JAEA-Review
2011-050

研究炉（JRR-3及びJRR-4）利用における研究成果集（平成１９年度）

Activity Report on the Utilization of Research Reactors (JRR-3 and JRR-4)
(Japanese Fiscal Year, 2007)

（編）研究炉利用課

(Ed.) Research Reactor Utilization Section

東海研究開発センター
原子力科学研究所
研究炉加速器管理部

Department of Research Reactor and Tandem Accelerator
Nuclear Science Research Institute
Tokai Research and Development Center

March 2012

Japan Atomic Energy Agency　日本原子力研究開発機構

JAEA-Review

本レポートは独立行政法人日本原子力研究開発機構が不定期に発行する成果報告書です。
本レポートの入手並びに著作権利用に関するお問い合わせは、下記あてにお問い合わせ下さい。
なお、本レポートの全文は日本原子力研究開発機構ホームページ（http://www.jaea.go.jp）
より発信されています。

独立行政法人日本原子力研究開発機構　研究技術情報部　研究技術情報課
〒319-1195　茨城県那珂郡東海村白方白根 2 番地 4
電話 029-282-6387, Fax 029-282-5920, E-mail:ird-support@jaea.go.jp

This report is issued irregularly by Japan Atomic Energy Agency
Inquiries about availability and/or copyright of this report should be addressed to
Intellectual Resources Section, Intellectual Resources Department,
Japan Atomic Energy Agency
2-4 Shirakata Shirane, Tokai-mura, Naka-gun, Ibaraki-ken 319-1195 Japan
Tel +81-29-282-6387, Fax +81-29-282-5920, E-mail:ird-support@jaea.go.jp

© Japan Atomic Energy Agency, 2012

JAEA-Review 2011-050

研究炉（JRR-3 及び JRR-4）利用における研究成果集（平成１９年度）

日本原子力研究開発機構 東海研究開発センター 原子力科学研究所
研究炉加速器管理部
（編）研究炉利用課

（2011 年 12 月 16 日受理）

平成 19 年度、非管理区域における汚染が発見されたことに伴う、再発防止のための安全確認調査で 7 月 12 日から 8 月 10 日まで原子炉を停止した。

JRR-3 は R3-19-4 サイクル(7 月 16 日～8 月 10 日)を安全確認調査で停止したが、R3-19-8 サイクル(12 月 3 日～12 月 26 日)を追加し、年間 7 サイクルの運転を行った。

JRR-4 は年間運転予定サイクルが 39 サイクルであったが、安全確認調査、反射体要素異常に伴う停止により年間 25 サイクルの運転を行った。

JRR-3 は、中性子散乱、即発ガンマ線分析、中性子ラジオグラフィなどの実験利用及び、放射化分析、原子炉燃料材料、ラジオアイソトープ製造、フィッショントラック年代測定の照射利用等、様々な目的に利用されている。

JRR-4 については、医療照射（Boron Neutron Capture Therapy：BNCT)、即発ガンマ線分析、放射線測定器の感度試験、原子炉研修運転実習等の実験利用、及び放射化分析、ラジオアイソトープ製造、フィッショントラック年代測定のための照射利用等、様々な目的に利用されている。

本報告書は、研究炉の利用者（原子力機構外を含む）から成果の提出を受け、中性子散乱 10 分野（構造、磁性、超伝導など)、中性子ラジオグラフィ、即発ガンマ線分析、放射化分析、その他、の分野別に研究成果を取りまとめたものである。

原子力科学研究所：〒319-1195　茨城県那珂郡東海村白方白根 2-4

JAEA-Review 2011-050

Activity Report on the Utilization of Research Reactors (JRR-3 and JRR-4) (Japanese Fiscal Year, 2007)

(Ed.) Research Reactor Utilization Section

Department of Research Reactor and Tandem Accelerator
Nuclear Science Research Institute
Tokai Research and Development Center
Japan Atomic Energy Agency
Tokai-mura, Naka-gun, Ibaraki-ken

(Received Decemder 16, 2011)

In the fiscal year 2007, the research reactor JRR-3 was operated for 7 cycles (cycle operation : 26days/cycle) and the JRR-4 was operated for 92 days.

JRR-3 is used for the purposes below;

- Experimental studies such as neutron scattering, prompt gamma-ray analyses, neutron radiography
- Irradiation for activation analyses, radioisotope (RI) productions, fission tracks
- Irradiation test of reactor materials

etc.

JRR-4 is used for the purposes below;

- Medical irradiation (Boron Neutron Capture Therapy : BNCT)
- Prompt gamma-ray analyses
- Sensitivity measurement of radiation detectors
- Experiment and practice in the nuclear reactor training
- Irradiation for activation analyses, RI productions, fission tracks

etc.

The volume contains 262activity reports, which are categorized into the fields of neutron scattering (10 subcategories), neutron radiography, neutron activation analyses, prompt gamma-ray analyses, and others submitted by the users in JAEA and other Organizations.

Keywords: JRR-3, JRR-4, Research Reactor, Neutron Scattering, Neutron Radiography, Neutron Activation Analysis, Neutron Beam, Irradiation

目　　次

はじめに 1
研究成果一覧 3
1. 中性子散乱 21
1) 構造・励磁 21
2) 磁　性 95
3) 強相関電子系 165
4) 非晶質･液体 211
5) 高分子 225
6) 生物 261
7) 基礎物理学･中性子光学 279
8) 装置 287
9) 超伝導現象 309
10) 残留応力 313
2. 中性子ラジオグラフィ 319
3. 即発ガンマ線分析 339
4. 放射化分析 347
5. その他 377
おわりに 398
謝 辞 399
付 録 401

Contents

Preface 1
Research Reports 3
1. Neutron Scattering 21
1) Structure・Excitation 21
2) Magnetism 95
3) Strongly Correlated Electron Systems 165
4) Amorphous・Liquid 211
5) Polymer 225
6) Biology 261
7) Fundamental Physics・Neutron Optics 279
8) Instrument 287
9) Superconductivity 309
10) Residual Stress 313
2. Neutron Radiography 319
3. Prompt Gamma-ray Analyses 339
4. Neutron Activation Analyses 347
5. Others 377
Conclusion 398
Acknowledgments 399
Appendixes 401

は じ め に

平成１９年度には、ＪＲＲ－３において７サイクルの共同利用運転、ＪＲＲ－４において２５サイクルの共同利用運転が行われ、これに伴いさまざまな利用が行われた。

本報告書は、利用者（原子力機構外利用者を含む）から当該利用の成果の提出を受け、取りまとめたものである。

提出して頂いた成果の件数は、中性子散乱２４０件、中性子ラジオグラフィ６件、即発ガンマ線分析５件、放射化分析７件、その他４件で合計２６２件であった。なお、本報告書の一部は、貴重な研究成果を公開する機会を広げるため、下記報告書の中から転載させて頂いたものである。

最後に、原稿を提出して頂いた利用者の皆様のご協力に感謝するとともに、今後も研究炉が有効に利用され、種々の研究がさらに進展されることを期待します。

研究炉利用課長
笹島　文雄

---

1)標　　題　：ACTIVITY REPORT ON NEUTRON SCATTERING RESEARCH issued by ISSP-NSL,University of Tokyo,Vol.15（東京大学物性研究所発行）
編　　者　：東京大学物性研究所
発 行 年　：２００８年

2)標　　題　：原子力機構施設利用共同研究成果報告書（平成１９年度）
編　　者　：東京大学大学院工学系研究科原子力専攻共同利用管理本部
発 行 年　：２００８年

This is a blank page.

研 究 成 果 一 覧

Research Reports

This is a blank page.

No.	「 Title 」	Page
	Neutron Scattering - Structure・Excitation -	
1-1-1	**Correlation between structural and thermoelectric properties in Zn13Sb10** G. Nakamoto, A. Tada, M. Kurisu, A. Tanaka, T. Tsutaoaka, Y. Andoh	23
1-1-2	**Dynamics of the water included in [H11O5][ZnCu(CN)4]** S. Nishikiori, Y. Minamimoto, O. Yamamuro	24
1-1-3	**Structural phase transition of one-dimensional semiconductor $C_5H_{10}NH_2PbI_3$** M. Takahashi, K. Kawasaki, K. Kataoka, Y. Fujii, M.Watanabe, K. Ohshima, Y. Noda	26
1-1-4	**Superspace Group Approach to the Crystal Structure of Chimney-Ladder Compound [Mn][Si]g** Y. Miyazaki, D. Igarashi, T. Kajitani	27
1-1-5	**Structure analysis of trehalose dihydrate by neutron diffraction** M. Takahashi, K. Kawasaki, K. Kataoka, M.Watanabe, K. Ohshima, Y. Noda	28
1-1-6	**QENS studies of Fast Molecular Reorientation in Liquid, Glass and Crystalline Phases of 8*OCB** H. Suzuki, A. Inaba, J. Krawczyk, M. Massalska-Arodz, T. Kikuchi, O. Yamamuro	29
1-1-7	**Crystal Structure of Tantalum Oxynitride TaON, a Visible Light Responsive Photocatalyst** M. Yashima, Y. Lee, K. Domen	31
1-1-8	**Diffusion Path of Oxide Ions in Apatite-type La9.25Si6.0O25.88** R. Ali, M. Yashima, Y. Matsushita, F. Izumi, S.Kikkawa, T. Wakita	33
1-1-9	**Structural investigation of the cubic perovskite-type doped lanthanum cobaltite La0.6Sr0.4CoO3-delta at 1258 degrees Celsius, - Possible diffusion path of oxygen ions in an electrode material** M. Yashima, T. Tsuji	35
1-1-10	**Low-Energy Phonon Anomaly of $CeOs_4Sb_{12}$** K. Iwasa, S. Itobe, C. Yang, Y. Murakami, M. Kohgi, H. Sugawara, H. Sato	37
1-1-11	**Observation of spin dynamics in Shastry- Shutherland lattice TbB4** K. Ohoyama, T. Matsumura, D. Okuyama, F. Iga, S. Michimura	38
1-1-12	**Crystal Structure of Chemically Modified Layered Cobaltates** Y. Miyazaki, D. Igarashi, T. Kajitani	39
1-1-13	**Structural disorder of cubic Ce0.5Zr0.5O2 solid solution** T. Wakita, M. Yashima, Y. Matsushita, T.Komatsu, Yong Phat, T. Ohta	40
1-1-14	**Magnetic structure in $CuFeP6_6$** M. Takahashi, E. Ahmed, K. Ohshima, Y. Noda	42
1-1-15	**Magnetic excitation in $CuFeP6_6$** M. Takahashi, E. Ahmed, K. Ohshima, N. Matsura	43
1-1-16	**Neutron scattering study of phonon dynamics on La3Pd20Ge6** C. H. Lee, H. Yoshizawa, I. Hase, Y. Nemoto, T. Goto	44
1-1-17	**Lattice dynamics of NaNbO3** I. Tomeno, Y. Tsunoda, M. Nishi, M. Matsuura, K. Oka	45
1-1-18	**Crystal Structure of Mg-doped apatite-type Ionic Conductor** Y. Matsushita, T. Wakita, H. Yoshioka, M. Yashima, F. Izumi	46
1-1-19	**Crystal structure and ionic conductivity of Ga system oxides for solid electrolyte of fuel cell** Y. Idemoto, T. Sugiyama, N. Kitamura	47
1-1-20	**Structural evaluation of nanotube and nanosheet layered titanate with novel nanostructures by neutron diffraction method** T. Kubo, M. Yashima, A. Nakahira	48

1−1−21	**Neutron Critical Diffuse Scattering of Quantum Relaxor KTaO3:Li** H. Yokota, Y. Uesu	50
1−1−22	**Dependence of crystal structure and ferroelectric property on composition and heat treatment for (Pb,Si)(Zr,Ti,Nb)O3 ferroelectric material** Y. Idemoto, S. Komiya	51
1−1−23	**Structural Defect and Ionic Conduction of Hydroxyapatite** H. Fujimori, K. Okanishi, K. Ohoyama, M. Yashima	52
1−1−24	**Neutron diffraction study on SnO2-CeO2 system** K. Nomura, H. Kageyama, T. Maekawa, C. Minagoshi, S. Nakamura , T. Ito	53
1−1−25	**Magnetic Phase Transition and Electric Polarization Flop of $TmMn_2O_5$** M. Fukunaga, K. Nishihata, H. Kimura, Y. Noda, K. Kohn	55
1−1−26	**Split-hydrogen sites in trioctahedral micas** K. Ishida, H. Fukazawa	56
1−1−27	**Powder Neutron Diffraction Measurements of One-dimensional Magnets $MPb_4Sb_6S_{14}$ (M = Fe, Mn)** Y. Matsushita, M. Nishi, S. Watanabe	57
1−1−28	**Crystal Structure of La-Ge-O Ionic Conductor** Y. Matsushita, N. Tsujii, K. Kobayashi, F. Izumi	59
1−1−29	**Low energy excitation in DyB_6** K. Tomiyasu, K. Takahashi	60
1−1−30	**High resorution inelastic neutron scattering by TiNi(Fe) alloy** T. Ohba, D. Kitanosono, T. Fukuda	61
1−1−31	**Crystal Structure Analysis of a Supramolecular Ferroelectric 55DMBP-H_2ia** R. Kumai, D. Okuyama, S. Horiuchi, T. Arima, M.Watanabe, Y.Noda, Y. Tokura	62
1−1−32	**Study suggests the existence of ferroelectric ice layer on a cold planet** H. Fukazawa, H. Yamauchi, A. Hoshikawa	64
1−1−33	**Structures and Phase Transitions in A2BO4-type Dielectrics** H. Shigematsu, K. Nomura	65
1−1−34	**Magnetic structure of Ni-Mn-Z(Z=In, Sn) shape memory alloys** T. Kanomata, K. Fukushima, Y. Yamaguchi	66
1−1−35	**Crystal Structure Determination of Ba2MgSiO7 by Neutron Diffraction** S. Seki, A. Komeno, K. Uematsu, K. Toda, M. Sato	67
1−1−36	**Diffuse Scattering Measurement on Protonic Conductor $K_3H(SeO_4)_2$** F. Shikanai, S. Itoh, K. Tomiyasu, N. Aso, S. Ikeda, T. Kamiyama	68
1−1−37	**Structural investigation of the cubic perovskite-type doped lanthanum cobaltite La0.4Ba0.6CoO3-x** T. Ohta, M. Yashima, T. Wakita, Y. Matsushita, T. Komatsu, Y. Phat	69
1−1−38	**Structural analysis of metavanadate phosphors AVO_3 (A: K, Rb and Cs)** T. Nakajima, M. Isobe, T. Tsuchiya, Y. Ueda, T. Kumagai	70
1−1−39	**Crystal structural change of potassium titanyl phosphate** T. Komatsu, M. Yashima, T. Wakita, Y. Phat, Y.Matsushita	71
1−1−40	**Li ion distributions of layered-structure type oxides LiNi1/2Mn1/2O2 prepared by ion-exchange** Y. Arachi, H. Maeda, H. Kobayashi, T. Asai	72
1−1−41	**High temperature neutron diffraction study of (La0.9Sr0.1)MnO3+d perovskite** K. Nomura, H. Kageyama, K. Kakinuma, T. Maekawa, S. Nakamura, H. Miyazaki H. Imabayashi, T. Ito	73
1−1−42	**Lithium Diffusion in LixFePO4** A.Yamada, S. Nishimura, G. Kobayashi, M. Yashima, K. Ohoyama, Y. Yamaguchi	74

1−1−43	**Soft modes in the relaxor ferroelectric compound $(Na_{0.5}Bi_{0.5})TiO_3$** M. Matsuura, H. Iida, K. Hirota, Y. Noguchi, M. Miyayama	75
1−1−44	**Anisotropic damping of transverse acoustic and optical modes in the relaxor ferroelectric 0.7 $Pb(Mg_{1/3}Nb_{2/3})O_3$-0.3 $PbTiO_3$** M. Matsuura, K. Hirota	76
1−1−45	**Behavior of Thermal Parameters through Phase Transition in KDP** H. Mashiyama, T. Miyoshi, T. Asahi, H. Kasano	77
1−1−46	**Crystal Structure Analysis of Ferroelectric Niobium Oxides** N. Kumada, Y. Yonesaki, T. Takei, N. Kinomura, M. Yashima	78
1−1−47	**Water Density Near Surface of DLC Films Having Various Surface Energies Measured by Neutron Reflectometry** T. Hirayama, T. Uno, T. Torii, T. Matsuoka, K. Inoue, T. Ebisawa, S. Tasaki, M. Hino N. Torikai	79
1−1−48	**Water Density Near Surface of DLC Films Having Various Surface Energies Measured by Neutron Reflectometry** T. Hirayama, T. Uno, T. Torii, T. Matsuoka, K. Inoue, T. Ebisawa, S. Tasaki, M. Hino N. Torikai	80
1−1−49	**Magnetic structure of Pr2-2xCa1+2xMn2O7(x=0.45)** Y. Tokunaga, D. Okuyama, T.J. Sato, T. Arima, Y. Tokura	81
1−1−50	**Neutron scattering in Ising-like one dimensional antiferromagnet $BaCo_2V_2O_8$** T. Masuda, S. Hondo, M. Matsuura	82
1−1−51	**Crystal structural analysis of rutile-type titania** Y. Phat, M. Yashima, T. Wakita, T. Komatsu	83
1−1−52	**Diffuse Scattering of PbF_2** Xianglian, K. Basar, S. Siagian, T. Sakuma, H. Takahashi, N. Igawa	84
1−1−53	**Structural Features of Lithium Ion Conductor $Li_{1+x}Ge_{2-x}Al_x(PO_4)_3$** Y. Fujita, H. Takahashi, T. Sakuma, N. Igawa	85
1−1−54	**Xe Motion in Clathrate Deuterohydrate Analyzed by Applying Rietveld/Maximum Entropy Method** N. Igawa, T. Taguchi, H. Fukazawa, H. Yamauchi, W. Utsumi, Y. Ishii	86
1−1−55	**Neutron Powder Diffraction and Difference MEM Analysis of Protium- and Deuterium-Dissolved $BaSn_{0.5}In_{0.5}O_{2.75+a}$** T. Nagasaki, S. Shiotani, M. Yoshino, K. Iwasaki, N. Igawa, H. Fukazawa, W. Utsumi	87
1−1−56	***In Situ* Powder Neutron Diffraction Experiment under High Pressure** W.Utsumi, K.Komatsu, H.Arima, H.Kagi, T.Okuchi, S.Sasaki, H.Yamauchi H.Fukazawa, N.Igawa, T.Kamiyama	88
1−1−57	**Pressure-Temperature Phase Diagram of Filled Skutterudite $PrFe_4P_{12}$** T. Osakabe, K. Kuwahara	89
1−1−58	**Cu Dimer Excitations in $Cu_2Fe_2Ge_4O_{13}$** T. Masuda, K. Kakurai	90
1−1−59	**Local Lattice Distortion in Giant Negative Thermal Expansion Material $Mn_3Cu_{1-x}Ge_xN$** S. Iikubo, K. Kodama, K. Takenaka, H. Takagi, S. Shamoto	91
1−1−60	**Existence of Ferroelectric Ice on Planets -a neutron study-** H. Fukazawa	92
1−1−61	**Nano-structure Analysis of ODS Ferritic Steels for Fast Reactor Application** S. Ohtsuka, J. Suzuki, T. Kaito, S. Kim, M. Inoue, S. Obara, T. Asayama	93

No.	「 Title 」	Page
	Neutron Scattering - Magnetism -	
1-2-1	**Neutron Inelastic Scattering of TbPd3S4** E. Matsuoka, K. Ohoyama, H. Onodera	97
1-2-2	**Spin Correlations of a Simple Cubic Antiferromagnet Pt_3Fe Alloy** R. Matsui, Y. Tsunoda	99
1-2-3	**Elastic Diffuse Scattering of Neutrons in Fe_3Pt Invar Alloys** M. Takasaka, Y. Tsunoda	100
1-2-4	**Magnetic structure of the n=3 frustrated square-lattice quantum spin system** (CuCl)Ca2Ta3O10 H. Kageyama, Y. Tsujimoto, A. Kitada, T.Watanabe, Y. Ajiro, K.Yoshimura M. Nishi, K. Hirota	101
1-2-5	**Neutron scattering study on (CuCl)LaTa2O7** H. Kageyama, A. Kitada, Y. Tsujimoto, Y. Ajiro, K. Yoshimura, M.Nishi N. Matsuura, K. Hirota	102
1-2-6	**Electric polarization induced by a proper helical magnetic ordering in a delafossite multiferroic $CuFe_{1-x}Al_xO_2$** T. Nakajima, S. Mitsuda, S. Kanetsuki, K. Tanaka, T. Fujii, N. Terada, M. Soda M. Matsuura, K. Hirota	103
1-2-7	**Electric field dependence of magnetic ordering of a delafossite multiferroic $CuFe_{1-x}Al_xO_2$** T. Nakajima, S. Mitsuda, H. Kimura, Y. Noda	104
1-2-8	**Effective random-field domain-state in a diluted frustrated magnet $CuFe_{1-x}Al_xO_2$** T. Nakajima, S. Mitsuda, H. Honma, H. Tsuchida	105
1-2-9	**Polarization analysis neutron scattering study of magnetic correlations in random magnet Fe65(Ni-Mn)35** K. Motoya, Y. Muro	106
1-2-10	**Magnetic excitations in the random-exchange Ising system (Fe-Zn)F2 near the percolation threshold** K. Motoya, Y. Muro, N. Aso, D. P. Belanger	107
1-2-11	**Inelastic Neutron Scattering Study on Triangular Lattice Antiferromagnet $CuFeO_2$** T. Nozaki, K. Hayashi, T. Kajitani	108
1-2-12	**Search for magnetic reflections in a heavy fermion antiferromagnet $CeTe_3$** N. Aso, K. Deguchi, G. F. Chen, N. K. Sato, H. Yoshizawa	109
1-2-13	**Magnetic structure of TbCoSn** M.Kurisu, A.Tada, G.Nakamoto, T.Tsutaoka, Y.Andoh	110
1-2-14	**Pressure induced incommensurate–commensurate magnetic phase transition in multiferroic $HoMn_2O_5$** H. Kimura, K. Nishihata, Y. Noda, N. Aso, T. Fujiwara, Y. Uwatoko	111
1-2-15	**Defect-induced short-range magnetic order in Co2(OD)3Cl** X.G. Zheng, M. Hagihala, T. Yamashita	112
1-2-16	**Inelastic neutron scattering on DyB4** T. Matsumura, D. Okuyama, T. Mouri	114
1-2-17	**Neutron diffraction in magnetic frustration systems with a 40T pulsed magnet** K. Ohoyama, K. Kurosawa, S. Yoshii, H. Nojiri, Y.H. Matsuda, H. Hiraka, S. Mitsuda	115
1-2-18	**Magnetic structure of an antiferro-octupolar ordering compound Tb0.94Gd0.06B2C2** E. Matsuoka, Y. Sasaki, D. Usui. K. Ohoyama, H. Onodera	116
1-2-19	**Magnetic structure of multipolar ordering compounds RPd3S4 (R = Ce, Pr)** E. Matsuoka, D. Usui, Y. Sasaki, K. Ohoyama, H. Onodera	118
1-2-20	**Study on low-temperature phase transitions in the $Ho_3Al_5O_{12}$** R. Morinaga, T. J. Sato, H. Kimura	120

1-2-21	**Magnetic and Crystallographic Study on R2CrS4 (R=Ho and Er)** K. Tezuka, Y. Yoshioka, S. Sato, S. Suzuki, K. Oshikane, Y. J. Shan, H. Imoto, K. Ohoyama	121
1-2-22	**Magnetic structure study of the multi-step metamagnet $CeIr_3Si_2$** Y. Muro, K. Motoya, K. Shigeto, T. Takabatake	122
1-2-23	**Magnetic phase diagram of the square lattice CuSb2-xTaxO6 with competing interactions J1 and J2** M. Nishi, M. Kato, K. Hirota, K. Ohyama	123
1-2-24	**Competing interactions in two dimensional square lattice CuSb2-xTaxO6** M. Nishi, M. Kato, K. Hirota, M. Matsuura	124
1-2-25	**Crystal Field Excitation of TmAg2In** T. Matsumura	125
1-2-26	**Magnetic Structure Analysis in Cr1-xMoxB2 (x = 0.15)** Y. Kousaka, E. Kaya, H. Kimura, Y. Noda, J. Akimitsu	126
1-2-27	**Chiral Helimagnetism in CuB2O4** Y. Kousaka, E. Kaya, M. Matsuura, K. Hirota, M. Nishi, J.Akimitsu	127
1-2-28	**Energy Range of Magnetic Excitations in Percolating Two-Dimensional Heisenberg Antiferromagnet, Rb2Mn0.598Mg0.402F4** S. Itoh, T. J. Sato	128
1-2-29	**Antiferromagnetic ordering of Ca3Ru2O7** Y. Yoshida, K. Iwata, N. Aso, S. Katano	129
1-2-30	**Relationship between Magnetic Structure and Ferroelectricity of LiVCuO4** Y. Yasui, Y. Naito, K. Sato, T. Moyoshi, M. Sato, K. Kakurai	130
1-2-31	**Magnetic Excitation Spectra of Honeycomb System Na3T2SbO6 (T=Cu, Ni, Co)** Y. Miura, Y. Yasui, T. Moyoshi, M. Sato, K. Kakurai	132
1-2-32	**Neutron diffraction studies on a Pr7Ni3 single crystal** T. Tsutaoka, A. Tanaka, Y. Andoh, A. Tada, G. Nakamoto, M. Kurisu	133
1-2-33	**Neutron Diffraction Studies on Y7Rh3Dx** T. Tsutaoka, A. Tanaka, A. Tada, G. Nakamoto, M. Kurisu, Y. Andoh	134
1-2-34	**Magnetic excitation spectrum in the frustrated triangular lattice antiferromagnet CuFe1-xAlxO2** S. Mitsuda, T. Nakajima, S. Iwamoto, N. Terada	135
1-2-35	**Magnetic Structure of Noncentrosymmetric heavy-Fermion $Ce_4Ni_3Pb_4$** T. Onimaru, K. Shigetoh, A. Ishida, T. Takabatake	136
1-2-36	**Crystal and magnetic structures of 12L-perovskites Ba4LnRu3O12 (Ln = Pr and Tb)** Y. Shimoda, Y. Doi, Y. Hinatsu	137
1-2-37	**Magnetic excitations in MCr_2O_4 (M=Fe, Ni)** K. Tomiyasu, H. Hiraka, K. Ohoyama, K. Yamada	138
1-2-38	**Spin Waves in MnP** S. Yano, Y. Kousaka, M. Nishi, M. Matsuura, K. Hirota, J. Akimitsu	139
1-2-39	**Magnetic structures and transitions of HoRh2Si2** T. Shigeoka, H. Shibasaki, T. Fujiwara, M. Nishi	140
1-2-40	**Neutron scattering study on the molecular magnet Mn6Sb2** K. Iida, T. J. Sato	141
1-2-41	**Neutron scattering in $Ba_2MnGe_2O_7$** T. Masuda, S. Kitaoka, M. Nishi	142

1−2−42	**Neutron scattering in O_2 adsorbed CPL-1** T. Masuda, K. Hirota	144
1−2−43	**Powder diffraction study on the ternary compound $Ce_5Ni_2Si_3$** T. J. Sato, K. Iida, H. Kitazawa, Y. S. Kwon	145
1−2−44	**Studies of a quadrupolar ordering and magnetic excitations in YbAs** A. Oyamada, K. Kuwahara, K. Iwasa, K. Ohoyama, M. Kohgi	146
1−2−45	**Magnetic property of Ag-In-Tb 1/1 approximant and its relation to Zn-Mg-RE quasicrystals** S. Ibuka, K. Iida, T. J. Sato	147
1−2−46	**Crystal Structure and Magnetic Properties of $CoZn(TeO_3)Br_2$** T. Kashi, Y. Yasui, T. Moyoshi, M. Sato, K. Kakurai, S. Iikubo, N. Igawa	148
1−2−47	**Linear Relation between Electric Polarization and Magnetic Chirality in the Commensurate Phase of RMn_2O_5 (R =Ho, Er)** S. Wakimoto, H. Kimura, M. Fukunaga, K. Nishihata, M. Takeda, K. Kakurai, Y. Noda Y. Tokura	149
1−2−48	**Polarization of the Spin-Wave Modes in the Kagome′Lattice Antiferromagnet $KFe_3(OH)_6(SO_4)_2$** K. Matan, J. S. Helton, D. Grohol, D. G. Nocera, S. Wakimoto, K. Kakurai, Y. S. Lee	151
1−2−49	**Investigation of in-plane Magnetic Structure in $NpFeGa_5$** T. Sugai, F. Mizuno, K. Kaneko, N. Metoki	153
1−2−50	**Unusual field-induced Antiferromagnetic Order in $NpIn_3$** F. Mizuno, T. Sugai, N. Metoki, K. Kaneko	154
1−2−51	**Magnetic Structure of $LiCu_2O_2$** Y. Yasui, K. Sato, T. Moyoshi, M. Sato, K. Kakurai	155
1−2−52	**Investigation of the Giant Magnetic Moments in Nitrogen-Martensites thin Films Using the Polarized Neutron Diffraction Technique** M. Takeda, K. Kakurai, K. Sunaga, M. Tsunoda, M. Takahashi	156
1−2−53	**Partial Disordered Phase of $RbCoBr_3$** Y. Nishiwaki, A. Oosawa, K. Kakurai, T. Kato	157
1−2−54	**Neutron Diffraction Study on Spinel $GeCo_2O_4$ under Magnetic Field** M. Matsuda, T. Hoshi, H. A. Katori, M. Kosaka, H. Takagi	158
1−2−55	**Magnetic Excitation in the Spin-1/2 Antiferromagnetic Alternating Chain Compound β-$AgCuPO_4$** M. Hase, M. Matsuda, K. Kakurai, K. Ozawa, H. Kitazawa, N. Tsujii, A. Dönni, H. Kuore	159
1−2−56	**Multi-step Magnetic Transition in Non-centrosymmetric Compound $CeCoGe_3$** K. Kaneko, N. Metoki, T. D. Matsuda, A.Thamizhavel, T. Takeuchi Y. Haga, R. Settai, Y. Onuki	160
1−2−57	**Pressure-Induced Magnetic Quantum Phase Transition in Coupled Spin Dimer System $KCuCl_3$** T. Ono, J. Kawakami, H. Tanaka, T. Osakabe, K. Kakurai	161
1−2−58	**Magnetic Structural Analysis of Magnetic Multilayers by Complementary Use of X-ray and Neutrons** M. Takeda, D. Yamazaki, K. Soyama, R. Maruyama, M. Hino, T. Hirano	162
1−2−59	**Small-Angle Neutron Scattering Measurements of Averaged Internal Structures in Nd-Fe-^{11}B Sintered Magnets** M. Takeda, J. Suzuki, D. Yamaguchi, T. Akiya, H. Kato, M. Sagawa, K. Koyama	163

No.	「 Title 」	Page
	Neutron Scattering - Strongly Correlated Electron Systems-	
1-3-1	**Magnetic excitations in halogen-bridged nickel complex** S. Itoh, K. Nakajima	167
1-3-2	**Charge and magnetic order in 2d cobaltate Pr2-xCaxCoO4** H. Yoshizawa, K. Masuda	168
1-3-3	**Variation of magnetic modulation for the antiferromagnetic states in $CeRh_{1-x}Co_xIn_5$(x = 0, 0.5 and ~ 0.7)** N. Oyama, M. Yokoyama, S. Oinuma, I. Kawasaki, H. Amitsuka, K. Tenya T. J. Sato, M. Matsuura, K. Hirota	169
1-3-4	**Evolution of Ferromagnetic and antiferromagnetic orders in Mn-doped $CaRuO_3$** M. Yokoyama, H. Hagiya, N. Oyama, Y. Nishihara, H. Kawanaka	170
1-3-5	**Modulated-structure analysis of the high-valence aperiodic chain compounds, Sr2k(Co1-xNix)O3 (k~0.635, 0<=x<=1)** M. Isobe, H. Kitazawa, K. Ohoyama	171
1-3-6	**Magnetic phase diagram under low temperature and high pressure in RVO3** D. Bizen, H. Nakao, K. Iwasa, Y. Murakami, T. Osakabe, S. Miyasaka, Y. Tokura	173
1-3-7	**Study on thermoelectric properties and misfit-structures in Y doped Ca3Co4O9** H.Nakatsugawa, H.M.Jeong, K.Nagasawa	174
1-3-8	**Magnetic excitation in a non-centrosymmetric pressure-induced superconductor $CeRhSi_3$** N. Aso, H. Miyano, H. Yoshizawa, N. Kimura, T. Komatsubara, H. Aoki	175
1-3-9	**Neutron diffraction under pressure in $CeRhIn_5$** N. Aso, K. Ishii, H. Yoshizawa, T. Fujiwara, Y. Uwatoko, G. F. Chen, N. K. Sato	176
1-3-10	**Two-dimensional magnetic excitations in $CeRhIn_5$** N. Aso, H. Miyano, H. Yoshizawa, G. F. Chen, N. K. Sato	177
1-3-11	**Search for magnetic excitation in a heavy fermion superconductor $CeCoIn_5$** N. Aso, H. Miyano, H. Yoshizawa, T. Fujiwara, G. F. Chen, N. K. Sato	178
1-3-12	**Correlation between ferromagnetism and superconductivity in UGe_2** N. Aso, S. Ban, K. Deguchi, T. Fujiwara, Y. Uwatoko, N. K. Sato	179
1-3-13	**Observation of magnetic form factor using detwinned single crystal of La_2CuO_4** H. Kimura, T. Adachi, Y. Noda, M. Fujita, K. Yamada	180
1-3-14	**Relation between low-energy phonons and a charge stripe order in $La_{2-x}Sr_xCu_{1-y}Fe_yO_4$** H. Kimura, Y. Ishikawa, Y. Noda, K. Enoki, M. Fujita, K. Yamada	181
1-3-15	**Search for magnetic scattering in Fe and Pb co-doped Bi2201** H. Hiraka, K. Yamada	182
1-3-16	**Magnetic Correlation in the Kondo-Semiconductor-like Material $CeOs_4Sb_{12}$** K. Iwasa, S. Itobe, M. Kohgi, C. Yang, K. Kuwahara, H. Sugawara, H. Sato, N. Aso	183
1-3-17	**Visualization of rattling in filled skutterudite compounds** K. Kaneko, N. Metoki, H. Kimura, Y. Noda, T. D. Matsuda, M. Kohgi	184
1-3-18	**Magnetic Excitation of Ferromagnetic System $NdFe_4P_{12}$ Exhibiting Heavy Electron Behavior** K. Iwasa, L. Hao, K. Saito, H. Sugawara, H. Sato	185
1-3-19	**Crystal-field excitation in $Pr(Ru_{1-x}Rh_x)_4P_{12}$** K. Iwasa, K. Saito, L. Hao, Y. Murakami	186
1-3-20	**Spin-lattice dynamics in rare earth antiferroquadrupolar ordering conpound HoB2C2** K. Ohoyama , H. Onodera, E. Matsuoka	187

1-3-21	**Coexistence of superconductivity and magnetism in a multi-layered cuprate** C. H. Lee, A. Iyo, K. Kihou, H. Kito, K. Yamada	188
1-3-22	**Flux line lattice in $ErNi_2B_2C$** H. K. Furukawa, R. Nagatomo, S. Konno, S. O. Kawamura, H. Yoshizawa, H. Takeya	189
1-3-23	**Magnetic and electronic nature of metallic ferromagnet Sn2Co3S2 and its related compounds** M. Matoba, A. Umetani, E. Nagoshi, S. Nakajima, T. Kubodera	190
1-3-24	**Charge and spin ordering in La1.85Ca0.15CoO4.17** K. Horigane, H. Haruhiro, K. Yamada, J. Akimitsu	192
1-3-25	**Lattice effects on the charge-spin ordering in layered cobaltates R1.5Sr0.5CoO4** K. Horigane, H. Haruhiro, K. Yamada, J. Akimitsu	193
1-3-26	**Cycloidal Spin Order in (Gd,Tb)MnO3 with Electric Polarization along the a-Axis** H. Sagayama, N. Abe, K. Taniguchi, T. Arima, Y. Noda, M. Soda, M. Matsuura K. Hirota, Y. Yamasaki, D. Okuyama, Y. Tokura	194
1-3-27	**Correlation between Electric Polarization and Sence of Helix in $MnWO_4$** H. Sagayama, N. Abe, K. Taniguchi, T. Arima, M. Soda, M. Matsuura, K. Hirota	195
1-3-28	**Magnetic excitations of NaxCoO2.yD2O** T. Moyoshi, Y. Yasui, M. Sato, K. Kakurai	196
1-3-29	**Magnetic structure of a pressure-induced magnetically ordered phase in YbAgGe with a quasi-kagome lattice** K. Umeo, H. Kubo, T. Onimaru, K. Katoh, T. Matsumura, N. Aso, T. Takabatake	197
1-3-30	**Spin excitations in $MgCr_2O_4$** K. Tomiyasu, H. Suzuki, M. Toki, S. Itoh, N. Aso, M. Matsuura, K. Yamada	198
1-3-31	**Magnetism and superconductivity in *RE* Ni_2B_2C** S. O. Kawamura, R. Nagatomo, S. Konno, H. K. Furukawa, H. Yoshizawa	199
1-3-32	**Electronic state in novel superconductor $CeCoIn_5$ studied by observation of the vortex state** H. K. Furukawa, S. O.Kawamura, S. Konno, R. Nagatomo, H. Shishido, T. Shibauchi Y. Matsuda	200
1-3-33	**Investigation of the magnetic excitations in high-*TC*** M. Matsuura, Y. Yoshida, H. Eisaki, N. Kaneko, K. Hirota	201
1-3-34	**Magnetic Structure in the Shastry-Sutherland Lattice Tb1-xYxB4** F. Iga, S. Michimura, K. Murakami, T. Takabatake, K. Suga, K. Kindo, K.Ohoyama	202
1-3-35	**1st order transition in $ErNi_2B_2C$** H. K. Furukawa, Y. Ishida , S. O. Kawamura, H. Yoshizawa, H. Takeya	203
1-3-36	**Study of spin fluctuations in $La_{1.94-x}Sr_xCe0.06CuO_4$** M. Fujita, M. Enoki, K. Yamada	204
1-3-37	**Search for transition of paring symmetry in electron-doped superconductor $Pr_{1-x}LaCe_xCeO_4$** M. Fujita, M. Nakagawa, K. Yamada	205
1-3-38	**Zn-doping effect on spin fluctuations in electron-doped $Pr_{1-x}LaCe_xCuO_4$** M. Fujita, M. Nakagawa, K. Yamada	206
1-3-39	**Order Parameter of Phase IV in (Ce,La)B6** K. Kuwahara, K. Iwasa, M. Kohgi, N. Aso, M. Sera, F. Iga, M. Matsuura, K. Hirota	207
1-3-40	**Neutron scattering study on PrFe4P12 under high pressure** K. Kuwahara, T. Osakabe, K. Iwasa, M. Kohgi, D. Kikuchi, Y. Aoki, H. Sato, H.Sugawara	208
1-3-41	**Rattling motion in PrOs4Sb12** K. Kuwahara, O. Yamamuro, K. Iwasa, M. Kohgi, D. Kikuchi, Y. Aoki, H. Sato, H.Sugawara	209

No.	「 Title 」	Page
	Neutron Scattering -Amorphous・Liquid-	
1-4-1	**Direct observation of supercooled water in hardened Low Heat Portland Cement** K. Mori, Y. Inamura, O. Yamamuro, T. Fukunaga	213
1-4-2	**Neutron Diffraction Study on the Intermolecular Structure in Highly Concentrated Aqueous Urea Solutions** Y. Kameda, A. Maki, H. Takahashi, Y. Amo, T. Usuki	214
1-4-3	**SANS Study on Mixing State of Ionic Liquid-Molecular Liquid Binary Solutions** T. Takamuku, Y. Honda, K. Fujii	216
1-4-4	**Amide-Induced Phase Separation of HFIP-Water Mixtures** T. Takamuku, H. Wada, K. Fujii	218
1-4-5	**Alkyl-chain Dependence on Micro-phase Separation of Room Temperature Ionic Liquids** K. Fujii, Y. Umebayashi, S. Ishiguro, T.Takamuku	220
1-4-6	**Structural Change of Supercritical Carbon Dioxide with Entrainer Molecule** T. Sato, M. Sugiyama, M. Misawa, K. Hamada, K. Itoh, K. Mori, T.Fukunaga	221
1-4-7	**Static and Dynamic Structure of Meso-scale fluctuations in liquid chalcogens near the metal-nonmetal transition** Y.Ohmasa, T.Hoshino R.Osada, M.Yao	222
1-4-8	**Small Angle Neutron Scattering Investigation of Aggregation of N,N-dialkylamide and Its Effect on Nitric Acid Extraction** S. Suzuki, T. Yaita, R. Motokawa, S. Koizumi	223

No.	「 Title 」	Page
	Neutron Scattering - Polymer -	
1-5-1	**Dynamical Study on Nanocomposite Hydrogel by Means of Neutron Spin Echo Technique** H. Endo, S. Miyazaki, M. Shibayama	227
1-5-2	**Hysteresis of bicelle/ULV transition in long- and short-chain lipid mixture** N. L. Yamada, N. Torikai	228
1-5-3	**Changes in flow-induced aggregated structures of shear-thickenning silica suspensions** M. Ando, H. Mizukawa, Y. Takahashi, M. Kawaguchi	229
1-5-4	**Simultaneous Evaluation of Lipid Exchange and Flip-Flop in Vesicles** Nakano, M. Fukuda, T. Kudo, H. Endo	231
1-5-5	**Structure Analyses of Nanoemulsion/polymer Mixtures Having Dilatancy Behavior** M. Shibayama, Y. Kawada, T. Kume, H. Endo, N. Osaka. N, T. Matsunaga	232
1-5-6	**Ionic Strength Dependence of Chain Conformation of Hydrophilic Polymers at Water Interface** M. Kobayashi, Y. Terayama, N. Hosaka, A. Takahara	233
1-5-7	**Surface and Interface Structure Analysis of (Multi-functionalized Silsesquioxane/Deuterated Polystyrene) Hybrid Thin Films** N. Hosaka, Y. Terayama, M. Kobayashi, A. Takahara	234
1-5-8	**Thermal fluctuation of a lipid bilayer in the anomalous swelling regime** M. Hishida, H. Seto, N. L. Yamada	235
1-5-9	**Melting and Re-crystallization Process of Shish-kebab Structure** G. Matsuba, Y. Hayashi, C. Ito, K. Nishida, T. Kanaya	236
1-5-10	**Gelation Mechanism of Clay-Polymer Nanocomposite Hydrogel using Contrast Variation SANS** M. Shibayama, S. Miyazaki , H. Endo , T. Karino , K. Haraguchi	237
1-5-11	**Structural Formation Process under Drawing** K. Nishida, T. Kanaya, G. Matsuba, Y. Hayashi, C. Ito	238
1-5-12	**Distribution of glass transition temperature in polymer thin films by neutron reflectivity** R. Inoue , H. Ogawa, T. Kanaya, K. Nishida , M. Hino	239
1-5-13	**A long-range periodic structure in a mixture of D_2O/3-methylpyridine/$NaBPh_4$ induced by solvation effect** K. Sadakane, N. Iguchi. H. Seto	241
1-5-14	**Effect of polymer on uni-lamellar vesicle in lipid mixture system** N. L. Yamada, N. Torikai	242
1-5-15	**Studies on Structural Nonuniformity of Natural Rubber** M. Shibayama , T. Suzuki, N. Oosaka, H. Endo, N. Higashitani, Y. Morita, Y. Kokubo Y. Ikeda, S. Kohjiya	243
1-5-16	**Temperature Effects on Shear-Induced Structural Transition in the Lamellar Phase of a Nonionic Surfactant -Change in the Orientation of Lamellae-** Y. Kosaka, M. Ito, Y. Kawabata, T. Kato	244
1-5-17	**Correlation between local dynamics and gas permeability of substituted polyacetylenes by quasielastic neutron scattering** T. Masuda, T. Kanaya, R. Inoue, O. Yamamuro	245
1-5-18	**Crowding effect on the shear induced structural transition of lamellar phase** S. Fujii, Y. Kawabata	246
1-5-19	**Nanostructure of Non-Surface Acitive Ionic Amphiphilic Diblock Copolymers in Aqueous Solutions** H. Matsuoka, H. Chen, F. Ozaki, T. Yamada	247
1-5-20	**2D-SANS Pattern Observed for Injection Molded Isotactic Polypropylene** T. Sakurai, Y. Nozue, S. Kimata, T. Kasahara, N.Yamaguchi, H. Endo, M. Shibayama	249

1-5-21	**Dynamical Properties of Syndiotactic Polystyrene (sPS) Crystalline Complex Phase** F. Kaneko, T. Kawaguchi, K. Ute	250
1-5-22	**Electrostatic Self-Assembly of Neutral and Polyelectrolyte Block Copolymer and Oppositely Charged Surfactant** M. Annaka, T. Matsuda, K. Morishita	251
1-5-23	**Effects of Molecular Weight and Surface Density on Conformation of Poly(N-isopropylacrylamide) Brushes Immobilized Onto A Substrate** M. Annaka, Y. Fujii, H. Atarashi, K. Tanaka, T. Nagamura, M. Hino	252
1-5-24	**Analysis of Adsorption Behavior for Proteins onto (Liquid/Polymer) Interface** Y. Fujii, H. Atarashi, K. Tanaka, T. Nagamura, M. Hino	254
1-5-25	**Lamellar to Micelle Transition of Nonionic Surfactant Assemblies Induced by Addition of Colloidal Particles** Y. Suganuma, N. Urakami, R. Mawatari, S. Komura, K. N. Yaegashi, M. Imai	256
1-5-26	**Nano-meter-sized domain formation in lipid membranes observed by small angle neutron scattering** Y. Sakuma, M. Imai, T. Masui, N. Urakami	257
1-5-27	**Sol-Gel Transition of Hydrophobically Modified Polyrotaxane** T. Karino, Y. Okumura, C. Zhao, M. Kidowaki, T. Kataoka, K. Ito, M. Shibayama	258
1-5-28	**Structural Study on Uniaxial Extension of Nanocomposite Hydrogel with High Clay Concentration by Means of Contrast Variation Neutron Scattering** T.Nishida, H. Endo, N. Osaka, K. Haraguchi, M. Shibayama	259

No.	「 Title 」	Page
	Neutron Scattering - Biology -	
1-6-1	**Control of Membrane Lipid dynamics by Transmembrane and Amphipathic Peptides** M. Nakano, M. Fukuda, T. Kudo, H. Endo	263
1-6-2	**Dynamics of folded and partial unfolded proteins observed by solution inelastic neutron scattering** H. Nakagawa, Y. Joti, O. Yamamuro, I. Tsukushi, M. Kataoka	265
1-6-3	**Hydration water dynamics at protein dynamical transition by quasi-elastic neutron scattering** H.Nakagawa, Y.Joti, O.Yamamuro, M.Kataoka	266
1-6-4	**Strctural torlance of complex of αA-crystallin and αB-crystallin** M. Sugiyama, N. Fuji, Y. Morimoto, T. Sato	267
1-6-5	**Measurements of slow dynamics of actin** S. Fujiwara, F. Matsumoto, H. Nakagawa, N. Takahashi, T. Oda	268
1-6-6	**Structure and dynamics of β-lactoglobulin aggregates by small-angle neutron scattering and neutron spin echo methods** K. Yoshida, T. Yamaguchi, H. Endo, M. Shibayama	269
1-6-7	**Neutron Diffraction Study of HIV-1 Protease in Complex with Inhibitor KNI-272** M. Adachi, T. Ohhara, K. Kurihara, T. Tamada, E. Honjo, N. Okazaki, S. Arai, Y. Shoyama H. Matsumura, H. Adachi, K. Takano, Y. Mori, K. Hidaka, T. Kimura, Y. Hayashi, Y. Kiso R. Kuroki	270
1-6-8	**Neutron Diffraction Study of ADP-ribose pyrophosphatase** M. Adachi, K. Kurihara, T. Tamada, T. Ooga, S. Kuramitsu, R. Kuroki	271
1-6-9	**Trial Diffraction Measurements of Protein Single Crystals in H_2O** S. Fujiwara, K. Kurihara, T. Chatake	272
1-6-10	**The State of Cryptobiosis of Larvae of Polypedilum Vandezplanki Studied by Incoherent Inelastic Neutron Scattering** H. Nakagawa, T. Okuda, M. Kataoka	273
1-6-11	**Dynamical Transition of DNA Studied by Neutron Inelastic Scattering** H. Nakagawa, H. Kono	274
1-6-12	**Glass Transition of Larvae of Polypedilum Vandezplanki Studied by Incoherent Inelastic Neutron Scattering** H. Nakagawa, T. Okuda, M. Kataoka	275
1-6-13	**Contrast Variation Measurements of Hen Egg White Lysozyme Amyloid Fibrils** S. Fujiwara, F. Matsumoto, H. Nakagawa	276
1-6-14	**Small-Angle Neutron Scattering Measurements of Rhodanase-GroEL-GroES Complex** K. Ichimura, Y. Matsuura, S. Fujiwara, Y. Kawata, H. Kihara	277
1-6-15	**Small-Angle Neutron Scattering Measurements of *α*-Synuclein and its Disease-Related Mutants** S. Naito, H. Mochizuki, T. Yasuda, J. Yamaguchi, Y. Mizuno, M. Furusaka, S. Ikeda M. H. Shimizu, S. Fujiwara	278

No.	「 Title 」	Page
	Neutron Scattering - Fundamental Physics・Neutron Optics -	
1−7−1	**Development of phase correction devices for high resolution NRSE spectrometer** M. Kitaguchi, M. Hino, Y. Kawabata, H. Hayashida, S. Tasaki	281
1−7−2	**Development of Jamin Type Cold Neutron Interferometer with Completely Separated Two Paths** Y. Seki, K. Taketani, H. Funahashi, M. Kitaguchi, M. Hino, Y. Otake, H.M. Shimizu	282
1−7−3	**Development of beam splitting etalons for pulsed neutrons II** M. Kitaguchi, Y. Seki, K. Taketani, H. Funahashi, M. Hino, H. M. Shimizu	283
1−7−4	**Possible improvement of thin magnetic film using Pd** S. Tasaki, S. Kuramoto, Y. Abe, M. Hino	284
1−7−5	**Development of neutron optics with a curved supermirror** K. Ikeda, H. Sato, K. Hirota, K. Mishima	285

No.	「 Title 」	Page
	Neutron Scattering - Instrument -	
1−8−1	**Thermal diffuse scattering effect on neutron holography** K. Hayashi, K. Ohyama, S. Orimo, Y. Nakamori, H. Takahashi, K. Shibata	289
1−8−2	**Development of A New Spin-Phase Contrast Imaging of Neutron** S. Tasaki, M. Kageyama, M. Hino, Y. Kawabata	290
1−8−3	**Development of transmittion geometry supermirror polarizer** M.Hino, M.Kitaguchi, H.Hayashida, Y.Kawabata, S. Tasaki	291
1−8−4	**Observation of superparamagnetic fluctuations in magnetic ferrofluid using MIEZE spectroscopy** M.Hino, H.Hayashida, M.Kitaguchi, N.Achiwa, Y. Kawabata	292
1−8−5	**Installation of a prototype of focusing-type small-angle neutron scattering instrument with an ellipsoidal supermirror** M. Furusaka, T. Satoh, Y. Sasaki, Y. Kawamura, T. Asami, Y. Otake, K. Ikeda P. Mikula, Y. Kiyanagi, S. Naito, H. Yoshizawa	293
1−8−6	**Development of 10 GPa class cubic anvil type high pressure apparatus for neutron scattering experiments** T. Fujiwara, K. Matsubayashi, Y. Uwatoko, N. Aso, M. Nishi, H. Yoshizawa	295
1−8−7	**Development of Large 2D-PSD under collaboration with HANARO** Y. Noda, M.Watanabe, H. Kimura, Y. Dohi, Y. Ishikawa, T. Yamazaki, M. Moon C. H. Lee	296
1−8−8	**Neutron imaging measurement using newly developed inorganic gadolinium scintillator** J. H. Kaneko, S. Satoh, J. Haruna, S. Saeki, S. Kawamura, Y. Ohtake, M. Furusaka Y. Kiyanagi	297
1−8−9	**Performance Test of Neutron Detector for Engineering Diffractometer in J-PARC** K. Sakasai, T. Nakamura, S. Harjo, A. Moriai, M. Katagiri, K. Soyama, S. Satoh E. Shooneveld, N. Rhodes	298
1−8−10	**Development of ^{3}He PSDs and Related Electronics for New Spectrometers in J-PARC** K. Nakajima, T. Yokoo, S. Satoh, K. Shibata, N. Takahashi, R. Kajimoto, T. Nakatani Y. Inamura, N. Kaneko, Y. Yasu, K. Nakayoshi, E. Inoue, H. Sendai, M. Arai	299
1−8−11	**Development of Asymmetric Reflection-type Germanium Monochromator for Beam Flux Enhancement on HRPD** H. Yamauchi, Y. Ishii, N. Igawa, H. Fukazawa, W. Utsumi	300
1−8−12	**Development of High Quality Neutron Mirrors with Upgrading Compact Cold Neutron Bender System II** I. Tamura, R. Maruyama, D. Yamazaki, K. Yamamoto, K. Nakamura, K. Soyama	301
1−8−13	**Development of High Reflectivity Neutron Supermirror Using Ion Beam Sputtering Technique** R. Maruyama, D. Yamazaki, T. Ebisawa, K. Soyama	302
1−8−14	**Neutron Reflectometer SUIREN: Status and Developments in 2007** D. Yamazaki, M. Takeda, R. Maruyama, M. Hino, K. Soyama	303
1−8−15	**Upgrading Compact Cold Neutron Bender System II** I. Tamura, R. Maruyama, D. Yamazaki, K. Yamamoto, K. Nakamura, K. Aizawa, K. Soyama	304
1−8−16	**Neutron Detection by a MgB2 Transition Edge sensor** S. Okayasu, M. Katagiri, K. Houjo, Y. Morii, S. Miki, H. Shimakage, Z. Wang, T. Ishida	305
1−8−17	**Application of a Magnetic Neutron Polarizing and Focusing Device to a Focusing-Geometry Small-Angle Polarized Neutron Scattering Instrument** T. Oku, T. Shinohara, T. Kikuchi, Y. Oba, H. Iwase, S. Koizumi, J. Suzuki	306

No.	「 Title 」	Page
	Neutron Scattering - Superconductivity -	
1-9-1	**Emergence of Magnetic Modulations in the Overdoped Phase of Bi2201 by by Fe Doping** H. Hiraka, S. Wakimoto, M. Takeda, K. Kakurai, K. Yamada	311
1-9-2	**Peculiar Field Response of Antiferromagnetism in non-centrosymmetric heavy fermion superconductor $CePt_3Si$** K. Kaneko, N. Metoki, T. Takeuchi, T.D. Matsuda, Y. Haga, R. Settai, Y. Onuki	312

No.	「 Title 」	Page
	Neutron Scattering - Residual Stress -	
1-10-1	**Strain Evaluation of Rebar in Reinforced Concrete Using Neutron Diffraction** M. Kanematsu, T. Noguchi, M. Yasuda, H. Suzuki	315
1-10-2	**Residual Stress and Deformation Behavior on $Zr_{55}Al_{10}Ni_5Cu_{30}$ Bulk Metallic Glass Containing ZrC Particles** H. Suzuki, J. Saida, M. Imafuku	316
1-10-3	**Bulky Measurement of Gradient Texture of an IF Steel by Neutron Diffraction** P.G. Xu, Y. Tomota, H. Suzuki, S. Machiya	317
1-10-4	**Engineering diffractometer "RESA" and "RESA-II"** H. Suzuki, T. Saito, S. Machiya, Y. Tsuchiya, A. Moriai, Y. Shimojo, K. Akita, Y. Morii	318

No.	「 Title 」	Page
	Neutron Radiography	
2−1	**Fundamental Experiments for the Development of an Advanced Neutron Tomography** M. Kureta	321
2−2	**Development of an Ultra-High-Speed Scanning Neutron Tomography System for High-Quality and Four-Dimensional Visualizations** M. Kureta, H. Iikura	322
2−3	**Development of Measurements for Multiphase Flow Dynamics -II by Using Neutron Beam of JRR-3M** K. Mishima	323
2−4	**Defense Responses of Trees and Dynamics of Water Distribution** T. Yamada, N. Nagaishi, K. Tanoi, T.M. Nakanishi	326
2−5	**Development of Imaging System for Neutron Image Intensifier** K. Mochiki, Y. Wada, M. Okazaki	331
2−6	**Analysis of water distribution in plant tissue.** T. Nakanishi	335

No.	「 Title 」	Page
	Prompt Gamma-ray Analyses	
3−1	**Development of a Method of Measuring the Cadmium Concentration in Agricultural Produce with Prompt γ-ray Analysis** Y. Sakurai, H. Matsue, S. Miyamoto, N. Kihou	341
3−2	**Measurements of Hydrogen-Containing Samples Using MPGA** Y. Toh, M. Oshima, M. Koizumi, K. Furutaka, A. Kimura, Y. Murakami	342
3−3	**Determination of Boron in Ceramic Reference Materials by Prompt Gamma-ray Analysis Using Focused Neutron Guided Beam of JRR-3M** T. Miura, H. Matsue, T. Kuroiwa, K. Chiba	343
3−4	**Non-Destructive Analysis of Ancient Egyptian Vitreous Relics by Neutron** S. Yoshida	344
3−5	**Development of Temperature Variable Neutron In-beam Mossbauer Spectrometer** M. K. Kubo, Y. Kobayashi, Y. Yamada, Y. Watanabe, T. Takayama, Y. Sakai H. Shoji, W. Sato, A. Shinohara, M. Segawa, H. Matsue	345

No.	「 Title 」	Page
	Neutron Activation Analyses	
4−1	**Survey of ^{129}I concentration in soil around the Tokai Reprocessing Plant** Y. kokubun, M. nakano, M. Takeishi	349
4−2	**Influence of water concentrations to chemical forms of tritium generated in mercury through a nuclear reaction** K. Manabe, S. Yokoyama	350
4−3	**Analysis of element in annually layered terrestrial carbonates (Tufa)** S. Sugihara, I. Morinaga, A. Hirose	351
4−4	**Studies on Phytoremediation of Soil Pollutions at the trace of a factory** Y. Kawanishi, N. Nogawa, Y. Makide, H. Sawahata, M. Kawate, M. Ishimoto, H. Matsue	354
4−5	**Instrumental Neutron Activation Analyses of volcanic rocks from Kyushu island: Characterization of Material Circulation through Volcanism** T. Hasenaka, M. Miyoshi, T. Nasu, M. Shimono, T. Edamura, K. Tanida, Y. Sekiguchi M. Morinaga, Y. Takae, H. Uemura	357
4−6	**Origin and fate of arsenic in volcanic hot spring area** Y. Kikawada, T. Oi, T. Hyatsu, J. Sano, A. Inoue, K. Oda, H. Fuji, Y. Ohno, K. Kyomen, N. Sato	361
4−7	**Accumulation of elements in an arable field with soil amendments (organic un-used resources) and its uptake by cultivated crop** H. Suzuki, H. Kumagaya, N. Nogawa	370

No.	「 Title 」	Page
	Others	
5−1	**Boron neutron capture therapy for head and neck malignancies.** J. Hiratsuka, T. Aihara, M. Uno, H. Kumada, K. Ono, T. Harada	379
5−2	**Study of Hyperfine Interaction using βray detected NMR-ON** S. Ohya,T. Ohtsubo, T. Izumikawa, S. Muto, K. Nisimura	381
5−3	**Basic & Clinical Research for Application of Neutron Capture Therapy to Highly Advanced Cancer** H. Yanagie, S. Mikado, N. Yasuda, S. Higashi, I. Ikushima, R. Mizumachi, Y. Murata, Y. Morishita A. Shinohara, K. Ogura, H. Sugiyama, N. Ryohei, S. Takamoto, M. Eriguchi, H. Takahashi	385
5−4	**Basic & Clinical Research for Application of Neutron Capture Therapy to Highly Advanced Cancer** H. Yanagie, K. Kakimi, A. Hosoi, A. Ogata, K. Mouri, K. Eguchi, Y. Morishita, A. Shinohara, H. Kumada, T. Nakamura, Y. Furuya, S. Takamoto, M. Eriguchi, H. Takahashi	391

1. 中性子散乱 1）構造・励磁

1. Neutron Scattering 1）Structure・Excitation

This is a blank page.

1-1-1

Correlation between structural and thermoelectric properties in Zn13Sb10

G. Nakamoto(A), A. Tada(A), M. Kurisu(A), A. Tanaka(B), T. Tsutaoaka(B), Y. Andoh(C)
(A)Japan Advanced Institute of Science and Technology, Ishikawa 923-1292, Japan,
(B)Graduate School of Education, Hiroshima University, Hiroshima 739-8524, Japan,
(C)Faculty of Regional Sciences, Tottori University, Tottori 690-8550, Japan

beta-Zn13Sb10 compound has been well known as a good thermoelectric material in the moderate temperature range because of its high dimensionless figure of merit, ZT=1.3 at 670 K. The high thermoelectric performance of this material originates mainly from the extremely low-thermal conductivity. Recently, it has been reported that such an extremely low-thermal conductivity is attributed to the disordered structure of Zn atoms or rattling motion of Sb-dimmers along the c-axis. However, the origin of the extremely low-thermal conductivity still remains an unresolved problem. More recentrly, it has been revealed that the occupation of Zn atoms at the interstitial sites has also strong influence on the structural property as well as thermoelectric one. Especially, the alpha to beta structural transtion at 260 K is largely dependent on Zn composition. Thus, there are many problems left about the correlation between the structural and thermoelectric properties of Zn13Sb10 compound.

In this experiment, powder neutron diffraction measurements were performed to examine the detailed crystal structure of Zn13Sb10 compound to clarify the correlation between the structural and thermoelectric properties.

Polycrystalline ingots were prepared by gradient freeze (GF) and vacuum-melt to quench (VMQ) methods. The constituent elements of Zn(5N) and Sb(6N) with the stoichiometric ratio 13:10 were encapsulated in a double quartz ampoule under vacuum. The GF ingot was grown in a vertical GF furnace at the growth rate of 3 mm/day. On the other hand, the VMQ ingot was melted in an electric furnace for 2 days and then quenched into ice water. Neutron diffraction experiment was carried out at T1-3 HERMES in JRR-3M at room temperature with a wave length of 1.82646(6) A. The data were collected by an MFC mode.

Figure 1 shows the powder neutron diffraction profile and result of Rietvelt analysis of the Zn13Sb10 GF ingot at room temperature. The Rietveld analysis was performed by using a pattern profile fittig program RIETAN-2000. Any reflections from an impurity phase are not detected. All the reflection peaks can be indexed by assuming a rhombohedric hexagonal structure (R3-c). The lattice parameters determined by this analysis are in good agreement with that obtained by the previous X-ray diffraction experiment. The goodness of fit, S, is obtained to be 1.40 at present. However, the relative intensity of the reflection peaks is not well fitted. This may be due to the difference in occupation of Zn atom at the interstitial sites from the starting structure model proposed by other groups. More presice analysis is now under way to determine the site occupancy especially for Zn atoms and to discuss the correlation between structural and thermoelectric properties of Zn13Sb10 compound.

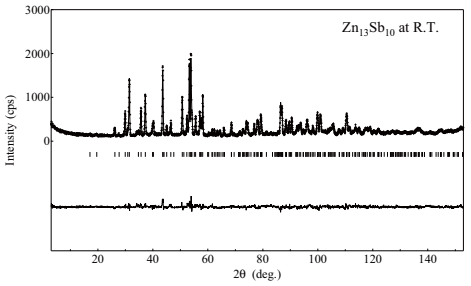


Fig. 1. Powder neutron diffraction profile and result of Rietveld analysis for Zn13Sb10 at room temperature.

1-1-2

Dynamics of the water included in [H11O5][ZnCu(CN)4]

Sin-ichi Nishikiori(A), Yoko Minamimoto(B), Osamu Yamamuro(B)
(A) Dept. of Basic Science, Graduate School of Arts and Sciences, Univ. Tokyo, (B) ISSP-NSL Univ. Tokyo

The title compound [H(H2O)5][ZnCu(CN)4] is a bimetal cyanide complex with a 3D framework structure built by bidentate behavior of cyanide linking tetrahedral Cu(I) and Zu(II) ions. The structure of the 3D framework is the tridymite-like structure as shown in Fig. 1 and the framework has negative electric charges. Inside the 3D framework void space is formed and water molecules and protons are included. The water molecules and protons are considered to form a hydrogen bonding network which penetrates the 3D framework of the bimetal cyanide complex. Although our previous X-ray structure analysis revealed the 3D framework structure, the structure of the hydrogen bonding network was unclear. The water molecules and protons are expected to be in a dynamic state. DSC measurement showed phase transitions at 160K-170K and 240K. 2H-NMR powder patters, which were measured using a deuterated sample, suggested a flip-flop motion about the C2 axis of a water molecule below 168K, a rotational motion about the C2 axis between 178K and 233K and an isotropic rotational motion above 253K for the water molecules. Although considerably activated rotational motion was confirmed near room temperature, there was no information about translational diffusion of the protons. If translational diffusion is observed, a possibility as a proton conductor comes up. In order to obtain information about such translational diffusion, we have carried out quasi-elastic neutron scattering (QENS) measurement on the title compound.

The sample was powdered and packed in a double walled cylindrical cell made of Al. The shape of the packed sample was a cylinder with a 13 mm diameter, a 50 mm height and a 1 mm thickness. The QENS measurement was carried out in the temperature range of 200K-323K on a time-flight type spectrometer AGNES(C3-1-1) installed at JRR-3M on JAEA(Tokai).

The data obtained were analyzed using the Chudley-Elliott model after several trials. This model is a jump diffusion model in which an atom stays and vibrates at a given position for an interval time and after that time the atom jumps rapidly to another position. In the case of a powder sample the jump direction is isotropic but the jump distance is fixed to a constant value. In our case, considering the results of the 2H-NMR experiments, we assumed that during the interval time the proton is undergoing reorientation among the four apexes of a tetrahedron which is a part of the hydrogen bonding network formed with the water molecules. At the center of the tetrahedron the O atom of a water molecule is positioned and the distance between the O and each apex is 0.97 A, which is the bond length of O-H. Fig.2 shows the HWHM vs Q plot and the best fit results based on our Chudley-Elliott model for the translational diffusion. From this fitting, the jump distance, the interval time, the diffusion constant and the activation energy were derived to be 2.9(1) A, 9(3) x 10^-15 sec, 6(3) x 10^13 A^2/sec and 16(1) kJ/mol, respectively. Considering the O-O distance in a O-H-O type hydrogen bond is 2.72(15) A, the jump distance obtained here means that the proton diffuses by a jump to an adjacent water molecule. The correlation time and the activation energy for the 4-site reorientation during the interval time were calculated to be 1.7(3) x 10^-12 sec and 11.2(5) kJ/mol, respectively.

Activity Report on Neutron Scattering Research: Experimental Reports **15** (2008)
Report Number: 327

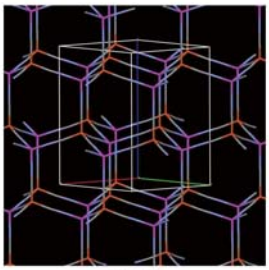


Fig. 1

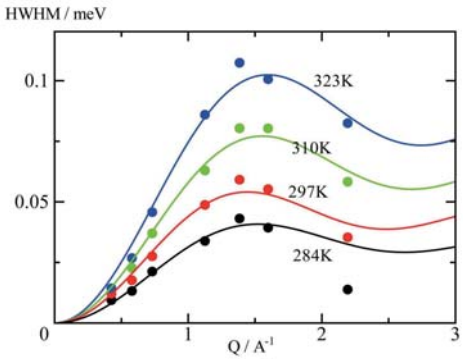


Fig. 2

Fig. 1. Fig.1. The structure of the 3D framework of [ZnCu(CN)4]-. Fig.2. HWHM vs Q plot and curve fitting using the Chudley-Elliott model for the translational diffusion.

1-1-3

Structural phase transition of one-dimensional semiconductor $C_5H_{10}NH_2PbI_3$

M. Takahashi[1], K. Kawasaki[1], K. Kataoka[1], Y. Fujii[1], M. Watanabe[2],
K. Ohshima[1] and Y. Noda[2]
Inst. of Mat. Sci., Univ. of Tsukuba[1], *IMRAM, Tohoku Univ.*[2]

Structural phase transition of one-dimensional lead-based inorganic-organic perovskites $C_5H_{10}NH_2PbI_3$ has been studied by using a single crystal diffractometer T2-2, FONDER. $C_5H_{10}NH_2PbI_3$ consists of semiconducting part composed of one-dimensional inorganic chains and barrier parts composed of inorganic $C_5H_{10}NH_2^+$ molecules. Studies with Raman scattering, DSC and optical absorption have shown that the material exhibits temperature-induced phase transitions involving rotational/orientational ordering of $C_5H_{10}NH_2^+$ molecules below room temperature. For detailed information on the structure of inorganic part, neutron diffraction measurement is indispensable.

Crystal structure at room temperature is determined by combination of X-ray and neutron analysis. Positional parameters for Pb and I are fixed by x-ray analysis [2] and those of atoms in inorganic parts are determined by 200 neutron intensity data with R values of 0.068. Figure 1(a) shows nuclear density distribution on (001) plane with equicontour surface at $\pm 0.8 fm/Å$ calculated by MEM. It clearly shows negative peaks (blue part) which indicate hydrogen atom positions. Nuclear density at 6-ring C_5N is found to be higher for the sites closer to the inorganic chains, indicating that N atom tends to occupy the closer sites to the semiconducting part.

Figure 1(b) shows temperature dependence of lattice parameters. It shows steplike changes at the transition temperatures with considerble large contraction of lattice b. Below 285K, 400 peak separates in two indicating that the crystal lattice changes from orthorhombic to monoclinic symmetries. The temperature dependence of angle α of the monoclinic lattice is shown in Fig.1(c). The results show that the successive phase transitions accompanied with large structural change take place below the room temperature. Further study to determine the structure at each phase is in planning.

[1] A. Masui *et al.*: Phys. Stat. Sol. (b) **223** (2001)501.
[2] G. V. Gridunova *et al.* : Soviet Physics, Doklady Akademii Nauk SSSR 278, 656 (1984).

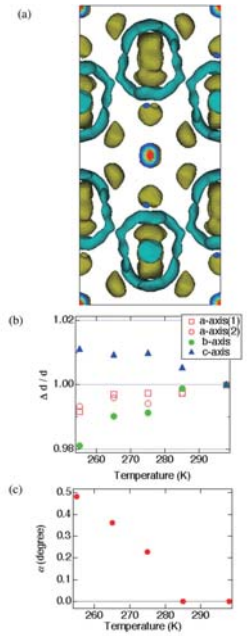


Fig. 1. (a)Nuclear density distribution on (001) plane.(b)Temperature dependence of lattice parameters. (c)Temperature dependence of angle α of the monoclinic lattice.

1-1-4

Superspace Group Approach to the Crystal Structure of Chimney-Ladder Compound [Mn][Si]g

Yuzuru Miyazaki, Dai Igarashi and Tsuyoshi Kajitani
Department of Applied Physics, Graduate School of Engineering, Tohoku University

Higher manganese silicide HMS (MnSi2-x) exhibits relatively high thermoelectric (TE) performance with the dimension-less figure-of-merit ZT = S2T/rho/kappa ˜0.7 around 800 K, where S, rho, kappa and T are the Seebeck coefficient, electrical resistivity, thermal conductivity and absolute temperature, respectively. Due to the natural abundance of constituent elements and high-temperature oxidation resistance, the compound is regarded as a potential p-type TE material. However, detailed structure of the compound has not been revealed due to the incommensurate superstructure. In this study, the crystal structure of HMS has been determined by means of the (3+1)-dimensional superspace group approach. Neutron powder diffraction (ND) measurement was carried out by means of HERMES diffractometer. Structural parameters have been refined with a superspace group of I41/amd(00gamma)00ss using the Rietveld refinement program JANA2000 designed for modulated structure analyses.

The compound can be regarded as a composite crystal which consists of tetragonal [Mn] and [Si] subsystems, with an irrational c-axis ratio (misfit parameter) g = c_Mn/c_Si˜ 1.74. The structure formula can be expressed as [Mn][Si]g. On the basis of the adopted superspace group, the modulated structure has been satisfactorily determined, by considering up to 4th order modulation amplitudes. A significant in-plane rotational modulation has been revealed in the ”chimney”-[Si] subsystem, while the positional modulation in the ”ladder”-[Mn] subsystem is less marked.

Fig.1 shows the Mn-Mn and Mn-Si interatomic distances plotted against an internal coordinate t’. In the present compound, t’ is defined as -gx3 + x4˜ -1.74x3 + x4. The coordinates x3 and x4 respectively correspond to the z coordinate in the [Mn] and [Si] subsystems. The modulation in Mn-Mn distances is relatively small, ranging from 2.913(9) angstrom to 3.062(15) angstrom. Reflecting the large in-plane modulation of Si atoms, the Mn-Si distances are significantly modulated, from 2.255(12) angstrom to more than 5 angstrom. Such a large modulation would be an origin of the observed low lattice thermal conductivity.

Activity Report on Neutron Scattering Research: Experimental Reports **15** (2008)
Report Number: 370

1-1-5

Structure analysis of trehalose dihydrate by neutron diffraction

M. Takahashi[1], K. Kawasaki[1], K. Kataoka[1], M. Watanabe[2],
K. Ohshima[1] and Y. Noda[2]
Inst. of Mat. Sci., Univ. of Tsukuba[1], IMRAM, Tohoku Univ.[2]

α,α-trehalose dihydrate is a non-reducing disaccharide, and very attractive from both academic and practical points of view, such as an additive for long term storage in food and pharmaceutical industries. It has high superiority as a protector of biological molecules compared with other carbohydrates such as sucrose. To understand the biological protective mechanism of α, α-trehalose, information on the hydrogen atom positions is indispensable.

Structure analysis of α, α-trehalose at room temperature was carried out by means of neutron diffraction method. Intensity data up to $\sin\theta/\lambda < 0.75$Å was collected using crystals with approximate dimensions of $15 \times 4.5 \times 2.7\text{mm}^3$ by a four-circle diffractometer, FONDER at T2-2. The space group of α, α-trehalose is orthorhombic $P2_12_12_1(Z = 4)$ and the obtained lattice parameters at 300 K were $a = 12.2380$Å, $b = 17.9087$Å and $c = 7.6032$Å. Least square fitting analysis were performed to refine structural parameters; in the analysis, parameters obtained by previous X-ray study[1,2] were used as initial parameters for atoms except for the hydrogen atom. Structure determined by 1711 neutron intensity data with R values of 0.068 is shown in Fig.1. Position of hydrogen atoms in both glucose(pink circle) and water molecules(red circle) are determined for the first time. It is found that the hydrogen atoms in water molecules are oriented to the glucose molecules, indicating that the molecules are connected to each other through the hydrogen bonding between the molecule and hydrogen atoms in water.

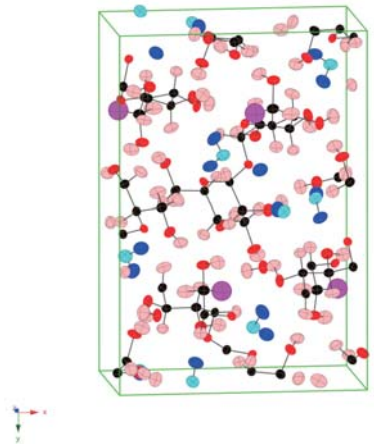


Fig. 1. Crystal structure of α, α-trehalose determined by neutron analysis. Hydrogen atom in glucose and water molecules are shown with pink and blue circles, respectively.

[1] G. M. Brown *et al*. Acta Crystallogr., B **283**(1972)3145.
[2] G. Taga *et al*. Acta Crystallogr., B **283**(1972)3258.

1-1-6

QENS studies of Fast Molecular Reorientation in Liquid, Glass and Crystalline Phases of 8*OCB

H. Suzuki(A), A. Inaba(A), J. Krawczyk(B), M. Massalska-Arodz(B), T. Kikuchi(C), O. Yamamuro(C)

(A)Osaka Univ., (B)Inst. Nuclear Physics, Krakow, Poland, (C)ISSP-NSL, Univ. Tokyo

Chain branching and chirality of molecules affect various physical properties substantially, such as phase behavior. Some of cyanobiphenyl compounds are good examples whose phase behavior varies depending on the presence of branch (chirality) in the alkyl side chain. We have been interested in their phase relation and dynamics. Here, we report the results obtained from quasielastic neutron scattering (QENS) measurements for (S)-4-(1-methylheptyloxy)-4-cyanobiphenyl (8*OCB) which is one of such cyanobiphenyl compounds.

Various kinds of measurements have already been made for 8*OCB. From the calorimetric measurements [1] and IR spectroscopy [2], the phase behavior of 8*OCB was established. The isotropic liquid is easily undercooled and forms glassy state on further cooling below 218 K. There exist two crystalline phase (metastable and stable). This phase behavior is entirely different from that of the non-chiral isomer, 8OCB, which has two liquid crystal phases (nematic and smectic). The dielectric relaxation measurements [3] have also been made, and they showed that the molecular reorientation around its short axis becomes quite slow near the glass transition temperature at 218 K. The purpose of this experiment was to investigate the molecular reorientation around its long axis and the internal molecular motions.

We performed QENS experiments on 8*OCB using AGNES spectrometer at JRR-3M. The measurements were made at 370 K, 350 K, 330 K, 310K, 290 K, 270 K for isotropic liquid phase with a low-resolution mode (delta E = 120?micro-eV). As a reference sample, 8OCB was also investigated at 370 K (isotropic liquid), 350 K (nematic), 330 K (smectic) and 310 K (crystal).

As a spectrum of rotational motion is approximately described by sum of a delta function (an elastic component) and a Lorentz function (a quasielastic component), we first fitted the spectra with these two functions. However, the result was not quite. We next tried to fit the data with two Lorentz functions, which was actually better. The HWHM of the Lorentz function for narrow component increases with increasing momentum transfer (Q), indicating the narrow component as a diffusive motion. The diffusion constants were obtained by using the continuous diffusion model. An Arrhenius plot for the diffusion constant gives the activation energy 23.5 kJ /mol (Fig. 1). The 8OCB spectra could also be fitted by two Lorentz functions. The HWHM of the narrow component was significantly broader than that of 8*OCB, which means that this diffusive motion of 8OCB is faster than that of 8*OCB. However, the diffusion constants of 8OCB determined in this QENS experiment were clearly larger than those obtained before by NMR measurements [4] (Fig. 1). In addition, rotational diffusion constants about its long axis for 8OCB, obtained by another NMR measurements [5], are about 10 nsˆ-1 at 340 K. This value is in the resolution-window of AGNES, so we must have observed this motion. Therefore, the narrow component should be interpreted as a coupled motion of translational diffusive motion and rotation around its long axis.

For the broad component, the activation energy was determined to be 4.8 kJ/mol by an Arrhenius plot of the HWHM. This motion may be some internal molecular motion such as rotation of the methyl groups

or tumbling motion of the alkyl chain. The rotational diffusion coefficient was estimated to be around 1.2 rad/ps at 350 K. For this broad component, the results of 8*OCB and 8OCB are almost same. It should be added that this motion was observed in the crystalline phase of 8OCB at 310 K as well, while it was not observed in the metastable or the stable crystal for 8*OCB at 270 K.

[1] K. Saito, M. Massalska-Arodz, S. Ikeuchi, M. Maekawa, J. Sciesinski, E. Sciesinska, J. Mayer, T. Wasiutynski, M. Sorai, J. Phys.Chem. B, 108 (2004) 5785.
[2] J. Sciesinski, E. Sciesinska, M. Massalska-Arodz, J. Mol. Struc., 596 (2001) 229.
[3] M. Massalska-Arodz, G. Williams, D. K. Thomas, G. Aldridge, IEEE Trans. Dielectr. Electr. Insul., 8 (2001) 377.
[4] M. Cifelli, P. J. McDonald, C. A. Veracini, Phys. Chem. Chem. Phys., 6 (2004) 4701.
[5] A. V. Zakharov, Ronald Y. Dong, Phys. Rev. E 63 (2000) 011704.

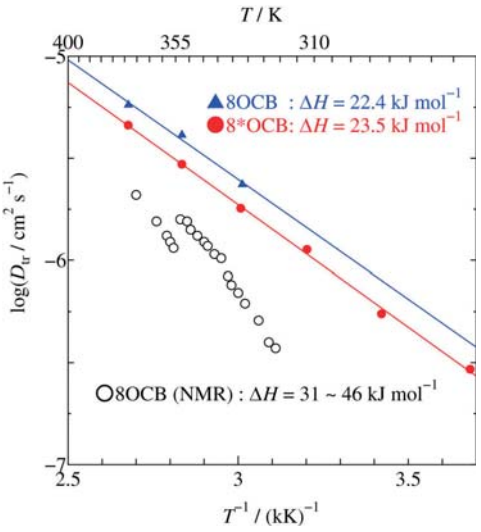


Fig. 1. Fig. 1 An Arrhenius plot of the diffusion constant for 8*OCB and 8OCB obtained in this QENS study, and the translational diffusion constant for 8OCB obtained by NMR measurements (Ref. 4).

1-1-7

Crystal Structure of Tantalum Oxynitride TaON, a Visible Light Responsive Photocatalyst

Masatomo Yashima, Yungi Lee*, and Kazunari Domen*
*Department of Materials Science and Engineering, Interdisciplinary Graduate School of Science and Engineering, Tokyo Institute of Technology, Nagatsuta-cho 4259, Midori-ku, Yokohama-shi, Kanagawa, 226-8502, Japan; * Department of Chemical System Engineering, School of Engineering, The University of Tokyo, 7-3-1 Hongo, Bunkyo-ku, Tokyo, 113-8656, Japan*

Metal oxide photocatalysts have attracted extensive research for the purposes of solar energy conversion and environmental remediation. Overall water splitting using a photocatalyst is an attractive solution for the supply of clean and recyclable hydrogen energy, while certain photocatalysts decompose waste materials and hazardous compounds. Although a large number of photocatalysts have been proposed to date, most function only in the ultraviolet (wavelength $<$ 400 nm) region (e.g., TiO2) due to the inherently large band gap of metal oxides. Metal oxynitrides are candidates for visible-light responsive photocatalysts, and promising results have been reported for TaON, N-doped TiO2, and (Ga1-xZnx)(N1-xOx). TaON has been demonstrated to be responsive to excitation at wavelengths up to ca. 530 nm, with a suitable band gap (2.3 eV) position for overall water splitting. In the present work, the crystal structure and electron density of an active TaON photocatalyst sample under visible-light excitation are investigated by neutron diffraction for confirmation of anion ordering, and synchrotron powder diffraction for high-precision analysis of the crystal structure and electron density. Density functional theory (DFT) is employed for theoretical calculations of the electron density distribution and partial density of states. This work was published in Masatomo Yashima, Yungi Lee and Kazunari Domen, "Crystal Structure and Electron Density of Tantalum Oxynitride TaON, a Visible Light Responsive Photocatalyst", Chem. Mater., 19, [4] 588-593 (2007).

Neutron powder diffraction experiments were performed using the Kinken powder diffractometer in order to ensure high-efficiency and high-resolution measurements. The diffractometer, HERMES [2], is installed at the JRR-3M Japan Research Reactor of the Japan Atomic Energy Agency (JAEA) in Tokai, Japan and is operated by the Institute of Materials Research of Tohoku University. Incident neutrons with a fixed wavelength of 0.18150 nm were obtained by a vertically focusing (331) Ge monochromator. Diffraction data were collected at step intervals of 0.1 deg. over a 2 theta range of 8-150 deg. using 150 3He counters set at 1° intervals. Structural refinement was performed using the Rietveld analysis program RIETAN-2000 [3]. The peak shape was assumed to be a modified pseudo-Voigt function with asymmetry. The cut-off value was 7.00 × FWHM (full-width at half-maximum). The background of each profile was approximated by a 12-variable polynomial in (2theta)^n (n = 0...11). The parameters n were refined simultaneously with the unit cell, structural and profile parameters. The nuclear density of TaON was investigated by the maximum-entropy method (MEM) with MEM-based pattern fitting (MPF) [4]. The MEM calculations were performed using the computer program PRIMA [4] with a 64 × 64 × 64 pixel unit cell.

All reflections in the neutron and synchrotron powder diffraction profiles were indexed as belonging to a monoclinic cell, indicating a single phase of baddeleyite-type TaON. Rietveld analyses of the neutron and synchrotron diffraction data were thus performed assuming a baddeleyite-type structure. All the occupancy factors were therefore fixed at unity in the final

refinement. Isotropic harmonic atomic displacement parameters were used for all atoms. In a preliminary analysis, the atomic displacement parameters B for the three atoms were refined independently. However, as the refined atomic displacement parameter was negative, final refinement was conducted assuming B(Ta) = B(N) = B(O), where B(X) denotes the atomic displacement parameter of X atom. The calculated intensity obtained after final refinement was in good agreement with the observed data. The neutron and synchrotron data sets both indicate that the TaON material has a baddeleyite-type structure (space group, P21/c), with estimated unit cell parameters of a = 0.494941(4) nm, b = 0.501662(4) nm, c = 0.516430(2) nm, alpha = 90 ° , beta = 99.6107(4) ° , gamma = 90 ° , and V = 0.126426(2) nmˆ3 (298 K). Occupational ordering of the anions occurs in alternate NTa4 and OTa3 layers normal to the [100] direction. The coordination numbers of Ta, N and O atoms are 7, 4 and 3, respectively. The NTa4 tetrahedron is linked with four corner-shared NTa4, four edge-shared NTa4, two corner-shared OTa3, and one edge-shared OTa3. The OTa3 triangle is linked with twelve corner-shared NTa4, one edge-shared NTa4, three corner-shared OTa3, and one edge-shared OTa3. These results indicate that the nitrogen atoms prefer to be four-coordinated in TaON, while oxygen atoms prefer to have three neighbors.

Figure 1 shows the refined crystal structure, MEM electron density distribution, MEM nuclear density distribution, and VASP valence electron density distribution on the b-c plane of the TaON photocatalyst over the range $1/4 < x < 3/4$. The nuclear density map shows an atom near the stable position, and the MEM and valence electron density maps clearly indicate covalent bonding between the Ta and N atoms. Again, the synchrotron-based electron density distribution (Fig. 1(b)) is in agreement with the DFT-based valence electron density distribution (Fig. 1(d)). These results suggest a two-dimensional network consisting of covalent bonds between Ta and N atoms, while the results of Ta-O layer indicate a two-dimensional network of covalent bonds between Ta and O atoms. The networks of Ta-N and Ta-O covalent bonds are arranged alternately along the c axis, corresponding to the ordering of NTa4 tetrahedra and OTa3 triangles.

References

[1] M. Yashima et al., Chem. Mater. 19 (2007) 588.
[2] K. Ohoyama et al., Jpn. J. Appl. Phys. 37 (1998) 3319.
[3] F. Izumi and T. Ikeda, Mater. Sci. Forum. 321-324 (2000) 198.
[4] F. Izumi and R. A. Dilanian, Recent Res. Develop. Phys. 3 (2002) 699.

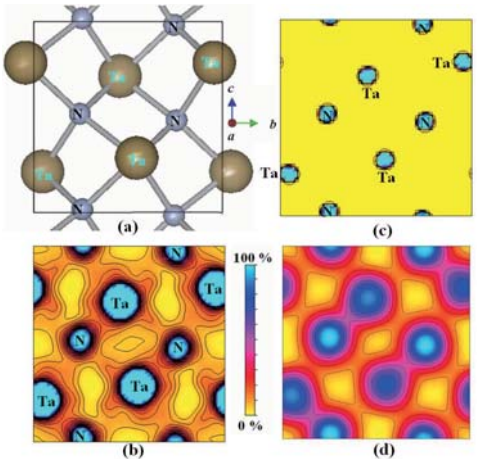


Fig. 1. (a) Refined crystal structure, (b) electron density, (c) nuclear density and (d) valence electron density distributions on the b-c plane of TaON over the range $1/4 < x < 3/4$.

1-1-8

Diffusion Path of Oxide Ions in Apatite-type La9.25Si6.0O25.88

Roushown Ali,*,** Masatomo Yashima,** Yoshitaka Matsushita,* Fujio Izumi,* Shinichi Kikkawa,*** Takahiro Wakita*

**Quantum Beam Center, National Institute for Materials Science, 1-1 Namiki, Tsukuba, Ibaraki 305-0044; **Department of Materials Science and Engineering, Interdisciplinary Graduate School of Science and Engineering, Tokyo Institute of Technology, 4259 Nagatsuta-cho, Midori-ku, Yokohama, 226-8502; ***Division of Material Science and Engineering, Graduate School of Engineering, Hokkaido University, Sapporo 060-8628, Japan*

Solid oxides exhibiting high ionic conductivity have been the subject of considerable research interest. In particular, the oxide-ion conductors are useful materials for fuel cells, catalysts, gas sensors and batteries. The development of improved electrolyte materials for these applications requires a thorough understanding of the crystal structure and diffusion path of mobile oxide ions, which determine the mechanism of ionic conduction. Lanthanum silicates La10-xSi6O26+delta having apatite-type structure are one of the promising groups exhibiting significant oxide ion conductivity but the understanding of the conduction mechanism in this structure remains subject to uncertainties. Here, we have investigated the crystal structure and diffusion pathway of oxide ions in apatite-type compound La9.25Si6.0O25.88 at 1558 degrees Celsius.

The neutron powder diffraction data were collected at 1558 degrees Celsius on HERMES installed at the JRR-3M reactor. Incident neutron beams with a fixed wavelength of 0.18265 nm were obtained by a vertically focusing (331) Ge monochromator. A furnace [1] with an MoSi2 heater was used to heat the sample and the sample temperature was maintained within +- 1.5 degrees Celsius. during the measurement. The resulting diffraction data were analyzed by the Rietveld method with RIETAN-FP [2] and whole-pattern fitting approach based on the maximum-entropy method (MPF) [3]. The MEM calculation was done with the unit cell divided into 100 X 100 X 80 pixels and whole-pattern fitting using RIETAN-FP.

The Rietveld refinement was performed with hexagonal space group P63/m through the neutron powder diffraction data measured at 1558 degrees Celsius. Attempts to refine the structure considering an interstitial oxygen atom site were not successful, so the refinement were performed without interstitial site. The calculated pattern agreed well with that of observed pattern. The reliability values obtained from the refinement were Rwp = 2.15 %, Rp = 1.67 %, RI = 1.20 % RF = 0.72 % and S = 2.05. The refinement was carried out with anisotropic thermal displacement parameters for all the cations and anions. The thermal displacement parameters of oxygen O3 atoms showed strong anisotropic along the a-axis with large U11 value (0.00123(3) nmˆ2) while that of O4 showed stronger anisotropic along the c-axis with larger U33 value (0.0025(1) nmˆ2). The structure consists of six isolated [SiO4] tetrahedra containing three kinds of oxygen atoms (O1, O2, O3). The oxygen atoms O3 and O4 displayed large displacement parameters, suggesting directionality in the movements of oxide ions around their stable positions. The probability densities of O4 atoms were connected with that of nearest-neighbor O4 atoms, indicating diffusion along a pathway parallel to the c axis. The O4 atoms migrated linearly to the nearest-neighbor O4 and followed one-dimensional tunnel extending along the c axis of the hexagonal P63/m framework. On the other hand, the probability densities of O3 atoms were largely distributed perpendicular to the c axis. The main diffusion pathway

Activity Report on Neutron Scattering Research: Experimental Reports **15** (2008)
Report Number: 396

involved one-dimensional migration along the hexagonal channels of the apatite-type structure. The directionality in the movements of oxide ion O3 also suggests another migration pathway perpendicular to the c-axis.

References

[1] M. Yashima, J. Am. Ceram. Soc. 85 (2002) 2925.
[2] F. Izumi and K. Momma. In Proc. XX Conf. Appl. Crystallogr., Solid State Phenom., Z rich, 2007. Trans Tech Publications. in press.
[3] F. Izumi and R. A. Dilanian, Recent Res. Dev. Phys., 3 (2002) 699.

1-1-9

Structural investigation of the cubic perovskite-type doped lanthanum cobaltite La0.6Sr0.4CoO3-delta at 1258 degrees Celsius, - Possible diffusion path of oxygen ions in an electrode material -

Masatomo Yashima and Takayuki Tsuji
Department of Materials Science and Engineering, Interdisciplinary Graduate School of Science and Engineering, Tokyo Institute of Technology, 4259 Nagatsuta-cho, Midori-ku, Yokohama-shi 226-8502, Japan

(1) Introduction

Perovskite-structured oxides that exhibit high ionic conductivity have attracted considerable attention due to their various applications in solid oxide fuel cells (SOFCs), batteries, catalysts and oxygen sensors. The development of better oxygen-ion and mixed conductors requires a better understanding of the diffusion paths and structural disorder of mobile oxygen ions at high temperatures at which the materials work efficiently. The lanthanum strontium cobaltites, La1-xSrxCoO3-delta, which have a perovskite-type structure, are promising electrode materials for the doped lanthanum gallate electrolyte in SOFCs. The crystal structure of rhombohedral R-3c La1-xSrxCoO3-delta has been the subject of a number of previous investigations. However, far less attention has been paid to the high-temperature cubic La1-xSrxCoO3-delta phase. The purpose of the present study is to investigate the crystal structure and structural disorder of the cubic Pm-3m perovskite-type La0.6Sr0.4CoO3-delta at 1258 degrees Celsius. This work was published in M. Yashima and T. Tsuji, "Structural investigation of the cubic perovskite-type doped lanthanum cobaltite La0.6Sr0.4CoO3-delta at 1531 K: possible diffusion path of oxygen ions in an electrode material", J. Appl. Crystallogr., 40, [6] 1166-1168 (2007).

(2) Experiments and data processing

La0.6Sr0.4CoO3-delta specimens were prepared through solid-state reactions by the Mitsubishi Materials Co. Neutron powder diffraction data were collected in air using HERMES, a diffractometer with a 150-multi-detector system, at room temperature and at 1258 degrees Celsius (Ohoyama et al., 1996). The HERMES diffractometer is located at the T1-3 port of the JRR-3M research reactor of the Japan Atomic Energy Agency at Tokai, Japan. The powder patterns were measured in the range from two theta = 5 degrees to 155 degrees. The wavelength of the incident neutrons was 0.18207 nm. The sample temperature was kept constant during the data collection at 1258.2degrees Celsius (+1.4 degrees Celsius, -0.8 degrees Celsius) using a furnace with MoSi2 heaters (Yashima, 2002).

The diffraction data obtained at 1258 degrees Celsius were analyzed by a combination of Rietveld analysis, the maximum-entropy method (MEM) and MEM-based pattern fitting (MPF) (Izumi & Dilanian, 2002). The computer programs RIETAN-2000 (Izumi & Ikeda, 2000), PRIMA (Izumi & Dilanian, 2002) and VESTA (Momma & Izumi, 2006) were utilized for the Rietveld and MPF analyses, MEM calculations and visualization of crystal structure and the nuclear-density distribution, respectively. The coherent scattering lengths (bc) adopted for Rietveld refinement were 8.24 fm for La, 7.02 fm for Sr, 2.49 fm for Co and 5.803 fm for O.

(3) Results and discussion

Neutron-diffraction data for La0.6Sr0.4CoO3-delta at room temperature indicated that the specimen consisted of a single phase of the rhombohedral La0.6Sr0.4CoO3-delta. All the peaks in the neutron diffraction pattern of

La0.6Sr0.4CoO3-delta at 1258 degrees Celsius were indexed by the cubic perovskite-type structure with Pm-3m symmetry, indicating phase transformation from a low-temperature rhombohedral to a high-temperature cubic phase. Rietveld analysis was performed using the diffraction data taken at 1258 degrees Celsius in the two theta range of 20 degrees to 153 degrees by a cubic perovskite-type structure. La and Sr atoms were placed at the special position 1b 1/2, 1/2, 1/2 of the Pm-3m symmetry. Co and O atoms were placed at the 1a 0, 0, 0 and 3d 1/2, 0, 0 sites, respectively. Isotropic and anisotropic atomic displacement parameters were used for the cations and anions, respectively. The calculated profile agreed well with the observed one. The atomic displacement parameters of the O atom exhibited large anisotropy, which reflects the rotational motion of O atoms in the rigid CoO6 octahedron. Similar anisotropy has been observed in other cubic perovskite-type compounds. The equivalent isotropic displacement parameter of O atom is larger than those of cations, suggesting the higher diffusivity of O atoms. The occupancy factor of the O atom at the 3d site was estimated to be 0.886(6), indicating an oxygen deficiency of delta =0.34(2) in La0.6Sr0.4CoO3-delta at 1258 degrees Celsius. The averaged valence of the Co cations was estimated to be 2.72 at 1258 degrees Celsius, which is consistent with the calculated bond valence sum value of 2.8. Here, the average value of the bond valence parameter of 1.698 was used for the calculation.

MEM-based pattern fitting (MPF) analysis was conducted using diffraction data in the two theta range from 20 degrees to 153 degrees, corresponding to d $>$ 0.107 nm (d: spacing of lattice planes), with the structure factors obtained from Rietveld analysis. A total of 16 structure factors were obtained. The 100 reflection appearing at the lowest two theta position (ca. 26.7 degrees) was included, since this peak provides information on the disordered arrangements of oxygen ions. The MEM calculations were performed with the unit cell divided into 64 X 64 X 64 pixels. The R factors for the Bragg intensities, RI and for the structure factors, RF were improved from 2.33 % in the Rietveld analysis to 1.71 % in the MPF, and from 1.72 % to 1.25 %, respectively. The nuclear-density map reveals that the oxygen ions in the cubic Pm-3m La0.6Sr0.4CoO3-delta exhibit a large thermal motion perpendicular to the Co-O bond, corresponding to large anisotropy of the atomic displacement parameters. The diffusion path does not follow the edge of the CoO6 octahedron shown as straight lines, but displays an arc shape away from the Co cation. It should be noted that the nuclear density of O atoms in La0.6Sr0.4CoO3-delta did not connect with that of nearest neighbor O atoms. On the contrary, the (La0.8Sr0.2)(Ga0.8Mg0.15Co0.05)O2.8 perovskite exhibited connected diffusion paths. This strongly suggests that the diffusivity of oxygen ions in La0.6Sr0.4CoO3-delta is lower than that in (La0.8Sr0.2)(Ga0.8Mg0.15Co0.05)O2.8.

1-1-10

Low-Energy Phonon Anomaly of $CeOs_4Sb_{12}$

K. Iwasa[1], S. Itobe[1], C. Yang[1], Y. Murakami[1], M. Kohgi[2], H. Sugawara[3], H. Sato[2]
Tohoku Univ.[1], *Tokyo Metropolitan Univ.*[2], *The Univ. of Tokushima*[3]

The rare-earth filled skutterudites RT_4X_{12} (R = rare earth, T = transition metal, X = pnictogen) have been studied in terms of the anomalously anharmonic lattice properties, as well as the various strongly correlated electron phenomena involving $4f$ electrons. The filled ions are located within the icosahedral X cage, and vibrate with large amplitude detected as the large Debye-Waller factors. Ultrasonic measurements of $PrOs_4Sb_{12}$ revealed dispersion of elastic constants indicative of anomalous Pr-ion motion within the Sb cage (T. Goto *et al.*: PRB **69** (2004) 180511). Recent inelastic x-ray scattering experiment of Sm-based compounds (S. Tsutsui *et al.*: Physica B **383** (2006) 142) and inelastic neutron scattering experiment of $CeRu_4Sb_{12}$ (C. H. Lee *et al.*: JPSJ **75** (2006) 123602) revealed low frequency flat phonon branches corresponding to the motion of filled atoms. We have reported the anomalous softening of phonon due to Pr vibration with decrease of temperature and the possible electron-phonon interaction in $PrOs_4Sb_{12}$ and $PrRu_4Sb_{12}$ (K. Iwasa *et al.*: Physica B **378-380** (2006) 194, J. Phys. Conference Series **92** (2007) 012122). In the present study, we have investigated the low-energy phonon spectra of $CeOs_4Sb_{12}$ using the triple-axis spectrometers TOPAN (6G) and HER (C1-1).

The figure shows phonon spectra of $CeOs_4Sb_{12}$ measured at the reciprocal lattice point **Q** = (0 3 3). It shows distinct decrease of excitation energy by 18% with decreasing temperature from 300 down to 15 K. This softening mode was confirmed to be less dispersive like an optical mode. We measured phonon spectra also at **Q** = (6 -0.4 -0.4), and it also exhibits softening by 10%. The energy region of this mode as well as the softening indicate that this phonon is composed of the vibration of the Ce atoms within the icosahedral Sb cage. The presence of such anharmonic low-energy phonon in the three measured compounds suggests that it is common feature in the rare-earth filled skutterudite. We will continue the study to reveal the mechanism of the softening behavior, which may be mode coupling effect or the electron-phonon interaction involving the anomalous rare-earth vibration mode.

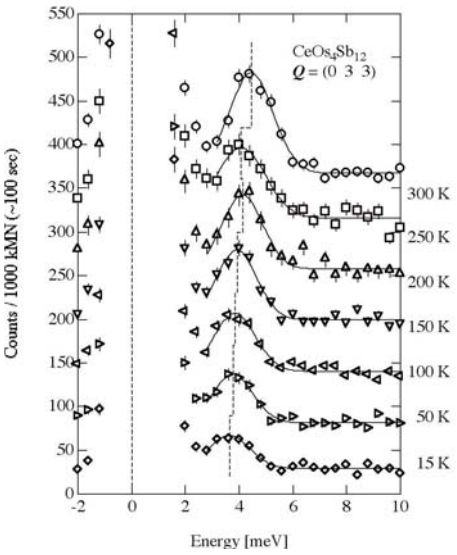


Fig. 1. Temperature dependence of the phonon spectra at **Q** = (0 3 3) of $CeOs_4Sb_{12}$.

1-1-11

Observation of spin dynamics in Shastry- Shutherland lattice TbB4

K. Ohoyama, T. Matsumura(A), D. Okuyama(A), F. Iga(B), S. Michimura(B)
IMR, Tohoku Univ., Faculty Science, Tohoku Univ.(A), ADSM, Hiroshima Univ.(B)

Rare earth compounds RB4 have attracted our interests because the geometrical alignment of the rare earth ions in the c-plane is equivalent with that of the Shastry-Sutherland lattice in which magnetic frustration is theoretically predicted. Of this system, TbB4 reveals successive magnetic transitions at TN1=42.1K and TN2=21.7K. An important characteristic point of TbB4 is that, in magnetization process for B//[001], TbB4 shows 9-steps metamagnetic transitions between 15T<H<30T below TN2, even though the magnetic structure under B=0T is an Heisenberg type antiferromagnetic one: all the magnetic moments below TN2 lies in the c-axis. The metamagnetic transitions in a Heisenberg-type magnet imply some unknown magnetic properties in RB4.

To understand magnetic properties in TbB4, it is indispensable to understand 4f ground state and low-lying 4f levels. Therefore, we are systematically investigating magnetic excitations in TbB4 under zero magnetic field. In 2007, we performed neutron inelastic scattering experiments on a single crystalline sample of Tb11B4 on 6G and T1-2, and found some characteristic behaviour of spin dynamics around the transition temperatures. The collimation condition were B-30-S-PG filter-30-B to obtain higher resolution. The constant Ef mode was selected with kf=2.67A-1.

Fig.1 shows the temperature dependence of energy spectra of TbB4 observed on 6G at the (100) reciprocal lattice point which corresponds to the magnetic zone centre. As shown in the figure, a magnetic excitation was observed at about 3meV at T=60K; the excitation energy decreases down to 1.5meV with decreasing temperature (top figure); the excitation can not be distinguished from the elastic scattering around TN2 under present resolution condition (middle figure). On the other hand below TN2, the excitation rapidly change the position to about 2meV and increases with decreasing temperature (bottom figure). This suggests that some kind of softening of excitation occurs above TN2. Furthermore, since the excitation energy near TN2 is smaller than the thermal energy, some quasi-degeneracy may play an important role for the magnetic properties in TbB4. To clarify the bahaviour of the low-lying 4f states around TN2, higher resolution experiments are in progress.

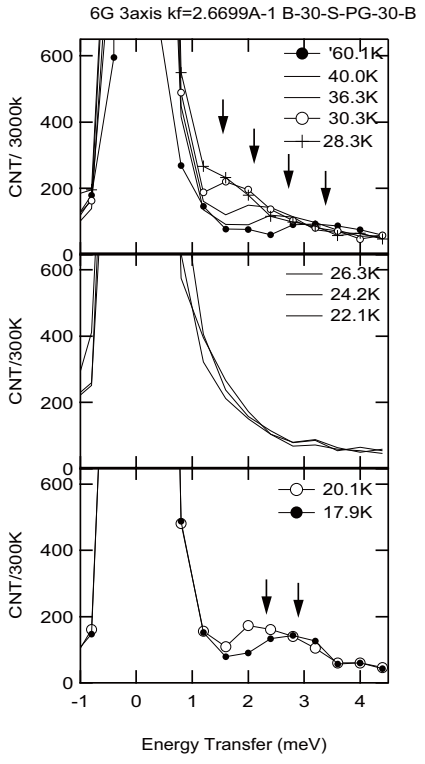


Fig. 1. Energy spectra of TbB4 observed on 6G at several temperatures at the (100) reciprocal point. Top: T>TN2, Middle: near TN2, Bottom: T<TN2

1-1-12

Crystal Structure of Chemically Modified Layered Cobaltates

Yuzuru Miyazaki, Dai Igarashi and Tsuyoshi Kajitani
Department of Applied Physics, Graduate School of Engineering, Tohoku University

Recently, a first-order structural transition has been discovered for the gamma-NaxCoO2 (x˜0.58) sample at the temperature range from T1 = 236 K to T2 =288 K. Above T2, the compound possesses an identical structure to well known gamma-NaxCoO2, in which the Na1 and Na2 atoms are randomly distributed. In this study, we have determined the crystal structure of the compound between T1 and T2. Neutron powder diffraction (ND) data were collected at several temperatures by the use of HERMES diffractometer. The ND data were analyzed using the Rietveld refinement program RIETAN2000. According to the electron diffraction pattern taken at 248 K, the compound has an order 'sqrt'7 x 'sqrt'7 ordered superstructure with the space group of P63/m. In Fig. 1, we show the revealed crystal structure of Na0.58CoO2 at 300 K and 240 K, projected parallel to the c-axis. The structure at 300 K is found to be isostructural to the potassium analogue, K4Co7O14, reported by Blangero et al[1]. At 240 K, the each single Co and O site split into two and three sites with different z-coordinations, respectively. This site-splitting yields an undulated CoO2 conduction plane with inequivalent Co-O lengths. The observed anomaly in resistivity and magnetic susceptibility at T2 can be understood by such a change in the bond lengths of the electronic conduction paths.

[1] M. Blangero et al, Inorg. Chem. 44 (2005) 9299.

1-1-13

Structural disorder of cubic Ce0.5Zr0.5O2 solid solution

Takahiro Wakita(A), Masatomo Yashima(A), Yoshitaka Matsushita(B), Takafumi Komatsu(A), Yong Phat(A), and Takashi Ohta(A)
(A)Department of Materials Science and Engineering, Interdisciplinary Graduate School of Science and Engineering, Tokyo Institute of Technology (B) Quantum Beam Center, National Institute for Materials Science

The crystal structure of the CeO2-ZrO2 solid solutions has been investigated by Yashima et al. [1,2]. They reported the existence of three metastable tetragonal forms of t, t' and t''. The three tetragonal forms belong to the P42/nmc space group. However, structural disorder and diffusion path of oxygen ions in Ce0.5Zr0.5O2 solid solution remain poorly understood. In this study, we demonstrate that there is considerable positional disorder of the oxygen ions in Ce0.5Zr0.5O2 solid solution. High-temperature neutron powder diffracrtion data at 1832 K are utilized because of the relatively high contributions to the structural disorder of oxygen ions, and it is easy to compare with CeO2, which has a cubic structure.

Ce0.5Zr0.5O2 powders were prepared by a coprecipitation route. Ce0.5Zr0.5O2 powders were pressed into pellets. CeO2 powders were prepared by a neutralization method. The powders were pressed into pellets. These pellets were used for high-temperature neutron diffraction measurements. Neutron diffraction measurements were performed in air with a 150-detector system, HERMES [3], installed at the JRR-3M reactor in Japan Atomic Energy Agency, Tokai, Japan. Neutrons with wavelength 1.8143 angstrom and 1.8207 angstrom were obtained by the (311) reflection of a Ge monochromator. Diffraction data were collected in air at 1832 K and at 1826 K. A furnace with MoSi2 heaters [4] was placed on the sample table, and used for neutron diffraction measurements at high temperatures. The experimental data were analyzed by a combination of Rietveld analysis, the maximum-entropy method (MEM) and MEM-based pattern fitting (MPF). Computer programs RIETAN-2000 [5], PRIMA [6] and VESTA [7] were utilized for the Rietveld and MPF analyses, MEM calculation and visualization of crystal structure and nuclear-density distribution, respectively.

Rietveld analysis of the neutron diffraction data of Ce0.5Zr0.5O2 at 1832 K and CeO2 at 1826 K was carried out based on a cubic fluorite-type structure with Fm-3m space group. The calculated profile is in good agreement with the observed data. Figures 1(a) and (b) show nuclear density contour maps on the (110) plane for Ce0.5Zr0.5O2 and CeO2 at 1832 K and 1826 K, respectively. The results reveal that the oxygen ions in Ce0.5Zr0.5O2 show complicated disorder and are spread over a wide area compared with CeO2 (Fig.1). The oxygen ions show a shift to the <111> directions (Fig.1). Possible diffusion paths of the oxygen ions can be seen along the <100> and <110> directions (see dotted arrows (A) and (B) in Figs. 1(a) and (b)). The spatial distribution of oxygen ions in Ce0.5Zr0.5O2 is greater than that of CeO2. The greater degree of positional disorder in Ce0.5Zr0.5O2 is responsible for higher diffusivity of the oxygen ions.

References

[1] M. Yashima et al., J. Am. Ceram. Soc. 76 (1993) 2865.
[2] M. Yashima et al., Appl. Phys. Lett. 72 (1998) 182.
[3] K. Ohoyama et al., Jpn. J. Appl. Phys. 37 (1998) 3319.
[4] M. Yashima, J. Am. Ceram. Soc. 85 (2002) 2925.
[5] F. Izumi and T. Ikeda, Mater. Sci. Forum. 321-324 (2000) 198.

[6] F. Izumi and R. A. Dilanian, Recent Res. Develop. Phys. 3 (2002) 699.
[7] K. Momma and F. Izumi, Commission on Crystallogr. Comput., IUCr Newslett. 7 (2006) 106.

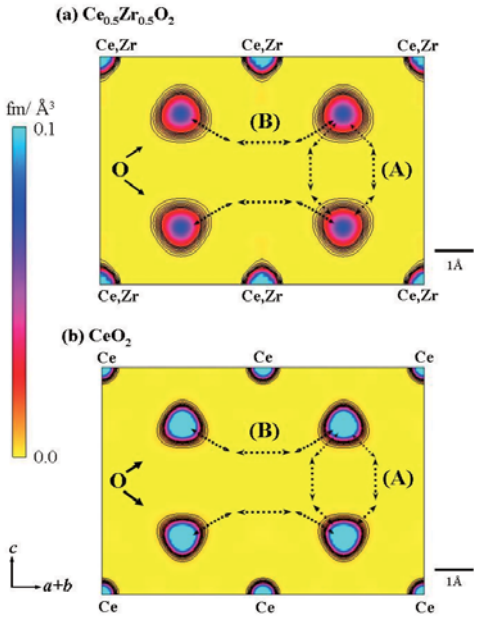


Fig. 1. Nuclear density distributions on the (110) planes of (a) Ce0.5Zr0.5O2 and (b) CeO2 with black contours in the range from 0.7 to 5.0 fm / angstrom3 (0.5 fm / angstrom3 step) at 1832 K and 1826 K, respectively.

1-1-14

Magnetic structure in CuFeP6$_6$

Miwako Takahashi[1], Ejaz Ahmed[1],Ken-ichi Ohshima[1] and Yukio Noda[2]
Inst. of Mat. Sci., Univ. of Tsukuba[1], IMRAM, Tohoku Univ.[2]

$CuFePt_6$ is one of the newly found ternary alloys $CuMPt_6$ (M; 3d elements). It has fcc fundamental structure and forms Cu_3Au-type ordered structure below 1313 K. Magnetic susceptibility shows different behavior for the alloys with disordered and ordered structures, indicating strong relation between magnetic properties and atomic ordered structures. Temperature dependence of magnetic susceptibility shows ferromagnetic transition for the alloys in both ordered and disordered state: at $T_C = 200$ K for the ordered state and at $T_C = 185$ K for the disordered state. Below T_C, susceptibility under FC and ZFC processes shows different behavior. The former shows normal ferromagnetic behavior but the latter shows successive antiferromagnetic-like transitions at $T_N = 100$ K for the ordered state and at $T_{N1} = 90$ K and $T_{N1} = 30$ K for the disordered state. On the other hand, variation of magnetization at 5 K shows typical ferromagnetic curves with little hysteresis for the alloys in both ordered and disordered states.

The magnetic structure of the alloy with both ordered and disordered state has been studied with a four-circle diffractometer, FONDER at T2-2. Figure 1(a) shows temperature dependence of the intensities of magnetic scattering in the alloy with disordered state. magnetic intensities appear at 1 1 0 (X-point of fcc) below T_C, and at 1/2 1/2 0 below T_{N1}. These magnetic intensities begin to decrease below T_{N2}; measurement at lower temperature is required for the study of magnetic phase below T_{N2}.

In the alloy with ordered state, magnetic scattering appears at 1 1 0 (Γ-point of sc) below T_C and at 1/2 1/2 0 (*M*-point of sc) below T_N, the same point as in the alloy with disordered state but with much stronger intensities. Figure 1(b) shows temperature dependence of intensity and position of 110 magnetic peak. Below T_C, peak position show gradual shift with increasing intensity and takes almost constant value below T_N. These results indicate strong correlation between magnetic and atomic structures.

[1] M. Takahashi, E. Ahmed, A. K. Das, Y. Fujii, H. Iwasaki and K. Ohshima : J. Alloys. Compd. in print.

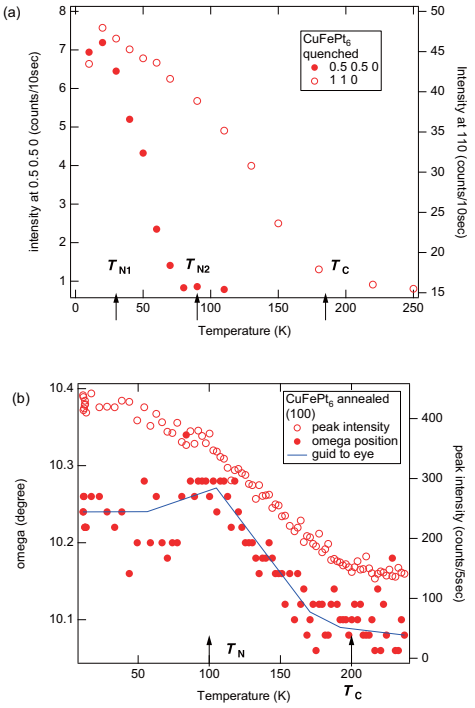


Fig. 1. (a)Temperature dependence of the intensities at 1/2 1/2 0 (closed circles) and 1 1 0 (open circles) in disordered state. (b) Temperature dependence of peak position (closed circles) and peak intensity (open circles) at 1 1 0 in ordered state.

1-1-15

Magnetic excitation in $CuFeP6_6$

Miwako Takahashi[1], Ejaz Ahmed[1],Ken-ichi Ohshima[1] and Naoto Matsura[2]
Inst. of Mat. Sci., Univ. of Tsukuba[1], ISSP, Univ. of Tokyo[2]

Ternary alloy $CuFePt_6$ shows anomalous magnetic behavior[1]. It has fcc fundamental structure and forms Cu_3Au-type ordered structure below 1313 K. The alloys with both ordered and disordered states undergo ferromagnetic and antiferromagnetic transitions, though the transitions take place at different temperatures in the different ordered states. Temperature dependence of magnetic susceptibility first shows ferromagnetic transition at $T_C = 200$ K for the ordered state and at $T_C = 185$ K for the disordered state. Below T_C, susceptibility under FC and ZFC processes shows different behavior. The former shows normal ferromagnetic behavior but the latter shows successive antiferromagnetic-like transitions at $T_N = 100$ K for the ordered state and at $T_{N1} = 90$ K and $T_{N1} = 30$ K for the disordered state. Magnetic diffraction under zero-magnetic field shows magnetic scattering at 110 (X-point in fcc disordered state and Γ-point in sc ordered state) below T_C, and 1/2 1/2 0 (M-point in sc ordered state) below T_N and T_{N1}. The results indicate competitive existence of the two types of magnetic structures in the alloy and the magnetic phase is sensitively dependent on the magnetic field and the atomic arrangement. To investigate dynamical fluctuation in the ferromagnetic and antiferromagnetic structures, inelastic neutron scattering was performed at the triple-axis-spectrometer PONTA.

Figure 1(a) shows observed inelastic peaks with ΔE below 4 meV (black closed circles) and above 4 meV (open circles) at 7 K on (hkk) plane in the alloy with ordered state. In the figure, green, blue and red closed circles represent 000 (Γ-point), 011 (Γ-point in ordered and X-point in disordered state), and 0 1/2 1/2 (M-point in ordered state), respectively. Inelastic peaks below $\Delta E < 4$ meV show no dispersion and do not appear at the equivalent points. Inelastic intensities along 0kk and 1kk at $\Delta E = 2$ and 3 meV are shown in Fig.1(b). At $k = 0.45$ and 0.65 of 0kk line, inelastic peaks with both $\Delta E = 2$ and 3 meV appear, though no clear peaks are observed along the symmetrical line of 1kk. The inelastic peaks are found to persist far above T_N. Further experiments should be necessary to clarify the origin of the magnetic excitation.

[1] M. Takahashi, *et al* : J. Alloys. Compd. in print.

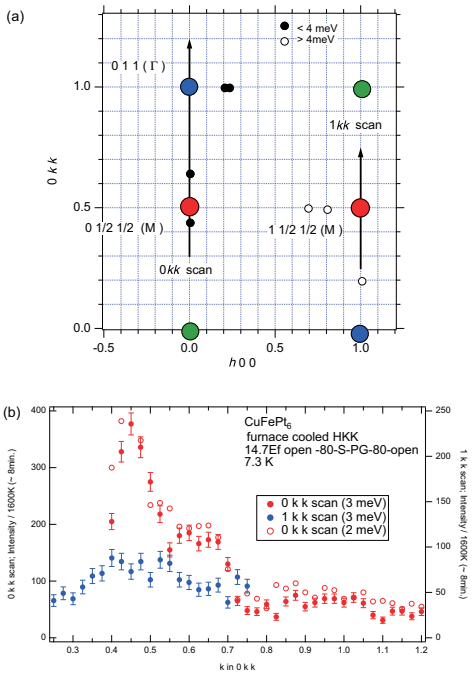


Fig. 1. (a)Inelastic peaks with ΔE below and above 4 meV (closed and open black circles) at 7 K. (b) Inelastic intensities along 0kk(red circles) and 1kk(blue circles) at $\Delta E = 2$ (open circles) and 3 meV (closed circles).

1-1-16

Neutron scattering study of phonon dynamics on La3Pd20Ge6

C. H. Lee(A), H. Yoshizawa(B), I. Hase(A), Y. Nemoto(C) and T. Goto(C)
(A) AIST, (B) ISSP, (C) Niigata Univ.

A large vibration of an atom in an oversized atomic cage, so called rattling, has attracted great interest since it can be the origin of exotic physical properties. La3Pd20Ge6 is one of those compounds that have large atomic cages filled with La guest atoms. Ultrasonic measurements show that the elastic constant C44 of La3Pd20Ge6 exhibits a Debye-type dispersion around T = 20K [1]. It is proposed that the phenomenon is originated from the rattling motion of La atoms, but there is still no direct evidence. Rather, the feature of a rattling motion is still controversial. In the present work, thus, we study phonon dynamics of La3Pd20Ge6 by inelastic neutron scattering and try to understand the reason of the Debye-type dispersion as well as the nature of rattling.

Neutron scattering measurements were carried out using the triple-axis spectrometer, TOPAN, GPTAS and HER, at the JRR-3 reactor of JAEA at Tokai. The final neutron energy was fixed at Ef = 14.8 meV or 5.4 meV using a pyrolytic graphite monochromator and an analyzer. The sequences of the horizontal collimators were 40′-40′-S-40′-40′, 40′-60′-S-60′-60′, open-S-80′-80′ or open-S-40′-40′, where S denotes the sample position. Total sample vomule of La3Pd20Ge6 single crystals used for the measurements was about 1.3cc.

Fig. 1 shows the phonon dispersion curve of La3Pd20Ge6 with propagation vector of [100]. The optical phonon mode observed at E = 1 meV around zone center corresponds to a guest mode, in which La atoms vibrate largely. Around q=(0.08,0,0), the guest mode shows anti-crossing behavior with acoustic phonon mode as other cage compounds[2-4]. Characteristically, the guest mode is quite dispersive, different with other cage compounds where guest modes are almost dispersionless. This suggests that an interaction between La-La atoms exists. Temperature dependence of the guest phonon energy exhibits hardening below T = 50 K, indicating strong anharmonicity. The relationship between the hardening and the Debye-type dispersion observed by ultrasound measurements is now under consideration.

[1] T. Goto et al., Phys. Rev. B 70 (2004) 184126
[2] C. H. Lee et al., J. Phys. Soc. Jpn. 75, (2006) 123602
[3] C. H. Lee et al., J. Phys.: Conf. Ser. 92, (2007) 12169
[4] C. H. Lee et al., J. Phys. Soc. Jpn. Suppl. (2008) in press

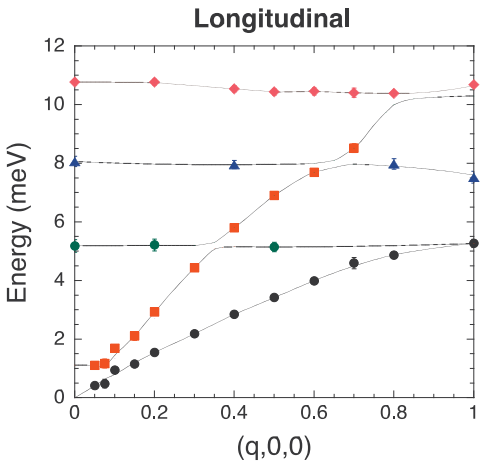


Fig. 1. Phonon dispersion curves of longitudinal phonon modes with propagation vector [100] in La3Pd20Ge6.

1-1-17

Lattice dynamics of NaNbO3

I. Tomeno(A), Y. Tsunoda(B), M. Nishi(C), M. Matsuura(C), K. Oka(D)
(A)Faculty of Education and Human Studies, Akita Univ., (B)School of Science and Engineering, Waseda Univ., (C)ISSP, Univ. of Tokyo, (D)Nanoelectrics Research Institute, AIST

Sodium niobate NaNbO3 exhibits a complex sequence of structural phase transitions as a function of temperature.[1] Above 913 K, NaNbO3 has a simple cubic perovskite structure. Below this temperature, there are at least six phases. Antiferrodistortive (AFD), antiferroelectric (AF), and ferroelectric (FE) phases have been identified in NaNbO3. The complexity of the phase transitions suggests the existence of competing structural instabilities in cubic NaNbO3.[2] We studied the lattice dynamics of cubic NaNbO3. Inelastic neutron scattering measurements were performed using the triple-axis spectrometer T-11 (HQR) at JRR-3M.

Figure shows constant-E scans for the [1, 1, 0] direction polarized along the [1, -1, 0] direction determined at 970K. In contrast, constant-E scans for the same direction polarized along the [0, 0, 1] showed that the TA phonon energy is approximately 8 meV at the M point. This indicates that the M-point TA phonons with polarization along [1, -1, 0] soften significantly in the cubic phase. Furthermore, we found out the softening of the R-point TA phonons. Softening of these zone-boundary phonons (the M3 and R25 modes) is interpreted by the instability of rotational modes of oxygen octahedra. In addition, preliminary experiments show the softening of long-wavelength TO phonons for the [1, 1, 0] direction polarized along the [0, 0, 1] direction. Present results roughly explain the diffuse X-ray scattering data in the cubic phase.[3] The complicated situation of soft modes at zone-center and zone-boundaries seems related with the existence of the sequence of phase transitions below 913 K. Further experiments are necessary to investigate phonon dispersion relations in cubic NaNbO3.

References
[1] C. N. W. Darlington and K. S. Knight, Physica B266, 368 (1999).
[2] W. Zhong and D. Vanderbilt, Phys. Rev. Lett. 74, 2587 (1995).
[3] F. Denoyer, R. Comes, and M.Lambert, Acta Cryst. A27, 414 (1971).

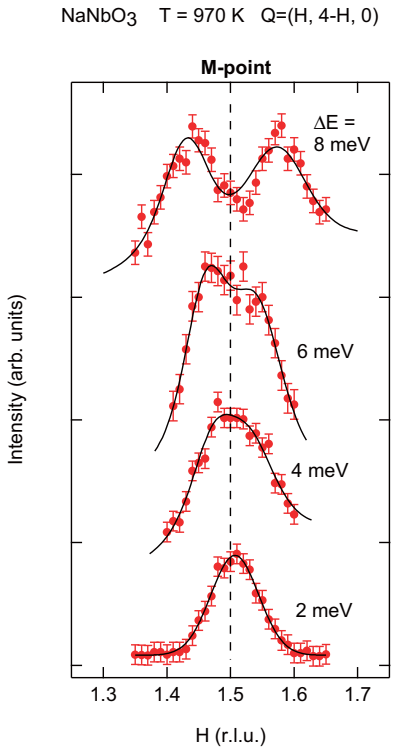


Fig. 1. Constant-E scans around the zone-boundary M point measured at 970 K.

1-1-18

Crystal Structure of Mg-doped apatite-type Ionic Conductor

Y. Matsushita[1], T. Wakita[2], H. Yoshioka[3], M. Yashima[2], and F. Izumi[1]
[1] *Quantum Beam Center, National Institute for Materials Science*
[2] *Interdisciplinary Graduate School of Science and Engineering, Tokyo Institute of Technology*
[3] *Hyogo Prefectural Institute of Technology*

Oxygen-ionic conductors are very important materials for various kinds of applications such as fuel cells and oxygen-gas sensors. In 1995, Nakayama found new type of oxygen-ionic conductor; Ln-Si-O apatites (Ln = Lanthanoids). [1] [2] These compounds show better oxygen ionic conductivity in middle range of temperature compared with other famous oxygen-ionic conductors (ZrO_2 and/or CeO_2-based materials). Recently, Yoshioka reported that Mg-doped apatites show the best ionic conduction. [3] However, in all of the apatite system, details of mechanism of ionic conduction are still under question. In this study, we carried out powder neutron-diffraction technique to understand crystallographic details of Mg-doped Apatite-type ionic conductor.

The Mg-doped apatite-type sample was prepared by sol-gel method. [3] The chemical composition of the sample, $La_{9.7}(Si_{5.7}Mg_{0.3})O_{26.3}$, was determined by inductively coupled plasma measurements.

The neutron powder-diffraction measurement at room temperature, was carried out using IMR-HERMES diffactmetor (T1-3), installed in the JRR-3M reactor. The wavelength of neutron was 0.18265 nm, which was vertically focused by a (331) Ge monochromator. The resulting diffraction data were analyzed by the Rietveld method with RIETAN-FP [4] and whole-pattern fitting approach based on the maximum-entropy method (MPF) [5].

The Rietveld refinement was performed with neutron powder diffraction data of $La_{9.7}(Si_{5.7}Mg_{0.3})O_{26.3}$ on the basis of hexagonal $P6_3/m$. The calculated pattern agreed well with that of observed pattern. The refinement was carried out with anisotropic thermal displacement parameters for all the lanthanum sites and the oxygen sites. The final convergent indexes were Rwp = 3.68 %, Rp = 2.67 %, RR = 5.04 %, Re = 0.75 %, RI = 1.08 %, and RF = 0.46 %. The obtained cell parameters from the Rietveld analysis were a = 0.97384(3) nm, and c = 0.72140(2) nm. On the Rietveld refinement process, the interstitial oxygen positions were not able to be clearly observed. However, the oxygens may locate around the La2 site from crystallochemical point of view.

References

[1] S. Nakayama *et al.*: J. Mater. Chem. **5** (1995) 1801.
[2] S. Nakayama *et al.*: Chem. Lett. **24** (1995) 431.
[3] H. Yoshioka *et al.*: Chem. Lett. **33** (2004) 392.
[4] F. Izumi and T. Ikeda: Mater. Sci. Forum **321-324** (2000) 198.
[5] F. Izumi and R. A. Dilanian: Recent Res. Develop. Phys. **3** (2002) 699.

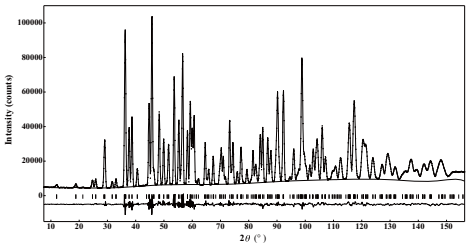


Fig. 1. Powder neutron diffraction profile of $La_{9.7}(Si_{5.7}Mg_{0.3})O_{26.3}$.

1-1-19

Crystal structure and ionic conductivity of Ga system oxides for solid electrolyte of fuel cell

Yasushi Idemoto, Tomomasa Sugiyama and Naoto Kitamura
Tokyo University of Science

Gallate-based oxides are regarded as promising candidates for the electrolyte of SOFC, because of their high conductivities and high chemical stabilities. In the oxides, partial substitution of aliovalent cations introduces oxygen vacancies and/or protons, and results in significant oxide ion and/or proton conduction above 500 K. Thus, it is important to clarify their crystal structures and nuclear densities of the oxide ion and the protons at elevated temperature. Due to the difficulty in structural analysis on such light atoms, however, there are not enough knowledge on them. In order to make these clearer, we focused on La0.8Sr0.2Ga0.8Mg0.2O3-d (LSGM) and La0.8Sr0.2Ga0.8Mg0.115Co0.085O3-d (LSGMC) as oxide ion conductor and La0.9Ba1.1GaO4 (LBG) as proton conductor, and investigated them with neutron diffraction measurements.

We obtained LSGM and LSGMC powders by heat-treating precursors prepared by AGC SEIMI CHEMICAL CO., LTD. LBG was synthesized with solid-state reaction using each oxide or carbonate as a starting material. As for the products, we characterized their phases by XRD, compositions by EDX, and oxygen nonstoichiometry by microbalance. Conductivity measurements were also performed at elevated temperatures. In order to clarify the crystal structures, neutron diffraction patterns were measured using HERMES of IMR at the JRR-3M, and these patterns were analyzed with the Rietan-2000. The measurements were performed at 298˜680 K. The nuclear densities were also estimated based on MEM using the PRIMA

From XRD patterns, it was considered that both LSGM and LSGMC had a single phase of the perovskite-type structure and the lattice constants became smaller by Co substitution. Taking the ionic radii of Mg and Co into account, the results reflect that Co occupies 4c (Ga, Mg) site. Rietveld analysis using neutron diffraction patterns indicated that both LSGM and LSGMC could be attribute to orthorhombic Pnma at 298˜680 K. The oxygen content calculated from the site occupancy decreased with increasing temperature in LSGMC while that was essentially independent of temperature in LSGM. These behaviors are consistent with results of oxygen nonstoichiometry measurements. Based on the refined structure, we estimated the nuclear densities with MEM. As a result, it was indicated that the oxygen nuclear density began to spread as temperature increased and that such a tendency was more significant in LSGMC than LSGM. This may correspond with higher conductivity of LSGMC than LSGM. From the difference between the nuclear densities at 298 K and 680 K in LSGMC, it was suggested that oxygen at O1 site diffused toward the neighboring O2 site and vice versa.

Activity Report on Neutron Scattering Research: Experimental Reports **15** (2008)
Report Number: 468

1-1-20

Structural evaluation of nanotube and nanosheet layered titanate with novel nanostructures by neutron diffraction method

Takashi Kubo*, Masatomo Yashima, Atsushi Nakahira*
**Department of Materials Science, Graduate School of Engineering, Osaka Prefecture University, 1-1 Gakuen-cho, Naka-ku, Sakai-shi, Osaka, 599-8531, Japan, Department of Materials Science and Engineering, Interdisciplinary Graduate School of Science and Engineering, Tokyo Institute of Technology, Nagatsuta-cho 4259, Midori-ku, Yokohama, 226-8502, Japan*

Currently, the development of synthetic processing for various nanoscale materials is under intensive investigation1-3. Especially, titanate or titanium oxide based nanotubes, which are prepared by a soft chemical hydrothermal treatment of TiO2 particles in a highly concentrated NaOH aqueous solution, received much attention, because they are expected to be useful for various applications such as photocatalysts and solar cells etc form their nanotubular structures and high surface areas4,5. Furthermore, these TiO2-derived nanotubes synthesized by a soft chemical hydrothermal treatment possess ion exchange ability, such as sodium or hydrogen and have unique layered structures6-8. However, the clarification of detailed structure of nanotubes is still insufficient for these TiO2-derived nanotubes synthesized by a soft chemical hydrothermal treatment by the conventional analysis technique. Especially, since these TiO2-derived nanotubes synthesized by a soft chemical hydrothermal treatment of TiO2 contain hydrogen in its nanotubular structure, the neutron powder diffraction analysis is useful for clarifing these nanotubular titanate. In this study, the fabrication of the titanate nanotubes have been attempted by a soft chemical hydrothermal treatment of TiO2 with a NaOH aqueous solution by the use of deuterated 10 M NaOH solution during a soft chemical hydrothermal treatment of TiO2.

Nanotubular titanate products were synthesized by the soft chemical processing, that is, hydrothermal treatment in NaOH solution and subsequently the evaluation of its structure was attempted by the neutron diffraction method. The detailed experimental procedures are described elsewhere6-8. Products were synthesized in deuterated 10 M NaOH solution at 383 K for 96 hours by the hydrothermal treatment. Products were filtered with Buchner and washed sufficiently with deuterated water. Samples were dried and crashed with Al2O3 mortar.

The neutron powder diffraction experiments were conducted using the neutron powder diffractometer installed on Tl-3 port of JRR-3M reactor in the Japan Atomic Energy Research Institute (JAERI), Tokai, Japan. Neutron powder diffraction experiments were carried out in air at room temperature. Neutron powder diffraction measurements were conducted in air atmosphere with a 150-detector system, HERMES. An incident neutron wavelength λ = 0.18196 nm was obtained from a Ge (311) monochromator. The ND data were collected on thoroughly ground powders by a multiscanning mode in the 2 θ range from 5° to 155° with a step width of 0.10°. The 3 g powder sample was wrapped by tungsten foil to form a cylindric shape (10 $\phi \times$ 30 mm). The characterization of as-prepared titanate products in deuterated NaOH solution by hydrothermal treatment and subsequently washed with deuterated water was evaluated.

These products possessed nanotubular nanostructure with a few nanometer in diameter and some hundred nm in length and identified to be H2TinO2n+1 as shown in Figure 1(A). From TEM ob-

servation (not shown here), these products were open-ended nanotubes with average inner diameter of approximately 5 nm and outer diameter of approximately 10 to 15 nm. The products had high surface are over 200 m2/g. Figure 1(B) shows the results of neutron powder diffraction for as-prepared titanate products in deuterated NaOH solution by hydrothermal treatment. In this study, some sharp peaks were confirmed by the neutron powder diffraction measurements. From the neutron powder diffraction measurements, the background of the neutron powder diffraction pattern was high. This is caused by the insufficient exchange of hydrogen and deuterium. These results suggest that TiO2-derived nanotubes synthesized by a soft chemical hydrothermal treatment at 383 K contained some anatase structures. Thus, the further study on the effect of synthetic condition on the structure of nanotube titanate derived from TiO2 is needed for the precise investigation.

1. S. Iijima, Nature, 354, 56 (1991).
2. P. Hoyer, Langmuir, 12, 1411 (1996)
3. T. Kasuga, M. Hiramatsu, A. Hosono, T. Sekino and Niihara, Langumuir, 14, 3160 (1998).
4. G. H. Du, Q. Chen, R. C. Che, Z. Y. Yuan and L. M. Peng, Appl. Phys. Lett., 79, 3702 (2001).
5. Q. Chen, W. Zhou, G. Du and L. M. Peng, Adv. Mater, 14, 1208 (2002).
6. A. Nakahira, W. Kato, M. Tamai, T. Isshiki, K.Nishio and H. Aritani, J. Mater. Sci., 39, 4239 (2004).
7. A. Nakahira, T. Kubo, Y. Yamasaki, T. Suzuki and Y. Ikuhara, Jpn. J. Appl. Phys., 44, 690 (2005).
8. T. Kubo, W. Kato, Y. Yamasaki and A. Nakahira, Key Eng. Mater., 317-318, 247 (2006).

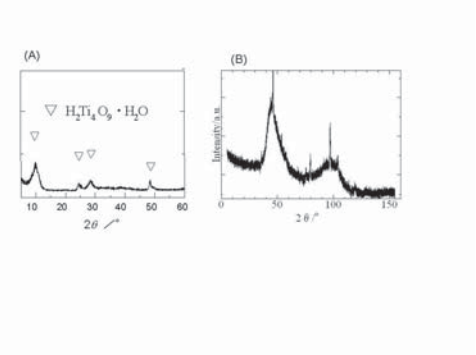


Fig. 1. Figure 1 (A) conventional XRD and (B) neutron diffraction result

1-1-21

Neutron Critical Diffuse Scattering of Quantum Relaxor KTaO3:Li

Hiroko Yokota and Yoshiaki Uesu
Deaprtment of Physics

Because the phase transition temperature of KLT-6.8% is 87 K, the distribution of the diffuse scattering is measured at 90 K. It is known in relaxors that polar nano regions (PNRs) starts to appear at the Burns temperature Td which is higher than the dielectric maximum temperature. Therefore, measurements to observe diffuse scatterings from PNRs should be performed above the phase transition temperature. In the diffuse scattering distributions around (110) at room temperature and 90K, a streak elongating along the [100] direction is observed at both temperatures. The origin is not clear at present. However it exists even at room temperature, therefore the existence is not related to the change in the polar state in KLT. So we neglect the effect when we analyze the diffuse scattering due to PNRs. At 90 K, the intensity along [-1 1 0] direction becomes stronger, which signifies the occurrence of the mosicity. It is observed that the tail of the diffuse scattering intensity expands along the [100] and [010] directions to form a crossed rod. The diffuse scattering from PNRs does not appear at the (220) reciprocal point. This phenomenon is coincident with the result of Toulouse et al. The temperature dependence of the diffuse scattering at (1.032, 1, 0) reciprocal point shows that below 80 K, the diffuse scattering intensity begins to increase with decreasing temperature probably because of the influence of Bragg intensity. With heating the specimen, the diffuse scattering increases abruptly and shows a peak around 85 K, which indicates the first order nature of the ferroelectric phase transition at Tp. the q dependence of the diffuse scattering is shown. Although a clear disappearance of the diffuse scattering intensity which is expected at Td is not observed, the intensity decreases toward 160 K. This fact does not contradict our conclusion that Td is located around 140 K by our X-ray diffraction measurement.

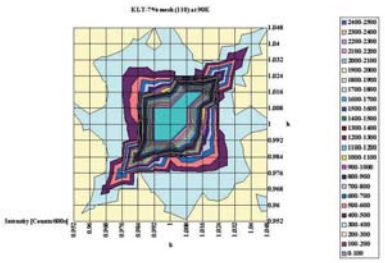


Fig. 1. 逆格子点 (1 1 0) 周辺における散漫散乱測定

1-1-22

Dependence of crystal structure and ferroelectric property on composition and heat treatment for (Pb,Si)(Zr,Ti,Nb)O3 ferroelectric material

Yasushi Idemoto and Shoko Komiya
Department of Pure and Applied Chemistry, Faculty of Scince and Technology, Tokyo University of Science, 2641 Yamazaki, Noda-shi, Chiba 278-8510

In Ferroelectric random access memory (FeRAM), PbZrzTi1-zO3 (PZT), which is one of the most widely study ferroelectric materials, is considered as a candidacy because of high remanent polarization (Pr). However, poor ferroelectric reliability of the PZT capacitor is a long-standing problem, and there are many studies on improvement of the electrode material. For improvement of these problems, we have synthesized the bulk samples of (Pb0.98Si0.02)(ZrzTi0.95-zNb0.05)O3, (z=0.2˜0.5) and (Pb1-ySiy)(Zr0.30Ti0.7-xNbx)O3, (x=0˜0.10; y=0.02, 0.04) [PZTNS] ferroelectric materials prepared by a solid-state reaction. We investigated the relationship between the properties, crystal structure and ferroelectric characteristics. Nb was substituted up to 0.05 in the samples by adding PbSiO3 (PSO).

As for the products, we characterized their phases by XRD, compositions by Inductively Coupled Plasma(ICP) and EDX. P-E hysterisis loop was measured at room temperature by TF-2000. Capacitance and tan δ was measured by using LCR meter. We measured powder neutron diffraction using HERMES of IMR at the JRR-3M, and determined the average crystal structures using the Rietveld method on the basis of space P4mm with Rietan-2000[1]. These measurements were performed at 298K. The nuclear densities were also estimated based on MEM using the PRIMA[2].

The lattice parameter ratio, a/c , of PZTNS samples decreased compared to PZT. The relative densities of pellets were almost over 95%. From the P-E hysteresis measurements, the hystersis loop of the Nb substituted PZTNS has a good square shape, and the remanent polarization (Pr) increased and the coercive field (Ec) decreased with Nb substitution. Moreover, Pr increased and Ec decreased with the increasing PSO addition content. From the crystal structure analysis, the position of the M(Zr, Ti, Nb) site moved to the ideal position with the Nb substitution. The formation of the oxygen vacancies was suppressed since the bond valence sum of the M(Zr, Ti, Nb)O6 octahedron increased. The flatness of the M(Zr, Ti, Nb)-O2 plane increased by the Nb substitution[3]. It is suggested that these factors lead to the squareness of the hystersis loop and improves the ferroelectric property.

References

[1] F. Izumi and T. Ikeda, Mater. Sci. Forum, 198,321(2000).
[2] F. Izumi and R. A. Dilanian, "Recent Research Developments in Physics," Vol. 3, Part II, Transworld Research Network, Trivandrum (2002), pp.699-726.
[3] Y. Idemoto, S. Komiya, Mater. Tech., in print.

1-1-23

Structural Defect and Ionic Conduction of Hydroxyapatite

H. Fujimori(A), K. Okanishi(A), K. Ohoyama(B), M. Yashima(C)
(A)Graduate School of Science and Engineering, Yamaguchi Univ, (B)Institute for Materials Research, Tohoku Univ., (C)Interdisciplinary Graduate School of Science and Engineering, Tokyo Institute of Technology

Hydroxyapatite is one of the most interesting materials in current technologies due to its wide possible applications as biomaterials and electrical devices. Its physical and chemical properties relating to such uses strongly depend on the crystal structure. Especially the stability of OH ion in the structure of hydroxyapatite has been suggested to be closely related to decomposition and ionic conductivity of hydroxyapatite. The OH lattice sites have been reported to be the conduction path of hydroxyapatite and to play an important role in the proton conduction. Thus, it is of vital importance to study OH ion at wide region of temperatures. However, information of hydrogen and oxygen ions is difficult to be detected by the powder X-ray diffraction (XRD) technique. The information contained in the characteristic spectral features of the OH group leads to the identification of important structural characteristics that cannot be made by XRD. Previously we performed Raman scattering of hydroxyapatite at temperatures up to 1200 oC by a new system of ultraviolet (UV) Raman spectroscopy. However, this technique is physically impossible to decide the position and diffusion path of proton. Thus, in this study we have successfully determined the position and diffusion path of deuterium in hydroxyapatite using neutron powder diffraction data by a whole-pattern fitting approach based on the maximum-entropy method (MEM).

Neutron powder diffraction data of deuterium-substituted hydroxyapatite were collected at 23 K, 300K, 673K, and 1073 K using the HERMES powder diffractometer installed at the JRR-3M research reactor of the Japan Atomic Energy Agency. Incident neutrons with a fixed wavelength of 1.8265(1) angstroms were obtained by a vertically focusing (331) Ge monochromator. The powder diffraction data were measured over a 2 theta range of 6-156 degrees. The diffraction data were analyzed by a combination of the Rietveld method and MEM using the computer programs RIETAN-FP and PRIMA. The space group was assumed to be P21/b for the structure at 23 K and 300 K. The refinements of the structure at 673 K and 1073 K were undertaken in P63/m. MEM analysis was conducted with the structure factors obtained from Rietveld analysis.

The figure 1 shows the scattering amplitude distribution of hydroxyapatite with P63/m structure at 1073 K, indicating deuterium ionic conduction along [001] direction. On the other hand, deuterium ion was almost localized at 673K, where the conductivity has been reported to be low.

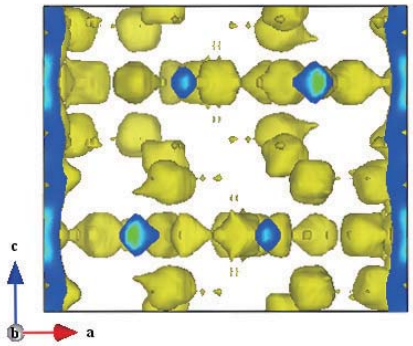


Fig. 1. The scattering amplitude distribution of hydroxyapatite with P63/m structure at 1073 K drawn by VESTA.

1-1-24

Neutron diffraction study on SnO2-CeO2 system

K. Nomura (A), H. Kageyama (A), T. Maekawa (B), C. Minagoshi (B), S. Nakamura (B), and T. Ito (B)
(A) National Institute of Advanced Industrial Science and Technology (AIST), (B) New Cosmos Electric Co., Ltd.

Recently, SnO2-based materials have been investigated as transparent conductive oxides, oxidation catalysts, and the sensing materials of semiconductor gas sensors [1]. Of these, as the sensing materials of sensors, SnO2-MOx (M = Al, Ce, etc.) systems have been mainly used. However, the detailed crystal structures of these systems are not clear yet. In the present study, we measured the neutron diffraction data of SnO2-CeO2 system at room temperature (297K), and investigated the crystal structure and the nuclear density distributions.

High purity (SnO2)(CeO2)x powder samples were prepared by a solid-state reaction method. Neutron diffraction measurements were performed with HERMES installed at JRR-3M in JAEA (Tokai) [2]. Neutron wavelength was 1.8265(1)A. Diffraction data were collected in the 2 θ range from 20 to 153 deg in the step interval of 0.1 deg. The diffraction data obtained were analyzed by the combination technique of Rietveld analysis using a computer program RIETAN-2000 [3] and a maximum-entropy method (MEM)-based pattern fitting. MEM calculation was carried out using a computer program PRIMA [4].

All the reflection peaks of (SnO2)(CeO2)x (x = 0, 0.03) were indexed by a tetragonal symmetry (P42/mnm, No.136). The assumed structure model was as follows: Sn4+ and Ce4+ ions occupy 2a sites (0, 0, 0) and oxide-ions occupy 4f sites (x, y, 0) (x = y ~ 0.36) [1]. The lattice parameters (a, c) and unit cell volume (V) increased with an increase in CeO2 content, suggesting an introduction of larger Ce4+ ions (0.97A) [5] into Sn4+ (0.64A) [5] sites. The pure SnO2 sample showed narrow peak width and low background intensities, whereas the CeO2-doped samples wide peak width and higher background intensities.

Figure 1 shows (a) the crystal structure and (b) the equicontour surfaces of scattering amplitude (0.05fm/A^3) of (SnO2)(CeO2)0.03. The nonsphere-shaped equicontour surfaces appeared at 4f (oxide-ion) sites.

References

[1] M. Batzill and U. Diebold, Progress in Surface Science, 79, 47 (2005).
[2] K. Ohoyama, T. Kanouchi, K. Nemoto, M. Ohashi, T. Kajitani, and Y. Yamaguchi, Jpn. J. Appl. Phys., 37, 3319 (1998).
[3] F. Izumi and T. Ikeda, Mater. Sci. Forum, 321-324, 198 (2000).
[4] F. Izumi and R.A. Dilanian, in: Recent Research Developments in Physics, vol.3, Transworld Research Network, Trivandrum, 2002, p.699.
[5] R.D. Shannon, Acta Cryst., A32, 751 (1976).

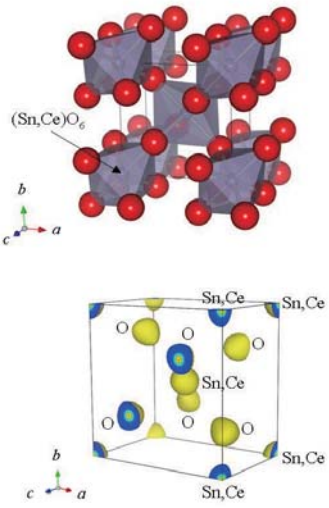


Fig. 1. (a) Crystal structure and (b) equicontour surfaces of scattering amplitude (0.05fm/A^3) of (SnO2)(CeO2)0.03.

1-1-25

Magnetic Phase Transition and Electric Polarization Flop of $TmMn_2O_5$

M. Fukunaga[1], K. Nishihata[1], H. Kimura[1], Y. Noda[1], and K. Kohn[2]
[1] *IMRAM, Tohoku University,* [2] *Waseda University*

We have performed simultaneous measurements of magnetic neutron diffraction, ferroelectric *D*–*E* hysteresis loops and the permittivity along the *a*-axis of $TmMn_2O_5$ at FONDER. $TmMn_2O_5$ is a rare-earth (R) manganese oxide of the form RMn_2O_5, which is known as multiferroic materials that exhibit coupling between ferroelectricity and magnetic ordering. It is believed that ferroelectricity of RMn_2O_5 appears only along the *b*-axis, and application of the electric field along the *a*-axis has not been performed. It was observed that neither the neutron diffraction profiles nor the phase transition temperatures depend on the applied electric field along the *a*-axis as well as the *b*-axis. But interesting results were obtained by the simultaneous measurement.

Figure 1 exhibits simultaneous measurement results of the magnetic propagation wave vector q_x, q_z, integrated intensity, and the remanent polarization along *a*- and *b*-axes of $TmMn_2O_5$ below 6 K, where a low-temperature incommensurate magnetic phase (LT-ICM1) changes into another magnetic phase (LT-ICM2). The filled symbols (with the electric field along the *a*-axis), the open symbols (*b*-axis) and q_x were measured separately. Although the dielectric properties along *a*- and *b*-axes of the same sample cannot be measured simultaneously, neutron diffraction results measured simultaneously with the dielectric properties guarantee the temperature axis of the two experiments. It was clearly obserbed that the decrease in the polarization along the *b*-axis coincides the decrease in the LT-ICM1 phase, and the increase in the polarization along the *a*-axis coincides the increase in the LT-ICM2 phase. As a result, it seems that the polarization flops from the *b*-axis to the *a*-axis. The polarization along the *a*-axis of RMn_2O_5 was observed probably for the first time. The inset shows the observed *D*–*E* hysteresis loop along the *a*-axis at 4.3 K, in which the linear permittivity component is subtracted.

The two magnetic phases exhibit almost the same magnetic propagation wave vector, but different magnetic structures cause the different dielectric properties. Magnetic structure analyses of both phases are required to discuss the difference between the two phases.

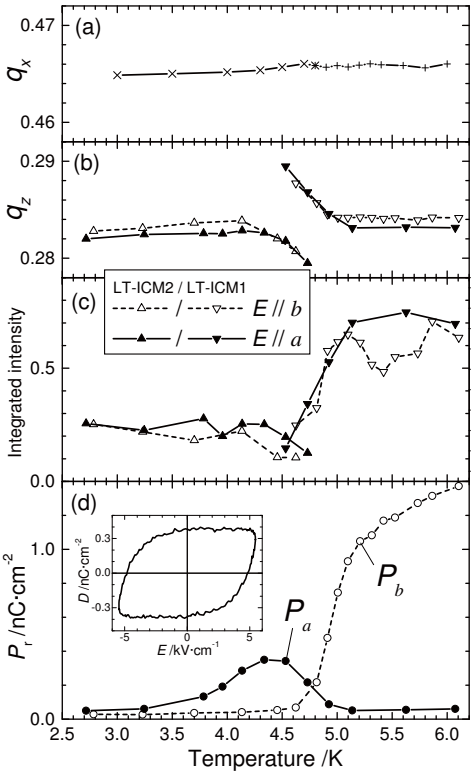


Fig. 1. Simultaneous measurement results of (a) the propagation wave vector q_x, (b) q_z,(c) integrated intensity, and (d) remanent polarization along *a*- and *b*-axes, P_a and P_b of $TmMn_2O_5$ during cooling.

1-1-26

Split-hydrogen sites in trioctahedral micas

Kiyotaka Ishida and Hiroshi Fukazawa
Kyushu University, Japan Atomic Energy Agency

Two kinds of the deuterated tetra-germanium magnesium micas, KMg2.5Ge4O10(OD)2 and KMg2.5(Ge3D4)O10(OD)2, have synthesized by a Tuttle type cold-seald hydrothermal equipment, and their neutron diffraction data were obtained in success by HERMES. Their crystal structure refinment have done by Rietan-2000. Further sructure analysis are on the move.

1-1-27

Powder Neutron Diffraction Measurements of One-dimensional Magnets $MPb_4Sb_6S_{14}$ (M = Fe, Mn)

Yoshitaka Matsushita[1], Masakazu Nishi[2], and Satoshi Watanabe[2]
[1] *Quantum Beam Center, National Institute for Materials Science*
[2] *Institute for Solid State Physics (ISSP), The University of Tokyo*

One-dimensional (1D) Heisenberg antiferromagnetic chain (HAF) compounds in magneto-chemistry and physics fields have attracted considerable interest, because most of them have been served as a prototypical model in quantum statics. Haldane theoretically predicted that 1D-HAF systems having integer spin quantum number ($S = 1, 2, \cdots$) should have a spin energy gap called as Haldane-gap between the ground state and the first excited state, in contrast to the case of half-integer spin quantum number ($S = 1/2, 3/2, \cdots$). [1] Since Haldane's prediction, extensive studies have been carried out on 1D-HAF systems with integer S. In 1986, the first $S = 1$ compound with Haldane gap, $[Ni^{2+}(en)_2NO_2](ClO_4)$ (so called as NENP) was discovered by Renard and his co-workers as the real system. [2] After the discovery of this compound, some of $S = 1$ Haldane gap compounds have been studied. [3]

We propose the rare $S = 2$ Haldane candidate mineral semiconductor compound, $Fe^{2+}Pb_4^{2+}Sb_6^{3+}S_{14}^{2-}$ (Jamesonite, hereafter FPSS). It is the isomorphic compound of $Mn^{2+}Pb_4^{2+}Sb_6^{3+}S_{14}^{2-}$ (Bénavidésite, hereafter MPSS). The several properties (structural, thermal, optical, electrical, magnetic properties) and synthetic condition of these compounds, had been reported. [4, 5, 6, 7] The monoclinic crystal structures of FPSS and MPSS consist of the lozenge-shaped $[Pb_4Sb_6S_{13}]$ and the rod-shaped $[MS_6]$ substructures (Fig. 1). In the structure, Fe^{2+} (d^6; $S = 2$) is located at the origin site (Wyckoff position; 2*a* in $P2_1/a$) and octahedrally coordinated by six sulfur atoms. The $[FeS_6]$ octahedra form the edge-shared 1D linear chain, running along the c-axis, as shown in Fig. 1. The shortest Fe$\cdots$Fe distance is 4.030(4) Å within the chain and 12.388(6) Å between the chains. Therefore, the magnetic inter-chain interaction should be weak, and FPSS can be regarded as an ideal 1D magnetic chain system with $S = 2$. From these crystallographic and magnetic properties, FPSS is expected to be a candidate of $S = 2$ Haldane compound. Apart from the argument of $S = 2$ Haldane compound, $S = 2$ 1D magnetic chain compound itself is rare. In the magnetic susceptibility measurements, FPSS showed 1D HAF behavior with a broad peak around 33.5 K, where a high-spin state ($S = 2$) of Fe^{2+} was estimated from a Curie-Weiss law fitting of magnetic susceptibility. Under 10K, FPSS shows two anomalies at $\sim$ 8 K and $\sim$ 3 K. [4, 5, 6] On the other hand, MPSS shows a broad peak around 25 K, and in lower temperature range small Curie tail are observed. However, both FPSS and MPSS did not show any long range ordering behaviors from results of magnetic susceptibilities (AC and DC), heat capacity and Mössbauer measurements, both compounds showed spin-glass behavior under low temperature range. [5, 6, 7] In 2004, Léone *et al.* reported powder neutron measurement using natural FPSS, and they observed extra peaks to be caused by magnetic long-range ordering. [8] The result is not consistent with our results. In this study, we carried out neutron powder-diffraction measurements using synthesized FPSS and MPSS compounds to understand magnetic behaviors these compounds.

The samples were prepared by solid-state reaction. [5] The neutron powder-diffraction measurement ($7^\circ \leq 2\theta < 157^\circ$)

was carried out using IMR-HERMES diffactmetor (T1-3), installed in the JRR-3M reactor. The wavelength of neutron was 1.8265(1) Å, which was vertically focused by a (331) Ge monochromator. The intensity data was observed at 4.0 K for FPSS and 1.4 K for MPSS, respectively.

Around 15.5° in 2θ, weak peaks are observed, but they are not matched with Léone's proposed magnetic ordering model. [8] To understand the details of magnetic behaviors of the compounds we need to examine under lower temperature with the higher resolution facilities.

References

[1] F. D.M. Haldane, Phys. Rev. Lett. **50** (1983) 1153.

[2] J. P. Renard *et al.*, Europhys. Lett. **3** (1987) 945.

[3] K. Katsumata, Current Opinion Solid State Mat. Sci. **2** (1997) 226, and references within.

[4] P. Léone *et al.*, Solid State Sci. **5** (2003) 771.

[5] Y. Matsushita, Y. Ueda, Inorg. Chem. **42** (2003) 7830.

[6] Y. Matsushita, Y. Ueda, Prog. Theor. Phys. **159** (2005) 179.

[7] S. Morimoto *et al.*, J. Mag. Mag. Materials **310** (2007) e962.

[8] P. Léone *et al.*, J. Mag. Mag. Materials **284** (2004) 92.

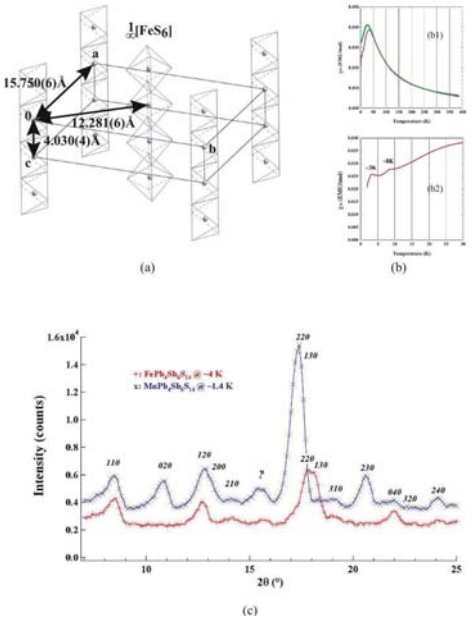


Fig. 1. 1) 1D-chain structure in FPSS. 2) Magnetic susceptibility of FPSS. 3) Neutron powder-diffraction diagram.

1-1-28

Crystal Structure of La-Ge-O Ionic Conductor

Yoshitaka Matsushita, Naohito Tsujii, Kiyoshi Kobayashi, and Fujio Izumi
Quantum Beam Center, National Institute for Materials Science

The La-T (T = Si and Ge) oxyapatites having chemical composition written as $Ln_{9.33\pm x}T_6O_{26\pm 3x/2}$, attract attention for the most promising oxygen-ionic conductor of next generation, and it has been measured the various kind of properties until now.[1, 2] These compounds show better oxygen ionic conductivity in the intermediate-temperature range compared with other famous oxygen-ionic conductors (ZrO_2 and/or CeO_2-based materials). However, the excess oxygen sites have not been found out, yet. The germanate compounds have low-temperature ($P\bar{1}$) and high-temperature ($P6_3/m$) forms. The two crystal structure models of low-temperature form had been proposed.[3, 4] In this study, we measured the intensity data using neutron powder-diffraction technique to identify the crystal structure of low-temperature germanate.

The germanate apatite sample ($La_{9.8}Ge_6O_{26.7}$) was prepared by solid-state reaction. All processes are carried out under air. The mixture of La_2O_3 and GeO_2 were calcined at 1273 K for 50 hours. Starting La_2O_3 was pre-heated at 1273 K for a night. The ground sample was pressed into the pellets, and re-heated up to 1273 K for 24 hours.

The intensity measurement at room temperature ($5^\circ \leq 2\theta < 156^\circ$), was carried out using IMR-HERMES diffactmetor (T1-3), installed in the JRR-3M reactor. The wavelength of neutron was 1.8265(1) Å, which was vertically focused by a (331) Ge monochromator. The resulting diffraction data were analyzed by the Rietveld method with RIETAN-FP [5] and whole-pattern fitting approach based on the maximum-entropy method (MPF)[6].

The cation compositions were fixed as chemical analysis result ($La_{9.8}Ge_6O_{26.7}$) on the Rietveld refinement. The space group was selected to $P\bar{1}$, and both reported structural models were examined. In current refinement process, the Pramana's model gave better fit. However, the refinement is not fully satisfied. The current convergent indexes were Rwp = 3.96 %, Rp = 2.93 %, RR = 6.15 %, Re = 0.78 %, RI = 0.89 %, and RF = 0.41 %. The obtained cell parameters from the Rietveld analysis were a = 9.929(2) Å, b = 9.920(2) Å, c = 7.2914(6) Å, α = 90.46(1) °, β = 89.04(1) °, and γ = 120.36(1) °.

References

[1] S. Nakayama *et al.*: J. Mater. Chem. **5** (1995) 1801.
[2] S. Nakayama *et al.*: Chem. Lett. **24** (1995) 431.
[3] L. Leon-Reina *et al.*: Chem. Mater. **15** (2003) 2099.
[4] S. P. Pramana *et al.*: Acta Crystal. **B63** (2007) 597.
[5] F. Izumi and T. Ikeda: Mater. Sci. Forum **321-324** (2000) 198.
[6] F. Izumi and R. A. Dilanian: Recent Res. Develop. Phys. **3** (2002) 699.

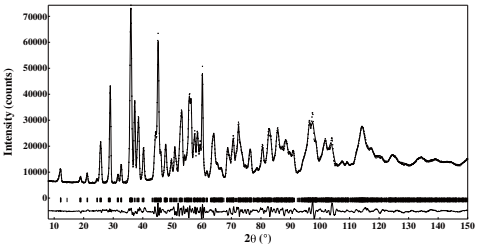


Fig. 1. Powder neutron diffraction profile of $La_{9.8}Ge_6O_{26.7}$.

1-1-29

Low energy excitation in DyB_6

K. Tomiyasu and K. Takahashi
WPI-AFIR Tohoku University and IMR Tohoku University

The freedoms of orbital and quadrupole are established as real existence. However, the excited states (the orbital wave and quadrupole wave) are not sufficiently studied in the experiments. Only few materials were measured by Raman scattering. Therefore, we submitted the trial measurements of low energy phonon in DyB_6 on HER (C1-1) in order to obtain the dispersivity of the quadrupole wave or the quadrupole-lattice coupling. DyB_6 exhibits the quite high transition temperature of ferro-type quadrupole ordering T_Q=32 K (3 meV), and the Q value and the temperature region of the ordering are distinguished from the antiferromagnetic order (T_N=23 K). The effect of quadrupole order on phonon can be extracted under 3 meV between T_Q and T_N.

The experimental conditions are summarized as follow: G-M-O-PGF-S-80'-BeF-flatA-80'-C, E_f=6 meV, narrowers (8×20 mm^2, 21×40 mm^2), GM-CTI, 1 single crystal with mm edge, hhk zone, standard Al-can. Figure 1(a) shows the constant-Q scans at hh2 (h=0.02, 0.04, 0.06, 0.08) at T=29 K ($T_N < T < T_Q$). The Q positions give us the TA phonon with the polarization along the [001] direction and the propagation vector along the [110] direction. Only the data at 0.04 0.04 2 show the appreciable peak. Figure 1(b) shows the temperature dependence of constant-Q scans at 0.04 0.04 2. The spectrum lines are fitted by the two Gaussians of the incoherent elastic scattering and the TA phonon. The fitting parameters are obtained to be E=1.02, 1.24 and 1.37 meV and ΔE(FWHM)=1.27, 1.47 and 0.95 meV at 29, 35 and 50 K, respectively. We now compare the neutron data with the ultrasound data, and discuss the softening of the phonon in connection with the spatial size of the quadrupole order domain, which is expected to be distributed from micro-m to nano-m.

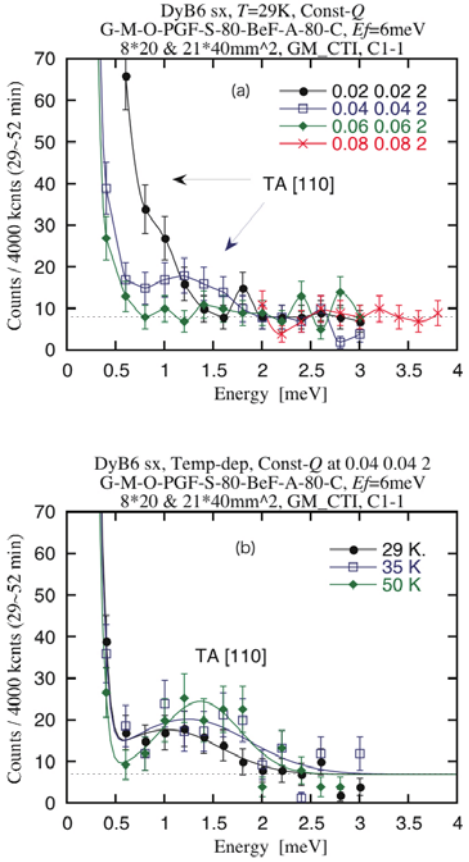


Fig. 1. (a) Constant-Q scans at T=29 K. (b) Temperature dependence of constant-Q scans at 0.04 0.04 2.

1-1-30

High resorution inelastic neutron scattering by TiNi(Fe) alloy

T. OHBA(A), D. KITANOSONO(A), T. FUKUDA(B)
(A) Department of Materials Science, Shimane University, (B) Materials Science and Engineerng, Osaka University

TiNi alloy system exhibits martensitic transformation, which shows typical first-order transformation. A few percent Fe added and substituted by Ni alloys were utilized for fundamental studies of martensitic transformation about 20 years ago. R-phase was found through the research and was thought at the beginning to be a precursor state of martensite. Later the R-phase was understood to be another type of martensite, whose structure was determined by Hara et al. Recently, systematic studies of Fe added alloys more than 2 percent were carried out. Calorimetric measurements and electrical resistivity measurements indicated different transformation behavior from first-order transformation for six or eight atomic percent alloys; that is Ti50Ni44Fe6 or Ti50Ni42Fe8. Calorimetric measurements show no transformation peak for those alloys. Electron diffraction studies and X-ray diffraction studies were also carried out for those alloys. Crystal structure of high temperature phase is B2 (CsCl) type. Diffuse peaks appeared around 1/3 of <110>* with lowering temperature. Those electron diffraction patterns were similar to diffraction patterns of R-phase. Since the martensitic transformation is known to be displacive transformation, phonon behavior is attractive mechanism for understanding the transformation. From the structural knowledge, [zz0]TA2 mode was expected to be soft at the transformation temperature. Ohba et al. measured phonon behavior for TiNi system previously. However no clear phonon softening was observed. Inelastic scattering measurements for larger than z=0.3, which is most important part of the phonon, showed disturbed peaks. Therefore, precise and high-resolution experiments were required. Inelastic scattering measurements for [zz0]TA2 mode were carried out at various temperatures. Figure 1 showed neutron inelastic experimental data for the alloy measured at 180K. Electron diffraction patterns at the temperature indicated R-phase like pattern. Incoherent intensities were subtracted from the observed data and shown in the figure, simultaneously. Inelastic phonon peak was found close to E=0, which may indicate almost complete softening of martensitic materials.

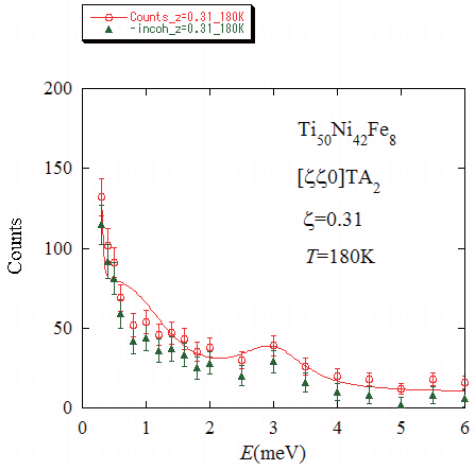


Fig. 1. Inelastic scattering data for [zz0]TA mode at 180K. The row data and incoherent intensities subtracted data were plotted.

1-1-31

Crystal Structure Analysis of a Supramolecular Ferroelectric 55DMBP-H_2ia

R. Kumai(A), D. Okuyama(B), S. Horiuchi(A), T. Arima(C), M. Watanabe(C), Y. Noda(C), and Y. Tokura(A,B,D)
(A)CERC AIST, (B)Multiferroic Project, ERATO, JST, (C)IMRAM, Tohoku Univ. (D)Dept. Appl. Phys., Univ. Tokyo

Ferroelectrics have been motivated not only by basic science but also by application because of those various utilizations for electronics. Recently Horiuchi et al. have reported a new ferroelectric realized by proton dynamics in a hydrogen-bonded chain with supramolecular structure, the cocrystal of 5,5′-dimethyl-2,2′-bipyridine (55DMBP, $C_{12}H_{12}N_2$) and iodanilic acid (H_2ia, $C_6H_2O_4I_2$).[1] The previous X-ray crystal structure analysis work suggests that the proton transfer occurs at Curie temperature ($T_C = 268$ K on cooling) and the corrective proton motion should be playing an important role for the development of the ferroelectricity in this material. Here, we report the crystal structure of 55DMBP-H_2ia obtained by the neutron diffraction in order to make clear the more precise hydrogen atom position.

Large single crystals of 55DMBP-H_2ia ($3 \times 1 \times 10$ mm^3) were prepared by slow evaporation from methanol solution. Neutron diffraction experiments were performed by utilizing a four-circle diffractometer FONDER with 1.245 Å neutron beam monochromized by a Ge(311) monochromater. We used the program DABEX for the absorption correction and the calculation of the diffraction path length which was used for extinction corrections. Using the corrected data sets, we used the program SHELX-97 for the least-square fitting in order to refine the parameters.[2]

Figure 1a shows the crystal structure of paraelectric phase of 55DMBP-H_2ia at $T =$ 300 K obtained by a neutron crystal structure analysis. Lattice parameters, space group ($P-1$), and atomic coordinates except for hydrogen atoms agree with those obtained by the X-ray diffraction experiments. It can be clearly observed that there are two types of hydrogen bonded site in the crystal. The significantly elongated thermal ellipsoid of hydrogen atom in the methyl group shows the rotational disordering of the methyl group. One can find the slightly elongated thermal ellipsoid of one hydrogen nuclei (H2), which indicates a broadly distributed hydrogen atom. From the interatomic distance table (inset of Fig. 1a), the migration of hydrogen atom of H2 site toward the center of the N$\cdots$O hydrogen bond can be found. The situation can be also observed in the nuclear density distribution obtained by the maximum entropy method (MEM) analysis of the diffraction data. Figure 1b shows the nuclear density distribution between N$\cdots$O hydrogen bond. The broadly distributed nuclear density at H2 site indicates the proton disorder in the short N$\cdots$O (2.58Å) hydrogen bonded site. In the low-temperature phase, we can be observed proton transfer at both H1 and H2 sites from the X-ray structure analysis. Neutron diffraction study of the ferroelectric phase of the 55DMBP-H_2ia, which is planned in near future, can provide us for more precisely information of the proton dynamics and the origin of polarization in the crystal.

References and notes [1] S. Horiuchi, R. Kumai, Y. Tokura, Angew. Chem. Int. Ed., 46, 3497 (2007). [2] 55DMBP-H_2ia 300K: $C_{18}H_{14}N_2O_4I_2$, $Z = 2$, Triclinic $P-1$, $a =$ 10.14(3) Å, $b =$ 8.81(5) Å, $c =$ 12.782(15) Å, $\alpha =$ 67.05(7)°, $\beta =$ 67.80(12)°, $\gamma =$ 67.06(10)°, $V =$ 933(3) Å^3, $R =$ 0.0343 for 1527 independent reflections ($|F_o| > 4\sigma(|F_o|)$).

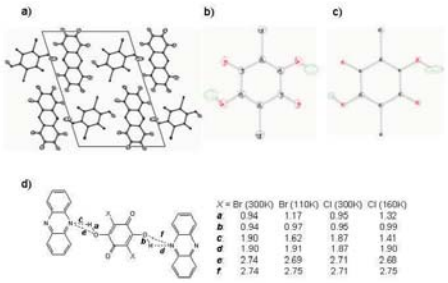


Fig. 1. (a) Crystal Structure, (b) nuclear density distribution map, and nuclear densities of hydrogen atom in the hydrogen bond for paraelectric phase (room temperature) obtained by the present neutron diffraction study.

1-1-32

Study suggests the existence of ferroelectric ice layer on a cold planet

Hiroshi Fukazawa, Hiroki Yamauchi, Akinori Hoshikawa
JAEA and Ibaraki Univ.

Whether ice in the outer solar system exists as hydrogen-ordered ices, is a question that has attracted scientific interest. Some ordered ices have ferroelectricity, and long range electrostatic forces caused by the ferroelectricity might be an important factor for planet formation. Features of the infrared spectrum of proton-ordered structures are unknown because of the difficulty in creating ordered ice in the laboratory. The aligned water ices are obtained only by doping of water samples with some catalysts, such as KOH or HCl, and the influence of the dopant on long-range ordering was not well resolved.

We produced KOD-doped D2O powder with a homogeneous concentration of KOD by rapid solidification of a mist of 0.001 - 0.1 M KOD solutions. Diffraction patterns were saved every 0.5 hours of collection time. These time-resolved measurements were performed at the HERMES in 04’ and 05’ [1, 2]. We have succeeded in making large quantities of ferroelectric ice, named ice XI, with the small amount of KOD, and then maintaining the samples in a 50 to 75 K temperature range over several days. From profile refinements with better values of reliability factors, which is the best way of investigating deuteron ordering, we found the temperature condition for the transformation of the largest fraction of ice Ih into ice XI. The finding confirms that ice XI is in a thermodynamically stable phase at low temperatures. We did longer experiments of same ice samples using a powder diffractometer, named the WAND, at the Oak Ridge National Laboratory, Based on the results, we propose that ice XI exists in the Universe [3]. It was picked out by US and Japanese press [4].

In spring and summer of 07’ we used the HERMES again and first measured in-situ time-resolved neutron diffraction of ice with 0.01 M KOD, which compressed at about 0.02 GPa using a sapphire cell of a large single crystal. We observed a transformation to the ferroelectric ice XI in a 60 to 75 K temperature range over tens hours. The results show that the ferroelectric ice is stable below 0.02 GPa. It suggests that a thick layer of ferroelectric ice exists on the surface of Pluto (Figure). Future telescope or planetary probe will be able to detecte the huge ferroelectric-ice mass.

We plan to do in-situ experiments on ice under much higher pressure conditions up to 10 GPa in 08’. We try to observe the phase transition from disordered phases to the ferroelectric ice or other ordered phases around 40-130 K (The value is the same as the temperature of Pluto’s surface and inner). The experiment will reveal the whole picture of low-temperature ice structures. It will show that myriad big icy-bodies in outer solar system, which exist as dwarf planets and KBO, consist of thick ferroelectric-ice surface and several inner layers of hydrogen ordered ices.

References

[1] H. Fukazawa, A. Hoshikawa, H. Yamauchi, Y. Yamaguchi and Y. Ishii, J. Crystal Growth 282 p.251 (2005).
[2] H. Fukazawa, et al., Physica B 385-386 p.113 (2006).
[3] H. Fukazawa et al., Astrophysical Journal Letters 652, pp.L57 (2006).
[4] Editor’s Choice, 2007, Science 315, 18; PhysOrg.com (http://physorg.com/news83862687.html); Asahi Daily Newspaper (2/2/07’ in Japanese); Tokyo Dainly Newspaper (7/10/07’ in Japanese).

1-1-33

Structures and Phase Transitions in A2BO4-type Dielectrics

H. Shigematsu(A) and K. Nomura(A)
(A)Department of Physics, Faculty of Education, Shimane University

Among a lot of A2BX4-type ferroelectrics (X = O, Cl, Br), a typical soft phonon-mode was observed in K2SeO4 clearly both above and below the normal-incommensurate (N-INC) phase transition point by neutron scattering. That is to say, the transition in K2SeO4 is interpreted as a displacive-type one. On the other hand, since the soft mode above the N-INC transition point in Rb2ZnBr4, Rb2ZnCl4 and K2ZnCl4 was not observed, it was thought that the transition type was an order-disorder one. For many A2BO4-type crystals such as K2SO4, K2CrO4, Rb2SeO4 and Cs2SeO4, the N-INC transition has never been reported. However, in the case of K2CrO4 and Rb2SeO4, the calculated dispersion curves contain an unstable sigma2 phonon branch whose qualitative and quantitative features are similar to those obtained for prototype incommensurate material K2SeO4. Indeed, a softening tendency of the sigma2 phonon branch around 0.7a* was observed in K2CrO4 and Rb2SeO4 [1]. The estimates hypothetical temperature in Rb2SeO4 is below -150 K.

In order to clarify the mechanism of low-temperature incommensurate phase transition and the hypothetical one in A2BO4-type crystals, we have to obtain additional information about the behavior of the low-energy sigma2-sigma3 optical branches in various A2BO4-type crystals. Therefore, we performed inelastic neutron scattering experiments by use of the triple-axis spectrometers (4G and T1-1) at JRR-3M of JAERI.

Figure 1 shows the phonon dispersion curves in an extended-zone scheme along the (x 0 0) direction for K2Se0.5Cr0.5O4. Two modes, which were anticrossed to each other around x ˜ 0.7, were observed. It is clear that low-frequency mode softens slightly in the vicinity of x = 1 with decreasing temperature, although the frequency will remain finite at 0 K. The estimated hypothetical temperature is about -160 K, which is lower than the calculated hypothetical temperature.

In Cs2SeO4, whose calculated hypothetical transition temperature was -151 K, the phonon dispersion frequency was essentially unchanged below room temperature. Our experimental results show that the plausible hypothetical temperature will be lower. The inelastic neutron scattering study on Rb2MoO4 is now in progress, because we found a new N-INC transition at 223 K.

References

[1] H. Shigematsu et al., J. Korean Phys. Soc. 46 (2005) 235.

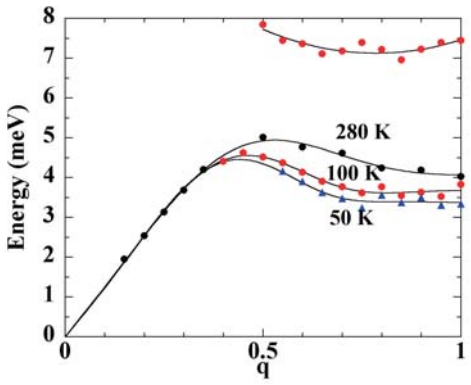


Fig. 1. Phonon dispersion curves in an extended-zone scheme on the (x 0 0) for K2Se0.5Cr0.5O4.

1-1-34

Magnetic structure of Ni-Mn-Z(Z=In, Sn) shape memory alloys

T. Kanomata, K. Fukushima, Y. Yamaguchi(A)
Faculty of Engineering, Tohoku Gakuin University, Institute for Materials Research, Tohoku University(A)

The Heusler alloys Ni2Mn1+xSn1-x(Z=In, Sn and Sb) show the martensitic transition from the L21 structure to an orthorhombic four-layered one. Unlike the case of conventional ferromagnetic shape memory alloys, the magnetization in the martensite phase for Ni2Mn1+xZ1-x(Z=In, Sn amd Sb) is much smaller compared to that in the austenite one. More recently, the present author's group has found an magnetic-field-induced martensitic transition from a nonmagnetic martensite phase to a ferromagnetic austenite one in the Ni-Mn-Sn Heusler alloy system. This alloy system opens up to the possibility of utilizing the magnetic-induced shape memory effect. Since then, the magnetic shape memory alloys Ni-Mn-Z(Z=In, Sn and Sb) have attracted much attention from the point of view of high performance materials being controlled by a magnetic field.

To investigate the magnetic structure of the nonmagnetic martensite phase in Ni-Mn-Sn magnetic shape memory alloys, we carried out the neutron powder diffraction experiments for Ni2Mn1+xSn1-x(x=0.44, 0.48 and 0.52).

The neutron powder diffraction pattern of Fig. 1(a) obtained at 370 K for Ni2Mn1.48Sn0.52, up the Curie temperature(TC= 313 K), shows strong Bragg reflections all of which could be indexed on the L21 fcc structure. The neutron powder diffraction pattern of Ni2Mn1.48Sn0.52 measured at 70 K, below the martensitic transition temperature (TM= 300 K), is shown in Fig. 1(b). It contains no residual cubic component. Most of the main reflections can be indexed using the 4O structure (space group: Pmma). It should be noted that no satellite reflections are observed. The analysis of the neutron powder diffraction is in progress to determine the magnetic structure of Ni2Mn1+xSn1-x(x= 0.44, 0.48 and 0.52) in the martensite phase.

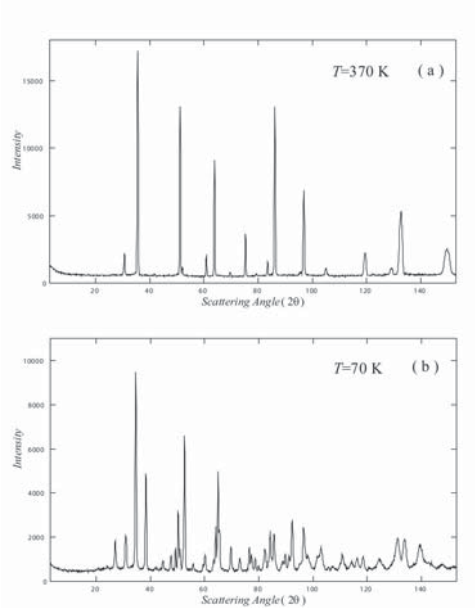


Fig. 1. Fig. 1 the neutron powder diffraction patterns of Ni2Mn1.48Sn0.52 at 370 K(a) and 70(b).

1-1-35

Crystal Structure Determination of Ba2MgSiO7 by Neutron Diffraction

Satomi Seki, Akira Komeno, Kazuyoshi Uematsu, Kenji Toda, Mineo Sato
Niigata University

The emission depends on the environment of the emission ion site in the host lattice. The silicate phosphors have relatively strong and rigid characteristics of partly covalent Si-O bond. In addition, rigid frameworks often provide relatively distorted coordination around the emission ion. Therefore, strong crystal fields were observed in many silicate phosphors. Alkaline earth silicate phosphor, M2MgSi2O7 (M = Ca, Sr and Ba) are expected as high luminance phosphor. However, the crystal structure of Ba2MgSi2O7 has not been reported up to now. The powder XRD pattern of Ba2MgSi2O7 differs from that of single crystal Ba2MgSi2O7. In this study, we show the crystallographic date on Ba2MgSi2O7 refined from the neutron powder diffraction patterns.

Crystal structures of Ba2MgSi2O7, were first reported by M. Shimizu et al. [1]. They refined Ba2MgSi2O7 on the basis of a tetragonal system with space group P-421m (a = 0.8425 nm). The crystal structure of Ba2MgSi2O7 differs from the tetragonal symmetry. Indexing of the XRD pattern for the powder sample, Ba2MgSi2O7 has monoclinic system with space group C2/c (a = 0.8426 nm). However, since these structures were deduced only from the electron and powder X-ray diffractions, the information on light elements, especially for oxygen atom, was quite poor.

Figure 1 and Table 1 shows the powder neutron diffraction pattern fitting and structural parameters for the Ba2MgSi2O7. All of the diffraction peaks were well indexed on monoclinic system C2/c. A good fitting profile were obtained with Rwp = 5.65 %.

Tetragonal and monoclinic structures take similarly layered structures with different barium coordination environments. It is considered that the synthesis temperature and annealing time are most important factors whether Ba2MgSi2O7 take the two-type structure, tetragonal or monoclinic.

[1] Y. Lin, C. W. Nan, X. Zhou, J. Wu, H. Wang, D. Chen, S. Xu. Mater. Chem. Phys., 82 (2003) 860-863.

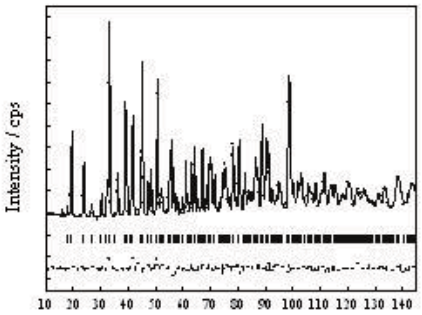


Fig. 1 Powder neutron fitting of $Ba_2MgSi_2O_7$.

Table 1 Structural parameter of $Ba_2MgSi_2O_7$.

Atom	Site	x	y	z	B / nm^2
Ba	8f	0.272(5)	0.044(1)	0.476(1)	0.0084(4)
Mg	4e	0.000	0.744(1)	0.250	0.009(2)
Si	8f	0.111(1)	0.282(5)	0.133(1)	0.007(1)
O(1)	8f	0.100(1)	0.142(1)	0.120(2)	0.015(3)
O(2)	8f	0.303(1)	0.342(1)	0.235(1)	0.003(1)
O(3)	8f	0.479(1)	0.149(1)	0.042(1)	0.001(4)
O(4)	4e	0.000	0.334(1)	0.250	0.009(4)

C 2/c (A-15), a = 0.8425(8) nm, b = 1.0732(8) nm, c = 0.8454(8) nm, Rwp = 5.65 %, Rp = 4.34 %, RR = 9.84 %, Re = 4.57 %, S = 1.23

Fig. 1.

1-1-36

Diffuse Scattering Measurement on Protonic Conductor $K_3H(SeO_4)_2$

F. Shikanai, S. Itoh, K. Tomiyasu[A], N. Aso[B], S. Ikeda and T. Kamiyama
Institute of Materials Structure Science, High Energy Accelerator Research Organization
[A] *Institute for Materials Research, Tohoku University*
[B] *Institute for Solid State Physics, University of Tokyo*

Much attention has been paid to some hydrogen bonded dielectric materials as the electrolytes for fuel cells which function above the boiling temperature of water. $K_3H(SeO_4)_2$ undergoes 1st order phase transition at 390 K (T_C). The material shows remarkable high electric conductivities above T_C (Phase I) and ferroelastic below T_C (Phase II). From the structural analyses by means of neutron diffraction, it developed that the slight deform of potassium lattice determine the hydrogen bonds orientation in the phase II, and alternate rotational displacements of SeO_4 tetrahedra which explained as zone boundary phonon mode correspond with the crystal structure in the phase II. [1, 2] We, therefore, have carried out inelastic neutron scattering (INS) experiments to clarify the mechanism of protonic conductivities and ferroelastic phase transition. No soft mode was obtained both of acoustic and zone boundary optical modes, however, diffusive spectra were obtained near the 0 meV at the L-point (0.5 2 0) above T_C. The results suggest that the rotational phonon mode of tetrahedra is to exist as over dumped phonon.

INS measurements were carried out using a high energy resolution triple axis spectrometer (C1-1 HER) installed at JRR-3M reactor, JAEA, Tokai, Japan. The energy scans were performed at zone boundary L-point with the energy transfer range from -2 meV to 4 meV. Final momentum vector k_f was fixed at 1.555 $Å^{-1}$. The h-scans from (0.25 2 0) to (0.75 2 0) were also performed to confirm that the INS spectra is obtained at only L-point.

Figure 1 shows INS spectra measured on the L-point by constant-Q mode at varied temperatures near T_C. Lorentzian shape spectrum increases with decreasing the temperature as shown in the figure. The result is close to the spectra of over dumped phonon of $CsPbCl_3$ due to the M_3 mode tilts of $PbCl_4$ octahedra. [3] It shows that the rotational mode of SeO_4 tetrahedra drives the improper ferroelastic phase transition, and plays an important role to the mechanism of proton conductivity in the phase I. It naturally expected that tilted tetrahedra form the hydrogen bonds locally even in the phase I, and the rotational mode over-dumped by the formation of hydrogen bonds. It developed that the hydrogen bonds disconnect and reconstruct due to the rotational tetrahedra mode in the phase I. It suggested that the rotational mode assists in the protons jumping to the inter-layer space in the metastable state.

References

[1] F. Shikanai *et. al.*: Physica B **385-386** (2006) 156.
[2] F. Shikanai *et. al.*: Ferroelectrics **347** (2007) 74.
[3] Y. Fujii *et. al.* : Phys. Rev. B **9**(1974) 4549.

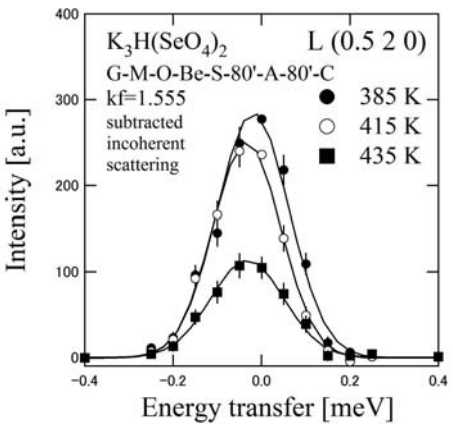


Fig. 1. INS spectra of $K_3H(SeO_4)_2$ at L-point

1-1-37

Structural investigation of the cubic perovskite-type doped lanthanum cobaltite La0.4Ba0.6CoO3-x

Takashi Ohta(A), Masatomo Yashima(A), Takahiro Wakita(A), Yoshitaka Matsushita(B), Takafumi Komatsu(A), and Yong Phat(A)
(A)Department of Materials Science and Engineering, Interdisciplinary Graduate School of Science and Engineering, Tokyo Institute of Technology, (B) Quantum Beam Center, National Institute for Materials Science

Lanthanum strontium cobaltites, La0.4Ba0.6CoO3-x, which have a perovskite-type structure, are promising electrode materials for the doped lanthanum gallate electrolyte in solid oxide fuel cells (SOFCs). The purpose of the present study is to investigate the crystal structure of the cubic Pm-3m perovskite-type La0.4Ba0.6CoO3-x at room temperature and at high temperatures.

La0.4Ba0.6CoO3-x pellets were supplied by Mitsubishi Materials Co., Tokyo, Japan. These pellets were used for room-temperature and high-temperature neutron diffraction measurements. Neutron diffraction data were collected in air using HERMES [1], a diffractometer with a 150 multi-detector system, at room temperature and at high temperatures. The HERMES is installed at the JRR-3M reactor in Japan Atomic Energy Agency, Tokai, Japan. Neutrons with wavelength 1.8143 angstrom and 1.8207 angstrom were obtained by the (331) reflection of a Ge monochromator. A furnace with MoSi2 heaters [2] was placed on the sample table, and used for neutron diffraction measurements at high temperatures.

The experimental data were analyzed assuming the cubic perovskite-type structure (space group Pm-3m) by Rietveld method with a computer program RIETAN-FP [3]. La and Ba atoms were placed at the special position 1b 1/2, 1/2, 1/2 of the Pm-3m symmetry. Co and O atoms were placed at the 1a 0, 0, 0 and 3d 1/2, 0, 0 sites, respectively. The calculated profile agreed well with the observed one (Fig. 1). The refined crystal structure of La0.4Ba0.6CoO3-x is similar with that of La0.6Sr0.4CoO3-x reported in our previous work [4]. Analyeses of diffraction data obtained at high temperatures are now in progress.

References

[1] K. Ohoyama et al., Jpn. J. Appl. Phys. 37 (1998) 3319.
[2] M. Yashima, J. Am. Ceram. Soc. 85 (2002) 2925.
[3] F. Izumi and K. Momma, Solid State Phenom. 130 (2007) 15.
[4] M. Yashima and T. Tsuji, J. Appl. Crystallogr., 40 (2007) 1166.

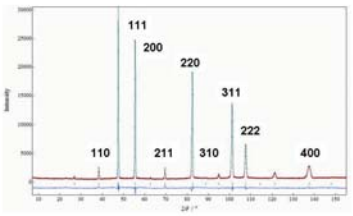


Fig. 1. Rietveld fitting result for the neutron-diffraction data of La0.4Ba0.6CoO3-x measured at room temperature.

1-1-38

Structural analysis of metavanadate phosphors AVO_3 (A: K, Rb and Cs)

T. Nakajima[1], M. Isobe[2], T. Tsuchiya[1], Y. Ueda[2], and T. Kumagai[1]

[1] *Advanced Industrial Science and Technology, 1-1-1 Higashi, Tsukuba, 305-8565*

[2] *Institute for Solid State Physics, Univ. of Tokyo, 5-1-5 Kashiwanoha, Kashiwa, 277-8581*

Metavanadate phosphors AVO_3 (A: K, Rb and Cs) were first discovered by Gobrecht *et al*. in 1957 [1]. The AVO_3 shows a broad-band emission at 380 – 700 nm. We have measured quantum efficiencies (η) of these compounds; the η of KVO_3, $RbVO_3$ and $CsVO_3$ were 4, 59 and 80%, respectively. The origin of intense luminesecence of the $CsVO_3$ has not been disccussed well in spite of its remarkable high value of η. In this work, we have studied the powder neutron diffraction for understanding luminescent properties of the AVO_3 from the viewpoint of the structural features.

The polycrystalline samples of AVO_3 (A: K, Rb and Cs) were prepared by a solid state reaction. The powder neutron diffraction measurements for the obtained powder samples were performed using the HERMES spectrometer installed at the research reactor JRR-3M in Japan Atomic Energy Agency, Tokai, Japan [2]. The wavelength of the incident neutron was selected to be 1.8265 Å. The diffraction data were collected in the 2θ range from 3 to 153 deg. in the step interval of 0.05 deg. at room temperature. The obtained data analyzed by the Rietveld method using a computer program RIETAN-FP [3].

Structural analysis of $CsVO_3$ was carried out by using a reported structural model, space group *Pbcm* [4]. The structural parameters were refined as follows: a = 5.3979(3) Å, b = 12.2553(8) Å and c = 5.7881(3) Å. The reliability factors were R_{wp} = 4.97%, R_e = 2.37%, R_I = 2.89% and R_F = 1.54%. Main diffraction peaks were almost fitted with the calculation result, however, the minor diffraction peaks can not be indexed by this structural model. In the KVO_3 and $RbVO_3$, the structural analyses were also carried out, and the some minor peaks were not indexed with *Pbcm* as similar with the case of $CsVO_3$.

For the discussion of luminescent properties of the AVO_3, the structural distortion should be correctly determined, because the emission intensity in these compounds could strongly depend on the distortion of the VO_4 tetrahedra in the crystal structure. In the conventional structural analysis using X-ray diffraction [4], the structural analysis of AVO_3 was carried out using the space group *Pbcm*, and clear differences were not observed among the VO_4 tetrahedra of the AVO_3 (A: K, Rb and Cs). Therefore, unindexed peaks in this neutron diffraction is expected to be a key point for the discussion of the origin for luminescent property of the AVO_3. The detailed structural analysis of these compounds are in progress.

References

[1] H. Gobrecht *et al.*: Z. Phys. **147** (1957) 350.

[2] K. Ohoyama *et al.*: Jpn. J. Appl. Phys. **37** (1998) 3319.

[3] F. Izumi *et al.*: Mater. Sci. Forum **321-324** (2000) 198.

[4] F. C. Hawthorne *et al.*: J. Solid State Chem. **22** (1977) 157.

1-1-39

Crystal structural change of potassium titanyl phosphate

Takafumi Komatsu, Masatomo Yashima, Takahiro Wakita, Yong Phat, Yoshitaka Matsushita*
*Department of Materials Science and Engineering, Interdisciplinary Graduate School of Science and Engineering, Tokyo Institute of Technology, * Quantum Beam Center, National Institute for Materials Science*

Nonlinear optical materials have received much attention in recent years. Potassium titanyl phosphate ($KTiOPO_4$, KTP) is one of them. The space group of KTP is $Pna2_1$ at room temperature. KTP exhibits a phase transition from ferroelectric to paraelectric phase at 1207 K. Second harmonic generation (SHG) effect disappears in the paraelectric phase. The crystal structure of the paraelectric phase of KTP has not been investigated yet, probably due to the difficulty of diffraction experiments above 1000 K. The purpose of this work is to study the crystal structure of paraelectric phase of KTP using neutron powder diffraction data measured at 1358 K.

A KTP sample was prepared by solid-state reactions at 1273 K for 3 hours. Neutron powder diffraction data were measured at 297, 639, 951, 1155, 1256 and 1358 K using the HERMES diffractometer. Wavelength of neutrons was 0.18265(1) nm. Crystal structure of KTP was refined by Rietveld method, using a computer program, RIETAN-FP.

All the reflections observed in the diffraction data collected below 1207 K were indexed by the space group $Pna2_1$, while those measured above 1207 K were indexed by the space group *Pnan*. Figure 1 shows the refined crystal structure of paraelectric KTP at 1358 K. The structure is characterized by helical chains of $Ti0_6$ octahedra that are linked at two corners and are separated by PO_4 tetrahedra. The potassium ion is located in channel along the *c*-axis.

Unit-cell parameters *a* and *b* increased with temperature up to 1358 K. The *c* parameter decreased with temperature up to 1155 K and did not change largely above the Currie temperature, 1207 K. The displacement of K atom along the *c*-axis decreased with an increase of temperature and disappeared at and above 1207 K, which indicates the displacive nature of the ferroelectric-paraelectric transition. The phase transition was also accompanied by the change of occupancy factors at the K sites, which indicates the order-disorder nature of this transition.

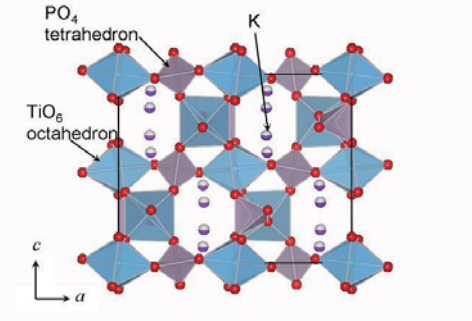


Fig. 1. Refined crystal structure of paraelectric $KTiOPO_4$ at 1358 K (space group *Pnan*).

1-1-40

Li ion distributions of layered-structure type oxides LiNi1/2Mn1/2O2 prepared by ion-exchange

Y. Arachi(A), H. Maeda(A), H. Kobayashi(B), T. Asai(A)
(A) Kansai University, (B) AIST

We have extensively investigated Li2MnO3-based oxides with layered-NaCl type to clarify the relationship between crystal structure and electrochemical property as cathode materials for Lithium ion battery. LiNi1/2Mn1/2O2 is one of those and it exhibits a specific capacity of 150 mAh/g in the voltage range of 2.5 to 4.3 V. It is known that conventional preparation produce about 10 % exchange of Li and Ni in the layered-structure and this Li/Ni disorder acts on increasing the activation energy of Li migration and effects on the cell performance[1,2]. We have confirmed that the phase transition associated with cation ordering occurs in discharged LiNi1/2Mn1/2O2. The objective of this study is to observe the change of Li position by preparation condition and to determine lower temperature structure as well. The samples were prepared by ion-exchange of Li for Na in NaN0.5Mn0.5O2. Neutron diffraction measurement of the compositions is of great useful to determine the ion distribution. It was performed by diffractometer, HERMES installed at JRR-3M in the Japan Atomic Energy Agency (JAEA) in Tokai, Japan (JAEA). The wavelength of neutron was 1.82646(6) . Diffraction data were collected in the 2 θ range from 3 to 153 degree in the step interval of 0.1 degree. Rietveld structural refinement was carried out by using a program RIETAN-2000 [3]. The obtained structure clearly depends on the ion-exchange reaction temperature and time. As increased reaction temperature and time the Li/Ni disorder became remarkable. However, disordering of Li and Ni was suppressed by this soft-chemical process compared to those by conventional preparation. The obtained diffraction patterns at 10 K will be applied for interpretation of the magnetic behavior that we have already observed a susceptibility cusp at 15 K.

[1]Y. Arachi,H. Kobayashi, S. Emura, Y. Nakata, M. Tanaka, T. Asai, H. Sakaebe, K. Tatsumi and H. Kageyama, Solid State Ionics, 176, (2005)895-903.
[2] K. Kang, Y. S. Meng, J. Breger, C. P. Grey, G. Ceder, Science, 311(2006)977.
[3] F. Izumi and T. Ikeda, Mater. Sci. Forum, 198 (2000) 321-324.

1-1-41

High temperature neutron diffraction study of (La0.9Sr0.1)MnO3+d perovskite

K. Nomura (A), H. Kageyama (A), K. Kakinuma (B), T. Maekawa (C), S. Nakamura (C), H. Miyazaki (C), H. Imabayashi (C), and T. Ito (C)
(A) National Institute of Advanced Industrial Science and Technology (AIST), (B) Kanagawa University, (C) New Cosmos Electric Co., Ltd.

Strontium-doped lanthanum manganite perovskites, (La1-xSrx)MnO3+d have been investigated as the electrode materials of solid oxide fuel cells, because of the high electronic and relatively high oxide-ion conductivity [1]. However, the detailed crystal structures at elevated temperatures have not been reported yet. In this study, we measured high temperature neutron diffraction data of 10 mol% Sr-doped LaMnO3, (La0.9Sr0.1)MnO3+d (LSM), to investigate the crystal structure and the conduction path of oxide-ions.

Neutron diffraction measurements were performed in air with a 150-detector system, HERMES [2], installed at the JRR-3M reactor in JAEA (Tokai). The neutron wave length was 1.8265(1)A and the diffraction data were collected in the 2 θ range from 20 to 153 deg in step interval of 0.1 deg, in the temperature range from 297 to 1473K and oxygen partial pressure, P(O2), range between 2x10^-4 and 0.21atm. A furnace with Pt-Rh heaters installed in a vacuum chamber was placed on the sample stage, and used for neutron-diffraction measurements at high temperatures. A tubular-type LSM sinter (outer diameter: 10 mm, inner diameter: 7 mm, length: 50 mm) was prepared, in order to obtain equilibrium conditions between the sinter and atmospheres at short times. The diffraction data obtained were analyzed using the Rietveld program RIETAN-2000 [3]

The diffraction data of LSM could be indexed assuming an orthorhombic symmetry (Pnma, No.62) (at 297 and 373K) or a trigonal one (R-3c, No.167) (between 473 and 1473K) in P(O2) = 0.21 atm. Figure 1 shows the Rietveld refinement result of LSM measured at 1473K in P(O2) = 0.21 atm. The number of chemical formula per unit cell, refined cell parameters, and refined unit cell volume were as follows: z = 6, a = 5.6029(5)A, c = 13.679(2)A, V = 371.87(7)A^3. The reliability factors were Rwp = 5.51%, RI = 2.35%, and RF = 1.74% Re = 2.96%. Goodness of fit (S = Rwp/Re) was 1.86.

References

[1] N. Minh, J. Am. Ceram. Soc., 76, 563 (1993).
[2] K. Ohoyama, T. Kanouchi, K. Nemoto, M. Ohashi, T. Kajitani, and Y. Yamaguchi, Jpn. J. Appl. Phys., 37, 3319 (1998).
[3] F. Izumi and T. Ikeda, Mater. Sci. Forum, 321-324, 198 (2000).

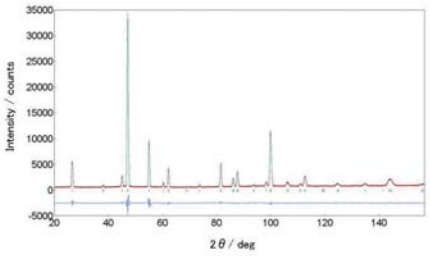


Fig. 1. Rietveld refinement result of (La0.9Sr0.1)MnO3+d at 1473K in P(O2) = 0.21 atm.

1-1-42

Lithium Diffusion in LixFePO4

Atsuo Yamada, Shin-ichi Nishimura, Genki Kobayashi, Masatomo Yashima, Kenji Ohoyama, Yasuo Yamaguchi
Tokyo Institute of Technology, Tohoku University

Chemical energy storage by batteries will provide an important function in the future greener society. Lithium ion battery is the most advanced energy storage system but the application has been limited to the portable electronics devices due to the cost and safety problems.

Neutron diffraction at high temperature as high as 350C was performed to understand the electrode reaction mechanism in the very important cathode material, LixFePO4, a use of which is now widely recognized as the most promising solution to get lithium ion batteries into the large-scale application such as plug-in hybrid vehicles. For example, more than 200 papers have been published on this material last year.

Scientific community has raised the important question as to why facile redox reaction is possible in insulating material; the fact that the battery with insulating LixFePO4 electrode can deliver much larger current density than the battery with conventional metallic LixCoO2 electrode. Geometric information on the movement of charge carrier should be the start point to answer this important question.

By the careful analysis by maximum entropy method, the long-awaited experimental evidence for one-dimensional lithium motion in LixFePO4 is displayed. This provides fundamental knowledge toward full understanding the peculiar redox mechanism.

Beyond LixFePO4, this is, to our knowledge, the first visual demonstration of ionic diffusion path in battery electrode.

Activity Report on Neutron Scattering Research: Experimental Reports **15** (2008)
Report Number: 598

1-1-43

Soft modes in the relaxor ferroelectric compound $(Na_{0.5}Bi_{0.5})TiO_3$

M. Matsuura[1], H. Iida[1], K. Hirota[1], Y. Noguchi[2], and M. Miyayama[2]

[1] *Institute for Solid State Physics, The University of Tokyo, 106-1 Shirakata, Tokai, 319-1106*
[2] *Institute of Industrial Science, The University of Tokyo, 4-6-1 Komaba, Meguro-ku, Tokyo 153-8505*

$(Na_{0.5}Bi_{0.5})TiO_3$ (NBT) forms perovskite structure with two different ions Na^+ and Bi^{3+} at the A site of ABO_3. NBT exhibits high and broad peak in the dielectric susceptibility which is very similar to that in typical relaxors and NBT regains attention as promising applications to piezoelectric devices containing no toxic lead. Last year, we studied the diffuse scattering and clarified that the diffuse scattering appears below about 800 K and has more intensity along transverse direction than that along longitudinal direction, suggesting a close connection between the diffuse scattering and soft transverse optical mode. The purpose of the present work is to study soft phonon modes to clarify the mechanism of the diffuse scattering in NBT. Neutron scattering experiments were performed on the triple-axis spectrometers PONTA.

Figure 1(a) shows a constant-Q scan measured at Q =(2.05, 1.95,0) and T = 670 K. The TO mode is strongly overdamped at this Q and the spectra is well reproduced by broad lorentzian centered at $\omega = 0$, shown by the solid line. The TA mode is not visible in panel (a) because its excitaton energy is below 2 meV. Figure 1(b) and (c) shows a similar constant-Q scan measured at Q =(2.15, 1.85, 0) and (2.25, 1.75, 0) . In addition to clear peaks for TA modes, a well-defined peak for the TO mode was observed at 13 meV for (2.25, 1.75, 0) while TO mode peak around 10 meV was rather broad for (2.15, 1.75, 0). To investigate TA and TO dispersions, a series of constant-Q scans with a step of 0.05 rlu from $q = 0$ to 0.25 rlu and constant-E scans with a step of 1 meV from 6 to 11 meV were taken, and the results are summarized in the inset to Fig.2. No propagating mode was observed for $q < 0.10$ rlu, indicating the so-called waterfall feature observed in relaxor ferroelecrics $Pb(Zn_{1/3}Nb_{2/3})O_3$-8%$PbTiO_3$ [2] and $Pb(Mg_{1/3}Nb_{2/3})O_3$. [3]

References

[1] J. Suchanicz and J. Kwapulinski, Ferroelectrics **165** 249 (1995).
[2] P. M. Gehring *et al.*, Phys. Rev. Lett. **84** 5216 (2000).
[3] P. M. Gehring *et al.*, Phys. Rev. Lett. **87** 277601 (2000).

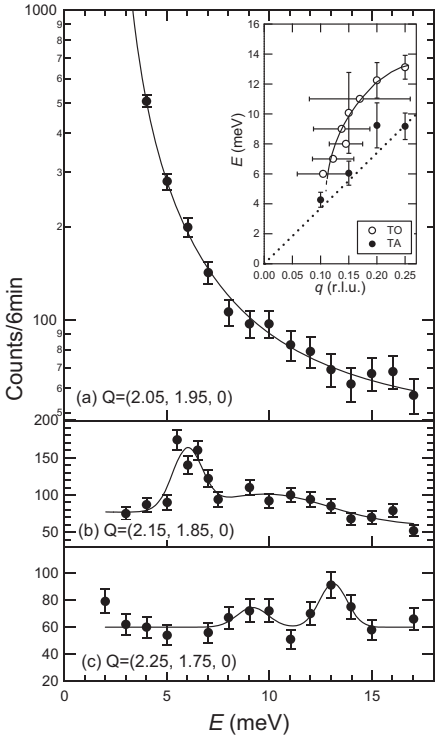


Fig. 1. Constant-Q scans measured at T = 670 K. Panel (a) shows a damped TO mode for $q = 0.05$ rlu. Panels (b) and (c) show underdamped TA and TO modes for $q = 0.15$ and 0.25 rlu. The inset shows the TA and TO dispersions at T = 670 K.

1-1-44

Anisotropic damping of transverse acoustic and optical modes in the relaxor ferroelectric 0.7 $Pb(Mg_{1/3}Nb_{2/3})O_3$-0.3 $PbTiO_3$

M. Matsuura and K. Hirota
Institute for Solid State Physics, The University of Tokyo, 106-1 Shirakata, Tokai, 319-1106

Relaxor ferroelectrics have gained great interest recently due to their promising application as piezoelectric devices. $Pb(Mg_{1/3}Nb_{2/3})O_3$ (PMN) is a typical relaxor which shows a broad and frequency dependent peak in dielectric susceptibility. It is widely believed that the polar nanoregions (PNR) occurring at temperatures much above T_c, the so-called Burns temperature T_d, play an important role in such relaxor behavior. The lattice dynamics in PMN are characterized by a soft, zone center, transverse optic (TO) mode observed below T_d, which is the so-called waterfall. Neutron scattering measurements by Naberezhnov *et al.* on PMN revealed the onset of strong diffuse scattering at or very near $T_d \sim 600$ K [1], indicating a close connection between the PNR and the diffuse scattering. Thus, it is expected that the local crystal distortion in PNR is driven by the soft TO. To elucidate the lattice dynamics in PNR, we investigated low energy phonon modes in PMN-30%PT. Neutron scattering experiments were performed on the triple-axis spectrometers HER installed at the JRR-3 Reactor of the JAEA.

Figures 1 show the constant Q spectrum at (2.15 1.85 0) and (2 -0.21 0) taken at $T = 600$, 400, and 200 K. If the lattice dynamics is isotropic, these spectrum show peaks for a transverse acoustic (TA) mode and a transverse optical (TO) mode at the same energies, because both Q's locate at the same $q = 0.21$ along the transverse direction from each Bragg position. At $T = 600$ K ($> T_C$), well-defined TA and TO modes were observed for (2 -0.21 0). For (2.15 1.85 0), while the TA mode looks very similar to that for (2 -0.21 0), the TO mode is softer and broader in energy than that for (2 -0.21 0). Below T_C, on the one hand, the TO mode for (2.15 1.85 0) becomes underdaped, on the other hand, the TA mode for (2.15 1.85 0) becomes overdamped as shown in Fig.1(b) and (c). The damped TA and TO modes were observed for $q =< 110 >$ directions which are the same directions of the anisotropic diffuse scattering. We speculated that PNR's trap soft phonon modes as a central peak. Besides, for the current case, PNR's may trap phonon modes anisotropically.

References

[1] A. Naberezhnov *et al.* , Eur. Phys. J. B, **11**, 13 (1999).

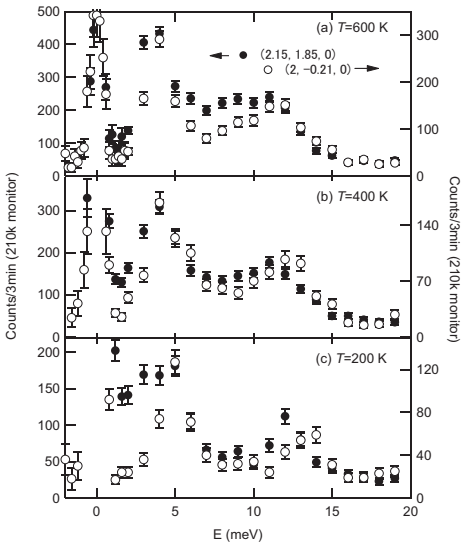


Fig. 1. Constant Q scan at (2.15 1.85 0) (closed circles) and (2 -0.21 0) (open circles) taken at $T = 600$, 400, and 200 K.

1-1-45

Behavior of Thermal Parameters through Phase Transition in KDP

H. Mashiyama, T. Miyoshi, T. Asahi and H. Kasano
Faculty of Science, Yamaguchi University, Yamaguchi 753-8512

KH2PO4 (KDP) is a well known ferroelectric (F) crystal which performs a phase transition at 123K. Whether the proton is tunneling or not in the paraelectric (P) phase has been controversial for a long time. Moreover, the zero temperature structure in which all degrees of freedom are frozen was not reported previously. Last year we refined the crystal structures down to 15 K, by using neutron scattering.[1] However, the detailed measurement lacked just around the transition temperature (Tc). Here we report full results, especially the temperature dependence of the Debye-Waller factor (U) through Tc.

A single crystal of KDP was set in a cryostat mounted on a diffractometer (FONDER) installed at JRR3M reactor in JARERI, Tokai. Diffraction data up to 2theta<156 (neutron wave length 1.2452A) were collected at two and three temperatures in phases P and F, respectively. Absorption and extinction correction was performed by using RADIEL. Atomic parameters were refined by least-squared calculations.

Figure 1 shows atomic displacements in the F phase. The PO4 tetrahedron deforms abruptly at Tc with accompanying a relative displacement of K to induce dipole moments. In the P phase, only proton takes a mean structure (split atom). With decreasing temperature, all the thermal parameters U's decrease monotonically, with a tiny change at Tc, as shown in figure 2.

The extrapolated values of U to T=0 demonstrate the zero-point vibration of nuclei (ground state wave function). It should be noted that the wave function of proton in the P phase is well described by superposing two ground state wave functions with a separation of 0.3A. Since the proton density is almost single peak, proton is considered to tunnel between two wells frequently. Below Tc each proton links one of two oxygen atoms to deform the PO4 tetrahedron. Comparing the magnitude of U with the atomic displacement below Tc, we can conclude that PO4 and K are not disordered units in the P phase.

References

[1] H. Mashiyama et al, ARNSR:ER Vol.14 (2007) Num.96.
[2] R. J. Nelmes et al, J. Phys. C 15 (1982) 59.

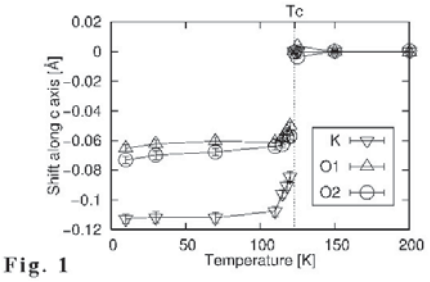


Fig. 1

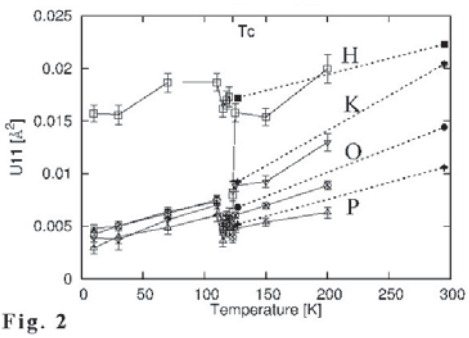


Fig. 2

Fig. 1. Atomic displacement along the c-axis of KDP.
Fig. 2 Temperature dependence of Debye-Waller factor along the a-axis of KDP. The unit cell is referred to the P phase. The previous results after Ref. [2] are shown by broken lines.

1-1-46

Crystal Structure Analysis of Ferroelectric Niobium Oxides

N. Kumada, Y. Yonesaki, T. Takei, N. Kinomura and M. Yashima*
*University of Yamanashi and *Tokyo Institute of Technology*

We performed the crystal structure refinement of two types of perovskite-type oxides, Ba(Cu1/3Nb2/3)O3 and (Ba,H)BiO3 by using powder neutron diffraction data which were collected in air with a 150-detector system, HERMES, installed at JRR-3M reactor in Japan Atomic Energy Research Institute (Tokai). High temperature neutron diffraction data was collected by using a furnace with MoSi2 heaters [1] which was placed on the sample table. The data was refined using the Rietveld method with the program RIETAN [2].

[1]Ba(Cu1/3Nb2/3)O3

Ba(Cu1/3Nb2/3)O3 has the perovskite-type structure with the tetragonal cell of a = 4.0218(4) and c = 4.1460(4) . The structure refinement by using neutron diffraction data was carried out for two types of models which have centrosymmetric P4/mmm(#123) and ancentrosymmetric P4mm(#99) space groups. The structure refinement by using the centrosymmetric space group P4/mmm led to the R-factors, Rwp =10.36, Rp = 7.60, RI = 3.17, RF = 1.56%, S = 3.579, while by using ancentrosymmetric space group, P4mm the lower R-factors (Rwp = 8.96, Rp = 6.63, RI = 1.94, RF = 0.98%, S = 3.010) were obtained. This result suggested that this compound had an ancentrosymmetric space group, P4mm. However, the displacement of z parameter for Ba and Nb atoms from that of O atoms was very small as shown in Fig. 1(a). We can not conclude that this compound has an ancentrosymmetric space group to exhibit ferroelectricity, and now are attempting to improve the structure refinement and to measure the electrical properties. This compound was found to be transformed from the tetragonal to cubic symmetry at 500 ~ 600 ° C. The structure refinement of the high temperature form by using neutron diffraction data was successful leading to the R-factors, Rwp = 9.82, Rp = 7.24, RI = 4.61, RF = 2.44%, S = 2.900 in assumption with the space group of Pm-3m (#221), and the lattice parameter was a = 4.0957(3) . The crystal structure is shown in Fig. 1(b). Since this perovskite-type niobium oxide has a possibility of ferroelcricity, its crystal structure and electrical properties are now under investigation.

[2](Ba,H)BiO3

A new perovskite-type bismuth oxide, (Ba,H)BiO3 was prepared by hydrothermal reaction using NaBiO3nH2O as a starting compound. The X-ray powder diffraction pattern of this compound could be indexed with the cubic cell of a = 8.5445(4) with the space group Pn3n(#222). The structure refinement by using neutron diffraction data led to the reasonable R-factors, Rwp = 8.72, Rp = 6.39, RI = 6.38, RF = 4.67%, S = 2.358.

References

[1] M. Yashima, J. Am Ceram. Soc.85 (2002) 2925.
[2] F. Izumi and T. IKeda, Mater. Sci. Forum 321 (2000) 198.

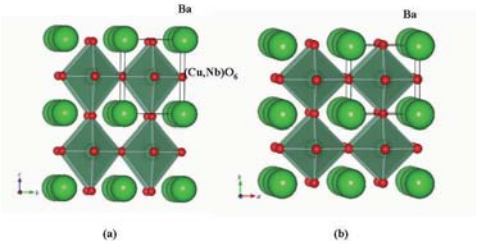


Fig. 1. Fig. 1 Crystal structure of BaCu1/3Nb2/3O3. (a) low and (b) high temperature forms.

1-1-47

Water Density Near Surface of DLC Films Having Various Surface Energies Measured by Neutron Reflectometry

Tomoko Hirayama#1, Tomoki Uno#1, Takashi Torii#1, Takashi Matsuoka#1, Kazuko Inoue#2, Toru Ebisawa#3, Seiji Tasaki#4, Masahiro Hino#5, Naoya Torikai#6
#1Doshisha Univ., #2Waseda Univ., #3JAEA, #4Kyoto Univ., #5KURRI, #6KEK

Lubricants generally contribute to achieve low friction on sliding surfaces in many kinds of mechanical components. It is well known that lubricants may form some absorption layers near surfaces. Though macroscopic relationships between lubricants (or absorption layers) and tribological properties have been studied everywhere, there are no reports on densities and thicknesses of the special ultrathin layers formed at the solid-liquid interface.

In our laboratory, densities of lubricants near solid surfaces are directly measured by neutron reflectometry and discussed in the series of studies. The neutron can go deeply into the inner region of common metals because neutrons physically interact not with electrons but with atomic nuclei, thus the in-situ observations of solid-liquid interface can be easily realized. The reflectometry is generally utilized for analysis of vertical microstructures of a sample or the interface through the reflectivity profile. In this paper, three kinds of DLC films having different surface energies were prepared as base materials, and water was selected as a lubricant. The DLC films were called 'normal DLC', 'hydrophilic DLC' and 'hydrophobic DLC'; the first was deposited by plasma CVD using CH4 gas on a silicone block, the second was treated by oxygen gas plasma on the surface of the normal DLC as post-processing treatment, and the third was deposited by plasma CVD using CH4 and C2F6. The DLC films were soaked in water in a specially-designed sample holder, and the neutron beam was directly entered to the DLC/water interface from the side of silicone block. Then, the instrument we used was a neutron reflectometer 'MINE' in Japan Atomic Energy Agency (JAEA), and the neutron reflectivity profiles from the interface between DLC films and water were obtained by the instrument. Through an analytical fitting approach with Parratt's theory to the obtained profiles, we can see that: (1) the thickness of hydrophilic layer (O2 plasma treated layer) formed in the surface of hydrophilic DLC is 15nm, (2) water infiltrates from the surface to the interior of hydrophilic DLC until 15 nm-depth, and the thickness of dense water layer infiltrated in the top surface of hydrophilic DLC is 2nm, and (3) the thickness of low-density water layer on the surface of hydrophobic DLC is 3nm, and its density is almost half of normal water, shown in Fig. 1.

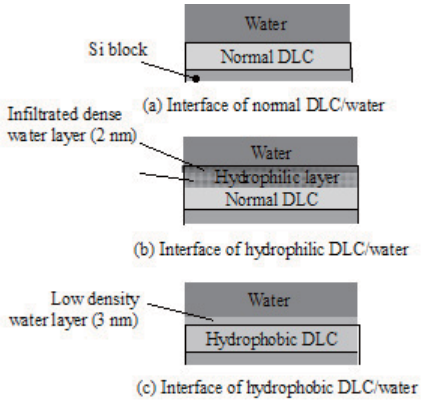


Fig. 1. Physical models estimated by neutron reflectometry

1-1-48

Water Density Near Surface of DLC Films Having Various Surface Energies Measured by Neutron Reflectometry

Tomoko Hirayama#1, Tomoki Uno#1, Takashi Torii#1, Takashi Matsuoka#1, Kazuko Inoue#2, Toru Ebisawa#3, Seiji Tasaki#4, Masahiro Hino#5, Naoya Torikai#6
#1Doshisha Univ., #2Waseda Univ., #3JAEA, #4Kyoto Univ., #5KURRI, #6KEK

Lubricants generally contribute to achieve low friction on sliding surfaces in many kinds of mechanical components. It is well known that lubricants may form some absorption layers near surfaces. Though macroscopic relationships between lubricants (or absorption layers) and tribological properties have been studied everywhere, there are no reports on densities and thicknesses of the special ultrathin layers formed at the solid-liquid interface.

In our laboratory, densities of lubricants near solid surfaces are directly measured by neutron reflectometry and discussed in the series of studies. The neutron can go deeply into the inner region of common metals because neutrons physically interact not with electrons but with atomic nuclei, thus the in-situ observations of solid-liquid interface can be easily realized. The reflectometry is generally utilized for analysis of vertical microstructures of a sample or the interface through the reflectivity profile. In this paper, three kinds of DLC films having different surface energies were prepared as base materials, and water was selected as a lubricant. The DLC films were called 'normal DLC', 'hydrophilic DLC' and 'hydrophobic DLC'; the first was deposited by plasma CVD using CH4 gas on a silicone block, the second was treated by oxygen gas plasma on the surface of the normal DLC as post-processing treatment, and the third was deposited by plasma CVD using CH4 and C2F6. The DLC films were soaked in water in a specially-designed sample holder, and the neutron beam was directly entered to the DLC/water interface from the side of silicone block. Then, the instrument we used was a neutron reflectometer 'MINE' in Japan Atomic Energy Agency (JAEA), and the neutron reflectivity profiles from the interface between DLC films and water were obtained by the instrument. Through an analytical fitting approach with Parratt's theory to the obtained profiles, we can see that: (1) the thickness of hydrophilic layer (O2 plasma treated layer) formed in the surface of hydrophilic DLC is 15nm, (2) water infiltrates from the surface to the interior of hydrophilic DLC until 15 nm-depth, and the thickness of dense water layer infiltrated in the top surface of hydrophilic DLC is 2nm, and (3) the thickness of low-density water layer on the surface of hydrophobic DLC is 3nm, and its density is almost half of normal water, shown in Fig. 1.

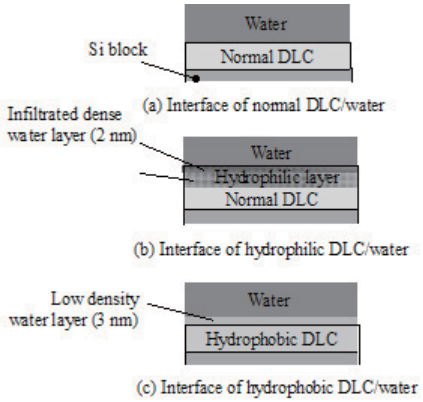


Fig. 1. Physical models estimated by neutron reflectometry

1-1-49

Magnetic structure of Pr2-2xCa1+2xMn2O7(x=0.45)

Y. Tokunaga(A), D. Okuyama(A), T.J. Sato(B), T. Arima(C), and Y. Tokura (A,D)
ERATO-MF, JST(A), ISSP, Univ. of Tokyo(B), IMRAM, Tohoku Univ.(C), Dept. Appl. Phys, Univ. of Tokyo(D)

Bilayer manganite Pr2-2xCa1+2xMn2O7(x=0.5) is a CE-type antiferromagnet with TN=143 K [1]. To study the robustness of the CE-AF state against the change of the hole concentration, we have examined the Pr2-2xCa1+2xMn2O7(x=0.45) system. Single crystal of Pr2-2xCa1+2xMn2O7(x=0.45) was prepared by floating-zone method. Neutron scattering measurements were carried out with the triple axis spectrometer GPTAS installed at JRR-3M. The measurements were done on the pseudo-tetragonal (hhl) reciprocal zone.

Figure (a) shows the results of q=(1/4, 1/4, l) scan taken at 200 K and 3 K. In the case of x=0.5, strong magnetic reflections are observed at l=integer positions, which results from CE-AF (see inset). For x=0.45, only diffuse scattering is observed even at 3 K, indicating that the correlation of the CE-type AF in this system is a shot-range one. Results of q=(h, h, 3) scan (Fig. (b)) suggest the anisotropic nature of the magnetic correlation. Figure (c) shows the temperature dependence of the diffuse intensity at q=(1/4, 1/4, 3). The intensity starts to increase below 120 K as decreasing temperature. These results are consistent with the magnetization and resistivity data.

Pr2-2xCa1+2xMn2O7 is the 2D analog of the similar minimal-disorder system of perovskite Pr1-xCaxMnO3. However, results of neutron diffraction measurements indicate the robustness of the CE-AF state against the change of the hole concentration is quite different from Pr1-xCaxMnO3, where long-range CE-AF is stable for x>0.3.

[1] Y. Tokunaga et al, to be published in PRB.

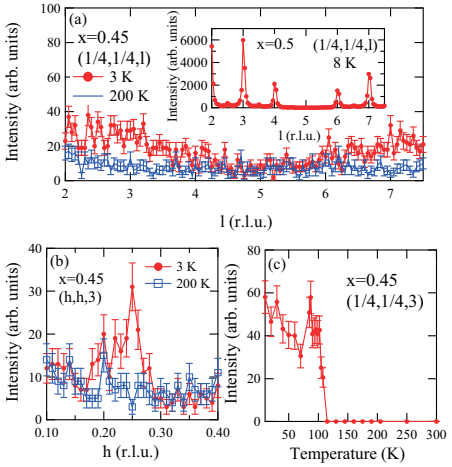


Fig. 1. Profiles of CE-type spin order observed along (a) q=(1/4,1/4,l) and (b) (h,h,3). (c) Temperature dependence of the diffuse intensity observed at q=(1/4,1/4,3).

1-1-50

Neutron scattering in Ising-like one dimensional antiferromagnet $BaCo_2V_2O_8$

T. Masuda, S. Hondo, and M. Matsuura[a]
International Graduate Schools of Arts and Sciences, Yokohama City University, 22-2 Seto, Kanazawa-ku, Yokohama, 236-0027
[a]Neutron Scattering Laboratory, Institute for Solid State Physics, University of Tokyo, 106-1 Shirakata, Tokai, Ibaraki, 319-1106, Japan

In one-dimensional antiferromagnetic XXZ model the phase diagram of the ground state contains characteristic nature of quantum fluctuation: Néel state in $\epsilon < 1$, quantum criticality at $\epsilon = 1$, and spin liquid at $\epsilon > 1$. Here ϵ is XXZ anisotropy parameter. In the uniform magnetic field characteristic behavior of Tomonaga-Luttinger liquid is identified by incommensurate spin correlation in longitudinal mode. Recently such experimental realization was discovered in $BaCo_2V_2O_8$ [1] by the combination of magnetization, ESR, and heat capacity measurements. The compound shows usual Néel transition at 5.4 K in zero field. In applied field at $h > 4$ T a new phase appears at $T < 1.4$ K which could be concerned with incommensurate spin correlation. The study of the spin dynamics by neutron scattering technique in $BaCo_2V_2O_8$ is a matter of importance. Eventually we noticed that another group in Europe is proceeding the similar study. We think that this study has priority over the original proposal titled "neutron scattering study in O_2 adsorbed CPL-p1." Hence we performed inelastic neutron scattering study in $BaCo_2V_2O_8$ in zero field in the 8th cycle in the fiscal year of 2007.

From the previous studies it is estimated that $J = 5.4$ meV, $\epsilon = 0.53$, and $J' = -0.065J$. Here J is the intrachain interaction and J' is the next nearest neighbor intrachain interaction. Exact diagonalization calculation predicts the anisotropy gap of 1.55 meV and the boundary energy of 7meV. Therefore we select thermal neutron with tight collimation setup: 36′ - 40′ - sample - PG - 40′ - 80′ with fixed final energy of E_f = 13.5 meV. The prepared crystal is cylindrical shape with ϕ8 mm × 20 mm. The chain axis is crystallo graphical c direction and we put scattering plane as $(h\ 0\ l)$.

We performed a series of constant q scans. Well defined peaks were observed as is shown in the typical scan in Fig. 1. The boundary energy is 7 meV and the anisotropy gap is 2 meV that are consistent with theoretical calculation. Since Co ions form 4-folded screw chain, four modes are predicted of which two modes are degenerated. Doing Fourier transformation of the Co position we obtained the structure factor with the modulation in a^* - b^* plane. By selecting adequate q we obtained a set of scans free of additional mode. The magnetic dispersion is mostly consistent with theory. Further analysis and calculation will appear in forthcoming paper.

References

[1] S. Kimura *et al.*, Phys. Rev. Lett. **99**, 087602 (2007), S. Kimura *et al.*, Cond-mat 0707.4713.

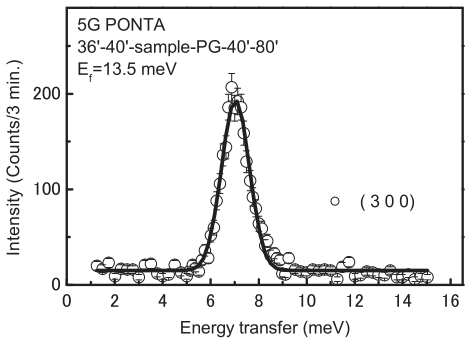


Fig. 1. Typical constant q scan in $BaCo_2V_2O_8$

1-1-51

Crystal structural analysis of rutile-type titania

Yong Phat, Masatomo Yashima, Takahiro Wakita, Takafumi Komatsu
Department of Materials Science and Engineering, Interdisciplinary Graduate School of Science, Tokyo Institute of Technology

Titanium dioxide (titania) is a technologically important material with applications in photocatalysis, paints, gas sensors, electrochromic devices, lithium ion batteries, and dye-sensitized solar cells. TiO2 crystallizes most commonly in either the rutile (space group P42/mmm) or anatase-type structure. For bulk titania crystals at ambient conditions, rutile is more stable than anatase and has therefore been more widely studied. In contrast to the extensive studies on its crystal structure, however structural properties of the rutile structure in high temperature have not been studied in detail and not well understood. In this study, we investigated the crystal structure of rutile-type titania at high temperatures by using neutron powder diffraction method.

Rutile-type titania powders were pressed into pellets. These pellets were used for high-temperature neutron diffraction measurements. Neutron diffraction measurements were performed in air with a 150-detector system, HERMES [1], installed at the JRR-3M reactor in Japan Atomic Energy Agency, Tokai, Japan. Neutrons with wavelength 1.8143 were obtained by the (331) reflection of a Ge monochromator. Diffraction data were collected in air from room temperature to high temperatures. A furnace with MoSi2 heaters [2] was placed on the sample table, and used for neutron diffraction measurements at high temperatures. The experimental data were analyzed by a combination of Rietveld analysis, the maximum-entropy method (MEM) and MEM-based pattern fitting (MPF). Computer programs RIETAN-FP, PRIMA and VESTA were utilized for the Rietveld and MPF analyses, MEM calculation and visualization of crystal structure and nuclear-density distribution, respectively. The data analysis is now in progress.

Reference

[1] K. Ohoyama et al., Jpn. J. Appl. Phys. 37 (1998) 3319.
[2] M. Yashima, J. Am. Ceram. Soc. 85 (2002) 2925.

1-1-52

Diffuse Scattering of PbF_2

Xianglian, K. Basar, S. Siagian, T. Sakuma, H. Takahashi[1] and N. Igawa[2]

Institute of Applied Beam Science, Ibaraki University, Mito 310-8512
[1]*Institute of Applied Beam Science, Ibaraki University, Hitachi 316-8511*
[2]*Japan Atomic Energy Agency, Tokai 319-1195*

Diffuse scattering contains information about a short-range-order in a disordered arrangement (static disorder) and thermal vibrations of atoms (thermal disorder) in crystals[1)]. The oscillatory diffuse scattering intensities were observed from ordered crystals at room temperature due to the correlation effects among thermal displacements of atoms[2)]. High temperature phase of PbF_2 is known as a superionic conductor with anion disorder. In order to clarify the influence of the correlation effects among thermal displacements of atoms and the disorder of anions, the neutron diffuse scattering profile in PbF_2 was studied.

Neutron scattering measurements were performed on powder PbF_2 at 295, 633 and 773 K by HRPD. Powder samples were set in a vanadium container of 10 mm in diameter. Incident neutron wavelength was 1.823 Å. The scattering data were collected in the range of scattering angle from 10° to 160° with step angle 0.05°. The observed diffuse neutron scattering intensities of PbF_2 are shown by broken lines in Fig. 1.

Rietveld refinement analysis has been performed on the neutron scattering intensities of PbF_2. Room temperature phase of PbF_2 belongs to orthorhombic system. The phase of PbF_2 at 633 K belongs to cubic system. The phase of PbF_2 at 773 K also belongs to cubic system and has disordered arrangements of F atoms. The calculated diffuse scattering intensities are shown by solid lines in Fig. 1. The values of correlation effects were included in the calculation for the interatomic distances less than 5 Å. The other values of correlation effects are assumed to be 0. The observed diffuse scatterings at 295 and 633 K are explained by correlation effects among thermal displacements of atoms. The diffuse scattering intensity at 773 K includes the contribution from disordered arrangements of F atoms and thermal vibrations of atoms.

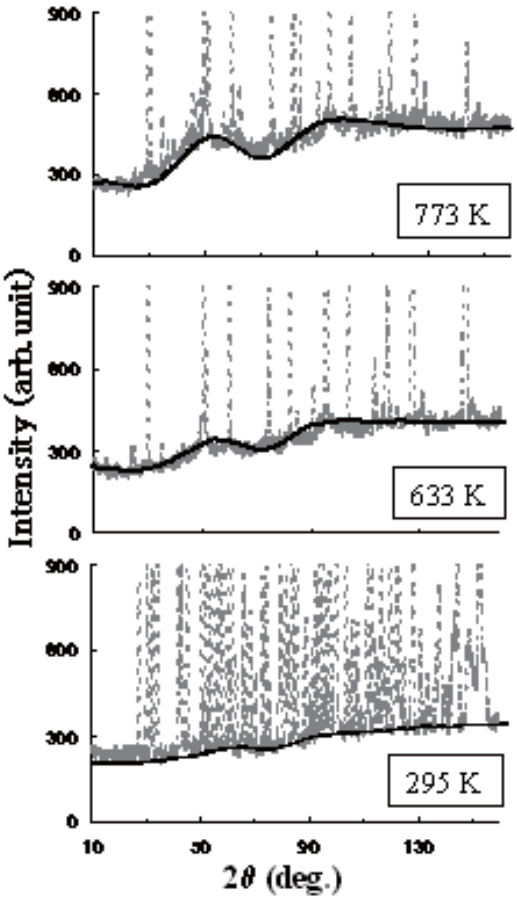


Figure 1: Neutron scattering intensities of powder PbF_2 above room temperature.

References

1) T. Sakuma: "J. Phys. Soc. Jpn.", 62, pp. 4150-4151 (1993).
2) T. Sakuma *et al.*: "Solid State Ionics", 176, pp. 2689-2693 (2005).

原子炉：JRR-3　　装置：HRPD(1G)　　分野：中性子散乱（構造）

1-1-53

Structural Features of Lithium Ion Conductor $Li_{1+x}Ge_{2-x}Al_x(PO_4)_3$

Y. Fujita, H. Takahashi, T. Sakuma[1] and N. Igawa[2]

Graduate School of Science and Engineering, Ibaraki University, Hitachi, Ibaraki 316-8511
[1] *Graduate School of Science and Engineering, Ibaraki University, Mito, Ibaraki 310-8512*
[2] *Quantum Beam Science Directorate, JAEA, Tokai, Ibaraki 319-1195*

$LiGe_2(PO_4)_3$ is a inorganic compound that has a so-called NASICON-type structure and indicates high Li^+ ion conduction. The substitution of Ge^{4+} ions by Al^{3+} ion leads to the increase of Li^+ ion concentration so that the charge neutrality in the compound is held. The chemical formula for Al-substituted compound is expressed as $Li_{1+x}Ge_{2-x}Al_x(PO_4)_3$, denoted as Al-LISICON. The space group of Al-LISICON is R-3c. The ionic conductivity increases with Li^+ ion concentration. In this case, excess Li^+ ions expressed by x in the chemical formula are distributed on 18e site. It has been reported that substituted Al^{3+} ion does not occupy Ge site but P site by NMR investigation [1]. In the present study, X-ray and neutron diffraction experiments were performed to clarify the characteristic features of the crystal structure for Al-LISICON at x=0.5. Neutron diffraction was done at 10, 150 and 300K by HRPD installed in JRR-3M. Diffraction pattern from HRPD at 300 K is shown in Fig. 1. Based on the Rietveld analysis, it is suggested that substituted Al^{3+} ion is distributed only on Ge site. It is known that strong diffuse scattering is observed especially in superionic conductors. Remarkable thermal diffuse scattering is expected in the diffraction profile of Al-LISICON, because of high Li^+ ion conduction in this compound. However the diffuse scattering intensity highlighted in the inset in Fig. 1 is almost the same as those in 150 and 10 K. These results suggest that the most of the diffuse scattering comes from not the thermal motion but the static disorder of constituted ions. Alami et al. reported that Li^+ ion at 6b site is slightly displaced to (001) direction in $LiGe_2(PO_4)_3$ [2]. Our structure refinement using Rietveld analysis gives unsatisfactory result at present. One of the reasons might arise from static disorder of Li^+ ions. More detailed analysis for Li^+ ion distribution in Al-LISICON is in progress.

References

1) P. Maldonado-Manso, M. C. Martin-Sedeño, S. Bruque, J. Sanz and E. R. Losilla :"Solid State Ionics", 178, 43(2007).
2) M. Alami, R. Brochu, J. L. Soubeyroux, P. Gravereau, G. Flem and P. Hagenmuller :"J. Solid State Chem.", 90, 185(1991).

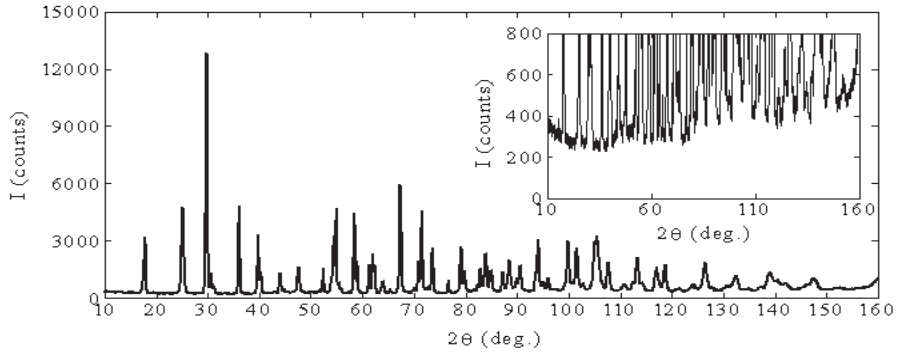


Figure 1: Neutron diffraction profile for $Li_{1.5}Ge_{1.5}Al_{0.5}(PO_4)_3$ at 300 K. The inset shows an expansion of the diffuse background portion.

原子炉：JRR-3　　装置：HRPD(1G)　　分野：中性子散乱（構造）

1-1-54

Xe Motion in Clathrate Deuterohydrate Analyzed by Applying Rietveld/Maximum Entropy Method

N. Igawa, T. Taguchi, H. Fukazawa, H. Yamauchi, W. Utsumi and Y. Ishii[1]

Quantum Beam Science Directorate, JAEA, Tokai, Ibaraki 319-1195
[1]*Radiation Application Development Association, Tokai, Ibaraki 319-1106*

Xenon hydrate is a structure I type clathrate hydrate at the atmospheric pressure and below the decomposed temperature. Although the three dimensional hydrogen-bonded framework in clathrate hydrate had been reported, the details of Xe gas motions in the framework are not clear. In this study, we analyzed the scattering length density distribution of Xe deuterohydrate by Rietveld and MEM analysis of neutron powder diffraction data to clarify the Xe motion.

We prepared deuterohydrate for the neutron diffraction to suppress the incoherent neutron scattering, which are especially caused by the H atoms. Neutron powder diffraction measurements were carried out using the HRPD at the temperatures of 10, 115, and 245 K. A neutron wavelength of 0.1823 nm was used. Crystal structures were determined from the diffraction patterns by the Rietveld method using the program "RIETAN-FP".[1)] After the Rietveld analysis, the scattering density distribution maps were analyzed by applying the maximum entropy method analysis using the program "PRIMA".[2)]

Figure 1 shows a result of Rietveld refinement at 10 K. All peaks were from the Xe deuterohydrate, and no reflections of impurities were observed. The R_{wp} and S are 3.42 % and 1.10. Structure I hydrates consist of 46 ice molecules in a framework of two dodecahedral cages (small cages) and six tetrakaidecahedral cages (large cages) in a unit cell. Figure 2 shows the temperature dependence of the scattering length density distribution maps of the small and large cages of Xe deuterohydrate. All maps were drawn with the same isosurface level, 1.0 fm/Å^3. In the small cage, a spherical positive scattering length density was observed at the center of the cage, which is attributed to Xe. An ellipsoid shaped scattering length density distribution at the center of the cage was observed in the large cage; the major axis of the density distributuion was directed toward the center of a hexagonal facet of the large cage. The distributions of Xe in the both cages were almost the same at any temperature.

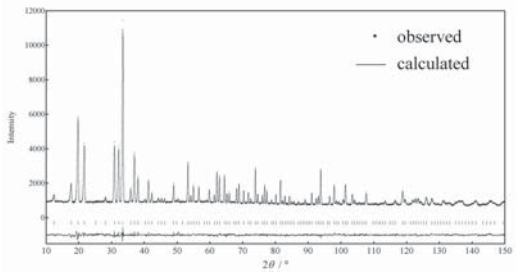


Figure 1: The result of the Rietveld analysis of Xe deuterohydrate at 10 K.

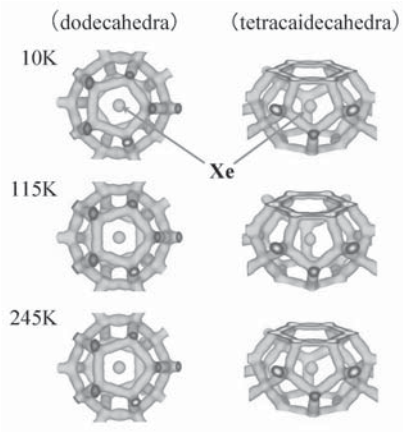


Figure 2: Scattering length density distribution maps for different temperatures.

References

1) F. Izumi et al.: "Solid State Phenom.", 13015(2007).
2) F. Izumi et al.: "Recent Research Development in Physics II", 3, 699(2002).

原子炉：JRR-3　　装置：HRPD(1G)　　分野：中性子散乱（構造）

1-1-55

Neutron Powder Diffraction and Difference MEM Analysis of Protium- and Deuterium-Dissolved $BaSn_{0.5}In_{0.5}O_{2.75+\alpha}$

T. Nagasaki[1], S. Shiotani[2], M. Yoshino[2], K. Iwasaki[2],
N. Igawa[3], H. Fukazawa[3] and W. Utsumi[3]

[1] *EcoTopia Science Institute, Nagoya University, Nagoya 464-8603*
[2] *Department of Materials, Physics and Energy Engineering, Graduate School of Engineering, Nagoya University, Nagoya 464-8603*
[3] *Quantum Beam Science Directorate, JAEA, Tokai, Ibaraki 319-1195*

Some perovskite oxides with dopant cations and oxide ion vacancies absorb water vapor in humid atmosphere to release mobile hydrogen ions (protons) into the structure, thereby becoming proton conductors. These materials are of fundamental interest as well as of practical one because of their potential applications to protonic devices including fuel cells.

Recently maximum entropy method (MEM) combined with neutron powder diffraction has been extensively used to investigate the crystal structures of ionic conductors including proton-conducting oxides [1–3]. It is because in general, the MEM is effective for revealing static and dynamic disorder in crystals. However, as we pointed out in the previous paper [4], the spatial resolution of 3D atomic distribution map deduced by MEM is limited especially when the neutron wavelength is long and the atomic concentration is low.

Therefore, we introduced a new method, the difference MEM analysis of neutron diffraction data, as a method to reveal detailed structure around hydrogen atoms in proton-conducting oxides. It is a MEM analysis of the differences between the structure factors of protium- and deuterium-dissolved crystals. Simulation has demonstrated that it not only provides the distribution of hydrogen atoms alone but also improves the spatial resolution of the MEM mapping around hydrogen atoms.

It should be noted that the MEM mapping in its own nature has a tendency to connect and merge the neighboring areas in the 3D atomic distribution. (We must take this behaviour into account when discussing minor distribution or diffusion pathways of atoms.) In the difference MEM analysis, however, we locate hydrogen atoms and other atoms in separate MEM calculations. In other words, they are not neighboring during the MEM calculations. That is why the difference MEM analysis drastically improves the separation between hydrogen and other atoms.

The difference MEM analysis was then applied to actual neutron diffraction data of protium- and deuterium-dissolved $BaSn_{0.5}In_{0.5}O_{2.75+\alpha}$. The result (Fig. 1, right) shows that O-H bonds mostly tilt towards the second nearest oxygen atoms and that distribution of hydrogen and/or oxygen atoms are insignificant in interstitial regions .

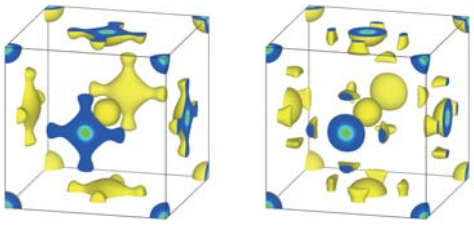


Figure 1: Scattering length density distributions in D_2O-dissolved $BaSn_{0.5}In_{0.5}O_{2.75+\alpha}$ deduced by the ordinary MEM analysis (left) and the difference MEM analysis (right). RIETAN-FP, PRIMA and VESTA were used for the analysis and the drawing.

References

1) T. Ito, T. Nagasaki et al. :"Solid State Ionics", 178, pp. 607-613 (2007).
2) X. Kuang et al. :"Nature Mater.", 7, pp. 498-504 (2008).
3) S. Nishimura et al. :"Nature Mater.", doi:10.1038/nmat2251 (2008).
4) T. Nagasaki et al. :"J. Nucl. Sci. Technol.", Suppl. 5, in print (2008).

原子炉：JRR-3　　装置：HRPD(1G)　　分野：中性子散乱（構造）

1-1-56

In Situ Powder Neutron Diffraction Experiment under High Pressure

W.Utsumi, K.Komatsu[1], H.Arima[1], H.Kagi[1], T.Okuchi[2],
S.Sasaki[3], H.Yamauchi, H.Fukazawa, N.Igawa and T.Kamiyama[4]

Quantum Beam Science Directorate, JAEA, Tokai, Ibaraki 319-1195
[1]*Graduate School of Science, The Tokyo University, Hongo, Bunkyo-ku, Tokyo 113-0011*
[2]*Institute for Study of the Earth's Interior, Okayama University, Misasa, Tottori 682-0193*
[3]*Department of Materials Science and Technology, Gifu University, Yanagido, Gifu 501-1193*
[4]*High Energy Accelerator Research Organization (KEK), Oho, Tsukuba, Ibaraki 305-0801*

Application of high pressure to materials often induces drastic changes in structure, physical properties, chemical reactions, etc., and sometimes remarkable phase transitions may occur. It is expected that high pressure material science and the investigation of the Earth's interior will greatly improve using the high flux pulse neutrons of J-PARC. We carried out a preliminary test experiment using the High Resolution Powder Diffractometer (HRPD) at JRR-3 to check the feasibility of the high pressure device[1)].

A Paris-Edinburgh cell, which is a standard high pressure device for the neutron experiment in Europe and USA, was mounted on the rotation stage of HRPD (Figure 1). A pair of anvils made of cubic born nitride (cBN) was used for the pressure generation. Diffraction profiles of Pb (initial size: 6mm in diameter and 1.6mm in height) placed in the high pressure cell were observed at 0 GPa (ambient conditions) and 2.9 GPa (applied load was 30 ton). Incident and diffracted neutron beams (wavelengh:1.823Å) pass through the anvil gap which is perpendicular to the compression axis. The exposure time was 2 and 10.5 hours for ambient and at high pressures, respectively.

Figure 2 shows the diffraction profiles thus obtained. Several peaks of Pb were clearly observed and the calculated lattice constants at 0 GPa and 2.9 GPa were 4.9518(3) and 4.8746(3) Å, respectively. Although the sample was surrounded by gasket and anvil materials, the background noise signals from these materials were reduced significantly due to the fine collimation of HRPD and the use of cBN anvils. Present results provide us useful information for the *in situ* high pressure experiments at J-PARC.

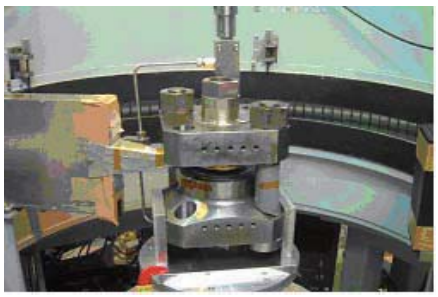


Figure 1: Paris-Edinburgh cell mounted on HRPD.

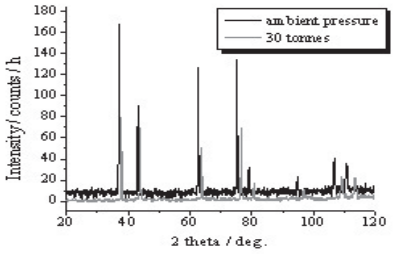


Figure 2: Diffraction profiles of Pb at 0 and 2.9 GPa.

References

1) K.Komatsu, H.Arima, H.Kagi, T.Okuchi, S.Sasaki, H.Yamauchi, H.Fukazawa, N.Igawa, W.Utsumi, and T.Kamiyama:"A high pressure experiment of powder neutron diffraction on the HRPD at JRR-3", Rev. High Press.Tech.(Japanese), 18, 170(2008).

原子炉：JRR-3　　装置：HRPD(1G)　　分野：中性子散乱（構造）

1-1-57

Pressure-Temperature Phase Diagram of Filled Skutterudite $PrFe_4P_{12}$

T. Osakabe and K. Kuwahara[1]

Quantum Beam Science Directorate, JAEA, Tokai, Ibaraki 319-1195
[1] *Graduate School of Science and Engineering, Ibaraki Univ., Mito, Ibaraki 310-8512*

Filled skutterudite compound $PrFe_4P_{12}$ shows a Γ_1-type electronic mulitipolar order below $T_A = 6.5$ K at ambient pressure [1,2]. The propagation vector is $\boldsymbol{q} = (1, 0, 0)$, which is closely related with the nesting property of the Fermi surface [3]. Applied pressure suppresses this orderd phase (A-phase, hereafter) and induces an insulating phase above 2.4 GPa at low temperature [4].

We performed neutron diffraction experiments under hydrostatic pressure up to 4.3 GPa to investigate the order parameter in the pressure-induced insulting phase. The experiments were carried out by using the TAS-1 spectrometer in JRR-3, JAEA at Tokai. The high pressure was generated by a newly-developed hybrid-anvil device composed of a large sapphire anvil and a tungsten carbide anvil [5]. Glycerin was employed as a pressure-transmitting medium, which transmits the hydrostatic pressure at least up to 7 GPa [6]. The sample size was about 0.8 ×0.6 ×0.2 mm^3.

Above 2.7 GPa, we found the AFM order with the propagation vector of $\boldsymbol{q} = (1, 0, 0)$, which is identical with that in the A-phase. The *Néel* temperature and ordered magnetic moment per Pr ion are summarized in fig. 1 as a pressure-temperature phase diagram together with the data in ref. [4]. As shown in fig. 1, the AFM ordered phase (M-phase, hereafter) corresponds to the pressure-induced insulating phase and highly stabilized by applied pressure. The magnetic structure in the M-phase is schematically shown in fig. 1. The transition from the A-phase to the M-phase is first order. The magnetic moment at 1.5 K is approximately 2.0 μ_B, which is consistent with the dipole moment in the CEF ground state of the Γ_1-$\Gamma_4^{(1)}$ with $d \sim 1$ quasi-quartet [7,8]. The drastic change in the order parameter from the A-phase to the M-phase at relatively low pressure is suppose to be originated from the comparable ordering energy between the multipoles in the highly degenerate ground state in this compound.

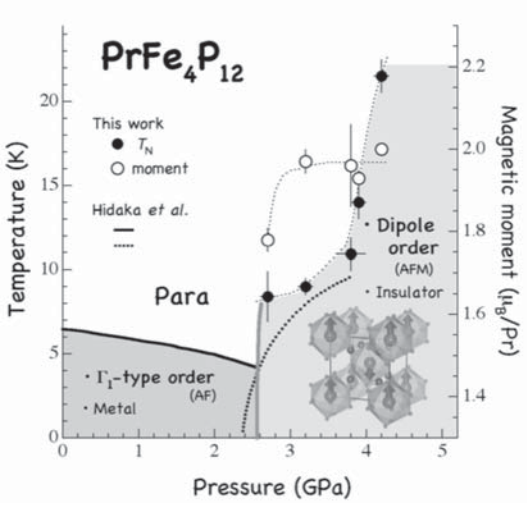


Figure 1: Pressure-temperature phase diagram of $PrFe_4P_{12}$.

References

1) Y. Aoki, T. Namiki, T. D. Matsuda, K. Abe, H. Sugawara, and H. Sato :,"Phys. Rev. B", 65, pp. 064446-1-7 (2002).
2) J. Kikuchi, M. Takigawa, H. Sugawara, and H. Sato : "J. Phys. Soc. Jpn.", 76, pp. 043705-1-4 (2007).
3) H. Harima, K. Takegahara, S. H. Curnoe, K. Ueda : "J. Phys. Soc. Jpn.", 71 Suppl. pp. 70-73 (2002).
4) H. Hidaka, I. Ando, H. Kotegawa, T. Kobayashi, H. Harima, M. Kobayashi, H. Sugawara and H. Sato :"Phys. Rev. B", 71, pp. 073102-1-4 (2005).
5) T. Osakabe, K. Kakurai, D. Kawana and K. Kuwahara : "J. Magnetism Magnet. Mater.", 310, pp. 2725-2727 (2007).
6) T. Osakabe and K. Kakurai :"Jpn. J. Appl. Phys.", 47, pp. 6544-6547 (2008).
7) A. Kiss and Y. Kuramoto :"J. Phys. Soc. Jpn.", 74, pp. 2530-2537 (2005).
8) Y. Kuramoto, A. Kiss, J. Otsuki and H. Kusunose :"J. Phys. Soc. Jpn.", 75 Suppl. pp. 209-214 (2006).

原子炉：JRR-3　　装置：TAS-1(2G)　　分野：中性子散乱（構造）

1-1-58

Cu Dimer Excitations in $Cu_2Fe_2Ge_4O_{13}$

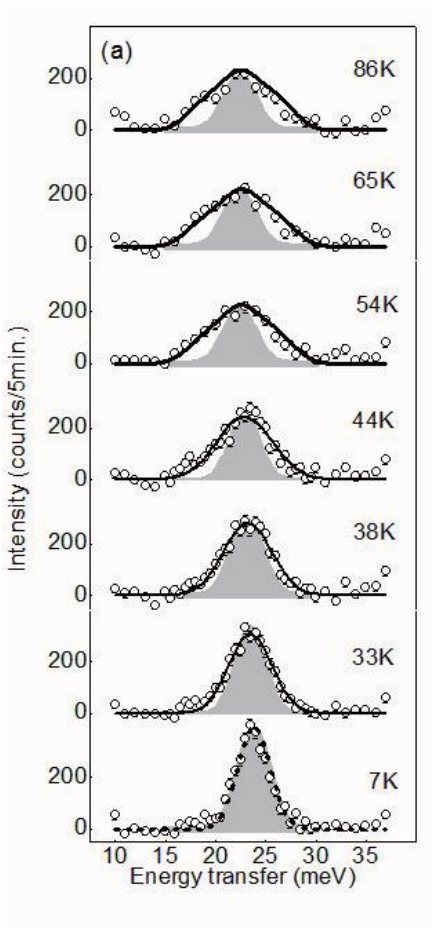
T. Masuda and K. Kakurai[1]

Yokohama City University, Yokohama, Kanagawa 236-0027
[1] *Quantum Beam Science Directorate, JAEA, Tokai, Ibaraki 319-1195*

$Cu_2Fe_2Ge_4O_{13}$ is a rare experimental realization of weakly coupled quantum dimers (Cu) and classical chains (Fe) compound [1)]. So far Fe centered magnetic excitations in lower energy range, which can be explained by weakly coupled Fe spins, had been studied in detail. For example, careful measurement of the magnetic dispersion in LTAS spectrometer revealed the existence of effective magnetic interaction by way of non-magnetic singlet Cu dimer [2)].

From the view of Cu dimers different type of effective models would be realized, namely Cu dimers in the staggered field from neighboring Fe moments at $T < T_N$ and dimers in random field at $T > T_N$. Such models have rarely been realized in external zero magnetic field. To verify the models in $Cu_2Fe_2Ge_4O_{13}$ we measured Cu centered dispersionless mode at $\hbar\omega \sim$24meV on TAS1 in JRR-3M.

Figure (a) is constant q scans in different temperatures. Well defined peaks due to Cu dimers are observed at $\hbar\omega = 24$ meV. At 7 K the peak is within resolution indicated by gray area. With the increase of temperature the width becomes wider and at $T >$54K (well above T_N) it reaches the saturation. The behaviors are qualitatively explained by density of state (DOS) of triplet excitations of spin dimers in staggered/random field. In the staggered field the triplet splits into singlet and doublet with $E_{doublet} = 1/2J + 1/2\sqrt{4h^2 + J^2}$, $E_{singlet} = \sqrt{4h^2 + J^2}$. In random field the triplets split intro the energy range of $J-h < E < J+h$. Here h is the field scaled in energy ($h = g\mu_B H$). Because h (5.48 meV) is small compared with J ($J = 24$ meV) [1] the DOS in the latter spreads in wider energy range than that in the former. Consequently the excitation in constant q scans at $T > T_N$ becomes broad. The dotted and bold solid curves are the theoretical calculations of neutron cross section based on dimers in staggered and random fields, respectively. Excellent agreements between the experiment and calculation mean that the proposed effective spin models are realized in $Cu_2Fe_2Ge_4O_{13}$.



References

1) T. Masuda et al., PRL 93, 077202 (2004).
2) T. Masuda et al., PRB 75, 220401(R) (2007).

原子炉：JRR-3　　装置：TAS-1(2G)　　分野：中性子散乱（構造）

1-1-59

Local Lattice Distortion in Giant Negative Thermal Expansion Material $Mn_3Cu_{1-x}Ge_xN$

S. Iikubo, K. Kodama, K. Takenaka[2,3], H. Takagi[3,4] and S. Shamoto

Quantum Beam Science Directorate, JAEA, Tokai, Ibaraki 319-1195
[1]*Department of Crystalline Materials Science, Nagoya University, Nagoya 464-8603*
[3]*RIEKN (TheInstituteofPhyscalandChemicalResearch), Wako, Saitama 351-0198*
[4] *CREST, Japan Science and Technology Agency, Kawaguchi, Saitama 332-0012*

$Mn_3Cu_{1-x}Ge_xN$ exhibits sharp magnetovolume effect (MVE) for $x \sim 0.15$, and with increasing x, MVE becomes broad against temperature (T), similar to Invar effect, leading to a giant negative thermal expansion coefficient[1]. Previous neutron diffraction measurement indicates that the system which exhibits large MVE ($0.15 \leq x \leq 0.7$), has so-called Γ^{5g}-type antiferromahentic ordering and the structure remains cubic below T_N[2]. In this study, we performed powder neutron diffraction on $Mn_3Cu_{1-x}Ge_xN$ to investigate the mechanism of the broadening of MVE.

T-dependence of the scattering intensity of magnetic (100) reflection is shown in main panel of Fig. 1. The intensity is normalized by the intensity of nuclear (100) reflection. The inset shows the T-dependence of the lattice constant from diffraction data. These results indicate that in the sample whose lattice constant gradually increases with decreasing T, the magnitude of the ordered moment gradually increases.

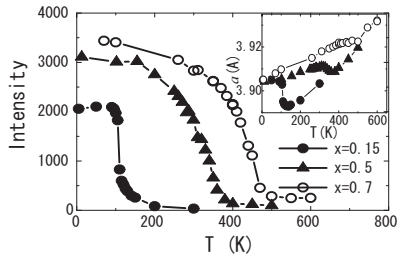


Figure 1: Main panel : T-dependence of the intensity of magnetic (100) reflection for x=0.15, 0.5 and 0.7. Inset : T-dependence of the lattice constant.

Figure 2 shows atomic pair distribution functions $G(r)$ of $Mn_3Cu_{1-x}Ge_xN$ obtained from pulsed neutron diffraction data collected on the powder diffractometer NPDF at the Los Alamos Neutron Science Center. Peak (1) indicates atomic correlation between Mn and N in Mn_6N octahedron. Peak (2) is a superposion of negative Mn-Cu (Ge) and positive Mn-Mn correlations. Peak (1) is a sharp single peak. In contrast, peak (2) splits into two peaks (shown by arrows). These indicate that Mn-octahedron rotates without the change of the shape. Although the periodic rotation of Mn-octahedron causes the structural transition to tetragonal structure in Mn_3GeN, the average strcuture of these samples remain cubic, indicating that the rotation is not periodic. It is found that the local Mn-octahedron rotation becomes larger with increasing x, by x-dpendence of the splitting of peak (2) shown by arrows. These results indicate that the local lattice distortion strongly correlates with the broadening of MVE, i.e., Invar effect.

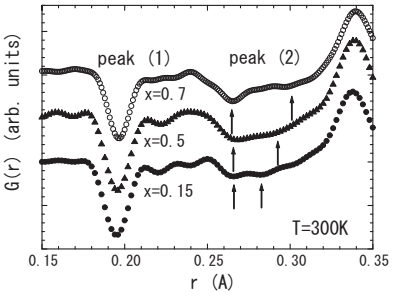


Figure 2: Atomic pair distribution functions $G(r)$ of $Mn_3Cu_{1-x}Ge_xN$ for x=0.7, 0.5 and 0.15 at 300 K.

References

1) K. Takenaka and H. Takagi :Appl. Phys. Lett. 87, 261902 (2005).
2) S. Iikubo *et al.* :Phys. Rev. B77, 020409(R) (2008).
3) S. Iikubo *et al.* : submitted to Phys. Rev. Lett.

原子炉：JRR-3　　装置：TAS-2(T2-4)　　分野：中性子散乱（構造）

1-1-60

Existence of Ferroelectric Ice on Planets -a neutron study-

H. Fukazawa

Quantum Beam Science Directorate, JAEA, Tokai, Ibaraki 319-1195

The complex behavior of water and the unusual properties of hydrogen ordering in ferroelectric ice crystal continue to attract much interest. Whether ice in the space exists as hydrogen-ordered ices, is an important question. Some ordered ices have ferroelectricity, and long range electrostatic forces caused by the ferroelectricity might be an important factor for planet formation.

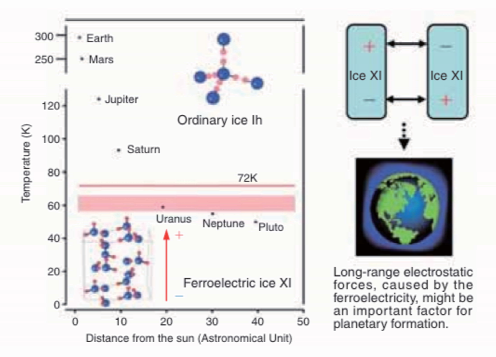


Figure 1: The area (below the red line of 72 K) where ice XI exists as a stable form in the solar system. Since water molecules are aligned along c-axis (vertical direction), ice XI has ferroelectricity.

Recently, Fukazawa et al [1,2] imitated the ice of cold space and measured neutron diffraction of the ice. The position of hydrogen became ordered at temperatures (below 76 K) of Uranus, Neptune and Pluto. H of the water molecule has a positive charge. Based on the neutron measurements, it is proposed that ferroelectric ice, named ice XI, exists in the Universe (Figure 1). Ice XI is the H-ordered structure and KOH accelerates the phase transition process.

Figure 2 shows the diffraction pattern (dotted line) of NaOD-doped ice, which was kept at 57 K for one day and kept at 68 K for 3 days. The solid lines, which are calculated from the best-fit model of the Rietveld refinement with f = 0.27, are in good agreement with the observed intensities drawn as dots. It confirms that ice XI is ferroelectric ice with aligned water molecules, as shown in Figure 1.

The particles of ice XI have long-range electric forces. The small ice XI of several micrometers in solar nebula may grow quickly and attract electrons and ions. This special character of ice XI becomes a key that solves the mystery of the planet formation and the material evolution. Furthermore, a preliminary work using TAS-2 shows a clear difference in the spectroscopic data between ice XI and ice Ih. This implies that future telescope and planetary exploration will find huge ferroelectric ice and hydrogen-ordered ices in our solar system.

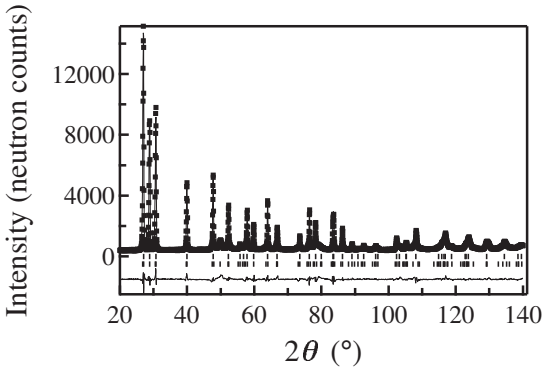


Figure 2: Neutron diffraction pattern of 0.01-M NaOD-doped ice at 68 K.

References

1) H. Fukazawa, et al. :“Astrophys. J. Lett.”, 652, pp. L57-L60 (2006).
2) H. Fukazawa, et al. :“Physica B”, 385-386, pp. 113-115 (2006).
3) H. Fukazawa :“JAEA R&D Review”, p. 43 (2007).
4) H. Fukazawa :“Planetary People”, 16, pp. 7-12 (2007).
5) H. Fukazawa :“Hamon (The Japanese Society for Nuetron Science)”, 18, pp. 97-102 (2007).

原子炉：JRR-3　　装置：TAS-2(T2-4)　　分野：中性子散乱（構造）

1-1-61

Nano-structure Analysis of ODS Ferritic Steels for Fast Reactor Application

S. Ohtsuka[1], J. Suzuki[2], T. Kaito[1], S. Kim[1], M. Inoue[1], S. Obara[1] and T. Asayama[1]

[1] *Core and Structural Materials Group, Advanced Nuclear System R&D directorate*
[2] *Neutron Optics Group, Quantum Beam Science Directorate*

The oxide dispersion strengthened (ODS) ferritic steel is a prospective material for fuel cladding tube of advanced fast breeder reactor (FBR). The most important task in the ODS ferritic steel development is high-temperature strength improvement because the maximum temperature of fuel cladding is designed to be as high as 973K for high thermal efficiency and economical plant operation. In this research, nano-structure analysis of ODS ferritic steel was carried out using SANS-J-II in JRR-3, and the correlation between nano-structure and high-temperature strength was quantitatively evaluated with a view to obtaining insights into nano-structure control technique for high-temperature strength improvement of ODS ferritic steel.

The ODS ferritic steel model alloys containing different concentrations of excess oxygen (Ex.O) and Ti were prepared, where the basic chemical composition of JAEA ODS steel for fast reactor application, i.e. 9mass%Cr-0.13C-2W-0.35Y_2O_3, was adopted. Excess oxygen is defined as the value obtained by subtracting O in Y_2O_3 from the total O in the steel. These steels were consolidated at 1423K (No.1, 3, 4) and 1473K (No.2), respectively. The size distribution and number density of nano-oxide particles were determined from the measured SANS profiles, where log-normal size distribution was adopted. Figure 1 clearly displays that decreasing Ex.O as well as increasing Ti provide for noticeable increase of nano-particle number density and size reduction of nano-particles. Comparison of the profiles between No.1 and No.2 proves that the lower consolidation temperature is favored in terms of high population nano-particle dispersion. The creep strength of 9Cr-ODS steel was plotted against the square root of nano-particles number density in Fig.2, which shows the creep strength of 9Cr-ODS steels is closely correlated with population of nano-oxide particles. The square root of nano-particles number density is known to be proportional to oxide dispersion strengthening. These results definitely give the important knowledge that delicate control of excess oxygen and titanium concentrations as well as appropriate choice of consolidation temperature are key points for high population nano-particle dispersion leading to drastic high-temperature strength improvement of ODS ferritic steel.

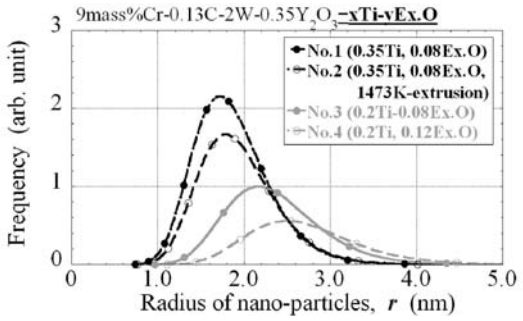


Figure 1: Size distribution of nano-scale oxide particles in 9Cr-ODS steels

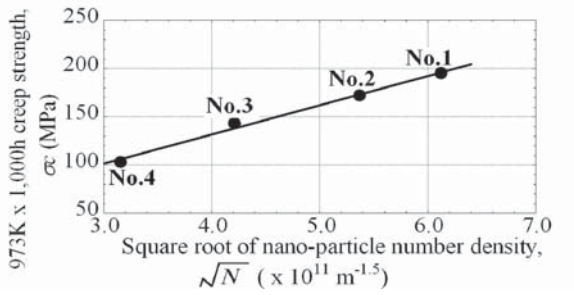


Figure 2: Creep rupture strength versus square root of nano-particle number densities.

原子炉：JRR-3　　装置：SANS-J-II　　分野：中性子散乱（構造）

This is a blank page.

1. 中性子散乱 2）磁　性

1. Neutron Scattering　2）Magnetism

This is a blank page.

1-2-1

Neutron Inelastic Scattering of TbPd3S4

E. Matsuoka, K. Ohoyama(A), and H. Onodera
Department of Physics, Tohoku University, (A)Institute for Materials Research, Tohoku University

The rare-earth (R) palladium bronzes RPd3S4 crystallizes into a cubic NaPt3O4-type crystal structure. R atoms form a body-centered cube and are subjected to a cubic crystalline electric field (CEF) represented by the cubic point group of Th [1]. Systematic studies along the R series have revealed that the CEF ground states of 4f electrons in RPd3S4 retain an orbital degeneracy [1].

In this system, DyPd3S4 with a quartet CEF ground state shows an antiferro-quadrupolar (AFQ) ordering at 3.4 K [2]. However, the order parameter of the AFQ phase has not been determined yet. For the determination of order parameter, we need to know the CEF scheme of 4f electrons. The best experimental method for the estimation of CEF scheme is a neutron inelastic scattering. Unfortunately, it is difficult to perform a neutron scattering of DyPd3S4 because of strong neutron absorption by natural Dy nuclei. In this study, neutron inelastic scattering of TbPd3S4 has been performed and CEF scheme of TbPd3S4 has been estimated. Our final purpose is to estimate CEF scheme of DyPd3S4 by analogy with that of TbPd3S4.

The temperature and Q dependence of energy spectra for the powder sample of TbPd3S4 have been measured by the triple-axis spectrometers HER (C1-1) and TOPAN (6G) with Ef = 3.6 and 14.7 meV, respectively.

The upper panel of Fig. 1 shows the energy spectra of TbPd3S4 at 7.2, 50 and 100 K for Q = 0.8 A-1 measured by HER. The intensity of a shoulder-like anomaly at 0.25 meV decreases with increasing temperature. From the specific-heat measurement, it has been expected that the first excited doublet or quartet is situated near ground triplet [3]. It is therefore very probable that the anomaly at 0.25 meV corresponds to the transition between the ground and the first excited states. The inset shows the energy spectra for Q = 0.8 A-1 above 1 meV. Four peaks were observed at 2, 3.8, 4.7 and 5 meV. The lower panel of Fig. 1 shows the energy spectra at 11, 104 and 300 K for Q = 4 A-1 measured by TOPAN. Several peaks and shoulder-like anomalies whose intensities show temperature dependence have been observed at energies indicated by dashed lines in the figure.

The ground J-manifold of Tb3+ splits into three triplet, one doublet and two singlets in cubic CEF. From the energy spectra obtained in this study, two possible CEF schemes have been deduced for TbPd3S4, i.e., 0 - 0.25 - 5 - 9.5 - 18 - 21 meV or 0 - 0.25 - 3.8 - 11 - 21 - 29 meV.

References

[1] K. Abe et al., Phys. Rev. Lett. 83 (1999) 5366.
[2] E. Matsuoka et al., J. Phys.: Condens. Matter 13 (2001) 11009.
[3] E. Matsuoka et al., J. Magn. Magn. Mater. 231 (2001) L23.

Activity Report on Neutron Scattering Research: Experimental Reports **15** (2008)
Report Number: 270

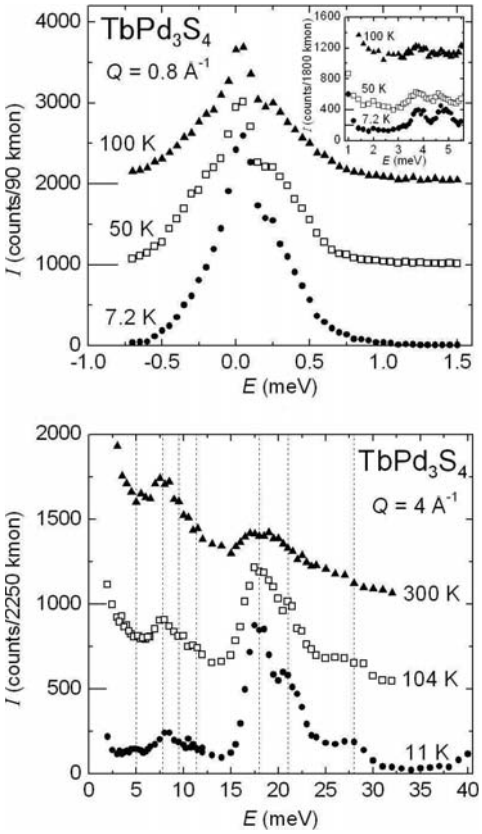


Fig. 1. Energy spectra of TbPd3S4 measured by HER (the upper panel) and TOPAN (the lower panel). The data above 50 K are drawn with appropriate offsets.

1-2-2

Spin Correlations of a Simple Cubic Antiferromagnet Pt_3Fe Alloy

R. Matsui, Y. Tsunoda
Waseda University

The ordered Pt_3Fe alloy has an $L1_2(Cu_3Au)$-type structure, in which the corner sites are occupied by Fe and the face center sites by Pt, respectively. Since Pt atoms carry no magnetic moments, Pt_3Fe alloy is considered to be a simple cubic antiferromagnet. Below the Néel temperature ($T_N \sim 180$ K), Pt_3Fe alloy undergoes an AF-AF phase transition at T_S ($T_S \sim 80$ K). At the high temperature phase, magnetic structure is a (1/2 1/2 0)-type, but at the low temperature phase, the (1/2 0 0) Bragg peak coexists with decreasing of the (1/2 1/2 0) Bragg peak intensity.

Among simple cubic antiferromagnetic structures, ferromagnetic and antiferromagnetic nearest neighbor spin couplings coexist in both the (1/2 1/2 0)-type and (1/2 0 0)-type structures, suggesting existence of spin frustration. To study the spin correlations of the simple cubic antiferromagnet, we carried out the neutron inelastic scattering experiments on a single crystal specimen of Pt_3Fe alloy in the paramagnetic phase. The measurements were performed at the T1-1 triple axis spectrometer, JRR-3M.

Fig. 1 shows inelastic scattering intensity map obtained at 200 K (1.11 T_N) on the (1 $\bar{1}$ 0) scattering plane (around the (1/2 1/2 1/2), (1/2 1/2 0) and (0 0 1/2) RLPs) using the constant-E mode of operation at $\Delta E = 5$ meV. Diffuse scattering peaks were observed around (1/2 1/2 0) and the (0 0 1/2) RLPs, which correspond to the high temperature phase and low temperature phase, respectively, but no peak around the (1/2 1/2 1/2) RLP. These data indicate that the spin correlations of the (1/2 1/2 0)-type and the (1/2 0 0)-type are competing in the paramagnetic phase of T / T_N = 1.11. We tried to reproduce the intensity contour map of the (1 $\bar{1}$ 0) plane using a simple classical Heisenberg model under the random-phase approximation (RPA). To reproduce the observed intensity map, we had to introduce up to the 4th neighbor exchange coupling and the exchange coupling parameters were combined rather strict conditions. The ratio of the exchange parameters were determined as $J_1 : J_2 : J_3 : J_4$ = -1.0 : -0.90 : -0.25 : 0.10 (where the plus[minus] shows [anti]ferromagnetic coupling.)

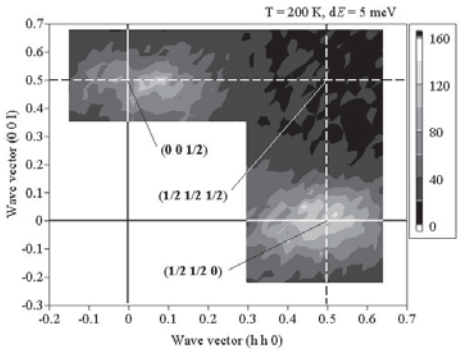


Fig. 1. Inelastic scattering intensity map obtained on the (1 $\bar{1}$ 0) scattering plane

1-2-3

Elastic Diffuse Scattering of Neutrons in Fe_3Pt Invar Alloys

M. Takasaka, Y. Tsunoda
Waseda University

The ordered Fe_3Pt alloy has an $L1_2(Cu_3Au)$-type structure, in which the corner sites are occupied by Pt and face center sites by Fe, respectively. However, by thermal treatment, disordered alloy is obtainable. Both ordered and disordered Fe_3Pt alloys are ferromagnetic and exhibit a small negative thermal expansion below the Curie temperature (ordered: T_C=400∼500K, disordered: T_C=280∼380K), which is well known as the Invar effect as well as $Fe_{65}Ni_{35}$ alloy. A martensitic phase transformation from fcc to bcc structure occurs at low temperature.

Recently, by the neutron scattering measurement we performed, elastic diffuse scattering with butterfly pattern was observed for typical Invar alloys $Fe_{65}Ni_{35}$ around the (200) and (002) Bragg peak positions. Since diffuse scattering seems to be strongly related with the Invar effect, we tried to examine existence of diffuse scattering for another Invar alloy Fe_3Pt. Because Fe_3Pt alloy is unstable against the martensitic phase transformation at low temperature, we used $Fe_{72}Pt_{28}$ alloy in both ordered and disordered specimens. The measurements were performed at the T1-1 triple axis spectrometer installed in the thermal guide of JRR-3M.

Fig. 1 shows elastic diffuse scattering intensity contour map for ordered $Fe_{72}Pt_{28}$ alloy obtained at room temperature around (002). Diffuse scattering with butterfly pattern is clearly observed. In this figure, sharp ridge (the body of the butterfly) is due to the mosaic spread of the sample. The similar diffuse scattering with butterfly type is also observed for disordered $Fe_{72}Pt_{28}$ alloy. Diffuse scattering with butterfly type is a characteristic of the local lattice distortion. Since diffuse scattering with special pattern is common for three typical Invar alloys, $Fe_{65}Ni_{35}$, ordered and disordered Fe_3Pt alloys, it is very likely that this lattice distortion is related to the Invar effect. There are many things to examine such as temperature dependence, magnetic field dependence, a difference by the degree of atomic order etc. These are remained for future program.

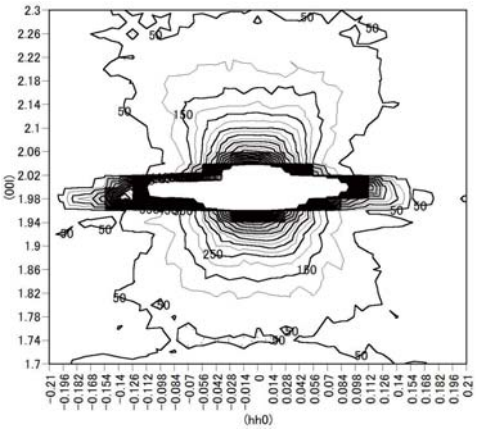


Fig. 1. elastic diffuse scattering intensity contour map for ordered $Fe_{72}Pt_{28}$ alloy obtained at room temperature around (002)

1-2-4

Magnetic structure of the n=3 frustrated square-lattice quantum spin system (CuCl)Ca2Ta3O10

H. Kageyama(A), Y. Tsujimoto(A), A. Kitada(A), T. Watanabe(A), Y. Ajiro(A), K. Yoshimura(A), M. Nishi(B), K. Hirota(B)
(A)Graduate School of Science, Kyoto University, (B)ISSP. University of Tokyo

A series of S=1/2 frustrated square-lattice antiferromagnets (CuX)A2B3O10 (X=Cl, Br; A=Ca, Sr, Ba, Pb; B=Ta, Nb) can be prepared by topotactic low-temperature ion-exchange reactions using corresponding triple-layered Dion-Jacobson type layered perovskite oxides A'A2B3O10 (A'=Cs, Rb), see Fig. 1. Quasi two-dimensional quantum magnetic properties could be expected because nonmagnetic A2B3O10 perovskite slabs act as a magnetically inert spacer, separating the magnetic CuX layer about 16 A.

We recently reported that (CuBr)Sr2Nb3O10 has a 1/3 magnetization plateau in the magnetization curve at low temperatures (Y. Tsujimoto et al., J. Phys. Soc. Jpn. 76, 063711 (2007)). This is quite unusual since the 1/3 plateau is normally expected in the triangule-based lattices such as a triangular lattice and kagome lattice. In order to understand the origin of the magnetization plateau in (CuBr)Sr2Nb3O10, we measured in 2006 the neutron diffraction of this material at low temperatures at HERMES, but no indication of magnetic order was obtained.

Therefore, as a next step, we measured the powder neutron diffraction of (CuCl)Ca2Ta3O10 which do not possess any magnetization plateau. The powder neutron diffraction patterns were obtained at 2 K and 20 K, which is below and above the temperature at which the temperature dependence of the magnetic susceptibility shows the maximum. We found the magnetic order described as the propagation vector q = (pi, 0, pi), indicating the so-called collinear magnetic ordering, where ferromagnetic chains along [010] are antiferromagnetically coupled along [100] . This spin structure is the same as that found in the double-layered material (CuBr)LaNb2O7 and shows that the next nearest neighbor Cu-Cu interactions are dominant with respect to the nearest neighbor interactions.

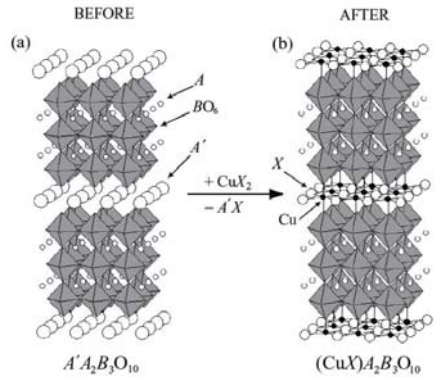


Fig. 1. Crystal structures of A'A2B3O10 and (CuX)A2B3O10 before and after ion exchange reactions, respectively.

1-2-5

Neutron scattering study on (CuCl)LaTa2O7

H. Kageyama(A), A. Kitada(A), Y. Tsujimoto(A), Y. Ajiro(A), K. Yoshimura(A), M. Nishi(B), N. Matsuura(B), K. Hirota(B)
(A)Graduate School of Science, Kyoto University, (B)ISSP. University of Tokyo

Spin-structure of the square-lattice antiferromagnet is trivial as long as the nearest neighbor interactions are considered. However, inclusion of antiferromagnetic next nearest neighbor interactions induces frustration, leading to non-trivial phases such as spin-liquid state.

We demonstrated from magnetic susceptibility and neutron scattering experiments that (CuCl)LaNb2O7, prepared by topotacic ion-exchange reaction of RbLaNb2O7 with CuCl2, does not show any sign of long range magnetic ordering at low temperatures, indicating spin-disordered ground state [1].Here, the S = 1/2 square lattices are formed by the Cu-Cl layers, which are separated by the nonmagnetic LaNb2O7 perovskite blocks. In contrast, the isostructural compound (CuBr)LaNb2O7 exhibits the long range magnetic order at 32 K. The neutron powder diffraction study at HERMES and 5G gave the spin structure of this material, a collinear type of order with a modulation vector of (pi, 0, pi). Such a spin structure is expected when the next nearest neighbor interaction dominates over the nearest neighbor one.The difference in the ground state between the Cl and Br compounds could be explained in terms of the difference in superexchange interactions between Cu-Cl-Cl and Cu-Br-Cu.

Under the proposal number 7535, we have performed the neutron inelastic and elastic scattering study on (CuCl)LaTa2O7, again isostructural of (CuCl)LaNb2O7. Sicne pentavalent Ta and Nb have nearly the same ionic radii, the two compounds have nearly same lattice parameters. However, (CuCl)LaTa2O7 show the magnetic ordering of the same type of (CuBr)LaNb2O7.This could not be explained by the abovementioned scenario. This observation indicates that the superexchange path via TaO6/NbO6 also contribute to the magnetism.

[1] H. Kageyama et al., J. Phys. Soc. Jpn. 74, 1702 (2005)
[2] N. Oba et al., J. Phys. Soc. Jpn. 75, 1133601 (2006)

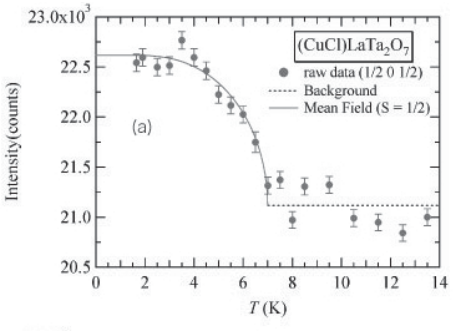


Fig. 1. Temperature dependence of the (1/2, 0, 1/2) magnetic reflection for (CuCl)LaTa2O7

1-2-6

Electric polarization induced by a proper helical magnetic ordering in a delafossite multiferroic $CuFe_{1-x}Al_xO_2$

T. Nakajima, S. Mitsuda, S. Kanetsuki, K. Tanaka, T. Fujii, N. Terada[1], M. Soda[2], M. Matsuura[2], K. Hirota[2].
Department of Physics, Faculty of Science, Tokyo University of Science, Tokyo 162-8601, Japan
[1]*ICYS, National Institute for Materials Science, Ibaraki 305-0044, Japan*
[2]*Institute for Solid State Physics, University of Tokyo, Kashiwa 277-8581, Japan*

Delafossite $CuFe_{1-x}Al_xO_2$ has been the subject of intense recent interest, because of the ferroelectricity accompanied by a proper helical magnetic ordering[1]. The local spin-polarization coupling in this system cannot be explained by the 'spin-current model' proposed by Katsura *et al.*[2], which successfully explains the ferroelectricity in cycloidal magnetic orderings of certain transition metal oxides such as $TbMnO_3$. Hence, we performed polarized neutron diffraction measurements on $CuFe_{1-x}Al_xO_2$ ($x = 0.02$) with applied electric field at the triple-axis neutron spectrometer PONTA installed at JRR-3, in order to identify the local spin-polarization coupling in this system.

A single crystal of $CuFe_{1-x}Al_xO_2$ with $x = 0.02$ of nominal composition was prepared by the floating zone technique. An incident polarized neutron with energy 34.05 meV was obtained by a Heusller (111) monochromator. The flipping ratio of the polarized neutron beam was ~ 19, and the polarization vector of the incident neutron, $\boldsymbol{p}_N$, was set to be parallel or antiparallel to the scattering vector, $\boldsymbol{\kappa}$, by a guide-field of a helmholtz coil and a spin flipper. The collimation was 40′-40′-40′-40′. The sample was mounted in a pumped ^{4}He cryostat with a hexagonal (hhl) scattering plane.

Typical diffraction profiles of magnetic reflections in the ferroelectric phase ($T = 2$ K) are shown in Figs. 1(c-1)-(d-2), in which I_{ON} and I_{OFF} denote the intensities measured when $\boldsymbol{p}_N \parallel -\boldsymbol{\kappa}$ and $\boldsymbol{p}_N \parallel \boldsymbol{\kappa}$, respectively. As shown in Figs.1(c-1) and 1(c-2), after cooling the sample under a poling electric field (128 kV/m) perpendicular to the helical axis, there was no difference between I_{ON} and I_{OFF} for both of $+\boldsymbol{q}$ and the $-\boldsymbol{q}$ magnetic satellites reflections (see Fig.1(b)). After cooling the sample under a poling electric field (120 kV/m) parallel to the helical axis, I_{ON} was greater than I_{OFF} for the $+\boldsymbol{q}$ reflection, and this relationship between I_{ON} and I_{OFF} was reversed for the $-\boldsymbol{q}$ reflection, as shown in Figs. 1(d-1) and 1(d-2). These results clearly demonstrate that proper helical magnetic ordering in $CuFe_{1-x}Al_xO_2$ generates a spontaneous electric polarization along the helical axis, and there is one-to-one correspondence between the polarity of local polarization vector and the spin helicity, as illustrated in Fig. 1(a).

References

[1] T. Nakajima *et al.*: JPSJ **76** (2007)043709.
[2] H. Katsura *et al.*: PRL **95** (2005)057205.

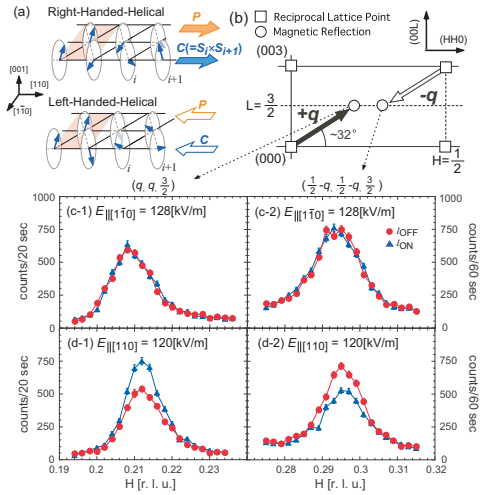


Fig. 1. (a)The relationship between spin arrangements and polarization vectors. (b)The location of the magnetic reflections. [(c-1)-(d-2)] The diffraction profiles at $T = 2$K.

1-2-7

Electric field dependence of magnetic ordering of a delafossite multiferroic $CuFe_{1-x}Al_xO_2$

T. Nakajima[1], S. Mitsuda[1], H. Kimura[2], and Y. Noda[2]

[1] *Department of Physics, Faculty of science, Tokyo University of Science 1-3 kagurazaka, shinjuku-ku, Tokyo, 162-8601*

[2] *Institute of Multidisciplinary Research for Advanced Materials, Tohoku University, Sendai 980-8577*

Delafossite $CuFe_{1-x}Al_xO_2$ has been of increasing interest as a new class of multiferroics, because of the ferroelectricity accompanied by a proper helical magnetic ordering. Recent polarized neutron diffraction measurements on $CuFe_{1-x}Al_xO_2$ with $x = 0.02$ under applied electric fields up to 160kV/m revealed the correspondence between the magnetic propagation wave vector and the local electric polarization vector[1]: specifically, the direction of the local electric polarization vector is parallel (or antiparallel) to the magnetic modulation wave vector projected in the hexagonal [001]-plane. Since this system has the three magnetic domains reflecting the three-fold symmetry of the crystal structure (see Fig. 1(b)), it is natural to anticipate that the poling electric field should favor the wave vector for which the electric polarization can be maximized. However, no significant changes are detected in the magnetic domain distribution under the electric field within $E < 160$kV/m applied along the [110] axis[1].

In present experiments, we have investigated the magnetic domain distributions in $CuFe_{1-x}Al_xO_2$ ($x = 0.02$) under electric fields up to 2200kV/m along [110] axis, using the four-circle neutron diffractometer FONDER(T2-2) installed at JRR-3. The wavelength of the incident neutron is 1.24Å. The closed-cycle He-gas refrigerator was used to provide access to the temperature down to 2.5K.

Fig. 1(a) shows the poling electric field dependence of the integrated intensities of the three equivalent magnetic reflections, which are proportional to the fractions of the magnetic domains. This shows that the application of a poling electric field within $|E| <\sim 2200$ kV/m does not affect the fractions of the three magnetic domains, implying that the fractions of the three magnetic domains are determined by the lattice distortion, which have been already occurred in the high-temperature (paraelectric) partially disordered phase [2].

However, we found that the diffraction profiles of the magnetic reflections in the ferroelectric phase are sharpened by applying the poling electric field, as shown in Fig. 1(c), suggesting that an application of the poling electric field improves the magnetic correlation in the ferroelectric phase. For the quantitative evaluation of the changes in magnetic correlation, further investigations are awaited.

References

[1] T. Nakajima *et al.*: PRB (in press).

[2] N. Terada *et al.*: JPSJ **75** (2006)113702.

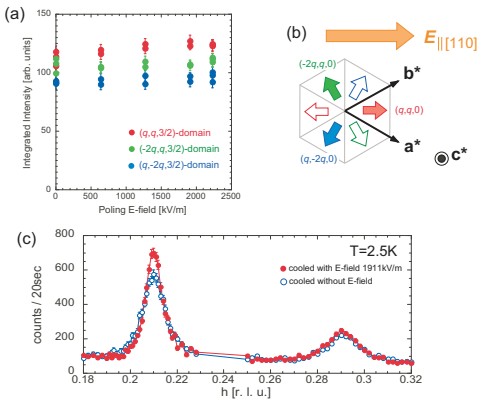


Fig. 1. (a) The poling E-field dependence of the intensities of the three equivalent magnetic reflections. (b) [001]-projection of the three equivalent propagation wave vectors. (c) Typical diffraction profiles in the ferroelectric phase.

1-2-8

Effective random-field domain-state in a diluted frustrated magnet $CuFe_{1-x}Al_xO_2$

T. Nakajima, S. Mitsuda, H. Honma, H. Tsuchida
Department of Physics, Faculty of science, Tokyo University of Science 1-3 kagurazaka, shinjuku-ku, Tokyo, 162-8601

Geometrically frustrated spin systems have been extensively investigated, because they exhibit a variety of exotic magnetic orderings, which spans from a complex noncollinear magnetic state to a spin-glass like disordered state. One of the unusual magnetic state in this system is the Partially-Disordered (PD) state, in which magnetically disordered sublattices exist. Recent studies on diluted triangular lattice antiferromangets such as $CsCo_{1-x}Mg_xBr_3$[1] and $CuFe_{1-x}Al_xO_2$ ($x = 0.10$)[2], which exhibit the PD magnetic orderings, revealed that a combination of the PD magnetic ordering and site-random magnetic vacancies can generate effective random-field even in the absence of external magnetic field.

For the systematic study on this effective random-field effect in the diluted frustrated magnet, we performed neutron diffraction measurements on $CuFe_{1-x}Al_xO_2$ samples with $x = 0.15$ and 0.20, using the triple-axis neutron spectrometer HQR(T1-1) installed at JRR-3. The collimation open-'40-'40-'40 was employed. The wavelength of the incident neutron is 2.44Å. The single crystal of $CuFe_{1-x}Al_xO_2$ samples were mounted in a ^{4}He-pumped cryostat with a hexagonal (hhl)-scattering plane. In order to evaluate the magnetic correlation length quantitatively, we analyzed the scattering profile, using Multi-Profile-Deconvolution method presented in Ref. [2].

Figs. 1(a) and (b) show the scattering profiles of the $x = 0.15$ and 0.20 sample at $T = 2$K and the results of MPD-analysis for these profiles. For both samples, the scattering function of the magnetic reflections are well described by the sum of a Lorentzian term and a Lorentzian-squared term with anisotropic width (see Fig. 1(d)). In particular, the existence of a Lorentzian-squared term indicates that the system breaks into a large number of small magnetic domains. We found that the width of the S(q), κ, increases with increasing Al^{3+}-concentration x (see Fig. 1(c)). This indicates that the average size of magnetic domains decreases with increasing x. We also found the contribution of the Lorentzian term in $S(q)$ increases with increasing x, as shown in Fig. 1(c). This implies that the system gradually changes from a random-field domain state to a spin-glass like disordered state, as the substitution increases. The further detailed analysis is now in progress.

References

[1] J. van Duijn *et al.*: PRL **92** (2004)077202.
[2] T. Nakajima *et al.*: JPCM **19**(2007)145216.

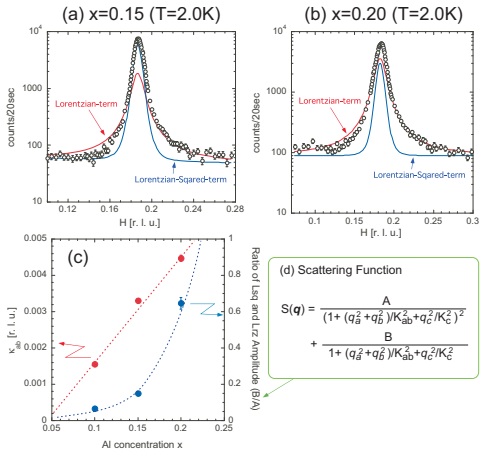


Fig. 1. Typical scattering profiles of (a) $x = 0.15$ and (b) $x = 0.20$ samples at $T = 2.0$K. (c) x dependence of the width of $S(q)$ and the ratio of amplitude of Lrz and Lsq term at $T = 2$K. The data of $x = 0.10$ is taken from Ref. [2] (d) Definition of the $S(q)$.

1-2-9

Polarization analysis neutron scattering study of magnetic correlations in random magnet Fe65(Ni-Mn)35

K. Motoya and Y. Muro
Department of Physics, Faculty of Science and Technology, Tokyo University of Science

A previous neutron scattering study showed that the short-range ferromagnetic and antiferromagnetic correlations coexist in wide concentration and temperature ranges of a random magnet system Fe65(Ni-Mn)35 [1]. Magnetic field variations of diffuse scattering patterns arising from these ferromagnetic and antiferromagnetic correlations have shown that the regions of these two kinds of correlations coexist separately in this system [2]. In this report, we present the result of polarization analysis experiment of this system.

The magnetic diffuse scattering patterns arising from ferromagnetic correlations (ferromagnetic clusters) observed around (111) Bragg point are well traced by a Lorentzian (LOR) function. Figure 1 (A) and (B) show the magnetic field variations of the amplitude (AL) and the width (κ L) of the spin-flip and non-spin-flip components, respectively. The result shows that the number and the average size of ferromagnetic clusters decrease with increasing field. This seems to be inconsistent with the magnetization behavior. We have made a scenario of magnetic field variation of ferromagnetic clusters consistent with the results of the neutron scattering and magnetization measurements [2].

The diffuse scattering signals arising from antiferromagnetic correlations (antiferromagnetic clusters) have been measured around (100) and (110) Bragg points. These patterns are well traced by a LOR function. The field variations of the amplitude and the width of the spin-flip and non-spin-flip components are shown in Fig.1 (C) and (D), respectively.

Based on the unpolarized [2] and the present polarization analysis measurements, we will determine the magnetic field variations of the number, size and orientation of the ferromagnetic clusters as well as the magnetic structure of the antiferromagnetic clusters.

[1] K. Motoya and K. Hioki, J. Phys. Soc. Jpn. 72 (2003) 930.

[2] K. Motoya et al., Phys. Stat. Sol. (submitted)

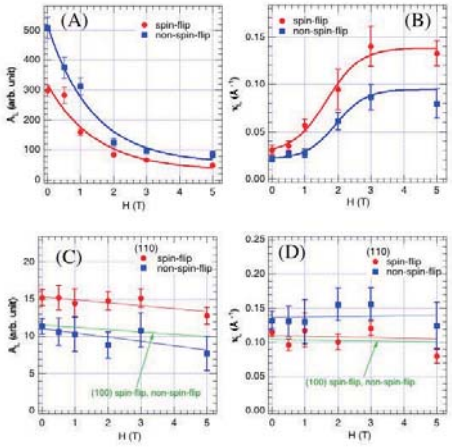


Fig. 1. Magnetic field variations of the amplitude and the width of the scattering patterns arising from ferromagnetic and antiferromagnetic clusters.

1-2-10

Magnetic excitations in the random-exchange Ising system (Fe-Zn)F2 near the percolation threshold

K. Motoya, Y. Muro, N. Aso (a) and D. P. Belanger (b)
Tokyo University of Science, (a) ISSP, (b) University of California, Santa Cruz

The diluted antiferromagnet (FexZn1-x)F2 has been extensively studied in the past as an ideal system for the studies of three-dimensional random-exchange Ising model. Previous neutron scattering studies of magnetic excitations of this system have revealed the following [1, 2]. For x=0.59 the spin-wave-like energy spectrum observed near q=0 changes to a form of localized excitations as q increases. The overall energy width and position of the spectrum at the zone boundary can be described by the local mean field (LMF) model. The spectrum from x=0.40 at q=0 consists of four evenly spaced excitation peaks. However, the overall structure is higher in energy than the predicted excitations of the LMF theory.

In order to clarify the total property of magnetic excitations of this system including the percolation threshold region (xp=0.24), we made high-energy-resolution inelastic neutron scattering measurements.

Two single crystals of x=0.25 (total weight 4.1g) were aligned with the c-axis vertical to the horizontal scattering plane. Measurements were performed using a horizontally-focusing analyzer on C1-1 spectrometer. The energy resolution varies from 0.08meV (FWHM) to 0.17meV as the energy transfer increases from 0 to 7meV with the final neutron energy fixed at Ef=3.1meV.

Figure 1 shows inelastic scattering intensity vs energy for x=0.25 measured at T=0.7K and various value of q. For all q values (from the zone center to the zone boundary) well resolved 6 peaks were observed. The position of each peak does not move with increasing q.

These features strongly suggest that the observed spectrum is attributed to the excitations of individual spins with various local environment. The bottom panel of Fig.1 shows the excitation spectrum of individual spins based on the LMF theory.

At T=10K no appreciable change was observed in the spectra. As increasing temperature the peaks gradually broaden and finally fade into a broad spectrum.
This shows that the system "freezes" below T=10K.

[1] C. Paduani et al., Phys. Rev. B 50 (1994) 193.

[2] Y. W. Rodriguez et al., J. Mag. Mag. Mater. 310 (2007) 1546.

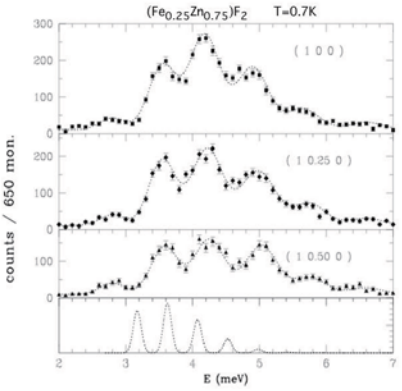


Fig. 1. The scattering intensity vs energy at T=0.7K measured at various q. The bottom panel is the LMF prediction.

1-2-11

Inelastic Neutron Scattering Study on Triangular Lattice Antiferromagnet $CuFeO_2$

T. Nozaki, K. Hayashi, and T. Kajitani
Department of Applied Physics, Graduate School of Engineering, Tohoku University, Sendai, 980-8579

Geometrically frustrated magnetic systems have received considerable attention in recent years due to the presence of extraordinary magnetic properties. As a model material of the magnetically frustrated triangular lattice antiferromagnet, $CuFeO_2$ shows successive magnetic phase transitions from an Ising-like 4-sublattice phase ($\uparrow\uparrow\downarrow\downarrow$) to a paramagnetic phase through a partially disordered phase ($T_{N2} \sim 10.5$ K $< T < T_{N1} \sim 14.0$ K).[1] To understand these complicated magnetic orderings, it is needed to elucidate magnons and phonons in the $CuFeO_2$ system in the wide temperature range. In this study, we measure inelastic neutron scattering spectra of powder $CuFeO_2$ below and over T_{N1} and T_{N2}.

Inelastic neutron scattering measurements were carried out by the use of a cold neutron spectrometer, AGNES. A wave length of the incident neutron was 4.22 Å. The energy value of the scattered neutron was determined by the time-of-flight method. The energy resolution was about 0.1 meV in the present experimental condition. The data acquisition time was about 20 h. Powder $CuFeO_2$ sample was synthesized by the solid state reaction method as described elsewhere.[2]

Figure 1 shows inelastic neutron scattering intensitiy, $S(\omega)$, of the $CuFeO_2$ powder taken at 7.5, 10, 11, 12.5, and 16 K, where ω is the angular frequency. The horizontal axis is the energy transfer values of the incidence. The negative side of the spectra corresponds to the energy loss side, i.e. the Stokes side. The central peaks at 0 meV are the elastic scattering components. There is a large and broad peak around -2 meV in each spectrum below 12.5 K, corresponding to the creation of locarized magnon mode. One possible reason of its broadning is the creation of magnon branches.[3, 4] As the temperature increases, the peak position moves closer to the central peak, i.e. the frequency of the magnon mode becomes lower. This temperature dependence is conceivably due to the spin-wave interactions.[5] It should be noted that a broad magnetic critical scattering component appears in the spectra taken at 12.5 K and 16 K.

References

[1] N. Terada *et al.*: Phys. Rev. B **74** (2006) 180404, and references therein.
[2] K. Hayashi *et al.*: Jpn. J. Appl. Phys. **46** (2007) 5226.
[3] N. Terada *et al.*: J. Phys.: Condens. Matter **19** (2007) 145241.
[4] F. Ye *et al.*: Phys. Rev. Lett. **99** (2007) 157201.
[5] T. Oguchi: Phys. Rev. **117** (1960) 117.

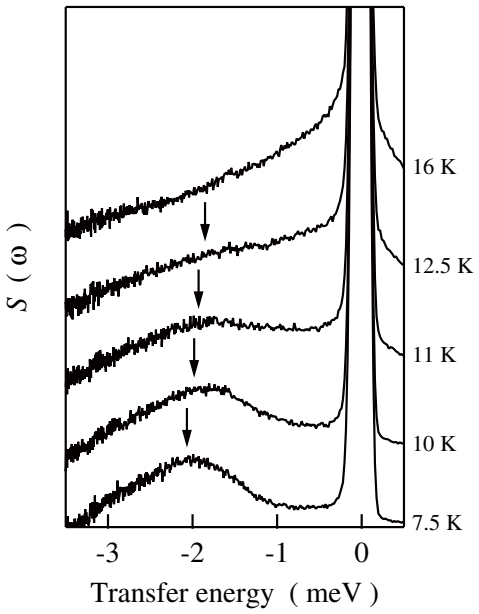


Fig. 1. Inelastic neutron scattering spectra of $CuFeO_2$ powder at 7.5, 10, 11, 12.5, and 16 K.

1-2-12

Search for magnetic reflections in a heavy fermion antiferromagnet $CeTe_3$

N. Aso, K. Deguchi[A], G. F. Chen[A], N. K. Sato[A], H. Yoshizawa
NSL-ISSP, Univ. of Tokyo, Graduate School of Sci., Nagoya Univ.[A]

$CeTe_3$ belongs to the family of quasi-two dimensional charge-density-wave (CDW) compounds RTe_3 (where R = Y, La-Sm, Gd-Tm). [1, 2] The crystal structure is weakly orthorhombic with the lattice parameters of $a \approx c \sim 4$ Åand $b \sim 25$ Å. In low temperature regin, there has been reported some magnetic ordering below $T \sim 3$K from the susceptibility measurements. [3] Very recently, Chen *et al.* found that $CeTe_3$ exhibits another (possibly) magnetic ordering below $T \sim 1.2$ K by the specific heat and susceptibility measurements. [4] From the susceptibility measurements, the phase below at $T \sim 1.2$ K seem to the 2nd-order antiferromagnetic ordering.

In this context, the main goal of this work is to determine the order parameters of the low-temperature two phases by neutron diffraction technique. Powder sample of $m \sim 10$ gram were prepare and put in a aluminum can filled with a He gas. It was cooled down to 0.75 K using a ^{3}He cryostat. [5] Neutron diffraction experiments were performed at PONTA and HQR in the research reactor JRR-3.

Figure 1 (a) shows powder pattern of $CeTe_3$ obtained at HQR with the incident energy $E_i \sim 13.5$ meV and the other configurations of G-Open-PGF-40′. Although one can clearly see some strong Nuclear Bragg peaks denoted by the indices in the figure, no distinct magnetic Bragg peak are observed. Thus we tried to subtract the scattering in the paramagnetic state of T = 5 K as the background one. Figure 1 (b) and (c) correspond to the scattering at T = 0.75 K and T = 3 K, respectively. One can clearly see no distinct magnetic Bragg peak in the both two phases. The possible reason is that the magnetic moment of the two phases is very small less than 0.3 μ_B/Ce. We now try to go to the single crystalline studies in the next.

References

[1] V. Brouet *et al.*, *Phys. Rev. Lett.* **93**, 126405 (2004).
[2] H. Komoda *et al.*, *Phys. Rev.* **B 70**, 195101 (2004).
[3] Y. Iyeiri *et al.*, *Phys. Rev.* **B 67**, 144417 (2003).
[4] G.F. Chen *et al.*, in preparation.
[5] TAIYO NIPPON SANSO CORPORATION. Tokyo 142-8558, Japan.

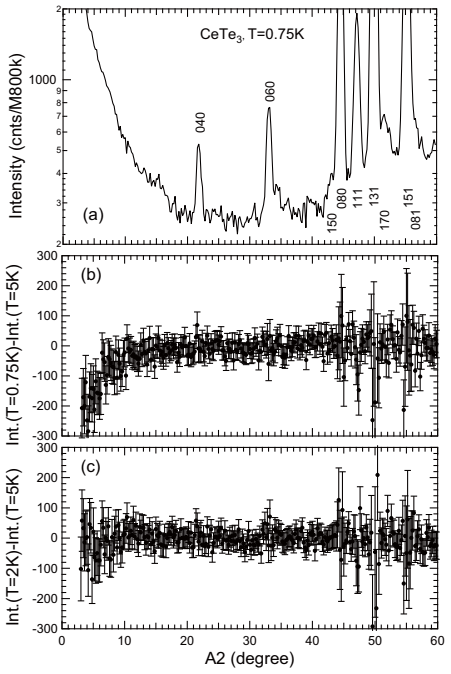


Fig. 1. (a) Powder pattern of $CeTe_3$ obtained at T = 0.75 K. (b) Subtracted profile at 0.75 K. Small deviation at small angles perhaps comes from the He gas scattering in the aluminum cell. (c) Subtracted profiles at 2 K.

1-2-13

Magnetic structure of TbCoSn

M.Kurisu, A.Tada, G.Nakamoto, T.Tsutaoka(1) and Y.Andoh(2)
Japan Advanced Institute of Science and Technology, Ishikawa 923-1292, Japan
(1)Graduate School of Education, Hiroshima University, Hiroshima 739-8524, Japan
(2)Faculty of Regional Sciences, Tottori University, Tottori 680-8551, Japan

RTX (R: rare earths, T: transition metals, X: metalloids) compounds crystallize in the epsilon-TiNiSi-type orthorhombic structure. Their magnetic property is characterized by
1. relatively lower antiferromagnetic ordering temperature TN below 20 K,
2. highest TN not at R=Gd but at Tb,
3. multi-step metamagnetic transitions in the ordered state along the easy axis of magnetization,
4. incommensurate magnetic structures in the series.[1]
Recently, it has been revealed that RRhGe (R=Tb and Dy) compounds also possess successive magnetic transitions below the Neel temperature from the magnetic and specific heat measurements. Our interest is in the role of crystalline electric field (CEF) effect and determination of magnetic structures in the series. In the present report, we show preliminary experimental results on TbCoSn.

Single-crystalline TbCoSn ingots were grown by a Czochralski method using a tetra-arc furnace in purified Ar atmosphere. The magnetic and specific heat measurements were performed by a SQUID magnetometer and a PPMS, respectively. The neutron diffraction measurements were performed at T1-1:HQR spectrometer installed at JRR-3M.

The magnetic susceptibility shows that antiferromagnetic ordering takes place at 20.2 K. Below TN, an anomaly indicative of another magnetic transition is observed at 4 K for the three principal axes. The specific heat measurement also indicates the two magnetic phases down to 1.8 K. The temperature dependence of the magnetic susceptibilities is well accounted for the three principal axes by the CEF calculation based on the point charge model. It is noted that the easy axis of magnetization is the a-axis in TbCoSn while it is the b-axis for other isostructural TbTX compounds. The sign of second order CEF parameter appears to be a dominant factor to determine the magnetic anisotropy.

The variation of magnetic reflection at (0 0.25 0) with temperature is displayed in Fig.1. This also supports the existense of low temperature phase below 4 K. A further data acquisition is needed to determine the magnetic structure of the compound.

References
[1] Y.Andoh, M.Kurisu, and S.Kawano, Journal of Magnetism and Magnetic Materials, 177-181 (1998) pp.1063-1064.

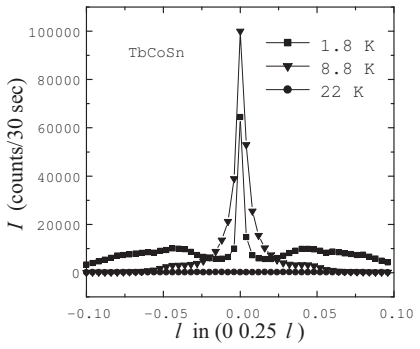


Fig. 1. Magnetic reflection at (0 0.25 0).

1-2-14

Pressure induced incommensurate–commensurate magnetic phase transition in multiferroic $HoMn_2O_5$

H. Kimura[1], K. Nishihata[1], Y. Noda[1], N. Aso[2], T. Fujiwara[3] and Y. Uwatoko[2]
[1]*IMRAM, Tohoku University*
[2]*ISSP, The university of Tokyo*
[3]*Department of Physics, Yamaguchi University*

$R Mn_2O_5$ is well known as "*multiferroics*" where the ferroelectric and antiferromagnetic order coexist and their order parameters couple with each other. This system essentially involves geometrical magnetic frustration, which leads to the long-period magnetic order and the complex magnetic phase diagram as a function of temperature. It was found that in $HoMn_2O_5$, magnetic-field-induced incommensurate–commensurate magnetic phase transition occurs in which the ferroelectic state are concomitantly induced[1]. This result indicates that the external field can control the dielectric phase through the control of competing magnetic ground states. Recently, it was found that the ferroelectric phase is induced by applying a hydrostatic pressure in $HoMn_2O_5$[2], indicating that the commensurate magnetic phase might appear by applying pressure. In the present study we thus performed neutron diffraction measurements under hydrostatic pressure to search the pressure induced magnetic phase transition in $HoMn_2O_5$.

Single crystal of $HoMn_2O_5$ was inserted in Cu-Be clamp cell and the pressure was applied up to 1.25 GPa. The measurement of magnetic peaks was performed using the triple-axis spectrometer AKANE installed at T_{1-2} thermal guide in JRR-3M. At 0 GPa, shown in Fig. 1 (a), a pair of magnetic peaks locate around (0.5±0.02 0 1.73), indicating that the magnetic order is incommensurate. Upon applied pressure, shown in Fig. 1 (b), there is a strong peak at the commensurate position (0.5 0 1.75) with a minor incommensurate peak, showing that the commensurate phase is induced. We mapped out the pressure–temperature phase diagram for the magnetic ordered phases, showing the one-to-one correspondence with that for the dielectric phases[2].

References

[1] H. Kimura *et al.*: JPSJ **75** (2006) 113701.
[2] C. R. Cruz *et al.*: PRB **76** (2007) 174106.

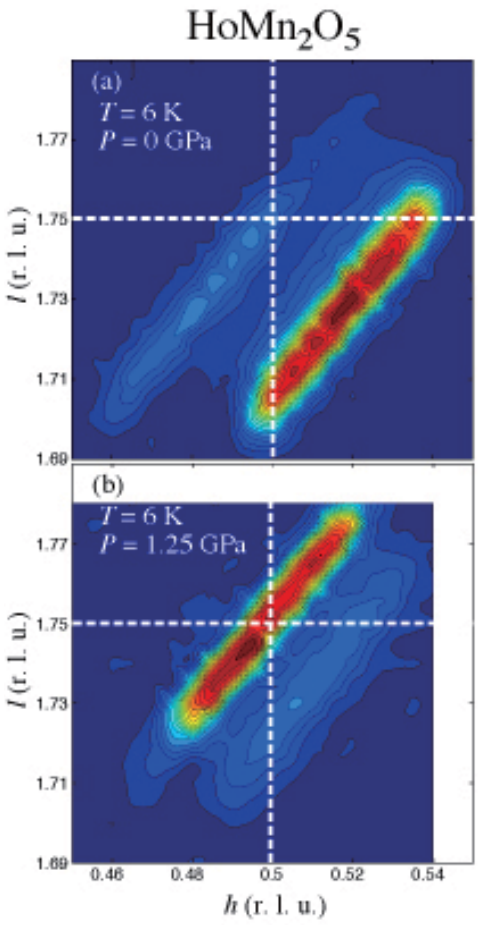


Fig. 1. Contour maps in $(H\ 0\ L)$ zone of magnetic Bragg reflection under (a) 0 GPa and (b) 1.25 GPa, taken at 6 K.

1-2-15

Defect-induced short-range magnetic order in Co2(OD)3Cl

X.G. Zheng, M. Hagihala, T. Yamashita
Faculty of Science and Engineering, Saga University, Saga 850-8502, Japan

In recent years we found a new geometric frustration system Cu2(OH)3Cl and Co2(OH)3Cl with a 3-dimensional network of corner-sharing tetrahedrons of the Cu2+ and Co2+ spins, respectively 1-3. We found coexisting antiferromagnetic order and spin fluctuation down to T=0 in ideal quantum spin material Cu2(OH)3Cl 2, and a kagome-ice-like partial ferromagnetic order in Co2(OH)3Cl 3, which raise great interest on this new material system. The latter compound can be compared with the rare-earth pyrochlore compounds Ho2Ti2O7, Dy2Ti2O7 and Ho2Sn2O7, i.e., the "spin ice" compounds. In these materials the spin alignment and the macroscopic quantum degeneracy are shown to be a magnetic equivalence of the ice rule in water ice. The spin ice has received intense attention because of the dynamics associated with the macroscopic degeneracy are experimentally accessible by many magnetic probes, and because the geometrical frustration of competing interactions is an essential element of important problems in fields extending to protein folding and neural networks. The experimentally observed degeneracy and zero-point residual entropy for water ice and spin ice apparently contradict a fundamental principle of thermodynamics (the 3rd law), which demands a single ordered ground state and hence zero entropy. As to the spin ice, a first-order phase transition to a true ground state is theoretically predicted, but has not been observed to date, despite rigorous efforts down to the experimentally attainable temperature of 10 mK. Whether the spin ice keeps the macroscopic quantum degeneracy down to 0 K remains an open and controversial issue.

Because Co2(OH)3Cl has a comparatively very higher transition temperature of TC = 10.5 K, we explored the possibility of a low-temperature order with impurity doping. For this purpose neutron diffraction experiment was carried out at T1-3 (Hermes) using powder sample of (Co0.9Al0.1)2(OD)3Cl.

Figure 1 shows the neutron diffraction patterns for (Co0.9Al0.1)2(OD)3Cl at typical temperatures. The results clearly show that a short-range spin correlation develops below around 4 K. AC and DC susceptibility measurements suggest that the remaining spin degree of freedom freeze completely below 4 K with a drastically increasing relaxation time.

The above-described result can be considered as an interesting analogy to the low-temperature anomaly in doped water ice, especially in the light of its relevance to the problem of residual entropy in ice-water or spin-ice transition. We hope it contributes to a complete understanding of the true ground state of geometrically frustrated systems.

References

1. X.G. Zheng et al., Phys. Rev. B 71, 052409 (2005).
2. X.G. Zheng et al., Phys. Rev. Lett. 95, 057201 (2005).
3. X.G. Zheng et al., Phys. Rev. Lett. 97, 247204 (2006).
4. X.G. Zheng et al., Phys. Rev. B, in press.

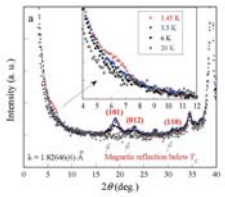


Fig. 1. Neutron diffraction result for (Co0.9Al0.1)2(OD)3Cl.

1-2-16

Inelastic neutron scattering on DyB4

Takeshi Matsumura, Daisuke Okuyama, and Takuya Mouri
Tohoku University

DyB4, belonging to a space group P4/mbm, has been attracting interest as a system where the quadrupolar and magnetic degrees of freedom exhibit anomalous correlations on the so-called Shastry-Sutherland lattice of Dy atoms. DyB4 exhibits two phase transitions at TN1=20.3 K and at TN2=12.7 K. It has already been established that the c-axis component of the magnetic moment orders antiferromagnetically below TN1, whereas the c-plane componet somehow remains paramagnetic until TN2 by magnetic susceptibility and elastic constant measurements. However, resonant x-ray diffraction and neutron diffraction experiments on single crystalline samples performed by us show short-ranged ordering of the c-plane magnetic component between TN2 and TN2, indicating that the time scale of the fluctuation is much longer than 10^(-12) sec, the time scale of neutron diffraction, but shorter than 10^(-7) sec, the time scale of ultrasonic measurement. Therefore, in order to investigate the difference in the magnetic states in the three phases, we have performed inelastic neutron scattering experiment on DyB4.

Inelastic neutron diffraction on DyB4 is very difficult because the absorption by natural Dy is quite large (~970 barn), even though we used enriched 11-Boron isotope to prevent absorption by 10-Boron. Then, we sliced the single crystal samples into the plates with thicknesses of 0.5 mm, maximizing the scattered neutrons. We prepared four sliced samples and orientated them within an error of 0.5 degree We performed constant-Q scans at positions close to (1, 0, 0), (2, 0, 0), (1, 0, 0.5), (1, 0, 1), (1, 0, 2), and (0, 0, 1) at three temperatures at 25 K, 15 K, and 4.0 K.

Figure shows the inelastic spectra at (1.05, 0, 0). At 25 K, we clearly observe two excitations at 4.5 meV and 6.5 meV. They are considered as the crystal field excitations since they are also observed at other Q-positons. In addition, we observe a low energy excitation below 2 meV. Fitting of the spectrum indicates that the excitation is at 1.4 meV. At 15 K in the intermediate phase, the energies of the higher enegy excitations shift to higher energies, while the low energy excitations remain unchanged. Below TN2, at 4 K, the low energy excitation vanishes and shifts to the well resolved excitation at 2.5 meV. This behavior is the same as that of HoB4. The high energy excitations also move to higher energies.

The change in the excitation spectra at three temperatures in the three phases shows that the magnetic state is obviously different. Phase I above TN1 is paramagnetic. In phase II between TN1 and TN2, the c-axis component is ordered. The c-plane component is also ordered in a short range, but it is not static. If it is static, the spectrum should have the same characteristic as in phase III below TN2, which is not the case.

To summarize, we have suceeded in measuring the inelastic excitation spectra on DyB4 with high absorption by Dy. The change in the spectrum for the three magnetic phases has been clearly observed.

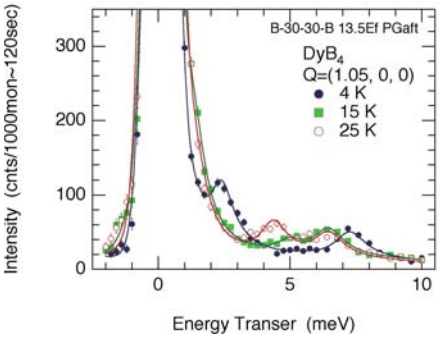


Fig. 1.

1-2-17

Neutron diffraction in magnetic frustration systems with a 40T pulsed magnet

K. Ohoyama, K. Kurosawa, S. Yoshii, H. Nojiri, Y.H. Matsuda, H. Hiraka, S. Mitsuda(A)
IMR, Tohoku Univ., Faculty Science, Tokyo Univ. of Science(A)

Neutron scattering experiments under magnetic field is indispensable for novel material science; however, feasible highest magnetic fields with conventional superconducting magnets for neutron diffraction are limited below 13T in Japan, and about 17T in the world, which is not sufficient to satisfy scientists' interests. The world record of magnetic field for neutron scattering experiments is B=25T, which was performed by Motokawa et al. using a repeating pulsed magnet in Neutron Science Laboratory of High Energy Accelerator Research Organization in Japan. However, neutron scattering experiments over B=10T are still difficult and limited for the present; therefore, easier and more diffusive techniques are ambitioned. Thus, aiming at neutron scattering experiments under B=40T, we are developing easier and diffusive experimental techniques with a compact pulsed magnet system.

In 2007, we developed a movable magnet system which consists of a compact condenser bank(C=5.4mF, 3kV) and a mini-coil (diameter:12mm, length:16mm). The coil is installed in a cooling system by liquid nitrogen, which ican be inserted in an Orange cryostat to cool the sample. The interval of each pulse was reduced to 6-7min. Neutron diffraction experiments were performed on Kinken spectrometer, AKANE, and T1-1.

The first target material was the triangular lattice compound CuFeO2, which shows characteristic multi-step matamagnetic transitions for B//c-axis. By using the developed magnet system, we succeeded in observing induced magnetic reflections under pulsed magnetic fields up to 31 T on AKANE. Fig.1 shows the time-dependence of magnetic filed (solid line) and intensity of magnetic reflection at the (1/3,1/3,2) reciprocal point (open circles). The reflection at the (1/3,1/3,2) position was observed only in the time region where the magnetic field was larger than 20T. This is direct evidence that the 3-sublattive structure is definitely realised in the phase of B>20T. In the experiments on AKANE, we also succeeded in observing the magnetic field dependence of 5-sublattice magnetic reflection of CuFeO2 under up to 31T; note that 31T is the highest magnetic field in the world for neutron scattering experiments.

We also tried to observe magnetic transitions in Shastry-Sutherland compound TbB4, which shows metamagnetic transitions for B//[001] in spite of its Heisenberg-type magnetic structures, on T1-1. We succeeded in the magnetic field dependence of the 100 magnetic reflection which correspond to the antiferromagnetic structure under B=0 T, and confirming the decrescence of the 100 reflection above B=17T.

Since we have confirmed that this magnet system can generate 40T magnetic fields safely, even 40T experiments are feasible by this system.

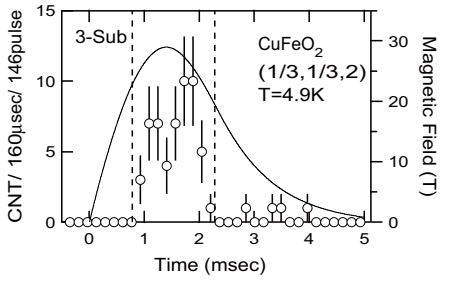


Fig. 1. Time-dependence of magnetic field (solid line) and the intensity of a 3-sublattice magnetic reflection observed at (1/3,1/3,2) at T=4.9K on Kinken neutron spectrometer AKANE (T1-2).

1-2-18

Magnetic structure of an antiferro-octupolar ordering compound Tb0.94Gd0.06B2C2

E. Matsuoka, Y. Sasaki, D. Usui. K. Ohoyama(A), and H. Onodera
Department of Physics, Tohoku University, (A)Institute for Materials Research, Tohoku University

The compound TbB2C2 shows an antiferromagnetic (AFM) ordering at TN = 21.7 K with a main [1 0 1/2] propagation vector and field-induced antiferroquadrupolar transitions [1]. The AFM phase in TbB2C2 that has been called phase IV shows some anomalous features in its magnetic behavior. The [1 0 1/2] wave vector in phase IV is peculiar to TbB2C2 since the other RB2C2 exhibit [1 0 0]-type AFM structure. Furthermore, the magnetic susceptibility anomalously increases below TN without any spontaneous magnetization. To obtain more precise information with respect to the anomalous magnetic behavior, effects of substitution of Tb3+ ions by Gd3+ have been examined and the T-x phase diagram of Tb1-xGdxB2C2 has been constructed [2]. The Gd substitution with a small content ($x<0.07$) induces drastic change of magnetic properties, namely, an intermediate magnetic phase named AFM1 appears at $TO<T<TN$. Here, TO is a transition temperature from AFM1 to phase IV. In ref. [2], the following assumption has been proposed: although the magnetic structure of AFM1 is a [1+delta delta 0]-type long periodic one, the antiferro-octupolar (AFO) ordering at TO forces to align the magnetic moments with their wave vector of [1 0 1/2]. The proposed assumption explains satisfactorily for the anomalous properties of TbB2C2 and the Gd-substitution effects [2].

To examine the assumption proposed in ref. [2], neutron powder diffraction experiments of Tb0.94Gd0.06B2C2 has been performed by using HERMES installed at the JRR-3M reactor in JAEA. Neutrons with a wavelength of 1.82646 A were obtained by the 331 reflection of the Ge monochromator. Since the natural boron is a strong neutron absorber, the 11B-enriched boron was used for the sample preparation.

Fig. 1 shows the neutron diffraction patterns of Tb0.94Gd0.06B2C2 measured at several temperatures. At paramagnetic region ($T>TN$), all of the Bragg peaks can be indexed as a LaB2C2-type tetragonal structure as shown in Fig. 1(a). On the other hand, weak satellite peaks around (100) and (101) are observed at 18 K ($TO<T<TN$) as shown in Fig. 1(b). The positions of these satellite peaks are almost identical to those observed in phase IV of TbB2C2 [1] as expected in ref. [2], implying that the magnetic structure of AFM1 is a long periodic one whose wave vector is [1+delta delta 0] with delta˜0.11. It is noteworthy that similar long periodic structure is observed for the intermediate magnetic phase of ErB2C2 [3]. In addition to the satellite peaks, strong magnetic peaks indexed by the wave vector of [1 0 1/2] are observed at 2.5 K ($T<TO$) as shown in Fig. 1(c). The results of present neutron diffraction support the assumption proposed in ref. [2].

[1] K. Kaneko et al., J. Phys. Soc. Jpn. 70 (2001) 3112.
[2] E. Matsuoka et al., J. Phys. Soc. Jpn. 75 (2006) 123707.
[3] K. Ohoyama et al., J. Phys. Soc. Jpn. 71 (2002) 1746.

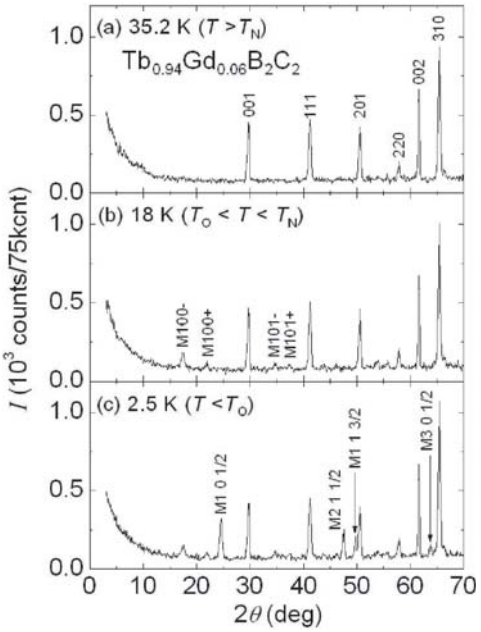


Fig. 1. Neutron powder diffraction patterns of Tb0.94Gd0.06B2C2 measured at several temperatures.

1-2-19

Magnetic structure of multipolar ordering compounds RPd3S4 (R = Ce, Pr)

E. Matsuoka, D. Usui, Y. Sasaki, K. Ohoyama(A), and H. Onodera
Department of Physics, Tohoku University, (A)Institute for Materials Research, Tohoku University

The rare-earth (R) palladium bronzes RPd3S4 crystallizes into a cubic NaPt3O4-type crystal structure. The R atoms form a body-centered cube and are subjected to a cubic crystalline electric field (CEF) represented by the cubic point group of Th [1]. Systematic studies along the R series have revealed that the CEF ground states of 4f electrons in RPd3S4 retain orbital degeneracy [1].

In this system, CePd3S4 shows anomalous magnetic properties: i) despite most RPd3S4 compounds show an antiferromagnetic (AFM) ordering, CePd3S4 shows a ferromagnetic (FM) one ii) the Curie temperature TC (6.0 K) is larger than the Neel temperature of R = Gd (5.5 K) [1]. On the other hand, it has been reported that PrPd3S4 does not show a magnetic ordering but a multipolar one at TM = 1.56 K [2]. To examine the origin of abovementioned anomalous properties of CePd3S4 and to confirm the occurrence of multipolar ordering of PrPd3S4, neutron powder diffraction experiments of CePd3S4 and PrPd3S4 have been performed by using HERMES installed at the JRR-3M reactor in JAEA. Neutrons with a wavelength of 1.82646 A were obtained by the 331 reflection of the Ge monochromator.

The upper panel of Fig. 1 shows the neutron diffraction patterns of CePd3S4. At 9 K (> TC), most peaks can be indexed as a NaPt3O4-type structure, although the small peaks by impurity phase (PdS) are discernible. At 2.2 K (< TC), two kinds of magnetic Bragg peaks are observed. One is an AFM component as observed at 15.4 degree indexed as "AFM100" in the figure. The appearance of (100) magnetic peak means that the magnetic structure of CePd3S4 is basically expressed by the wave vector of [100], i.e., type-I AFM structure as observed for TbPd3S4 [3]. The other is a FM component indexed as "FMhkl". Therefore, we can consider that the magnetic structure of CePd3S4 is not a simple FM structure but a canted-AFM one expressed by two wave vectors of [100] and [000], which probably implies that the ordered phase is a coexistent one of AFM and antiferroquadrupolar order similar to the phase in DyPd3S4 [4].

The lower panel of Fig. 1 shows the diffraction patterns of PrPd3S4 measured at 3 K (> TM) and 0.7 K (<TM). Unexpectedly, the magnetic Bragg peaks shown as "Mhkl" in the figure are observed at 0.7 K. All of magnetic peaks can be indexed by considering a wave vector of [100], that is, type-I AFM structure is realized below TM. Note that TM defined by the specific-heat measurements shifts to higher temperatures by magnetic fields, begins to shift to lower temperatures above 2 T, and disappears above 3.6 T [2]. Such a "re-entrant" behavior of TM means that the transition at TM is not due to magnetic ordering but a multipolar one [2]. To explain the inconsistency between the specific-heat measurements and the present neutron diffraction, we now consider that a multipolar ordering (e.g. antiferro-octupolar ordering) occurs at TM and the AFM ordering is concomitant with it.

[1] K. Abe et al., Phys. Rev. Lett. 83 (1999) 5366.
[2] E. Matsuoka et al., J. Phys. Soc. Jpn. 76 (2007) 073707.
[3] E. Matsuoka et al., J. Magn. Magn. Mater. 231 (2001) L23.
[4] L. Keller et al., Phys. Rev. B 70 (2004) 060407.

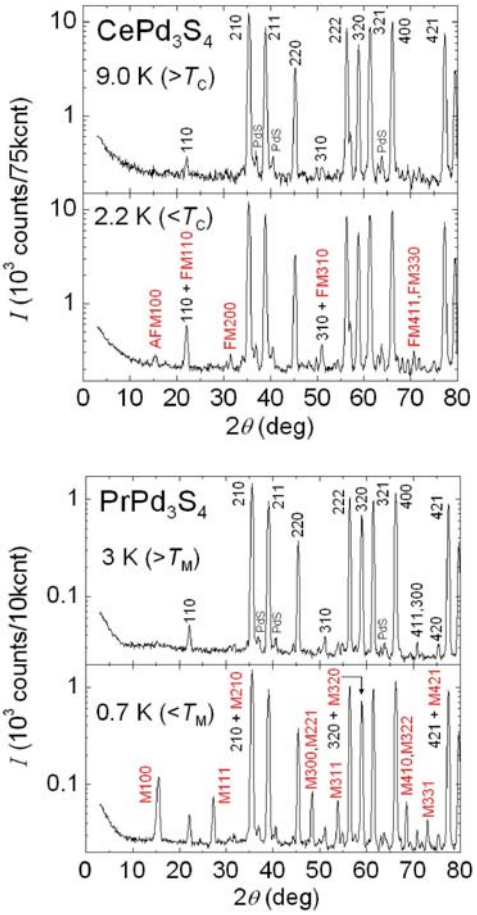


Fig. 1. Neutron powder diffraction patterns of CePd3S4 (upper panel) and PrPd3S4 (lower panel).

1-2-20

Study on low-temperature phase transitions in the $Ho_3Al_5O_{12}$

R. Morinaga, T. J. Sato, and H. Kimura[A]
ISSP-NSL Univ. Tokyo, [A]IMEL NIMS

Geometrically frustrated systems have attracted special interests for more than three decades. The antiferromagnetic rare-earth(RE) garnet $A_3B_5O_{12}$ is one of a classical and prototypical frustrated system consisting of three-dimensinally connected triangular motif. The ground-state degeneracy becomes highest for the isotropic magnetic moments such as RE = Gd. Therefore, $Gd_3Ga_5O_{12}$ is the most intensively studied for many years. Nevertheless, other RE garnets have been studied mainly as the optical matirials; the magnetic study focusing the effect of geometrical frustration is rather less conducted.From the low-temperature specific heat and magnetic susceptibility measurements of one of RE garnet $Ho_3Al_5O_{12}$, it is known that there is an antiferromagnetic transition at T_N = 0.839 K in addition to Weiss temperature θ_{Weiss} = - 2.92 K [1]. This difference between T_N and θ_{Weiss} suggests formation of the short range antiferromagnetic correlations at $T_N < T < |\theta_{Weiss}|$. Last year we performed neutron powder diffraction and found the development of magnetic short range correlations both in the elastic and inelastic channels.

Here, we report neutron scattering study on the single crystal $Ho_3Al_5O_{12}$. Experiments have been performed at the triple-axis spectrometer 4G-GPTAS for elastic and C11-HER for low energy inelastic scattering. Single crystals of $Ho_3Al_5O_{12}$ were grown by the floating zone method. Data shown here were taken with a double-axis mode with incident energy E_i = 14.8 meV at 4G. A single crystal was mounted in a Lq-He3 cryostat and cooled down to 0.51 K.

Figure 1 shows the elastic contour map of two temperature differences between T = 1.3 and 0.51 K in the (*H0L*) zone. In this figure, solid lines indicates the Brillouin zone boundary. Strong diffuse scattering is distributed from magnetic Bragg points to zone center. Furthermore, another type of diffuse scattering can be seen around nuclear Bragg peak point 202. However, at 402 nuclear Bragg peak there is no diffuse scattering. As the diffuse scattering follows the magnetic form factor and is temperature dependence, magnetic diffuse scattering around 202 originates from the ferromagnetic coupling of the Ho^{3+} ions. From the analysis of the powder neutron scattering measurements, the second nearest neighbor Ho^{3+} magnetic moments in the same sublattices have the major contributions to the magnetic diffuse scattering. Detailed analysis is now in progress.

[1] S. Nagata et al. J. Phys. Chem. Solids. **62** (2001) 1123.

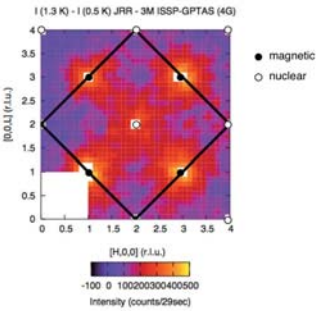


Fig. 1. Magnetic diffuse scattering intensity map $S(Q)|_{T=1.4K}$ - $S(Q)|_{T=0.5K}$ in the (*H0L*) plane.

1-2-21

Magnetic and Crystallographic Study on R2CrS4 (R=Ho and Er)

Keitaro Tezuka, Yuta Yoshioka, Seiji Sato, Satoshi Suzuki, Keita Oshikane, Yue Jin Shan, Hideo, Imoto, and Kenji Ohoyama *
*Department of Applied Chemistry, Faculty of Engineering, Utsunomiya University, Utsunomiya 321-8585; *Institute for Materials Research, Tohoku University, Sendai 980-8577*

A series of sulfides R2CrS4 (R = Ho-Tm, Y) with the Er2CrS4-type structure (Pca21, No. 29) gives good examples of the magnetic interactions between Jahn-Teller Cr2+ ions and rare earth ions. Recently we found that Y2CrS4 with no magnetic rare-earth ions showed an antiferromagnetic transition at ca. 65 K while other members of the series showed magnetic anomalies at ca. 60 K and also at lower temperatures. We could refine the magnetic structure of YCr2S4 at 10 K and of Tm2CrS4 at 3 K. Both of their magnetic structures have the same unit cell as their crystal structures though their magnetic structures are different [1?3].

In this study, neutron diffraction measurements of Ho2CrS4 (80 K, 40 K, 20 K, 9 K, 5 K, and 3 K) and Er2CrS4 (80 K, 50 K, 40 K, and 3 K) were performed on the high efficiency and resolution powder diffractometer, HERMES, of Institute for Materials Research, Tohoku University, installed at the JRR-3M Reactor in JAEA (Tokai). The wavelength of a neutron incident was 1.8265(1) .

Either Ho2CrS4 or Er2CrS4 did not have any distinct crystallographic phase transition between 80 K and 3 K and were isomorphous with Er2CrS4. At 80 K, cell parameters of Ho2CrS4 and Er2CrS4 were determined to be a = 12.4990(16) , b = 7.4947(9) , and c = 12.4488(17) , and a = 12.4711(13) , b = 7.4718(7) , and c = 12.4399(12) , respectively, which decreased with decreasing temperature. Below the magnetic transition temperatures, ca. 60 K, both compounds showed several magnetic peaks and their intensities gradually increased with decreasing temperature (see Fig. 1). The magnetic diffractions suggested that paramagnetic chromium and lanthanide ions were ordered as found in Tm2CrS4. These magnetic peaks could be indexed on the same crystallographic unit cell (Fig. 1) as observed in Y2CrS4 and Tm2CrS4. However, intensities of the magnetic peaks showed that all of the four members of the series have different magnetic structures.

References

[1] K. Tezuka et al., J. Phys. Chem. Solids, 68 (2007), 2133-2137.
[2] K. Tezuka et al., Activity Report on Neutron Scattering Research: Experimental Reports, Vol. 13, nact06-33342.
[3] K. Tezuka et al., Activity Report on Neutron Scattering Research: Experimental Reports, (2007), 214.

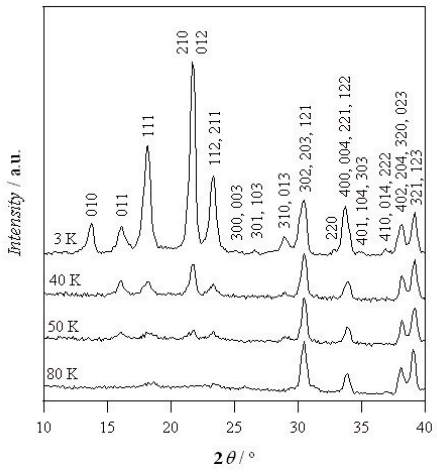


Fig. 1. Neutron diffraction patterns of Er2CrS4.

1-2-22

Magnetic structure study of the multi-step metamagnet $CeIr_3Si_2$

Y. Muro(A), K. Motoya(A), K. Shigeto(B), T. Takabatake(B)
(A)Department of Physics, Faculty of Science and Technology, Tokyo University of Science,(B)ADSM, Hiroshima University

$CeIr_3Si_2$ crystallizes in the orthorhombic $ErRh_3Si_2$-type structure (Imma, No. 74), which is a derivative of the hexagonal $CeCo_3B_2$-type. The lattice parameters are a = 7.1765 Å, b = 9.7274 Å and c = 5.5971 Å. The results of electrical resistivity, specific heat and magnetic susceptibility measurements reveal that $CeIr_3Si_2$ is a Kondo-lattice compound showing two successive magnetic transitions at T_{N1}=4.1 K and T_{N2}=3.3 K[1]. Below 3.3 K, the isothermal magnetization of polycrystalline sample displays mult-step metamagnetic transitions at 0.6 T, 0.9 T and 1.2 T. Recent study of a single-crystal $CeIr_3Si_2$ has revealed that the metamagnetic transitions at 0.6 T and 1.2 T occurs when the magnetic field H applyed along the b-axis while that at 0.9 T occurs when $H//c$-axis[2]. We need to obtain the magnetic structures between each transition field in order to study the origin of multi-step metamagnetism of $CeIr_3Si_2$. Thus we have been carrying out the elastic neutron scattering of powder and single-crystal samples.

In order to search magnetic reflections, elastic scans were performed in three scattering planes of (HK0), (H0L) and (0KL). At 1.5 K, we observed four magnetic Bragg peaks at Q =(0 4/3 ±2/3) and Q =(0 5/3 ±1/3). Temperature dependence of the peak at Q =(0 4/3 −2/3) was shown in Fig. 1(a). The observed magnetic reflections agree with those observed in the previous measurement using a powder sample. These non-integer Q's indicate that the lattice parameters of b- and c-axis below T_{N2} becomes three time as large as those above T_{N1}.

Figure 1(b) shows the temperature dependence of integrated intensity at Q=(0 4/3 −2/3) and Q=(0 5/3 −1/3). The intensities of all magnetic reflections display a maximum at 2.7 K in spite of no further phase transition down to 0.5 K. This behavior may indicate the cluster glass-like transition at T_{N2} possibly due to partial disorder between Ir and Si rigands.

References

[1] Y. Muro, Y. Ohno, T. Okada, K. Motoya, *J. Magn. Magn. Mater.* 310 (2006), p. 389.
[2] K. Shigetoh, A. Ishida, Y. Ayabe, T. Onimaru, K. Umeo, Y. Muro, K. Motoya, M. Sera, T. Takabatake, *Phys. Rev. B* 76 (2007), p. 184429.

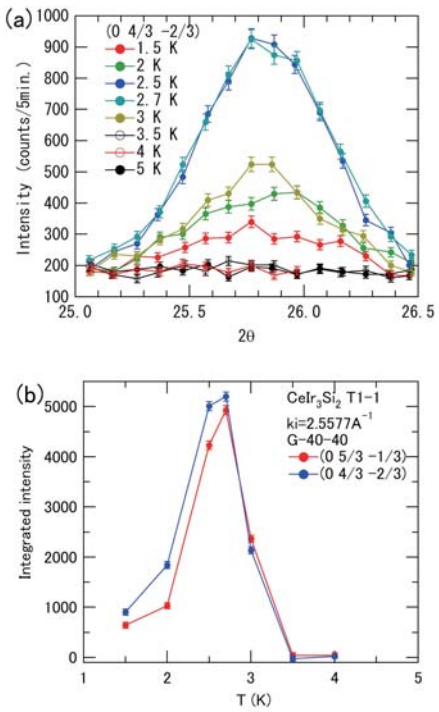


Fig. 1. (a)Temperature dependence of magnetic reflection at (0 4/3 -2/3). (b)Temperature dependences of integrated intensity at (0 4/3 -2/3) and (0 5/3 -1/3).

1-2-23

Magnetic phase diagram of the square lattice CuSb2-xTaxO6 with competing interactions J1 and J2

M. Nishi, M. Kato(A), K. Hirota(A) and K. Ohyama(B)
ISSP Univ. Tokyo, (A) Inorganic Chemistry Lab. Doshisya Univ. (B)IMR Tohoku Univ.

Low-dimensional magnetism of Heisenberg antiferromagnets (HAF) has been a focus of intensive research since discover of high Tc copper oxides. CuSb2O6 compound has a tri-rutile type structure in which Cu2+ ions form a square lattice similar to La2CuO4 [1]. The magnetic susceptibility of CuSb2O6 indicates a typical behavior for S=1/2 one-dimensional HAF above 20K and shows a antiferromagnetic long-range order at 8.7 K in which Cu spins are aligned ferromagnetically along b-axis (namely collinear order) with a propagation vector (1/2, 0, 1/2) [2, 3]. If nearest neighbor coupling J1 is too stronger than next nearest coupling J2 along diagonal, Neel order will be stabilized. Then J2 interaction through Cu-O-O-Cu bond is dominant on the collinear order of CuSb2O6.
The substitution of Ta atom instead of Sb atom causes the decreasing of transition temperature of long-range order which disappears above x=1 [4]. TaO6 octahedron occupies inter CuO layers and the inter layer coupling may be decreased with the substitution of Ta atom; x. When J2 coupling is HAF, there are the spin frustrations between J1 and J2 couplings even if J1 coupling is ferromagnetic or antiferromagnetic [5].
Neutron diffraction measurements of CuSb2-xTaxO6 powder samples with x=0.3, 0.7 and 0.8 were carried out on the neutron powder diffractometer HERMES (T13) installed at the JRR-3M reactor at JAEA. Magnetic Bragg peaks were observed at (1/2, 0, 1/2), (1/2, 0, 3/2) and (3/2, 0, 3/2). Temperature dependences of Bragg peak for three kinds of samples were carried out on the neutron triple axis spectrometer HQR (T11) installed at the JRR-3M in JAEA. The transition temperature of antiferromagnetic long-range order were determined as 8.0K for x=0.0, 3.5K for x=0.7 and 3.8K for x=0.8. These data were plot in the figure 1 with the data of magnetic susceptibilities and heat capacities. In comparison of the experimental results of x=0.7 and 0.8 samples magnetic Bragg intensity of x=0.8 becomes extremely weaker than that of x=0.7 in spite of nearly same Tn. Then it is expected that above x=0.8 new magnetic phase will be appear.

References

[1] A. M. Nakua et al., J. Solid State Chem. 91 (1991) 105.
[2] M. Kato et al., J. Phys. Soc. Jpn. 71S (2002) 187.
[3] B. J. Gibson et al., J. Mag. Mag. Mater. 272-6 (2004) 927.
[4] M. Kato et al., J. Phys. Chem. Sol. 63 (2002) 1129.
[5] N. Shanon et al., Eur. Phys. J. B38 (2004) 599.

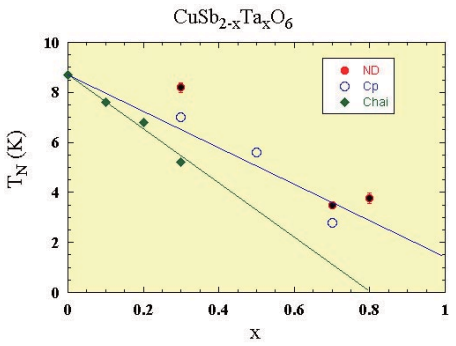


Fig. 1. Magnetic phase diagram of CuSb2-xTaxO6 obtained by neutron diffraction, heat capacity and magnetic susceptibility. The antiferromagnetic transition temperature decreases with increasing of substitution of Ta atom.

1-2-24

Competing interactions in two dimensional square lattice CuSb2-xTaxO6

M. Nishi, M. Kato(A), K. Hirota(A) and M. Matsuura
ISSP Univ. of Tokyo, (A)Inorganic Chemistry Lab. Doshisya Univ.

Low-dimensional magnetism of Heisenberg antiferromagnets (HAF) has been a focus of intensive research since discover of high Tc copper oxides. CuSb2O6 compound has a tri-rutile type structure in which Cu2+ ions form a square lattice similar to La2CuO4 [1]. The magnetic susceptibility of CuSb2O6 indicates a typical behavior for S=1/2 one-dimensional HAF above 20K and shows a antiferromagnetic long-range order at 8.7 K in which Cu spins are aligned ferromagnetically along b-axis (namely collinear order) with a propagation vector (1/2, 0, 1/2) [2, 3]. If nearest neighbor coupling J1 is too stronger than next nearest coupling J2 along diagonal, Neel order will be stabilized. Then J2 interaction through Cu-O-O-Cu bond is dominant on the collinear order of CuSb2O6.
The substitution of Ta atom instead of Sb atom causes the decreasing of transition temperature of long-range order which disappears above x=1 [4]. TaO6 octahedron occupies inter CuO layers and the inter layer coupling may be decreased with the substitution of Ta atom; x. In this reason we can study the J1 and J2 couplings about CuO layer only at the compound with x=1. When J2 coupling is HAF, there are the spin frustrations between J1 and J2 couplings even if J1 coupling is ferromagnetic or antiferromagnetic [5].
Neutron inelastic scattering measurements of CuSbTaO6 powder samples were carried out on the neutron triple-axis spectrometer PONTA (5G) and HQR (T11) installed at the JRR-3M reactor at JAEA. Magnetic excitation peak was observed at Q=0.5A-1 for constant E=1.5 meV scan and this position shifts to Q=0.55A-1 for constant E=3.5meV scan at the temperature 1.5K. CuSbTaO6 powder sample does not become antiferromagnetic long-range order until 1.5K. With the reason that scattering intensity at Q=0.4A-1 is regarded to background intensity, the magnetic net intensity deducting from the data of Q=0.5A-1 to that of Q=0.4A-1 were obtained from E=0.5meV to 1.7meV with energy resolution 1meV. We found distinctly the spin gap with E=0.8meV for CuSbTaO6 sample as shown in figure 1. If there is short-range order, the diffuse scattering is observed usually. Then spin gap of 0.8meV will be come from spin frustration mechanism among magnetic interactions.

References

[1] A. M. Nakua et al., J. Solid State Chem. 91 (1991) 105.
[2] M. Kato et al., J. Phys. Soc. Jpn. 71S (2002) 187.
[3] B. J. Gibson et al., J. Mag. Mag. Mater. 272-6 (2004) 927.
[4] M. Kato et al., J. Phys. Chem. Sol. 63 (2002) 1129.
[5] N. Shanon et al., Eur. Phys. J. B38 (2004) 599.

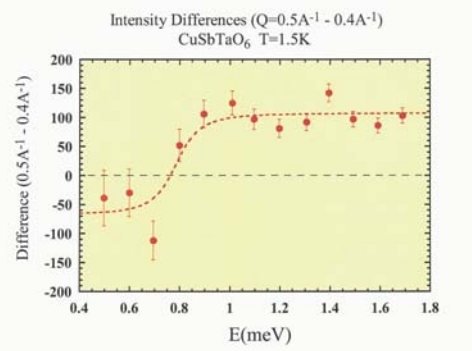


Fig. 1. The experimental results of CuSbTaO6 powder sample in inelastic neutron-scattering. Magnetic spin gap was distinctly observed at E=0.8meV.

1-2-25

Crystal Field Excitation of TmAg2In

Takeshi Matsumura
Department of Physics, Graduate School of Science, Tohoku University

A ternary compound RAg2In (R=rare earth) crystallizes into cubic Heusler-type structure. This system has a characteristic that the magnetic ordering temperatures are very low. Here, in TmAg2In, the specific heat and magnetic susceptibility measurements have suggested that the ground state is gamma5 and it has been clarified that the magnetic order does not occur down to 0.5 K. However, the specific heat exhibits an anomalous peak around 1 K, which is much lower than the 1st excited state at about 15 K. Then, the possibility of Kondo effect has been suggested for TmAg2In.

The purpose of the present neutron scattering study is to investigate the possibility of Kondo effect in TmAg2In. Determining the crystalline electric field (CEF) level scheme also is another important purpose.

We have performed inelastic neutron scattering experiments on powder sample using TOPAN(6G) and HER(C11) 3-axis spectrometers. First, using TOPAN, we measured the inelastic spectrum up to an energy transfer of 20 meV, and found the CEF excitation peaks around 1.5 and 2.7 meV. The spectrum and its temperature dependence was successfully explained by the CEF model. However, because of the limited energy resolution, it was not possible to discuss the possibility of Kondo effect. Next, using HER spectrometer, we measured the spectrum with much higher resolution.

The figure shows the energy spectrum at T=0.75 K, below the anomaly of the specific heat. We can clearly see two CEF excitation peaks at 1.68 meV and at 2.87 meV. By investigating the temperature dependence, the CEF level scheme has been determined as G_5,1(0)-G_3(19.5)-G_4(33.4)-G_1(35.3)-G_5,2(52.8)-G_2(72.5 K), which is experessed by the parameters of x=-0.013 and W=0.239 K.

Solid line is a fit to the data assuming three Lorentzians at E=0 (quasi-elastic) and at two CEF levels. At temperatures higher than 3 K, the data can be well fitted by this model. However, below 1.5 K, the data gradually deviate from the Lorentzian shape, and at 0.75 K, the spectrum cannot be simply expressed by three Lorentzians. It also seems that the CEF excitation peaks are slightly splitted.

A simple scenario is that the CEF level is slightly modified (~ 1 K) by the possible local distortion that reduces the cubic symmetry. Such a disorder can happen in Heusler structure where the Tm and In sites can exchange relatively easily. At temperatures higher than this splitting, the peak can be expressed by a single Lorentzian. But at low temperatures, it is not the case. The width of the peaks about 0.1 meV is comparable to the Kondo temperature estimated by the specific heat. It is also a typical value for localized f-electron systems. It can also be caused by extrinsic effect of disorder.

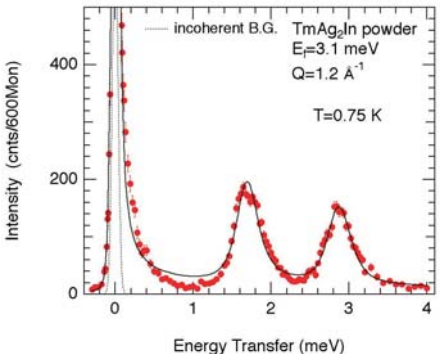


Fig. 1.

1-2-26

Magnetic Structure Analysis in Cr1-xMoxB2 (x = 0.15)

Y. Kousaka(A), E. Kaya(A), H. Kimura(B), Y. Noda(B) and J. Akimitsu(A)
(A)Department of Physics and Mathematics Aoyama-Gakuin University, (B)Institute of Multidisciplinary Research for Advanced Materials Tohoku University

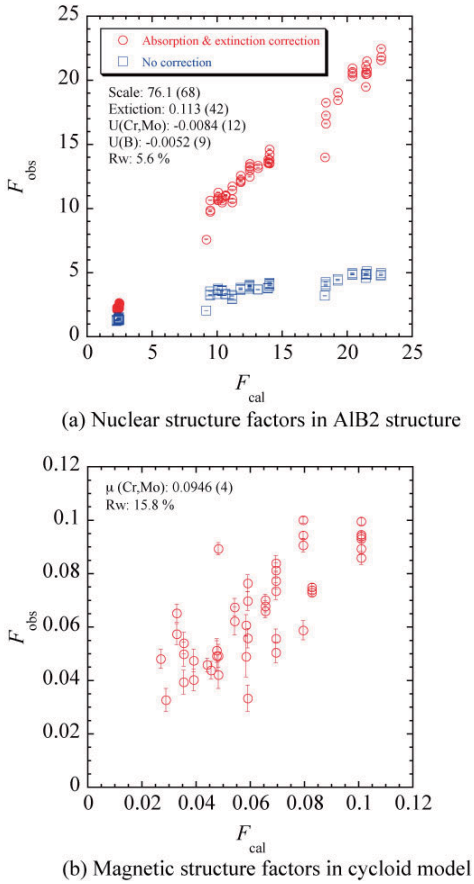
CrB2, which shows a cycloidal magnetic structure along <1,1,0>, has a hexagonal AlB2-type structure with a space group of P6/mmm. With substituting 15 % Mo to Cr in CrB2, NMR results indicate that magnetic structure changes to Spin Density Wave (SDW) [1]. However, it is quite difficult to explain the change of magnetic structure by substituting 15 % Mo to Cr in CrB2, and no other experiments has not been performed for decades.

In order to examine the magnetic structure of Cr1-xMoB2, we performed neutron diffraction experiments at the 4-circle diffractometer T2-2 (FONDER), JRR-3M reactor in JAEA (Tokai). The single crystal was grown by floating zone method using enriched 11B to avoid large absorption of 10B. The data were taken at 10 K. Firstly, we determined the magnetic propagation vector to be (0.286, 0.286,0). Then, in order to determine crystal and magnetic structure, we observed nuclear and magnetic scattering intensities. We corrected the absorption and extinction effect in nuclear scattering, using DABEX and RADIEL. The crystal structure was AlB2 structure, which is the same with CrB2. Fig.1 (a) shows comparison between observed and calculated nuclear structure factors. Determined temperature factors showed negative value, because small contamination of 10B makes it difficult to estimate absorption coefficient. Though the nuclear structure factors were severely affected by a extinction effect, the magnetic scattering intensities were too weak to be affected by the extinction effect. We compared the observed and calculated magnetic structure factor in cycloid and SDW model. As shown in Fig.1 (b), magnetic structure was basically described by the cycloidal structure with 15.8 % of weighted R factor, compared with SDW structure with 25.3 %.

In order to determine the magnetic structure in detail, we are now analyzing the experimental results by the use of different magnetic structure like an elipsoidal cycloid structure.

Reference

[1] K. Yoshimura et al.: J. Magn. Magn. Matter. 90 (1990) 709.



(a) Nuclear structure factors in AlB2 structure

(b) Magnetic structure factors in cycloid model

Fig. 1. Comparison between observed and calculated structure factors.

1-2-27

Chiral Helimagnetism in CuB2O4

Y. Kousaka(A), E. Kaya(A), M. Matsuura(B), K. Hirota(B), M. Nishi(B) and J. Akimitsu(A)

(A)Department of Physics and Mathematics Aoyama-Gakuin University, (B)Institute for Solid State Physics of the University of Tokyo

Helical magnet copper metaborate CuB2O4 with the space group I-42d has been paid attention from the viewpoint of chiral helimagnetic ordering. It shows various magnetic phase transitions at low temperature: paramagnetic state above TN (= 20 K), commensurate phase with weak ferromagnetic ordering in the range of T* (˜ 10 K) < T < TN and incommensurate phase with helimagnetic ordering below T*. In the temperature close to the incommensurate-to-commensurate transition, neutron diffraction experiments show higher order satellite, which is an evidence for the formation of magnetic soliton lattice [1]. With increasing an applied magnetic field perpendicular to the helical c-axis, incommensurate phase II is observed in the region which was supposed to be commensurate magnetic structure [2]. The magnetic property of CuB2O4 can be interpreted by the lattice chiral XY model: commensurate-to-incommensurate transition is understood by the formation of chiral magnetic soliton lattice [3]. Moreover, symmetry operation based on its space group, I-42d, allows antiferro-chiral helimagnetic ordering, which alternates right and left handed screws.

In order to detect the antiferro-chiral helimagnetic ordering, we performed polarization analysis experiments in the incommensurate phase. The single crystal was grown by the spontaneous crystallization technique; slow cooling of CuO, Li2CO3 and B2O3 [3], using enriched 11B2O3 to avoid the large neutron absorption due to 10B. The polarized neutron diffraction experiments were performed at PONTA (5G), JRR-3M reactor in JAEA (Tokai). The data was taken at 8 K under an applied magnetic field parallel or perpendicular to the scattering vector, due to aligning the neutron polarization parallel or perpendicular to the scattering vector. Accoring to the calculation of the antiferro-chiral helimagnetic ordered magnetic structure factors in (h, 0, 2h+-q) (h: even), spin flip process should be observed when the neutron polarization is parallel to the scattering vector. In case of the neutron polarization perpendicular to the scattering vector, non-spin flip process should be observed. However, the experimental results in (2, 0, 4+-q) indicates that the both processes are observed in case of parallel and perpendicular neutron polarization. The experimental data was considered to be affected by several magnetic domains. As this compound shows commensurate-to-incommensurate magnetic ordering with cooling temperature, makeing a single magnetic domain in commensurate phase is enough to guarantee the single mangetic domain in incommensurate phase.

Therefore, in order to make a uniform magnetic domain, we should cool the sample with appling field parallel to the b-axis.

Reference

[1] B. Roessli et al.: Phys. Rev. Lett. 86 (2001) 1885.
[2] Y. Kousaka et al.: J. Phys. Chem. Sol. 68 (2007) 2170.
[3] Y. Kousaka et al.: J. Phys. Soc. Jpn.76 (2007) 123709.

1-2-28

Energy Range of Magnetic Excitations in Percolating Two-Dimensional Heisenberg Antiferromagnet, Rb2Mn0.598Mg0.402F4

S. Itoh and T. J. Sato*
*High Energy Accelerator Research Organization, Tsukuba 305-0801; *The University of Tokyo, Tokai 319-1106*

Magnetic excitations in the percolating two-dimensional Heisenberg antiferromagnet, Rb2MncMg1-cF4, with c= 0.598 were investigated on the triple-axis spectrometer, GPTAS (4G) at JRR3M in JAEA (Tokai), in the energy range up to 20 meV. The magnetic concentration of this system is very close to the percolation threshold for a square lattice (cp = 0.593). The N el temperature of this system was determined to be 4 K by measuring the temperature dependence of the intensity of the magnetic (100) reflection. The inelastic spectra at (1+q,0,0) with q = 0 - 0.5 were measured with a fixed final energy Ef = 14.7 meV, at 1.5 K well below TN and at 200 K. The energy resolution was 0.7 meV (FWHM) at the elastic point.

In 2004 and 2005, we performed similar experiments to determine the energy range of magnetic fractons in this system, and it was reported the observation of dispersive excitations more than 10 meV on GPTAS [1]. However, the peak positions of the dispersive component were not consistent with the experiments on HER (C1-1) at JRR3M and on IRIS at ISIS. At present, we improved the shielding of the spectrometer, GPTAS, and preformed the experiment again. Figure 1 shows the observed excitation spectrum at the magnetic zone boundary (1.5,0,0) at 1.5 K. The dispersive component at around 12 meV observed in the previous experiment disappeared by the improvement of the shielding, and therefore, it was found to be spurious. We can still see a small peak at around 12 meV, and it was found to be phonon from its temperature dependence. Therefore, we found the energy range of the magnetic excitations to be less than 10 meV at the present experiment.

Also we previously reported dispersive excitations observed on HER and on IRIS. From the result of the precise analysis of the data taken on IRIS, the observed spectra on IRIS was found to quantitatively agree with the predicted dynamical structure factor of magnetic fractons [2], and the zone boundary energy of fractons was estimated to be less than 10 meV. And the dispersive spectra observed on HER can be interpreted as the Ising cluster excitations with a small dispersion. In the present experiment, we determined the energy range of the magnetic excitations in this system, and consistently demonstrated the magnetic fractons and other magnetic excitations.

References

[1] S. Itoh et al, Activity Report on Neutron Scattering Research Vol. 13 (ISSP, Univ. Tokyo 2006).
[2] K. Yakubo et al., J. Phys. Soc. Jpn. 62 (93) 2196.

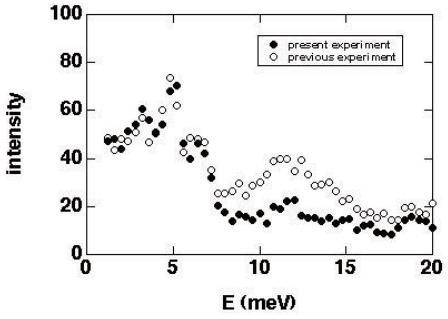


Fig. 1. Excitation spectra at (1+q,0,0) with q=0.5 at 1.5 K in Rb2Mn0.598Mg0.402F4 observed on GPTAS.

1-2-29

Antiferromagnetic ordering of Ca3Ru2O7

Y. Yoshida(A), K. Iwata(B), N. Aso(C), S. Katano(B)
(A)AIST, (B)Saitama univ., (C)ISSP-NSL Univ. Tokyo,

Double layered Ruddlesden-Popper (R-P) type Calcium ruthenate, Ca3Ru2O7, shows an antiferromagnetic ordering below 56K and a metal-nonmetal transition at 48K.[1] Recent study revealed that Ca3Ru2O7 shows anisotropic behavior in the transport properties, and is a quasi-two-dimensional metal below 30K.[2] Powder neutron diffraction study and thermal expansion measurement clarified that the transition at 48K accompanies jumps of all lattice parameters.[3,4] As to the magnetic structure of Ca3Ru2O7, it was speculated by the magnetic peak from the powder neutron diffraction study. In the magnetic ground state, magnetic moments align ferromagnetically along b-axis within the double layer and antiferromagnetically between the double layers.[4] Since the magnetic anisotropy in the magnetic susceptibility was changed at the structural transition, the magnetic structure between 48 and 56K has not been clarified yet.

In order to clarify the magnetic structure of Ca3Ru2O7, we performed a neutron diffraction study with a single crystalline Ca3Ru2O7. Elastic neutron scattering experiments were performed on the triple-axis spectrometer T1-1 installed at the reactor hall at JRR-3. The incident neutron wave number was 2.555 -1. The spectrometer was operated with a 2-axis mode with the holizontal collimaitons of G-80'-60'. A PG filter was used to reduce the higher-order contaminations. The sample was placed in an aluminum can filled with He gas, and mounted in a conventional cryocooler. The nuclear and magnetic peaks were obtained below 70K.

Besides nuclear peaks, inequivalent 22 magnetic peaks were observed at 10K in both (0, k, l) and (h, 0, l) planes. Figure 1 shows temperature dependence of the peak intensities of the magnetic Bragg (0,0,1) and (0,2,1). With increasing temperature, the peak intensity of (0,0,1) suddenly decreased at 48K, while that of (0,2,1) increased abruptly. This indicates that the direction of magnetic moments changes from the b-axis to the a-axis at the structural transition.

[1] G. Cao et al., PRL 78, 1751, (1997).
[2] Y. Yoshida et al., PRB 69, 220411 (2004).
[3] E. Ohmichi et al., PRB 70, 104414 (2004).
[4] Y. Yoshida et al., PRB 72, 054412 (2005).

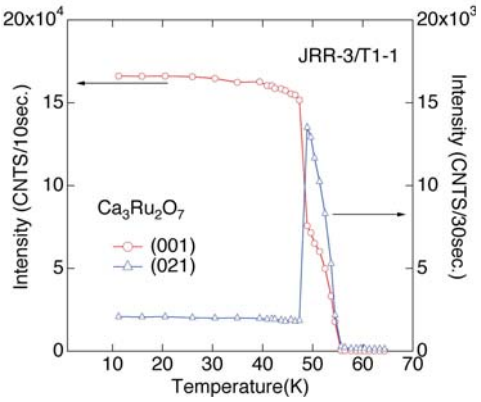


Fig. 1. Temperature dependence of the peak intensities of (0,0,1) and (0,2,1)

1-2-30

Relationship between Magnetic Structure and Ferroelectricity of LiVCuO4

Y. Yasui, Y. Naito, K. Sato, T. Moyoshi, M. Sato and K. Kakurai*
*Dept of Phys., Nagoya Univ., *JAEA*

LiVCuO4 has one-dimensional (1D) chains of the edge-sharing CuO4 squares along b, which are separated by the nonmagnetic Li+ and V5+ ions. For this system, the antiferromagnetic transition was found at TN = 2.4 K, where the dielectric susceptibility epsilon measured along a also exhibits an anomaly, indicating that the ferroelectric transition takes place almost simultaneously with the magnetic transition. This simultaneous occurrence of the two transitions or their coexistence is called the multiferroic phenomenon [1]. While almost all multiferroic systems ever reported have the magnetic moments with spin S>1 and/or have more than two magnetic sites, LiVCuO4 has spins S=1/2 of Cu2+ in the 3d x2-y2 orbital and only one crystallographically distinct Cu site. It is considered to be the first example of spin 1/2 multiferroic systems, which does not bring about any complications due to the multi-orbital and multi-site effects in the study of the mechanism of the multiferroic nature.
Neutron scattering studies as well as measurements of the dielectric susceptibility epsilon and ferroelectric polarization P have been carried out in various magnetic fields H for single-crystal samples of LiVCuO4, and the relationship between the magnetic structure and ferroelectricity has been studied [2]. Neutron scattering measurements were carried out using the triple axis spectrometer HQR(T1-1), where the double axis condition was adopted. For H = 0, the neutron scattering intensities were measured at Q = (h, k, 0) and (0, k, l) in the reciprocal space at 1.6 K (<TN) and 5 K (>TN). At 1.6 K, we observed magnetic superlattice reflections at Q = (h, k+-delta, 0) and (0, k+-delta, l) (h and l = odd, k = even) with delta=0.466. The magnetic structure that can reproduce the observed magnetic scattering intensities, is the ab-plane helical one shown schematically in the figure. It is consistent with the structure reported by Gibson et al.[3]. Considering the ferroelectric polarization P observed along a, we have found that the relation P=Q*e3 holds, which is consistent with the existing theories. The ferroelectric polarization along a, Pa at H=0 is found to be proportional to the neutron magnetic scattering intensity, indicating that the magnetic order is closely related to the appearance of the ferroelectricity.
The behaviors of epsilon and Pa drastically change with the applied magnetic field. Neutron diffraction measurements were carried out in the (0kl) scattering plane under the applied field H (//a) and the magnetic structure has been determined, where the spins have the bc-plane helical structure at least in the region H > 2 T. These results are consistent with the observed suppression of Pa by the applied field H along a above 2 T.
According to the existing theories, the ferroelectricity is expected to be along c for the bc-plane helical structure. However, we have not observed the ferroelectricity along c under the field H>2 T applied along a, where the bc-plane helical structure is actually realized. (Note that Schrettle et al.[4] have reported in the recent paper that they observed the weak ferroelectric polarization along c for the bc-plane helical structure.) To understand the origin of this discrepancy remains as a future problem.

References

[1] Y. Naito, K. Sato, Y. Yasui, Y. Kobayashi, Y. Kobayashi, and M. Sato: J. Phys. Soc. Jpn. 76 (2007) 023708.
[2] Y. Yasui, Y. Naito, K. Sato, T. Moyoshi, M. Sato, and K. Kakurai: to be published in J. Phys. Soc. Jpn. 77 (2007) No2.
[3] B. J. Gibson et al.: Physica B 350 (2004)

e253.
[4] F. Schrettle et al.: cond-mat/ 0712.3583.

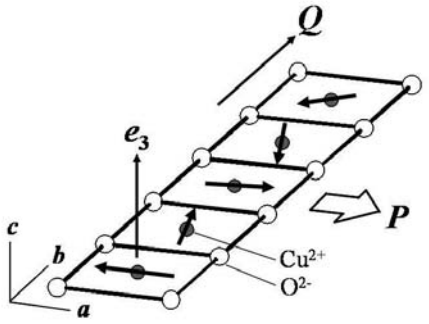


Fig. 1. The magnetic structure and ferroelectric polarization P of LiVCuO4 (Q and e3 are modulation vector and helical axis, respectively)

1-2-31

Magnetic Excitation Spectra of Honeycomb System Na3T2SbO6 (T=Cu, Ni, Co)

Y. Miura, Y. Yasui, T. Moyoshi, M. Sato and K. Kakurai*
*Nagoya University, JAEA**

Na3Cu2SbO6 is composed of Cu2SbO6 layers with Na layers between them. The former layers consist of edge-sharing CuO6 octahedra, which form the distorted honeycomb lattice with SbO6 octahedron at the center of each hexagon of the CuO6 octahedra (left figure). The Cu valence is +2 and the spin S=1/2. The temperature (T) dependences of the spin component of the magnetic susceptibility chi-spin and the specific heat C-spin indicate that a spin gap exists in the system. The superexchange interactions between two Cu spins, J1 and J1' via Cu-O-Cu paths and that of the Cu-O-O-Cu path J2 are defined as shown in the left figure. Taking into account of both the large Jahn-Teller distortion and the characteristics of the shape of the electron orbits in which the spins exist, we expect that J2 is the largest and J1' is much smaller than the other two, rationalizing that a model of the alternating chains along b is a proper one to describe the present spin system. We carried out detailed analyses of the spin-gap behavior using the (chi-spin)-T and (C-spin)-T data, and found, as described in ref. 1, that the antiferromagnetic (AF)-ferromagnetic (F) alternating chain model successfully describes it.

Inelastic neutron scattering experiments have been performed on aligned single crystals of Na3Cu2SbO6 to directly observe the spin-gap in the magnetic excitation spectra. The measurements were carried out on the triplet-axis-spectrometer ISSP-PONTA at JRR-3 in Tokai. Pyrolytic graphites (PG) were used as the monochromator and the analyzer. A PG filter after the sample was used to suppress the higher order contaminations. Horizontal collimations were effectively 40'-40'-80'-80'. The aligned crystals were oriented with the [100] and [010] axes in the scattering plane. The condition of the fixed final neutron energy Ef=14.7 meV was adopted.

Scattering intensities were collected at 10 K by the k-scans along (h, k, 0) with the transfer energy (E) of 9 meV. Peaks of the singlet-triplet excitaions were found at the k points of 0.5, 2.5 and 3.5 in the region of k<4.0 (see the right figure shown below for h=1). We also carried out similar scans at several different values of h and found that these peaks extend along h, having the one-dimensional character of the spin system, which is consistent with the above description that the system can be understood by the AF-F alternating chain model. Then, the E-scan profiles were obtained at Q=(1, 2.5, 0) at several fixed temperatures in the region of 10<T<200 K, where the gap energy were found to be 9 meV, which also agreed with the results obtained by our previous studies of chi-spin and C-spin.

The dispersion curve was also measured by the E-scans at various Q points. Analyses to estimate the J1 and J2 values from the dispersion curves are underway.

[1]Y. Miura et al.: J. Phys. Soc. Jpn. 75 (2006) 084707.

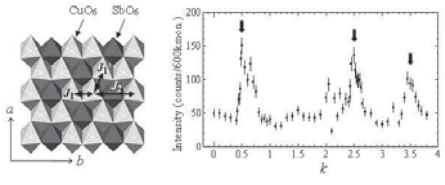


Fig. 1. (Left) Schematic figure of the honeycomb layer. At the corners of the octahedra, O atoms exist, and a Cu or Sb atom is within each octahedron. (Right) The Q-scan profile of (1, k, 0) at 10 K for E=9 meV.

1-2-32

Neutron diffraction studies on a Pr7Ni3 single crystal

T. Tsutaoka(A), A. Tanaka(A), Y. Andoh(B), A. Tada(C), G. Nakamoto(C) and M. Kurisu(C)

(A)Graduate School of Education, Hiroshima University, Hiroshima 739-8524, Japan
(B)Faculty of Regional Sciences, Tottori University, Tottori 680-8551, Japan
(C)Japan Advanced Institute of Science and Technology, Ishikawa 923-1292, Japan

The rare earth compound Pr7Ni3 crystallizes in the hexagonal Th7Fe3 type structure with the space group P63mc [1]. From the magnetic measurements, it possesses the two magnetically ordered states; one is an antiferromagnetic state between TN = 4.2 K and Tt = 2.1 K and ferrimagnetic like state below Tt. [2]. In this study, neutron diffraction measurements have been carried out on a Pr7Ni3 single crystal in the a* - c* reciprocal plane using the HQR spectrometer of JRR-3M of in the temperature range from 1.5 to 10 K.

Figure 1(a) shows the magnetic and nuclear reflections in the a* - c* reciprocal plane at 1.5 K. The magnetic reflections appear at the positions indexed by the propagation vector k = (0.5, 0, 0). A magnetic reflection was also observed at the nuclear position (1, 0, 0) indicating a small spontaneous magnetization along the c-axis. Ferrimagnetic magnetization curve is also observed at 1.9 K [2]; a canted magnetic structure along the c-axis can be possible.

Figure 1(b) shows the intensity of the magnetic reflection at (0.5, 0, 2) and (1, 0, 0) as a function of temperature. The magnetic reflection at (0.5, 0, 2) shows a maximum at Tt and decreases; it disappears around TN. On the other hand, the ferromagnetic component at (1, 0, 0) disappears at Tt. The kx was constant up to TN.

Magnetic structure analysis using a Rietveld method for each state is now in progress.

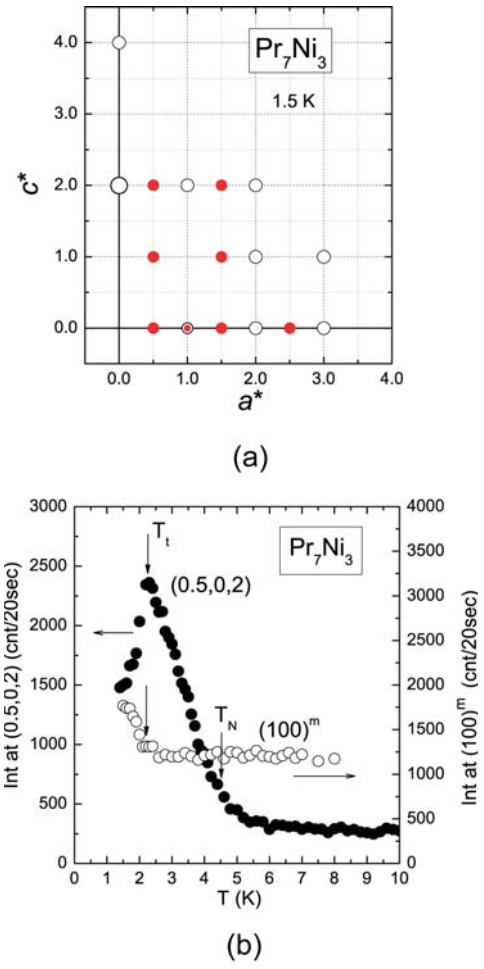


Fig. 1. Magnetic and nuclear reflections of a Pr7Ni3 single crystal in the a* - c* reciprocal plane at 1.5 K (a). The intensity of (0.5, 0, 2) magnetic reflection and the magnetic component of (1, 0, 0) as a function of temperature (b).

References

[1] G. L. Olcese, J. Less-Common Met. 33 (1973) 71.

[2] Y. Haga et al., Meeting Abstracts of the Phys. Soc. Jpn. 62, 1-3 (2007) 420.

1-2-33

Neutron Diffraction Studies on Y7Rh3Dx

T. Tsutaoka(A), A. Tanaka(A), A. Tada(B), G. Nakamoto(B), M. Kurisu(B) and Y. Andoh(C)
(A)Graduate School of Education, Hiroshima University, Hiroshima 739-8524, Japan
(B)Japan Advanced Institute of Science and Technology, Ishikawa 923-1292, Japan
(C)Faculty of Regional Sciences, Tottori University, Tottori 680-8551, Japan

The rare earth intermetallic compounds R7Rh3 based hydrides can have the hexagonal Th7Fe3 type structure with the space group P63mc in the relatively high hydrogen content up to R7Rh3H30[1]. Magnetic property of the Tb7Rh3 and Dy7Rh3 changes from antiferromagnetic to ferromagnetic and the electrical property changes from semimetallic to metallic by the hydrogenation[1]. We have carried out the neutron diffraction experiments for the parent compounds and their deutrids R7Rh3Dx (R = Dy and Ho) [2]. In this study, we have performed powder neutron diffraction measurements on the nonmagnetic deutride Y7Rh3D20 to investigate the deuterium configuration. Neutron diffraction measurements have been carried out by using the HERMES spectrometer of JRR-3M in the temperature range from 10 to 100 K with a wave length of 1.82645(6) A. The data were collected by an MFC mode.

Figure 1(a) shows the powder neutron diffraction profiles of Y7Rh3 at 10 K. All peaks in Y7Rh3 can be indexed by the Fe7Rh3 type structure and the lattice paramters and atomic positions were refined. Obtained lattice parameters are a=9.772(5) and c=6.174(4), respectively.

Figure 1(b) shows the powder neutron diffraction profile of Y7Rh3D20 at 16 K. The simulation result with the expanded lattice parameter a=10.246 and c=6.626, which is determined from X-ray diffraction analysis, and diffraction peak positions are also indicated. In the Y7Rh3D20, all peaks for Th7Fe3 type structure were shifted toward lower angle side indicating the lattice expansion; the diffraction pattern is different from Y7Rh3. Three diffraction peaks, which are indicated by the vertical arrows, can not be indexed by the Th7Fe3 type structure. Thus these diffraction peaks can be from the deuterium configuration. The analysis of the crystal structure and the deuterium configuration of Y7Rh3Dx with the Rietveld analysis are now in progress.

References

[1] R. Sato, T. Tsutaoka, S.M. Filipek, J. Alloys and Comp., 446-447 (2007) 610.
[2] T. Tsutaoka et al., Activity report on Neutron Scattering Research, Report #120 (2006).

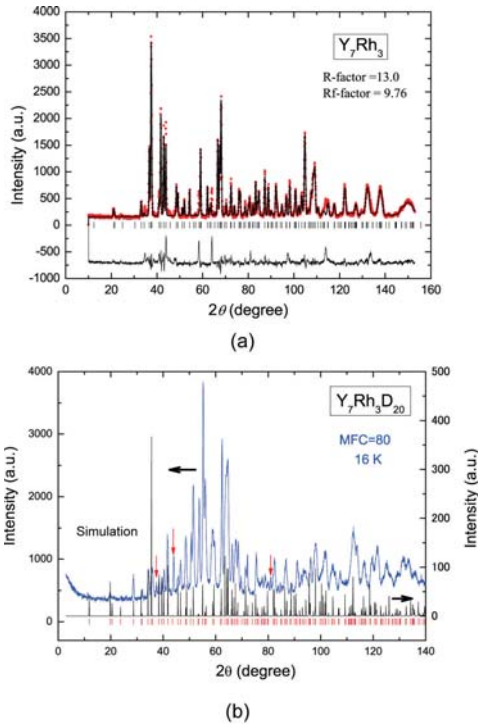


Fig. 1. Neutron diffraction profiles for Y7Rh3 (a) and Y7Rh3D20. Simulation result with the expanded lattice parameter a = 10.246, c =6.626 and diffraction peak positions are also indicated.

1-2-34

Magnetic excitation spectrum in the frustrated triangular lattice antiferromagnet CuFe1-xAlxO2

S. Mitsuda, T. Nakajima, S. Iwamoto, N. Terada1
Department of Physics, Faculty of Science, Tokyo University of Science, Tokyo 162-8601, Japan,
1 ICYS, National Institute for Materials Science, Ibaraki 305-0044, Japan

Magnetic oxide CuFe1-xAlxO2 has been extensively investigated to elucidate the spin-polarization coupling in the ferroelectric incommensurate (FEIC) phase that is magnetic field- or impurity-induced (see Fig.1 b) from the 4-sublattice ground state. Beyond multiferroic study on static coupling between spin and electric polarization, we have started inelastic neutron scattering study, aiming to investigate its dynamical spin-polarization coupling. However, since higher-temperature-partially disordered (PD) state is spatially co-existing in the FEIC phase at low temperature, quantitative inelastic neutron scattering measurement in the FEIC phase under zero magnetic field has been difficult for the Al-doped CuFeO2, although PD-contamination-free FEIC phase can be obtained by transverse magnetic field cooling [1].

Taking accounts of that coexistence of PD state might be due to local distortion around doped Al3+ ions with smaller ionic radius than that of Fe3+, we newly choose Ga-doped system, CuFe1-xGaxO2, where ionic radius of doped Ga3+ ions seems to be close to that of Fe3+. As was in previous studies on CuFe1-xAlxO2 [2-3], we performed elastic as well as inelastic neutron scattering measurements on the single crystal CuFe1-xGaxO2 sample with x = 0.35, using the triple-axis neutron spectrometer HER(C1-1) installed at JRR-3.

As shown in Fig.1 a, diffraction profile of magnetic (q, q, 1.5) reflection in the FEIC phase is resolution-limited single peak as is in the OPD phase, clearly suggesting that the FEIC phase in Ga-doped system, CuFe1-xGaxO2, is PD-contamination-free. Actually, the discontinuous phase transition between PD state and FEIC state is quite sharp. Adapting magnetic phase transition temperatures obtained from present experiment to the magnetic phase diagram of CuFe1-xAlxO2, Ga-doping with x=0.035 effectively corresponds to Al-doping with x=0.019 as is shown in Fig.1 b. Since, in preliminary inelastic measurement on the Ga-doped system, relatively clear magnetic excitation spectrum than that in previous measurement [3] has been observed, further systematic inelastic study using Ga-doped system is desired.

References

[1] T. Nakajima et al.: JPSJ 76 (2007) 043709,
[2] N. Terada et al.:JPSJ 74 (2005) 2604,
[3] N. Terada et al.: JPCM 19(2007) 145241.

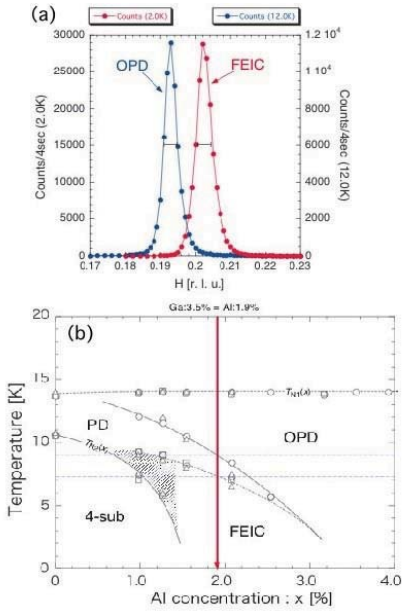


Fig. 1. (a) magnetic diffraction profiles for PD and FEIC state,(b) x-T magnetic phase diagram of CuFe1-xAlxO2[2]

1-2-35

Magnetic Structure of Noncentrosymmetric heavy-Fermion $Ce_4Ni_3Pb_4$

T. Onimaru[1], K. Shigetoh[1], A. Ishida[1], and T. Takabatake[1,2]
[1]*AdSM, Hiroshima Univ.*, [2] *IAMR, Hiroshima Univ.*

Cerium-based ternary intermetallic compound $Ce_4Ni_3Pb_4$ crystallizes in the trigonal $La_4Ni_3Pb_4$-type structure (space group $R3$) without inversion symmetry.[1] The lattice parameters are a=9.931 Å and c=9.464 Å. In the unit cell, the Ce atoms contain 9*b* and 3*a* sites, the Ni atoms 9*b*, and the Pb atoms 9*b* and 3*a* sites, respectively. Magnetic property of polycrystalline $Ce_4Ni_3Pb_4$ has already been reported by Shigetoh *et al.*[2] Both the temperature dependence of the specific heat and electric resistivity show anomalies at T_M=4 K and T_N=3 K. M/B shows no anomaly at T_M, however, it exhibits a considerable increase below T_N in magnetic fields of B<1 T. This ferromagnetic-like behavior probably results from the Dzyaloshinsky-Moriya interaction due to the lack of the inversion symmetry. In much higher magnetic fields than 1 T, a characteristic peak due to an antiferromagnetic transition appears.

To determine a magnetic structure of $Ce_4Ni_3Pb_4$, We have performed neutron diffraction experiments on a powder sample and a single-crystalline one. The powder neutron diffraction experiments were performed with the ISSP triple-axis diffractometer HQR(T1-1) . The sample was mounted at a coldhead of an 1K refrigerator and cooled down to 0.74 K. Fig. **??** shows results of the powder neutron diffraction experiments at T=0.74 K and 7.0 K . Difference between the diffraction patterns at T=0.74 K and 7.0 K is appearance of superlattice reflection labeled "Mag." in the figure at around the scattering angle of 2θ=18.1 deg which should be corresponding to $|\boldsymbol{Q}|$=0.80 Å^{-1} . In the temperature dependence of the intensity, the intensity decreases with increasing temperatures and reaches to the background intensity at around 3 K corresponding to T_N. Above 3 K, no difference between the patterns at 0.74 K and 7 K was observed. Furthermore, in order to determine a propagation vector of the magnetic structure, we performed the neutron diffraction measurements on the single-crysalline sample using the ISSP triple-axis spectrometer GPTAS(4G). The sample was mounted at a coldhead of an Orange cryostat and cooled down to 1.4 K. Searches for the position of the superlattice reflection were performed on the scattering plane of the ($H0L$), (HHL) and ($0KL$). Below 3 K, it appears at $\boldsymbol{Q}$=(0, 1, 1/2) and its equivalents, suggesting that an antiferromagnetic transition should occur at around T_N=3 K. The determination of the magnetic structure is now in progress.

References

[1] L. D. Gulay *et al.*: J. Alloys Compd. **392** (2005) 165.
[2] K. Shigetoh *et al.*: J. Phys. Soc. Jpn. **75** (2006) 033701.

1-2-36

Crystal and magnetic structures of 12L-perovskites Ba4LnRu3O12 (Ln = Pr and Tb)

Shimoda Y., Doi Y., and Hinatsu Y.
Division of Chemistry, Graduate School of Science, Hokkaido University

Crystal structure and magnetic properties of new perovskites Ba4LnRu3O12 (Ln = Pr and Tb) were investigated. The schematic crystal structure is illustrated in Fig. 1. In this structure, two kinds of the B site ions, Ru and M, occupy the face-sharing octahedral sites (Ru3O12 trimer) and the corner-sharing octahedral ones (LnO6 octahedron), respectively. From the magnetic susceptibility and specific heat measurements, it is found that both compounds show magnetic anomalies at low temperatures.

In order to determine their crystal and magnetic structures, the neutron diffraction measurements were performed using the high efficiency and resolution powder diffractometer, HERMES, of Institute for Materials Research, Tohoku University, installed at the JRR-3M Reactor in JAEA (Tokai). The wavelength of a neutron incident is 1.82035 . The data were analyzed by the Rietveld technique.

As results of the Rietveld analyses of the neutron diffraction data at room temperature, the crystal structures of Ba4LnRu3O12 (Ln = Pr and Tb) were determined. Both compounds have a perovskite-related structure which consists of the 12-layer (12L) of the BaO3 sheets. The Ba4TbRu3O12 has a hexagonal unit cell with space group R-3/m; the cell parameters are a = 5.8314 and c = 29.0212 . On the other hand, the crystal structure of the Ba4PrRu3O12 is monoclinically (space group C2/m) distorted with a = 10.157 , b = 5.869 , c = 29.315 , and beta = 90.910 degree.

The neutron diffraction measurements at low temperatures were performed for Ba4TbRu3O12. In the diffraction profile at 2.5 K, some additional reflection peaks were found at lower angles, which were not observed at room temperature. These peaks can be indexed using a propagation vector k = (0, 0, 3/2). The magnetic structure was by the Rietveld analysis of the data. In this magnetic structure, the magnetic moments of Ru ions in the Ru3O12 trimer order antiferromagnetically (up-down-up). The ferrimagnetic moments remaining in the Ru3O12 trimers and magnetic moments of Tb ions order antiferromagnetically along the c-axis.

Activity Report on Neutron Scattering Research: Experimental Reports **15** (2008)
Report Number: 556

1-2-37

Magnetic excitations in MCr_2O_4 (M=Fe, Ni)

K. Tomiyasu[1], H. Hiraka[2], K. Ohoyama[2], and K. Yamada[1]
WPI-AIMR Tohoku Univ.[1] and IMR Tohoku Univ.[2]

The geometric frustration is expanded to even the systems with magnetic moments on a non-frustrated sub-lattice in addition to a frustrated one. In the spinel chromites, MCr_2O_4 (M=Mn, Fe, Co, Ni, Cu, Zn, Mg, Cd, Hg), the M ions and the Cr^{3+} (S=3/2) ions occupy the non-frustrated A sites (diamond) and the frustrated B sites (corner sharing tetrahedra), respectively. The chromites with nonmagnetic ions M=Zn, Mg, Cd, Hg at A sites are well known as the highly frustrated systems, but the materials with magnetic and non-Jahn-Teller ions M=Mn and Co exhibit the simultaneous formation of long-range ferrimagnetic order and short-range spiral order, meaning the partial frustration.

Meanwhile, the other ions M=Fe, Ni, Cu lead to only the long-range magnetic order because of the large Jahn-Teller distortion (3-10%), which should eliminate the geometric frustration. However, $ZnCr_2O_4$ and $MgCr_2O_4$ exhibit the anomalous spin excitations without dispersion at 4.5 meV around Q=1.5 $Å^{-1}$ by powder neutron inelastic scattering even in the tetragonal and antiferromagnetic ordered phase. Therefore, we also suspected that such excitations are hidden in the $FeCr_2O_4$, $NiCr_2O_4$ and $CuCr_2O_4$. In the present experiments, we performed the elastic and inelastic scattering experiments on the powder specimens of $FeCr_2O_4$ and $NiCr_2O_4$ on HERMES and AKANE.

Figures 1(a) and 1(b) show the data of $S(Q)$ on $FeCr_2O_4$ and $NiCr_2O_4$ at 12 K, respectively. The appreciable signal of magnetic diffuse scattering is observed around Q=1.5 $Å^{-1}$ in both of the materials. Figures 1(c) and 1(d) show the data of $S(Q,E)$ on the two materials, respectively. It is revealed that the diffuse scattering, measured in the diffraction experiments, comes from the component of inelastic scattering around 6 and 5.5 meV, respectively. The excitations are almost non-dispersive, and the energy is roughly comparable to that of $Zn/MgCr_2O_4$, suggesting that the magnetic modes in the different systems are the same in origin. We have clarified the mode in $MgCr_2O_4$ to be the antiferromagnetic hexamer, which is the same as in the paramagnetic phase, in another experiments on a single-crystal specimen in the last year and is emblematic of the geometric frustration. Thus, it is becoming plausible that even the Jahn-Teller materials also exhibit the geometric frustration as the inelastic component with a finite gap energy.

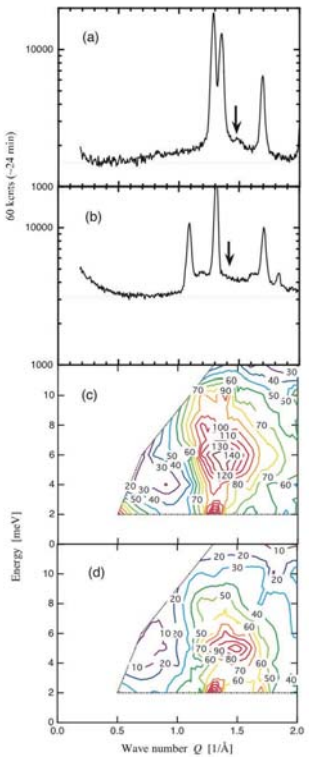


Fig. 1. Present neutron scattering data on powder speciments of $FeCr_2O_4$ and $NiCr_2O_4$.

1-2-38

Spin Waves in MnP

S. Yano(1), Y. Kousaka(1), M. Nishi(2), M. Matsuura(2), K. Hirota(2) and J. Akimitsu(1)
(1)Department of Physics and Mathematics, Aoyama-Gakuin Univ., 5-10-1 Fuchinobe, Sagamihara, (2) Institute for Solid State Physics, The Univ. of Tokyo 106-1 Shirakata, Tokai 319-1106

Manganese phosphide MnP is a ferromagnetic intermetallic compound below TC = 291K, and it transforms into a proper screw spiral state at T* = 47K.

The crystal structure is a slightly distorted NiAs structure with the lattice parameters of a = 5.916 Å, b = 5.260 Å, c = 3.173 Å at room temperature. In the ferromagnetic state, the easy-axis of the magnetization is the c-axis. In the spiral state, the spin rotates in the b-c plane with a propagation vector 0.117a* along the a-axis.

The ferromagnetic spin-waves along the three principal axes had been measured by Todate et al[1]. They reported that the dispersion relation along the a-axis exhibits anomalous wave vector and temperature dependences, and also the quadratic q dependence was observed along both the b and c-axis. However, the measurements were taken only in ferromagnetic state, so that the information about the spiral state is still missing.

In order to elucidate the mechanism of the spiral state, the information of spin wave in the whole Brillouin zone is crucially important. We focus our attention on the spin wave dispersion of the spiral state in MnP, in order to investigate the magnetic mechanism of the spiral state.

We performed the neutron inelastic scattering experiments at triple-axis spectrometer PONTA (5G), JRR-3M reactor in JAERI (Tokai).

The single crystal of MnP, whose size is length 40mm × diameter 9mm was grown by the Bridgman method.

The measurements were taken at 18 K, as shown Fig1 and Fig2, the spin wave dispersions have been mearsured along the a- and b-axis. From these experimental results, however, it is difficult for to obtain the precise exchange parameters of magnetic interaction. Additional measurements are needed to determine the magnetic exchange parameters.

Further measurements of spin waves at large-q and ω region are now in progress.

References

[1] Y Todate et al.: Jou Phys Soc Jpn. 56 36 (1987).

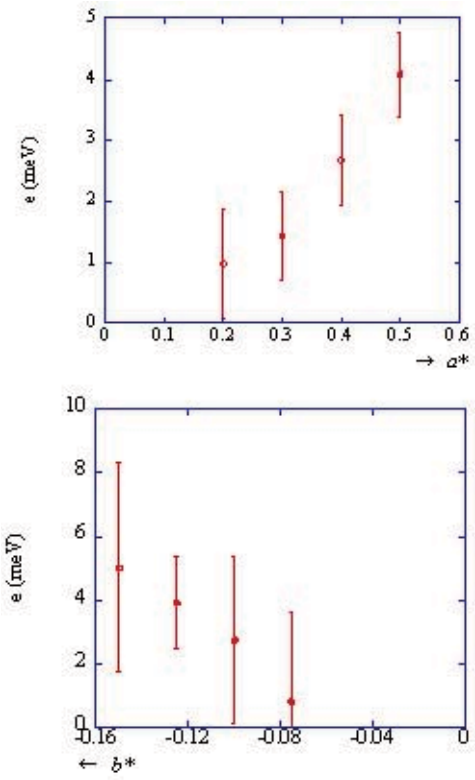


Fig. 1. Spin wave relations along the a- and b-axis

1-2-39

Magnetic structures and transitions of HoRh2Si2

T. Shigeoka(A), H. Shibasaki(A), T. Fujiwara(A), M. Nishi(B)
(A) Grad. Sch. of Sci. Eng. Yamaguchi Univ, (B) ISSP Univ. of Tokyo

Neutron diffraction measurements by Slaski et al. have revealed that the ternary compound HoRh2Si2, having the tetragonal ThCr2Si2-type crystal structure (space group: I4/mmm), orders antiferromagnetically below TN=27 K [1]. The antiferromagnetic structure reported is characterized by the wave vector k= (0, 0, 1), having Ho moments tilted by 28+-3 degree from the c-axis. Recent magnetic study shows that HoRh2Si2 has three transitions: T1=12.4 K, T2=27.5 K and TN=29.5 K. The magnetic structures have been, however, unknown yet.

In order to investigate the magnetic structures for each temperature region: T<T1 ,T1<T<T2 and T2<T<TN, neutron diffraction studies have been performed on a HoRh2Si2 single crystal using the triple axis spectrometer HQR installed at JAERI, Tokai, Japan. The a-axis of the single crystal was vertically oriented to obtain the distribution of neutron intensities in the a*-c* reciprocal plane.

The single crystal has been grown by the tri-arc Czochralski method. The single phase nature has been confirmed by X-ray powder diffraction

At low temperatures below T1, an appearance of antiferromagnetic reflections associated with the propagation vector k= (0, 0, 1) has been confirmed. Both (001) and (100) reflections are observed, indicating that magnetic moments tilt from the c- and a-axis. This result is consistent with the previous report [1]. An analysis for magnetic structure for low temperature is now in progress. The temperature dependence of peak intensity for antiferromagnetic reflections (001) and (100) is shown in Fig. 1. The (001) reflection disappears above T1. The temperature dependency of intensity of (100) peak changes at T1. In intermediate temperature region T1<T<T2, only antiferromagnetic reflections associated with the AFI-type structure are observed. All magnetic reflections disappear above T2; for T2<T<TN, magnetic reflections could not detected at all. We believe that new magnetic reflections should appear for T1<T<T2 and T2<T<TN. Further neutron study should be required.

[1] M. Slaski et al., J. Magn. Magn. Mat. 39(1983)268.

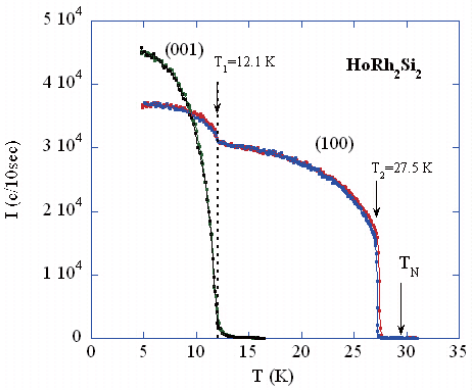


Fig. 1. Temperature dependence of antiferromagnetic (001) and (100) peak intennsity of HoRh2Si2

1-2-40

Neutron scattering study on the molecular magnet Mn6Sb2

Kazuki Iida and Taku J Sato
ISSP

Mn_6Sb_2 is a molecular magnet. Mn^{2+} ions with $s = 5/2$ are forming a approximately eqational hexagon and coupled by ferromagnetic exchange interaction between nearest neighbor ions, and the ground state is $S = 15$.

We performed inelastic neutron scattering experiments and succeeded to observe the magnetic excitations. There were two inelastic peak at 0.26 and 0.54 meV in the inelastic neutron scattering spectrum at 1.5 K. They are confirmed to be magnetic excitations from their temperature dependences and Q dependences. On the other hand, magnetic susceptility result expects that the first excitation mode from $S = 15$ to 14 exists at 0.52 meV. We measure the Q-scans at the peak energies 0, 0.26 and 0.54 meV, and at two temperatures 1.5 and 6.0 K. Fig. 1 shows the temperature subtractions of the obtained Q-scans. The Q dependence of 0.26 meV is different from that of 0.54 meV. Thus, the inner-cluster Heisenberg Hamiltonian cannot explain the peak at 0.26 meV. At the elastic position, diffuse scattering was observed shown in Fig. 1, and its shape is good agreement with the Q dependence of 0.26 meV. This fact suggests that a short-range correlation is developed at low temperature and have the excitation mode at 0.26 meV.

The peak of diffuse scattering is at $Q = 0.2$ A^{-1}, corresponding to $2\pi/0.2 \sim 30$ A in real space which is comparable with the distance between Mn_6Sb_2 clusters. We suppose that there are antiferromagnetic interaction between cluster spins ($S = 15$), resulting in the diffuse scattering. The origin of the inter-cluster interactions may be the dipole and/or exchange interactions. D, the constance of a dipole interaction is $(g\mu_B)^2/R^3 = 0.028$ μeV, and thus the dipole interaction cannot account for the peak at 0.26 meV. Hence we add the innter-cluster exchange interaction between Mn_6Sb_2 cluster with $S = 15$ as a perturbation to inner-cluster Heisenberg model. Taking account of the layered triangular structure of the Mn_6Sb_2 system, we found that antiferromagnetic short-range-spin correlations on the triangular lattice reproduce the observed diffuse scattering pattern. The Q dependence of the 0.26 meV peak is also reproduced as the elementary excitation in the short-range ordered cluster spins. Thus the inter-cluster interaction can explain not only the diffuse scattering but also the peak at 0.26 meV.

Ferromagnetic inter-cluster interactions have been know in the magnetic molecules, such as in Mn_{12} where inter-cluster interactions give rise to the long-range magnetic order. However, the antiferromagnetic interactions were quite rare; Mn_6Sb_2 is the first system in which antiferromagnetic interactions are confirmed by the neutron spectroscopy. The inter-cluster interaction is the second-dominant term which does not perturb the inner-cluster ferromagnetic coupling (i.e., $S = 15$ is the ground state even with the inter-cluster coupling). Since the cluster spin forms 2D triangular net, the intrinsic geometrical frustration may prohibits the long-range order in the Mn_6Sb_2 system.

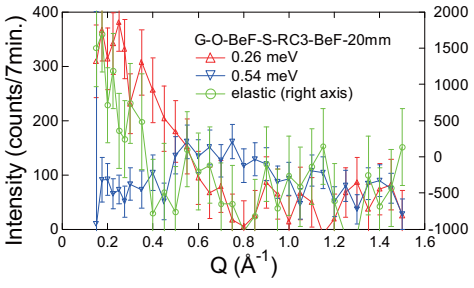


Fig. 1. The subtractions of Q dependency at 6.0 K from that at 1.5 K of 0.26, 0.54 and 0 meV

1-2-41

Neutron scattering in $Ba_2MnGe_2O_7$

T. Masuda, S. Kitaoka and M. Nishi[a]
International Graduate Schools of Arts and Sciences, Yokohama City University, 22-2 Seto, Kanazawa-ku, Yokohama, 236-0027
, [a]Neutron Scattering Laboratory, Institute for Solid State Physics, University of Tokyo, 106-1 Shirakata, Tokai, Ibaraki, 319-1106, Japan

$Ba_2MnGe_2O_7$ is an ideal 2D square-lattice antiferromagnet (AFM) with Mn^{2+} spin of $S = 5/2$. The crystal structure is tetragonal with space group $P-421m$, a = 8.4952 Å, and c = 5.5256 Å. From the magnetic susceptibility measurement the antiferromagnetic (AF) exchange interaction is estimated to be $J \sim 0.05$ meV. The spin wave calculation based on the obtained parameter predicts that the boundary energy would be about 0.8 meV; ideal energy scale for cold neutron scattering. This magnetic energy scale is also adequate for high magnetic field study. Since the saturation field is estimated to be 10 T, the exotic behavior of the spin dynamics in very high field[2] could be observed by using conventional superconducting magnet. Hence it is important to study the basic magnetic property of $Ba_2MnGe_2O_7$ in zero field as the first step of study in spin dynamics in high magnetic field. We performed magnetic diffraction in 5G PONTA and also in T11 HQR. The crystal is cylindrical shape with $\phi 7$ mm $\times$ 7mm. Since the isostructural compound $Ba_2CuGe_2O_7$ [1] is well known as spiral magnet with Dzyaloshinskii-Moriya and KSEA interaction with the propagation vector of $(1-\zeta\ 1-\zeta\ 0)$, we searched the magnetic Bragg peak in the scattering plane of $(hk0)$ in the first experiment 5G. However any magnetic signal was not detected. Then we try next experiment in $(h\ 0\ l)$ plane in T11. The experimental set up was Guide - 40′ - PG filter - sample - 40 ′ - 60′. To our surprise we found the magnetic peak at commensurate position of $(h\ 0\ n/2)$ (n is integer.) We collected 10 inequivalent magnetic peaks and we are now doing magnetic structure analysis. Next we performed inelastic neutron scattering in C11 HER. The sample size is $\phi 7$ mm $\times$ 40 mm. The experimental setp up was guide - open - Be filter - sample - 80′ - 80 ′ with e_f = 3meV. We performed a series of constant q scans in the $(h\ 0\ l)$ plane. We observed well defined magnetic excitation in $\hbar\omega \leq 0.6$ meV. The obtained dispersion relation is shown in Fig. **??**. The data is well explained by weakly coupled square lattice AFM with weak diagonal interaction with the exchange parameters of $J_1 = 0.029$ meV, $J_2 = 0.0015$ meV, and $J_{\rm inter} = 0.0007$ meV. Here J_1 is main interaction, J_2 is diagonal interaction, and $J_{\rm inter}$ is interplane interaction. As is deduced from crystal structure and bulk magnetic susceptibility measurement, $Ba_2MnGe_2O_7$ is an ideal square lattice AFM with moderate energy scale for both neutron scattering and magnetic field study.

References

[1] A. Zheludev *et al.,* Phys. Rev. B **54**, 1563 (1997).
[2] Z. E. Zhitomirsky *et al.,* Phys. Rev. Lett. **82**, 4536 (1999).

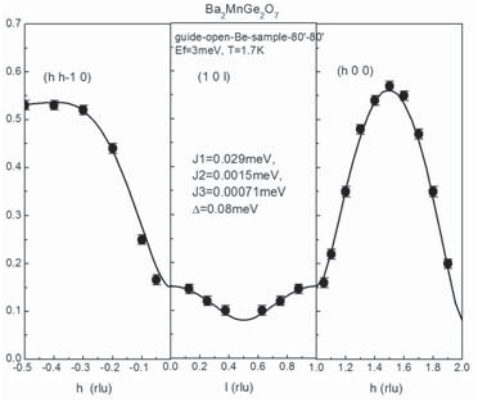


Fig. 1. The magnetic dispersion of $Ba_2MnGe_2O_7$. The solid line is the fitting by SW calculation.

1-2-42

Neutron scattering in O_2 adsorbed CPL-1

T. Masuda and K. Hirota[a]
International Graduate Schools of Arts and Sciences, Yokohama City University, 22-2 Seto, Kanazawa-ku, Yokohama, 236-0027
[a]Neutron Scattering Laboratory, Institute for Solid State Physics, University of Tokyo, 106-1 Shirakata, Tokai, Ibaraki, 319-1106, Japan

Oxygen is a rare diatomic magnetic molecule. Recently trial to utilize the oxygen as magnetic entity has been conducted in some types of nanoporous metal-organic compounds. The physically adsorbed O_2 molecule forms magnetic framework and O_2 based magnet is realized. Among them in CPL-1 ($C_{16}H_{12}Cu_2N_6O_{10}$) [1], O_2 molecules forms ladder-like structure and the spin-gap behavior is expected. Indeed the magnetic susceptibility [1] and magnetization measurements [2] suggests the spin gap of 60 $\sim$ 88 K (5.2 $\sim$ 7.6 meV).

Hence we started the thermal neutron scattering study on the O_2 based magnet since the fiscal year of 2006. We succeeded in observing the magnetic signal of the adsorbed oxygen and obtained preliminary data set of constant q scans and constant E scans (Fig.1). The difficulty of the study was that we had to collect all the data set in one allocated machine time due to the following technical reason.

The sample contains many hydrogen atoms and the background is large. Therefore, we performed scans on non-O_2 adsorbed sample for background measurement and then we repeat the same scan on O_2 adsorbed sample. It is not until we finish a set of scans that we obtain the net magnetic excitation of the adsorbed oxygen. Usually we noticed that some additional scans were necessary in the end of experiment. In the next allocated experiment we found that the obtained background was slightly different from that in the previous one. This is probably due to slightly different instrumental configuration; e.g., effective volume of the sample in the specially designed Al can, detailed optical set up, and so on. Even though small the difference is, the absolute intensity of the background is large and we have to redo the background measurements. This is why we obtained only preliminary data in the year of 2006. Figure 1 was the best data.

In the year of 2007 we know exactly what we need and what we should do. We focused on obtaining publication quality data in (i) a series of constant q scans at T = 2 K (4 days), (ii) constant energy scan at 8 meV (4 days), and (iii) a constant q scans at various temperatures (4 days). We successfully collected the data set. The detail of this study will appear in a forthcoming publication.

Now we have some technique and budget to obtain deuterated samples. In the next fiscal year we will proceed the project more efficiently.

References

[1] R. Kitagawa, *et al.*, Science **20**, 2358 (2002).
[2] T. C. Kobayashi *et al.*, Prog. Theor. Phys. Suppl. **159**, 271 (2005).

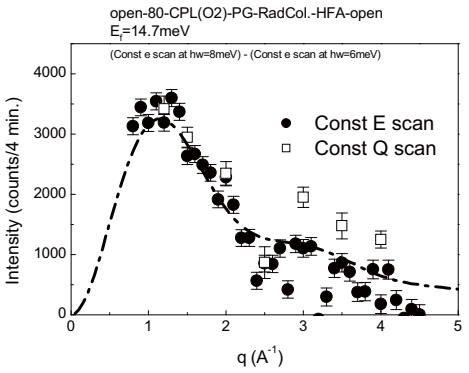


Fig. 1. Constant E scan.

1-2-43

Powder diffraction study on the ternary compound $Ce_5Ni_2Si_3$

T. J. Sato, K. Iida, H. Kitazawa[1], and Y. S. Kwon[2]
ISSP-NSL, University of Tokyo, Tokai, Ibaraki 319-1106, Japan
[1] *NIMS, Tukuba, Ibaraki 305-0047, Japan*
[2] *Department of Physics, Sung Kyun Kwan University, Suwon 440-476, Korea*

Effect of geometrical frustration in the localized spin systems has been intensively studied to date. A number of novel low-temperature phenomena have been reported there, exemplified by the spin freezing, spin liquid and spin ice, to note a few. Geometrical frustration may also bring about non-trivial magnetic ordering in the metallic system at low temperatures. In particular, competition/interplay between the strong electron correlations and geometrical frustration is an intriguing issue to study.

The ternary compound $Ce_5Ni_2Si_3$ crystallizes in the hexagonal Ce_2NiSi-type structure with the space group $P6_3/m$. The Ce Atoms are at the corners of trigonal prisms, forming a locally triangular lattice net [1]. The linear Sommerfeld coefficient γ is about 300 mJ/Ce mol K^2, which is a sign of heavy fermion formation in this compound. An antiferromagnetic order was observed at $T_N = 7.3$ K, whereas the Weiss temperature $\theta = -61.3$ K, resulting in the frustration index $f \sim 8$. Although macroscopic magnetic properties have been reported to a large extent, spin structure in the ordered phase has not been determined yet.

In this study, we performed the powder neutron diffraction experiments to determine the crystal as well as the spin structure at low temperatures in $Ce_5Ni_2Si_3$. The experiments have been performed at IMR-HERMES powder diffractometer. A powdered sample (about 4 grams) was loaded in the vanadium cell with the diameter of 7 mm, and then attached to the closed cycle refrigerator. The powder diffractgrams were recorded at 2 K, 15 K, and 300 K.

Figure 1 shows the resulting powder diffraction patterns at the low temperatures 2 K and 15 K. The overall diffraction patterns are mostly the same for two temperatures, inferring absence of the structural transition. At the lowest temperature 2 K, however, there appear several weak Bragg peaks [see arrows in Fig. 1(b)]; since this temperature is well below T_N, they are most likely the magnetic Bragg peaks associated to the macroscopically observed antiferromagnetic ordering. Magnetic as well as crystallographic structure analysis is now in progress using homemade Rietveld analysis code with the group theoretical representation analysis for the magnetic structure determination [2].

References:

[1] B. K. Lee *et al.*, Phys. Rev. B **70** (2004) 224409.
[2] I. Nakanowatari *et al.*, Phys. Rev. B **76** (2007) 184427.

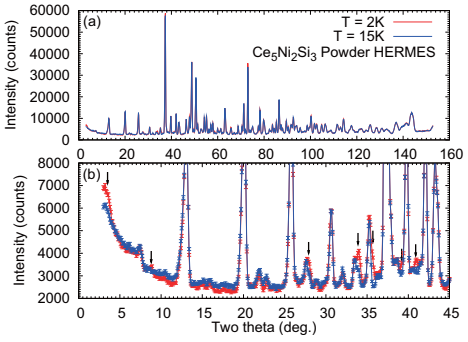


Fig. 1. Neutron powder diffraction patterns at $T = 2$ K (red) and 15 K (blue) measured at IMR-HERMES.

1-2-44

Studies of a quadrupolar ordering and magnetic excitations in YbAs

A. Oyamada, K. Kuwahara, K. Iwasa, K. Ohoyama and M. Kohgi
Kyoto Univ. , Tokyo Metropolitan Univ., Tohoku Univ.

YbAs is a possible candidate of a quadrupolar ordering system at high temperature (80 K). It was reported by ETH group that the first excitation level of crystal field splitting (Gamma8) is split below 80 K. This splitting was attributed to a quadrupolar ordering.
In order to investigate the splitting of Gamma8 state, we observed the Gamma6-Gamma8 excitation of YbAs by inelastic neutron scatterings.
We found a Gamma6-Gamma8 splitting below 80 K.
The splitting has temperature dependence which confirms the previous data reported by ETH group.
Furthermore we found that the phonon spectra does not change at 80 K.
These results suggest that a transition at 80 K is a quadrupolar one.
Further experiments on q-dependence are required.

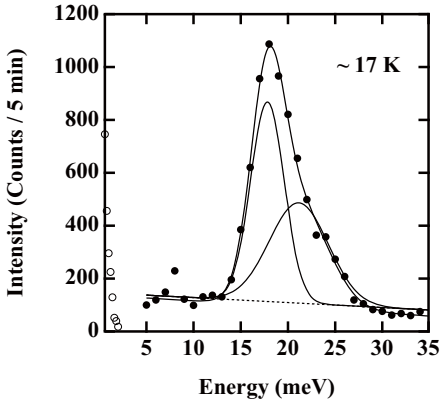


Fig. 1. Energy spectra of YbAs at 17 K.

1-2-45

Magnetic property of Ag-In-Tb 1/1 approximant and its relation to Zn-Mg-RE quasicrystals

S. Ibuka, K. Iida and T. J. Sato
ISSP-NSL Univ. Tokyo,

Quasicrystals are characterized by sharp Bragg reflections with a point symmetry which is forbidden in a periodic lattice, such as the five-fold symmetry. For magnetic quasicrystals, non-trivial spin ordering arranged on a quasiperiodic lattice is expected theoretically. But up to now the long-range order has not been observed in any magnetic quasicrystals. Even Zn-Mg-RE(RE=rare earth) quasicrystals which have well localized and large 4f magnetic moments just indicate spin-glass-like transition or no transition[1]. The absence of the long-range order evokes a new question whether quasiperiodicity is essentially incompatible with the long-range magnetic order or not.

An approximant is a periodic crystal that has a similar or identical atomic cluster in a finite length scale. Therefore, by studying magnetism of the approximants, one may separately elucidate the effect of the long-range quasiperiodicity and that of the short-range clusters. Fortunately, a magnetic approximant to the icosahedral quasicrystal has been found in Ag-In-RE systems. They seem to have well localized moments as is the case in Zn-Mg-RE, and are more suitable for neutron scattering than Cd-RE approximants in terms of the absorption. Our measurement of static magnetization of Ag-In-Tb 1/1 approximant showed that it has a spin-glass-like transition at $T = 3.7$ K, which is similar to that of Zn-Mg-Tb at 5.8 K[1]. To elucidate difference from Zn-Mg-RE quasicrystals in magnetic ordering, we have performed neutron powder diffraction study at 4G-GPTAS and T1-3-HERMES.

The sample was prepared by melting constituent elements and by annealing the resultant as-cast alloy in an appropriate manner. The data shown in Figure 1 are taken with incident energy $E_i = 13.7$ meV in the double-axis mode. They show clear nuclear Bragg reflections, which are independent of temperature; no magnetic Bragg reflection was observed at the lowest temperature. we also confirmed the absence of the magnetic Bragg reflection using T1-3-HERMES. Figure 1 also shows temperature difference of the powder diffraction patterns measured at 3.5 K and 60 K. It clearly shows two broad peaks at 0.6 and 1.9 $Å^{-1}$, indicating the development of the short-range-spin correlations at low temperatures. This contrasts to the three-peak feature of the magnetic diffuse scattering pattern in Zn-Mg-Tb. The peak at 0.6$Å^{-1}$ develops below 40 K, which is much higher than the freezing temperature of 3.7 K. Further study using a single crystalline sample is desired to elaborate the short-range-spin correlations in the approximant.

[1] T. J. Sato, Acta Cryst. A**61** (2005) 39.

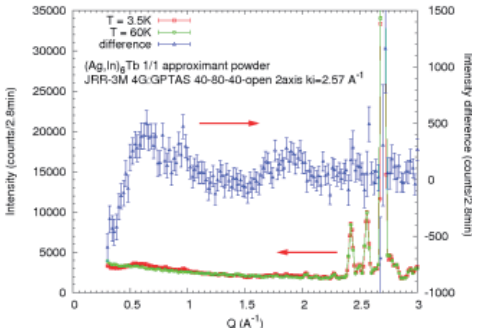


Fig. 1. Neutron powder diffraction patterns at $T =$ 3.5 K(red) and 60 K(green) obtained at 4G-GPTAS. Temperature difference [I(3.5 K) - I(60 K)] as a magnetic scattering contribution is also shown by the blue triangles.

1-2-46

Crystal Structure and Magnetic Properties of $CoZn(TeO_3)Br_2$

T. Kashi, Y. Yasui, T. Moyoshi, M. Sato, K. Kakurai[1], S. Iikubo[1], N. Igawa[1]

Department of Physics, Nagoya University, Furo-cho, Chikusa-ku, Nagoya 464-8602
[1]*Quantum Beam Science Directorate, JAEA, Tokai, Ibaraki 319-1195*

$CoZn(TeO_3)Br_2$ has been newly synthesized and its crystal and magnetic structures have been determined by powder neutron diffraction studies.[1)] T-Te-O-X systems (T=transition metals, X=Cl, Br) exhibit a variety of interesting magnetic properties. For example, $Co_2(TeO_3)Cl_2$ with the saw-tooth lattice of Co^{2+} ions exhibits two successive magnetic orderings at temperatures T_{N1} ∼73 K and T_{N2} ∼15 K.[2)] Another example $Co_2(TeO_3)Br_2$ has the linkage of $Co(2)O_4Br_2$ octahedra and $Co(1)O_2Br_2$ tetrahedra, forming a two dimensional Co spins, which order at T_N ∼29 K.[3)] Here, to add a new member to the T-Te-O-X systems, we have synthesized $CoZn(TeO_3)Br_2$. This new system has been found to be isomorphic to $Co_2(TeO_3)Br_2$ by neutron structural analysis and can be derived by the total substitution of Co(1) sites with Zn atoms. Because the Zn atoms decouple the magnetic interaction among the chains of Co(2) moments of the corner-sharing $Co(2)O_4Br_2$ octahedra, inducing the one-dimensionality of Co spins, the magnetic characteristics of the new system is quite different from that of $Co_2(TeO_3)Br_2$. It is interesting to study what magnetic characteristics are observed for this new Co^{2+} one dimensional spin system. We have carried out measurements of the magnetic susceptibility χ and specific heat C. Neutron magnetic structure analysis has also been carried out in parallel with the neutron crystal structure analysis. The powder neutron diffraction studies have been carried out at the high resolution powder diffractometer (HRPD) of JRR-3 of JAEA in Tokai. Rietveld analyses were carried out by using the computer program Rietan 2000.

A transition to an antiferromagnetic state accompanied by the weak ferromagnetic moment has been observed at the Neel temperature T_N=9.0 K. The Weiss temperature θ_W is estimated to be ∼68.5 K from the magnetic susceptibility data. The absolute ratio of the Neel and Weiss temperatures $|T_N/\theta_W|$ is ∼0.13. A broad peak at T_N exists in the C/T-T curve.

The magnetic structure below T_N has been determined by a powder neutron diffraction study, where Co spins within a chain are found to order basically in an antiferromagnetic way with the spins along the c direction (chain direction), but they are canted from the c-axis toward the b-axis by an angle of 17 (±3) °. The ordered moment is 1.78(±0.03) μ_B. To explain the ferromagnetic magnetization of the powder samples (∼0.024 μ_B), the spins should have another canting possibly toward the a-axis at an angle of 7.9 °. Then, for the understanding of the non-collinear and complicated magnetic structure of $CoZn(TeO_3)Br_2$, we should consider the competition of effects originating from the single ion anisotropy and Dzyaloshinski-Moriya interaction, for example. The existence of the T-linear component of the specific heat has been reproducibly observed. We note that the ordered moment at T=3 K is 1.78 μ_B, much smaller than the value of 3 μ_B usually expected for the high spin state Co^{2+} state. These results suggest that a significant fraction of Co spins remains in the disordered or glassy state.

References

1) T. Kashi *et al.*; J. Phys. Soc. Jpn. **77** (2008) 084707.
2) T. Kashi *et al.*; J. Phys. Soc. Jpn. **76** (2007) 084713.
3) R. Becker *et al.*; J. Solid. State. Chem. **179** (2006) 836.

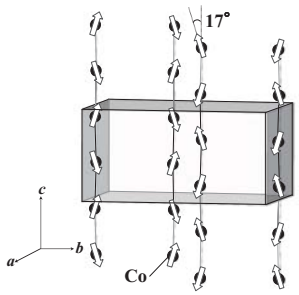


Figure 1: Magnetic structure of $CoZn(TeO_3)Br_2$.

原子炉：JRR-3　　装置：HRPD(1G)　　分野：中性子散乱（磁性）

1-2-47

Linear Relation between Electric Polarization and Magnetic Chirality in the Commensurate Phase of $R\mathrm{Mn_2O_5}$ (R =Ho, Er)

S. Wakimoto, H. Kimura[1], M. Fukunaga[1], K. Nishihata[1], M. Takeda, K. Kakurai, Y. Noda[1], and Y. Tokura[2]

Quantum Beam Science Directorate, JAEA, Tokai, Ibaraki 319-1195
[1]*Institute of Multidisciplinary Research for Advanced Materials, Tohoku University, Sendai 980-8577*
[2]*Department of Applied Physics, University of Tokyo, Tokyo 113-8656*

Multiferroic materials $R\mathrm{Mn_2O_5}$ (R: rare earth) show antiferromagnetic order and ferroelectricity concomitantly at low temperatures with strong coupling, resulting in a remarkable magnetoelectric effect [1,2]. The understanding of the coupling mechanism is one of the central issues.

To date, two distinct models have been suggested as an origin of the magnetoelectric coupling in the Mn multiferroics. One is an inverse Dzialoshinski-Moriya (DM) interaction model [3] and the other is called exchange striction model [4]. The former produces polarization from a cross term of spins $\mathbf{S}_i \times \mathbf{S}_j$, while the latter based on $\mathbf{S}_i \cdot \mathbf{S}_j$ products. Recently, it is shown that the commensurate (CM) magnetic structure of the ferroelectric phase of $R\mathrm{Mn_2O_5}$ (R=Y, Er, Ho) contains spirals of the Mn spins with magnetic unit cell of $(2a, b, 4c)$ [5], which create the polarization based on the inverse DM mode. Therefore, the role of the magnetic spiral in the magnetoelectric coupling is of great interest. Here we report results of polarized neutron scattering experiments under electric field in the CM phase of $\mathrm{HoMn_2O_5}$ and $\mathrm{ErMn_2O_5}$.

Polarized neutron scattering experiments were done at TAS-1. A combination of a pyrolytic graphite (PG) monochromator and a Heusler analyzer has been used with a spin flipper in front of the analyzer. A guide field around the sample was kept either parallel to the momentum transfer $\mathbf{Q}$ (horizontal field) or vertical by a Helmholtz coil. The incident neutron energy $E_i = 14.7$ meV and the collimator sequence of 40′-80′-80′-open were used. PG and sapphire filters were located in front of the sample to eliminate higher order and fast neutrons, respectively. In this configuration, we can analyze the polarization of the diffracted neutrons where the incident beam is unpolarized.

Disk-shaped single crystals of $R\mathrm{Mn_2O_5}$ (R =Ho, Er) with a thickness of $\sim$ 1 mm along the b-axis were placed in a closed-cycle He-gas refrigerator. The b-axis was set vertical, so that one can access to $(H, 0, L)$ type reflection. Electrodes were attached on gold masks on the b-surface. In the measurements, we cooled the sample from 65 K to 20 (23) K for R =Er (Ho) under electric fields up to 1 kV, then measure neutron scattering followed by a warming procedure without field. In warming, pyrocurrent has been measured to evaluate the electric polarization.

The polarization of the incident and diffracted neutrons, $\mathbf{P_i}$ and $\mathbf{P_f}$, are connected by the following formula in the magnetic scattering cross section from a magnetic structure with chirality:

$$\mathbf{P_f}\sigma = \{-\mathbf{P_i} + 2(\mathbf{P_i}\cdot\hat{\mathbf{M}})\cdot\hat{\mathbf{M}}\}\cdot\sigma_m + i(\mathbf{M}\times\mathbf{M}^*), \quad (1)$$

where

$$\mathbf{M} = \sum_j \mathbf{S}_{j\perp}\cos\mathbf{Q}\cdot\mathbf{r}_j + i\sum_j \mathbf{S}_{j\perp}\sin\mathbf{Q}\cdot\mathbf{r}_j. \quad (2)$$

Here, σ_m is the magnetic cross-section without chirality, $\mathbf{S}_{j\perp}$ is a component of the $j-$th spin perpendicular to $\mathbf{Q}$. The first term in Eq. (1) means that the neutron polarization makes π-precession with respect to $\mathbf{M}$. The second term expresses the chiral structure contribution indicating that the final polarization is forced to align along the chiral vector $i(\mathbf{M}\times\mathbf{M}^*)//\mathbf{Q}$. In our experimental set-up, therefore, the difference in the spin (+) and (-), $(\sigma_+ - \sigma_-) \propto P_f$, in the horizon-

原子炉：JRR-3　　装置：TAS-1(2G)　　分野：中性子散乱（磁性）

tal field mode observes the magnetic chirality directly.

Figures 1 (a) and (b) show magnetic chirality in the CM phase of $HoMn_2O5$ and $ErMn_2O5$, respectively, as a function of the electric polarization of the bulk sample along the b-axis. The data at $\sim$ 5 nC for Fig. 1 (a) and those for $\sim$ 2 nC for Fig. 1 (b) are measured after cooling under a zero field, while the others are either data measured after cooling in ± 1 kV. We note that our samples show spontaneous polarization after the zero-field-cooling. This is because of a sample-dependent peculiarity that polarized domains are imbalanced even after the zero-field-cooling process [6]. The chirality has been measured at both Q-positions near the a^*-axis, $(1.5, 0, \pm 0.25)$ for $HoMn_2O_5$ and $(2.5, 0, \pm 0.25)$ for $ErMn_2O_5$, and near the c^*-axis, $(0.5, 0, \pm 1.75)$ for $HoMn_2O_5$ and $(0.5, 0, \pm 2.25)$ for $ErMn_2O_5$. Since the neutrons see magnetic component that is perpendicular to $\mathbf{Q}$, the former corresponds to the magnetic chirality in the bc-plane while the latter in the ab-plane. For both samples, particularly for $HoMn_2O_5$, it is demonstrated that the chirality is proportional to the electric polarization even with the zero-field-cooling data. Also we have confirmed that the high-temperature ICM phase, which is paraelectric, does not show the chirality. Thus, the magnetic chirality universally connected to the electric polarization for the CM phase of RMn_2O_5 with R =Ho and Er, and the ferroelectric phase of $TbMnO_3$ [7] However, there is an important question for the RMn_2O_5 system why the large electric polarization achieves in the CM structure. To address this, detailed magnetic structure analyses for the high-temperature as well as low-temperature ICM phase are necessary.

References

1) T. Kimura *et al.*, Nature **426**, 55 (2003).
2) N. Hur *et al.*, Nature **429**, 392 (2004).
3) H. Katsura, N. Nagaosa, and A. V. Balatsky, Phys. Rev. Lett.**95**, 057205 (2004).
4) L. C. Chapon *et al.*, Phys. Rev. Lett.**96**, 097601 (2006).
5) H. Kimura *et al.*, J. Phys. Soc. Jpn.**76**, 074706 (2007).
6) M. Fukunaga *et al.*, J. Korean Phys. Soc. **51**, 768 (2007).
7) Y. Yamasaki *et al.*, Phys. Rev. Lett.**98**, 147204 (2006).

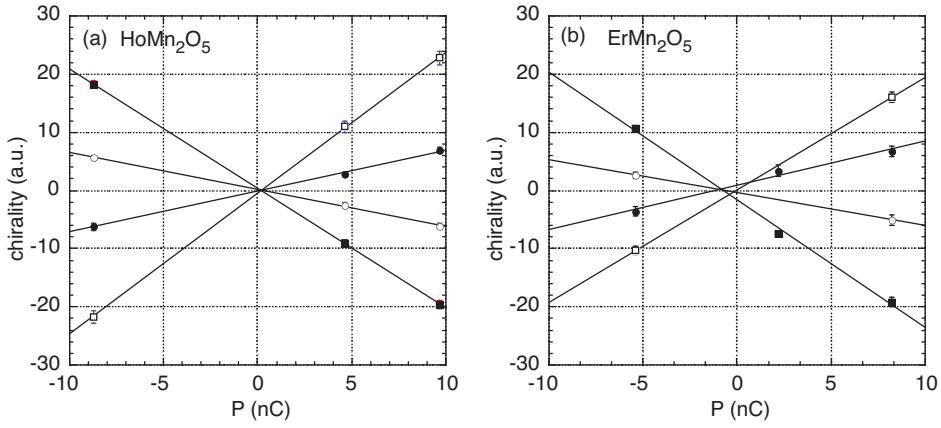


Figure 1: Chiral terms for (a) $HoMn_2O_5$ and (b) $ErMn_2O_5$ as a function of the electric polarization of bulk crystal along the b-axis. The chirality is determined by $\sigma_+ - \sigma_-$. For $HoMn_2O5$, the chirality is measured at $(1.5, 0, 0.25)$ (filled circles), $(1.5, 0, -0.25)$ (open circles), $(0.5, 0, 1.75)$ (filled squares), and $(0.5, 0, -1.75)$ (open squares). For $ErMn_2O_5$, it is measured at $(2.5, 0, 0.25)$ (open circles), $(2.5, 0, -0.25)$ (filled circles), $(0.5, 0, 2.25)$ (open squares), and $(0.5, 0, -2.25)$ (filled squares).

1-2-48

Polarization of the Spin-Wave Modes in the Kagomé Lattice Antiferromagnet $KFe_3(OH)_6(SO_4)_2$

K. Matan[1], J. S. Helton[1], D. Grohol[2], D. G. Nocera[3], S. Wakimoto[4], K. Kakurai[4], and Y. S. Lee[1]

[1]*Department of Physics, Massachusetts Institute of Technology, Cambridge, MA USA*
[2]*The Dow Chemical Company, Core R&D, Midland, MI 48674, USA*
[3]*Department of Chemistry, Massachusetts Institute of Technology, Cambridge, MA 02139, USA*
[4]*Quantum Beam Science Directorate, JAEA, Tokai, Ibaraki 319-1195*

Collective behavior in strongly correlated systems often leads to unconventional ground states. One example of such systems is geometrically frustrated spins, where the incompatibility between the topology of an underlying lattice and spin interactions prevents the system to be in a unique ground state, prompting the presence of novel spin dynamics. The kagomé lattice antiferromagnet is a highly frustrated two-dimensional lattice, being comprised of corner-sharing triangles. One of the hallmarks of this system is the "zero energy modes", which result from the highly degenerate, but connected, ground state manifold. One ideal realization of the kagomé lattice antiferromagnet is jarosite $KFe_3(OH)_6(SO_4)_2$. Due to the presence of the Dzyaloshinskii-Moriya (DM) interaction in this material, the spins order in a $q = 0$ structure with small canting forming an "umbrella" spin configuration below the Néel temperature $T_N = 65$ K[1,2]. The DM interaction also lifts the "zero energy mode" to a finite energy, making it measurable by neutron scattering. We have previously reported on the first observation of this lifted zero energy mode in jarosite, and determined all relevant spin Hamiltonian parameters[3].

Inelastic polarized neutron scattering measurements were performed on TAS-1 spectrometer at Japan Atomic Energy Agency, Tokai, Japan. This state-of-the-art instrument utilizes double-focusing Heussler crystals to monochromate and analyze the incident and scattered neutron beams. The beam polarization of more than 90% is achieved. The final neutron energy was fixed at 14.7 meV. Horizontal collimations of open−80′−sample−open−open were employed. However, due to the small sample, effective horizontal collimations of $48' - 18' -$ sample $- 25' - 240'$ were used to calculate the resolution function. Pyrolytic graphite filters were placed in the scattered beam to reduce higher-order contaminations. The energy resolution of about 1.2 meV and background of about one count per minute were achieved. A single crystal of jarosite of mass 48 mg was oriented in the (HK0) zone. The sample was cooled by a ^{4}He close-cycle displex.

The spin-wave calculations of the spin Hamiltonian show three branches of low energy spin excitations, which correspond to two out-of-plane excitations and one in-plane excitation[4]. By choosing proper orientations of a polarization vector **P**, which is defined by the direction of a guide field, and wave vector **Q**, one can distinguish between the in-plane and out-of-plane spin excitations. If **P** and **Q** are parallel, both in-plane and out-of plane magnetic excitations will give rise to scattering intensity in the spin-flip (SF) channel. On the other hand, if **P** is perpendicular to **Q**, then the magnetic scattering in the SF channel is due to the excitations that are perpendicular to both **Q** and **P**, and the magnetic scattering in the non-spin-flip (NSF) channel is due to the excitations parallel to **P**.

Fig. 1 shows constant-**Q** scans at (1,0,0), the center of the Brillouin zone (Γ−point), measured at 10 K. The observed peaks were fit with narrow Gaussian convoluted with the experimental resolution function assuming the empirical dispersion[3]. For the guide field along **Q** (HF) (Fig. 1(a)), both spin-wave excitations at 2 meV and 7 meV were observed

原子炉：JRR-3　　装置：TAS-1(2G)　　分野：中性子散乱（磁性）

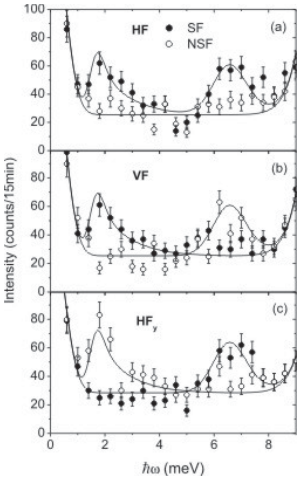


Figure 1: Inelastic polarized neutron scattering measurements of spin-wave excitations at the zone center.

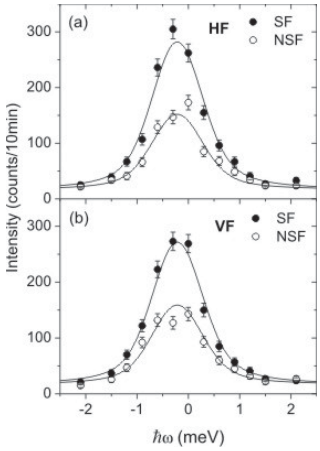


Figure 2: Quasi-elastic scattering centered at (1 0 0) measured by polarized neutrons at 67 K.

in the SF channel, while there is no magnetic scattering in the NSF channel. For the guide field perpendicular to **Q**, and perpendicular to the scattering plane (VF) (Fig. 1(b)), the peak at 2 meV was observed in the SF channel, and the peak at 7 meV was observed in the NSF channel. On the other hand, if the guide field was perpendicular to **Q**, but lay within the scattering plane (HF_y) (Fig. 1(c)), then the peak at 2 meV was observed in the NSF channel and the peak at 7 meV was observed in the SF channel. The equivalent intensities in the VF SF (VF NSF) and HF SF (HF SF) channels and the absence of intensity in the VF NSF (VF SF) channel at 2 meV (7 meV) indicate that the 2 meV (7 meV) excitation is predominantly the in-plane (out-of-plane) excitation, consistent with the spin-wave analysis.

The polarization of the spin fluctuations were also studied using polarized neutron scattering. Fig. 2 shows constant-**Q** scan at (1 0 0) through a quasi-elastic peak measured at $T = 67$ K. The observed quasi-elastic peak was fit to Lorentzian convoluted with the experimental resolution function. Backgrounds and peak widths were kept constant for all data sets. The intensities in the HF SF and VF SF channels indicate that the spin fluctuations are predominantly the in-plane fluctuations, providing the direct evidence for the presence of XY symmetry previously reported in Ref. 2.

In jarosite, the spin gaps are a result of the antisymmetric DM interaction. To the leading order, the analytic expressions show that the in-plane gap is proportional to $|D_p|$ while the two out-of-plane gaps are proportional to $\sqrt{J_1 D_z}$[3,4]. Therefore, despite the similar D_p and D_z, the out-of-plane gap is significantly larger than the in-plane gap. Above T_N only the in-plane rotational (XY) symmetry is restored. This result immediately suggests the existence of the out-of-plane gap above T_N. In fact, our polarized neutron scattering around the quasi-elastic peak above T_N exhibits the in-plane-only spin fluctuations, which imply that the out-of-plane gap remains at a finite energy. Therefore, in the critical regime, $KFe_3(OH)_6(SO_4)_2$, whose interlayer coupling is negligibly small[1], is a promising candidate for studying the 2D XY universality class in magnetic systems.

References

1) D. Grohol *et al.*, Nature Mater. 4 (2005) 323.
2) T. Inami *et al.*, Phys. Rev. B 61 (2000) 12181.
3) K. Matan *et al.*, Phys. Rev. Lett. 96 (24) (2006) 247201.
4) T. Yildirim, A. B. Harris, Phys. Rev. B 73 (21) (2006) 214446.

1-2-49

Investigation of in-plane Magnetic Structure in $NpFeGa_5$

T. Sugai[1,2], F. Mizuno[1,2], K. Kaneko[1] and N. Metoki[1,2]

[1] *Advanced Science Research Center, JAEA, Tokai, Ibaraki 319-1195*
[2] *Department of Physics, Tohoku University , Sendai 980-8578*

$NpTGa_5$(T=Fe, Co, Ni, Rh and Pt) is an isostructual family of heavy fermion superconductors $CeTGa_5$ and $PuTGa_5$. The magnetic structures of $NpTGa_5$ were studied by our recent systematic neutron scattering experiments. We found the variety of the magnetic structures and double transitions, which can be understood in terms of a localized model. For example, our neutron polarization analysis revealed that $NpFeGa_5$ shows C-type AFM with magnetic moment parallel to the $\langle 110 \rangle$ direction, while below 78K, magnetic moment rotates to c-axis at the angle 25°. Kiss *et al.* [1] explained this unusual magnetic moment direction with quadrupole order parameter $\langle O_{zx} \rangle$, which induces both in-plane($\vec{\mu} \| c$-axis) and out-of-plane($\vec{\mu} \perp c$-axis) dipole moment. Furthermore S. Kambe *et al.* [2] proposed that magnetic moment slightly rotate, i.e. $\vec{\mu} \| [110]+[1\bar{1}0]$, from the splitting of NMR spectra at Ga site, due to mixing of small $\langle O_{zx} \rangle$ and large $\langle O_{yz} \rangle$. Neutron spin polarization analysis of single domain sample of $NpFeGa_5$ with application of vertical magnenic feld has been carried out in order to reveal this additional in-plane component.

Neutron scattering experiments have been carried out using triple-axis spectrometer TAS-1 installed at the research reactor JRR-3 at the Japan Atomic Energy Agency. The sample dimension was 1.75×1.75×1.25 mm^3.

We studied (1/2 1/2 0) AFM Bragg scattering from single domain sample with the [*hhl*] scattering plane(stabilized via vertical magnetic field along $[1\bar{1}0]$). With this configration, non spin flip(NSF) cross section detects vertical component perpendiculer to the scattering plane, while spin flip(SF) component is proportional to the squared moment along the c-axis.

Fig.2 shows the NSF cross section signal of the (1/2 1/2 0) at 1.5 K. We observed a very weak scattering intensity above the background level. After correcting depolarization obtained by flipping ratio, we concluded that a possible magnetic moment of about <0.1 μ_B. This small moment would be consistent with small splitting in NMR study by S. Kambe *et al.*. In order to get the final conclusion about the existence of the small in-plane component, we need to improve signal statics.

[Figure]

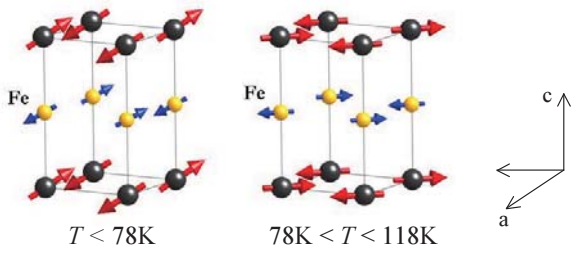


Figure 1: Magnetic structure of $NpFeGa_5$.

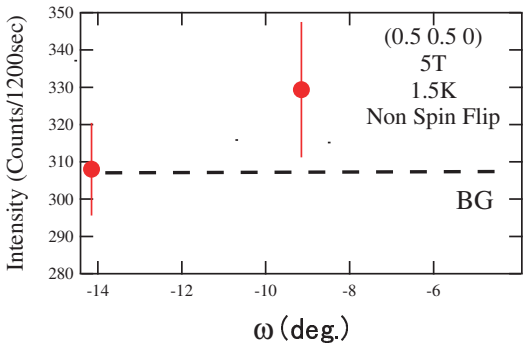


Figure 2: Non Spin flip(NFS) scattering at (1/2 1/2 0) . The broken line indicates back ground.

References

1) A. Kiss *et al.* :"J. Phys. Soc. Jpn.", 75, 034709(2006).
2) S. Kambe *et al.* :"Phys. Rev. B", 76, 144433(2007).

原子炉：JRR-3　　装置：TAS-1(2G)　　分野：中性子散乱（磁性）

1-2-50

Unusual field-induced Antiferromagnetic Order in $NpIn_3$

F. Mizuno[1,2], T. Sugai[1,2], N. Metoki[1,2] and K. Kaneko[2]

[1] *Advanced Science Research Center, JAEA, Tokai, Ibaraki 319-1195*
[2] *Department of Physics, Tohoku University , Sendai 980-8578*

Very recently we have systematically revealed the magnetic structure of NpTGa$_5$ which is an iso-structural family of havy fermion superconductors CeTGa$_5$ and PuTGa$_5$. We reported possible quadrupole order in many body itinerant 5f electron system. NpTGa$_5$ has layered structure with sequential stacking of NpGa$_3$ and TGa$_2$ layers. Thus our study recalls renewed interests in NpX_3 mother crystal with AuCu$_3$ structure. The triplet state under cubic symmetry provides a more suitable situation for the orbital degree-of-freedom as a possible origin of the multiple phase diagram, successive transition and meta-magnetic behavior. We have studied the magnetic structure and the magnetic phase diagram of $NpIn_3$ systematically under horizontal and vertical magnetic field with use of neutron spin polarization technique.

For H=0 we observed ferromagnetic (FM) scattering at (001) for $T_N < T < T_C$, and antiferromagnetic (AFM) modulation with q = (3/8 3/8 3/8) at the ground state for $T < T_N$, which is consistent with a previous study [1]. We observed a sharp transition between FM and AFM structure. No coexistence of both FM and AFM has been observed.

We observed that the AFM peak disappeared with application of magnetic field H=5 T along [110]. We found (1/2 1/2 0) AFM modulation accompanied by the meta-magnetic phase. Surprisingly, we found that the AFM modulation amplitude is parallel to the field direction. Namely Np subllatice has two different size of Np magnetic moment which is parallel to the external field. This is revealed by the horizontal field experiments with H//[110] applied on the [$hk0$] scattering plane. The AFM reflection at Q=(1/2 -1/2 0) for $Q \perp H$, while no peak observed at (1/2 1/2 0) with Q // H, indicative of the AFM moment parallel to the field direction as shown in Figures. The direction of the AFM modulation was also confirmed by the neutron spin polarization analysis.

AFM modulation in spin flip phase is perpendicular to the external field as a result of the energy gain from induced moment by external field, where there is a slight energy loss of exchange energy due to small tilting of the AFM moment. A similar structure has been reported in the field induced phase of $PrOs_4Sb_{12}$, where the quadrupole order appears for high field [3]. Therefore this unusual structure would be a signature of field induced quadrupole order in $NpIn_3$.

[Figure]

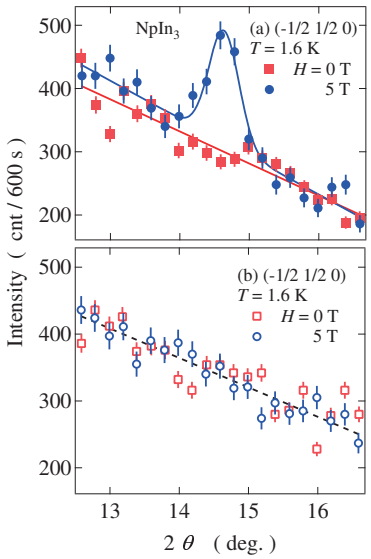


Figure 1: Field induced antiferromagnetic reflection of $NpIn_3$ for (a) $Q \perp H$ and (b) $Q//H$, respectively.

References

1) E. Colineau : Ph.D. Thesis.
2) D. Aoki *etal.* :"J. Phys. Soc. Jpn", 75, 084710(2006).
3) K. Kaneko *etal.* :"Phys. Rev. B", 75, 094408(2007).

原子炉：JRR-3　　装置：TAS-1(2G)　　分野：中性子散乱（磁性）

1-2-51

Magnetic Structure of $LiCu_2O_2$

Y. Yasui, K. Sato, T. Moyoshi, M. Sato, K. Kakurai[1]

Department of Physics, Nagoya University, Furo-cho, Chikusa-ku, Nagoya 464-8602
[1]*Quantum Beam Science Directorate, JAEA, Tokai, Ibaraki 319-1195*

Materials with magnetic and ferroelectric coexisting orders are called multiferroics and attract much attention. While almost all multiferroic systems ever reported have the magnetic moments with spin $S \geq 1$ and/or have more than two magnetic sites, the authors' group have found that $LiVCuO_4$ is a multiferroic with Cu^{2+} spins S=1/2 in the 3d, x^2-y^2 orbital and only one crystallographically distinct Cu site.[1,2] To understand the multiferroic nature, studies of the spin 1/2 multiferroic systems are very useful, because there are not any complications due to the multi-orbital and multi-site effects. $LiCu_2O_2$ with similar structural characteristics to those of $LiVCuO_4$, but with two crystallographically distinct Cu sites has also been reported to be multiferroic.[3] However, we think that certain problems remain on the reported multiferroic behavior[3] and magnetic structure[4] of $LiCu_2O_2$, because an inconsistency exists in the relationship between the magnetic structure and observed ferroelectiric polarization. Moreover, the *ab*-helical magnetic structure reported in ref. 4 cannot explain the ^{7}Li-NMR spectra obtained by our group. (Due to the existence of the double CuO_2 ribbon chains shown in the inset of Fig. 1 makes it difficult to determine the magnetic structure of $LiCu_2O_2$.)

Neutron scattering studies have been carried out on single crystals using the triple axis spectrometer TAS-1 installed at JRR-3 of JAEA in Tokai. To avoid the large neutron absorption of Li, we used ^{7}Li isotope in the growth of crystals. The neutron scattering intensities were measured at $\boldsymbol{Q}$=(h, k, 0) and (h, k, 2h) in the reciprocal space at 3.2 K ($< T_N \sim$22.5 K) and 50 K ($> T_N$). At 3.2 K, we observed magnetic superlattice reflections at $\boldsymbol{Q}$=(h, $k \pm \delta$, 0) and (h, $k \pm \delta$, 2h) (h=half-integer and k=integer) with $\delta \sim$0.172. Figure 1 shows the temperature dependence of the integrated intensity of 1/2 δ 1 magnetic reflection. From the figure, the magnetic ordering is found to grow with decreasing T below T_N. The Cu^{2+} spins have incommensurate magnetic structure with modulation vector of $\delta \boldsymbol{b}^*$ (or the pitch angle along the CuO_2 ribbon chains is $\sim$62°). First, we analyzed the obtained magnetic scattering intensities at 3.2 K by using the initial spin directions and angles of four chains in the unit cell as the parameters, assuming that the magnetic structure is sinusoidal or helical type. We found that the observed scattering intensities cannot be reproduced by the magnetic structures described by varying the above parameters. (Note that the *ab*-plane helical structure reported in ref. 4 can be obtained by varying the above parameters.) At 3.2 K the magnetic structure is, we think, very complicated and spins have nonzero components in all of the three directions. Detailed magnetic structure analysis is being carried out by adopting other possible models.

References

1) Y. Naito *et al.*; J. Phys. Soc. Jpn. **76** (2007) 023708.
2) Y. Yasui *et al.*; J. Phys. Soc. Jpn. **77** (2008) 023712.
3) S. Park *et al.*; Phys. Rev. Lett. **98** (2007) 057601.
4) T. Masuda *et al.*; Phys. Rev. Lett. **92** (2004) 177201.

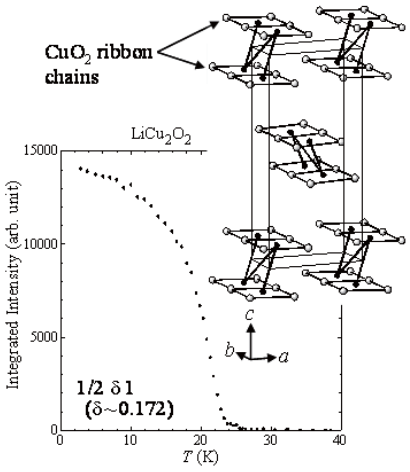


Figure 1: T-dependence of scattering intensity for 1/2 δ 1 ($\delta \sim$0.172) reflection. Inset shows the schematic structure of $LiCu_2O_2$.

原子炉：JRR-3　　装置：TAS-1(2G)　　分野：中性子散乱（磁性）

1-2-52

Investigation of the Giant Magnetic Moments in Nitrogen-Martensites thin Films Using the Polarized Neutron Diffraction Technique

M. Takeda[1,2,3], K. Kakurai[1], K. Sunaga[4],M. Tsunoda[4], M. Takahashi[4]

[1] *Quantum Beam Science Directorate, Japan Atomic Energy Agency, Tokai-mura, Naka-gun, Ibaraki, 319-1195, Japan*
[2] *J-PARC Center, Tokai-mura, Naka-gun, Ibaraki, 319-1195, Japan*
[3] *New Industry Creation Hatchery Center, Tohoku Univ., Aramaki Aoba, Aoba-ku, Sendai-shi, Miyagi, 980-8579, Japan*
[4] *Graduate School of Engineering, Tohoku Univ., Aramaki Aoba, Aoba-ku, Sendai-shi, Miyagi, 980-8579, Japan*

Since the discovery of a giant magnetic moment of 2.9 T in $Fe_{16}N_2$ thin films by Kim *et al.*, a lot of research have been done to try to show clear evidence of the giant magnetic moments. It has been, however, enable to conclude because of inhomogeneity of the sample. The $Fe_{16}N_2$ films consists of α' and α" phases of $Fe_{16}N_2$, but it was difficult to control the ratio. Takahashi *et al.* have successfully synthesized the $(\alpha' + \alpha")-Fe_{16}N_2$ films, and have performed magnetization measurements, Mössbauer spectroscopy and so on[2]. They did not find out the giant magnetic moment in their films. We performed the polarized neutron diffraction measurements of the $Fe_{16}N_2$ films to give the final conclusion.

The samples were prepared by the reactivity sputtering with N_2 gas on MgO substrates. 15 pieces of the films were glued on a plate of the single crystal of Si so as to align the [001] and $[1\bar{1}0]$ axes of $Fe_{16}N_2$ of the films (Fig. 1). The diameter of each films is 5 mm ϕ, and the thickness of the films 300 nm. The films have a buffer layer of Fe with the thickness of 5 nm, and a cap layer of Cu with 50 nm.

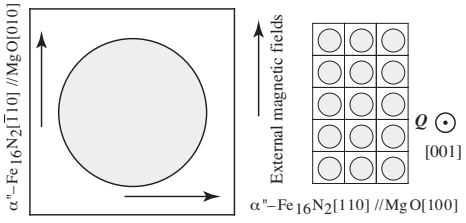


Figure 1: Epitaxial relations (left) and schematic representation of an assemble of 15 films (right).

An external magnetic field of 10 kOe was applied to the sample to saturate the Fe magnetization in the films. The neutron energy was fixed at 14.7 and 80 meV(λ = 0.237 and 0.098 nm) by a Cu_2MnAl polarizing monochromator. Neutron spin was set to parallel or antilarallel to the magnetization of the sample using a spin-flipper set before the sample. Each intensity with the spin-flipper off (I_+) and with on (I_-) was independently counted, and then a flipping ratio (I_+/I_-) was obtained (Fig. 2).

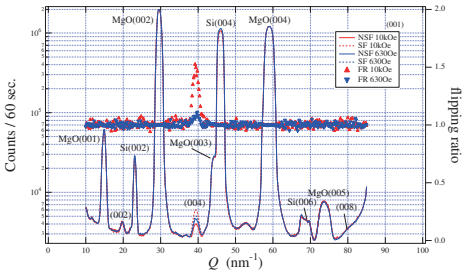


Figure 2: Polarized neutron diffraction intensities and flipping ratios. Scans were done along the [00l].

We determined the magnetic moments of Fe on three different sites in the unit cell as 2.19 (Fe I), 2.08 (Fe II), and 2.55 μ_B (Fe III) from analysis of the data in Fig. 2 and another data with scans along [hh0]. There is no evidence of the giant magnetic moments of the $Fe_{16}N_2$ films.

References

1) T. K. Kim and M. Takahashi, Appl. Phys.Lett., **20**, 492 (1972).
2) H. Takahashi, H. Shoji, and M. Takahashi, J. Magn. Magn. Mater., **174**, 57 (1997).

原子炉：JRR-3　　装置：TAS-1(2G)　　分野：中性子散乱（磁性）

1-2-53

Partial Disordered Phase of $RbCoBr_3$

Y. Nishiwaki, A. Oosawa[1], K. Kakurai[2] and T. Kato[3]

Department of Physics, Tokyo Women's Medical University, Shinjuku-ku, Tokyo 162-8666
[1]*Department of Physics, Sophia University, Chiyoda-ku, Tokyo 102-8554*
[2]*Quantum Beam Science Directorate, Japan Atomic Energy Agency, Tokai, Ibaraki 319-1195*
[3]*Faculty of Education, Chiba University, Inage-ku, Chiba 273-8522*

$RbCoBr_3$ realizes the distorted triangular-lattice antiferromagnet with the Ising spin system.[1)]. The crystal structure is distorted through structural phase transitions from the $CsNiCl_3$ structure. The lattice distortion is characterized by -$CoBr_3$- chain shift and the geometrical frustration is released partially. The antiferromagnetic phase transition of $RbCoBr_3$ was identified at T_N = 37.2 K, which agrees with the ferroelectric transition temperature $T_C = T_N$. A previous neutron diffraction study reported that a partial disordered (PD) phase was absent in $RbCoBr_3$.[1)] The PD phase was found to appear on $CsCoCl_3$ and $CsCoBr_3$, which have a nondistorted triangular lattice, at temperatures between the ground-state ferrimagnetic phase and the paramagnetic phase.[2,3)] In the PD phase, one of the three sublattices is disordered and the other sublattices are aligned antiferromagnetically. However, recent theoretical and experimental studies indicate that $RbCoBr_3$ should undergoes successive magnetic and structural phase transitions. Therefore, we reexamine the existence of the PD phase.

The temperature dependence of the $(\frac{1}{3}\ \frac{1}{3}\ 1)$, $(\frac{2}{3}\ \frac{2}{3}\ 1)$, and (1 1 1) neutron diffraction peak heights is shown in Fig. 1. The $(\frac{2}{3}\ \frac{2}{3}\ 1)$ peak is observed below 37.2 K but the (1 1 1) peak is observed only below 30.5 K. When the spin structure is PD, the (1 1 1) peak disappears and the $(\frac{2}{3}\ \frac{2}{3}\ 1)$ peak appears. Therefore, the intermediate PD phase is exhibited between T_{N1} = 37.2 K and T_{N2} = 30.5 K.

Compared with the results of $CsCoCl_3$ and $CsCoBr_3$,[2,3)], the temperature dependence of the (1 1 1) peak of $RbCoBr_3$ exhibits an almost linear increase below T_{N2} with decreasing temperature. The results can be explained by considering a lattice distortion affecting the spin system. We considered the spin-lattice model and performed Monte Carlo simulations.[4)] In the model, the up-down shifts of -$CoBr_3$- chains are represented using the pseudospin variable. The pseudospin system has frustration in the same way as the real-spin system. The exchange interactions between real spins depend on the pseudospin of the lattice variables. Details of the model Hamiltonian and analysis are reported elsewhere.[4)] As a result, the linear temperature dependence of the (1 1 1) peak is well reproduced by the spin-lattice model, as shown in Fig. 1.

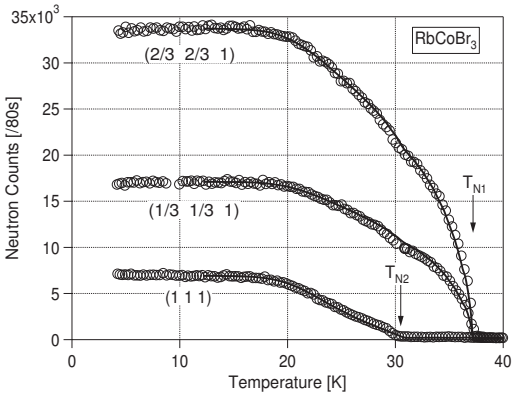


Figure 1: Temperature dependence of (1 1 1), $(\frac{1}{3}\ \frac{1}{3}\ 1)$, and $(\frac{2}{3}\ \frac{2}{3}\ 1)$ neutron diffraction peak heights. The numerical results of the model simulations are shown by lines.

References

1) Y. Nishiwaki, T. Kato, Y. Oohara, and K. Iio: J. Phys. Soc. Jpn. **73** (2004) 2841.
2) M. Mekata: J. Phys. Soc. Jpn. **42** (1977) 76.
3) W. B. Yelon, D. E. Cox, and M. Eibschütz: Phys. Rev. B **12** (1975) 5007.
4) T. Nakamura and Y. Nishiwaki: cond-mat/0803.1710.

原子炉：JRR-3　　装置：TAS-2(T2-4)　　分野：中性子散乱（磁性）

1-2-54

Neutron Diffraction Study on Spinel $GeCo_2O_4$ under Magnetic Field

M. Matsuda, T. Hoshi[1,2], H. Aruga Katori[2], M. Kosaka[1] and H. Takagi[2]

Quantum Beam Science Directorate, JAEA, Tokai, Ibaraki 319-1195
[1]*Graduate School of Science and Engineering, Saitama University, Saitama, Saitama 338-8570*
[2]*RIKEN, Wako, Saitama, 351-0198*

The spinel $GeCo_2O_4$ has the pyrochlore lattice of Co^{2+} ions, in which the kagomé and triangular planes stack alternatively along the (111) direction. It shows an antiferromagnetic ordering with a characteristic wave vector of Q=(1/2, 1/2, 1/2) below $T_N \sim 21$ K [1)] accompanied by a structural phase transition from cubic to tetragonal symmetry. [2)] The spin arrangement is ferromagnetic in the kagomé and triangular planes and antiferromagnetic between the kagomé and triangular planes. [3)] Recently, magnetic properties of $GeCo_2O_4$ in magnetic field were studied. [2)] It was reported that $GeCo_2O_4$ exhibits a magnetic phase transition at $H_c \sim 4$ T when the field is applied along the (110) and (111) directions. The magnetic transition is probably related with the frustrating interactions.

In order to clarify the magnetic structure in magnetic field, we performed neutron diffraction experiments using a powder sample of $GeCo_2O_4$. The experiments were performed on the triple-axis spectrometer TAS-2 at JRR-3 at JAEA. Vertical magnetic field was applied up to 10 T using a new type of split-pair superconducting magnet that uses cryocoolers.

Magnetic field dependence of some magnetic Bragg peak intensities was measured. For example, the (1/2, 1/2, 1/2) Bragg intensity increases with increasing magnetic field up to 4 T and gradually decreases above 4 T as shown in Fig. 1(a). This characteristic field ($\sim$4 T) is consistent with H_c determined from the magnetization measurments. [2)] Furthermore, the hysteresis behavior was observed between 0 and 4 T at 4 K. It becomes less distinct at 15 K as shown in Fig. 1(b). This behavior probably originates from a reorientation of the magnetic domains in magnetic field. Therefore, the field dependence of the intensity probably originates from the combined effects of the redistribution of the magnetic domains and a magnetic phase transition. We need more experiments using a single crystal to distinguish the two effects and clarify the detailed magnetic structure in magnetic field.

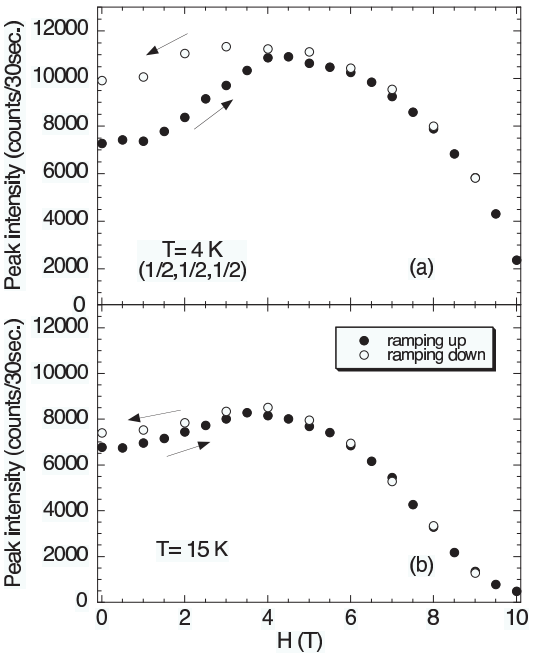


Figure 1: Magnetic field dependence of the (1/2, 1/2, 1/2) magnetic Bragg intensity measured at T=4 K (a) and 15 K (b).

References

1) J. Hubsch and G. Gavoille: "J. Magnetism Magnet. Mater.", 66, pp. 17-22 (1987).
2) T. Hoshi, H. Aruga Katori, M. Kosaka and H. Takagi: "J. Magnetism Magnet. Mater.", 310, pp. e448-e450 (2007).
3) S. Diaz, S. de Brion, G. Chouteau, B. Canals, V. Simonet and P. Strobel: "Phys. Rev. B", 74, pp. 092404/1-4 (2006).

原子炉：JRR-3　　装置：TAS-2(T2-4)　　分野：中性子散乱（磁性）

1-2-55

Magnetic Excitation in the Spin-1/2 Antiferromagnetic Alternating Chain Compound β-$AgCuPO_4$

M. Hase, M. Matsuda[1], K. Kakurai[1], K. Ozawa, H. Kitazawa,
N. Tsujii, A. Dönni and H. Kuore[2]

National Institute for Materials Science (NIMS), 1-2-1 Sengen, Tsukuba, Ibaraki 305-0047
[1]*Japan Atomic Energy Agency (JAEA), 2-4 Shirakata Shirane, Tokai, Naka, Ibaraki 319-1195*
[2]*Department of Physics, Sophia University, 7-1 Kioi-cho, Chiyoda, Tokyo 102-8854*

The calculated results based on spin-dimer analysis indicate that an exchange interaction in a Cu-Cu bond with a long distance (5.20 Å) is the strongest (the J_4 interaction in Fig. 7 of Ref. 1) in insulating β-$AgCuPO_4$, although there are short Cu-Cu bonds (3.10 and 3.20 Å). The J_1 interaction in the same figure is the second strongest: the ratio J_1/J_4 is 0.17. The two interactions form an antiferromagnetic (AF) alternating chain. Actually, the magnetic susceptibility of β-$AgCuPO_4$ shows the existence of a spin-singlet ground state with a spin gap.[1)] Because we usually speculate that the strongest interaction exists in a short Cu-Cu bond, the calculated results cannot be accepted easily. Consequently, we performed inelastic neutron scattering (INS) measurements to determine experimentally the spin system.[2)] INS measurements were carried out on the thermal neutron triple-axis spectrometer TAS-2. The final neutron energy was fixed at 13.7 meV. The collimation was guide-80'-sample-80'-oepn.

The circles in the inset of Fig. 1 show a constant-Q (scattering vector magnitude) scan spectrum. An asymmetric broad inelastic magnetic peak is observed. We measured constant-ω (energy transfer) scan spectra at 5.1 K and at 5, 6, 7, and 8 meV and summed the four spectra (circles in Fig. 1). A clear Q dependence is visible. The line in Fig. 1 indicates the spherical average of the scattering function of the alternating chain with the Cu-Cu distance of 5.20 Å in the strongest interaction and is consistent with the experimental result. In an alternating chain with strong dimerization ($J_4 \gg J_1$), the scattering intensity is strong at the bottom (spin gap) and top of the dispersion. For that reason, we fitted a summation of two Gaussians (solid line) to the experimental spectrum in the inset of Fig. 1. The summation reproduces well the experimental spectrum. Two peak energies are about 6.2 and 8.0 meV (72 and 93 K). The susceptibility of the AF alternating chain with $J_4 = 80$ K and $J_1 = 14$ K ($\alpha \equiv J_1/J_4 = 0.18$) agrees well with the experimental one.[2)] The value 0.18 of α is almost the same as 0.17 in the calculated results.[1)] The spin gap value in the AF alternating chain is 72 K and is the same as obtained in the INS measurements. The higher energy 93 K is close to the energy at the top of the dispersion in the AF alternating chain ($J_4 + 1/2J_1 = 87$ K). Consequently, we could conclude that the spin system was the AF alternating chain with $J_4 = 80$ K and $J_1 = 14$ K and that the J_4 bond with the long Cu-Cu distance had the strongest exchange interaction.

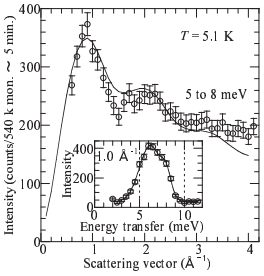


Figure 1: Constant-ω and Q (inset) scan spectra.

References

1) H. B. Yahia et al. : "Inorg. Chem.", 45, pp. 5501-5509 (2006).
2) M. Hase et al. : "Phys. Rev. B", 76, pp. 134403 1-5 (2007).

原子炉：JRR-3　　装置：TAS-2(T2-4)　　分野：中性子散乱（磁性）

1-2-56

Multi-step Magnetic Transition in Non-centrosymmetric Compound $CeCoGe_3$

K. Kaneko[1], N. Metoki[1], T. D. Matsuda[1], A.Thamizhavel[3], T. Takeuchi[2], Y. Haga[1],R. Settai[3], Y. Ōnuki[1,3]

[1]*Advanced Science Research Center, Japan Atomic Energy Agency, Tokai, Naka, Ibaraki 319-1195*
[2]*Low Temperature Center, Osaka University, Toyonaka 560-0043*
[3]*Graduate School of Science, Osaka University, Toyonaka 560-0043*

A discovery of the heavy fermion superconductivity in non-centrosymmetric compounds $CePt_3Si$[1)] and $CeTSi_3$ (T=Rh[2)], Ir[3)]) attracts a considerable interest, since exotic superconducting properties are expected under the lack of inversion symmetry. Following the discovery of $CeTSi_3$, superconductivity was also found in isomorphous $CeCoGe_3$ with T_{sc}=0.7 K under pressure of 5.5 GPa [5)]. At ambient pressure, $CeCoGe_3$ exhibits multi-step magnetic transitions at T_{N1}=20 K, T_{N2}=11.5 K and T_{N3}=7.5 K[4)]. The magnetic structure of the ground state and the nature of the multi-step transitions have not been clarified so far. The present work aims to reveal the magnetic structure of the ground state in $CeCoGe_3$ by neutron diffraction.

A single crystalline sample of $CeCoGe_3$ was grown by flux method. Neutron diffraction experiments were carried out on the two-axis diffractometer MUSASI and thermal triple-axis spectrometer TAS-2, both installed at JRR-3. Neutrons with a wavelength of 2.44 Å and 2.359 Åwere used in MUSASI and TAS-2, respectively, with the PG filter in order to remove the higher order contamination. The single crystal was mounted with the $(h\,0\,l)$ horizontal scattering plane.

Figure 1 shows the line scan profile along the $(1\,0\,l)$ in the reciprocal space of $CeCoGe_3$ taken at 2.9 K. The superlattice reflection was observed at $(1\,0\,1/2)$. The additional weak peak at $(1\,0\,1/4)$ was also found together with its higher order harmonics of $(1\,0\,3/4)$, indicated by arrows. At 25.0 K above T_{N1}, these superlattice peaks were not observed. Therefore the propagation vectors of the ground state are determined to be $\boldsymbol{q}_1$=$(0\,0\,1/2)$ and $\boldsymbol{q}_2$=$(0\,0\,3/4)$. The inset of Fig. 1 shows $(0\,0\,l)$ scan profiles at respective positions to $\boldsymbol{q}_1$ and $\boldsymbol{q}_2$ measured at 2.9 K. Since no trace of magnetic peak was found in the $(0\,0\,l)$ line, the directions of the magnetic moment corresponding to both $\boldsymbol{q}_1$ and $\boldsymbol{q}_2$ are parallel to the tetragonal c-axis. This direction of the magnetic moment is consistent with an anisotropy in the magnetization measurement[4)] and is in contrast to $CeTSi_3$ (T=Rh[2)], Ir[3)]). The coexistence of $\boldsymbol{q}_1$ and $\boldsymbol{q}_2$ suggests that the size of the ordered moment is not unique in the ground state. The detailed magnetic structure analysis is now in progress.

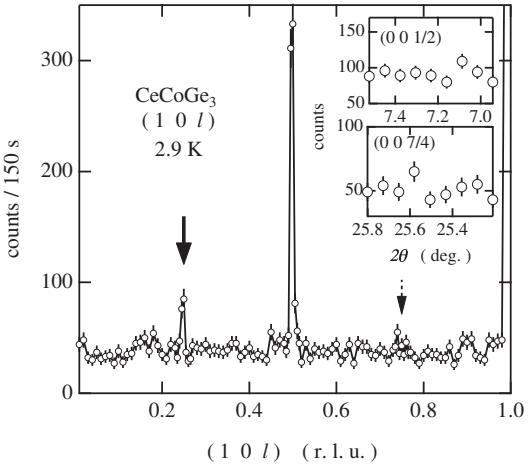


Figure 1: The line scan profile along the $(1\,0\,l)$ of $CeCoGe_3$ taken at 2.9 K The inset shows the $(0\,0\,l)$ scan at l=1/2 and 7/4 measured at the same temperature.

References

1) E. Bauer *et al.*, Phys. Rev. Lett. **92**, 027003 (2004).
2) N. Kimura *et al.*, Phys. Rev. Lett. **95**, 247004 (2005).
3) I. Sugitani *et al.*, J. Phys. Soc. Jpn. **75**, 043703 (2006).
4) A. Thamizhavel *et al.*, J. Phys. Soc. Jpn. **74**, 1858 (2005).
5) R. Settai *et al.*, Physica B **310**, 844 (2007).

原子炉：JRR-3　　装置：TAS-2(T2-4)　　分野：中性子散乱（磁性）

1-2-57

Pressure-Induced Magnetic Quantum Phase Transition in Coupled Spin Dimer System $KCuCl_3$

T. Ono, J. Kawakami, H. Tanaka, T. Osakabe[1] and K. Kakurai[1]

Department of Physics, Tokyo Institute of Technology, Meguro-ku, Tokyo 152-8550
[1] *Quantum Beam Science Directorate, JAEA, Tokai, Ibaraki 319-1195*

$KCuCl_3$ is an interacting spin dimer system, which undergoes a pressure-induced quantum phase transition (QPT) from a gapped ground state to an antiferromagnetic state at a critical pressure of $P_c \simeq 8.2\,\mathrm{kbar}$ [1]. An analysis of magnetic susceptibilities has revealed that the intradimer interaction decreases with pressure and the sum of interdimer interactions increases. This causes the shrinkage of the gap, which leads to the pressure induced QPT, as summarized in Fig. 1. To clarify the pressure dependence of individual magnetic interactions in $KCuCl_3$, we investigated the magnetic excitations under hydrostatic pressures by neutron inelastic scattering experiments. This experiment is the continuation of the published study for the pressure at $P = 4.7\,\mathrm{kbar}$ [2].

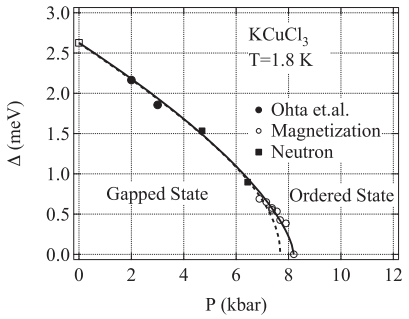


Figure 1: Pressure dependence of the gap Δ.

Neutron inelastic scattering experiments was performed using LTAS spectrometer with the collimation sequence guide-80'-80'-open and with a fixed final neutron energy $E_f = 3.5\,\mathrm{meV}$. The cylindrical high-pressure cell used was identical to that was used in Ref. 2).

Figure 2 shows the dispersion relations for $\boldsymbol{Q}$ along $(0, 0, 1 + 2h)$ and $(h, 0, 1)$ measured at $P = 6.4\,\mathrm{kbar}$ together with the preceding results. The softening of magnetic excitations due to applied pressure is clearly observed. The solid lines are the calculated results using

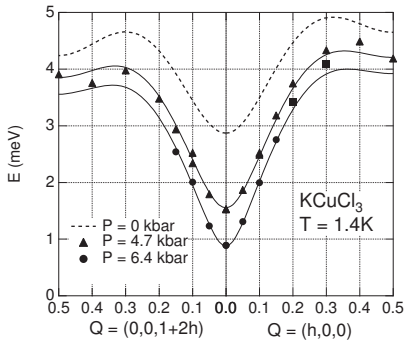


Figure 2: Dispersion relations in $KCuCl_3$ measured at 4.7 and 6.4 kbar for $\boldsymbol{Q}$ along $(0, 0, 1+2h)$ and $(h, 0, 1)$.

RPA approximation [3] with effective exchange parameters listed in Table 1. The experiments above the critical pressure is ongoing.

Table 1: Intradimer and effective interdimer interactions in $KCuCl_3$ in meV unit for $P = 0$, 4.7 and 6.4 kbar. The notational used here follows Ref. 3).

P [kbar]	J	J_1^{eff}	J_2^{eff}	J_3^{eff}
ambient	4.34	-0.42	0.90	0.56
4.7	3.65	-0.62	0.86	0.86
6.4	3.29	-0.52	0.82	0.82

References

1) K. Goto, M. Fujisawa, H. Tanaka, Y. Uwatoko, A. Oosawa, T. Osakabe, and K. kakurai: "J. Phys. Soc. Jpn.", 75 064703(2006).
2) K. Goto, T. Osakabe, K. Kakurai, Y. Uwatoko, A. Oosawa, J. Kawakami, and H. Tanaka: "J. Phys. Soc. Jpn.", 76 053704(2007).
3) A. Oosawa, T. Kato, H. Tanaka, K. Kakurai, M. Müller and H. -J. Mikeska: "Phys. Rev. B"65 094426 (2002).

原子炉：JRR-3　　装置：LTAS(C2-1)　　分野：中性子散乱（磁性）

1-2-58

Magnetic Structural Analysis of Magnetic Multilayers by Complementary Use of X-ray and Neutrons

M. Takeda[1,2,3], D. Yamazaki[1,2], K. Soyama[1,2], R. Maruyama[2], M. Hino[4], T. Hirano[5]

[1]*Quantum Beam Science Directorate, Japan Atomic Energy Agency (JAEA), Tokai-mura, Naka-gun, Ibaraki, 319-1195, Japan*
[2]*J-PARC Center, Tokai-mura, Naka-gun, Ibaraki, 319-1195, Japan*
[3]*New Industry Creation Hatchery Center, Tohoku Univ., Aramaki Aoba, Aoba-ku, Sendai-shi, Miyagi, 980-8579, Japan*
[4]*Kyoto University Reactor, Kyoto University, Kumatori-cho, Sennan-gun, Osaka, 590-0494,Japan*
[5]*Hitachi Research Laboratory, Hitachi Ltd., Ohmika-machi, Hitachi-shi, Ibaraki, 319-1292, Japan*

A read sensor head of a hard disk drive has a layered structure and consists of several ferromagnetic (F), antiferromagnetic (AF), and nonmagnetic layers. Much attention is now paid to the magnetic structure near the interfaces between the F and the AF layers in development of the high performance read sensors because a stable pinning of magnetization of F layer by AF layer is very sensitive to the magnetic structure near the interfaces. Complementary use of X-ray and neutron reflectometry is the most powerful and nondestructive tool to investigate such buried internal magnetic structures.

Figure 1 (a) shows the polarized neutron reflectivities from a multilayer which is a part of a read sensor under a magnetic field of 1.8 kOe using SUIREN. The structure of the sample is described as Si/Ta(5nm)/Ru(5nm)/MnIr(5nm)/CoFe(2nm)/Cu(1nm)/Ru(2nm). The length of the sample in the scattering plane was 35 mm, and the height was 25 mm. The angle divergence of the incident beam was controlled by two sets of horizontal slits and was approximately 4 % ($\Delta\theta/\theta$) in the whole scan range.

The reflectivities with the spin-flip clearly indicate the existence of perpendicular component of internal magnetization under this field. X-ray reflectivity of the same sample is also displayed in Fig. 1 (b). This information is not able to be obtained by the X-ray reflectivity measurements. On the other hand, the statistics and the Q resolution of data in Fig. 1 (b) are better than those of polarized neutron reflectivities in Fig. 1 (a) even though measuring time of the data in Fig. 1 (a) was much longer than that of Fig. 1 (b). The layered internal structural information (paramagnetic one) is more accurately obtained from the X-ray reflectivity data. The complementary use of X-ray and neutron reflectometry will give the reliable depth profile of magnetization of this multilayer on the basis of the structural information from the X-ray reflectivity measurements. Analyses of both data are now in progress, and the results will be reported elsewhere.

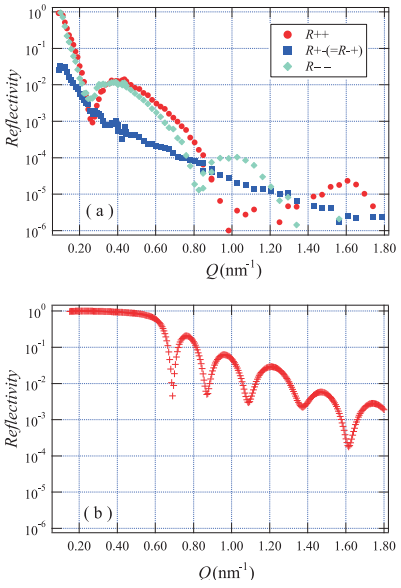


Figure 1: Four kinds of polarized neutron reflectivities (a), and X-ray one (b) from the same multilayer which is a part of multilayer structure of a read sensor.

原子炉：JRR-3　　装置：SUIREN(C2-2)　　分野：中性子散乱（磁性）

1-2-59

Small-Angle Neutron Scattering Measurements of Averaged Internal Structures in Nd-Fe-^{11}B Sintered Magnets

M. Takeda[1,2,3], J. Suzuki[1,2], D. Yamaguchi[4], T. Akiya [3], H. Kato[3,5], M. Sagawa[3,6], K. Koyama[7]

[1] *Quantum Beam Science Directorate, Japan Atomic Energy Agency (JAEA), Tokai-mura, Naka-gun, Ibaraki, 319-1195, Japan*
[2] *J-PARC Center, Tokai-mura, Naka-gun, Ibaraki, 319-1195, Japan*
[3] *New Industry Creation Hatchery Center, Tohoku Univ., Sendai, Miyagi, 980-8579, Japan*
[4] *Advanced Science Research Center, Japan Atomic Energy Agency (JAEA), Tokai-mura, Naka-gun, Ibaraki, 319-1195, Japan*
[5] *Department of Applied Mathematics and Physics, Yamagata Univ., Yonezawa, Yamagata, 992-8510, Japan*
[6] *Intermetallics Co., Ltd., Kyodaikatsura #303, 1-36 Goryo Ohara, Nishikyo-Ku, Kyoto, 615-8245, Japan*
[7] *Institute for Materials Research, Tohoku University, Sendai, Miyagi, 980-8577, Japan*

Neodymium iron boron (Nd-Fe-B) sintered magnets are now widely used because of the highest $(BH)_{\max}$ among the commercially available permanent magnets. At the present, Dy, which is one of the rare metals, has to be added to keep the coercivity especially in the operational temperatures higher than the room temperature. The key to achieve the high-cercivity Dy-free Nd-Fe-B sintered magnets is how to control the grain size and the structure near the grain boundary. We have performed the small-angle neutron scattering (SANS) measurements of the Nd-Fe-^{11}B sintered magnets using unpolarized and polarized neutrons to obtain the averaged internal structures of samples with the different coercivity introduced by applying high magnetic fields during the annealing[1)].

We found that both of the integrated intensities along the $\vec{q}//\vec{M}$ and $\vec{q} \perp \vec{M}$ clearly correlated with the coercivity values (H_c): The sample with the higher H_c has the higher SANS intensity. Furthermore, imbalance of the intensities between the spin-flip (SF) and the non-spin-flip (NSF) components of the SANS using the polarized neutrons along the $\vec{q} \perp \vec{M}$ direction was induced by the magnetic fields applied parallel to $\vec{M}$ (Fig. 1), while SF and NSF components were equal to each other in zero external magnetic field. The degree of imbalance is different among the samples with the different H_c. This suggests that the magnetic inhomogeneity in the scale of 100 - 200 nm seems to affect the H_c. Such inhomogeneity inside the grain has been thought to have little effect on H_c. Present work gives a hint to achieve the high-coercivity Dy-free Nd-Fe-B sintered magnet.

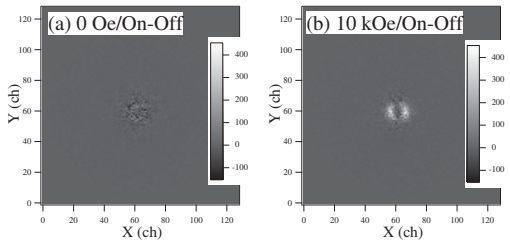


Figure 1: Differences of the intensity between SF and NSF components along the $\vec{q} \perp \vec{M}$ direction on the 2D-PSD: (a) the map in zero magnetic field and (b) in the field of 10 kOe applied parallel to $\vec{M}$.

This work was partially supported by the Ministry of Economy, Trade and Industry (METI), and New Energy and Industrial Technology Development Organization (NEDO), Grant-in-Aid for "Development of technology for reducing dysprosium usage in a rare-earth magnet" in "Rare Metal Substitute Materials Development Project".

References

1) H. Kato, T. Miyazaki, M. Sagawa, and K. Koyama, Appl. Phys. Lett., **84** (2004) 4230. (2007) s474.

原子炉：JRR-3　　装置：SANS-J-II(C3-2)　　分野：中性子散乱（磁性）

This is a blank page.

1. 中性子散乱 3) 強相関電子系

1. Neutron Scattering 3) Strongly Correlated Electron Systems

This is a blank page.

1-3-1

Magnetic excitations in halogen-bridged nickel complex

S. Itoh and K. Nakajima*
*High Energy Accelerator Research Organization, Tsukuba, 305-0801, *Japan Atomic Energy Agency, Tokai, 319-1195*

Halogen-bridged metal complexes with a one-dimensional (1D) mixed-valence -X-M(II)-X-M(IV)-X- structure have been studied as a Peierls distorted chain system with a strong electron-lattice interaction resulting from the off-centered position of halogen between neighboring metal atoms. Among these compounds, [NiBr(chxn)2]Br2 (chxn:1R, 2R-cyclohexanediamine) have a non-distorted 1D structure expressed as -Br-Ni(III)-Br-Ni(III)-Br-[1,2]. This spin structure implies antiferromagnetic Heisenberg chains with S = 1/2. Magnetic susceptibility measurements up to the room temperature suggested a large exchange constant of J ˜ 0.3 eV [2]. Optical studies have been revealed that this system exhibits a 1D charge transfer insulator [3]. The observed optical properties can be explained by a 1D extended Hubbard model [4], and it suggested J ˜ 0.4 eV, which is consistent with the result on the susceptibility.

In order to detect magnetic excitations, we previously performed an inelastic neutron scattering experiment on HER (C1-1) at JRR3M in JAERI (Tokai) in 2002, by using 20 g of a single-crystal sample. However, we could not detect meaningful magnetic signals at the magnetic zone center at energy transfers up to 1.5 meV at 1.4 K.

Recently, this system has been suggested to be a spin-Peierls system with Tsp˜40K from magnetic susceptibility study as well as 81Br NQR study [5]. By applying the BCS theory to the spin-Peierls system, the gap energy can be estimated to be approximately 6 meV from Tsp. At present, in order to investigate the spin-Peierls nature in this system, an experiment was performed on PONTA (5G) at JRR3M in JAEA (Tokai), by using the same sample. Since, from the previous experiment in 2005, we thought that we could detect tiny magnetic signals at low energy region at the magnetic zone, we again tried to measure inelastic signals to improve statistics at present. The experiment was performed at 8 K and 100 K (below and above TSP), however, we could not detect meaningful magnetic signals because of huge incoherent inelastic signals from hydrogen atoms. In order to detect magnetic signals, deuteration of the sample is essential. For the next time, we try to observe magnetic signals using a deuterated sample.

References

[1] K. Toriumi et al., J. Am. Chem. Soc. 111 (1989) 2341.
[2] H. Okamoto et al., Phys. Rev. B 42 (1990) 10381.
[3] H. Okamoto et al., Phys. Rev. B 54 (1996) 8438.
[4] N. Tomita and K. Nasu, Phys. Rev. B 56 (1997) 3779.
[5] S. Takaishi et al., J. Am. Chem. Soc. 126 (2004) 1614.

1-3-2

Charge and magnetic order in 2d cobaltate Pr2-xCaxCoO4

H. Yoshizawa and K. Masuda
Neutron Science Laboratory, ISSP, The University of Tokyo

We studied the charge and spin order in the 2d cobaltate Pr2-xCaxCoO4 in JFY2005 and 2006. For $0.39 < x < 0.5$ where the hole concentration is less than but close to x = 0.5, the spin and charge order in the cobaltates has the checkerboard-type as shown in Fig. 1 (a). On the other hand, for $x > 0.5$ where the hole concentration is larger than half the number of the Co sites, incommensurate (IC) peaks appear with two characteristic wave vectors, (δ , 0, 1) and (2 δ , 0, 1), with δ = 1-x. From their Q-dependences, we identified the IC peaks with (δ , 0, 1) to be magnetic and those with (2 δ , 0, 1) to be structural. This indicates that the charge and spins form stripes as shown in Fig. 1 (b). This stripe order is similar to those observed in the underdoped region of cuprates and nickelates. It is however to note that in the overdoped ($x > 0.5$) cobaltates the magnetic Co2+ ions form the domain boundaries that separate the nonmagnetic Co3+ ions.

In order to understand an origin of this unusual spin-charge order, we studied its spin dynamics in the JFY2007, and found that its spin dynamics is governed by a strong planar anisotropy and spin state transiton from an intermediate to low spin state. The detailed quantitative analysis is now underway.

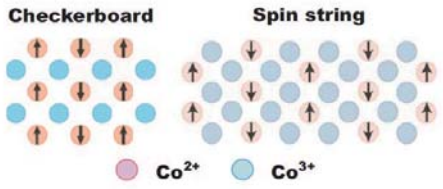


Fig. 1. Schematic models for the checkerboard-type spin-charge order (left) and spin string order (right) in PCCO.

1-3-3

Variation of magnetic modulation for the antiferromagnetic states in $CeRh_{1-x}Co_xIn_5 (x = 0, 0.5 \text{ and } \sim 0.7)$

N. Oyama[1], M. Yokoyama[1], S. Oinuma[2], I. Kawasaki[2], H. Amitsuka[2], K. Tenya[3], T. J. Sato[4], M. Matsuura[4] and K. Hirota[4]

[1]*Ibaraki University,* [2]*Hokkaido University,* [3]*Shinshu University,* [4]*ISSP, The University of Tokyo*

For a decade, there has been a growing interest in physical property near the quantum critical point (QCP) in the heavy-fermion systems. The heavy-fermion compound $CeRhIn_5$ orders in an incommensurate antiferromagnetic (AF) phase with a modulation of $q_h = (1/2, 1/2, 0.297)$ [1]. It is revealed in the Co-doped alloys $CeRh_{1-x}Co_xIn_5$ [2] that the AF phase is suppressed with increasing x, and then disappears at $x_c \sim 0.7$. At the same time, superconductivity (SC) appears between $x = 0.4$ and $x = 1$. Furthermore, recent elastic neutron scattering experiments for $CeRh_{1-x}Co_xIn_5$ with intermediate Co concentrations [3, 4] revealed that a commensurate magnetic order with a wave vector $q_c = (1/2, 1/2, 1/2)$ develops at low temperatures. To elucidate the nature of these AF phases, we have performed the neutron scattering experiments for $CeRh_{1-x}Co_xIn_5$ $(x = 0, = 0.5, \sim 0.7)$.

Single crystals of $CeRh_{1-x}Co_xIn_5$ were grown by the In-flux method. The samples were shaped into bar (typical size: $\sim 3\ mm^2 \times 10\ mm$) in order to minimize the effects of the neutron absorption caused by Rh and In. Elastic neutron scattering experiments were carried out using triple-axis spectrometers GPTAS and PONTA at the JRR-3M research reactor of JAEA. Measurements were performed in the (*hhl*) scattering plane.

Figure 1 shows the neutron scattering pattern obtained from the $(1/2, 1/2, 1 + \xi)$ $(0 \leq \xi \leq 1)$ scan at 1.6 K. The incommensurate magnetic Bragg peaks were observed for $x = 0$, whose wave vector corresponds to $q_h \sim (1/2, 1/2, 0.297)$. For $x = 0.5$, we observed of the commensurate magnetic Bragg peak with the modulation of $q_c = (1/2, 1/2, 1/2)$. In addition, for $x \sim 0.7$, we have found that the q_h peak position moves toward $q_1 \sim (1/2, 1/2, 0.42)$, together with the apperance of the q_c peak.

From these results, we suggest that the commensurate magnetic correlation is tightly coupled with SC.

References

[1] W. Bao *et al.*, Phys. Rev. B **62** (2000) R14621; Phys. Rev. B 67 (2003) 099903(E).

[2] V.S. Zapf *et al.*, Phys. Rev. B **65** (2001) 014508.

[3] M. Yokoyama *et al.*, J. Phys. Soc. Jpn. **75** (2006) 103703.

[4] S. Ohira-Kawamura *et al.*, Phys. Rev. B 76 (2007) 132507.

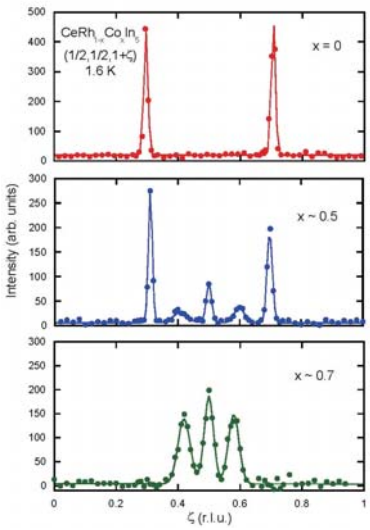


Fig. 1. Antiferromagnetic Bragg-peak profiles at 1.6 K for $CeRh_{1-x}Co_xIn_5$.

1-3-4

Evolution of Ferromagnetic and antiferromagnetic orders in Mn-doped $CaRuO_3$

M. Yokoyama, H. Hagiya, N. Oyama, Y. Nishihara and H. Kawanaka[1]
Ibaraki University, [1] *National Institute of Advanced Industrial Science and Technology*

The relationship between metal-insulator transition and magnetism in the transition-metal oxides is one of the intriguing issues in the condensed-matter physics. The distorted perovskite compound $CaRuO_3$ (the $GdFeO_3$-type orthorhombic structure; space group *Pnma*) is considered to be a paramagnetic metal located in the vicinity of the metal-insulator transition. It is revealed that the ionic substitutions for the Ru site dramatically enhance the magnetic correlation [1, 2, 3, 4]. We recently found that the substitution of Mn for Ru induces both ferromagnetic and antiferromagnetic (AF) components in the magnetization, accompanying the variation of the electrical resistivity from metallic to insulating behavior. These features are expected to be attributed to the change of the d electronic state. To investigate the microscopic properties of the d electrons in the intermediate Mn concentration range, we have performed powder neutron diffraction experiments for $CaRu_{1-x}Mn_xO_3$.

The polycrystalline samples of $CaRu_{1-x}Mn_xO_3$ with $x = 0.4$ were prepared by the solid-state method. The neutron diffraction measurements for powdered samples were performed in the temperature range between 15 K and 290 K, using the HERMES spectrometer (IMR, Tohoku Univ.) installed at the guide hall of the research reactor JRR-3M of JAEA. The wavelength of the incident neutron was selected to be 1.8264 Å. Figure 1(a) shows low-angle part of the neutron powder diffraction profiles at 15 K and 290 K for $x = 0.4$. The (110) and (011) Bragg peaks are clearly observed at 15 K, which attributes the occurence of the G-type AF order. In addition, the enhancement of the (020) Bragg-peak intensity due to ferromagnetic order was also detected. Temperature variations of these Bragg-peak intensities [Fig. 2(b)] are consistent with characteristics seen in the magnetization: the magnitude of magnetization is markedly suppressed below ~ 90 K.

References

[1] I. Felner *et al.*: Phys. Rev. B 66 (2002) 054418.
[2] V. Hardy *et al.*: Phys. Rev. B 73 (2006) 094418.
[3] V. Durairaj *et al.*: Phys. Rev. B 73 (2006) 214414.
[4] A. Maignan *et al.*: Phys. Rev. B 73 (2006) 024410.
[5] A.I. Shames *et al.*: Phys. Rev. B 70 (2004) 134433.

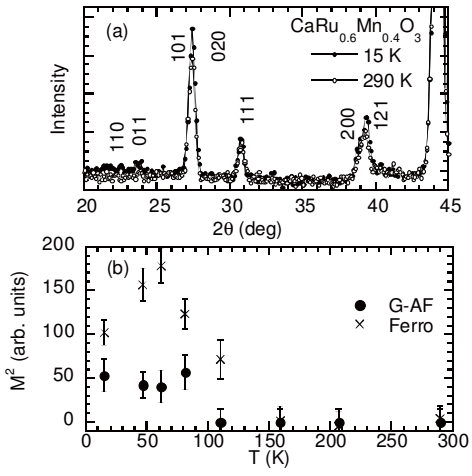


Fig. 1. (a) Neutron powder diffraction profiles at 15 K and 290 K, and (b) Temperature variations of the square of the ferromagnetic and antiferromagnetic moment for $CaRu_{1-x}Mn_xO_3$ with $x = 0.4$.

1-3-5

Modulated-structure analysis of the high-valence aperiodic chain compounds, Sr2k(Co1-xNix)O3 (k˜0.635, 0<=x<=1)

Masaaki ISOBE (A), Hideaki KITAZAWA (B), Kenji OHOYAMA (C)
(A) Advanced Nano Materials Laboratory, National Institute for Materials Science; (B) Quantum Beam Center, National Institute for Materials Science; (C) Institute for Materials Research, Tohoku University

The A2kMO3 (A: alkali-earth elements, M: transition metals)-type compounds belong to a hexagonal class in Bravais lattices. This system has two types of one-dimensional chain sub-lattices of [MO3] blocks and A ions, running along the c-axis in the crystal structure. The atomic positions are incommensurately modulated due to irrational-ratio periodicity of the sub-lattices (c1/c2=k). Recently, we found from static-magnetic measurements that solid-solution phases Sr2k(Co1-xNix)O3 (k˜0.635, 0<=x<=1) can possess an unusual high-valence (˜3.5+) state of the Co and Ni ions throughout the x compositions. The purpose of this experimental subject is to make clear the true valence of the ions in the Sr2k(Co1-xNix)O3 system, by precisely analyzing the modulated crystal structure, including oxygen positions.

Neutron diffraction data for the polycrystalline samples with compositions of Sr14Co11O33, Sr14Co8Ni3O33, Sr9Co3.5Ni3.5O21 and Sr9Co2Ni5O21 were collected using the HERMES diffractometer (IMR, Tohoku Univ.) at room temperature in a 2theta range from 7 to 157.95 degrees, in a step size of 0.05 degree. Incident thermal neutron beams were monochromatized to a wavelength of 1.8265 A with the 331 reflection of a bent-crystalline Ge monochromator. The modulated crystal structures of Sr2k(Co1-xNix)O3 were analyzed by the Rietveld method using a computer software, PREMOS91 [1], on the basis of a superspace-group approach. The initial structure model was constructed by making reference to the structure model proposed by Onoda et al. for Sr1.145TiS3 [2]. The super-space groups, P-R3m/1s and R-P31c/111, were adopted for the first- ((Co,Ni)O3) and the second- (Sr) subsystems, respectively.

Figures 1 (a) and (b) show crystal structures illustrated using the refined structure parameters for the sample of Sr14/11(Co8/11Ni3/11)O3 (Rwp=5.44%). The (a) is a projection along the c-axis, and the (b) is a projection perpendicular to the c-axis of one of the [(Co,Ni)O3] chains and the neighboring Sr atoms. The lattice parameters are a=9.4761(2) A, c1=2.54105(8) A, and k(=c1/c2)=0.63505(5). The figure (b) reveals sequence of the polyhedron types, i.e. a trigonal prism (TP) and an octahedron (Oh), around the Co and Ni atoms.

Figure 1 (c) shows Co,Ni-O distances as a function of the internal forth coordinate t' for the (3+1)-dimensional incommensurate structure model of Sr14/11(Co8/11Ni3/11)O3. The O(+z) and the O(-z) curves indicate oxygen atoms above and below the Co/Ni atom along the c-axis, respectively. The shaded area corresponds to the TP sites, and the non-shaded area to the Oh sites. The [(Co,Ni)O3] chain comprises 27% TP and 73% Oh sites. The figure (c) indicates that in most of the TP sites, both the Co,Ni-O lengths, O(+z) and O(-z), are simultaneously lengthened as compared to those in the Oh sites. We also analyzed occupancy probabilities of the Co and Ni atoms at the M site, as a function of t'. It was found that the Ni atoms prefer the TP sites to the Oh sites, and that the Co atoms are selectively situated at the Oh sites. The bond valences were calculated from the Co,Ni-O distances and the occupancy probabilities. The values are ˜2.3+ for the TP sites and ˜3.4+ for the Oh sites on average. It suggests that the high-valence

Activity Report on Neutron Scattering Research: Experimental Reports **15** (2008)
Report Number: 299

state can appear exclusively at the Oh sites.

References

[1] A. Yamamoto, Acta Crystallogr. A49 (1993) 831; ibid. A52 (1996) 509.
[2] M. Onoda, M. Saeki, A. Yamamoto, and K. Kato, Acta Crystallogr. B49 (1993) 929.

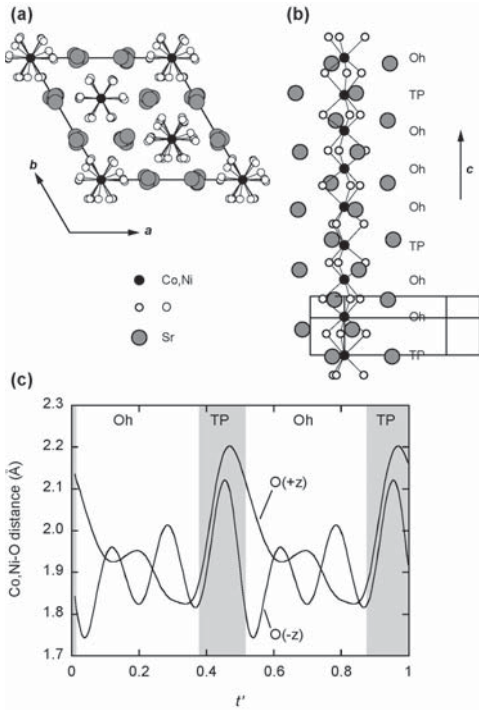


Fig. 1. (a, b) Crystal structure of Sr14/11(Co8/11Ni3/11)O3; (c) Co,Ni-O distances as a function of the internal forth coordinate t'.

1-3-6

Magnetic phase diagram under low temperature and high pressure in RVO3

D. Bizen(A), H. Nakao(A), K. Iwasa(A), Y. Murakami(A), T. Osakabe(B), S. Miyasaka(C), Y. Tokura (D,E)
(A) Tohoku Univ., (B) JAEA, (C) Osaka Univ., (D) The Univ. of Tokyo, (E) CERC

RVO3 (R: rear earth or Y) shows various physical properties coupled with the spin and orbital states. [1] The orbital state is strongly coupled with the lattice distortion, i.e. Jahn-Teller distortion. Hence the pressure effect for the orbital state interests us, and the pressure-temperature phase diagram of the V 3d-orbital state was investigated by x-ray diffraction under high-pressure and low-temperature. [2] It elucidated that the C-type orbital ordering (C-OO) is stabilized as compared with the G-type orbital ordering (G-OO) by applying hydrostatic pressure. The spin state coupled with the orbital state is also an important problem for this system. Therefore, the spin state in TbVO3, of which the ground state of 3d-orbital changes from the G-OO to the C-OO by applying pressure, was investigated under high-pressure and low-temperature using a hybrid anvil cell.

In order to determine the magnetic ordering, the magnetic scattering was measured by using the triple-axis spectrometer TOPAN. The temperature dependence of the magnetic peak intensities was measured at several pressures as shown in the figure. At ambient pressure (0 GPa), the magnetic peak at (0 1 0) reflecting the C-type spin ordering (C-SO) was observed below the magnetic transition temperature. With increasing pressure, the C-SO phase is suppressed and finally disappears. On the other hand, the magnetic peak at (0 1 1) reflecting the G-type spin ordering (G-SO) appears above 1.0 GPa, and the magnetic transition temperature remarkably increases with applying pressure. As compared with the orbital phase diagram [2], it becomes clear that the G-SO phase corresponds to the C-OO phase and the C-SO phase appears in the G-OO phase. Namely, we could clearly determine the changing the spin state when the orbital ordering of the ground state is changed by applying pressure. The result indicates a strong coupling between the spin state and the orbital state in RVO3 system.

[1] S. Miyasaka et al., Phys. Rev. B 68 (2003) 100406.
[2] D. Bizen et al., J. Magn. Magn. Mater. 310 (2007) 785.

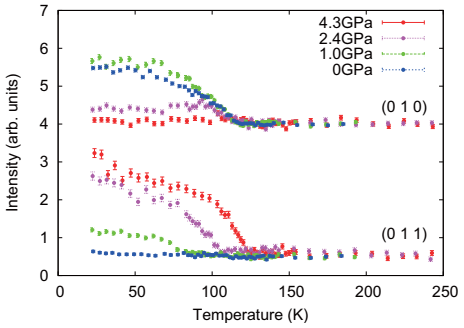


Fig. 1. Temperature dependence of the magnetic peak intensities at (0 1 1) and (0 1 0), which correspond to G-OO and C-SO, respectively.

1-3-7

Study on thermoelectric properties and misfit-structures in Y doped Ca3Co4O9

H.Nakatsugawa, H.M.Jeong, and K.Nagasawa
Yokohama National University 79-5 Tokiwadai Hodogaya Yokohama 240-8501 Japan

Since the discovery of large thermoelectric power in the layered compounds NaCo2O4 and Ca3Co4O9, misfit-layered cobalt oxides particularly have attracted much interest as candidates for thermoelectric (TE) materials. The polycrystalline Ca3Co4O9 sample typically exhibits S=130 μ V/K, ρ =15m Ω cm and κ =1.0W/mK at room temperature. For practical use, an appreciable decrease in ρ must be achieved because ρ =15m Ω cm at room temperature is about one order of magnitude higher than that of Bi2Te3-based TE materials. In this study, we have employed a high-resolution powder neutron diffraction technique to investigate the weak modulated crystal structure of trivalent Y ion doped Ca3Co4O9 polycrystalline samples. This study was carried out to investigate the valence state of Co ions both in the CoO2 sheet and in the RS-type BL subsystems.

The polycrystalline samples of [(Ca1-xYx)2CoO3]0.62CoO2 (0 ≦ x ≦ 0.04) were prepared by the conventional solid-state reaction method. The sample homogeneity and crystallinity were confirmed by means of the powder Neutron diffraction (ND) technique. Tne ND data were collected at 293K using the Kinken powder diffractometer for high efficiency and high resolution measurements (HERMES) of Institute for Materials Research (IMR), Tohoku University, installed at the JRR-3M reactor in Japan Atomic Energy Research Institute (JAERI), Tokai. The incident neutron beam was monochromatized at λ =1.8265 Å. The ND data were analyzed using a Rietveld refinement program PREMOS 91 designed for modulated structure analyses. The crystal structures and interatomic distance plots were obtained with the use of PRJMS and MODPLR routines, respectively, both were implemented in the PREMOS 91 package.

First, we assumed the superspace group of C2/m(0 p 0)s0 for the crystal structure of [(Ca0.98Y0.02)2CoO3]0.62CoO2 (x = 0.02), and assigned the CoO2 sheet for subsystem 1 and the RS-type BL for subsystem2. In this superspace group, the CoO2 sheet has C2/m symmetry while the RS-type BL subsystem has C21/m symmetry.

After two or three refinement cycles, the modulation of the atomic positions in x=0.02 was introduced, considering up to the second order of cosine and sine components of the Fourier terms, i.e., Ai (i = 0, 1, 2) and Bi (i = 1, 2). Figure 1 shows the observed, calculated and difference intensities of the HERMES data for x = 0.02. Short vertical lines below the patterns indicate the peak positions of the main (upper) and satellite (lower) reflections for the CoO2 sheet and RS-type BL subsystems. The difference between the observed and calculated patterns is shown below the vertical lines. The final Rwp factor is 5.91 % and the lattice parameters are refined to a = 4.8300(5) Å, b1 = 2.8220(1) Å for CoO2 sheet, b2 = 4.5517(1) Å for RS-type BL subsystem, c = 10.838(9) Å and β = 98.13(8)° .

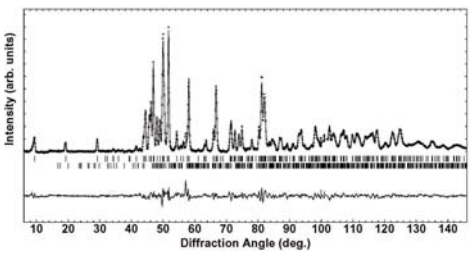


Fig. 1. Observed, calculated and difference intensities of ND data for [(Ca0.98Y0.02)2CoO3]0.62CoO2 (x=0.02).

1-3-8

Magnetic excitation in a non-centrosymmetric pressure-induced superconductor $CeRhSi_3$

N. Aso, H. Miyano, H. Yoshizawa, N. Kimura[A], T. Komatsubara[A], H. Aoki[A]
NSL-ISSP Univ. of Tokyo, Graduate School Sci. Tohoku Univ.[A]

Coexistence between magnetism and superconductivity (SC) is the central issue in condensed matter physics. Recently non-centrosymmetric heavy-fermion superconductor $CePt_3Si$ and UIr were reported. From the fundamental point of view of symmetry, the discovery of these materials are very surprising because there are two basic symmetries which are considered indispensable to form Cooper pair: time reversal symmetry and parity. The former is important for Cooper pairing in any case while the latter is mandatory for pairing in the triplet channel. Thus there is a lot of discussions for the non-centrosymmetric SC at present.

Kimura *et al.* [1] discovered another non-centrosymmetric superconductor $CeRhSi_3$ with the crystal structure of $BaNiSn_3$-type ($I4mm$). [2] $CeRhSi_3$ exhibits the antiferromagnetic (AFM) ordering below $T_N = 1.6$ K at ambient pressure (P). By increasing the P, T_N shows a maximum around 0.7 GPa, then gradually decreases. SC appears in a wide P range from 1.2 to 2.3 GPa (and more). Concerning the magnetic structure, there was only one neutron diffraction work on polycrystalline samples, [3] which exhibits no magnetic reflections with possible maximum magnetic moment of 0.25 μ_B/Ce. In the last year we have first determined the magnetic structure using the single crystalline $CeRhSi_3$, [5] indicating the longitudinal spin density wave (LSDW) with the wave vector of k = (0.215, 0, 0.5) and the Ce staggered moment of $\sim$ 0.1 μ_B/Ce.

This year we tried to examine the low-energy magnetic excitations below $T_N = 1.6$ K. Figure 1 shows the inelastic scattering profile at Q = (0.215, 0, 1.5) and T = 0.76 K obtained at the HER spectrometer with the fixed energy of $k_f = 1.55$ $\AA^{-1}$ using the horizontally focused analyzer. One can recognize an energy-broad magnetic signal at the energy loss side, which is almost wave vector independent. Thus we did not observe any signal corresponding to the LSDW ordering wave vector. We will plan to go to the lower energy in the next.

References

[1] N. Kimura *et al.*, *Phys. Rev. Lett.* **95**, 247004 (2005).
[2] Y. Muro *et al.*, *J. Phys. Soc, Jpn.* **67**, 3601 (1998).
[3] A. Krimmel *et al.*, *Appl. Phys.* **A 74** Suppl., S695 (2002).
[4] N. Kimura *et al.*, *Physica* **B 294-295**, 280 (2001).
[5] N. Aso *et al.*, *J. Magn. Magn. Mater.* **310** (2007) 302.

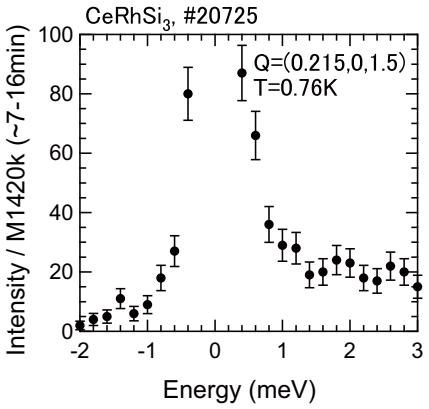


Fig. 1. Inelastic neutron scattering profile at Q = (0.215, 0, 0.5).

1-3-9

Neutron diffraction under pressure in $CeRhIn_5$

N. Aso, K. Ishii, H. Yoshizawa, T. Fujiwara[A], Y. Uwatoko[B], G. F. Chen[C], N. K. Sato[C]
NSL-ISSP, Univ. of Tokyo, Graduate School of Sci. and Engineering, Yamaguchi Univ.[A],
ISSP, Univ. of Tokyo[B], *Graduate School of Sci., Nagoya Univ.*[C]

The interplay between magnetism and superconductivity (SC) is the interesting and important issue on condensed matter physics. In $CeRhIn_5$ [1, 2], it was very difficult to establish the coexistence of both two phases under pressure (P) because of the inhomogeneity of the P. There was open to argument if the coexistence is intrinsic.

Very recently G.G. Chen et al. [3] reported that high-quality single crystalline $CeRhIn_5$ display the SC at $T_{SC} \sim 90$ mK even under ambient P and its P-T phase diagram is drastically renewed. These findings indubitably indicate that the identical f electron plays both roles of SC and AFM. Therefore $CeRhIn_5$ is a very important material for the investigations on the coexistence of SC and AFM. To elucidate the coexistence mechanism of both SC and AFM, it is very useful to perform neutron diffraction under P which is a very powerful tool to directly determine the magnetic structure of the system.

The main goal of our study is to observe any changes through the SC transition temperature T_{SC} in $CeRhIn_5$. On the other hand, since the strong neutron absorption of Rh, In nuclei and pressure cell itself make the magnetic neutron diffraction under P extremely difficult, there has been little good information on the magnetic structure under P [4, 5].

In this work, we prepared a small CuBe-based pressure cell and succeeded in detecting magnetic reflections under P up to 1.5 GPa at the ISSP/GPTAS and HQR spectrometers in the research reactor JRR-3/JAEA. Figure 1 shows neutron diffraction profile thorough $Q = (0.5, 0.5, L)$ at $P \sim 0.25$ GPa. One can clearly recognized a pair of magnetic peaks at $L \sim 1.298$ and 1.702 at $T = 0.75$ K (below T_N), which are truly of magnetic origin since they disappear at 4.9 K (above T_N). Here we would like to emphasize that our results surpassed the past ones [4, 5] for the intensity of about 70 counts/min and SN ratio of ~ 1.3. These arise from the optimization of both the crystal and pressure cell sizes.

The incommensurability δ in the propagation vector $\tau = (0.5, 0.5, \delta)$ smoothly increase from 0.297 at $P = 0$ to 0.326 at 1.22 GPa, which is qualitatively different from the previous results. [4, 5] We believe that these difference comes from the used pressure transmitting media.

References

[1] H. Heeger *et al.*, *Phys. Rev. Lett.* **84**, 2986 (2000).
[2] T. Park *et al.*, *Nature* **440**, 65 (2006).
[3] G. F. Chen *et al.*, *Phys. Rev. Lett.* **97**, 17005 (2006).
[4] S. Majumdar *et al.*, *Phys. Rev.* **B** 66, 212502 (2002).
[5] A. Llobet *et al.*, *Phys. Rev.* **B** 69, 024403 (2004).

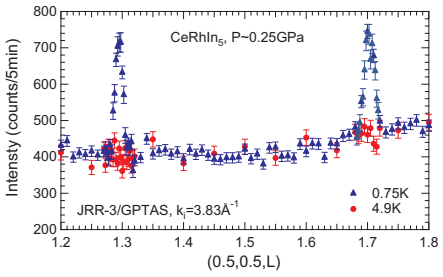


Fig. 1. Incommensurate magnetic Bragg reflections at $P \sim 0.25$ GPa.

1-3-10

Two-dimensional magnetic excitations in $CeRhIn_5$

N. Aso, H. Miyano, H. Yoshizawa, G. F. Chen[A], N. K. Sato[A]
NSL-ISSP, Univ. of Tokyo, Graduate School of Sci., Nagoya Univ.[A]

The interplay between magnetism and superconductivity (SC) is the interesting and important issue on condensed matter physics. Although it has been considered to be exclusive over quantum critical point (QCP), it is now widely accepted that both SC and antiferromagnetism (AFM) coexist in the vicinity of QCP in the systems of the pressure (P)-induced superconductor $CePd_2Si_2$, $CeIn_3$, and $CeRhIn_5$ [1, 2] and so on after a lot of energetic investigations. Since it, however, was very difficult to establish the coexistence of both two phases under P because of the inhomogeneity of the P, there was open to argument if the coexistence is intrinsic. Very recently G.G. Chen et al. [3] reported that high-quality single crystalline $CeRhIn_5$ display the SC at $T_{SC} \sim 90$ mK even under ambient P and its P-temperature (T) phase diagram is drastically renewed. These findings indubitably indicate that the identical f electron plays both roles of SC and AFM. Therefore $CeRhIn_5$ is a very important material for the investigations on the coexistence of SC and AFM. To elucidate the coexistence mechanism of both SC and AFM, it is very useful to perform inelastic neutron scattering which is a very powerful tool to directly observe the dynamical spin susceptibility (DS) of the system. The main goal of our study is to determine the wave vector dependence and its energy scale of the DS in $CeRhIn_5$, and to find out the connection between SC and the DS.

On the other hand, since the Rh and In nuclei are strong neutron absorbers, there has been little information on low-energy magnetic excitations by inelastic neutron scattering studies. In the last year, we succeeded in detecting the low energy magnetic excitations at the AFM ordering wave vector Q = (0.5, 0.5, 2.7) by using a lot of large single crystals of $CeRhIn_5$. [4]

This year we have been continuing to study the DS in $CeRhIn_5$ at the ISSP/HER spectrometer in the research reactor JRR-3/JAEA. Figure 1 shows inelastic neutron scattering spectrum at constant energy of $\hbar\omega$ = 0.8 meV in the (h, h, l)-zone at and T = 1.4 K. One can clearly recognize a strong intensity along the (0.5, 0.5, l) line, indicating that the low-energy magnetic excitation is a two-dimensional nature. We are now continuing to study the overview of the low-energy part of its DS in $CeRhIn_5$.

References

[1] H. Heeger *et al.*, *Phys. Rev. Lett.* 84 (2000) 4986; S. Kawasaki *et al.*, *Phys. Rev.* B 65 (2002) 20504; T. Muramatsu *et al.*, J. Phys. Soc. Jpn. 70 (2001) 3362.
[2] T. Park *et al.*, *Nature* 440 (2006) 65.
[3] G. F. Chen *et al.*, *Phys. Rev. Lett.* 97 (2006) 17005.
[4] N. Aso *et al.*, NSL-ISSP Activity Report **14** (2007) 227.

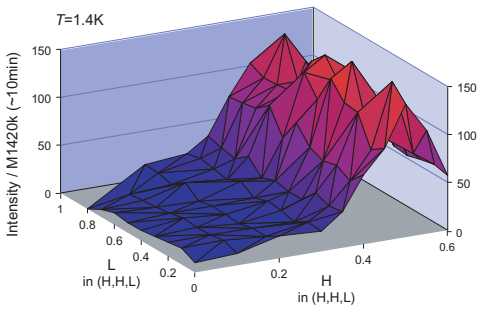


Fig. 1. Inelastic neutron scattering profiles in the (h, h, l)-zone at $\hbar\omega$ = 0.8 meV and T = 1.4 K.

1-3-11

Search for magnetic excitation in a heavy fermion superconductor $CeCoIn_5$

N. Aso, H. Miyano, H. Yoshizawa, T. Fujiwara[A], G. F. Chen[B], N. K. Sato[B]

ISSP, Univ. of Tokyo, Graduate School of Sci. and Engineering, Yamaguchi Univ.[A], *Graduate School of Sci., Nagoya Univ.*[B]

The interplay between magnetism and superconductivity (SC) is the interesting and important issue on condensed matter physics. A recently discovered series of $CeMIn_5$ (M = Rh, Co and Ir) has the highest SC transition temperature T_c = 2.3 K for heavy fermion materials. [1] It is believed that such a high T_c can be realized by strong antiferromagnetic (AFM) fluctuations. For example, $CeRhIn_5$ exhibits an incommensurate AFM ordering with the wave vector of τ= (0.5, 0.5, 0.297). [2] Very recently G.G. Chen et al. [3] reported that high-quality single crystalline $CeRhIn_5$ display the SC at $T_c \sim$ 90 mK even under ambient pressure (P) and its P-T phase diagram is also drastically renewed. These findings indubitably indicate that the identical f electron plays both roles of SC and AFM. Therefore $CeRhIn_5$ is a very importance material for the investigations on the coexistence of SC and AFM. To elucidate the nature of both SC and AFM, it is very useful to perform inelastic neutron scattering which is a very powerful tool to directly observe the dynamical spin susceptibility of the system.

In this context, we first succeed in observing the low-energy magnetic excitations in $CeRhIn_5$. [4] Inelastic neutron scattering spectrum at constant energy of $\hbar\omega$ = 0.8 meV in the (h, h, l)-zone and T = 1.4 K clearly showed a strong intensity along the (0.5, 0.5, l) line, indicating that the low-energy magnetic excitation is a two-dimensional nature. Thus the main goal of our study is to detect the low-energy magnetic excitations in $CeCoIn_5$ and to determine its energy scale of the dynamical susceptibility $CeCoIn_5$, and to compare them between $CeRhIn_5$ and $CeCoIn_5$.

Single crystals of $CeCoIn_5$ were grown by In-flux method. Inelastic neutron scattering experiments were carried out at 4G (GPTAS) and C1-1 (HER) spectrometers in the research reactor JRR-3. (*hhl*)-zone was selected as the scattering plane. The crystals with the total mass of $\sim$ 0.5 gram were aligned with the total area of $\sim$ 300 mm^2 and were cooled down to T = 1.5 K.

We observed very weak low-energy excitations below 1.5 meV at Q = (0.5, 0.5, 2.3), (0.5, 0.5, 2.5) and (0.5, 0.5, 2.7). Unfortunately we can not identify whether these intensities are Q-dependent nor identify that this signal is of magnetic origin. The possible reasons are that the used crystals are not enough for the inelastic neutron scattering study and that the temperature of 1.5 K is not low enough for T_c = 2.3 K.

Note: After our work, we noticed that the group of Collin Broholm detected the low-energy magnetic excitations around the commensurate AFM wave vector τ = (0.5, 0.5, 0.5) in $CeCoIn_5$ with total mass of $\sim$ 5 gram. A sharp spin resonance ($\hbar\Gamma <$ 0.07 meV) at $\hbar\omega$ = 0.60 $\pm$ 0.03 meV develops in the SC state and disappears above T_c. [5]

References

[1] C. Petrovic *et al.*, *J. Phys.: Condens. Matter* **13**, L337 (2001).

[2] W. Bao *et al.*, *Phys. Rev.* **B 62**, R14621 (2000); *ibid* **63**, 219901(E) (2001); *ibid* **67**, 099903(E) (2003).

[3] G. F. Chen *et al.*, *Phys. Rev. Lett.* 97 (2006) 17005.

[4] N. Aso *et al.*, NSL-ISSP Activity Report **14** (2007) 227; *ibid* **15** (2008) in these repot.

[5] C. Stock *et al.*, arXiv:0712.0172v1.

1-3-12

Correlation between ferromagnetism and superconductivity in UGe_2

N. Aso, S. Ban[A], K. Deguchi[A], T. Fujiwara[B], Y. Uwatoko[C], N. K. Sato[A]
NSL-ISSP, Univ. of Tokyo, Graduate School of Sci., Nagoya Univ.[A],
Graduate School of Sci. and Engineering, Yamaguchi Univ.[B], *ISSP, Univ. of Tokyo*[C]

Saxena *et al.* discovered the ferromagnetic (FM) superconductor UGe_2 in which superconductivity (SC) occurs at high pressure range between ∼1.0 and ∼ 1.5 GPa. [1]. In the FM phase, there seems to be another phase transition or crossover at T_x ($\simeq$ 32 K at ambient pressure). This characteristic temperature T_x also decreases with increasing P and becomes suppressed to zero at a critical pressure P_x ($\simeq$ 1.2 GPa) where a maximum SC transition temperature (T_{SC} $\sim$ 0.7 K) appears. In our previous work [2], we presented the temperature dependence of magnetic Bragg peak intensities under P by the neutron diffraction (ND) technique to reveal the nature of the transition at P_x. We have found that the low-T behavior of the uniform magnetization can be explained by a conventional Stoner model, indicating that the FM state below P_x can be understood as the perfectly polarized state.

Very recently, Ban *et al.* reinvestigated a SC phase diagram of UGe_2 by AC magnetic susceptibility measurements. [3] They found that the T_{SC} and volume fraction show a "M-shaped" structure as a function of P and suggested that both of two critical points play an important role in the occurrence of SC. These observations are possibly ascribed to the improved homogeneity of the P transmitting medium. To examine the correlation between SC and FM in UGe_2, we have to perform ND measurements by simultaneously detecting the superconductivity in UGe_2.

A single crystal was grown by Czochralsky pulling method with a tetra-arc furnace. The P was generated by a beryllium-copper pressure cell [4] using deutride methanol and ethanol mixture as a P transmitting medium. [2, 4] Coils of ac susceptibility measurements are wound in the outside of the cylinder as shown in fig. 1. The P was estimated by determining the T_{SC} of Sn. Elastic ND experiments has been performed on the triple-axis spectrometer PONTA (5G) at temperature down to 0.1 K using a dilution refrigerator.

In this study, although the pressure was tuned just at P_x, unfortunately only 20 % volume fraction of SC at 0.1 K were seen with T_{SC} ∼ 0.4 K in UGe_2. Furthermore we have to tilt the dilution fridge by ∼ 4 degrees and then the outer coil may touch the radiation shield of the fridge. Thus we are now analyzing the obtained neutron data.

References

[1] S.S. Saxena *et al.*, it Nature (London) **406**, 587 (2000).
[2] N. Aso *et al.*, *Phys. Rev.* **B 73**, 054512 (2006).
[3] S. Ban *et al.*, *J. Magn. Magn. Mater.* **310**, e120 (2007).
[4] N. Aso *et al.*, *AIP Conf. Proc.* **850** (2006) 705.



Fig. 1. Pressure cell together with the AC susceptibility coil.

1-3-13

Observation of magnetic form factor using detwinned single crystal of La_2CuO_4

H. Kimura[1], T. Adachi[1], Y. Noda[1], M. Fujita[2] and K. Yamada[2]
[1]*IMRAM, Tohoku University*
[2]*IMR, Tohoku University*

Imaging of spin density distribution has been tried to understand the 3*d*-electron orbital state which contributes to a large variety of physics in strongly correlated electron systems. A polarized neutron diffraction has been used for this trial and clarified the orbital order in ferromagnetic $YTiO_3$[1]. In the present study, we performed crystal- and magnetic structure analyses by using four-circle diffractometer with unpolarized neutron to observe accurate magnetic form factor of 3*d*-electron orbital. The target material of this study is La_2CuO_4 (LCO). LCO is an antiferromagnet with $3d^9$ configuration for Cu^{2+} ion and thus $S = 1/2$ spin should localize on $d_{x^2-y^2}$ orbital.

The single crystal of LCO was grown by TSFZ method. The crystal was cut and polished perpendicular to orthorhombic *a*-axis. The shaped crystal was heated above structural phase transition temperature from orthorhombic to tetragonal phase under uniaxial strain along *a*-axis to make the detwinned crystal in the orthorombic phase. As a result, we succeeded in obtaining 97 % detwinned single crystal of LCO. The measurements were performed using the four-circle diffractometer FONDER installed at T_{2-2} thermal guide in JRR-3M. The wavelength of neutron was 1.243 Å. The maximum values of $\sin\theta/\lambda$ for magnetic Bragg reflections were about 0.6 $Å^{-1}$.

Crystal structure analysis was firstly performed to obtain the exact scale factor, which was well solved with a reliability factor of $R = 4.2$ %. The magnetic structure with an assumption of $< j_0 >$ magnetic form factor was solved with $R_M = 16.9$ %. On the contrary, as shown in Fig. 1, F_{calc} derived using the magnetic form factor of $d_{x^2-y^2}$ orbital much better reproduces the F_{obs} comparing the case of $< j_0 >$ form factor. The present result is consistent with the results obtained from the magnetic form factor in Nd_2CuO_4[2].

References

[1] H. Ichikawa *et al.*: Physica B **281&282** (2000) 482.
[2] H. Kimura *et al.*: Physica B **385&386** (2006) 133.

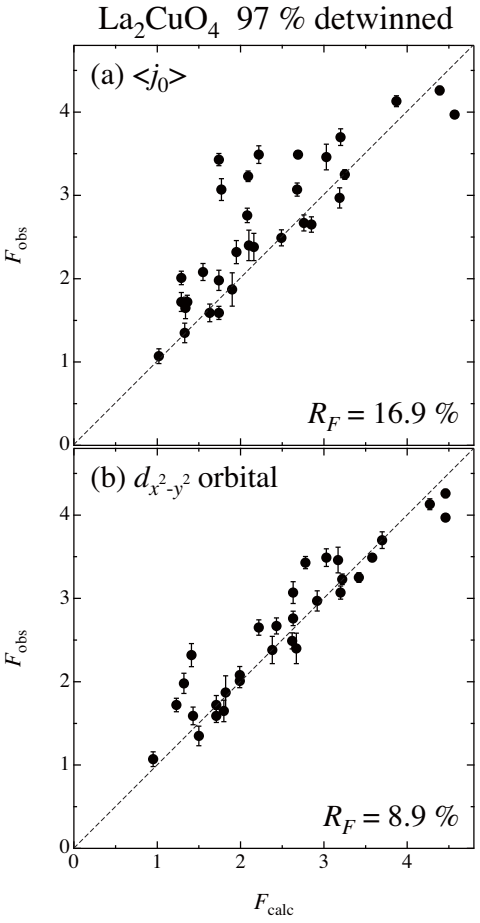


Fig. 1. F_{obs} *vs.* F_{calc} plot. F_{calc}'s are calculated using (a) isotropic $< j_0 >$ form factor and (b) anisotropic $d_{x^2-y^2}$ orbital.

1-3-14

Relation between low-energy phonons and a charge stripe order in $La_{2-x}Sr_xCu_{1-y}Fe_yO_4$

H. Kimura[1], Y. Ishikawa[1], Y. Noda[1], K. Enoki[2], M. Fujita[2] and K. Yamada[2]
[1]*IMRAM, Tohoku University*
[2]*IMR, Tohoku University*

It is well known that the charge stripe order in high-T_c cuprates competes with superconductivity. The previous neutron and X-ray diffraction studies have shown that the stripe order stabilizes only in La-214 compounds in which the concentration of doped hole is the vicinity of 1/8 and the crystal structure is so-called low-temperature tetragonal (LTT) or low-temperature less orthorhombic (LTLO). However, it was recently found in neutron and X-ray diffraction study that the charge stripe order is induced by substituting a small amount of iron with a large magnetic moment for copper, where the system is believed not to be the LTT or LTLO phase but to be the low-temperature orthorhombic (LTO) phase. This is the first discovery of magnetically induced charge stripe order in the LTO phase. However, the origin of this charge order is not clarified yet. In the present study, we measured soft phonons associated with the structural phase transition from the LTO to the LTT/LTLO, to confirm whether the structural phase transition into LTT/LTLO phase really occurs.

The single crystal of $La_{2-x}Sr_xCu_{1-y}Fe_yO_4$ with $x = 0.13$ and $y = 0.01$ (LSCFO) was grown by TSFZ method. Inelastic neutron scattering measurements for soft phonons were performed at triple-axis spectrometer HER installed at C_{1-1} cold neutron guide in JRR-3M. The final energy of neutrons was fixed at 4 meV with the energy resolution of 0.2 meV.

Figure 1 (a) shows the energy of soft phonons at $\mathbf{Q} = (1\ 0\ 4)$ as a function of temperature. Although the phonon becomes soft with decreasing temperature, there is no complete condensation of phonons down to $T = 10$ K and also no anomaly around $T = 55$ K ($\equiv T_{\rm charge}$), below which the charge stripe order occurs. This clearly shows that there is no structural phase transition below $T_{\rm charge}$ and the system retains the LTO structure. On the contrary, as shown in Fig. 1 (b), the linewidth in the phonon spectra starts narrowing below $T_{\rm charge}$, indicating that the life time of phonons gets longer in the stripe ordered phase. More systematic studies are required to clarify the relevance between the charge stripe order and the narrowing of the phonon.

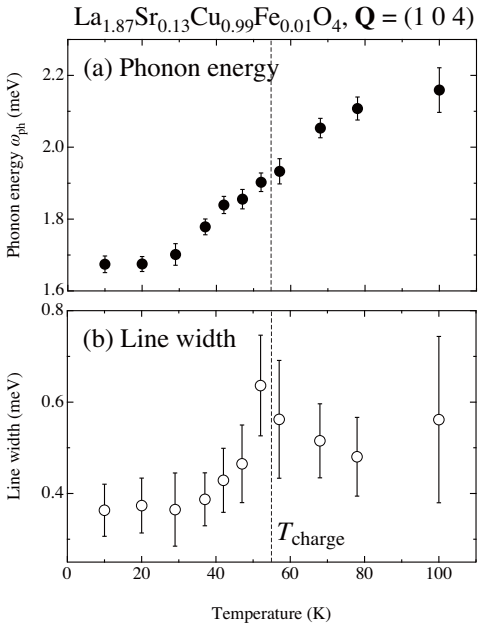


Fig. 1. Temperature dependences of (a) Phonon energy $\omega_{\rm ph}$ and (b) Line width for $(1\ 0\ 4)$ phonon.

1-3-15

Search for magnetic scattering in Fe and Pb co-doped Bi2201

H. Hiraka and K. Yamada
IMR, Tohoku University

There is no conclusion yet about the origin of attractive force that creates Cooper pairs and eventually high-T_c superconductivity. Recent inelastic neutron scattering studies revealed that the so-called "hourglass-like" magnetic dispersion relation commonly exists in La214 [1], Y123 [2], and Bi2212 [3] systems, thus indicating the magnetic interaction as a prime candidate of pairing mechanism. However, no magnetic cross section has been experimentally reported yet in one of the most typical cuprate superconductors, $Bi_2Sr_2CuO_{6+\delta}$ (Bi2201). So, we tried to find magnetic signals from this CuO_2 mono-layer system to establish universal features among high-T_c superconductors. Because Cu-site substitution enhances elastic and low-energy neutron magnetic scattering in La214 system [4, 5], we doped Fe atoms in this study by expecting a substantial impact on magnetic correlations due to its large magnetic moment. In addition, Bi atoms were partially substituted by Pb atoms, so that large single crystals (∼cm-size in length) could be easily grown by TSFZ techniques.

Neutron scattering experiments were carried out on triple-axis spectrometers AKANE and TOPAN using as-grown single crystals of $Bi_{1.74}Pb_{0.38}Sr_{1.88}Cu_{1-y}Fe_yO_{6+\delta}$ (y =0, 0.01, 0.03, and 0.05). Figure 1 shows a contour map of intensity difference of elastic scattering between 3 K and 300 K, measured on AKANE under the triple-axis mode using 3%-Fe doped sample around $(1,0,0)_{\rm ortho}$, or (π,π). A pair of broad peaks is clearly seen at $(0.8,\pm0.2,0)_{\rm ortho}$, in addition to the nuclear peak at $(1,0,0)_{\rm ortho}$. Later on, another pair was confirmed at $(1.2,\pm0.2,0)_{\rm ortho}$, and the same four-fold structure was observed in $(3,0,0)_{\rm ortho}$ zone with weak intensity. The onset temperature of this diffuse scattering (∼30 K) is comparable to that in spin-glasses of La214 [6]. These facts strongly support that this symmetric cross section has the magnetic origin. (Indeed, we confirmed it by polarized neutron experiments.) This magnetic scattering is incommensurate and similar to that in La214 system, except the large incommensurability ($\delta \sim 0.20$). We conjecture that Fe spins may reflect underlying magnetic modulations in pure Bi2201 system. Search for the dynamical magnetic component is now in progress.

References

[1] J.M. Tranquada *et al.*, Nature **429**, 524 (2004).
[2] C. Stock *et al.*, Phys. Rev. B **71**, 024522 (2005).
[3] B. Fauque *et al.*, cond-mat/0701052.
[4] K. Hirota *et al.*, Phys. B **241-243**, 817 (1998).
[5] H. Hiraka *et al.*, Phys. C **408-410**, 775 (2004).
[6] S. Wakimoto *et al.*, Phys. Rev. B **60**, R769 (1999).

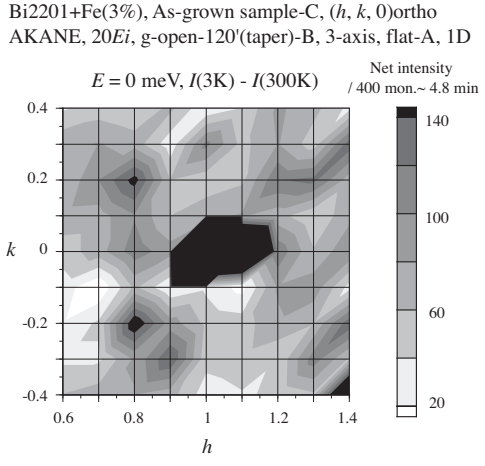


Fig. 1. Contour map of intensity difference of elastic scattering between 3 K and 300 K.

1-3-16

Magnetic Correlation in the Kondo-Semiconductor-like Material $CeOs_4Sb_{12}$

K. Iwasa[1], S. Itobe[1], M. Kohgi[2], C. Yang[1], K. Kuwahara[2], H. Sugawara[3], H. Sato[2], N. Aso[4]

Tohoku Univ.[1], *Tokyo Metropolitan Univ.*[2], *The Univ. of Tokushima*[3], *Univ. of Tokyo*[4]

$CeOs_4Sb_{12}$ has been considered as a Kondo semiconductor characterized by a band gap of around 10 K estimated from the temperature dependence of electrical resistivity, while it shows the large T-linear coefficient of specific heat γ = 200 mJ/K^2/mol (E. Bauer *et al.*: J. Phys.: Condens. Matter **13** (2001) 4495, H. Sugawara *et al.*: Phys. Rev. B **71** (2005) 125127). Previous inelastic neutron scattering experiment revealed no clear crystal filed excitation, in contrast to the Curie-Weiss behavior of magnetic susceptibility above 100?K (C. P. Yang *et al.*: J. Phys. Soc. Jpn. **74** (2005) 2862). It is notable that this material shows a phase transition at 0.9 K under zero magnetic field and the ordering temperature is enhanced by applied magnetic fields. The low-temperature magnetic instability is expected to be a formation of spin density wave (SDW) by the enhanced density of state at the Fermi level under magnetic field, as discussed in the theoretical arguments based on the periodic Anderson model (T. Ohashi *et al.*: Phys. Rev. B **70** (2004) 245104).

We performed neutron diffraction experiment using the triple-axis spectrometers TOPAN (6G) and HER (C1-1) and the dilution refrigerator of ISSP, Univ. of Tokyo. We succeeded in observing weak antiferromagnetic reflections characterized by the wave vector **q** = (1 0 0) below the ordering temperature. Assuming the magnetic ordering at the Ce-ion sites forming the bcc lattice, we evaluated the ordered moment magnitude of $(0.07 \pm 0.02)\mu_B$/Ce that is consistent with the SDW scenario. On the other hand, the antiferromagnetic peak disappears above 1 T in contrast to the reported enhancement of the transition temperature. The electronic state changes from the less-conductive state with the antiferromagetic ordering in the low field region to the metallic one above 1 T without the antiferromagnetic state. We have tried to identify an order parameter in the higher magnetic field region above 1 T, and carried out the polarized neutron diffraction using PONTA (5G) and TOPAN (6G). The observed flipping ratio intensities were transformed into the magnetic form factor, as shown in Fig. 1. Although the data points scatter owing to low statistics from the tiny magnetic moment even under magnetic moment, the overall feature against the scattering vector coincides with the calculated one for Ce^{3+} based on the dipole approximation shown by the solid line. No clear change was seen in the form factor across the phase boundary, thus the magnetic moment distribution has no trace of the ordering nature. We will continue the measurement to reveal the order parameter in the high magnetic field region.

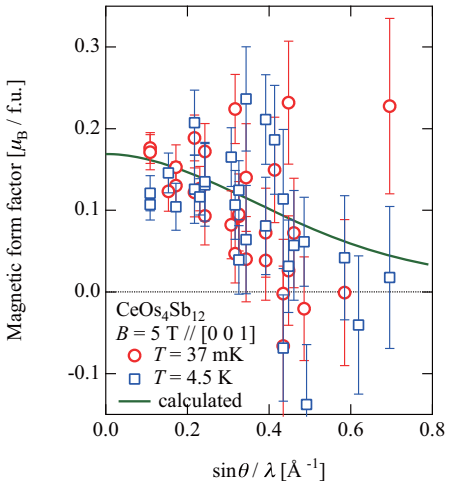


Fig. 1. Magnetic form factors of $CeOs_4Sb_{12}$ at 5 T.

1-3-17

Visualization of rattling in filled skutterudite compounds

K. Kaneko[A], N. Metoki[A,B], H. Kimura[C], Y. Noda[C], T. D. Matsuda[A], M. Kohgi[D]
[A]*Advanced Science Research Center, Japan Atomic Energy Agency*
[B]*Department of Physics, Tohoku University*
[C]*Institute of Multidisciplinary Research for Advanced Materials, Tohoku University*
[D]*Department of Physics, Tokyo Metropolitan University*

Filled skutterudite compounds LnT_4X_{12} where Ln is rare earth, T is transition metal and X is pnictogen, exhibit wide variety of physical properties by combination of Ln, T and X. Recently, large thermal vibration of a rare earth ion, so-called ratting, becomes one of the key issue as a possible origin of interesting physical properties including unconventional heavy-fermion superconductivity in $PrOs_4Sb_{12}$, Nd-based heavy-fermion behavior in $NdOs_4Sb_{12}$ and so on. In order to reveal detailed pictures of the rattling and its relationship with f-electron, single crystal neutron diffraction experiments on $PrOs_4Sb_{12}$ and $NdOs_4Sb_{12}$ were carried out on 4-circle diffractometer FONDER. The maximum entropy method is employed in the structural analysis to avoid arbitrariness, which was achieved using software PRIMA and VESTA.

Figure 1 shows obtained nuclear scattering length density (hereafter, nuclear density) distributions of $PrOs_4Sb_{12}$ and $NdOs_4Sb_{12}$ at room temperature. These results correspond to the space- and time averaged nuclear density reflecting thermal vibration. Taking into account the difference in the coherent scattering length between Pr and Nd, b_{Pr}=4.58 fm and b_{Nd}=7.69 fm, isosurface levels in Fig. 1 are set at 4.58 fm/Å^3 and 7.69 fm/Å^3 for(a) $PrOs_4Sb_{12}$ and (b) $NdOs_4Sb_{12}$, respectively.

Widely spread nuclear density distributions could be seen at the center of the cage, corresponding to Pr and Nd. Note that the shapes for both Pr and Nd are not spherical, namely, both ions exhibit anisotropic thermal motion. A contrast between Pr and Nd is found in anisotropy and magnitude of spatial extent. In $PrOs_4Sb_{12}$, the distribution of Pr has an almost cubic shape with the edge parallel to the ⟨100⟩ direction and the width is broadest along the ⟨111⟩ direction. The spatial extent of Nd distribution in $NdOs_4Sb_{12}$ is wider than that of Pr, and becomes rather isotropic. The width along the ⟨100⟩ direction is slightly larger than that along ⟨111⟩ in $NdOs_4Sb_{12}$, which is contrary to $PrOs_4Sb_{12}$. It should be pointed out that both ⟨100⟩ and ⟨111⟩ directions for Ln ion correspond to the voids of the Sb icosahedron cage. In contrast, the nuclear distribution of Os and Sb in $PrOs_4Sb_{12}$ quite resembles to those in $NdOs_4Sb_{12}$. Further diffraction studies on detailed temperature dependence and extension to $LaOs_4Sb_{12}$ could provide keen insights on anisotropy with regard to a role of $4f$ electron and its relationship to various physical properties.

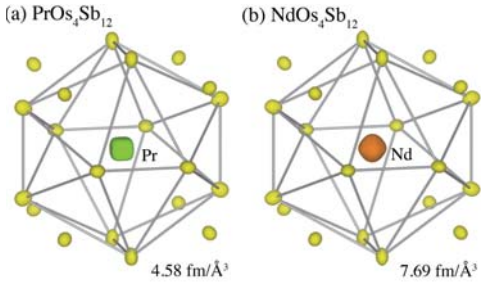


Fig. 1. Nuclear density distributions of $PrOs_4Sb_{12}$ and $NdOs_4Sb_{12}$ at room temperature.

Activity Report on Neutron Scattering Research: Experimental Reports **15** (2008)
Report Number: 433

1-3-18

Magnetic Excitation of Ferromagnetic System $NdFe_4P_{12}$ Exhibiting Heavy Electron Behavior

K. Iwasa[1], L. Hao[1], K. Saito[1], H. Sugawara[2], H. Sato[3]
Tohoku Univ.[1], *The Univ. of Tokushima*[2], *Tokyo Metropolitan Univ.*[3]

In the study of strongly correlated electron phenomena of rare-earth filled skutterudite compounds, heavy electron state in the system having two or more $4f$ electrons per rare-earth ion has been a topic. $PrFe_4P_{12}$ with $4f^2$ configuration of Pr^{3+} is a typical system, which shows the Sommerfeld coefficient for electronic specific heat γ = 1.4 J/mol/K^2 and the clear -log$T$ behavior of electrical resistivity (Y. Aoki *et al.*: Phys. Rev. B **65** (2002) 064446, H. Sugawara *et al.*: Phys. Rev. B **65** (2002) 134411). Our inelastic neutron scattering experiment revealed the quasielastic magnetic response indicating the strongly hybridized state (K. Iwasa *et al.*: Acta Physica Polonica B **34** (2003) 1117). A similar $-$ log$T$ behavior is also found in $NdFe_4P_{12}$ with $4f^3$ configuration of Nd^{3+} (H. Sato *et al.*: Phys. Rev. B **62** (2000) 15125). However, it undergoes a ferromagnetic phase transition at T_C = 1.9 K and the magnitude of ordered magnetic moment was evaluated as $1.6\mu_{B/Nd}$ (L. Keller *et al.*: J. Alloys and Compounds **323-324** (2001) 516), which is much larger than the typical heavy electron materials and seems not to be consistent with the singlet formation due to Kondo effect. Thus, the heavy electron behavior in electrical resistivity of $NdFe_4P_{12}$ together with well localized $4f$ electrons is a mysterious property. In order to investigate the $4f$ electron state of this material, we performed inelastic neutron scattering experiments. The triple-axis spectrometers TOPAN (6G) and HER (C1-1) were used to measure energy spectra from a single-crystalline sample.

Figure 1 shows energy spectra at **Q** = (0.85 0.85 0) of $NdFe_4P_{12}$ at 0.7 and 3 K above and below T_C, respectively. We observed a peak at 1 meV at 0.7 K and it disappears at 3 K above T_C. This peak can be assigned to a collective excitation in the ferromagnetic ordered state, and no distinct dispersion relation is detected near the ferromagnetic zone center **Q** = (1 1 0). It is indicative that the magnetic excitation has energy gap of 1 meV, which may come from the anisotropy of crystal field. The magnetic excitation is consistent with the ferromagnetic ordering, so that the anomalous behavior of $NdFe_4P_{12}$ can not simply be attributed to the magnetic Kondo effect.

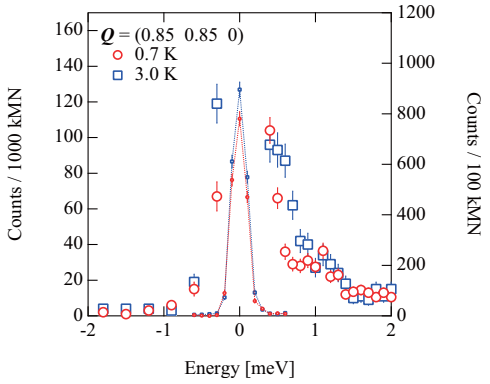


Fig. 1. Energy spectra at **Q** = (0.85 0.85 0) of $NdFe_4P_{12}$ at 0.7 and 3 K.

1-3-19

Crystal-field excitation in $Pr(Ru_{1-x}Rh_x)_4P_{12}$

K. Iwasa[1], K. Saito[1], L. Hao[1], Y. Murakami[1]
Tohoku Univ.[1]

Higher-rank multipolar ordering of $4f$ electron state of Pr-filled skutterudite has been a fascinating topic. $PrRu_4P_{12}$ is a typical system, in which the antiferro-type hexadecapolar (rank-4 multipolar) ordering occurs below the metal-nonmetal transition at 63 K. This phase transition is interpreted as a new type of charge density wave formation due to the Fermi surface nesting property strongly coupled with the modulated $4f$ multipolar arrangement. p-f hybridization between $4f$ and conduction electrons plays an essential role in the ordering mechanism. However, some properties have remained unsolved. The low-temperature resistivity does not diverge with decrease of temperature, and the nonmetallic state is easily suppressed by magnetic field of 1 T. The weak nonmetallic state is expected to originate from other mechanism in addition to p-f hybridization. The substitution of Rh to Ru gives rise to rapid suppress of metal-nonmetal transition; the electrical resistivity at low temperature in the Rh 10% system becomes the same magnitude at around 60 K. Thus, the doping effect is a key to understand the weak nonmetallic phase of $PrRu_4P_{12}$. Then we have carried out inelastic scattering experiments to measure crystal-field excitation of $Pr(Ru_{1-x}Rh_x)_4P_{12}$.

We performed the experiments using the triple-axis spectrometers HER (C1-1) and TOPAN (6G) for polycrystalline sample of $Pr(Ru_{1-x}Rh_x)_4P_{12}$ ($x = 0$, 0.03, 0.05, 0.10 and 0.15). Figure 1 depicts the low-energy spectra of the samples of x=0 and 0.03 at 7 K. The peak at 3.2 meV of the $x = 0$ sample corresponds to the exitation from the ground state triplet $\Gamma_4^{(2)}$ to the first excited state singlet Γ_1, which exhibit strong temperature dependence below the transition temperature. On the other hand, a strong peak at 2.4 meV in the data of the $x = 0.03$ sample appears, which is not observed in the $x = 0$ sample. The 2.4 meV peak is common for the Rh doped samples, and the excitation energy does not depend on temperature. Moreover, the integrated intensity increases with the increment of the Rh concentration. The Rh doping modifies the Pr $4f$ crystal-field levels not to shift against temperature variation, then the hexadecapolar ordering with the level shifts is suppressed. An additional $4d$ electron of Rh is expected to be doped in the conduction band. The metal-nonmetal transition of $PrRu_4P_{12}$ is sensitive not only to the p state originating from the pnictogen P but also to the $4d$ state by the transition-metal site.

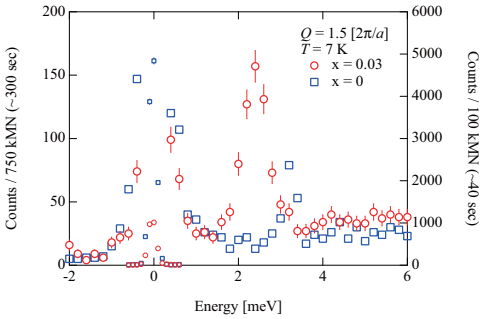


Fig. 1. Crystal-field excitations of $PrRu_4P_{12}$ and $Pr(Ru_{0.97}Rh_{0.03})_4P_{12}$ at 7 K.

1-3-20

Spin-lattice dynamics in rare earth antiferroquadrupolar ordering conpound HoB2C2

K. Ohoyama , H. Onodera(A), E. Matsuoka(A)
IMR, Tohoku Univ., Faculty Science, Tohoku Univ.(A)

The RB2C2 (R=rare earth) compounds, which have the tetragonal LaB2C2 type structure with P4/mbm symmetry, show diversified magnetic properties caused by coexistence of antiferroquadrupolar (AFQ) and antiferromagnetic (AFM) interactions. In particular, DyB2C2 is the first tetragonal rare earth compound in which an AFQ ordering is realised. Since the exact ground state by crystalline electric field under tetragonal symmetry has no degree of freedom on electric quadrupolar moments, it was thought that no AFQ ordering can be realised in the tetragonal rare earth compounds.

On the contrary, we have proved that some of RB2C2 are AFQ ordering compounds with higher TQ than other typical AFQ compounds. Thus, to understand necessary conditions of AFQ orderings in rare earth compounds, it is indispensable to clarify characters of the AFQ ordering in RB2C2. Of the RB2C2 system, HoB2C2 is particularly unique because of the following points: (i) the AFQ ordering in HoB2C2 is realised at TQ=4.5K below the magnetic ordering temperature, TN=5.9K[2], (ii) anomalous magnetic diffuse scattering is observed above TQ up to 2TQ[3].

To understand the magnetic properties of HoB2C2 around the transition temperatures, we think clarifying spin-lattice dynamics is indispensable because magnetism and lattice is strongly coupled though the strong LS coupling. Therefore, we performed inelastic scattering experiments to observe higher energy excitations on 6G, and low-energy excitations on C1-1. In 2007, we succeeded in observing dispersion relations of some modes of magnetic excitations below 4meV in the ordered state. Figure 1 shows dispersion relations from the (100) to (101/2) reciprocal position at T=1.56K observed on C1-1. We found two magnetic modes at about 3meV and 0.8meV at the zone centre (100). The lower excitation shows obvious dispersion, while the dispersion of the higher mode is relatively weak. We also observed dispersion relations along the a*-direction.

From the temperature dependence of the magnetic excitation spectra, we confirmed that the lower mode becomes weak near the transition temperatures, and disappears above the transition temperatures, indicating that the lower dispersive mode is important for the AFQ and AFM ordering in HoB2C2.

References

[1] H. Yamauchi et al.: J. Phys. Soc. Jpn. 68 (1999) 2057.
[2] H. Onodera et al.: J. Phys. Soc. Jpn. 68 (1999) 2526..
[3] A. Tobo et al.: Physica B 312-313 (2002) 853-854.

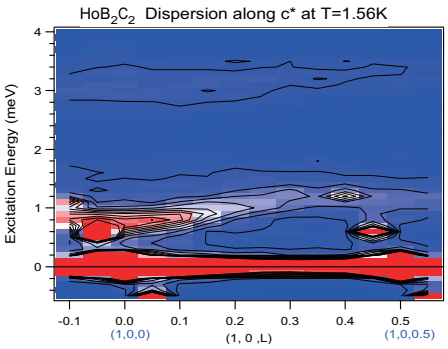


Fig. 1. Dispersion of magnetic excitations along the c* direction in HoB2C2 at T=1.56K

1-3-21

Coexistence of superconductivity and magnetism in a multi-layered cuprate

C. H. Lee(A), A. Iyo(A), K. Kihou(A), H. Kito(A) and K. Yamada(B)
(A) AIST, (B) IMR Tohoku Univ.

One of the most significant feature in high-Tc cuprates is that superconductivity is inextricably linked with antiferromagnetism. Crucial issue for understanding the mechanism of cooper pairs formation is whether the same carrier is responsible for both magnetic long range ordering and superconductivity. Recently, NMR and uSR measurements show that antiferromagnetism exists in superconducting phase of multilayered cuprates. In particular, NMR measurements suggest that antiferromagnetism coexists with superconductivity microscopically on a single CuO2 plane in underdoped HgBa2Ca4Cu5O12+d. Experiments using diffraction technique are highly required to clarify whether it is a long range ordering or not.

Neutron scattering measurements were carried out using a powder diffractometer, HERMES, and a triple-axis spectrometer, AKANE, at the JRR-3 reactor of JAEA at Tokai. On the experiments with HERMES, the incident neutron wavelength was fixed at 1.8265 A using (311) reflection of the Ge monochromator. The sequences of horizontal collimators were 12′-blank-S-22′ where S denotes the sample position. On the other hand, on the expermiments with AKANE, the incident neutron wavelength was fixed at 2.044 A using a pyrolytic graphite (PG) monochromator. The sequences of horizontal collimators were 12′-blank-S-15′. Powder of HgBa2Ca4Cu5O12+d was used as a sample.

Fig. 1 shows spectra of theta-2theta scan in HgBa2Ca4Cu5O12+d sample at T=12K and 300K. A peak around 2theta = 15.7 at T = 12K is also observed at T=300K, indicating that the peak include a fundamental nuclear peak of (003) or even some impurity phases. Even if magnetic component exists, the intensity should be quite small comparing to the observed peak intensity. A solid line depicts calculated spectra assuming magnetic moment of Cu atoms on inner CuO2 plane as 0.67uB estimated by NMR measurements. Clearly, such a well defined magnetic peak is not observed, indicating that the magnetic moment should be quite small. We also checked that well defined magnetic peak is not observable in a wide 2theta region.

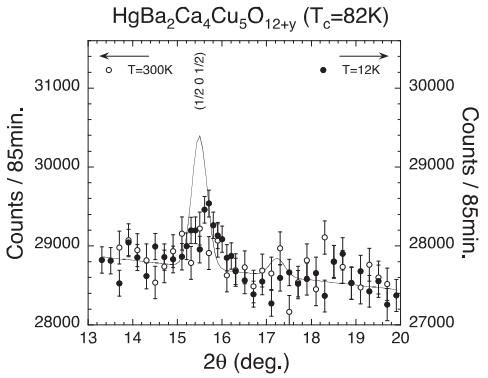


Fig. 1. Spectra of theta-2theta scan in HgBa2Ca4Cu5O12+d at T=12K and 300K. A solid line depict the result of simulation assuming 0.67 uB as magnetic moment of Cu atoms on inner CuO2 plane.

1-3-22

Flux line lattice in $ErNi_2B_2C$

H. Kawano-Furukawa, R. Nagatomo, S. Konno, S. Ohira-Kawamura, H. Yoshizawa[a] and H. Takeya[b]

Ochanomizu Univ., ISSP NSL Univ. of Tokyo[a] and NIMS[b]

In ferromagnetic superconductors, an internal magnetic field H_{int} mediated by the ferromagnetic moments may lead a spontaneous vortex phase [1,2,3]. But there is no experimental report for a realization of the phase so far.

$ErNi_2B_2C$ ($T_c \sim 10.5$ K, $T_N \sim 6$ K, $T_{WFM} \sim 2.3$ K) is one of possible candidates for the spontaneous vortex phase, because H_{c1} of the system shows an abrupt decrease below T_{WFM} and it seems to become zero at around 1.8K, which satisfies the condition of the spontaneous vortex phase [4,5,6,7]. To check this possibility, we started to study the flux line lattice on $ErNi_2B_2C$ by a small angle neutron scattering (SANS) technique.

In this study, we used un-anealed single crystals of $ErNi_2^{11}B_2C$ ($T_c \sim 8.6$ K) grown by a floating zone method. The SANS experiments were performed at the SANS-U spectrometer in JRR-3, JAERI, Japan. External fields H_{ext} were applied parallel to both the crystallographic b axis and the incident neutron beam. Neutrons with wavelength λ_n = 11 Å were selected by a velocity selector, and an area detector at the end of a 16 m long evacuated chamber counted neutrons scattered by the FLL. To maximize neutron transmissions the sample were cut with 1 mm thickness along the neutron beam.

Figures show temperature dependence of FLL diffraction patterns observed under H_{ext} = 6400 Oe. The upper panels show data measured after field cooled processes (FC) but the bottom ones were recorded after field cooled and oscillated processes (FCO). Down to 4K, all figures show rhombic FLL patterns. However, at lower temperatures, these two processes give different results. Namely, the FLL patterns after the FC processes remain the rhombic FLL but those after the FCO processes show cubic one. From this result, we lead two conclusions: (1) the rhombic FLL in FC process is due to vortex pinning and (2) an oscillation field of 800 Oe is enough to release the vortex pinning. From the present study, we succeeded in construction of a phase diagram of the FLL structure on $ErNi_2^{11}B_2C$.

We are on the process to verify the spontaneous vortex phase in this compound and the further experiments are planed.

[1] E. I. Blount et al., Phys. Rev. Lett. 42, 1079 (1979).

[2] M. Tachiki et al., Solid State Commun. 31, 927 (1979); ibid. 34, 19 (1980).

[3] H. S. Greenside et al., Phys. Rev. Lett. 46, 49 (1981).

[4] H. Kawano et al., J. Phys. Chem. Solids 60, 1053 (1999).

[5] T. K. Ng et al., Phys. Rev. Lett. 78, 330 (1997).

[6] H. Kawano-Furukawa et al., in Rare Earth Transition Metal Borocarbides (Nitrides): Superconducting, Magnetic and Normal State Properties, Vol. 14 of NATO advanced Study Institute, Series II, edited by K. H. Muller and V. Narozhnyi (Kluwer Academic, Dordrecht, 2001), p. 223.

[7] Mariko V. Jarić, Phys. Rev. B 20, 4486 (1979).

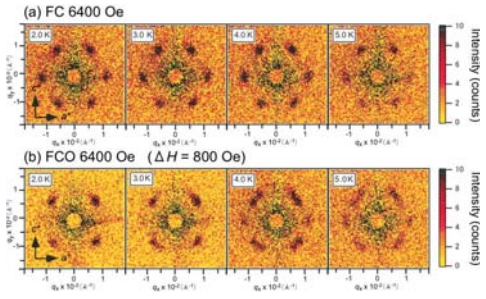


Fig. 1. Temperature dependence of FLL patterns after FC and FCO processes.

1-3-23

Magnetic and electronic nature of metallic ferromagnet Sn2Co3S2 and its related compounds

M. Matoba, A. Umetani, E. Nagoshi, S. Nakajima, and T. Kubodera
Center for Applied Physics and Physico-Informatics, Keio University, 3-14-1 Hiyoshi, Yokohama 223-8522

Pyrite- and shandite-type Co disulfides are both mineral-related materials that can be artificially synthesized. Pyrite-type ferromagnetic CoS2 (TC=120K) and its related compounds have been the subject of the intense research because of their variety of interesting physical properties [1] to reveal their correlated electron nature. On the other hand, few studies have been made of shandite-type ferromagnetic Sn2Co3S2 (TC=177K) [2-4].

Recently, crystallographic and electronic structure effects in (Sn,In)2Co3S2 has been investigated by X-ray diffraction (XRD) and local spin density approximation (LSDA) band calculations to discuss its structural nature from the viewpoint of the half antiperovskite (SnCo3/2S) [3]. However, electronic and magnetic properties of Sn2Co3S2 has not been examined in detail beyond LSDA and the electronic bonding nature is not clear. In this paper, we report the hitherto unknown magnetic and electronic nature of shandite-type A2Co3S2 (A=Sn, In) as the strong correlated electron system (SCES).

Polycrystalline A2Co3S2 (A=Sn, In) samples were carefully prepared by a solid state reaction method in a evacuated quartz tube [4]. Obtained samples were characterized by powder XRD, powder neutron diffraction (PND) by the high efficiency and high resolution measurements (HERMES) [5], and Rietveld analysis using the programs Rietan2000 and PRIMA [6]. The electronic and magnetic nature were analysed by XPS spectro- and SQUID magnetometers, and the electronic structure of Sn2Co3S2 was calculated by LSDA+U method (the LMTART code [7]).

Figure 1 (top-left panel) displays Co 2p core-level XPS spectra of Sn2Co3S2 in comparisson with those of reference compounds [8-10]. One can see that each of spin-orbit components (2p3/2 and 2p1/2 peaks) indeed shows a strong satellite feature at higher binding energy side of the main peak. Co 2p XPS spectrum of Sn2Co3S2 exhibits a complicated feature, and it can be considered as the spectrum with two shape components by XPS peak shape analysis. In the top-left panel of Fig.1, the solid curve (a) is the total estimated spectrum with two shape components (curves (b) and (c)), demonstrating the very good agreement between experimental and calculated spectra of Sn2Co3S2. The shape of component (b) is similar to main peak shapes of Co and TlCo2S2; the shape of component (c) resembles the satellite shape of TlCo2S2, and is quite similar to that of strongly correlated Co compound K2CoF4. These feature might contain some information on the Co-Sn/Co-S bonding nature and the electron correlation in Sn2Co3S2. Thus, the effects of metallic Co-Sn and inoic/covalent Co-S bondings are considered to be seen as the complicated feature in the Co 2p XPS spectra. This is indeed similar to the situation in ThCr2Si2-type TlCo2S2 indicating that the effect of Co-S bonding is seen as satellite structures in the Co 2p XPS spectra [10]. We therefore analyzed the spectrum by the configuration interaction cluster model [8] to estimate the on-site d-d Coulomb repulsion energy U=4 eV, indicating that the electronic nature of the Co3S2 units in Sn2Co3S2 belongs to SCES.

The bond-valence-sum (BVS) calculation [11] was carried out to evaluate the valence state of the Co ions (formal charge of Co is 1.14) indicating that Co atoms have mixed valence; the ratio (Coˆ{0+}:Coˆ{2+})

Activity Report on Neutron Scattering Research: Experimental Reports **15** (2008)
Report Number: 491

is roughly 1:2. The mixed valence like complicated feature of Co 2p XPS spectrum of Sn2Co3S2 would be explained by two different metallic Co-Sn and ionic/covalent Co-S bondings. Figure 1 (bottom panel) dispalys electron-density maps obtained by maximum entropy method (MEM)-based whole pattern fitting and LSDA+U calculation to suggest the layered structural nature and reveal that electron density at the saddle point in Co-S bond is indeed three times larger than those of Co-Sn bonds, indicating the difference of Co-Sn/Co-S bonding nature and supporting the BVS result.

Finally, we would like to comment the electronic nature of (Sn,In)2Co3S2 in which TC is gradually decreased with x to be zero at x=1. Fig.1 (top-right panel) shows magnetic susceptibilities and electrical resistivities of (Sn,In)2Co3S2. Interestingly, Rietveld refinement of XRD and PND indicates that Sn atoms on the Sn1(3a) site are regioselectively substituted by In atoms for Sn2Co3S2. Furthermore, the ferromagnetic metal to pseudo-gap semiconductor transition is indeed observed at x=1 in (Sn,In)2Co3S2. Further experimental and theoretical studies of the spin, charge and orbital degrees of freedom for Sn2Co3S2 as SCES would be of great interest, and the so-called chemical tuning research is now in progress.

References

[1] S. Ogawa, J. Appl. Phys. 50, 2308 (1979).
[2] S. Natarajan et al., J. Less. Common. Metals. 138, 215 (1988).
[3] R. Weihrich and I. Anusca, Z. Anorg. Allg. Chem. 632, 1531 (2006).
[4] T. Kubodera et al., Physica B 378-380, 1142 (2006).
[5] K. Ohoyama et al., Jpn. J. Appl. Phys. 37, 3319 (1998).
[6] F. Izumi and T. Ikeda, Mater. Sci. Forum, 321-324, 198 (2000).
[7] S. Y. Savrasov, Z. Kristallogr. 220, 555 (2005).
[8] A. Fujimori et al., J. Electron. Spectrosc. Relat. Phenom. 62, 141 (1993).
[9] L. Sangaletti, F. Parmigiani, and E. Ratner, Phys. Rev. B 57, 10175 (1998).
[10] M. V. Yablonskikh et al., J. Phys. Condens. Matter 18, 1757 (2006).
[11] J. L. Tallon, Physica C 168, 85 (1990).

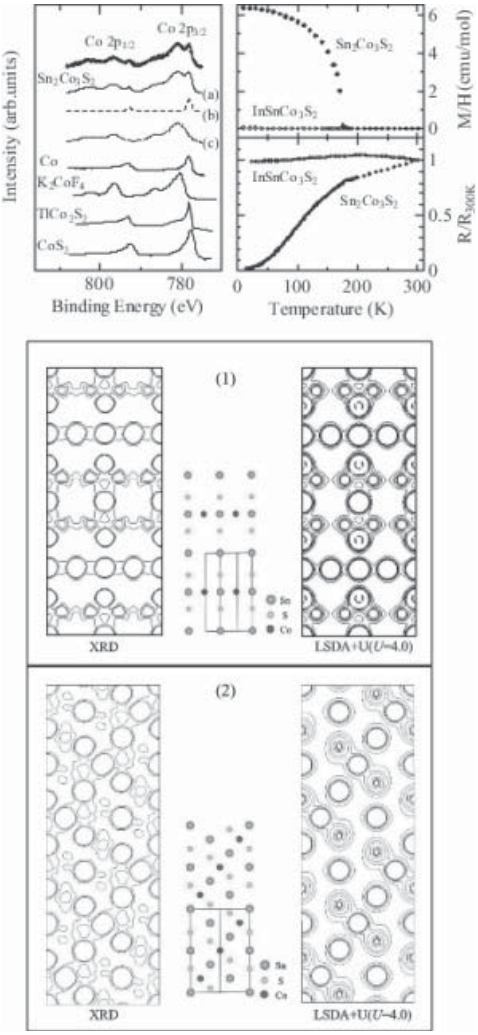


Fig. 1. (Top) Co 2p XPS spectra, magnetic susceptibilities, electrical resistivities, and (bottom) electron-density maps in (100) and (110) planes of Sn2Co3S2.

1-3-24

Charge and spin ordering in La1.85Ca0.15CoO4.17

K. Horigane, H. Haruhiro*, K. Yamada* and J. Akimitsu
Department of Physics and Mathematics, Aoyama-Gakuin University, Sagamihara 229-8558;
**Institute for Materials Research, Tohoku University, Sendai 980-8577*

In the neutron scattering experiments of layered cobaltate, we studied the hole-doping dependence of the charge and magnetic orderings[1]. Charge order peaks were insensitive to x, while the magnetic diffraction pattern changed dramatically below and above x=0.5. The type-1 reflections arised below x=0.5, whereas it switches to the type-2 reflections avobe x=0.5. From these results, we found that the type-1 and 2 stacking domains were changed by Ca doncentration or Co-valence. However, it is not straightforward to understand the origin of magnetic structure by Ca doping. In order to understand the essence for magnetic domains in this system, we examined the charge and magnetic ordering in excess oxygen system La1.85Ca0.15CoO4.17, of which cobalt valence is about Co2.5+.

Single crystal of La1.85Sr0.15CoO4.17 was grown by the TSFZ method, of which volume was about 1.0 cc. It was mounted in a refrigerator with the b-axis vertical, allowing to observe the (h,0,L) reciprocal lattice plane. To index the superlattice peaks, we use a unit cell with dimensions $\sqrt{2}a \times \sqrt{2}a \times c$. The neutron scattering experiments were carried out on the 3-axis spectrometer TOPAN(6G). The incident neutron energy was fixed to be Ei=30.5meV, typecally with a sequence of collimation of blank-30'-60'-blank.

Figure 1-(a) shows the charge order spectrum of (1,0,L). An integer-peak structure was clearly observed, and it is consistent with the checkerboard-type charge order in La1.5Ca0.5CoO4. If the Ca concentration is essential for magnetic domains, it is expected that magnetic peaks due to type-1 stacking are only observed. Figure 1-(b) shows the magnetic scattering in La1.85Ca0.15CoO4.17. We observed the strong intensity at L=half-integer. This result indicates that type-1 stacking domain is dominant in a lower doping range, suggesting that the magnetic domains are changed by Ca concentration around x=0.5. To understand the relationship, we should study other cobaltates which are substituted at A-site with various rare-earth and alkaline earth metals.

Reference

[1] K. Horigane et al.: JPSJ 76 (2007) 114715.

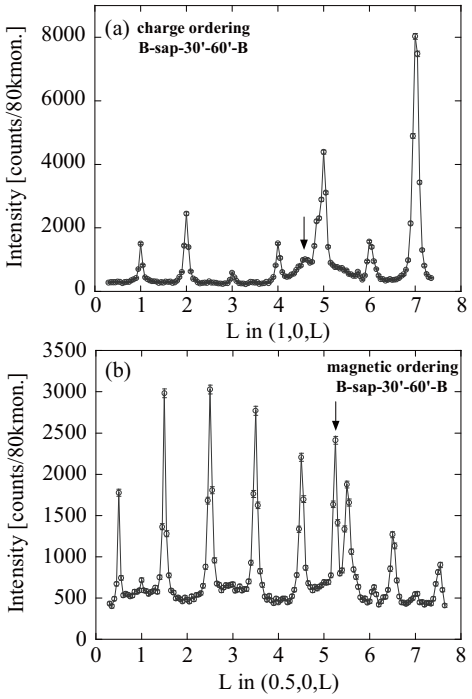


Fig. 1. (a)Structural scattering due to checkerboard charge order at (1, 0, L) in La1.85Ca0.15CoO4.17. The arrow indicate aluminum scattering. (b)Magnetic peaks at (0.5, 0, L) in La1.85Ca0.15CoO4.17.

1-3-25

Lattice effects on the charge-spin ordering in layered cobaltates R1.5Sr0.5CoO4

K. Horigane, H. Haruhiro*, K. Yamada* and J. Akimitsu
Department of Physics and Mathematics, Aoyama-Gakuin University, Sagamihara 229-8558;
**Institute for Materials Research, Tohoku University, Sendai 980-8577*

Layered transition metal oxides have been much attention due to their wide variety of magnetic, electrical and structural properties. In some of the doped transition metal compounds, there is a real space ordering due to the charge carriers in a certain carrier concentration, resulting in an orbital ordering (OO) and sometimes a charge ordering (CO). In a recent neutron scattering study, Zaliznyak el al. investigated a short ranged checkerboard charge order of Co2+/Co3+ (ξ co=23 Å) and magnetic order at L=odd in the half-doped cobaltate La1.5Sr0.5CoO4 (LSCO:rA=1.19 Å) [1]. More recently, we performed neutron scattering experiments on La1.5Ca0.5CoO4 (LCCO: rA=1.15 Å) [2]. Comparing the results between LSCO and LCCO systems, we found that long-ranged checkerbord charge order (ξ co(Ca)=115 Å) and new type of magnetic reflections at L=half-integer were observed in LCCO system. Our purpose of this study is to clarify the relationship between A site radius, rA, and charge-spin ordering. Thus, we studied about charge and magneic orderings in Nd1.5Sr0.5CoO4(NSCO: rA=1.16 Å) system.

Single crystal of Nd1.5Sr0.5CoO4 was grown by the TSFZ method, of which volume was about 1.0 cc. It was mounted in a refrigerator with the b-axis vertical, allowing to observe the (h,0,L) reciprocal lattice plane. To index the superlattice peaks, we use a unit cell with dimensions $\sqrt{2}a \times \sqrt{2}a \times c$. The neutron scattering experiments were carried out on the 3-axis spectrometer AKANE(T1-2).

Figure 1-(a) shows structural scatterings due to checkerboard charge ordering of R1.5Sr0.5CoO4 (R=La, Nd) in (1, 0, L). We observed the scatterings with L=integer in Nd system, while those of intensity in La system was very small. This result indicate that A site radius, which corresponds to bandwidth, is coupled with the charge order in layered cobaltates.

Magnetic scatterings at q=(0.5, 0, L) in Nd1.5Sr0.5CoO4 is shown in Fig.1-(b). We observed scatterings with L=odd, and this result is same as that of LSCO system. Contrary to the case of charge ordering, magnetic ordering is hardly coupled with A site radius.

Reference

[1] I. A. Zaliznyak et al.: PRL 85 (2000) 4353.
[2] K. Horigane et al.: JPSJ 76 (2007) 114715.

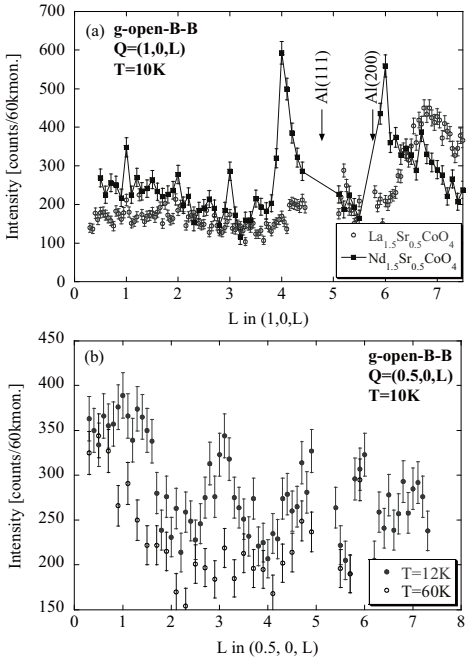


Fig. 1. (a)Structural scattering due to checkerboard charge order at (1, 0, L) in R1.5Sr0.5CoO4. The arrows indicate aluminum scattering. (b)Magnetic peaks at (0.5, 0, L) in Nd1.5Sr0.5CoO4.

1-3-26

Cycloidal Spin Order in (Gd,Tb)MnO3 with Electric Polarization along the a-Axis

H. Sagayama(A), N. Abe(A), K. Taniguchi(A), T. Arima(A), Y. Noda(A), M. Soda(B), M. Matsuura(B), K. Hirota(B), Y. Yamasaki(C), D. Okuyama(D), Y. Tokura(C,D)
(A)IMRAM, Tohoku Univ., (B)ISSP, Univ. Tokyo, (C)Dept. Appl. Phys., Univ. Tokyo, (D)ERATO-MF, JST

In a orthorhombically distorted perovskite $TbMnO_3$, ferroelectric polarization appears along the c axis below $T_C \sim 27$ K. The polarization flops by 90 degrees to the a direction by the application of a magnetic field along the b or a axis. This magnetically-induced polarization flop should be regarded as a magnetic phase transition accompanied by the ferroelectric transition.

The zero-field magnetic state below T_C was pinned down to a cycloid with the spin spiral plane perpendicular to the a axis. The cycloid should induce electric polarization through the inverse effect of Dzyaloshinski-Moriya (DM) interaction. In contrast, the magnetic structure of the high-field phase was not settled yet. From the theoretical point of view, there are at least two possible spin arrangements which can induce electric polarization along the a axis. One is of the cycloid type with the spiral plane perpendicular to the c axis, and the other is of the commensurate collinear type with the propagation vector (0 1/4 1). A synchrotron x-ray diffraction measurement in high magnetic fields revealed that the propagation vector changes from incommensurate ($0 \approx 0.27$ 1) to commensurate (0 1/4 1). Judging from the phase diagram of the $Gd_{1-x}Tb_xMnO_3$, the origin of the ferroelectric polarization along the a axis should be common to the high-field phase of $TbMnO_3$ and the zero-field phase of $Gd_{1-x}Tb_xMnO_3$ with $x \sim 0.3$. As a full analysis of the magnetic structure in a high magnetic field is not easy, we investigated the magnetic structure of $Gd_{1-x}Tb_xMnO_3$.

A single crystal of $^{160}Gd_{0.7}Tb_{0.3}MnO_3$ was grown by a floating zone method. Intensity data of magnetic reflections were collected at 15 K by using a four-circle neutron diffractometer FONDER. The wavelength of 1.24Å was used for the measurement. The absorption of the neutron beam by the crystal was 5.80/cm. Spin polarized neutron diffraction measurements were performed with a triple-axis spectrometer PONTA. The intensity of a magnetic reflection (0 1/4 3) were investigated for the incident neutron spin parallel and antiparallel to the scattering vector. In this configuration, the c component of the spin vector chirality should cause a difference in the intensity.

Figure 1 shows the profiles of magnetic satellites at $Q_s = (0\ 1/4\ 3)$ for the ferroelectric state at 20 K after cooling in an electric field. The intensity clearly depends on the neutron spin direction. This result evidently indicates the chiral spin structure in $Gd_{0.7}Tb_{0.3}MnO_3$. The magnetically induced polarization flop in $TbMnO_3$ is ascribed to the flop of spiral plane around the b axis.

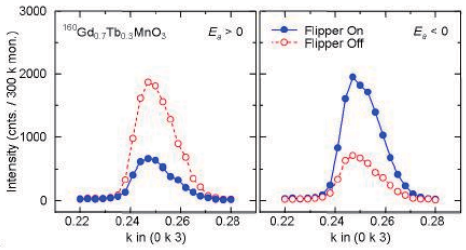


Fig. 1. Profiles of a magnetic reflection (0 1/4 3) in $^{160}Gd_{0.7}Tb_{0.3}MnO_3$ with the incident neutron spin polarized (open red circles) parallel and (solid blue circles) perpendicular to the scattering vector.

1-3-27

Correlation between Electric Polarization and Sence of Helix in $MnWO_4$

H. Sagayama(A), N. Abe(A), K. Taniguchi(A), T. Arima(A), M. Soda(B), M. Matsuura(B), K. Hirota(B)
(A)IMRAM, Tohoku Univ., (B)ISSP, Univ. Tokyo

In a magnetoelectric compound $MnWO_4$, sinusoidal incommensurate antiferromagnetic ordering of the Mn^{2+} moments takes place at $T_{N1} = 13.5$ K with a magnetic wave vector with $k \approx (-0.214\ 1/2\ 0.457)$. The ferroelectric polarization along the b axis (P_b) emerges upon the magnetic phase transition from collinear to spiral spin structure at $T_{N2} = T_C = 12.7$ K. Below $T_{N3} = 7.6$ K, the spin structure alters into a commensurate collinear type with k =$(-1/4,\ 1/2,\ 1/2)$ and the ferroelectricn polarization is dismissed. We report here the quantitative elucidation of such magnetically induced ferroelectricity in terms of the spin ellipticity as the order parameter and show the successful electric control between the clockwise (CW) and counter-clockwise (CCW) spin helixes.

Spin-polarized neutron diffraction measurements were performed with a triple-axis spectrometer PONTA at JRR-3. A single crystal was mounted on a sapphire plate in a closed-cycle helium refrigerator and irradiated with a spin-polarized neutron beam. A Heusler monochromator was utilized to obtain the spin-polarized neutron beam. The spin of the neutron beam could be flipped by a spin-flipper, so as to be parallel or anti-parallel to the scattering vector Q_s with a guide-field of about 10 gauss applied by a Helmholtz coil.

All the neutron diffraction measurements were performed in zero electric field after cooling the sample from the paramagnetic phase in a poling electric field. Peak profiles of magnetic satellite reflections with Q_s =$(-1\ 0\ 2)\pm k$ were measured along the $(-1\ 0\ 2)$ line in the reciprocal lattice.

Figure 1(a) shows the profiles of the magnetic satellites for the ferroelectric state at 9 K. The flipping ratios are far from one only for the ferroelectric phase ($T_{N3} < T < T_{N2}$). Moreover, the result shows that the sense of the spiral is controlled by the ferroelectric polarization direction. Such a behavior seems to be common to the recently discovered magnetic ferroelectrics. However, the short principal axis of the spiral of $MnWO_4$ at 8K is estimated to be more than 90 % of the long axis. This is rather a contrast to the case of $TbMnO_3$, where the spiral is more elliptic with $m_c/m_b \sim 0.7$. The small ellipticity in this material is advantagious for the investigation of low energy excitations in the multiferroic.

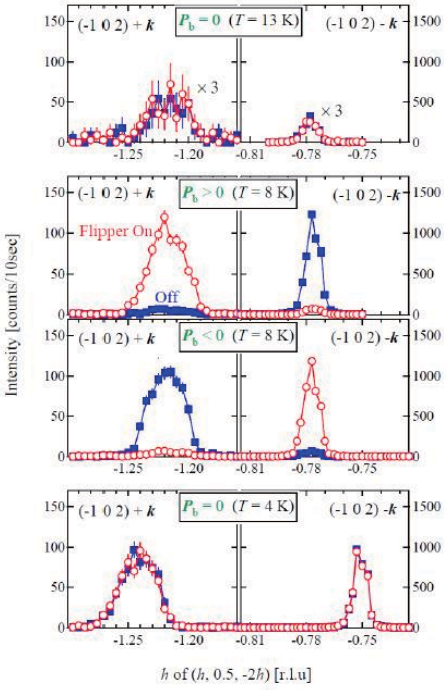


Fig. 1. Profiles of magnetic satellites $(-1\ 0\ 2\ )\pm k$ in three magnetic phases.

1-3-28

Magnetic excitations of NaxCoO2.yD2O

Taketo Moyoshi, Yukio Yasui, Masatoshi Sato and Kazuhisa Kakurai1
Nagoya University, JAEA1

Na0.3CoO2.1.3H2O with the 2-dimensional triangular lattice of Co atoms exhibits the superconducting transition at Tc of 4.5 K [1]. Because it attracted much attention as the first oxide superconductor with 3d-electrons found after the high-Tc Cu-oxides, various experimental and theoretical studies have been carried out to identify the superconducting mechanism.

Here, we have carried out the neutron magnetic inelastic scattering to investigate the relationship between the magnetism and the superconductivity. We used aligned crystals of NaxCoO2.yD2O, in which the volume fraction of the superconducting phase (bilayer phase, y~1.3) was about 75% and the remaining non-superconducting phase was found to be the non-deuterated phase y~0. Because parts of crystals exhibit the superconducting transition at Tc~ 4.5 K and other parts exhibits the anomalies at 6 K by in the T dependences of the magnetic susceptibility and specific heat, we estimate the nuQ value of crystals to be at around 12.5 MHz from the T-nuQ phase diagram reported in reference 2 (nuQ : 59Co-nuclear quadrupole frequency).

The neutron measurements were carried out using the spectrometer 5G installed at JRR-3 with the triple-axis condition. The aligned crystals were used with the [100] and [001] axes in the scattering plane.

Constant-E scans along (h, 0, 2.8) have been carried out at the energy transfer of 3 meV at several temperatures between 5 K and 100 K. In the measurement, the l value of 2.8 was chosen, because where the neutron background count becomes almost minimum in the scan along (0, 0, l). Two magnetic scattering peaks have been observed at h = 0 and h = 1/2. The peak at h = 0 is the two-dimensional ferromagnetic fluctuation and expected to appear when the eg' band pockets exist at the Fermi surface. The spectral weight chi"(Q, omega=3meV) at h = 0 decreases with decreasing temperature and disappears below 25 K. This result indicates that the two-dimensional ferromagnetic fluctuation decreases with decreasing temperature and that the top of the eg' band is below the Fermi energy. In contrast, the intensity at h = 1/2 seems to increase slightly with decreasing temperature from 100 K to 5 K. Because the intensities of the magnetic excitations observed at h = 0 at relatively high temperatures and h = 1/2 down to 5 K are almost constant with varying l, the magnetic correlations are two-dimensional character.

The present results exclude the possibility of the triplet-pairing of the superconductivity, and are consistent with the results of the NMR Knight shift reported by the present authors' group [3, 4].

Reference

[1] K. Takada et al., Nature 422 (2003) 53
[2] Y. Kobayashi, M. Yokoi, T. Moyoshi and M. Sato, J. Phys. Soc. Jpn. 76 (2007) 103705.
[3] Y. Kobayashi, H. Watanabe, M. Yokoi, T. Moyoshi, Y. Mori and M. Sato, J. Phys. Soc. Jpn. 74 (2005) 1800.
[4] Y. Kobayashi, T. Moyoshi, H. Watanabe, M. Yokoi and M. Sato, J. Phys. Soc. Jpn. 75 (2006) 074717.

1-3-29

Magnetic structure of a pressure-induced magnetically ordered phase in YbAgGe with a quasi-kagome lattice

K. Umeo(A), H. Kubo(B), T. Onimaru(B), K. Katoh(C), T. Matsumura(B), N. Aso(D) and T. Takabatake(B)
(A)N-BRAD, (B)ADSM, Hiroshima Univ., (C)NDA, (D)ISSP, Univ. Tokyo

The heavy-fermion antiferromagnet YbAgGe with the ZrNiAl-type structure undergoes two magnetic transitions at TM1=0.8 K with an incommensurate propagation vector k1=[0, 0, 0.324] and TM2=0.65 K with k2=[1/3, 0, 1/3] .[1,2] An expanded tail in specific-heat C(T) above TM1 is consistent with the magnetic frustration.[1] Recently, an anomalous phase diagram of YbAgGe under pressures has been constructed from the resistivity and C(T) measurements.[3,4] With applying pressure above 0.5 GPa, the resistivity anomalies at TM1 and TM2 merge into a sharp drop at TM=0.85 K.[3] In the pressure range $0.5 < P < 1.5$ GPa, magnetic ordering temperature TM(P) remains constant, while above P* = 1.6 GPa, TM(P) increases linearly. Concomitantly, the anomaly of C(T) at TM converts from a first-order type sharp peak to a second-order type jump of a conventional magnetic compound without geometrical frustration. Additionally, the magnetic entropy at TM rises for $P > P^*$, while Kondo temperature does not change.[4] These findings suggest that the sudden rise of TM(P) for $P > P^*$ is a due to the release of the magnetic frustration. In the present work, in order to determine a magnetic structure above 1.6 GPa, we performed neutron diffraction experiments under high pressure.

Measurements were preformed on a single crystalline sample prepared by the Bridgman method. In neutron diffraction experiments, the sample was cooled down to 35 mK with a 3He-4He dilution refrigerator. A pressure of 0.6 GPa was applying by a piston-cylinder cell (Cu-Be alloy, outer diameter=14mm) using Daphne oil as a pressure transmitting medium.

We found magnetic Bragg reflections at Q=(1/3, 0, 1/3), (1/3, 0, 2/3), (2/3, 0, 1/3) and (2/3, 0, 2/3) at T=35 mK. Fig. 1 shows the omega scan of the magnetic Bragg reflection at Q=(2/3, 0, 2/3) performed at T=0.3 K and 1.13 K > TM. However, we observed no super lattice reflection with the propagation vector k1=[0, 0, 0.324]. In order to investigate the magnetic structure above 1.6 GPa, we are planning to perform neutron diffraction measurements under higher pressures.

[1] K. Umeo et al.: J. Phys. Soc. Jpn, 73 (2004)537.
[2] B. Fak et al.: Physica B378-380 (2006)669.
[3] K. Umeo et al.: Physica B 359-361 (2005)130.
[4] H. Kubo et al.: J. Phys. Soc. Jpn, 77 (2008) in press.

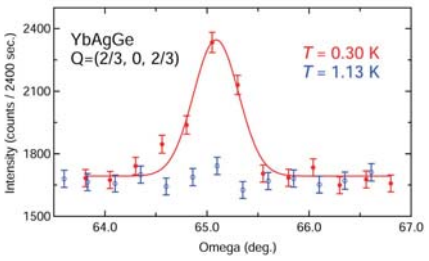


Fig. 1. Omega scan of the magnetic Bragg reflection at Q=(2/3, 0, 2/3). The closed and open circles correspond to the data at T=0.3 and 1.13 K, respectively. The curves is a result of Gaussian fitting.

1-3-30

Spin excitations in $MgCr_2O_4$

K. Tomiyasu[1], H. Suzuki[2], M. Toki[3], S. Itoh[4], N. Aso[5], M. Matsuura[5], K. Yamada[1]
WPI-AIMR Tohoku Univ.[1], *Waseda Univ.*[2], *PF KEK*[3], *KENS KEK*[4], *ISSP Tokyo Univ.*[5]

The geometric spin frustration is widely accepted as a concept to bring out a novel paramagnetic state. However, we measured two magnetic modes with discrete energies in an antiferromagnetic ordered phase in a geometrically frustrated magnet $MgCr_2O_4$ (spinel) by inelastic neutron scattering on a single-crystal specimen, and clarified the spatial spin correlations of the two levels: one is an antiferromagnetic hexamer and another is an antiferromagnetic heptamer.

Figures 1(a) to 1(d) show the present neutron scattering data, the constant-E map at E=4.5 and 9.0 meV in the $hk0$ and hhl zones in the antiferromagnetic phase ($T\sim$5 K). The data of (a) and (b) were measured on HER, and those of (c) and (d) were measured on PONTA and TOPAN, respectively. Figures 1(a) and 1(b) are the same pattern as the quasielastic scattering in the paramagnetic phase, meaning the hexamer. Figure 1(d) looks alike that of the independent seven-spin clusters (heptamers), proposed in the pyrochlore material $Tb_2Ti_2O_7$ with the same magnetic lattice as the B sites in a spinel material. We also confirmed that the intensity pattern in another scattering plane in Fig. 1(c) can be reproduced by the heptamer.

We now discuss the experimental fact that the one material includes the different spatial correlations, which have been emblematic of the geometric spin frustration in the paramagnetic phases of different systems. Also, such experiments will be able to be expanded to the other frustrated magnets in the magnetic *ordered* phases.

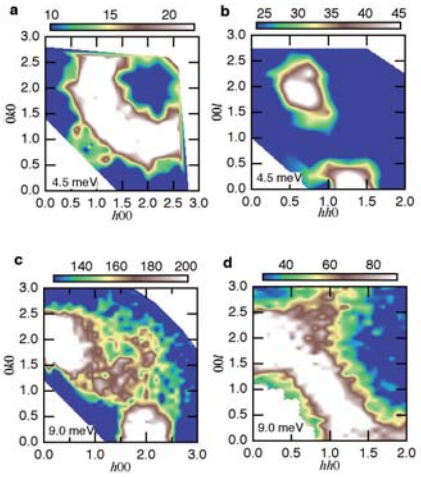


Fig. 1. Color images of single-crystal inelastic scattering of $MgCr_2O_4$, measured in a constant energy mode. The horizontal gauges indicate the scattering intensity in arbitrary units.

1-3-31

Magnetism and superconductivity in $RENi_2B_2C$

S. Ohira-Kawamura[1], R. Nagatomo[2], S. Konno[3], H. Kawano-Furukawa[3], H. Yoshizawa[4]
[1]*Academic and Information Board, Ochanomizu University*
[2]*Department of Physics, Ochanomizu University*
[3]*Graduate School of Humanities and Sciences, Ochanomizu University*
[4]*ISSP-NSL, University of Tokyo*

$RENi_2B_2C$ (*RE* is a rare earth or Y) has been studied intensively since a series of the materials exhibit various physical properties such as superconductivity, magnetic order, or their microscopic coexistence with substituting the *RE* site. For instance, one of them, $ErNi_2B_2C$, has attracted much attention because it exhibits the coexistence of the superconductivity and weak ferromagnetism. Recently, we have made $Lu_{0.5}Tb_{0.5}Ni_2B_2C$ as another promising candidate in which the superconductivity and weak ferromagnetism coexist. In order to understand the magnetically ordered state in this system in detail, we performed a neutron diffraction measurement.

The single crystal sample of $Lu_{0.5}Tb_{0.5}Ni_2B_2C$ was prepared, and the magnetic transitions at 9.5 K and 5.5 K were confirmed by a magnetization measurement. The sample was cooled down to 0.7 K using a 1K cryostat. The experiment was carried out at the 4G spectrometer (GPTAS), and neutrons with a momentum $k_i = 2.67$ Å^{-1} were used. ($h0l$) was selected as the scattering plane.

The neutron magnetic diffraction profiles in the (h01) direction at 0.7 and 15 K are shown in Fig. 1(a). At 0.7 K, a clear magnetic Bragg peak is observed at $Q = (0.44, 0, 1)$, which corresponds to the propagation vector for the SDW state. In the case of the pure $TbNi_2B_2C$ system in the SDW state, the higher-order peaks are also observed at the $3q$, $5q$ and $7q$ positions in addition to $q = 0.55a^*$. However, any other magnetic peaks were not observed in the present study, indicating clear difference from the pure system. The temperature dependence of the integrated intensity for the Bragg peak at $Q = (0.44, 0, 1)$ is displayed in Fig. 1(b). The SDW phase appears below ~9.5 K. The q position of the observed peak is not shifted with temperature. More detailed studies will be planned.

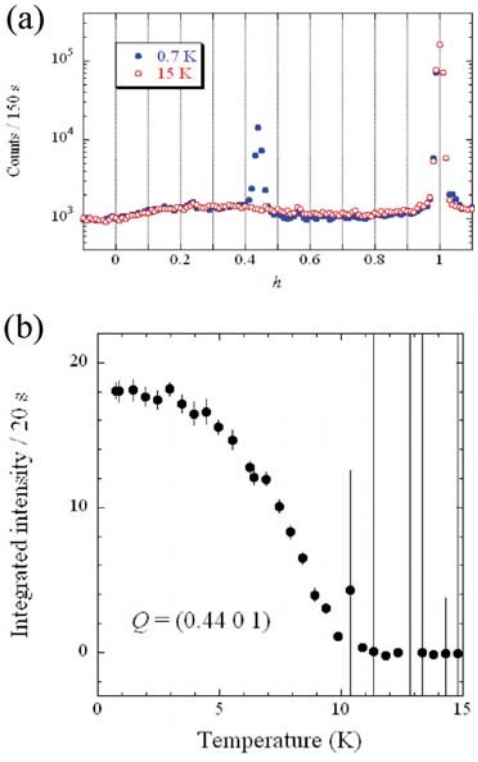


Fig. 1. (a) Neutron magnetic diffraction profiles in the (h01) direction at 0.7 and 15 K. (b) Temperature dependence of the integrated intensity of the magnetic Bragg peak at $Q = (0.44, 0, 1)$.

1-3-32

Electronic state in novel superconductor $CeCoIn_5$ studied by observation of the vortex state

H. Kawano-Furukawa[1], S. Ohira-Kawamura[2], S. Konno[1], R. Nagatomo[3], H. Shishido[4], T. Shibauchi[4], Y. Matsuda[4,5]
[1]*Graduate School of Humanities and Sciences, Ochanomizu University*
[2]*Academic and Information Board, Ochanomizu University*
[3]*Department of Physics, Ochanomizu University*
[4]*Department of Physics, Kyoto University*
[5]*ISSP, University of Tokyo*

$CeCoIn_5$ is a new heavy fermion superconductor with quasi two-dimensional electronic structure and the superconducting transition temperature $T_c = 2.3$ K. The vortex state of this system has attracted a great deal of attention, because some interesting phenomena have been reported. For instance, a possible FFLO state has been suggested in the low-T/high-H corner of the H-T phase diagram[1]. Recently we performed a SANS experiment on this system in the perpendicular field ($H \parallel c$), and found that the square flux line lattice (FLL) structure which was observed above 1 T exhibited reorganization to a triangular one above 4 T and that the internal field inside the vortex cores was unexpectedly enhanced by the external field[2]. In order to investigate its FLL structure of $CeCoIn_5$ in $H \parallel a$, we carried out a SANS experiment on this material.

The measurement was carried out at the C1-2 spectrometer (SANS-U). Neutrons with wavelength of 7.08 Åwere used, and the PSD was set at the 12 or 16 m position from the sample. The single crystal samples (the average size of $3 \times 0.5 \times 0.5$ mm^3) were aligned to cover the $\sim 8 \times 8$ mm^2 area so that the a axis is parallel to the neutron beam and the c axis is parallel to the vertical direction. A ^{4}He cryostat with a 3 T horizontal magnet was used, and the sample was cooled down to 1.6 K. The magnetic field was applied parallel to the a axis and the neutron beam.

The measurements were carried out at 0.1 T and 0.2 T. The data were collected at 1.6 K ($T < T_c$), and the background data collected at 3.5 K ($T > T_c$) were subtracted. We spent 6 hours to collect the data at each temperature. However, no reflections from the FLL were observed. The signal was not detected even in the scattering vector (Q) dependence and the azimuthal angle (θ) dependence of the scattering intensity. We note that, in the case of the measurement for $H \parallel c$, the diffraction spots from the FLL are clearly observed in shorter time.

The $CeCoIn_5$ crystal has the tetragonal symmetry (space group $P4/mmm$), and the symmetry axis corresponds to the crystallographic c axis. When the magnetic field is applied parallel to the a axis (equivalent for the b axis), the magnetic penetration depths for the b and c directions, λ_{ab} and λ_c, are expected to be significantly different (λ_{ab} is several times longer than λ_c). In this case, the supercurrent is expected to be no longer circular but anisotropic. Namely, the FLL structure should be distorted. On the other hand, the sample angle ω was calculated assuming isotropic triangular or square FLL. Therefore, we currently expect that the reason why the reflections were not observed in the present study is that the chosen sample angle ω did not satisfy the Bragg condition.

[1] See, for example, K. Kumagai et al., Phys. Rev. Lett. 97 (2006) 277002.

[2] S. Ohira-Kawamura et al., J. Phys. Soc. Jpn. (2008) in press.

1-3-33

Investigation of the magnetic excitations in high-T_C

M. Matsuura[1], Y. Yoshida[2], H. Eisaki[2], N. Kaneko[2], and K. Hirota[1]
[1] *Institute for Solid State Physics, The University of Tokyo, 106-1 Shirakata, Tokai, 319-1106*
[2] *AIST, 1-1-1 Umezono, Tsukuba, Ibaraki 305-8568*

The interplay between antiferromagnetic (AF) spin fluctuations and superconductivity is the central issue in the physics of high-transition temperature superconductivity because of the persistent AF fluctuations in the superconducting phase. Recently, a characteristic hourglass magnetic excitation have been reported from two families of high-Tc materials, LBCO and YBCO. If spin fluctuations are important for the mechanism of high-T_c superconductivity, they should be universal for all copper-oxide systems, however, it is still not clear. To resolve this issue, we explored another high-T_c system, optimmaly doped $Bi_{2.1}Sr_{1.9}CaCu_2O_{8+\delta}$ (Bi2212). Single crystals of Bi2212 were grown using travelling-solvent-floatingzone method. Neutron scattering experiments were performed on the triple-axis spectrometer PONTA installed at the JRR-3 Reactor of the JAEA. We have aligned 9 single crystals on Al plates. The total mass of aligned crystals is 6.4g (0.98cc), which is 16 times as large as the crystal used in the previous report[1].

Constant-Q spectrum taken in 2007 August show three peaks at 22, 36, and 46 meV (Fig.1a). We found 22- and 46 meV-peaks are spurious peaks arising from incoherent scattering of analyzer. Therefore, we improved 5G analyzer to reduce the incoherent scattering and the spurious peaks disapper for the 2007 Dec. spectrum (Fig.1a). Thus, the scattering around 34 meV comes from sample, in addition, it increases below T_c as previous works.[1, 2] (Fig.1b) Constant-E scan along the [110] direction at $E = 34$ meV shows a peak at (π,π) which is slightly enhanced below T_c (Fig.1c). One shoud note that large peak at (π,π) and $E = 34$ meV remains even at $T = 100$ K ($> T_c$). This suggests that strong spin fluctuations exist in the normal state, which has been neglected in the study of magnetic excitations in Bi2212.

References

[1] H. F. Fong *et al.*, Nature (London) **398**, 588 (1999).
[2] H. He et al., Phys. Rev. Lett. **86**, 1610 (2001).

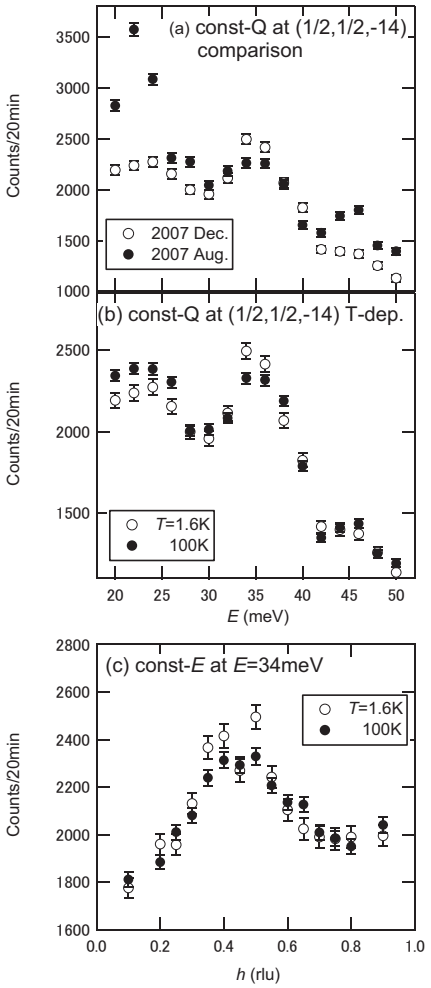


Fig. 1. Const-Q spectra at (1/2 1/2 -14) and $T = 1.2$ K ($T < T_c$) and 100 K ($T > T_c$). b) Constant-Energy profiles at $\hbar\omega = 34$ meV with (*hh*-14).

1-3-34

Magnetic Structure in the Shastry-Sutherland Lattice Tb1-xYxB4

F. Iga(a), S. Michimura(a), K. Murakami(a), T. Takabatake(a), K. Suga(b), K. Kindo(b), K. Ohoyama(c)

(a)ADSM, Hiroshima Univ., (b) ISSP, Univ. of Tokyo, (c) IMR, Tohoku University

Rare-earth tetraborides RB4 have a tetragonal crystal structure with a space group P4/mbm which is characterized by the 2-dimensional orthogonal dimers in the c-plane. Such dimer systems are equivalent to the Shastry-Sutherland lattice (SSL) where nearest-neighboring dimers have geometrical frustration.

TbB4 has successive antiferromagnetic transitions at TN1 = 44 K and TN2 = 24 K. The magnetization curve of TbB4 at 1.3K shows at least nine magnetization jumps above 16T for B//c and it is remarkable concerning the origin. In order to approach the mechanism of multi-step magnetization, we studied Y-substitution effect on TbB4 for magnetic susceptibility, magnetoresistance and specific heat. From these macroscopic measurements the characteristic temperature TN2 was found to be smeared out around x=0.2.

In order to clarify whether such lower temperature phase below TN2 truly disappears at x=0.2 or not, we have measured the powder neutron diffraction for x=0.10 and 0.25. The isotope boron 11 enriched up to 99.75% was used for sample preparation and these samples were crushed to powder. The neutron powder diffraction experiment was performed by using HERMES. Measured temperature region were from 3 to 50 K. For x=0.1 this alloy shows successive antiferromagnetic phase transition at TN1 = 40 K and TN2 = 20 K. Below TN1, magnetic peaks at (100), (210) and (111) gradually grow with decreasing temperature. Furthermore these magnetic peaks grow again below TN2 = 20 K. On the other hand, magnetic peaks for x=0.25 gradually grow below TN1 = 35 K and these intensities saturate at 20 K. From these measurement, we could not find another phase transition correspondent to TN2 for x=0.25.

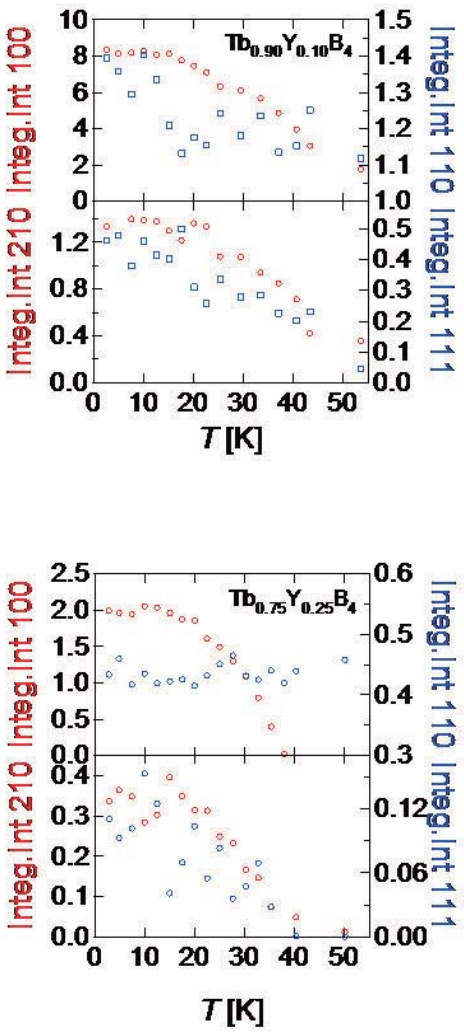


Fig. 1. Temperature dependences of some magnetic peaks at (110), (111) and (210) in x=0.10 and 0.25.

1-3-35

1st order transition in $ErNi_2B_2C$

H. Kawano-Furukawa, Y. Ishida , S. Ohira-Kawamura, H. Yoshizawa[a] and H. Takeya[b]
Ochanomizu Univ., ISSP NSL Univ. of Tokyo[a] and NIMS[b]

$ErNi_2B_2C$ is the first material in which a microscopic coexistence of weak ferromagnetism (WFM) and superconductivity (SC) was directly confirmed by a neutron scattering measurements in zero field [1]. $ErNi_2B_2C$ transforms to a superconducting state at $T_c = 10.5$ K, a SDW state at $T_N = 6$K and a weak ferromagnetic state at $T_{WFM} =$ 2.3K. At early stage of the study, Zarestky *et. al.* [2] and Sinha *et. al.* [3] independently performed neutron diffraction measurements and both group independently observed that clear magnetic peaks develope below T_N at incommensurate wave vector $q \sim 0.553$a* and spins on Er atoms order transversely polarized planar sinusoidal structure. After these works, we performed unpolarized and polarized neutron diffraction measurements and succeeded in confirming microscopic coexistence between the WFM and the SC by showing an appearance of an interferance term below $\sim$ 2.3K at both (0 0 2) and (0 0 6) nuclear Bragg positions of the $ErNi_2B_2C$ crystal [1,4]. In those studies, however, we noticed that temperature dependence of the magnetic intensity shows a hysteresis behavior around 2.3K. To check an origin of this anomaly, we performed further neutron diffraction measuremtns.

In the present study, we used single crystals of $ErNi_2^{11}B_2C$ grown by a floating zone method. T_c of our un-annealed sample is determined to be $\sim$ 8.6 K which is same crystal with the one used in the previous experiment [1].

Figures show temperature dependence of neutron diffraction intensities at (a) (1 0 0) and (2) (0 0 1). These two points are equivalent Bragg positions for the WFM order parameter. But data show different temperature dependence around 2.3K. This result indicates a rotation of spins. To check this behavior in more detail we measured neutron diffraction profiles along (h 0 1) and (h 0 0) (not shown). With such date, we concluded that that the ferromagnetic order in $ErNi_2B_2C$ first develops with spins along the a-axis below 2.3K but it rotate along the b-axis at 1.8K through a first order transition.

[1] H. Kawano *et al*., J. Phys. Chem. Solids **60**, 1053 (1999)

[2] J. Zarestky *et al*., Phys. Rev. B **51**, R678 (1995).

[3] S.K. Sinha *et al*., Phys. Rev. B **51**, R681 (1995).

[4] H. Kawano-Furukawa *et al*., Phys. Rev. B **65**, 180508 (2002)

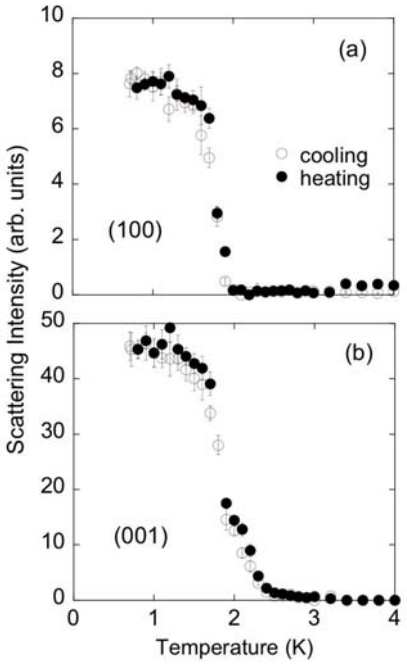


Fig. 1. Temperature dependence of Bragg intensities at (a) (1 0 0) and (b) (0 0 1).

1-3-36

Study of spin fluctuations in $La_{1.94-x}Sr_xCe_{0.06}CuO_4$

M. Fujita[1], M. Enoki[2], and K. Yamada[3]

[1] *Institute for Materials Research, Tohoku University, Katahira, Sendai 980-8577, Japan*
[2] *Department of Physics, Tohoku University, Aramaki, Sendai 980-8578, Japan*
[3] *World-Premier-International Research Center Initiative, Tohoku University, Katahira, Sendai 980-8577, Japan*

It is widely believed that spin correlations play an important role in the mechanism of high-T_c superconductivity[1]. Since, the static spin order competes with the superconductivity and such order is stabilized in the system with corrugated CuO_2 planes[2], a study of spin fluctuations in the system with flat CuO_2 plane, where the ideal superconducting state is considered to be realized, is more important. In order to shed light on this issue, we have carried out neutron-scattering experiments to investigate the effect of distortion of CuO_2 planes on the low-energy spin correlation of $La_{1.94-x}Sr_xCe_{0.06}CuO_4$ with x=0.14, 0.18 and 0.24, of which orthorhombic lattice distortion is smaller than that in $La_{2-x'}Sr_{x'}CuO_4$ (LSCO) with comparable hole concentration.

As shown in Fig. 1, clear gap structure was observed in the energy spectrum of local dynamical susceptibility $\chi''(\omega)$ for both x=0.18 ($p\sim$0.14) and x=0.24 ($p\sim$0.20) samples, similar to the results for optimally-doped LSCO[3]. On the other hand, in the x=0.14 ($p\sim$0.10) sample, a low energy component showing the increases of intensity below 2$\sim$3meV with lowering ω was observed within the gap-like structure. Such a $\chi''(\omega)$ in x=0.14 is quite different from that for LSCO with x'=0.10, although the effective hole concentration in two samples is comparable[3]. These experimental results suggest that the gap-strucure is robust against the lattice distortion, while the low-eneryg component is strongly influenced by the lattice distortion. We speculate that such reduction of the low-energy component is caused by the relaxation of corrugation of CuO_2 planes. In other words, the slowing down of spin fluctuations occurs in the system with corrugated CuO_2 planes. Moreover, the appearance of gap-like structure in $\chi''(\omega)$ by reducing the lattice distortion would be the evidence for the existence of spin-gap states in the underdoped La214 system. Further systematic neutron-scattering experiments are required to clarify the intrinsic spin correlations in the high-T_c superconductors.

References

[1] M. A. Kastner *et al.*: Rev. Mod. Phys. **70**, (1998)897.
[2] M. Fujita *et al.*: Phys. Rev. Lett. **88** (2002)167008.
[3] C.H. Lee *et al.*: J. Phys. Soc. Jpn. **69** (2000)1170.

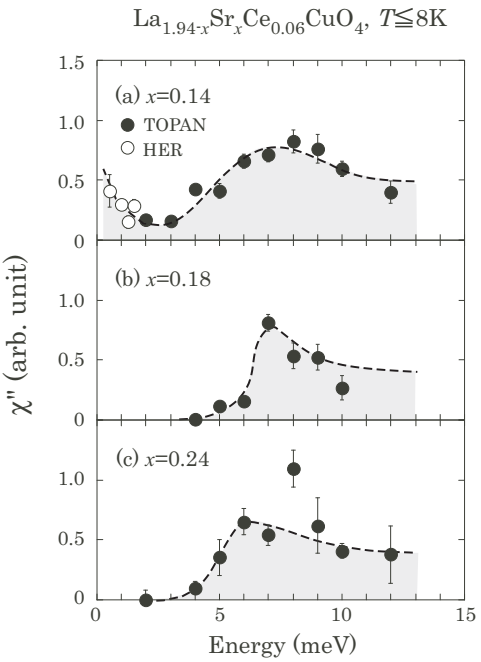


Fig. 1. Local spin susceptibility for $La_{1.94-x}Sr_xCe_{0.06}CuO_4$ with (a) x=0.14, (b) 0.18 and (b) 0.24 measured below 8 K.

1-3-37

Search for transition of paring symmetry in electron-doped superconductor $Pr_{1-x}LaCe_xCeO_4$

M. Fujita[1], M. Nakagawa[2], and K. Yamada[3]
[1] *Institute for Materials Research, Tohoku University, Katahira, Sendai 980-8577, Japan*
[2] *Department of Physics, Tohoku University, Aramaki, Sendai 980-8578, Japan*
[3] *World-Premier-International Research Center Initiative, Tohoku University, Katahira, Sendai 980-8577, Japan*

Research of mechanism of high-T_c superconductivity remains one of central issues in the strongly correlated electron system. Extensive research on the magnetism in the cuprate superconductors revealed the close relation between the spin correlations and the hihg-T_c superconductivity. On the other hand, a possible role of lattice vibrations in the mechanism of the high T_c superconductivity has also been intensely studied[1,2]. Quite recently, an evidence for the transition or crossover of superconducting paring symmetry from being *d*-wave to *s*-wave in nature upon doping was reported for the electron-doped (*n*-type) cuprate[3,4]. This suggests that in the *n*-type superconductors the *d*-wave superconductivity mediated by spin fluctuations can change to the conventional *s*-wave superconductivity mediated by lattice vibrations with increasing doping concentration. In comparison, such symmetry crossover has not been reported in the case of the *p*-type cuprates, suggesting that the $d_x{}^2$-$_y{}^2$-wave symmetry favoring a spin-mediated mechanism seems to be common in the whole range of *p*-type high-T_c cuprates. Therefore, to understand common mechanism of high-T_c superdonductivity, it is quite important to clarify the origin of *s*-wave superconductivity in the electron-doped system.

Motivated by above reason, we have started the neutron-scattering study on the *n*-type $Pr_{1-x}LaCe_xCuO_4$ system to confirm the evidence of *s*-wave superconductivity. In Fig. 1, preliminary results for the measurement of an acoustic phonon around (0 0 4) position in x=0.15 sample (T_c=16 K) are shown. Intensity of phonon gradually increases upon heating. The increase of intensity can be reproduced by thermal factor and no clear anomalous temperature dependence of phonon was observed in this sample within the experimental accuracy. However, to conclude the absence of anomaly in phonon, more precise measurement with high energy resolution is required and comprehensive study for wide concentration range is important for the next step.

References

[1] M. Tachiki *et al.*: Phys. Rev. B **67** (2003)174506.
[2] S. Ishihara and N. Nagaosa: Phys. Rev. B **69** (2004)144520.
[3] J.A. Skinta *et al.*: Phys. Rev. Lett **88** (2002)207005.
[4] V.A. Khodel *et al.*: Phys. Rev. B **69** (2004)144501.

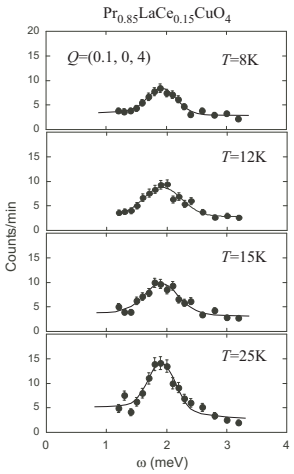


Fig. 1. Constant-momentum spectra with Q=(0.1, 0, 4) in $Pr_{0.93}LaCe_{0.07}CuO_4$ measured at temperatures around T_c(=16 K).

1-3-38

Zn-doping effect on spin fluctuations in electron-doped $Pr_{1-x}LaCe_xCuO_4$

M. Fujita[1], M. Nakagawa[2], and K. Yamada[3]

[1] *Institute for Materials Research, Tohoku University, Katahira, Sendai 980-8577, Japan*
[2] *Department of Physics, Tohoku University, Aramaki, Sendai 980-8578, Japan*
[3] *World-Premier-International Research Center Initiative, Tohoku University, Katahira, Sendai 980-8577, Japan*

In the hole-doped (*p*-type) high-T_c cuprates, extensive neutron-scattering measurement clarified that antiferromagnetic spin fluctuations in doped Mott insulators show close connection with high-T_c superconductivity. However, less is known about the spin correlations in the electron-doped (*n*-type) supercondcuting cuprates. Neutron-scattering experiment on *n*-type $Nd_{2-x}Ce_xCuO_4$ revealed the existence of commensurate low-energy spin correlations in both AF ordered and SC phases [1]. This is qualitatively different from the well-defined incommensurate structure observed in the *p*-type cuprates, and it implies that the microscopic origin of the superconductivity in cuprates might be asymmetric against the type of charge carriers. To clarify the nature of spin correlations in the electron-doped system through impurity effect, we performed inelastic neutron-scattering measurement on $Pr_{0.89}LaCe_{0.11}Cu_{1-y}Zn_yO_4$ with y=0.014.

Fig. 1 shows constant-q spectra measured at 3 meV, 7 meV and 10 meV. Well-defined commensurate peak was observed at all energies, analogous to the results for Zn-free $Pr_{0.89}LaCe_{0.11}CuO_4$. However, the peak is somewhat broader than that in Zn-free sample. In Fig. 2, peak-width (half-width at half-maximum) as a function of ω obtained by fitting to a single Gaussian without convoluting the instrumental resolution is shown. The results for Zn-free sample is also plotted as a reference. In both samples, the width increases linearly with increases ω. However, the slope, κ/ω, is larger in the Zn-doped sample. Such a increase of slope by Zn-doping is similar to the result for the evolution of spin correlations by electron-doping[2], and therefore the similarity suggest that the doped electrons dilute Cu spins on CuO_2 planes.

References

[1] K. Yamada *et al.*: Phys. Rev. Lett **90** (2003)137004.
[2] M. Fujita *et al.*: arXiv:0707.0150.

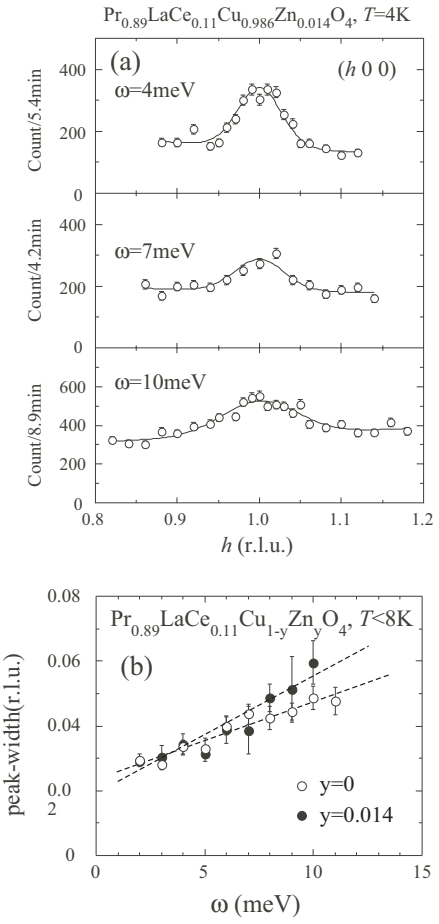


Fig. 1. (a) Constant energy spectra for $Pr_{0.89}LaCe_{0.11}Cu_{0.986}Zn_{0.014}O_4$. (b) ω-dependence of peak-width for Zn-free and Zn-doped samples.

1-3-39

Order Parameter of Phase IV in (Ce,La)B6

K. Kuwahara, K. Iwasa(A), M. Kohgi, N. Aso(B), M. Sera(C), F. Iga(C), M. Matsuura(B), K. Hirota(B)

Department of Physics, Tokyo Metropolitan University, Department of Physics Tohoku University(A), Neutron Science Laboratory, Institute for Solid State Physics, University of Tokyo(B), Department of Quantum Matter, ADSM, Hiroshima University(C)

Cerium hexaboride CeB6 undergoes successive phase transitions from paramagnetic phase (Phase I) to antiferroquadrupolar ordering and to antiferromagnetic ordering (Phase III). By doping La into the Ce site in this system, a new phase called phase IV appears in CexLa1-xB6 for $x < 0.8$.

Recently we have observed weak but distinct superlattice reflections at Q = (h/2,h/2,l/2) (h, l = odd number) from phase IV of Ce0.7La0.3B6 for the first time by elastic neutron scattering. The intensity of the superlattice reflections is stronger for high scattering vectors. This unusual Q dependence of the intensity evidences that the order parameter of phase IV has a complex magnetization density, consistent with the recent experimental and theoretical prediction in which the order parameter is the magnetic octupoles T_beta with Gamma_5 symmetry of Oh. However, it still remained possible that such a Q dependence of intensity might arise from lattice distortions, since the scattering intensity due to lattice distortions also increases with increasing Q in proportion to the square of Q. To rule out this possibility, we have performed further neutron scattering experiments.

A large single crystal of Ce0.7La0.3B6 was grown by the floating zone method, using 99.52% enriched 11B to avoid the large neutron absorption due to 10B. The neutron diffraction experiments were performed on the thermal neutron triple axis spectrometer TOPAN (6G) & PONTA (5G).

Figure 1 shows the result of the polarized neutron scattering experiment at PONTA (5G). Spin-flip neutron scattering have been clearly observed. This provides direct evidence that the observed superlattice reflections are magnetic and not due to lattice distortions.

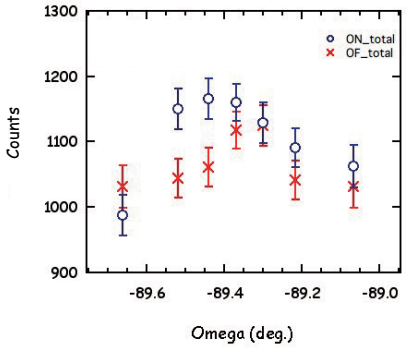


Fig. 1. Neutron scattering patterns of rocking curves at the scattering vector Q = (5/2,5/2,5/2), where the spin of the incident neutrons is parallel (the spin flipper was off) or antiparallel (the spin flipper was on) to the scattering vector Q.

1-3-40

Neutron scattering study on PrFe4P12 under high pressure

K. Kuwahara, T. Osakabe(A), K. Iwasa(B), M. Kohgi, D. Kikuchi, Y. Aoki, H. Sato, H. Sugawara(C)

Department of Physics, Tokyo Metropolitan University, Neutron Materials Research Center, Japan Atomic Energy Agency(A), Department of Physics, Tohoku University(B), Faculty of Integrated Arts and Sciences, The University of Tokushima(C)

PrFe4P12 undergoes the non-magnetic phase transition at TA = 6.5 K under ambient pressure. By applying pressure, the non-magnetic ordered phase disappears and the metal-insulator (M-I) transition occurs around Pc = 2.4 GPa (Hidaka et al.: Phys. Rev. B 71 (2005) 073102). In the insulating phase, we have observed the distinct antiferromagnetic magnetic Bragg peak with a wave vector q =(1,0,0) above Pc by using a new hybrid-type pressure cell (HAC) which is composed of a large sapphire anvil and a tungsten carbide anvil (Osakabe et al.: J. Mag. Mag. Mat. 310 (2007) 2725).

In order to get further microscopic information about the pressure-induced antiferromagnetic order, we have performed high-pressure neutron diffraction measurements on PrFe4P12 single crystal at low temperatures under high pressure and magnetic fields using the triple-axis spectrometer TOPAN at JRR-3M in JAEA and the HAC. Single crystals were grown by tin-flux method. The HAC was set inside a superconducting magnet with the [0,0,1]-axis vertical to the (h,k,0) scattering plane.

Figure 1 shows the temperature and magnetic field dependences of the antiferromagnetic Bragg peak with q = (1,0,0) under 3.2 GPa. The pressure-induced antiferromagnetic order is clearly suppressed by applying magnetic field. This result agrees with the reported field dependence of the electrical resistivity. This strongly indicates that the pressure-induced M-I transition is caused by the antiferromagnetic order. However, it is difficult to explain the mechanism of the M-I transition by a simple superzone gap formation at the Fermi surface due to the antiferromagnetic order, since the Fermi surface of an extra hole-like band exists. Further studies are necessary to clarify the mechanism of the M-I transition.

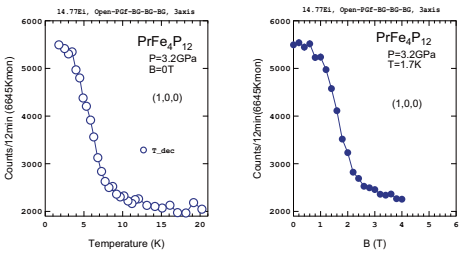


Fig. 1. Temperature and magnetic field dependences of the antiferromagnetic Bragg peak with q = (1,0,0) under 3.2 GPa.

1-3-41

Rattling motion in PrOs4Sb12

K. Kuwahara, O. Yamamuro(A), K. Iwasa(B), M. Kohgi, D. Kikuchi, Y. Aoki, H. Sato, H. Sugawara(C)

Department of Physics, Tokyo Metropolitan University, Neutron Science Laboratory, Institute for Solid State Physics, University of Tokyo(A), Department of Physics, Tohoku University(B), Faculty of Integrated Arts and Sciences, The University of Tokushima(C)

The filled skutterudite compounds RT4X12 (R: rare earth or actinide, T: transition metal, X: pnictogen) crystallize in the body-centered cubic space group Im-3, in which R ion is surrounded by a cage of X-icosahedron. This characteristic "cage" structure provides a wide variety of thermal, magnetic and transport properties. Among the filled skutterudite compounds, PrOs4Sb12 received much attention because it is the first Pr-based heavy-fermion superconductor and a field-induced antiferro-quadrupolar (AFQ) ordered phase exists near the superconducting phase. In addition to the relation between the AFQ fluctuations and the superconductivity, interestingly, the possibility that the heavy-fermion superconductivity is related to a rattling motion due to a weakly bounded Pr-ion in the Sb cage has been argued. Especially, a Debye-type dispersion in the elastic constants observed by high resolution ultrasonic measurements (T. Goto et al.: Phys. Rev. B 69 (2004) 180511R) shows the importance of the rattling motion in this system. In order to microscopically study the dynamical property of the rattling motion, we started doing inelastic neutorn scattering experiments with high energy resolution.

The powder sample of PrOs4Sb12 was grown by Sb-self-flux method. The total mass is about 39 g. The inelastic neutorn scattering experiments were done by using the Angle Focusing Cold Neutron Spectrometer (AGNES) at JRR-3M in JAEA.

Figure 1 shows inelastic spectra at 10 K and 100 K. The difference between spectrum at 10 K and that at 100 K has been observed below around 0.2 meV. The observed excitation might be due to the rattling motion of Pr-ion. To clarify this possibility, further studies, such as measurements of Q-dependence of the excitation, are needed.

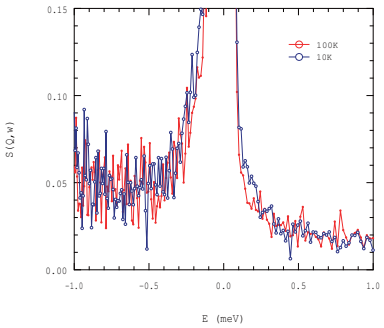


Fig. 1. Inelastic spectra of PrOs4Sb12 at 10 K and 100 K.

This is a blank page.

1. 中性子散乱 4)非晶質･液体

1. Neutron Scattering 4) Amorphous・Liquid

This is a blank page.

1-4-1

Direct observation of supercooled water in hardened Low Heat Portland Cement

K. Mori(A), Y. Inamura(B), O. Yamamuro(B), T. Fukunaga(A)
(A)Research Reactor Institute, Kyoto University, (B)ISSP, University of Tokyo

Frost damage on concrete buildings is one of the most serious problems in cold districts like Hokkaido in Japan. Freezing of water makes its own volume increase up to as much as 9%, inducing internal pressure within concrete materials. However, the freezing and thawing cycle of water is very complicated due to an existence of supercooled water below 273 K. In this work, we performed directly to observe the freezing and thawing water in hardened Low Heat Portland Cement (LHPC) by using the quasi-elastic neutron scattering (QENS) method.

The LHPC clinkers were hydrated with light water (H2O) at 301 K in air. The H2O to LHPC mass ratio is 0.5. After a couple of days, the hardened LHPC was soaked in water. QENS data of the hardened LHPC were measured at temperatures between 202 K and 302 K on the high-resolution pulsed cold neutron spectrometer, AGNES, installed at the ISSP at University of Tokyo. The energy resolution of the AGNES is 120 μ eV when the neutron wavelength is 4.22 angstrom.

Figure 1 (a), (b), (c) and (d) show QENS spectra at 302 K, 272 K, 262 K and 242 K. The closed and opened circles indicate the freezing and thawing processes, respectively. The solid line is the QENS spectrum at 202 K, corresponding to the energy resolution of the AGNES. This means that the water in the hardened LHPC freezes completely below 202 K. Above 242 K, the QENS was clearly observed, that is, the supercooled water exists at temperatures between 242 K and 273 K. Furthermore, it was found that the freezing and thawing cycle of water in the hardened LHPC has a little hysteresis below 273 K.

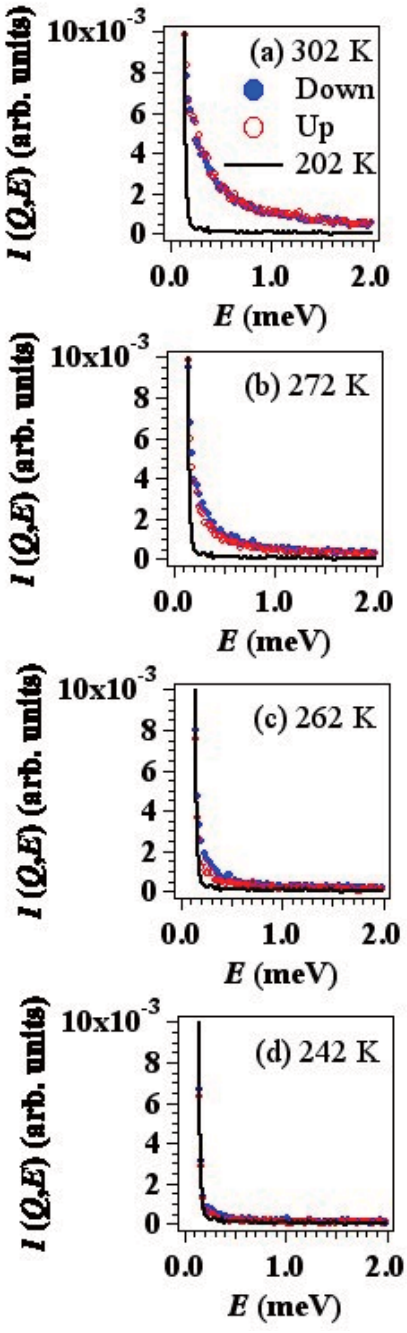


Fig. 1. QENS spectra at 302 K, 272 K, 262 K and 242 K.

1-4-2

Neutron Diffraction Study on the Intermolecular Structure in Highly Concentrated Aqueous Urea Solutions

Yasuo Kameda, Asami Maki, Hiroaki Takahashi, Yuko Amo, Takeshi Usuki
Department of Material and Biological Chemistry, Faculty of Science, Yamagata University, Yamagata 990-8560

Intermolecular hydrogen-bonded structure in the concentrated aqueous urea solution has been received much attention because of its importance for various fields of chemical and biological sciences. A number of neutron diffraction studies have been conducted in order to investigate the hydration structure of the urea molecule [1-6], however, direct experimental information on the structure of urea-urea interaction has not yet been obtained. In the present report, we describe results of neutron diffraction measurements on 14N/15N and H/D isotopically substituted aqueous 25 mol% urea solutions in order to obtain the N(urea)-N(urea) partial structure factor and corresponding N-N partial distribution function.

Five isotopically substituted aqueous 25 mol% urea solutions were used in the present study, namely,

I. [(14ND2)2C=O]0.25(D2O)0.75,
II. [(15ND2)2C=O]0.25(D2O)0.75,
III. [(14-15ND2)2C=O]0.25(D2O)0.75,
IV. [(14NZ2)2C=O]0.25(Z2O)0.75, and
V. [(15NZ2)2C=O]0.25(Z2O)0.75,

where 14-15N is the 1:1 mixture of 14N and 15N, and "Z" denotes the null mixture of H and D. Sample solutions were sealed in a cylindrical quartz cell (12.0 mm in inner diameter and 1.1 mm in thickness).

Neutron diffraction measurements were carried out at 298 K using the ISSP diffractometer 4G (GPTAS) installed at the JRR-3M research reactor with an incident neutron wavelength of 1.099(4) A. Scattered neutrons were collected over the angular range of $3 < 2\theta < 118$ deg. corresponding to $0.30 < Q < 9.80$ 1/A. Preset time was 230 s for each data point. Measurements were made in advance for an empty cell, a vanadium rod of 10 mm in diameter, and an instrumental background. After correction for the background, absorption and multiple scattering, the observed count rates were converted to the scattering cross section by the use of corrected scattering intensities from the vanadium rod.

The intermolecular first-order difference function, delta-N-inter(Q) [7], was derived from the difference in observed scattering cross sections between sample solutions that have different average coherent scattering length of the nitrogen atom. The observed delta-N(Q) function can be described by a linear combination of the partial structure factors involving contribution from the nitrogen atom. Numerical values of the coefficients A - D are summarized in Table 1.

delta-N(Q) = A[aNO(Q)-1] + B[aNH(Q)-1] + C[aNC(Q)-1] + D[aNN(Q)-1],

where,

A = 4x delta bN bO,
B = 8x(1+x) delta bN bH,
C = 4x**2 delta bN bC, and
D = 4x**2(bN**2 - bN'**2).

Table 1. Weighting factor for partial structure factors in the first- and second-order difference functions (in barns).

Difference	A	B	C	D
I - III	0.0830	0.2383	0.0238	0.0618
III - II	0.0830	0.2383	0.0238	0.0516
(I-III)-(III-II)	0	0	0	0.0102

The N-N partial structure factor was successfully obtained from the second-order difference between two first-order difference functions, between samples I - III and III - II. Although observed intermolecular difference functions between samples I - III and III - II look very similar, the derived N-N partial structure factor clearly indicates the first diffraction peal at Q = 1.5 1/A. Difference distribution functions GN(r) between samples I - III and III - II, and the N-N partial distribution function are represented in Fig. 1. The observed intermolecular N-N partial distribution function, gNN(r), is characterized by a well-resolved first peak at r = 5 A, which may imply that that the stable urea cluster is present in the concentrated aqueous solution. Detailed structural information on the N-H and N-O partial structure functions can be obtained from the combination of the observed scattering cross sections for samples I - II and IV - V, respectively. Further data analysis is in progress.

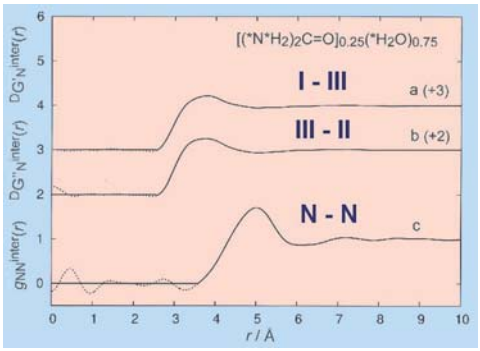


Fig. 1. a, b) Intermolecular difference distribution functions and c) N-N partial distribution function observed for aqueous 25 mol% urea solutions.

References

[1] J. L. Finney, J. Turner, Ann. N.Y. Acad. Sci., 482 (1986) 127.
[2] J. L. Finney, J. Turner, Electrochim. Acta, 33 (1988) 1183.
[3] J. L. Finney, A. K. Soper, Chem. Soc. Rev., 23 (1994) 1.
[4] Y. Kameda, H. Naganuma, K. Mochiduki, M. Imano, T. Usuki, O. Uemura, Bull. Chem. Soc. Jpn., 75 (2002) 2579.
[5] A. K. Soper, E. W. Castner, A. Luzar, Biophys. Chem., 105 (2003) 649.
[6] Y. Kameda, M. Sasaki, S. Hino, Y. Amo, T. Usuki, Bull. Chem. Soc. Jpn., 79 (2006) 1367.
[7] J. E. Enderby, G. W. Neilson, "Water, A Comprehensive Treatise", Plenum Press, New York, (1979), Vol. 6, p. 1.

1-4-3

SANS Study on Mixing State of Ionic Liquid-Molecular Liquid Binary Solutions

Toshiyuki Takamuku, Yusuke Honda, and Kenta Fujii
Saga University

Recently, ionic liquids and their mixtures of molecular liquids are frequently examined as a novel solvent for electric devices, organic syntheses, and solvent extractions. However, physicochemical properties of ionic liquids and ionic liquid-molecular liquid mixtures are still unknown at the molecular level. The properties are essential to understand chemical reactions and equilibria in ionic liquids and their mixtures of molecular liquids.

In the present study, mixing state of binary solutions of imidazolium-based ionic liquids and water, methanol, acetonitrile, and benzene has been observed at a mesoscopic level by using small-angle neutron scattering (SANS) technique. Two ionic liquids, 1-ethyl-3-methylimidazolium (EMI+) chloride (Cl-) (m.p. = 360 K) and EMI+ bis-(trifluoromethanesulfonyl) amide (TFSA-) (m.p. = 256 K) were examined. Based on the present results, the effects of the properties of the molecular liquids on mixing state of ionic liquid-molecular liquid binary solutions have been discussed.

Sample solutions were prepared by dissolving EMICl into deuterated liquids of water, methanol, and acetonitrile and by mixing EMITFSA with deuterated methanol, acetonitrile, and benzene at various mole fractions. However, EMICl-benzene and EMITFSA-water solutions were not prepared because of their very low miscibility. SANS spectra of the sample solutions at 298 K were measured on the SANS-U spectrometer with the camera lengths of 1 and 4 m. The scattering intensities for the sample solutions were accumulated on the detector at the camera lengths of 1 and 4 m for 10 min and 1 h, respectively.

For the EMICl systems, as seen in Fig. 1(a), the SANS intensities for the EMICl-acetonitrile mixtures are significantly observed at the high acetonitrile mole fractions of 0.8, 0.9, and 0.95. However, the SANS intensities for the EMICl-water and EMICl-methanol mixtures were scarcely observed. Thus, EMICl and acetonitrile molecules form each cluster in the mixtures, whereas EMICl is homogeneously dissolved into water and methanol. On the other hand, for the EMITFSA systems, the SANS intensities for the EMITFSA-methanol mixtures are significant at the methanol mole fractions of 0.8, 0.9, and 0.95 as shown in Fig. 1(b), while those for the EMITFSA-acetonitrile and EMITFSA-benzene mixtures were not observed. Hence, both EMITFSA and methanol are inhomogeneously mixed each other in the mixtures, but acetonitrile and benzene are homogeneously mixed with EMITFSA.

The present results can be explained as follows. In the EMICl systems, acetonitrile molecules may not strongly interact with Cl- due to the low electron-acceptability of acetonitrile, while water and methanol molecules strongly solvate Cl-. However, benzene molecules cannot solvate highly charged Cl- i.e., EMICl is not dissolved into benzene. These are the reasons for the most inhomogeneous mixing of the EMICl-acetonitrile mixtures among the EMICl systems. On the contrary, methanol molecules weakly interact with TFSA- because of the low charge-density of TFSA-. However, acetonitrile molecules can easily interact with TFSA- due to the suitable polarity of acetonitrile. In contrast, water molecules hardly interact with hydrophobic TFSA-, i.e., a small amount of water is only dissolved in EMITFSA. In the EMITFSA-benzene mixtures, benzene molecule may contact with EMI+ by the pi-pi interaction between them [1,2]. Additionally, benzene molecule may easily interact with low-charged TFSA-. It results in the homo-

Activity Report on Neutron Scattering Research: Experimental Reports **15** (2008)
Report Number: 332

geneous mixing of the EMITFSA-benzene mixtures. Thus, the inhomogeneity of the EMITFSA-methanol is the highest among the EMITFSA systems.

[1] C.G. Hanke, A. Johansson, J.B. Harper, and R.M. Lynden-Bell, Chemical Physics Letters 374, 85-90 (2003).
[2] M. Deetlefs, C. Hardacre, M. Nieuwenhuyzen, O. Sheppard, and A. K. Soper, J. Phys. Chem. B, 109, 1593-1598 (2005).

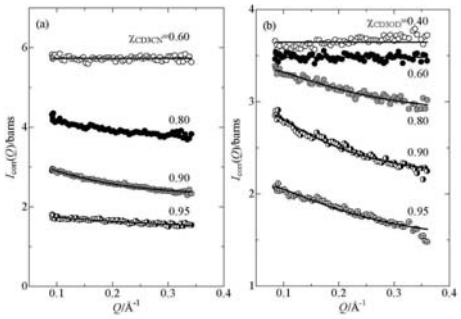


Fig. 1. SANS spectra for (a) EMICl-acetonitrile and (b) EMITFSA-methanol mixtures.

1-4-4

Amide-Induced Phase Separation of HFIP-Water Mixtures

Toshiyuki Takamuku, Hiroshi Wada, and Kenta Fujii
Saga University

Aqueous mixtures of several water-miscible organic solvents, such as propanol and acetonitrile, separate into organic solvent-rich and water-rich phases, when salt is added into mixtures. The key of the salt-induced phase separation is preferential solvation of both cation and anion by water molecules [1-4]. Thus, water clusters are evolved around both ions with increasing salt concentration, and organic molecules, which are excluded from water clusters, simultaneously aggregate to form clusters. Finally, phase separation takes place, when the size of both water clusters and organic solvent clusters reaches a macroscopic scale. Recently, we have found that addition of amphiphilic molecules, such as amide, also induces phase separation of 1,1,1,3,3,3-hexafluoro-2-propanol (HFIP)-water mixtures. The phase diagrams obtained for the HFIP-water-amide ternary systems at 298 K have shown a closed-circle region of phase separation, and the more hydrophobic the amides, the larger the region of phase separation.

To clarify the mechanism of amide-induced phase separation of HFIP-water mixtures, in the present study, SANS experiments have been made on HFIP-water-amide mixtures with three different amides, N-methlyformamide (NMF), N-methylacetamide (NMA), and N-methylpropionamide (NMP). The hydrophobicity of the amides is larger in the order of NMF $<$ NMA $<$ NMP.

HFIP-D2O-amide ternary solutions below the lower critical composition and above the upper critical one were prepared in accordance with the phase diagrams. SANS measurements at 298 K were made on the sample solutions by using the SANS-U spectrometer with the camera lengths of 1 and 4 m. The scattering intensities were accumulated on the detector at the camera lengths of 1 and 4 m for 10 min and 1 h per sample, respectively.

Fig. 1(a) shows the Ornstein-Zernike correlation lengths xi estimated from the SANS intensities for the HFIP-D2O-amide mixtures below the lower critical composition as a function of amide mole fraction. For each amide system, the xi value increases with increasing amide mole fraction. It is suggested that the heterogeneity of the mixtures increases with the increase in the amide concentration toward the critical one. The NMP system requires the smallest amount of amide to enhance the heterogeneity among the systems. Fig. 1(b) shows that the amide mole fraction dependence of the xi values for the HFIP-D2O-amide mixtures above the upper critical composition. The xi value for each system gradually decreases when the amide concentration increases apart from the critical one. The NMP system requires the largest amount of amide to recover the homogeneous mixing.

Below the lower critical composition, a small amount of amide added may be easily solvated by hydrophobic HFIP molecules rather than water ones, resulting in the enhancement of HFIP clusters around amide molecules. Hence, phase separation occurs when clusters are evolved to a macroscopic size. Above the lower critical composition, on the contrary, amide molecules further added may play a role as an interface between HFIP and water clusters because of the amphiphilicity of amide molecule, i.e., HFIP, water, and amide molecules are homogeneously mixed again. Thus, the HFIP-water-amide systems reveal a closed-circle region of phase separation, and the region for the HFIP-water-NMP system is the largest among the three systems due to the most hydrophobic NMP.

Activity Report on Neutron Scattering Research: Experimental Reports **15** (2008)
Report Number: 361

[1] K. Yoshida, M. Misawa, K. Maruyama, M.; Imai M. Furusaka, J. Chem. Phys., 113, 2343-2348 (2000).
[2] T. Takamuku, D. Matsuo, A. Yamaguchi, M. Tabata, K. Yoshida, T. Yamaguchi, M. Nagao, T. Otomo and T. Adachi, Chem. Lett., 2000, 878-879.
[3] T. Takamuku, A. Yamaguchi, D. Matsuo, M. Tabata, M. Kumamoto, J. Nishimoto, K. Yoshida, T. Yamaguchi, M. Nagao, T. Otomo and T. Adachi, J. Phys. Chem. B, 105, 6236-6245 (2001).
[4] T. Takamuku, Y. Noguchi, E. Yoshikawa, T. Kawaguchi, M. Matsugami and T. Otomo, J. Mol. Liquids, 131/132, 131-138 (2007).

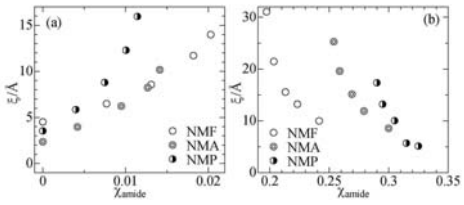


Fig. 1. Xi values for HFIP-water-amide mixtures (a) below the lower critical composition and (b) above the upper critical one as a function of amide mole fraction.

1-4-5

Alkyl-chain Dependence on Micro-phase Separation of Room Temperature Ionic Liquids

Kenta Fujii (A), Yasuhiro Umebayashi (B), Shin-ichi Ishiguro (B), and Toshiyuki Takamuku (A)
(A) Saga Univ., (B) Kyushu Univ.

Room temperature ionic liquid has attracted attention as a new solvent of negligible vapor pressure and incombustibility. Recently, it has been reported by simulation and thermodynamic studies [1,2] that nonpolar (alkyl-chain group) and polar (cationic imidazolium ring and anion) domains are formed in 1-alkyl-3-methylimidazolium (C(n)mim+) hexafluorophosphate ionic liquids with the alkyl-chain length longer than n = 4, thus micro-phase separation occurs in the ionic liquids. In this work, small-angle neutron scattering (SANS) measurements for the C(n)mim+ bis(trifluoromethanesulfonyl) amide (TFSA-) were carried out at 298 K to elucidate experimentally the effect of varying the alkyl-chain length on the micro-phase separation.

SANS measurements were made on the C(n)mim+TFSA- (n = 2, 4, 6, 8, 10 and 12) by using SANS-U spectrometer with the camera length of 1 and 4 m. The scattering intensities for the sample liquids were accumulated on the detector at the camera lengths of 1 and 4 m for 10 min and 1 h, respectively.

Figure 1 shows SANS spectra obtained for the C(n)mim+TFSA- with the alkyl-chain length from 2 to 12. The SANS profiles for all the ionic liquids at low Q region do not show the Orstein-Zernike behavior. Indeed, a peak appears in the range of $0.15 < Q/A\text{-}1 < 0.35$ with increasing the alkyl-chain length and shifts to lower Q side. A peak fitting using Lorentzian function was performed on the SANS spectra, as shown by solid line in Fig. 1, to obtain the peak position Q0, and then the spatial correlation (= 2pi/Q0) were estimated to be 15, 22 and 26 A for n = 8, 10 and 12, respectively. The spatial correlation obviously depends on the alkyl-chain length, indicating that the alkyl-chain groups aggregate to form domains or clusters in the ionic liquids with n = 8 up to 12, but do not aggregate with n = 2 to 6. Here, according to our large-angle high-energy X-ray scattering measurements, it has found that the carbon - carbon interactions among the alkyl-chain groups of the C(n)mim+ strengthen with increasing n. This is consistent with the present SANS results, i.e., the experimental evidence for the long-range ordering of room-temperature ionic liquids at the molecular level.

References

[1] J. N. A. C. Lopes, A. A. H. Padua, J. Phys. Chem. B 110, 3330-3335 (2006)
[2] L. M. N. B. F. Santos, J. N. C. Lopes, J. A. P. Coutinho, J. M. S. S. Esperanca, L. R. Gomes, I. M. Marrucho, L. P. N. Rebelo, J. Am. Chem. Soc. 129, 284-285 (2007)

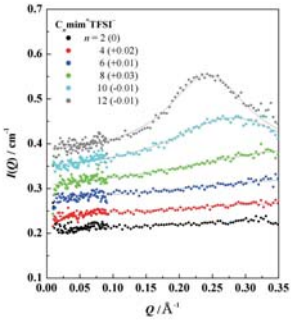


Fig. 1. SANS profiles of C(n)mim+TFSA- ionic liquids

1-4-6

Structural Change of Supercritical Carbon Dioxide with Entrainer Molecule

T. Sato[A], M. Sugiyama[B], M. Misawa[C], K. Hamada[A], K. Itoh[B], K. Mori[B], and T. Fukunaga[B]

[A]*Grad. Sch. Eng. Kyoto Univ.,* [B]*KUR, Kyoto Univ.,* [C]*KEK*

Recently, supercritical carbon dioxide (sc-CO_2) has attracted much attention as an environmentally accepted solvent. The solvent power of sc-CO_2 extremely increases with adding a small amount of entrainer molecule such as alcohol, carbon hydride, and water. Since the solubility of sc-CO_2 is strongly connected with its fluctuation structure, it is quite important to investigate the effects of entrainer for meso-scale structure of sc-CO_2. In the present study, the structural change of sc-CO_2 induced by adding the entrainer has been observed with small-angle neutron scattering (SANS).

A SANS experiment was performed using SANS-U of the Institute for Solid State Physics, the University of Tokyo installed at JRR-3M in Tokai, Japan. Scattering intensity with a Q range between 0.02 and 0.2 Å^{-1} can be measured by using 7 Å neutron in 2 m camera length. Methanol (CD_3OD) or ethanol (C_2D_5OD) was added into sc-CO_2 with 1 mol% concentration as entrainer. Measurement temperature was fixed at 38 °C and pressure was varied from 7.66 to 10.36 MPa.

The ovserved SANS intensity was simply analyzed with Ornstein-Zernike (OZ) equation to obtain OZ correlation length, ξ, and $I(0)$. Although the system consisted of both density and concentration fluctuations, all the SANS data can be well analyzed with a single OZ equation. Since the concentration of entrainer was dilute, the scattering intensity mainly came from the density fluctuation of the mixed solution. The pressure dependences of ξ and $I(0)$ along the isotherm are shown in Fig. 1(a) and 1(b), respectively. Results of both pure and alcohol entrained sc-CO_2 are displayed in this figure. Each data has a maximum along the isotherm corresponding to the ridge structure in supercritical region. The maximum values of ξ and $I(0)$ of sc-CO_2 with alcohol become considerably larger than those of pure sc-CO_2. Moreover, the pressure at which the fluctuation becomes maximum sifts to the lower. It was suggested that these changes could be induced by attractive interaction between the alcohol and CO_2 molecules. Magnitude of the interaction with the ethanol is stronger than that with the methanol. It is considered that these structural changes with alcohol molecules associate with the increase of solvent power of sc-CO_2.

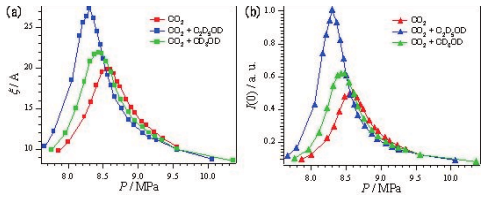


Fig. 1. Change of structural parameters ξ and $I(0)$ along the isotherm of 38 °C induced by adding 1 mol% methanol and ethanol.

1-4-7

Static and Dynamic Structure of Meso-scale fluctuations in liquid chalcogens near the metal-nonmetal transition

Y.Ohmasa, T.Hoshino R.Osada and M.Yao
Department of Physics, Graduate School of Science, Kyoto University

Liquid Te-Se mixtures exhibit a metal-nonmetal (M-NM) transition in a relatively narrow temperature range [1]. This transition is accompanied by anomalies in thermodynamic properties such as the thermal expansion coefficient and compressibility. Recently, sound attenuation measurements for liquid Te-Se mixtures revealed that there occur dynamic anomalies in the M-NM transition region [2]. From the frequency dependence of the sound attenuation coefficient α, their relaxation time is estimated to be of the order of nanoseconds. These anomalies may be related to the relaxation between the metallic and non-metallic states in the liquid, and it is interesting to study the space- and time-structure of the mesoscale fluctuations.

In the present work, we studied the static and dynamic structure of meso-scale fluctuations in liquid Te-Se mixtures near the metal-nonmetal transition by using Neutron Spin-Echo (NSE) and Small Angle Neutron Scattering (SANS) techniques.

The closed and open circles in Fig.1 show the intermediate scattering function $I(Q,t)/I(Q,0)$ of Te_7Se_3 sample in a quartz cell observed at Q =0.046A^{-1} and 0.064A^{-1}, respectively, at 490°C. These data indicate that there exists a relaxation process in the nsec region. In addition, from the SANS measurement, we observed a strong peak at $Q \sim 0.2$A^{-1} for the liquid Te-Se mixtures for the first time. This peak may be related to the meso-scale fluctuations in the M-NM transition region.

References

[1] M. Yao and H. Endo, J. Non-Cryst. Solids **205-207** (1996) 85, and references therein.

[2] M. Yao, N. Itokawa, H. Kohno, Y. Kajihara and Y. Hiejima, J. Phys.: Condens. Matter **12** (2000) 7323

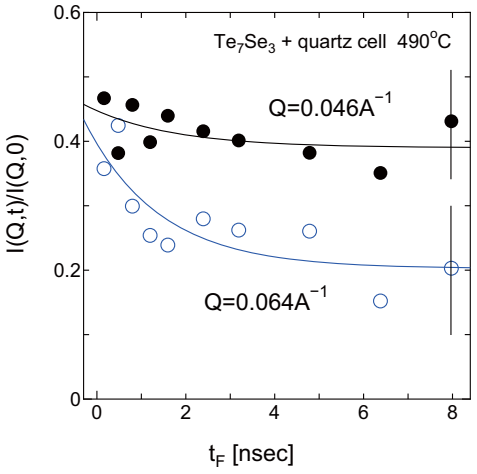


Fig. 1. Intermediate scattering function I(Q,t)/I(Q,0) for liquid Te7Se3 in a quartz cell at 490C. The solid lines indicate the fitting curves.

1-4-8

Small Angle Neutron Scattering Investigation of Aggregation of *N,N*-dialkylamide and Its Effect on Nitric Acid Extraction

S. Suzuki, T. Yaita[1], R. Motokawa[2] and S. Koizumi[2]

Nuclear Science and Engineering Directorate, JAEA, Tokai, Ibaraki 319-1195
[1]*Quantum Beam Science Directorate, JAEA, Harima, Hyogo, 679-5148*
[2]*Advanced Science Research Center, JAEA, Tokai, Ibaraki, 319-1195*

Small Angle Neutron Scattering (SANS) is a powerful technique in structural studies of polymers and micelles[1)]. Recent studies have shown the applicability of the SANS technique to solvent extraction chemistry[2)]. SANS has ability to elucidate the size and the shape of the extractant aggregates formed upon metal cations and inorganic acid extraction.

In solvent extraction chemistry, this extractant aggregate with metal ions (likes uranium and plutonium) and/or inorganic acid makes heavy organic phase (it is called the third phase) between an aqueous phase and an organic phase. This aggregate in the nuclear spent fuel reprocessing causes serious problems, such as a criticality accident and inhibition of stable process operation. In order to understand this aggregate with metal ions and inorganic acid, the structure analysis of high concentration metal ion and/or inorganic acid loaded organic phase as a reprocessing process is required. However, large extractant aggregates or polymeric species are often formed under reprocessing conditions, which has not been studied in detail.

N,N-dialkylamide extractants strongly aggregate with uranium or nitric acid in non-polar diluents has been reported[3)]. SANS studies of the aggregation of *N,N*-dihexyloctanamide (DHOA) dissolved in deuterated n-octane have been preformed.

The samples were made as following procedure, 2 ml of deuterated n-octane as an organic solvent containing 1.0 mol/dm^3 DHOA was shaken with the same volume of the various nitric acids (2.0, 4.0, 6.0, 9.0 mol/dm^3). After centrifugation this sample, 0.5 ml of the organic solution was separated to use as a sample. 0.5 ml of DHOA solution was enclosed in Quartz cell. SANS measurement were performed by the SANS-J instrument with λ =0.706 nm at the JRR-3M reactor in JAEA. The scattering data of extracted samples were collected for 1 hour at room temperature.

Figure 1 shows the first obtained scattering profiles of nitric acid (2.0, 4.0, 6.0, 9.0 mol/dm^3) extracted DHOA samples.

In next step, data analysis for these results should be carried out. Furthermore, SANS measurement, vapor pressure osmometry, interfacial tension measurement for radioactive samples (uranium(VI) and thorium(IV)) should be investigated.

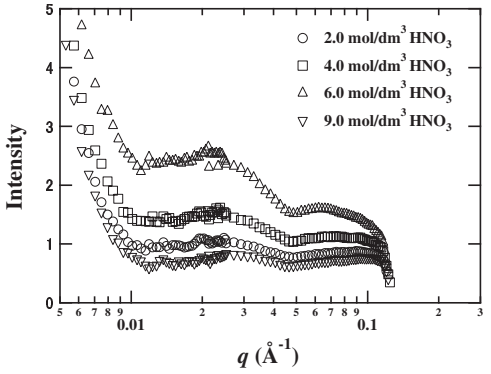


Figure 1: SANS curves of DHOA-nitric acid extracted samples.

References

1) L.J.Magid :"Structure and Dynamics by Small-Angle Neutron Scattering, in nonionic Surfactants, Physical Chemistry", M.J.Schick Ed., Surfactant Science Series, 23, Maercel Dekker, Inc., New York, (1987).
2) M.P.Jansen, T.Yaita, and R. Chiarizia :"Langmuir", 23(9), pp. 4765 (2007).
3) G.M.Gasparini, and G. Grossi :"Solv. Extr, Ion Exch.", 4(6), 1233 (1986).

原子炉：JRR-3　　装置：SANS-J(C3-2)　　分野：中性子散乱（液体・不規則物質）

This is a blank page.

1. 中性子散乱 5) 高分子

1. Neutron Scattering 5) Polymer

This is a blank page.

1-5-1

Dynamical Study on Nanocomposite Hydrogel by Means of Neutron Spin Echo Technique

Hitoshi Endo, Sho Miyazaki and Mitsuhiro Shibayama
ISSP, The University of Tokyo

"Nanocomposite" is a current key aspect for development of advanced materials [1], e.g., polymer-clay nanocomposite in synthetic systems [2]. Recently, polymer-clay nanocomposite hydrogels (NC gel) have been developed by Haraguch et al. [3, 4], which have extraordinary superior properties as large deformability with high elasticity, quick shrinkage after large deformation, non-destructivity, high optical transsparency, and so on. Since conventional organogels are very fragile, these characteristics of NC gels are great advantages for material use.

We have studied the static structure of NC gel in detail by means of contrast variation SANS [5], and confirmed that the polymer chains are adsorbed on clay surface, then the clay nanoparticles work as 2-dimensional cross-linkers.

In this study, dynamical property of the nanocomposite hydrogel was investigated by means of neutron spin echo technique. Since 10.8 Åwavelength neutron beam was unsed for low Q region ($0.04 \leq Q[\text{Å}^{-1}] \leq 0.07$), the achieved maximum Fourier time was a bit more than 40ns, while 7.3 Åwavelength neutron beam was unsed for high Q region ($0.09 \leq Q[\text{Å}^{-1}] \leq 0.2$), so that the maximum Fourier time was 15ns in that case. Fig. 1 shows the measured normarized intermediate scattering functions from the nanocomposite gel consisting of 4 vol% of polymer and 1 vol% of clay with deuterated water. The curves in Fig. 1 show the fitting results with

$$\frac{I(Q,t)}{I(Q,0)} = \exp(-\Gamma t) \qquad (1)$$

at short Fourier times ($<$ 5ns). It is clearly shown that the measured intermediate scattering functions decay as like as liquids, but do not decay exponentially at longer Fourier time, which may be due to the gel structure, i.e., the polyer gels are macroscopically solids but microscopically liquids, and the polymers can flow in short time scale but their center of masses are frozen for longer time scale.

References

[1] L. A. Utracki, *Clay-Containing Polymeric Nanocomposites* (Repra Tech. Ltd., London, 2004).
[2] A. Okada and A. Usuki, *Macromol. Mater. Eng.* **291**, 1449 (2006).
[3] K. Haraguchi and T. Takehisa, *Adv. Mater.* **14**, 1120 (2002).
[4] K. Haraguchi, T. Takehisa and S. Fan, *Macromolecules* **35**, 10162 (2002).
[5] S. Miyazaki, H. Endo, T. Karino, K. Haraguchi, and M. Shibayama, *Macromolecules* **40**, 4287 (2007).

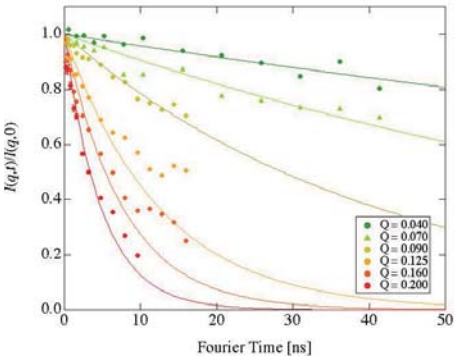


Fig. 1. Normalized intermediate scattering functions I(Q,t)/I(Q,0) obtained from the nanocomposite hydrogel.

1-5-2

Hysteresis of bicelle/ULV transition in long- and short-chain lipid mixture

Norifumi L. YAMADA, Naoya TORIKAI
High Energy Accelerator Research Organization

In the aqueous solutions of dimyristoylphosphatidylcholine (DMPC) and dihexanoylphosphatidylcholine (DHPC) mixture, bilayered-micelle, so called bicelle, were formed at low temperature. These bicelles fuse into large uni-lamellar vesicles (ULVs) above the chain melting temperature, T_c, of DMPC molecules (about 24°C) when lipid membranes were charged [1]. Although these disk-fused ULVs usually fissure into small disk micelles below T_c, the ULVs are stable even below T_c when the lipid concentration is very low [2]. However, the mechanism of the stable ULV formation has not been clarified yet.

In this study, we observed the structure in the lipid mixture system below and above T_c by SANS, and quantitatively discussed the stability of ULVs. The experiments were performed at 20°C and 50°C with changing lipid concentration. DMPC and DHPC were mixed in the molar ratio of [DMPC]:[DHPC] = 4.6:1, and dissolved in the D_2O solution of 3 mM $CaCl_2$. The SANS experiments were carried out at SANS-U, JRR-3M, JAEA, Tokai, Japan [3].

Figure 1 shows the temperature dependence of SANS profile with changing lipid concentration. While no hysteresis was observed at high lipid concentration (2.11 wt.%), the SANS profiles at low lipid concentration (0.35 wt.%) show the hysteresis as shown by previous study [2]: the profile of bicelles at 20°C changed to ULVs with increasing temperature up to 50°C, and the profile of ULVs remained even after decreasing temperature down to 20°C. Although such the hysteresis was observed even at intermediate lipid concentration (1.06 wt.%), large bicelles appeared instead of ULVs after annealing. In this case, the volume of bicelle evaluated by the fitting is almost same to that of ULV shell. This means that one ULV at high temperature phase opened to one bicelle with decreasing temperature. Therefore, bicelles after annealing is larger than before annealing, since some small bicelles fuse into one ULV at the ULV formation. This new histeresis would be a important help to understand the mechanism of the hysteresis of bicelle/ULV transition.

References

[1] M.-P. Nieh *et al.*, *Biophys. J.* **82** (2002) 2487.
[2] M.-P. Nieh *et al.*, *Langmuir* **21** (2005) 6656.
[3] S. Okabe *et al.*, *J. Appl. Cryst.*, **38** (2005) 1035.

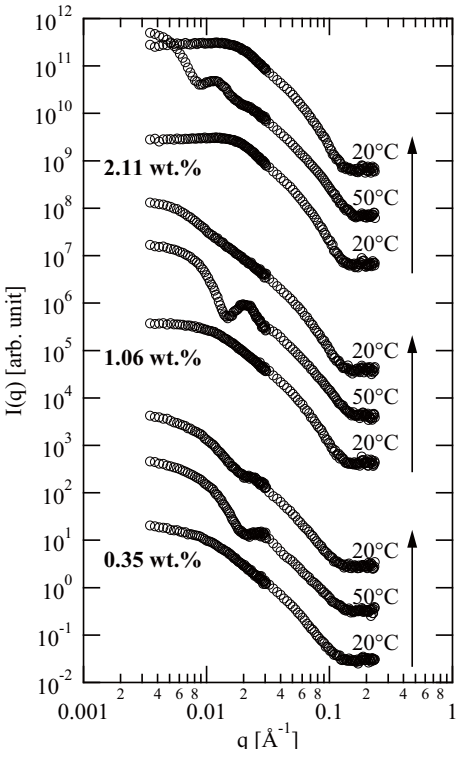


Fig. 1. Temperature dependence of SANS profile with changing lipid concentration. Temperature sequence is indicated by the arrows.

1-5-3

Changes in flow-induced aggregated structures of shear-thickenning silica suspensions

M. Ando (A), H. Mizukawa (A), Y. Takahashi (B), and M. Kawaguchi (A)
(A) Mie University, (B) Kyushu University

In this report, we performed small-angle neutron scattering (SANS) under shear for the 4.93 vol% fumed hydrophobic silica particles, whose surface is chemically coated by dimethyl n-hexadecane silicone, suspended in dioxane and n-hexadecane. The wavelength was selected to be 0.7 nm. The suspensions pre-conditioned by a debubbling mixer were transfered to a quartz co-axial rheometer cell with the gap length of 1 mm. The sample to detector distances were 4 m and 12 m. The resulting scattering intensity was normalized to the isotropic scattering intensities of the respective dispersants after substraction of the background due to the corresponding dispersants. The SANS experiments were performed under applied shear rates ranged from 0 to 600 1/s at 27 oC.

The rheological measurements of the corresponding silica suspensions were performed using a commercial rheometer of MCR-300: rheochaos response, namely irregular time variation in the stress/shear rate at a constant shear rate/stress arising from nonlinearities in the viscoelastic constitutive equations, was observed for the silica suspension in dioxane at limitted shear rates, whereas such a response was not detective for the silica suspensions in n-hexadecane during the shear rates examined. Similar rheochaos responses were observed in several soft matters, such as worm-like micelle solutions, lamellar, onion, and sponge phases of surfactants, and dense colloidal suspensions.

Figure 1 shows a double logarithmic plots of the scattering intensity (I(q)) as a function of the wave vector (q) for the silica suspesnion in dioxane. The values of I(q) apparently superimpose on the same curve, irrespective of the shear rate. The respective log-log plots of I(q) versus q scale linearly a slope of - 2.0 below q = 0.2 1/nm and - 4.0 above this q value, where the I(q) tends toward Porod's law. The former slope corresponds to the mass fractal dimension (Dm) for the aggregated objects, while the latter slope gives the surface fractal dimension (Ds) according to the relationship, I(q)˜ qˆ- (6-Ds), leading to the Ds value of 2.0. The resulting Ds value is smaller than that for the hydrophobic R202 silica particles, whose surface is chemically coated by silicone oil with the degree of polymerzation of 6 in trans-decalin. Moreover, the q value intercected between the slopes of - 2.0 and - 4.0 gives the size of the primary silica particle and leads to 11.5 nm, which is almost equivalant to the diamater of the corresponding fumed silica. However, we can notice that the magitude of the I(q) vales at the shear rate ranges from 20 to 300 1/s where rheochaos response is observed, is clearly larger than that without rheochaos response by the plots of I(q) as a function of log q.

On the other hand, the scattering curves for the silica suspensions in n-hexadecane can be much better superimposed than those in dioxane, irrespective of the applied shear rate. This means that changes in the scattering intensities are not clearly observed when shear rate is varied. However, the difference between the scattering curves of the silica suspensions in dioxane and n-hexadecane was observed at the q values higher than 0.1 1/nm, where the former scattering intensity was clearly larger than the latter one if both scattering curves in dioxane and n-hexadecane at lower q regions were supperimposed.

In conclusion, this SANS experiment shows that the rheochaos response is well correlated with the changes in the scattering curves and the fractal strucures of the

Activity Report on Neutron Scattering Research: Experimental Reports **15** (2008)
Report Number: 297

silica suspensions can not be easily broken out by the applied shear rates.

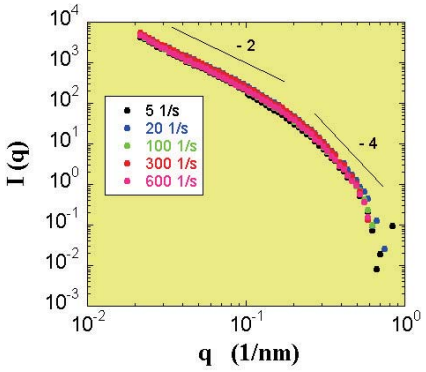


Fig. 1. SANS scattering curves of the silica suspensions in dioxane under the applied shear rates.

1-5-4

Simultaneous Evaluation of Lipid Exchange and Flip-Flop in Vesicles

Nakano(A), M. Fukuda(A), T. Kudo(A), H. Endo(B)
(A)Graduate School of Pharmaceutical Sciences, Kyoto Univ., (B)ISSP-NSL, Univ. of Tokyo

We recently succeeded in determining the rates of interbilayer exchange and flip-flop of dimyristoylphosphatidylcholine (DMPC) in large unilamellar vesicles (LUVs) by small-angle neutron scattering (SANS) technique [1]. This technique takes advantage of the large difference in the scattering length density between hydrogenated and deuterated lipids, and the exchange of these lipids between LUVs results in a decrease in the scattering intensity, which can be detected by time-resolved SANS (TR-SANS) measurements. In this study, effect of cholesterol (Chol) on the rate of interbilayer and transbilayer transfers of DMPC was evaluated by TR-SANS measurements.

DMPC, d54-DMPC, were obtained from Avanti Polar Lipids Inc. (Alabaster, AL). Cholesterol (Chol) was from Sigma (ST. Louis, MO). LUVs consisting of deuterated (D-LUV) or hydrogenated DMPC (H-LUV) and Chol (0, 20, and 40 mol% of total lipids) with a diameter of ca. 100 nm were prepared by extrusion method using Tris-buffered saline prepared from mixtures of D2O and H2O. LUVs consisting of 1:1 mixture of deuterated and hydrogenated lipids (D/H-LUV) were also prepared by mixing these lipids and Chol before hydration. Volume fraction of D2O in the Tris-buffer was 0.5, 0.45, and 0.4 for LUVs with 0, 20, and 40 mol% Chol, respectively, which corresponds to the contrast-matching condition between D/H-LUV and solvent. Phospholipid concentration of each LUV preparation was set to 20 mM. SANS measurements were performed at 37 ° C using SANS-U with 7 angstrom of incident neutron beam. Sample-to-detector distance was set to 4 m.

First, we confirmed that D-LUV and H-LUV had almost identical scattering profile, while D/H-LUV exhibited little scattering at the contrast matching condition.

TR-SANS measurement was started immediately after mixing equivalent volume of D-LUV and H-LUV. Time-course of the normalized contrast was calculated from the scattering intensity and plotted in Figure 1. The contrast decay profiles depend on the mole fraction of Chol. In the absence of Chol, the normalized contrasts reached below 0.5, suggesting an involvement of flip-flop, and the obtained contrast decays were well reproduced by the kinetic model that takes account of both the interbilayer and transbilayer exchange. These exchange rates were reduced in the presence of Chol, and the flip-flop was vanished at 40 mol% Chol, where lipids are known to form liquid-ordered phase.

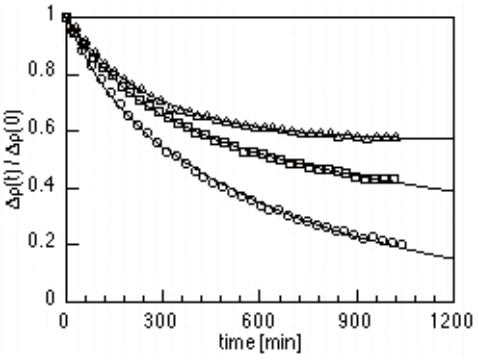


Fig. 1. Contrast decays of DMPC/Chol LUVs with 0 (circles), 20 (squares), and 40 mol% Chol (triangles) after mixing D- and H-LUV at 37 ° C.

1-5-5

Structure Analyses of Nanoemulsion/polymer Mixtures Having Dilatancy Behavior

M. Shibayama[A], Y. Kawada[B], T. Kume[B],H. Endo[A],N. Osaka N.[A],T. Matsunaga[A]
[A]*ISSP-NSL, University of Tokyo*
[B]*Beauty Care Res. Lab., Kao Co., Ltd.*

The microscopic structure of shear-induced gels for a mixed solution of 2-hydroxyethyl cellulose (HEC) and nanometer-size spherical droplets (NE) has been investigated by in-situ small-angle neutron scattering (SANS) with a Couette geometry as a function of shear rate, $\dot{\gamma}$. The following facts were disclosed.
(1) There is a suitable range of NE and HEC concentrations necessary for a shear-induced sol-gel transition. The size of the polymer chains needs to be comparable with the inter-particle distance, a, of the oil-droplets in NE. (2) In the stationary state, the polymer chains do not bridge neighboring droplets and are localized to one or a few droplets via weak molecular interaction, such as van der Waals interaction and/or hydrogen bond. (3) Nanodroplets are dispersed in the solution with the electrostatic repulsive interaction and keep the inter-particle distance. (4) With increasing $\dot{\gamma}$, the viscosity increased rapidly at $\dot{\gamma} \simeq 4.0$ s^{-1}, followed by a shear thinning. After cessation of shear, the system exhibited an extraordinarily large steady viscosity. This phenomenon was observed as a shear induced sol-gel transition. (5) Real-time SANS measurements showed an increase in the scattering intensity exclusively at low scattering angle region. However, neither orientation of polymer chains nor droplet deformation was detected and the SANS patterns remained isotropic irrespective of $\dot{\gamma}$. It took about a few days for the gel to recover its original sol state. (6) Shear-induced sol-gel transition occurs when the system is percolated with deformed polymer chains via droplets. (7) For systems having highest dilatancy ratio, the shear stress at the transition σ_{tr} is simply estimated by the interparticle distance, a, i.e., $\sigma_{tr} \approx k_B T/a^3$, and is independent of the molecular weight of the polymer, where k_B and T are the Boltzmann constant and the absolute temperature, respectively. This means that the shear (or shear rate) necessary for the transition is of the order of unity, i.e., $\gamma_{tr} \approx 1$. (8) The shear thickening is not necessarily ascribed to a non-Gaussian chain deformation, such as an inverse Langevin chain conformation, but to a Gaussian chain statistics with a filler-assisted percolation. A possible mechanism of gelation is proposed from the viewpoint of shear-induced percolation transition.[1]

References

[1] M. Shibayama, H. Kawada, T. Kume, T. Matsunaga, H. Iwai, T. Sano, N. Osaka, S. Miyazaki, S. Okabe, and M. Shbayama, *J. Chem. Phys.* **127**, 144507-1-7 (2007).

1-5-6

Ionic Strength Dependence of Chain Conformation of Hydrophilic Polymers at Water Interface

M. Kobayashi1, Y. Terayama2, N. Hosaka2, A. Takahara*1,2
1Institute for Materials Chemistry and Engineering, 2Graduate School of Engineering, Kyushu University

In general, an isolated polyelectrolyte in pure water forms a relatively expanded state due to the electrostatic repulsion of ionic functional groups in the chain, while it would shrink in salt solution by the reduction of electrostatic repulsion between polymer chains. However, the influence of the ionic strength on a dimension of charged polymers should largely depend on chain flexibility and environment. Polymer brush, for example, is the densely tethered polymer chains on a solid substrate through the covalent bonds.[1] Brush layer in a solution affords unusual high concentration of polymer and high osmotic pressure, resulting in a fairly extended conformation of the brush chains. In this study, interface structure of surface-grafted polyelectrolyte brush at aqueous solution containing a salt was analyzed by neutron reflectivity (NR) measurements.

High-density polyelectrolyte brushes on quartz were prepared by surface-initiated atom transfer radical polymerization of 2-methacryloyloxyethyl phosphorylcholine (MPC) [2] and N,N-dimethylaminoethyl methacrylate, which was transformed to 2-(methacryloyloxy)ethyltrimethylammonium iodide (META). NR measurements were carried out with the multilayer interferometer for neutrons (MINE), using wavelength of 0.88nm. Neutron beam irradiated from quartz to the interface between heavy water and swollen brush on quartz glass. Scattering length density profiles of PMETA brush in heavy water calculated from the reflectivity curves indicated that the PMETA chains were stretched up to 70 nm in heavy water forming concentration gradient of heavy water. Interestingly, quite similar reflective curve was observed from the interface of PMETA brush at 1.0 M of NaCl deuterium oxide solution. Salt ion cannot be diffused into a high-density polymer brush layer due to the high osmotic pressure and high local charge density. Therefore, the thickness of PMPC brush in solution was supposed to be hardly changed even in a salt solution. Similar results in another type of polyelectrolyte have also been discussed by Matsuoka[3] and Kurihara[4] using X-ray reflectivity and surface-force measurement, respectively.

References

[1] W. J. Brittain et al, Polymer Brushes, Wiley-VCH, Weinheim (2004).
[2] M. Kobayashi, Y. Terayama, N. Hosaka, M. Kaido, A. Suzuki, N. Yamada, N. Torikai, K. Ishihara, A. Takahara, Soft Matter, 3, 740 (2007).
[3] P. Kaewsaiha, K. Matsumoto, H. Matsuoka, Langmuir, 20, 6754 (2004).
[4] S. Hayashi, T. Abe, N. Higashi, M. Niwa, K. Kurihara, Langmuir 18, 3932 (2002).

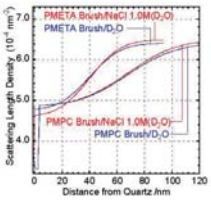


Fig. 1. Figure 1. Scattering length density profiles of PMETA and PMPC brush in D2O and 1.0 M NaCl solution.

1-5-7

Surface and Interface Structure Analysis of (Multi-functionalized Silsesquioxane/Deuterated Polystyrene) Hybrid Thin Films

N. Hosaka1, Y. Terayama1, M. Kobayashi2, A. Takahara*1,2
1Graduate School of Engineering, 2Institute for Materials Chemistry and Engineering, Kyushu University

Polymer thin films have gained much interest because of their numerous technological applications, however, producing stable and defect-free films is problematic since the polymer thin films tend to break up and dewet from a substrate. Previously, it was shown that the addition of polyhedral oligomeric silesequioxane (POSS) nanofiller stabilized the polystyrene (PS) thin film against dewetting [1]. POSS, which is characterized by the formula of (RSiO1.5)8, has a nanosized cage structure with a silica core and organic groups on its surface. The dispersion state of POSS in the film seemed to be an important factor to understand the film stabilization effect [2], and the systematic study using designed nanofillers to control its dispersion state is a challenge for further development of this technique.

The present work is focused on the control of the dispersion state of POSS nanofillers in PS thin films through the introduction of the several substituents onto POSS surface. The dispersion states of the surface-modified POSS in deuterated PS (d-PS) thin films were investigated by neutron reflectivity. Figure 1 shows the depth profile models of scattering length density (b/V) of ca. 130 nm thick d-PS film and POSS/d-PS (10/90, w/w) films. POSS with phenethyl groups (PhPOSS) was homogeneously dispersed into d-PS film because of the high affinity of phenethyl groups with d-PS. The b/V of the film was decreased by the addition of PhPOSS compared with d-PS film. In contrast, POSS having seven cyclopentyl groups and a low energy fluoroalkyl group (CpPOSS-Rf) strongly segregated to the film surface and formed thin layer with low b/V. The difference of the surface energy between CpPOSS-Rf and d-PS provides a driving force for the segregation of CpPOSS-Rf to the film surface. The formation of low b/V layer was also observed at the surface and film?substratet interface of d-PS film containing POSS with seven cyclopentyl groups and a dihydroxylpropyl group (CpPOSS-2OH). CpPOSS-2OH segregated to the surface and the interface of the film because of the lower surface energy of cyclopentyl groups than that of d-PS and the affinity of the hydroxyl groups with the substrate, respectively. These results revealed that the dispersion state of POSS can be controlled by tuning the surface substituents on POSS, and expected to contribute to the design of the polymer thin film properties by the addition of nanofillers with controlled structures.

References

[1] N. Hosaka, K. Tanaka, H. Otsuka, A. Takahara, CompositeInterfaces, 11, 297 (2004).
[2] N. Hosaka, N. Torikai, H. Otsuka, A. Takahara, Langmuir, 23, 902 (2007).

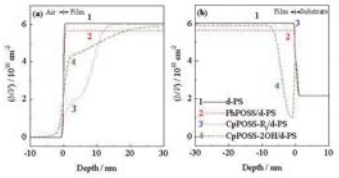


Fig. 1. Figure 1. The depth profile models of b/V of d-PS film and POSS/d-PS (10/90, w/w) films near (a) the surface and (b) the film?substrate interface.

1-5-8

Thermal fluctuation of a lipid bilayer in the anomalous swelling regime

Hishida M., Seto H., Yamada N.L.
Department of Physics, Kyoto Univ.

Biomembrane is mainly composed of a phospholipid bilayer, which is spontaneously formed by mixing of lipid and water. A various kinds of physical and chemical properties of phospholipid bilayers have been investigated, and a number of applications have been provided. Spontaneously formed structure of phospholipid by mixing with water is multi-lamellar vesicles, while living cell membranes are uni-lamellar vesicles. It is important to understand the formation of cell membrane self-organization of lipid bilayers in context with the interactions between bilayers such as van der Waals interaction, hydration repulsion and steric repulsion by thermal fluctuation of bilayer.

In order to understand interactions of lipid bilayers, we focused on a phenomenon called "anomalous swelling" [1]. In the anomalous swelling regime, i.e., temperature just above the main transition temperature from the liquid-crystalline phase to the gel phase, the repeat distance between stacked bilayers increase drastically. The driving force for the increase has been considered to be amplified steric repulsion due to the softening of lipid bilayer [2]. However, the softening is not confirmed enough especially by microscopic picture, and the mechanism of anomalous swelling is under dispute.

In the present experiment, we performed neutron spin echo spectroscopy (NSE) for the lipid bilayers in the anomalous swelling regime at iNSE, JRR-3, JAEA. Both multi-lamellar vesicles and uni-lamellar vesicles of DMPC were measured in the same condition. Figure 1 shows the typical intermediate correlation functions of DMPC small uni-lamellar vesicles. The bending modulus of lipid bilayer is calculated using the theory by Zilman and Granek, and the values exhibit that bilayers become harder in the anomalous swelling regime. The same tendency is observed in the case of multi-lamellar vesicles. This tendency is reasonable since the hydrocarbon chain of lipid molecules freeze in the gel phase. The value of the bending modulus estimated from the experiment is two orders of magnitude larger than kT. This result suggests that static disordering of stacking of bilayers such as metastable ripple phase is induced just above the main transition temperature, and the multi-lamellar structure is swollen.

[1]J. F. Nagle et al., Phys. Rev. E 58 7769 (1998)
[2]N. Chu et al., Phys. Rev. E 71 041904 (2005)

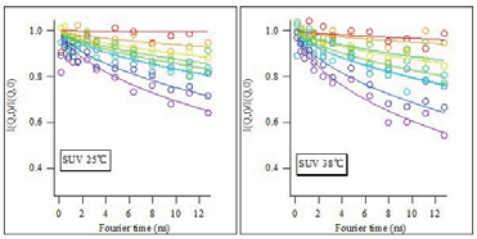


Fig. 1. Intermediate correlation functions of DMPC small uni-lamellar vesicles at 25 C and 38 C. Open circles are the data from NSE and solid lines are fitting results by Zilman and Granek theory.

1-5-9

Melting and Re-crystallization Process of Shish-kebab Structure

Go Matsuba, Yuji Hayashi, Chie Ito, Koji Nishida, Toshiji Kanaya
Institute for Chemical Research, Kyoto University

When polymer are crystallized under elongational or shear flows, the so-called shish-kebab structure could be observed. The shish-kebab structure consists of long central fiber core (shish-structure) and lamellar crystal (kebab structure) periodically attached along the shish-structure and surrounded by the shish-structure. We studied the hierarchic structure of the shish-kebab structure using three neutron spectrometers [1].

In the present experiment, we carried out the time-resolved small angle neutron scattering (SANS) measurements on melting and re-crystallization processes of shish-kebab structure with hand-made temperature cell [2]. The initial shish-kebab structure was made from drawing blends of deuterated low molecular weight components and protonated ultra-high molecular weight polyethylene (PE) at 150 C. The molecular weight of low molecular weight deuterated and protonated ultra-high molecular weight PE (dPE/hPE) is 56,500 and 2,000,000. The SANS measurements were performed on SANS-U spectrometer on JRR-3M, JAEA, Tokai, Japan. We observed temperature change of the shish-kebab structure during the heating process from room temperature to above the melting temperature and then quenching it to room temperature.

Figure 1 shows that 2D-SANS images at various temperatures during the heating process and after quenching. In the heating process, the position of spot-like scattering parallel to the drawing direction shifts to lower angle. This result suggests the spacing of kebab structure grows larger. The kebab structure melts at 133 C. When the sample was heated up 180 C above the melting temperature, the shish-kebab structure was not observed after quenching to room temperature, but the isotropic crystal morphology was shown as in Figure 1(a). However, as seen in Figure 1(b), when the sample was molten at 136 C and then quenched to room temperature, the shish-kebab structure appeared again. These results suggest that the melt of PE blends on 180 C is isotropic, on the other hand, some “oriented structure” in melt is reserved at 136 C. For detailed analysis, we evaluated the scattering profiles normal to the drawing direction in order to clarify the shish-structure melting process. The scattering intensity in lower q-range below 0.15 Aˆ-1 vanished at about 138 C, while that of higher q-range above 0.15Aˆ-1 still remained at141 C.

References

[1] T. Kanaya et al., Macromolecules, 40, 3650, 2007.
[2] K. Nishida et al., Activity Reports on Neutron Scattering Research, ISSP, U of Tokyo, 13, 2006.

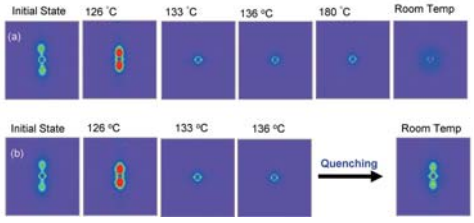


Fig. 1. Temperature dependence of 2D SANS profiles for melting and recrystallization process of shish-kebab.

1-5-10

Gelation Mechanism of Clay-Polymer Nanocomposite Hydrogel using Contrast Variation SANS

Shibayama M.[A], Miyazaki S.[A], Endo H.[A], Karino T.[A], Haraguchi K.[B]
[A]*ISSP-NSL, University of Tokyo* [B]*Kawamura Institute of Chemical Research*

Recently, clay-polymer nanocomposites have been focused much attention because of their excellent physical properties. Haraguchi et al. reported a novel clay-polymer nanocomposite gels (NC gels) consisting of synthetic hectorite (Laponite) and poly(*N*-isopropylacrylamide) (PNIPA)[1]. This NC gel has excellent physical properties, such as toughness, large deformability, large swelling ration, rapid shrinking capability, and high transparency. We carried out structure investigation of NC gels of various concentrations by small-angle neutron scattering using contrast variation technique (contrast-variation SANS) in order to learn the gelation mechanism.

We prepared NC gels of four different concentrations, two dense samples were in gel state and two dilute samples remained sol state. Investigating the microscopic structures of these samples near galation threshold, we can learn the galation mechanisms of NC gels. Since NC gel is a three components system, consisting of clay, PNIPA, and water, the scattering intensity is given by clay-clay, clay-polymer, polymer-polymer correlations. Thus using water of more than three different scattering length densities, we can decompose the scattering intensities into their partial scattering functions. In this case, we used contrast controlled water with different D_2O fraction.

Fig.1(a) shows the scattering intensities of the most dense sample and the partial scattering functions. Scattering intensity of NC gel is minimum in the case of D_2O fraction was 56%. With increasing D_2O fraction, the scattering intensity became large. Fig.1(b) shows the partial scattering functions obtained from the scattering intensities of Fig.1(a) by singular value decomposition. In order to check the validity of decomposition, the reconstructed scattering intensities are added in Fig.1(a) with solid line. Comparing these scattering intensities, the decomposition was successful. The most important result is that the sign of $S_{CP}(q)$, which corresponds to the clay-polymer cross-correlation, is positive. It indicates that there are spatial cross-correlation between clay and polymer. Then we assumed that clay platelets are surrounded by polymer layers and these surrounded clay platelets are tied by polymer network. Thus we calculated the scattering function from this model and we can successfully fit these partial scattering functions. From the fitting, clay platelets are surrounded by polymer layers, whose volumes are about 2.5 times of the clay platelets. Furthermore, this model represented the scattering functions of the other samples, regardless of gel and sol. It indicates that the microscopic structures of NC gel are almost identical regardless of gel and sol.

[1] K. Haraguchi and T. Takehisa, *Adv. Mater.* **14**, 1120 (2002).

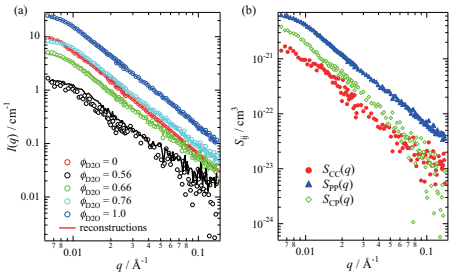


Fig. 1. (a)Scattering intensities and (b)obtained partial scattering functions.

1-5-11

Structural Formation Process under Drawing

Koji Nishida, Toshiji Kanaya, Go Matsuba, Yuji Hayashi, Chie Ito
Institute for Chemical Research, Kyoto University

Crystallization of polymers under drawing has been extensively investigated because drawing process quite affects the properties and strength of fibers and plastics. When polymers crystallize under drawing, the so-called shish-kebab structure could be observed. The shish-kebab structure consists of long central fiber core (shish-structure) and lamellar crystal (kebab structure) periodically attached along the shish-structure and surrounded by the shish-structure. It is believed that the shish structure is formed by completely stretched polymer chains and the kebabs are folded chain lamella crystals and grow to the direction normal to the shish-structure. In previous paper, we have revealed the hierarchic structure of the shish-kebab in a wide special scale using three kinds of neutron spectrometers [1].

In the present experiment, we carried out the time-resolved small angle neutron scattering (SANS) measurements on structural formation processes of blends of deuterated polyethylene and ultra-high molecular weight protonated polyethylene (dPE/hPE) with the hand-made shear cell [2], which was modified to observe drawing processes in this experiment. The range of drawing rate is from 6 micron/s to 7.2 mm/s. We employed a large torque motor with a maximum load capacity of about 3.5 Nm and then could draw very rigid sample. Polymer crystallization experiments require precise temperature control. Hence, the temperature was controlled within 0.3 C in a range from room temperature to 200 C. The maximum drawing ratio is about 5 in normal setting. The SANS measurements were performed on SANS-U spectrometer on JRR-3M, JAEA, Tokai, Japan.

Figure 1 shows 2D SANS images during the drawing process at 125 C. Before drawing, we could observe only isotropic scattering from spherulites or isotropic lamella. In the beginning, the scattering profiles look like ellipsoid because the long period spacing increases in a direction parallel to the drawing, and then they become two spots patterns. Now we are analyzing the shish-kebab structure formation process during the drawing process at various crystallization temperatures.

References

[1] T. Kanaya et al., Macromolecules, 40, 3650, 2007.
[2] K. Nishida et al., Activity Reports on Neutron Scattering Research, ISSP, U of Tokyo, 13, 2006.

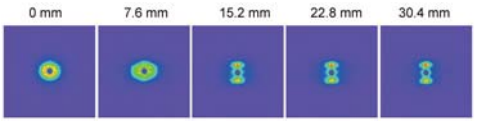


Fig. 1. 2D SANS images during drawing process annealed at 125 C.

1-5-12

Distribution of glass transition temperature in polymer thin films by neutron reflectivity

Inoue R[1], Ogawa H[1], Kanaya T[1], Nishida K[1], and Hino M[2]
Institute for Chemical Research, Kyoto University[1], *Reserch Reactor Institute, Kyoto University*[2]

With the recent progress of evaluation methods for polymer thin films, it was found that the physical properties of polymer thin films were very different from those of bulk state. Among them, thickness dependence of glass transition temperature (T_g) is one of the most attractive topics and the decrease of T_g with thickness was observed for polystyrene (PS) [1-3]. The singularity of Tg behaviour of polymer thin film is now understood in terms of multilayer or heterogeneous structure, however the definite mechanism of glass transition in polymer thin films is still missing. In order to reveal the mechanism of glass transition of polymer thin films, we have to study multi-layer structure of polymer thin films in more detail. We studied the distribution of glass transition temperature in polymer thin films using multi-layered thin film by stacking hydrogenated PS (h-PS) and deuterated PS (d-PS) with neutron reflectivity. Neutron can discern h-PS layer and d-PS layer clearly due to the difference of neutron scattering length density, hence we can evaluate T_g at a given position. We used h-PS with molecular weight (M_w) of 769K and molecular weight distributions (M_w/M_n) 1.18 and d-PS with M_w of 731K and M_w/M_n of 1.08 and we prepared d-PS/h-PS/d-PS tri-layered thin film. In order to minimize the effect of inter-layer diffusion between h-PS layer and d-PS layer, we annealed this tri-layered thin film at 365K that is about 10K below bulk T_g for 12 h. The neutron reflectivity measurements were done with MINE-II reflectometer installed in JRR-3M reactor and the measurements were performed from 298K to 403K in a vacuum cell. Figure 1(a) indicates the neutron reflectivity profiles from d-PS/h-PS/d-PS tri-layered thin films at 298K and 403K. Solid and dashed curves are the results of fit using a three-layer model with the formula derived by Parratt. The agreements of the fits are very good for both below and above bulk T_g, therefore we used three-layer model for the evaluation of film thickness and roughness of each layer. Temperature dependence of thickness of each layer is shown in Figure 1(b). At low temperature, thickness began to increase due to the thermal expansion, however thickness began to shrink at around 360K. It was supposed that this was caused by the unrelaxed structure of polymer thin film due to lack of annealing. Kanaya et al. reported that T_g value of polymer thin film was not affected by annealing condition [4], hence we evaluated T_g of each layer from the intersection of solid lines, as shown by arrows in Figure 1 (b). The evaluated T_g of each layer from top to bottom is 363K, 390K, and 383K, respectively. Although we have to study the annealing effect in order to disclose the distribution of T_g in polymer thin films, we could roughly withdraw the distribution of T_g in polymer thin film.

References [1] J. L. Keddie et al. Europhys. Lett. 27, 59 (1994).

[2] T. Miyazaki et al. Phys. Rev. E 69, 061803 (2004).

[3] S. Kawana et al. Phys. Rev. E 63, 21501 (2001).

[4] T. Kanaya et al. Polymer, 44, 3769 (2003).

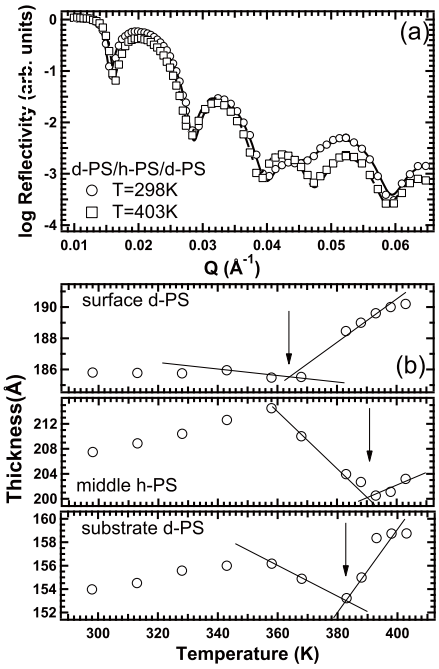


Fig. 1. (a) Neutron reflectivity profiles from dPS/hPS/dPS stacked thin films. (b) Temperature dependence of thickness for each layer.

1-5-13

A long-range periodic structure in a mixture of D_2O/3-methylpyridine/$NaBPh_4$ induced by solvation effect

Sadakane K., Iguchi N. and Seto H.
Department of Physics, Kyoto University, Kitashirakawa, Sakyo, Kyoto 606-8502

The solvation effect plays an important role in various fields of natural science. One of the most interesting issues is its influence on water and organic solvent mixtures. Recently, Onuki and Kitamura theoretically showed that the solvation effect of salt ion induces a long-range periodic structure in conjunction with a concentration fluctuation of those mixtures. [1]

The binary mixture of water and 3-methylpyridine (3MP), which shows LCST type phase separation, is known to have a large salt effect on the phase separation. Thus, we have investigated the concentration fluctuation and structural formation of the mixture of D_2O, 3MP and salt at SANS-U. In this study, we focused on the effect of sodium tetraphenylborate ($NaBPh_4$) because the solvation effect of anions and cations should be very large.

The SANS profile of D_2O/3MP without salt could be explained by the Ornstein-Zernike function, which is generally applied to near-critical binary mixture,

$$I_{OZ}(Q) = \frac{I_0}{1+\xi^2 Q^2}\,, \qquad (1)$$

where ξ is the correlation length and I_0 the forward scattering proportional to the osmotic compressibility.

On the other hand, the SANS profiles from D_2O/3MP/$NaBPh_4$ can not be explained by Eq. (1) because a single peak is observed around $Q = 0.1$ Å^{-1} (See Fig. 1). Thus, we tried to apply the scattering function proposed by Onuki and Kitamura [1], which shows the existence of a long-range periodic structure induced by solvation effect of salt ion,

$$I_{OK}(Q) = \frac{I_0}{1+(1-\gamma^2/(1+\lambda^2 Q^2))\xi^2 Q^2}\,, \qquad (2)$$

where γ is a dimensionless parameter corresponding to the difference of the strengths of the cation and anion, and λ the Debye screening length. In this expression, the peak position Q_m is given by $Q_m = \sqrt{\gamma - 1}/\lambda$. All the SANS profiles of D_2O/3MP/$NaBPh_4$ can be well explained by Eq. (2), and the characteristic repeat distance d increase with increasing temperature (See Fig. 1).

This result could be interpreted that the long-range periodic structure is induced by a cooperation of the solvation effect and the concentration fluctuation [2].

[1] A. Onuki and H. Kitamura, J. Chem. Phys., **121**, 3143 (2004).
[2] K. Sadakane, H. Seto, H. Endo and M. Shibayama, J. Phys. Soc. Jpn., **76**, 113602 (2007).

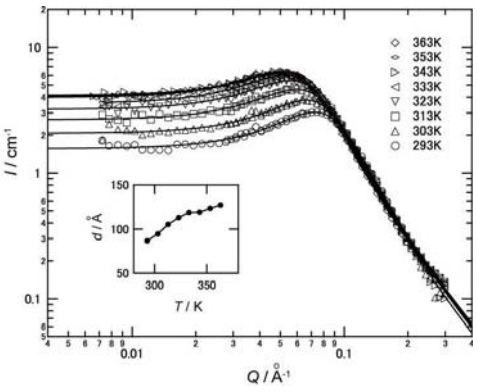


Fig. 1. SANS profile of D_2O/3MP (the weight fraction of 3MP is 0.32) with 100 mM of $NaBPh_4$. The solid line shows the fitting function given by Eq. (2). The inset shows the temperature dependence of repeat distance, d.

1-5-14

Effect of polymer on uni-lamellar vesicle in lipid mixture system

Norifumi L. YAMADA and Naoya TORIKAI
High Energy Accelerator Research Organization

It has been well known that natural swelling of a dry phospholipid film usually produces large multi-lamellar vesicles (MLVs) [1]. These mimic biomembranes produced from synthetic phospholipid molecules have been extensively studied to understand the actual behavior of real biomembranes. Living cells and their organelle, however, exist as unilamellar vesicles (ULVs). Therefore, effective methods to create the ULVs have been studied so far [2].

For a phospholipid mixture system consisting of long- and short-chain lipids, ULVs were spontaneously formed at high temperature when lipid bilayers are charged by adding ions or charged lipids [3]. Since these ULVs are uniform in size and very easy to make, the ULV production method from bicelles appears promising to create ideal model cells. In this study, we investigated the effect of polyethylene glycol (PEG), as mimic-biomolecules, on ULV formation in a lipid mixture system.

To observe the ULV structure, we have performed SANS experiments on a typical lipid mixture system, dimyristoylphosphatidylcholine (DMPC) and dihexanoylphosphatidylcholine (DHPC) mixture, at SANS-U, JRR-3M, JAEA, Tokai, Japan [4]. The mixture of lipids in the molar ratio of [DMPC]:[DHPC] = 3.2:1 was dissolved in the PEG solution to be the same volume fraction of lipids (0.35 wt.% for PEG-less sample). The molecular weight of PEG was 4000 g/mol and the concentration of PEG solutions were 0, 16.6, 33.3, 50.0, 66.6, 83.3, and 100 mg/ml.

Figure 1 shows the obtained SANS profiles of vesicles at high temperature phase (50°C). As shown by previous study, homogeneous ULVs were observed in the profile of 0 mg/ml. With increasing PEG concentration, ULVs became polydisperse in size, and a new Bragg peak due to MLVs appeared around $q = 0.1$ Å^{-1} above 50.0 mg/ml. From these results, we conclude that the addition of PEG stabilize MLV structure instead of ULV structure. This would be resulted from the entropic effect due to the addition of PEG.

References

[1] Reeves J. P. and Dowben R. M., *J. Cell. Physiol.* **73** (1969) 49.
[2] N. L. Yamada *et al.*, *Europhys. Lett.* **80** (2007) 48002.
[3] M.-P. Nieh *et al.*, *Biophys. J.* **82** (2002) 2487.
[4] S. Okabe *et al.*, *J. Appl. Cryst.*, **38** (2005) 1035.

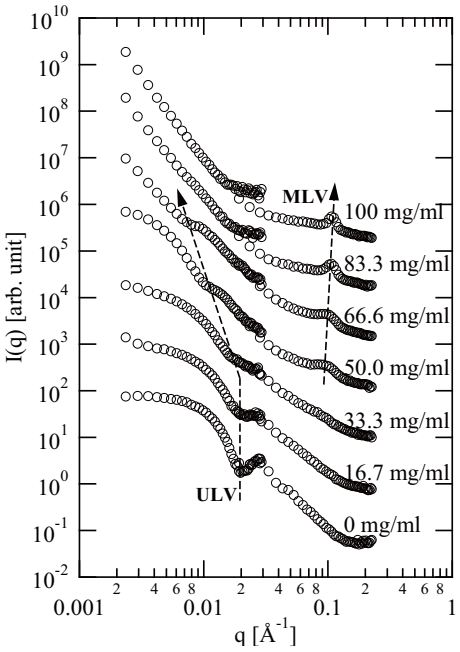


Fig. 1. SANS profiles of vesicles from bicelle with changing PEG concentration.

1-5-15

Studies on Structural Nonuniformity of Natural Rubber

M. Shibayama(A) , T. Suzuki(A), N. Oosaka(A), H. Endo(A), N. Higashitani(B), Y. Morita(B), Y. Kokubo(B), Y. Ikeda(B), and S. Kohjiya(C)
(A)ISSP-NSL, Univ. Tokyo, (B)Grad. Sch. Sci. Technol., Kyoto Inst. Tech., (C)Fac. Sci., Mahidol Univ.

Crosslinked rubbers are one group of the traditional soft matters. It is well known that the crosslinked rubber has nonuniformity in its microstructure. However, this network nonuniformity has not been sufficiently elucidated due to the complexity of the composition and the complex preparatory processes. The goal of the study is an elucidation of nonuniformity of crosslinked natural rubber (NR). An upturn scattering was detected in SANS profiles of crosslinked and uncrosslinked NR, which were ascribed to the non-rubber components in NR [1]. Thus, a model research using a synthetic analogue of NR becomes necessary. In this study, the microscopic structure of peroxide-crosslinked and sulfur-crosslinked isoprene rubber (abbreviated as P-IR and S-IR, respectively) is investigated by SANS.

P-IR and S-IR were prepared by milling with crosslinking reagents and heat-pressed for curing at 155 ° C and 140 ° C, respectively. SANS experiments were carried out at SANS-U (C1-2), JRR3M in JAEA (Tokai). The wavelength was 7 . The sample-to-detector distances were 2.00 and 8.00 m. The scattered intensity was collected with an area detector and then circularly averaged. Swollen samples in deuterated (D-) toluene were subjected to SANS measurements.

The following conclusions were obtained: (i) In both samples, the inhomogeneity in their network structures was detected, which was speculated to be due to the presence of poor and rich phases of crosslinking sites. (ii) The scattering curves of swollen P-IR and S-IR in D-toluene were successfully reproduced by the Squared-Lorentz and Lorentz functions. (iii) The mesh size (ξ) and the scale of inhomogeneity ascribed to the rich phase (Ξ) in P-IR were decreased and increased, respectively, by the increase of network-chain density (ν) as shown in Fig.1. (iv) For S-IR, ξ was almost constant regardless of the amounts of sulfur and accelerator, whereas Ξ increased with the increase of these amounts when definite amounts of stearic acid and ZnO were mixed. (v) The increase of ZnO resulted in the decrease of ξ and Ξ. The obtained results will be useful for a more systematic material design of future rubber products.

Reference

[1] T. Karino et al., Biomacromolecules, 8, 693(2007).

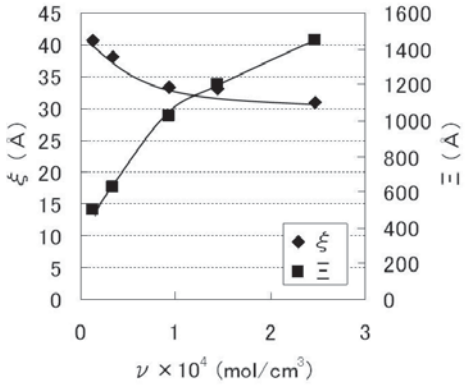


Fig. 1. Fig.1 ν dependence of ξ and Ξ for P-IR. The lines are guides for eyes.

1-5-16

Temperature Effects on Shear-Induced Structural Transition in the Lamellar Phase of a Nonionic Surfactant -Change in the Orientation of Lamellae-

Yuriko Kosaka, Makiko Ito, Youhei Kawabata, and Tadashi Kato
Tokyo Metropolitan University

In the past 15 years, much attention has been paid to the effects of shear flow on the structure of a lamellar phase owing to the development of the apparatus which enables us to determine their structures directly under shear flow. In the previous studies, we have measured small angle neutron scattering (SANS) on the lamellar phases of a nonionic surfactant C16H33(OC2H4)7OH (C16E7) in D2O at 70C under shear flow with shear rate of 0.01 - 10 s-1. We have found anomalous decrease in the lamellar spacing (d) for the shear rate of 0.1-1 s-1 [1-3]. In addition, abrupt change of d has been observed at around 70C when the temperature is raised from 60C to 80C. In the present study, we have investigated effects of temperature in more detail focusing on the change in the azimuthal intensity distribution.

Measurements of SANS were carried out at the instrument SANS-U of Institute for Solid State Physics of University of Tokyo in JRR-3M at Tokai with a Couette shear cell [4].

Figure 1a shows azimuthal intensity distribution for the shear rate of 3 s-1 at different temperatures and at 48 wt% of C16E7. At 60C, the lamellae is oriented to the neutral direction (90 and 270 degree) after the application of shear flow. The orientation becomes even more strong at 71 C. In Figure 1b, temperature dependences of the peak intensity for the neutral and flow direnctions are presented. This figure demonstrates that the orientation of lamellae becomes abruptly strong at 71 C and then changes towards isotropci orientation with the further increase in temperature. It should be noted that the repeat distance also abruptly increases at 71C as described in the previous report. These results suggest lamellar to onion transition with increasing temperature, which is not observed at rest.

References

[1] T. Kato et al. Langmuir 20 (2004) 3504.
[2] T. Kato et al. J. Phys. Cond. Matt. 17 (2005) S2923.
[3] K. Miyazaki et al. J. Appl. Cryst. 40 (2007) s332.
[4] Y. Takahashi et al. J. Soc. Rheol. Jpn. 28 (2000) 187.

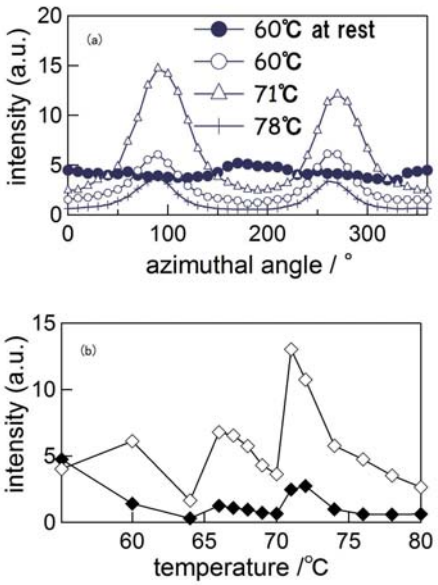


Fig. 1. Azimuthal intensity distribution at different temperatures (a) and temperature dependences of the peak intensity for the neutral (open diamond) and flow (closed diamond) direnctions (b) at the shear rate of 3 s-1 and at 48 wt% of C16E7.

1-5-17

Correlation between local dynamics and gas permeability of substituted polyacetylenes by quasielastic neutron scattering

T. Masuda[1], T. Kanaya[2], R. Inoue[2] and O. Yamamuro[3]
[1]*Department of Polymer Chemistry, Kyoto University,* [2]*Institute for Chemical Research, Kyoto University,* [3]*Institute for Solid State Physics, University of Tokyo*

It is well known that some substituted polyacetylenes show high gas permeability among all the examined polymers [1]. We synthesized a variety of substituted polyacetylenes [2,3] and investigated the relationship between gas permeability and side-group structure. Through these studies, we observed that local mobility of side group structure in glassy state plays an important role for gas permeability. In order to confirm this idea, we have investigated local dynamics of several polyaetylene with bulky substitutes using a quasielastic neutron scattering spectrometer AGNES installed at the cold neutron guide C3-2-1.

In this study, we mainly focused on the correlation between local picosecond dynamics and the gas permeability of these polymers. Although glass transition temperatures of investigated polymers are far above room temperature, investigated polymers exhibited quasielatic-like spectrum at room temperature, as shown in Figure.1 (a). It suggests that certain stochastic motion exists even in glassy state. In order to extract the dynamical feature of these polymers, we performed curve fit to the obtained S(Q, ω). First, we tried to fit with single Lorentizan function, however we failed to describe observed spectrum with single Lorentizan. Hence, we employed two Lorentzian functions and we could describe the observed spectrum well with two Lorentzian functions. We termed broad quasielatic component and narrow quasielatic component as broad component and narrow component, respectively. Neither relaxation rate Γ and fraction A of broad component depend on permeability, however both Γ and A of narrow component exhibited positive correlation with on permeability coefficient of O_2. These findings suggest that slow local motion plays major role in gas permeability. This tendency is also visible for the permeability coefficient of O_2 dependence of product of Γ and A for both quasielatic components, as indicated in Figure 1 (b). The behavior of dynamics of these polymers seemed to be explained by the model suggested by Kanaya et al [2]. The detailed analysis is now under progress.

References [1] K. Tsuchihara et al. Macromolecules, 25, 8548 (1991). [2] T. Kanaya et al. Macromolecules, 35, 5559 (2002).

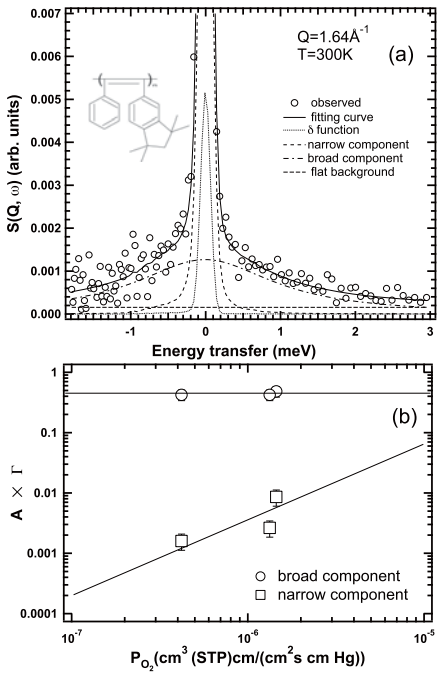


Fig. 1. (a) An example of fits to S(Q, ω) of one polymer and the quasielastic components were well fitted by two Lorentzians. (b) P_{O_2} dependence of the product of fraction (A) and relaxation rate of both quasielastic components.

1-5-18

Crowding effect on the shear induced structural transition of lamellar phase

Shuji Fujii(A) and Yohei Kawabata(B)
(A) Dept. Material Sci. and Tech., Nagaoka Univ. Tech. (B) Dept. Chem., Tokyo Metropolitan Univ.

It is well known that the shear flow applied on a lyotropic lamellar phase induces an onion (multilamellar vesicle) structure. Although it is also well known that polymers grafted on the lamellar membrane affect its dynamics, much less is known how the grafted polymer chain influences the viscoelasticity of lamellar phase, especially how the shear induced lamellar to onion structural transition is influenced by grafted polymer chain. On the shear induced lamellar to onion transition for the polymer-grafted lamellar phase, we should clarify the bilayer membrane structure in the microscopic scale.
In the present study, we have measured the small angle neutron scattering (SANS) on the polymer-grafted lamellar phase in D2O under shear flow field. Samples used in this study were nonionic surfactant (C10E3)/PEO-PPO-PEO type amphiphilic triblock copolymer (P105)/water system. Triblock copolymer concentration was fixed to the mole fraction of 0.01.

The Rheo-SANS measurements were performed by using SANS-U spectrometer equipped with quartz Couette shear cell at Institute for Solid State Physics, The University of Tokyo in JRR-3M at Tokai. Fig.1 shows the SANS profiles for surfactant lamellar and polymer-grafted lamellar phases at shear rate of 50s-1. For the surfactant lamellar phase (fig.1a), SANS profile shows an Onion formation with one Bragg peak. However, for the polymer-grafted lamellar phase (fig.1b), no Onion formation is observed but SANS profile shows the emergence of the second Bragg peak, which indicates the lamellar-lamellar phase separation. Thus, the present results suggest that lamellar-lamellar phase separation significantly affects the shear-induced Onion formation behavior.

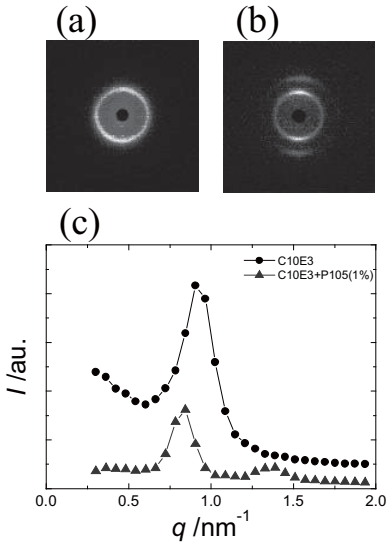


Fig. 1. SANS profiles of the surfactant lamellar and polymer-grafted lamellar phases.

1-5-19

Nanostructure of Non-Surface Acitive Ionic Amphiphilic Diblock Copolymers in Aqueous Solutions

Hideki Matsuoka, Hao Chen, Fumiaki Ozaki, Tasuku Yamada
Department of Polymer Chemistry, Kyoto University

I.Introduction

"Non-Surface Acitive Amphiphilic Polymer" is a new class of substance which has been found by our group. It is diblock copolymer consists of ionoc segment and hydrophilic chain. It shows a very curious character which has been never observed for any kind of other molecules: The polymer forms micelles in aqueous solution but does not adsorbed on the air/water interface. This behavior of out-of-common sense of surface and interface science and makes a strong impact on the definition of "Surfactants", which is a combination of "Suraface" "Active" "Agent". The origin of this strange behavior should be electrostatic origin since non-ionic polymer never shows similar behavior. By our systematical investigation, the image charge effect at the air/water interface is considered to be an important factor for this phenomenon. Also, by our study using polymers with various chain lengths and length ratios, It has been found that the degree of polymerization of each segment of, at least, 20 is required to show non-surface active nature. Hence, "non-surface activity" is some kind of "Polymer Effect". In this study, the nanostructure of micelles of non-surface active polymers was investigated by SANS, and the effect of chain length ratio was duly examined.

II.Experimental

The polymers used were diblock copolymers of poly(n-butyl acrylate) and poly(styrene sulfonate sodium salt) with various chain length with keeping constant block ratio of 1:1. The block copolymers were synthesized by nitroxy radical mediated living radical polymerization as reported previously. The SANS experiments were carried out with SANS-U spectrometer of ISSP, University of Tokyo, at Tokai, Ibaragi, Japan. The measurements were performed at two different camera length, i.e., 2m and 8m. The effect of salt was also investigated with using 0.5M NaCl aq. as solvent.

III. Results and Discussion

Figure 1 shows SANS profiles for solutions of polymers with block ratio, m:n, =18:13, 28:32, and 37:35. The concentration of polymer is 0.5 wt.%. A strong scattering was observed for each solution, which means micelle formation in aqueous solution. Although the detailed analysis has not yet performed since SANS experiments were carried out only a few weeks ago, the trends that short chain polymer forms rod-like micelles and long chain polymer forms mixture of spherical and rod-like micelles. The blob scattering from micelle corona is also observed. No significant difference is observed SANS profiles for no salt and 0.5M NaCl conditions, which means very tough nature of micelle structure against salt addition.

The SANS profiles will be analyzed by core-shell model and core-corona model fittings to evaluate nanostructural parameters of micelles such as core size, shell thickness, radius of gyration of shell chains, and fraction of spherical and rod-like micelles when coexist. The structural parameter thus evaluated will be duly examined with single chain properties such as non-surface activity and cmc (critical micelle concentration). These information will make a large contribution to correct understanding of "non-surface active" polymer, which is a novel class of molecules.

Activity Report on Neutron Scattering Research: Experimental Reports **15** (2008)
Report Number: 594

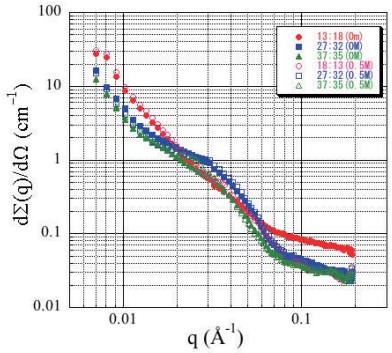


Fig. 1. SANS profiles of poly(n-butyl acrylate)-b-poly(sodium styrenesulfonate) block copolymers with different block lengths at no and 0.5M NaCl conditions.

1-5-20

2D-SANS Pattern Observed for Injection Molded Isotactic Polypropylene

T. Sakurai, Y. Nozue, S. Kimata, T. Kasahara, N.Yamaguchi, H. Endo*, M. Shibayama*
Petrochemicals Research Laboratory, Sumitomo Chemical. Co. Ltd. Chiba 299-0295, Japan
**Institute for Solid State Physics, The University of Tokyo, Kashiwa 277-8561, Japan*

Recently we have successfully demonstrated time-resolved Small-angle neutron scattering (SANS) measurements for observing melting behavior of injection molded isotactic polypropylene (iPP) using deuterium labeling to distinguish different chain lengths within an overall distribution. For SANS pattern with streak and spot shapes in the direction perpendicular and parallel to the flow direction, we clarified that the streak pattern disappeared at higher temperature compared to the spot pattern. This result strongly suggests that the streak pattern derives from the formation of "shish" structure in the material and the spot pattern due to the stacking lamellae structure ("kebab") [1].

In order to perform the quantitative analysis for shish structure, the SANS data in wider q range is desirable. In this study, we tried to SANS measurements of injection molded iPP in lower q range.

The deuterated and hydrogenated iPPs having molecular weight (MW) of ca. 1,200,000, 180,000 and 40,000 with narrow MW distribution were polymerized by metallocene catalyst system. The ratio of High, Middle and Low MW component in the blend was H:M:L=2:4:1. Total weight of the sample was 7g, and 1g of the sample was deuterated polymer. Blended samples were selectively deuterated in High or Middle or Low MW component, the deuterated blend samples being called High-D, Mid-D and Low-D. For the preparation of pseudo-injection sample, compact injection machine developed by co-worker was applied. Detailed preparation method is described elsewhere [1], [2].

SANS measurement was performed at SANS-U apparatus, at Institute for Solid State Physics, The University of Tokyo, Tokai, Japan. The wavelength was 7.0 and the scattered intensity was collected with an area detector during 7200 sec. The sample-to-detector distance was set to be 12 m for lower q measurement, and the experiment was carried out at room temperature.

Fig. 1 shows 2D-SANS data of High-D, Mid-D and Low-D. As like 2D-SANS pattern observed for camera length of 8m [1], the streak pattern was observed in the direction perpendicular to the flow direction. The shape of streak pattern depended on the deuterated MW component, and the degree of anisotropy was in the order of Low-D > Mid-D > High-D. The High-D sample showed 2D-SANS pattern with slight anisotropy even in the present camera length.

References

[1] S. Kimata et al., Science 316, (2007) 1014.
[2] M. Seki et al., Macromolecules 35, (2002) 2583.

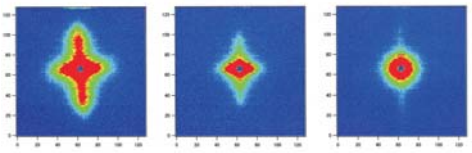


Fig. 1. Figure 1: 12m SANS data in Low-D (left), Mid-D (center) and High-D (right). Vertical direction is the flow direction.

1-5-21

Dynamical Properties of Syndiotactic Polystyrene (sPS) Crystalline Complex Phase

Fumitoshi Kaneko, Tatsuya Kawaguchi, Koichi Ute
Graduate School of Science, Osaka University; Graduate School of Engineering, Tokushima University

Syndiotactic polystyrene (sPS) is a relatively new commodity polymer, which exhibits a variety of solid states. One of the important properties of sPS is the formation of crystalline complex phase, where organic compounds are stored in the cavities formed between sPS helices with TTGG conformation. Formerly it was considered that only relatively small molecules could be incorporated into sPS complex phase. However, recent our studies have clarified that sPS has an ability to form crystalline complexes with larger and bulkier molecules, exceeding the size limit expected in the previous studies. By using the help of a plasticizing agent, a wide variety of molecular compounds can now be introduced into the crystalline matrix of sPS. In this study, we have investigated the dynamical properties of such sPS complex systems containing relatively large molecules.

We chose several molecules consisting of ethyleneoxide (-CH2CH2O-) groups as guests. All QNS spectra were measured with AGNES spectrometer of JRR3M (Tokai). The mean-square displacement <u^2> of hydrogen atoms was evaluated from the Q dependence of the elastic scattering intensity I(Q) by using the following the Debye-Waller formula: I(Q)=I(0) exp[-(1/3)<u^2> Q^2], where I(0) is the elastic intensity at Q=0.

Figure 1 shows the temperature dependence of <u^2> for sPS complexes with triethylene glycol dimethyl ether (TEGDM) and an oligomeric sample (PEG1000). The <u^2>s of the two sPS complexes show similar tendencies to temperature variations, but <u^2> is clearly larger in sPS/TEGDM than in sPS/PEG at 160 and 230 K. The quasielastic component is also more intense in sPS/TEGDM. These experimental results indicate that TEMDM is more mobile than PEG1000 in this temperature region. The temperature dependence of <u^2> can be interpreted as follows. The molecular motions of both the guest molecules confined in the cavities are restricted by the host-guest interaction in low temperatures, but the shorter molecule, TEMDM, having two mobile methyl terminals starts large diffusive motions from lower temperatures. For more detailed analysis, we are planning the experiment to evaluate the contribution of each component (sPS host framework, amorphous region and guest molecules) to QNS.

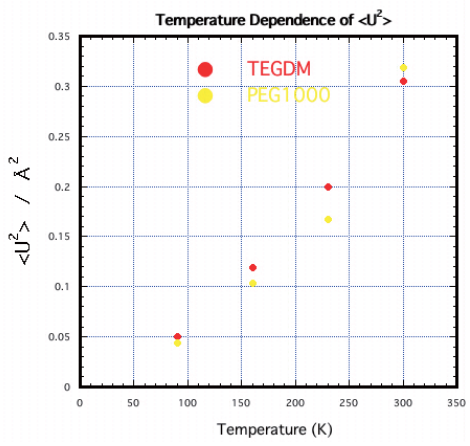


Fig. 1. Temperature dependence of <u2> for sPS crystalline complex phase

1-5-22

Electrostatic Self-Assembly of Neutral and Polyelectrolyte Block Copolymer and Oppositely Charged Surfactant

Masahiko Annaka, Tsuyoshi Matsuda, Kanae Morishita
Department of Chemistry, Kyushu University

Interactions between polyelectrolytes and oppositely charged amphiphiles have attracted a great deal of interest in the last decades, due to their importance both in fundamental polymer physics/biophysics and in biological and industrial applications. The interactions between polyelectrolytes and oppositely charged surfactants are quite strong and can induce a complex formation, often resulting in highly ordered structures. These well-defined supramolecular structures of the polyelectrolyte-surfactant complexes have unusual properties. We investigate the microscopic structure of colloidal complex made from poly(N-isopropylacrylamide)-block-poly(acrylic acid) (PNIPAM-b-PAA) (Fig. A) as thermosensitive neutral-anionic block copolymer and dodecyltrimethylammonium bromide (DTAB) as cationic surfactant under various conditions, specifically the effects of the DTAB concentration (surfactant-to-polymer charge ratio and temperature.

PNIPAM-b-PAA with low polydispersity was prepared by RAFT polymerization in methanol. SANS (Fig. B) clearly indicates that the aqueous solution of PNIPAM-b-PAA and DTAB associate into colloidal complexes. For low surfactant-to-polymer charge ratio Z(= [S]/n[P], [S]: DTAB conc., [P]: PNIPAM-b-PAA conc., n: degree of polym. of PAA block) lower than the critical value Zc, the colloidal complexes are single DTAB micelles dressed by a few PNIPAM-b-PAA (Fig C-i). Above the critical value Zc ˜ 0.7, the colloidal complexes form a core-shell microstructure (Fig. C-ii). The core of the complex consists of densely packed surfactant micelles (DTA+), and PAA block chains bind to these micelles, displace their counteranions (Br-) and bridge them together. The core radius is ranging between 150-160 A depending on the charge ratio and temperature, and the intermicellar distance of the DTAˆ+ micelles is ˜39 A, which is independent of the charge ratio Z as well as temperature. The corona of the complex is constituted from the thermosensitive PNIPAM. The aggregation number expressed in terms of DTA+ micelles per complex is also determined using the analogy with the homopolyelectrolyte/surfactant system, and found to be 200-250 depending on the charge ratio and temperature.

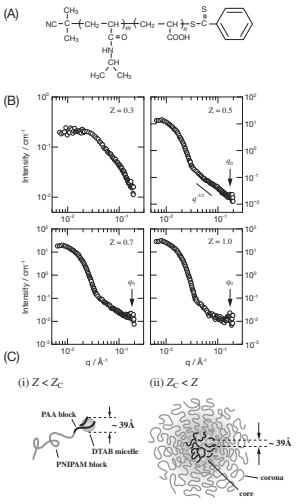


Fig. 1. (A) Chemical structure of PNIPAM-b-PAA. (B) SANS profiles for 0.4 wt% aqueous solutions of PNIPAM-b-PAA. (C) Schematic representation of complex (i) Z < ZC, and (ii) ZC < Z.

1-5-23

Effects of Molecular Weight and Surface Density on Conformation of Poly(N-isopropylacrylamide) Brushes Immobilized Onto A Substrate

Masahiko Annaka(1), Yoshihisa Fujii(2), Hironori Atarashi(2), Keiji Tanaka(2), Toshihiko Nagamura(2), Masahiro Hino(3)

1. Department of Chemistry, Kyushu University, Fukuoka 812-8581, Japan.
2. Department of Applied Chemistry, Kyushu University, Fukuoka 819-0395, Japan.
3. Research Reactor Institute, Kyoto University, Kumatori, Osaka 590-0494, Japan.

In the future, the quantity of polymeric materials used for medical diagnosis and treatment will continue to increase. Poly(N-isopropylacrylamide) (PNIPAm) is well known to exhibit LCST-type phase behavior in water. This property has been cleverly utilized in number of biomedical application. In such an application, the polymer surface is in contact with a water phase and polymer is used in various temperatures. Previously, we studied interfacial structure of water/poly(methyl methacrylate), which was a simple model for water/PNIPAm. As a result, the water/PMMA interface was diffuse in comparison with the air/PMMA one due to the interfacial roughening and the partial dissolution of segments at the outermost region of the film. [1] In addition, the PMMA film was discernibly swollen even in water. Then, our interest is what happens with the aggregation structure of the PMMA film in water if the temperature increases.

A film of perdeuterated PMMA (dPMMA) was prepared from a toluene solution, spin-coated onto a quartz block. The film thickness, evaluated by ellipsometry, was 60.7 nm. The density profile of the dPMMA film along the direction normal to the surface was studied by the multilayer interferometer for neutrons (C3-1-2-2, MINE) at ISSP, the University of Tokyo. Prior to the measurement, the dPMMA film was aged in water at 360 K for 12 hr, which was enough to cause swelling. Incident neutrons with the wavelength of 0.88 nm and the resolution of 5.1 % were guided into the specimen from the quartz side, which was vertically mounted on a goniometer. The reflectivity was calculated on the basis of the scattering length density profile using Parratt32, which is a freeware from the Hahn-Meitner Institute.

Fig. 1(a) shows the scattering vector, q dependence of reflectivity for dPMMA film in water. Solid line denote the best-fit calculated reflectivity, to the experimental data, on the basis of model scattering length density (b/V) profile in the panel (b). Since the calculated curve is in good agreement with the experimental data, it can be claimed that the model (b/V) profile used well reflect the density profile of the dPMMA film along the direction normal to the interface. The water content in the interior region, namely constant density region, of the film was 4.0 vol%. Moreover, the overall water content of the entire film was 9.5 vol%, being much larger than the reported value of 3.4 vol% at room temperature.[1] Since the dPMMA film contained water molecules after being immersed in the water, it became much thicker than before, the thickness increasing from 60.7 to 66.5 nm. The increment of the film thickness was almost identical to the value calculated on the basis of the overall water content through the mass balance. In the case of the film aged in a hot water, the most striking feature is that water molecules were preferentially segregated at the substrate interface. Taking into account that the film sometimes peels off from the substrate during the aging process in the hot water, this result was quite reasonable. Such an interfacial segregation of water was not observed for the film aged in water at room temperature. A more conclusive discussion about an effect of temperature on the aggregation structure of the dPMMA film in water will be reported in

the future.

Reference

[1] K. Tanaka, Y. Fujii, H. Atarashi, M. Hino and T. Nagamura, Langmuir, 24, (2008) 296.

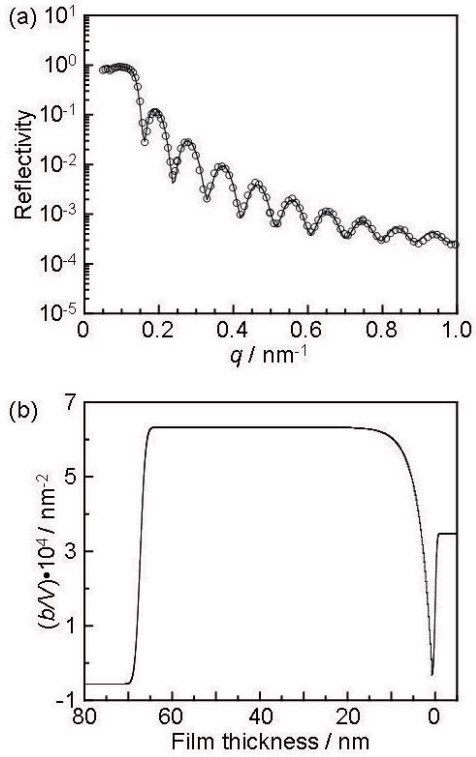


Fig. 1. (a) Neutron reflectivity for a dPMMA film in water. Open symbols depict experimental data, and solid line is reflectivity calculated on the basis of the scattering length density profile shown in (b).

1-5-24

Analysis of Adsorption Behavior for Proteins onto (Liquid/Polymer) Interface

Yoshihisa Fujii(1), Hironori Atarashi(1), Keiji Tanaka(1), Toshihiko Nagamura(1), Masahiro Hino(2)

1. Department of Applied Chemistry, Kyushu University, Fukuoka 819-0395, Japan
2. Research Reactor Institute, Kyoto University, Kumatori, Osaka 590-0494, Japan

Recently, polymer films have been widely used in a wide variety of applications. In biomaterials and biosensors, the polymer surface is in contact with a water phase. Thus far, a density profile of a perdeuterated poly(methyl methacrylate) (dPMMA) film spin-coated on a substrate was examined in water along the direction normal to the interface by specular neutron reflectivity (NR).[1] The interface of dPMMA with the water was much more diffused than the pristine air/dPMMA interface. This was because segments at the outermost region of the film could be dissolved into the water phase. If the length of the segments can be controlled, adsorption behaviors of lipids and protein even onto PMMA in water might be controlled. Since the former will be realized by the technique of a precise synthesis in the near future, adsorption behavior of protein onto a PMMA film was studied as a first benchmark.

A film of dPMMA was prepared from a toluene solution, spin-coated onto a quartz block. The film thickness, evaluated by ellipsometry, was 60.4 nm. As protein and buffer solution, bovine serum albumin (BSA) and 0.1 mol/l phosphate buffer solution were used, respectively. The density profile of the dPMMA film along the direction normal to the surface was examined by the multilayer interferometer for neutrons (C3-1-2-2, MINE) at ISSP, the University of Tokyo. Incident neutrons with the wavelength of 0.88 nm and the resolution of 5.1 % were guided into the specimen from the quartz side, which was vertically mounted on a goniometer. The reflectivity was calculated on the basis of the scattering length density profile using Parratt32, which is a freeware from the Hahn-Meitner Institute.

Fig. 1(a) shows the scattering vector, q dependence of reflectivity for a dPMMA film. For clarity, each data set for the dPMMA film in buffer and BSA buffer solution is off-set by a decade. Since just one film was used for all measurements, the NR curves can be directly compared. Solid and broken lines denote the best-fit calculated reflectivity, to the experimental data, on the basis of model scattering length density (b/V) profiles in the panel (b). The (b/V) values for quartz, dPMMA, buffer and BSA were 3.48x10-4, 6.62x10-4, -5.44x10-5 and 2.40x10-6 nm-2, respectively. Since the calculated curves are in good agreement with the experimental data, it can be claimed that the model (b/V) profiles used well reflect the density profiles of the dPMMA film along the direction normal to the interface. In buffer, the model (b/V) profile was almost the same as the one in water reported before.[1] And, as shown in the (b/V) profile, segments at the outermost region of the film were dissolved into the buffer phase. The interface of dPMMA with the BSA buffer solution became rougher than the one with buffer solution because of increasing interfacial roughness via the adsorption of BSA. This roughening was asymmetric to the interface; only the solution side became rougher. This interfacial roughening after the BSA adsorption was in excellent accord with the direct observation for the interface using atomic force microscopy. More conclusive study will be reported in the near future.

Reference

[1] K. Tanaka, Y. Fujii, H. Atarashi, M. Hino and T. Nagamura, Langmuir, 24, (2008) 296.

Activity Report on Neutron Scattering Research: Experimental Reports **15** (2008)
Report Number: 622

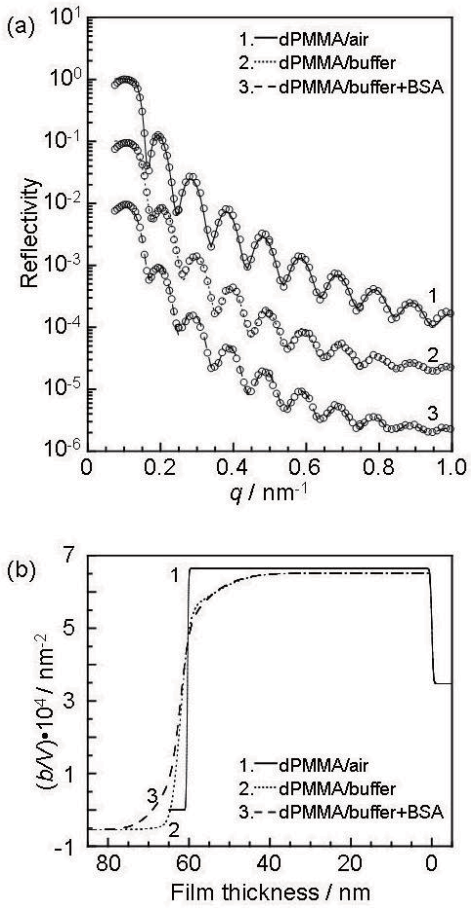


Fig. 1. (a) Neutron reflectivity for a dPMMA film in air, buffer and BSA buffer solution. Open symbols depict experimental data, and solid lines are reflectivity calculated on the basis of the scattering length density profiles shown in (b).

1-5-25

Lamellar to Micelle Transition of Nonionic Surfactant Assemblies Induced by Addition of Colloidal Particles

Y. Suganuma, N. Urakami*, R. Mawatari, S. Komura**, K. Nakaya-Yaegashi, M. Imai
*Ochanomizu University, *Yamaguchi University, ** Tokyo Metropolitan University*

We have investigated the depletion interaction between lamellar membranes and spherical colloidal particles using a small angle neutron scattering (SANS) technique. By adding colloidal particles into lamellar membrane slits, the first lamellar peaks in SANS profiles become intense and the second and higher harmonics begin to appear, indicating that the membrane fluctuations are suppressed by the colloidal particles. We estimate the inter-lamellar interaction potential in the presence of the colloidal particles from the layer compressibility obtained by the SANS profile analysis and propose a phenomenological free energy model based on the restriction of membrane fluctuations. Further addition of the colloidal particles brings a lamellar membrane to flexible rod-like micelle transition. In order to release the strong frustration due to the restriction of membrane fluctuations, the surfactant assemblies transform the morphology from the two dimensional sheets to the one dimensional rods. We estimate free energies of the lamellar membrane + colloidal particle mixture and the rod-like micelle + colloidal particle mixture to explain the observed lamellar to micelle transition.

Activity Report on Neutron Scattering Research: Experimental Reports **15** (2008)
Report Number: 625

1-5-26

Nano-meter-sized domain formation in lipid membranes observed by small angle neutron scattering

Sakuma Y., Imai M., Masui T., *Urakami N.
*Ochanomizu University, *Yamaguchi University*

Using a contrast matching technique of small angle neutron scattering (SANS) and small unilamellar vesicles (SUVs) composed of ternary mixture of deuterated-saturated (d-DPPC), unsaturated (DOPC) phosphatidylcholine lipids and cholesterol we have investigated macroscopic liquid-disordered and liquid-ordered phase coexistence on model biomembranes but the equilibrium size of these domains is constrained to less than 10 nm by the system size. Above a miscibility temperature the ternary vesicles with the matching composition show no significant scattering, which represents that the lipids are mixed homogeneously. However below the miscibility temperature, a characteristic scattering profile with a maximum is observed, indicating the formation of domains on SUVs. The observed profiles are well described by a multi-domain model. In order to explain the obtained results, we have performed a molecular dynamics simulation with a coarse grained model. Both experimental and simulation results show that the domains on the SUVs are agitated by thermal fluctuations and repeat coalescence and rupture even below the miscibility temperature. These domains are stabilized by decreasing temperature and form a mono-domain. In addition based on the SANS data and phase diagram of the ternary system we determine the compositions of the domain and the matrix regions, i.e. tie-lines in the phase diagram, which shows that d-DPPC molecules concentrate in the domain region with decreasing temperature.

Activity Report on Neutron Scattering Research: Experimental Reports **15** (2008)
Report Number: 628

1-5-27

Sol-Gel Transition of Hydrophobically Modified Polyrotaxane

Takeshi Karino, Yasushi Okumura, Changming Zhao, Masatoshi Kidowaki, Toshiyuki Kataoka, Kohzo Ito, and Mitsuhiro Shibayama
Institute for Solid State Physics, The University of Tokyo, Graduate School of Frontier Sciences, The University of Tokyo

Recently, we succeeded in preparation of water-soluble polyrotaxanes by introducing hydrophobic groups. In the case of methyl group substitution, i.e., methylated polyrotaxane (Me-PR), Me-PR aqueous solutions exhibited thermosensitivity and underwent a sol-gel transition by increasing temperature. The introduction of methyl groups to PRs leads to thermosensitivity. It is noted here that substitution with larger hydrophobic functional groups, such as ethyl groups and propyl groups, resulted in a macrophase separation even at ambient temperature.

In this report, the sol-gel transition and thermosensitivity of Me-PR aqueous solutions were investigated by means of small-angle neutron scattering (SANS) and dynamic light scattering (DLS). It is known that water-solubility of polyrotaxane (PR), consisting of poly(ethylene glycol) (PEG) and R-cyclodextrin (R-CD), is very low due to stacking of neighboring R-CD molecules on a PEG chain. Methylation of the hydroxyl groups on R-CD molecules resulted in a significant improvement of water-solubility, and Me-PR exhibited a thermoreversible sol-gel transition in water depending on the degree of methylation. For low degrees of methylation ($<30\%$), a Me-PR solution was transparent even up to 80 $^{\circ}$ C. On the other hand, for high degrees of methylation ($>60\%$), it became opaque with increasing temperature and a gelation took place at high temperature. The temperature dependence of the sliding motion of CD molecules along the PEG chains and the mechanism of sol-gel transition are discussed on the basis of SANS and DLS results.

References

[1] Y. Okumura and K. Ito, Adv. Mater. 13, 485 (2001).
[2] T. Kataoka, M. Kidowak, C. Zhao, H. Minamikawa, T. Shimizu and K. Ito, J. Phys. Chem., B, 110, 24377 (2006).
[3] T. Karino, Y. Okumura, C. Zhao, M. Kidowaki, T. Kataoka, K, Ito and M. Shibayama, Macromolecules, 39, 9435 (2007).

1-5-28

Structural Study on Uniaxial Extension of Nanocomposite Hydrogel with High Clay Concentration by Means of Contrast Variation Neutron Scattering

T.Nishida[1], H. Endo[1],N. Osaka[1], K. Haraguchi[2] M. Shibayama[1]
Institute for Solid State Physics, The University of Tokyo, Kashiwanoha 5-1-5, Kashiwa, Chiba 277-8581, Japan[1], Kawamura Institute of Chemical Research, 631 Sakada, Sakura-shi, Chiba 285-0078, Japan[2]

In these days, mechanically excellent gels are developed such as topological gels, double network gels, and nanocomposite gels (NC gels). NC gels are hybrid materials consisting of organic polymers (poly(N-isopropyl acrylamide)) and inorganic clay nanoparticles (hectorite) , which have excellent physical properties, such as toughness, high modulus, deformability, etc. It is interesting and important to account for these mechanical properties on the molecular level for material science as well as industrial applications. In order to elucidate the microscopic structure of NC gels under elongation, we carried out contrast variation SANS (CV-SANS) experiments by varying the D_2O fraction in the aqueous solvent. Since NC gels are ternary systems consisting of clays, polymers, and water, observation of partial scattering functions reflecting each component is straightforward for quantitative structural analyses of the multicomponent system. So the CV-SANS techniques are essential for our system. NC gels are synthesized by polymerization with a mixture of N-isopropyl acrylamide monomers and Laponite clay nanoparticles in aqueous solutions. To apply CV-SANS techniques, we prepared five different NC gels consisting of 0, 22.6, 70, 80 and 100vol% D_2O fraction. SANS experiments were performed at SANS-U diffractometer of Institute for Solid State Physics, the University of Tokyo. This experiment has been the first attempt to apply the CV-SANS techniques to uniaxially-stretched hydrogels. With CV-SANS anisotropic 2-dimentional SANS patterns were clearly observed (see Fig. 1). The stretching ratio is $\lambda = 1, 3, 7$. The upper 6 figures indicate scattering from clays, i.e., the scattering contrast between polymer and solvent was matched, and bottom 6 ones are from polymers, i.e., the scattering contrast between clay and solvent was matched. The high-Q (detector length=2m) 2-dimensional patterns show elliptic pattern reflecting the similar orientations of clay and polymer for the uniaxial stretch. The low-Q (detector length=8m) patterns show similar two-lobe patterns for both clay and polymer scattering at $\lambda = 3$, which differ at $\lambda = 7$. This tendency clearly indicates that polymers are adhered to clay surfaces, which start to be torn off at $\lambda = 7$. **Reference**

S. Miyazaki et al., *Macromolecules* **39**, 8112, (2006).

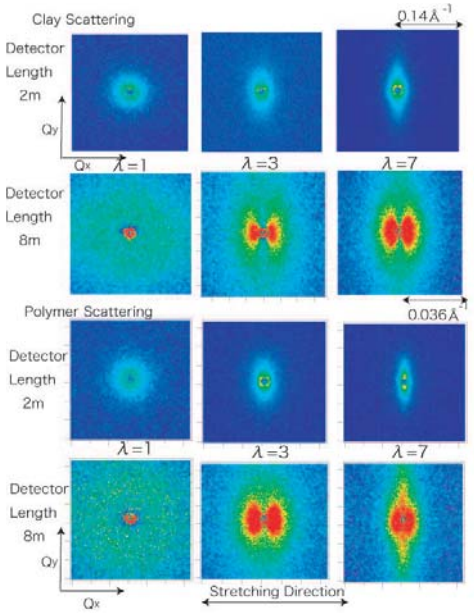


Fig. 1. 2-dimentional SANS patterns for uniaxially stretched NC gels at high-Q and low-Q.

This is a blank page.

1. 中性子散乱 6）生物

1. Neutron Scattering 6）Biology

This is a blank page.

1-6-1

Control of Membrane Lipid dynamics by Transmembrane and Amphipathic Peptides

M. Nakano(A), M. Fukuda(A), T. Kudo(A), H. Endo(B)
(A)Graduate School of Pharmaceutical Sciences, Kyoto Univ., (B)ISSP-NSL, Univ. of Tokyo

Controlled lipid traffic in biological membranes is important for cell growth, development and survival [1]. For example, phospholipids that are produced in the cytosolic leaflet of the endoplasmic reticulum (ER) membrane can flip to the other side, which is required to ensure balanced growth of the bilayer. Although this transbilayer movement of lipids is considered protein-mediated, it is unclear whether it involves a dedicated flippase or the mere presence of proteins in the ER bilayer. Kol et al. have observed that peptides that mimic the alpha-helices of transmembrane proteins can stimulate flip-flop of fluorescence-labeled phospholipids in liposomes [2], which indicates that the ability to catalyse flip-flop in the ER is not necessarily restricted to one specific protein.

We recently succeeded in determining the rates of interbilayer exchange and flip-flop of dimyristoylphosphatidylcholine (DMPC) in large unilamellar vesicles (LUVs) by small-angle neutron scattering (SANS) technique [3]. In this study, similar experiments were carried out with longer acyl chain lipid, 1-palmitoyl-2-oleoylphosphatidylcholine (POPC) and its analogue with smaller polar headgroup, 1-palmitoyl-2-oleoylphosphatidic acid (POPA), and the effect of the transmembrane peptide on the transbilayer transfers of lipids was investigated.

POPC, POPA, d31-POPC, and d31-POPA were obtained from Avanti Polar Lipids Inc. (Alabaster, AL). Transmembrane peptide, KALP23, was obtained from Hayashi Kasei Co. (Osaka). Methyl-beta-cyclodextrin (MCD) was from Aldrich (Milwaukee, WI). LUVs consisting of deuterated (D-LUV) or hydrogenated lipids (H-LUV) with a diameter of ca. 100 nm were prepared by extrusion method using Tris-buffered saline (10mM Tris-Hcl, 150 mM NaCl, pH 7.4) prepared from mixtures of D2O and H2O. LUVs consisting of 1:1 mixture of deuterated and hydrogenated lipids (D/H-LUV) were also prepared. Transmembrane peptide (if necessary) was mixed (0.5 mol%) with lipids before hydration. Volume fraction of D2O in the Tris-buffer was 0.3, which corresponds to the contrast-matching condition between D/H-LUV and solvent. Phospholipid concentration of each LUV preparation was set to 30 mM. SANS measurements were performed at 37 $^\circ$ C using SANS-U with 7 angstrom of incident neutron beam. Sample-to-detector distance was set to 4 m.

TR-SANS measurement was started immediately after mixing equivalent volume of D-LUV and H-LUV. Time-course of the normalized contrast was calculated from the scattering intensity and plotted in Figure 1. POPC showed extremely slow interbilayer exchange with the half-life of exchange of more than 90 h. Moreover, POPA, which has smaller polar headgroup than POPC, showed no exchange. Addition of MCD, which is known to catalyze the interbilayer lipid migration, indeed enhanced the rate of exchange. In the presence of MCD, the normalized contrast for POPC LUVs reached to 0.56 and became constant, which suggests that POPC does not flip-flop at all. Deviation of the constant value (0.56) from 0.5 is presumably due to the existence of multilamellar species in LUV preparation. On the other hand, the contrast decay of POPA LUVs reached well below 0.5, suggesting an involvement of flip-flop.

We performed the TR-SANS experiments on LUVs with peptide, KALP23. However, no stimulating effect of the peptide on the

Activity Report on Neutron Scattering Research: Experimental Reports **15** (2008)
Report Number: 309

flip-flop of POPC and POPA was observed. This result suggests that a mere insertion of transmembrane helices into bilayer does not mediate the lipid flip-flop.

References

[1] J. C. M. Holthuis and T. P. Levine, Nat. Rev. Mol. Cell Biol. 6 (2005) 209.
[2] M. A. Kol, A. N. C. van Laak, D. T. S. Rijkers, J. A. Killian, A. I. P. M. de Kroon, B. de Kruijff, Biochemistry 42 (2003) 231.
[3] M. Nakano, M. Fukuda, T. Kudo, H. Endo, T. Handa, Phys. Rev. Lett. 98 (2007) 238101.

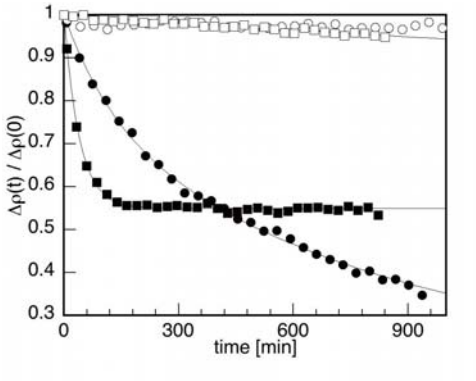


Fig. 1. Contrast decays of POPC (squares) and POPA (circles) LUVs after mixing D- and H-LUV at 37 ° C in the absence (open symbols) and presence (closed symbols) of 1mM MCD.

1-6-2

Dynamics of folded and partial unfolded proteins observed by solution inelastic neutron scattering

H. Nakagawa[A], Y. Joti[B], O. Yamamuro[B], I. Tsukushi[C], M. Kataoka[A,D]
[A]*JAEA,* [B]*Univ. Tokyo,* [C]*Chiba Inst. Tech.,* [D]*NAIST*

Protein has biological function under the physiological condition, which is usually in a solution. So far most inelastic neutron scattering experiments with biological samples are limited in the hydrated powder condition due to the strong solvent scattering. But recently solution inelastic neutron scattering experiments have emerged in the literature, which is even now challenging work [1].

We performed solution scattering experiment with AGNES using Staphylococcal nuclease (SNase) of native and truncated mutant. The energy resolution of ANGNES is 120 μeV. Truncated mutant is SNase without C-terminal 13 residues, which is in the partial unfolded state under the physiological condition.

Figures are the scattering profiles of two samples at 280 K and 300 K. Under the temperatures the native SNase is in the folded state. Elastic incoherent structure factor (EISF) of the folded state hardly decreases upon heating from 280 K to 300 K. This indicates that the folded structure is thermally stable in these temperatures. On the other hand, EISF of the partial unfolded state notably decreases upon the heating. The difference of EISF between two temperatures suggests that conformational entropy of the unfolded protein at 300 K is significantly larger than that at 280 K.

The quantitative analysis of solution inelastic neutron scattering will make it possible to characterize the dynamical properties of protein structure and give important insight into the protein folding problem.

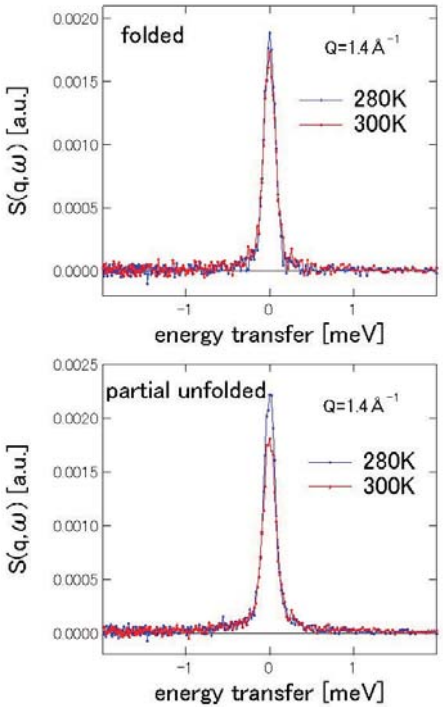


Fig. 1. Solution inelastic neutron scattering spectra of SNase in folded and partial-unfolded states.

[1] J. Fitter et al. :"Chem.Phys.", 292, 405 (2003).

1-6-3

Hydration water dynamics at protein dynamical transition by quasi-elastic neutron scattering

H.Nakagawa(A), Y.Joti(B), O.Yamamuro(C), M.Kataoka(A,D)
(A)JAEA, (B)Univ.Tokyo, (C)ISSP-NSL Univ. Tokyo, (D)NAIST

A protein dynamical transition around 180˜240 K has been observed for the hydrated protein [1]. It was reported for various proteins that their functions are suppressed with the loss of anharmonic dynamics by dehydration or by cooling down below the transition temperature. In order to elucidate the role of water at the protein-water interface, it is essential to understand protein dynamics and function properly. In this study the hydration water dynamics were examined by quasi-elastic neutron scattering below and above the dynamical transition temperature at a hydration level of 0.39 (g D2O/g protein). The scattering from the hydration water on the protein can be selectively estimated by the subtraction of the scattering profile of a D2O-hydrated protein from that of a H2O-hydrated protein. The neutron inelastic scattering experiments were performed with AGNES, in the JRR-3M reactor in Tokai, which has an energy resolution of 120 μ eV. Figure (a) shows the mean-square displacements (MSD) of protein and hydration water at various temperatures. Below the dynamical transition temperature ˜240 K, the MSD of the protein and the hydration water are almost identical, while above the transition temperatures the MSD of the hydration water are significantly larger than those of the protein. Figure (b) shows that the inelastic spectrum of the hydration water is almost identical to the resolution function at 100 K and Figure (c) shows that quasi-elastic scattering of the hydration water was observed at 300 K. These results indicate that above the dynamical transition temperatures the hydration water has the diffusive motions. It was reported that a relaxation time of the protein-water hydrogen bond network is 18 ps at 300 K [2]. The observed hydration water dynamics involves such a network relaxation. The dynamical coupling between hydration water and protein is essential for the protein dynamical transition.

1) W.Doster et al.: “Nature”,337,754(1989).
2) M.Tarek et al.: “Phys.Rev.Lett”,88(2002).

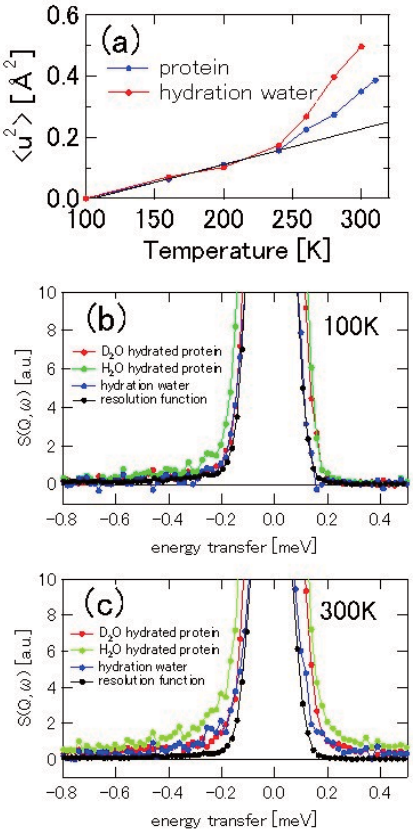


Fig. 1. Figure Mean-square displacement of protein and hydration water (a), inelastic neutron scattering of protein, hydration water and resolution function at 100K (b) and 300K (c).

1-6-4

Strctural torlance of complex of αA-crystallin and αB-crystallin

M. Sugiyama[1], N. Fuji[1], Y. Morimoto[1], T. Sato[2],
[1] *Research Reactor Institute, Kyoto Univ., Osaka, 590-0494*

Alpha-crystallin is one of chaperones to prevent from abnormal aggregation of proteins in human eye lens. This protein is a water-soluble aggregate consisting of two kinds of polypeptide, αA-crystallin and αB-crystallin. These two polypeptide have similar aging acid sequences. Here, it leads a simple question, *why does α-crystallin need two similar polypeptides?* In order to answer this question, we have investigated structural responses of αA-crystallin and αB-crystallin under environmental stresses, such as low temperature, UV irradiation, γ-ray irradiation and so on. By our previous studies, it has been revealed that αA-crystallin and αB-crystallin show different structural responses against low temperature and UV irradiation: αA-crystallin has higher structural stability against UV irradiation but lower one against low temperature whereas αB-crystallin shows opposite structural stability against two stresses. We supposed that by consisting of two polypeptide which have opposite stability against low temperature and UV irradiation, α-crystallin could develop tolerance to two external stress.

In order to prove this hypothesis, we should reveal the structural response of the complex consisting of αA-crystallin and αB-crystallin under the external stresses. For this purpose, we observed the structural evolution of the complex of αA-crystallin and αB-crystallin under UV irradiation with small-angle neutron scattering. The UV light had wavelength range with 280-360 nm (UV-B) and the SANS intensity was recorded every 30 minutes for 8 hours.

Figure 1(a) shows the SANS profiles of the complex before and after 8 hr UV irradiation at 37 C and Fig. 1(b) also shows those at 37C for 0 and 8 hr without UV irradiation. This result clearly indicates that the complex has tolerance against UV irradiation even though it includes αB-crystallin. Therefore, we can conclude that the role of αA-crystallin in the complex is to prevent from making abnormal aggregation against UV irradiation.

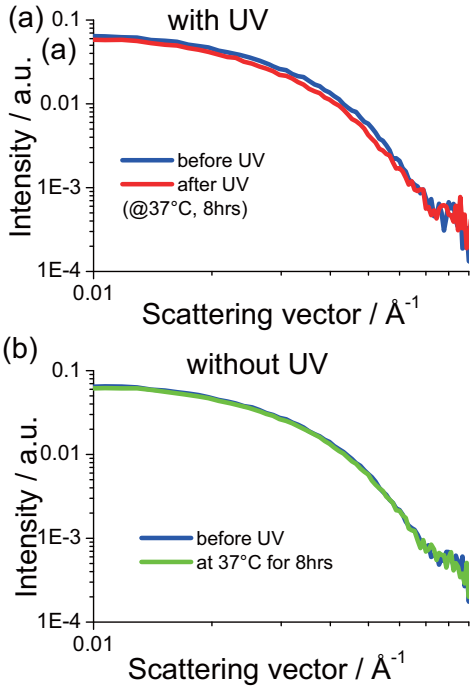


Fig. 1. SANS profiles of the complex αA-crystallin and αB-crystallin.

1-6-5

Measurements of slow dynamics of actin

Satoru Fujiwara, Fumiko Matsumoto, Hiroshi Nakagawa, Nobuaki Takahashi, and *Toshiro Oda
*Japan Atomic Energy Agency and *RIKEN SPring8-center*

F-actin, a helical polymer formed by polymerization of the monomers (G-actin), plays crucial roles in various aspects of cell motility. Flexibility of F-actin has been suggested to be important for such a variety of functions. Understanding the flexibility of F-actin requires characterization of a hierarchy of dynamical properties, from internal dynamics of the actin monomers through domain motions within the monomers and relative motions between the monomers within F-actin to large-scale motions of F-actin as a whole. As one of the ongoing projects towards this ultimate goal, we have been studying the dynamics of actin in a pico- to nanosecond time range by neutron spin-echo (NSE) spectroscopy.

As a continuation to the experiments done in 2006, we carried out two kinds of the NSE measurements: one was the measurements with a wider Q-range in order to obtain the detailed Q-dependency of the relaxation times, from which information on the collective motions such as the actin protomers in F-actin and the domain motions in the actin protomer were obtained; the other was the measurements on longer time scales, in order to make more accurate estimation of the relaxation times possible.

G-actin and F-actin were purified from rabbit skeletal muscles, and suspended in D2O. The NSE measurements on these solutions were carried out on the spectrometer iNSE, run by the University of Tokyo, installed at the guide hall of the research reactor, JRR-3M, Ibaraki, Japan. Two experimental set-ups enabled us to measure the intermediate scattering functions in the Q-range between 0.04 Aˆ-1 and 0.2 Aˆ-1 at the Fourier time up to 15 nsec, and those in the Q-range between 0.03 Aˆ-1 and 0.12 Aˆ-1 at the Fourier time at least up to 30 nsec. Figure 1 shows the combined results of these two measurements. It is shown that although the relaxation times of the intermediate scattering functions of F-actin is very slow compared to those of G-actin, each intermediate function can be fit with a single exponential, from which effective diffusion coefficients can be estimated. Behavior of the effective diffusion coefficients of G-actin as a function of Qˆ2 corresponds to free diffusion in solution whereas that of F-actin seems to reflect the collective motions within F-actin. Detailed analysis is currently underway.

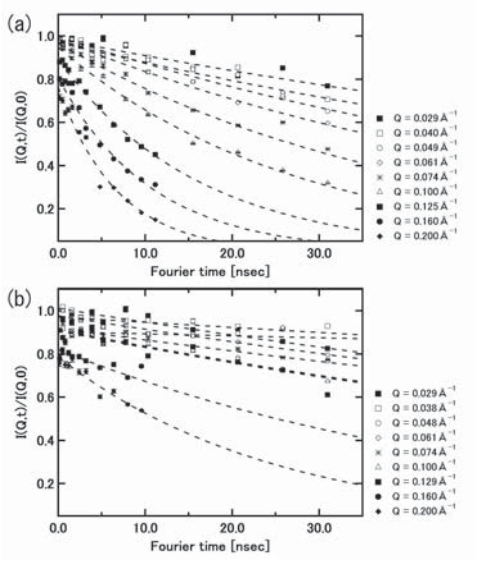


Fig. 1. The normalized intermediate scattering functions of (a) G-actin and (b) F-actin

1-6-6

Structure and dynamics of β-lactoglobulin aggregates by small-angle neutron scattering and neutron spin echo methods

K. Yoshida[1], T. Yamaguchi[1], H. Endo[2], M. Shibayama[2]

[1] *Department of Chemistry, Faculty of Science, Fukuoka University,*[2] *Institute for Solid State Physics, The University of Tokyo*

Many proteins aggregate and gelate when they take a misfolded state. The gelation of β-lactoglobulin(BLG) is triggered by heat, pressure, and addition of alcohol. The pH dependence of the aggregation state of a heat-induced gel has been studied[1], however, the mechanism of alcohol-induced gelation is not clear. Understanding the mechanism of aggregation of denatured BLG would provide a hint to reveal how misfolded protein forms an aggregate such as amyloid fibril. Small-angle neutron scattering and neutron spin echo measurements provide useful information of the structure and dynamics of the BLG aggregates.

BLG was lyophilized from D_2O solution to substitute exchangeable hydrogen of BLG to deuterium. The BLG powder was dissolved into ethanol- and trifluoroethanol(TFE)-water mixtures at various volume fractions of alcohol and followed by addition of 100 mM of DCl and the BLG concentrations were 10 and 20 mg ml^{-1}. A sample was kept in a quartz cell of 2-mm path length for SANS measurement. The cell was inserted into a temperature-controlled chamber at 298 K. The distances between the sample and detector were 1 and 4 m, corresponding to Q of 0.007 - 0.3 Å^{-1}. Measurements were also made for background and lupolen used for intensity normalization. A quartz cell of 4-mm path length for NSE measurement. The scattering vector Q covered was 0.055 - 0.12 Å^{-1}. The Fourier time was varied from 0.15 to 15 ns. The temperature of sample was controlled at 298 $\pm$ 0.3 K with circulated water.

Figure 1 shows the SANS intensity of BLG in ethanol-water mixture. This indicates that BLG exists as a monomer up to 20 vol% of ethanol and the aggregation occurs above 30 vol% where the secondary structure BLG changes. A similar trend was also found in TFE-water mixture. The alcohol-induced BLG aggregation could be well related to the secondary structure change. The relaxation of BLG obtained from NSE intermediate scattering functions retards drastically by addition of ethanol and TFE. The relaxation was hardly found at an energy resolution of the NSE spectrometer at 30 vol% of ethanol and 20 vol% of TFE where the solutions gelate, indicating the formation of a rigid BLG network structure.

The present results will be compared with those of heat- and pressure-induced aggregation of BLG. We will discuss the role of solvent on gelation of BLG at the molecular level.

References

[1] S. Takata, T. Norisuye, N. Tanaka, M. Shibayama, Macromolecules **33**, 5470-5475 (2000).

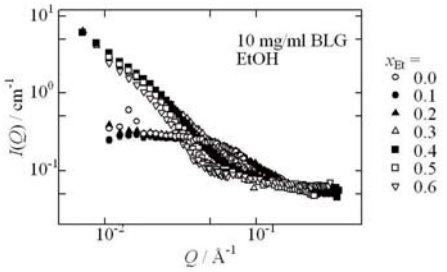


Fig. 1. SANS intensity curves of BLG at various volume fraction of ethanol in ethanol-water mixture with 100 mM DCl.

1-6-7

Neutron Diffraction Study of HIV-1 Protease in Complex with Inhibitor KNI-272

M. Adachi[1], T. Ohhara[1], K. Kurihara[1], T. Tamada[1], E. Honjo[1], N. Okazaki[1], S. Arai[1], Y. Shoyama[1], H. Matsumura[2,3], H. Adachi[2,3], K. Takano[2,3], Y. Mori[2,3], K. Hidaka[4], T. Kimura[4], Y. Hayashi[4], Y. Kiso[4] and R. Kuroki[4]

[1]*Quantum Beam Science Directorate, JAEA, Tokai, Ibaraki, 319-1195*
[2]*Graduate School of Engineering, Osaka University, Suita, Osaka 565-0871*
[3]*SOSHO Inc., Osaka 541-0053*
[4]*Kyoto Pharmaceutical University, Kyoto, Kyoto 607-8412*

The HIV-1 protease (EC 3.4.23.16) is an aspartic protease that functions to cleave the nascent viral polyprotein and plays an essential role in viral replication. Currently, the development of HIV-1 protease inhibitors is regarded as a major success of structure-based drug design, and the inhibitors of HIV protease are important compounds to establish highly active antiretroviral therapy for AIDS. The investigation of catalytic mechanism of HIV-1 protease will help to improve the design of inhibitor against HIV-1 protease. Thus, in order to identify the location of key hydrogen atoms, we aimed to determine the structure of HIV-1 protease with its transition state analog, KNI-272 by neutron crystallography.

For neutron crystallography of protein, a large crystal in size is required for data collection. We prepared 1.4 mm^3 HIV-1 protease crystal in volume by two-liquid system and macro seeding method using the recombinant HIV-1 protease which is refolded and purified from *Eschericha coli* cells. The crystal was soaked into deuterated solution and mounted at BIX-4 of the neutron diffractometer at JAEA. Diffraction data were collected at room temperature using a monochromatic neutron beam (λ= 2.6 Å) and recorded on a neutron imaging plate. For the efficient data collection, a- and c-axes of the crystal lattice was leaned at about 45 degree angle relative to phi rotation axis. A total rotation range of 50.7 was covered by 169 images with an exposure time of 6h/image by rotation angle of 0.3 from a rotation about one independent axis. The data were processed with the programs DENZO and SCALEPACK. Whole data set was integrated and scaled to 2.3 Å. Data collection and refinement statistics are summarized in Table 1. Moreover, same crystal was used to obtain X-ray diffraction data to 1.4 Åresolution. From the crystallographic refinement using both x-ray and neutron diffraction data by a joint refinement program PHENIX, the structure has been refined to R-factor of 16.0 %.

Table 1: Data collection and refinement statistics

Data collection	
Space group	$P2_12_12$
Unit cell dimensions	
a, b, c (Å)	59.5, 87.4, 46.8
Resolution range (Å)	43.9-2.3 (2.38-2.30)
I/σ(I)	7.7 (2.5)
R_{merge}	0.081 (0.226)
Completeness (%)	83.4 (80.3)
Refinement	
Data range for refinement (Å)	49.2-2.3
R_{work}	0.160
R_{free}	0.226
No of atoms	
total	3,845
H atom	1,586
D atom	529

原子炉：JRR-3　　装置：BIX-4(1G-B)　　分野：中性子散乱（生物）

1-6-8

Neutron Diffraction Study of ADP-ribose pyrophosphatase

M. Adachi[1], K. Kurihara[1], T. Tamada[1], T. Ooga[2], S. Kuramitsu[2] and R. Kuroki[4]

[1] *Quantum Beam Science Directorate, JAEA, Tokai, Ibaraki, 319-1195*
[2] *Graduate School of Science, Osaka University, Toyonaka, Osaka 563-0043*

ADP ribose pyrophosphatase (ADPRase) catalyzes the hydrolysis of ADP ribose to ribose 5 ' phosphate and AMP. The postulated role of ADPRase is to control the cellular concentration of toxic nucleoside diphosphate derivatives or physiological methabolites. Yoshiba et al[1)] reported x-ray crystal structures of ADPRase derived from an extreme thermophile [*Thermus thermophilus*] and proposed the catalytic mechanism including ionization state of catalytic residues and role of water molecules for the catalytic function and substrate recognition of ADPRase. However, hydrogen atoms of the enzyme, substrate and water molecules have not been detected directly because of lower scattering length of hydrogen atom by X-ray compared to other atoms. It is necessary to obtain information of hydrogen atoms by neutron crystallography for understanding the catalytic mechanism in detail. For neutron crystallography of a protein, large crystal in size is required for data collection. We prepared 8 mm^3 ADPRase crystal in volume by macro seeding method using recombinant ADPRase purified from *Eschericha coli* cells. The crystal growth experiment was performed using PEG4000 as a precipitant and it took about two months at 20 degrees to obtain the appropriate size of crystal. The crystal was soaked into deuterated solution and mounted at BIX-3 of the neutron diffractometer at JAEA. Diffraction data were collected at room temperature using a monochromatic neutron beam (λ= 2.9 Å) and recorded on a neutron imaging plate. Although c-axis of the crystal lattice is rather too long (119Å) for data collection in BIX-3, some diffraction peaks were overlapped. After the separation of diffraction peaks and completeness were predicted, full data set was collected along two independent axes. A total rotation range of 103.8 degrees was covered by 346 images with a rotation angle of 0.3 degree, and the exposure time was 4h/image. The data were processed with the programs DENZO and SCALEPACK. Whole data set was integrated and scaled to 2.1 Å. Data collection and current refinement statistics are summarized in Table 1. From the crystallographic refinement using both x-ray and neutron diffraction data by a joint refinement program PHENIX, the structure has been refined to R-factor of 17.4 %.

Table 1: Data collection and refinement statistics

Data collection	
Space group	$P3_221$
Unit cell dimensions	
a, b, c (Å)	50.7, 50.7, 119.2
Resolution range (Å)	43.9-2.1 (2.18-2.10)
I/σ(I)	20.3 (6.0)
R_{merge}	0.080 (0.338)
Completeness (%)	73.1 (61.2)
Refinement	
Data range for refinement (Å)	43.9-2.1
R_{work}	0.174
R_{free}	0.252
No of atoms	
total	2,975
H atom	1,103
D atom	503

References

1) Yoshiba S, Ooga T, Nakagawa N, Shibata T, Inoue Y, Yokoyama S, Kuramitsu S, Masui R. J. Biol. Chem. 279, 163-174 (2004).

原子炉：JRR-3　　装置：BIX-4(1G-B)　　分野：中性子散乱（生物）

1-6-9

Trial Diffraction Measurements of Protein Single Crystals in H_2O

S. Fujiwara, K. Kurihara and T. Chatake[1]

Quantum Beam Science Directorate, JAEA, Tokai, Ibaraki 319-1195
[1]*Research Reactor Institute, Kyoto University, Kumatori, Osaka 590-0494*

Among various methods for structural studies of biological macromolecules, neutron scattering and diffraction provide unique information that cannot be obtained from other methods. Because of a large difference in the scattering length density of water and heavy water (-0.00562 $\times$ 10^{-12} cm Å^{-3} for H_2O and 0.064 $\times$ 10^{-12} cm Å^{-3} for $^2H(=D)_2O$) due to the difference in the scattering length of hydrogen (-0.3742 $\times$ 10^{-12} cm) and deuterium (0.6671 $\times$ 10^{-12} cm), it is possible to vary widely the scattering length density of solvent by changing the fraction of D_2O in the solvent. This "contrast variation" technique has found wide applications not only in small-angle neutron scattering but also in neutron crystallography. Application of the contrast variation technique in neutron crystallography provides information on individual components in a very large macromolecular complex such as nucleic acid regions within viruses and nucleosomes, and on disordered components in the complex such as detergent moiety in membrane proteins[1)]. Essence in these applications is obtaining structural information of the region having distinct scattering length density. Thus, there is a possibility that the scattering density of amino acids is estimated because each amino acid has distinct scattering length density. Furthermore, we have obtained the results from the neutron fiber diffraction measurements using the contrast variation technique, suggesting a possibility of distinguishing the static disorder and dynamic fluctuations (Fujiwara et al., in preparation).

To explore such a possibility of the contrast variation technique in neutron crystallography, we started a project of collecting the neutron diffraction from crystals soaked in various fractions of D_2O. As a first step, we prepared a single crystal of proteins in H_2O, and performed a trial measurement to see if diffraction patterns could be collected.

A crystal of TAKA amylase was used in the measurements. The crystal, grown in H_2O solution to the size of about 1 mm^3, belongs to orthorhombic $P2_12_12_1$ with cell dimensions of a = 51 Å, b = 67 Å, and c = 133 Å. Diffraction images were collected at room temperature using monochromatic neutron beam (λ = 2.6 Å) and recorded on a neutron imaging plate on a single-crystal diffractometer (BIX-4) at JRR-3 in JAEA. We tried to record the diffraction patterns under different conditions of exposure times and oscillation ranges. A pattern collected by 8 hours exposure under the no-oscillation condition showed diffraction spots up to 9 Åresolution. This implies that the diffraction measurements are feasible on single crystals in H_2O, but, for the measurements to be done within a reasonable machine time, larger crystals with preferably smaller cell dimensions will be required. Exploration of suitable crystals is underway.

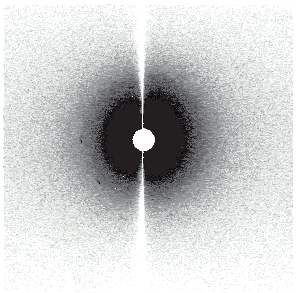


Figure 1: Example of the diffraction patterns collected at BIX-4.

References

1) P. A. Timmins and G. Zaccai: "Eur. Biophys. J." 15, 257 (1988): P. A. Timmins: "Neutron Scattering in Biology" Springer, pp. 73-83 (2006).

原子炉：JRR-3　　装置：BIX-4(1G-B)　　分野：中性子散乱（生物）

1-6-10

The State of Cryptobiosis of Larvae of Polypedilum Vandezplanki Studied by Incoherent Inelastic Neutron Scattering

H. Nakagawa, T. Okuda[1] and M. Kataoka

Quantum Beam Science Directorate, Japan Atomic Energy Agency, Tokai, Ibaraki, 319-1195
[1]*Institute of Molecular and Cellular Biosciences, The University of Tokyo, Yayoi, Tokyo, 113-0032*

Larvae of an African chironomid, Polypedilum vanderplanki live in temporal rock pools and they can stand complete desiccation in a cryptobiotic (ametabolic) state [1]. One of the most characteristic phenomena is remarkable accumulation of trehalose in the cryptobiotic larva. Slowly-dehydrated larva (Slow sample) accumulated sufficient trehalose successfully enters the state of cryptobiosis, whereas quickly-dehydrated one (Quick sample) with a small amount of trehalose fails to do. It is suggested that the vitrification of the trehalose is important for cryptobiosis. Generally the glassy materials exhibits a glass transition. This study aimed to examine the vitrified state in cryptobios in terms of glass transition by incoherent inelastic neutron scattering using slow and quick samples. The incoherent neutron inelastic scattering experiments were performed with the triple axis spectrometer, TAS-2, in the JRR-3M reactor in Tokai. The data were then collected at 100 and 280 K. Figure shows the inelastic neutron scattering around the elastic peak of the slow and quick samples of Larvae of Polypedilum vandezplanki at 100 and 280 K. At 100 K significant difference was not observed between the slow and quick samples. At 280 K, the elastic intensity of the slow sample is higher than that of the quick sample. This suggests that the relaxation process of the slow sample is inhibited and/or the timescales of the process is slower than quick one. This suggests the appearance of a glass transition with the quick sample, and the glassy state with the slow one even in the physiological temperature. These observations imply that the importance of the vitrification by the trehalose for the cryptobiosis mechanism of Larvae.

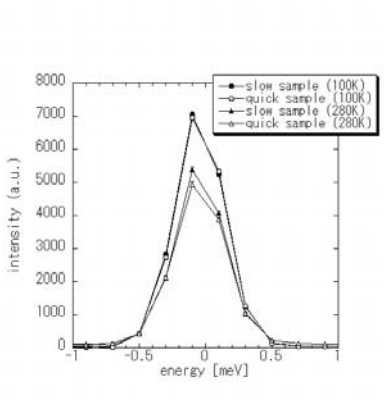


Figure 1: Inelastic neutron scattering around the elastic peak of the slow and quick samples of Larvae of Polypedilum vandezplanki at 100 and 280 K.

References

1) T. Okuda et al. :"Proc.Arthropod.Embryol.Soc.Jpn",39, 1(2004).

原子炉：JRR-3　　装置：TAS-2(T2-4)　　分野：中性子散乱（生物）

1-6-11

Dynamical Transition of DNA Studied by Neutron Inelastic Scattering

H. Nakagawa, and H. Kono

Quantum Beam Science Directorate, Japan Atomic Energy Agency, Tokai, Ibaraki, 319-1195

Protein recognize specific DNA sequences not only through direct contact between amino acids and bases, but also indirectly based in the sequence-dependent conformation and deformability of the DNA [1]. Therefore, the relationship between DNA sequence and its flexibility should be known. MD simulation shows that DNA tetramer sequences AATT and TTAA are conformationally more rigid and flexible, respectively. This relationship should be confirmed experimentally. In this study, as a preliminary experiment, we measured the flexibility of the hydrated DNA with sequence of AATT (rigid sequence) by incoherent neutron scattering. The neutron scattering experiments were performed with the triple axis spectrometer, LTAS, in the JRR-3M reactor in Tokai with an energy resolution of 69 μ eV. The hydration level of DNA sample is 0.49 g water/g DNA. Figure shows the temperature dependent atomic mean-square displacement (MSD) of hydrated DNA. As the temperature increase, the MSD monotonously increases. At around 240 K, DNA shows the sharp rise in the MSD. This is so called dynamical transition, which is generally observed with the hydrated biomacromolecules [2]. The slope of the regression line of the temperature-dependent MSD gives the resilience of molecular structure as a force constant [3]. Analytical equation is as below, k=0.00276/(d(MSD)/dT) [N/m]. Above the transition temperature, the resilience of DNA structure was estimated as 0.27 N/m. This study demonstrated that neutron scattering experiment is applicable for estimating of DNA structural flexibility. In the future, we will measure DNA with a sequence of TTAA (flexible sequence), and compare it with AATT (rigid sequence).

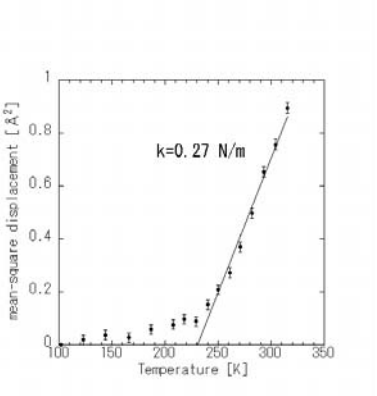


Figure 1: The atomic mean-square displacement of the hydrated DNA with a sequence of AATT and the force constant above the dynamical transition temperature is 0.27 N/m.

References

1) S. Fujii et al. :"Nuc.Acid.Res",35, 6063(2007).
2) W. Doster et al. :"Nature",337, 754(1989).
3) G. Zaccai et al. :"Science",288, 1605(2000).

原子炉：JRR-3　　装置：LTAS(C2-1)　　分野：中性子散乱（生物）

1-6-12

Glass Transition of Larvae of Polypedilum Vandezplanki Studied by Incoherent Inelastic Neutron Scattering

H. Nakagawa, T. Okuda[1] and M. Kataoka

Quantum Beam Science Directorate, Japan Atomic Energy Agency, Tokai, Ibaraki, 319-1195
[1]*Institute of Molecular and Cellular Biosciences, The University of Tokyo, Yayoi, Tokyo, 113-0032*

Larvae of an African chironomid, Polypedilum vanderplanki live in temporal rock pools and they can stand complete desiccation in a cryptobiotic (ametabolic) state [1]. One of the most characteristic phenomena is remarkable accumulation of trehalose in the cryptobiotic larva. Slowly-dehydrated larva (Slow sample) accumulated sufficient trehalose successfully enters the state of cryptobiosis, whereas quickly-dehydrated one (Quick sample) with a small amount of trehalose fails to do. It is suggested that the vitrification of the trehalose is important for cryptobiosis. Generally the glassy materials exhibit a glass transition. This study aimed to examine the vitrified state in cryptobios in terms of glass transition by incoherent elastic neutron scattering using slow and quick samples. The experiments were performed with the triple axis spectrometer, LTAS, in the JRR-3M reactor in Tokai with an energy resolution of 61 μ eV. The data were then collected at every 10 K between 100 and 290 K. The q-dependence of the elastic intensity gives the atomic mean-square displacement (MSD) in the samples by Gaussian approximation analysis. Figure shows the MSD of the slow and quick samples of Larvae of Polypedilum vandezplanki between 100 K and 300 K. As the temperature increases, the MSDs of both samples monotonously increase. At the lower temperatures a significant difference was not observed between the slow and quick samples. The MSDs of the slow sample deviate from that of the quick one above about 250 K, indicating the appearance of the glass transition. This suggests that the relaxation process of the slow sample is inhibited and/or the timescales of the process is faster than quick one. These observations imply that the importance of the vitrification by the trehalose for the cryptobiosis mechanism of Larvae.

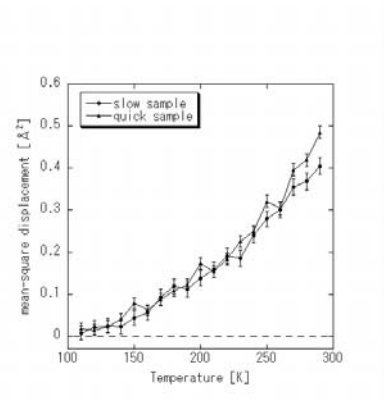


Figure 1: Mean-square displacement of the slow and quick samples of Larvae of Polypedilum vandezplanki.

References

1) T. Okuda et al. :"Proc.Arthropod.Embryol.Soc.Jpn",39, 1(2004).

原子炉：JRR-3　　装置：LTAS(C2-1)　　分野：中性子散乱（生物）

1-6-13

Contrast Variation Measurements of Hen Egg White Lysozyme Amyloid Fibrils

S. Fujiwara, F. Matsumoto and H. Nakagawa

Quantum Beam Science Directorate, JAEA, Tokai, Ibaraki 319-1195

Amyloid fibrils, filamentous protein aggregates found in a wide variety of proteins, are thought to be related to pathogenesis of neurodegenerative diseases such as Altzheimer's disease and Parkinson's disease. Understanding the mechanism of the amyloid fibril formation is therefore important for the development of therapeutic strategies against the amyloid diseases. Moreover, since the amyloid fibrils are found to be formed by proteins that have nothing to do with diseases, it should be of considerable help to gain an insight into the generic properties of proteins related to the mechanisms of folding and stability. It was found that hen egg white lysozyme (HEWL) forms the amyloid fibrils in highly concentrated ethanol solution[1]. The HEWL-water-ethanol system is suitable to study the general mechanism of the amyloid fibril formation. From small-angle X-ray and neutron scattering (SAXS and SANS) measurements, we showed that a pathway of the amyloid fibril formation of HEWL consists of three stages; the formation of the dimers, the formation of the protofilaments, and the formation of the amyloid fibrils via a lateral association of the protofilaments[2)3)].

In order to understand the mechanism by which the amyloid fibril formation occurs in more detail, it is necessary to obtain detailed structural information of each intermediate structure. Here, we performed SANS experiments of HEWL solutions in 90% ethanol at two HEWL concentrations, 2 mg/ml and 10 mg/ml, which correspond to the state where protofilaments are formed and the state where the lateral association of the protofilament occurs, respectively. SANS curves of these HEWL solutions, prepared in various fractions of deuterated solvents, were measured with SANS-J at the guide hall of the reactor JRR-3M in JAEA, and cross-sectional Guinier analysis was done to estimate the cross-sectional radius of gyration at each contrast. Figure 1 shows the Stuhrmann plots[4], the plots of square of the cross-sectional radius of gyration against a reciprocal of the contrast, of these solutions. The data were fit with a quadratic function of $1/(\Delta\rho)$, suggesting that a center of the scattering density shifts with contrasts. Detailed analysis with aid of model calculation is currently underway.

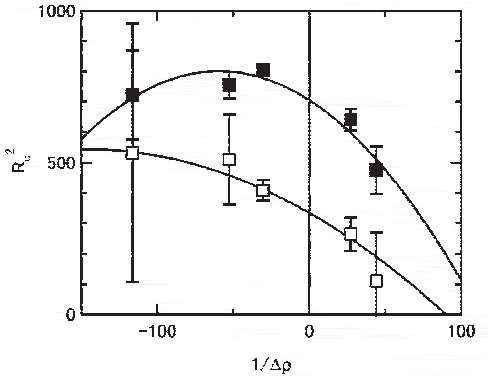


Figure 1: The Stuhrmann plots of the cross-section of the amyloid protofilament of HEWL. Filled and open squares denote the data at 10 mg/ml and 2 mg/ml, respectively.

References

1) S. Goda et al: "Protein. Sci." 9, 369 (2000).
2) Y. Yonezawa et al.: "J. Mol. Biol." 323, 237 (2002).
3) S. Fujiwara et al: "J. Mol. Biol." 331, 21 (2003).
4) H. B. Stuhrmann: "J. Appl. Cryst." 7, 173 (1974).

原子炉：JRR-3　　装置：SANS-J(C3-2)　　分野：中性子散乱（生物）

1-6-14

Small-Angle Neutron Scattering Measurements of Rhodanase-GroEL-GroES Complex

K. Ichimura, Y. Matsuura[1], S. Fujiwara[2], Y. Kawata[3] and H. Kihara[1]

Department of Biochemistry, Dokkyo University Medical Schoo, Mibu, Tochigi 321-0293
[1]*Department of Physics, Kansai Medical University, Hirakata 573-1136*
[2] *Quantum Beam Science Directorate, JAEA, Tokai, Ibaraki 319-1195*
[3]*Department of Biotechnology, Tottori University, Tottori 680-8552*

When proteins are synthesized *in vivo*, they are apt to fold with the aid of chaperon proteins. GroEL, a chaperon protein from *E. coli*, forms hydrophobic bonds with the newly synthesized target protein, assisting the folding of the target protein. In order to elucidate the molecular mechanism of folding the target protein with the aid of the chaperon protein, it is important to elucidate various intermediate structures including the structure of the target protein when they are bound to chaperon protein, and the structure of GroEL in the ternary complex formed with GroES. As a first step towards this purpose, we employed neutron scattering to investigate the structure of the target protein bound to GroEL.

We used rhodanase as a target protein. Rhodanase is a monomeric protein of the molecular weight of 33-kDa, and its folding intermediate is known to bind to GroEL. Employing the mutated GroEL[1)], which forms stable complex with the target proteins and binds GroES at its complex with the target protein, made it possible to measure small-angle neutron scattering (SANS) curves of the rhodanase-GroEL complex. We prepared deuterated (d-) and undeuterated (h-) rhodanase, and mixed with GroEL and GroES at 1:1:1 stoichiometry in solvent containing 42% D_2O, at which the scattering length density of the solvent was matched to that of the undeuterated proteins.

We measured SANS curves of d-rhodanase-GroEL-GroES complex and h-rhodanase-GroEL-GroES complex with the Small-Angle Neutron Scattering Instrument (SANS-J) at the guide hall of the reactor JRR-3M in Japan Atomic Energy Agency. The measurements were done with the incident neutrons of the wavelength of 6.5 Å($\lambda/\Delta\lambda$=13.4%), and the sample-to-detector distance was 2.5 m. Temperature of the samples were kept at 15℃ during the measurements. Figure 1 shows the SANS curve of d-rhodanase-GroEL-GroES, that of h-rhodanase-GroEL-GroEs, and the difference curve between these two. Because of the unfortunate breakdown of the detector of SANS-J during our machine time, we obtained only the curves with poor statistics. They, however, show that the reasonable difference curve were obtained, indicating that the SANS curve arising from rhodanase within the GroEL-GroES complex can be extracted.

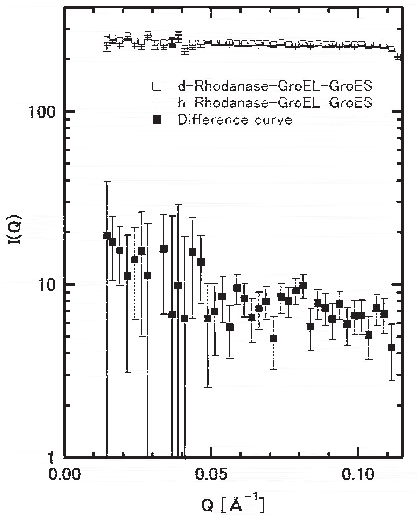


Figure 1: SANS curves of d-rhodanase-GroEL-GroES, h-rhodanase-GroEL-GroES, and the difference curves.

References

1) Y. Kawata et al: "Biochemistry" 38, 15731 (1999).

原子炉：JRR-3　　装置：SANS-J(C3-2)　　分野：中性子散乱（生物）

1-6-15

Small-Angle Neutron Scattering Measurements of α-Synuclein and its Disease-Related Mutants

S. Naito[1,2], H. Mochizuki[1], T. Yasuda[1], J. Yamaguchi[1], Y. Mizuno[1], M. Furusaka[3], S. Ikeda[2], M. H. Shimizu[2] and S. Fujiwara[4]

[1] *Dept. of Neurol., Juntendo Univ. Sch. of Med.,Tokyo 113-8421*
[2] *KEK, Tsukuba, Ibaraki 305-0801*
[3] *Dept. of Mech. Intell. Eng., Grad. School of Eng., Hokkaido Univ., Sapporo 060-8628*
[4] *Quantum Beam Science Directorate, JAEA, Tokai, Ibaraki 319-1195*

Parkinson's disease (PD) is a neurodegerative disorder that is characterized by the loss of dopaminergic neurons from the substantia nigra, and the formation of fibrillar intraneuronal inclusions called Lewy bodies, the major component of which are filaments consisting of α-synuclein. It has been postulated that the fibril formation by α-synuclein is closely associated with pathogenesis of PD. In particular, the facts that α-synuclein found in the fibrils in Lewy bodies is phosphorylated at the residue Ser129 and that missense mutants of α-synuclein (A30P and A53T), found in the patients of rare, autosomal dominant early-onset PD, form fibrils imply that fibril formation induced by abnormal state of α-synuclein is associated with PD. It is thus important to investigate relationship between the structural states of α-synuclein and fibril formation.

As a first step towards this purpose, we prepared three kinds of samples; the wild-type α-synuclein, the mutant A53T, and the mutant S129D, which mimics the phosphorylation at this residue, and investigate the structures of these proteins in solution. We employed small-angle neutron scattering (SANS). We prepared the solutions containing these proteins under the condition where the fibril formation does not occur, and SANS curves of these solutions were measured with the Small-Angle Neutron Scattering Instrument (SANS-J) at the guide hall of the reactor JRR-3M in Japan Atomic Energy Agency. The measurements were done with the incident neutrons of the wavelength of 6.5 Å($\lambda/\Delta\lambda$= 12.9%), and the sample-to-detector distance was 6 m. Temperature of the samples were kept at 20˚C during the measurements.

Figure 1(a) shows the SANS curves of the wild type α-synuclein, the mutant A53T, and the mutant S129D. Differences in the SANS curves are clearly observed between the wild type, A53T, and S129D, indicating the structural differences in these proteins. Figure 1(b) shows the Kratky plots of these SANS curves. Linear increases with increasing Q imply that these proteins have a random-coil like conformation rather than a globular structure. The differences in the plots appear to be consistent with the development of the beginnings of a tightly packed core in the mutants. Detailed analysis is currently underway.

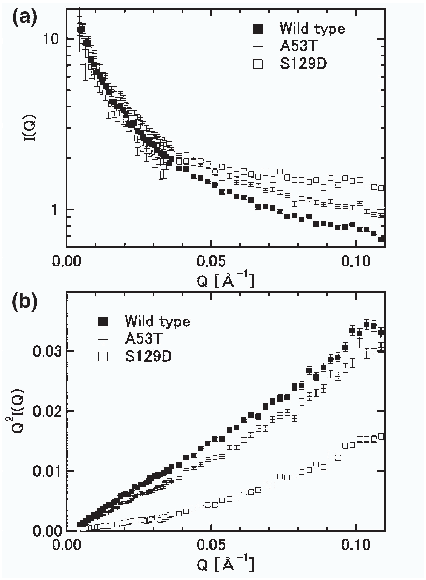


Figure 1: (a) SANS curves and (b) Kratky plots of the wild type α-synuclein, the mutant (A53T), and the mutant (S129D).

原子炉：JRR-3　　装置：SANS-J(C3-2)　　分野：中性子散乱（生物）

1. 中性子散乱 7) 基礎物理学・中性子光学

1. Neutron Scattering 7) Fundamental Physics・Neutron Optics

This is a blank page.

1-7-1

Development of phase correction devices for high resolution NRSE spectrometer

Kitaguchi M.(A), Hino M.(A), Kawabata Y.(A), Hayashida H.(B), Tasaki S.(B),
Maruyama R.(C), Ebisawa T.(C)
KURRI(A), Kyoto Univ.(B), JAEA(C)

Neutron spin echo (NSE) spectrometer is one of the techniques with the highest energy resolution for quasi-elastic scattering[1]. In the case of spin echo the beam divergence makes the deviation of the relative phase between up- and down-spin components, which is equivalent to spin precession, because the relative phase is proportional to the neutron flight length. The deviation of the phase can be corrected by using three magnetic fields with the strength which is proportional to the square of the radius. In the conventional NSE with the spin quantization axis along to the beam direction, such magnetic fields are made with Fresnel coils [2]. In neutron resonance spin echo (NRSE) spectrometer [3], however, the spin quantization axis is generally transverse to the beam. Magnetic fields for adiabatic transition of the quantization axis for the correction with Fresnel coils make the vertical asymmetric distribution of the field integral. That makes the contrast of spin echo signal disappear.
We consider the devices which make the transition of spin quantization axis only at the resonance spin flippers (RSFs). The quantization axis of the incident neutrons changes from longitudinal direction into vertical direction just before a RSF. After the flip of the spin, the quantization axis changes to longitudinal direction. We call the devices which provides the transition field as "coupling coils". By using a set of coupling coils provides parabola distribution of field integral, which is the same representation as the correction field only for the vertical divergence. Numerical simulation of the phase distribution for the beam divergence was performed for the system including coupling coils. We demonstrated that the phase through the system can be uniform for the wide beam divergence. Test experiments are in progress at cold neutron beam line MINE1 and MINE2.

References

[1] F. Mezei: Z. Phys. 255 (1972) 146.
[2] F. Mezei: The Principles of Neutron spin echo, proceedings of the ILL Workshop, Grenoble 1979, Lecture Notes in Physics, vol. 128, Springer, Heidelberg, 1979, pp. 3-26.
[3] R. Gaehler, R. Golub: Z. Phys. B65 (1987) 43.
[4] M. Kitaguchi, et. al., Meas. Sci. Techno., to be published in 2008.

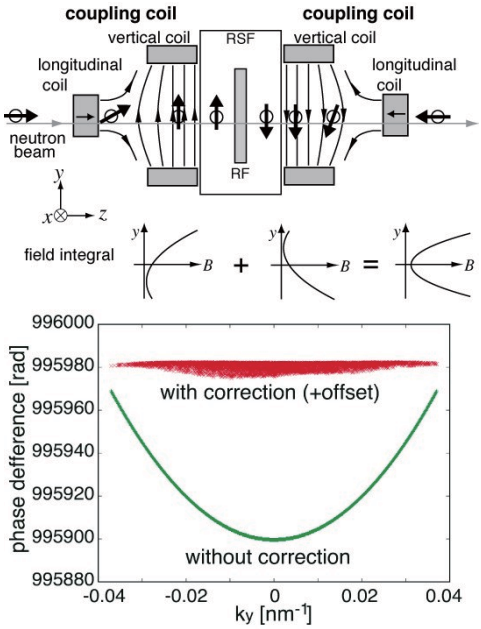


Fig. 1. Top: Concept of coupling coils. Bottom: Simulation of the phase distribution for beam divergence. The phase is uniform for wide beam divergence at a proper set of current for the coupling coils.

1-7-2

Development of Jamin Type Cold Neutron Interferometer with Completely Separated Two Paths

[1,4]Y. Seki, [1]K. Taketani, [2]H. Funahashi,
[3]M. Kitaguchi, [3]M. Hino, [4]Y. Otake, [5]H.M. Shimizu
Department of Physics, Kyoto University, Kyoto 606-8502, Japan
Osaka Electro-Communication University, 18-8 Hatsucho, Neyagawa, Osaka 572-8530, Japan
Research Reactor Institute, Kyoto University, Kumatori, Sennan, Osaka 590-0490, Japan
RIKEN, 2-1 Hirosawa, Wako, Saitama 351- 0198, Japan
KEK, 1-1 Oho, Tsukuba, Ibaraki 305-0801, Japan

We are developing large-dimensional cold-neutron interferometers with multilayer mirrors in order to investigate small interactions.

The success of Jamin-type interferometer made up of two 'beam splitting etalons (BSEs)' [Fig. 1] with a 10 μm gap have confirmed the accuracy of manufacturing of etalons. However, even if the beam width was collimated to 100 μm, the two beams were almost overlapped. When we enlarge the gap of the BSE up to 200 μm, we can separate the beam spatially and realize various experimental configuration, for example, inserting the some devices between paths of the interferometer.

One of our experimental targets is the precision measurement of Aharonov-Casher effect. The AC effect is a dual of the Aharonov-Bohm effect. When a neutral particle with a magnetic moment goes around change density the topological phase shift is induced. The AC phase shift was detected for the first time by using the Si crystal neutron interferometer, however, the observed value was inconsistent with the expected value. Our large-dimensional cold-neutron interferometer with separated long paths can measure the topological AC phase shift precisely enough.

The development is performed at cold-neutron beam line MINE2 at JRR-3M reactor in JAEA. The beam has a wave length of 0.88nm and a bandwidth of 2.4% in FWHM. The typical longitudinal, vertical and horizontal coherence lengths in our setup are about 17 nm, 50 nm and 2 μm, respectively. Therefore the tolerances for alignment of two BSEs are

$$\alpha < 40 \quad \mu\text{rad}, \quad \beta < 130 \quad \mu\text{rad}, \qquad (1)$$

where α and β are the relative angle between two BSEs in the horizontal and vertical planes, respectively.

In order to arrange BSEs meeting this coherence condition, we have developed a new jig employing a precise planar substrate (SIGMA KOKI OFPXP-150S20-4). The 150-cm-square substrate is made of PYREX with flatness of $\lambda_{He-Ne}/4$. Each BSEs was fixed closely to the substrate at three points with screws. We have obtained reasonable signals of the interference fringe, and are trying to find a way to stabilize and improve its contrast.

In addition, we studied the thermal, magnetic and vibration stability in the experimental environment. It was understood that phase drifts of neutron spin interferometry ($\sim$ 34 mrad) were almost followed by the magnetic fluctuations ($\sim$ 16 mG).

References

[1] M. Kitaguchi *et al.*: Phys. Rev. **A 67** (2003) 033609.

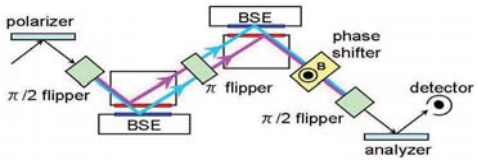


Fig. 1. Jamin-type interferometer with two BSEs

1-7-3

Development of beam splitting etalons for pulsed neutrons II

Kitaguchi M.(A), Seki Y.(B), Taketani K.(B), Funahashi H.(C), Hino M.(A), and Shimizu H. M.(D)
(A)KURRI, (B)Kyoto Univ., (C)Osaka Electro-Comunication Univ., (D)KEK

A large dimensional interferometer for long wavelength neutrons has the advantage to increase the sensitivity to small interactions. Multilayer mirror is suitable for Bragg reflection of cold neutrons. We demonstrated Jamin-type interferometer for cold neutrons using ' beam splitting etalons (BSEs), ' which enables us to align the four independent multilayer mirrors in the interferometer within required precision [1]. We are preparing for high-resolution measurement of Aharonov-Casher effect [2,3] by using this type of interferometer.

The interferometer for pulsed neutrons can increases neutron counts available for AC measurement because the phase shift is independent from the velocity of incident neutrons. Neutron interferometer with multilayer mirrors can be applied to pulsed neutrons by replacing the mirrors with supermirrors. The supermirrors can reflect neutrons with wide range of wavelength at a proper incident angle. In the case of neutron spin interferometer of Jamin type, a magnetic supermirror on the one plane of the BSE reflects only up-spin component of the neutrons and a non-magnetic supermirror on the other plane reflects transmitted down-spin component. The second BSE with supermirrors recombines the two components. High polarization of both of reflected and transmitted beam for magnetic mirror is required in order to split the beam into two paths according to the spin states.

We deposited magnetic supermirrors on silicon wafers by using both of ion beam sputtering instrument and vacuum evaporation instrument at KURRI for test of BSE. The reflectivity of the magnetic supermirrors were measured by scanning of incident angle instead of neutron wavelength. Test experiments were performed using the cold neutron beam line MINE2 at the JRR-3M reactor in JAEA. The beam had a wavelength of 0.88 nm and a bandwidth of 2.7% in FWHM. The magnetic mirrors required external magnetic field for magnetic saturation of the mirror. Strong magnetic field in local area in neutron spin interferometer would decrease the visibility of interferogram due to depolarization or deviation of the relative phase between the two spin states. We are continuing the development of the magnetic supermirror for lower external field. The interferometer for the AC measurements must have perfectly separated two paths enclosing an electrode. We are also continuing on the constructing of interferometer using BSEs with large gaps.

References

[1] M. Kitaguchi et al.: Phys. Rev. A 67 (2003) 033609.
[2] Y. Aharonov and A. Casher: Phys. Rev. Lett. 53 (1984) 319.
[3] A. Cimmino et al.: Phys. Rev. Lett. 63 (1989) 380.

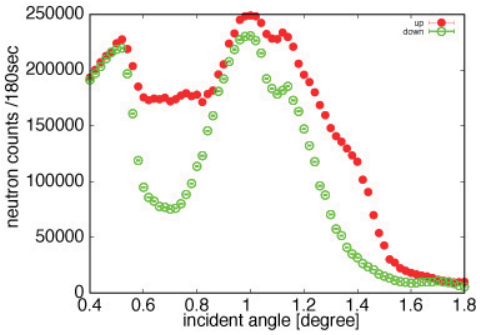


Fig. 1. Reflectivity of multilayer spin splitter with the magnetic supermirror. Because the mirror was not saturated, the reflectivity for up-spin was not high for BSEs.

1-7-4

Possible improvement of thin magnetic film using Pd

Seiji Tasaki, Satoshi Kuramoto, Yutaka Abe, Masahiro Hino
Department of Nuclear Engineering Kyoto University

Multilayers consisting of alternative stack of a magnetic material and a non-magnetic material is widely used as neutron spin polarizers. Such multilayers are also a key element for consisting multilayer spin splitter, consisting of polarizing mirror, gap layer and reflection mirror, which can be used to measure precise quantity of absorbed material by the gap layer material.

One way to the improvement of polarizing efficiency of the multilayer polarizer is to make the saturated magnetic field higher. Higher field strength allows us higher potential contrast between neutron eigenstates, and higher reflectivity for neutron with field-parallel spin. Recently, Noma et al. [1] reported that saturated magnetic field of FeCo was increased by being sandwiched by Pd thin films. In the present study, we studied the effect of Pd thin layer over Fe films in polarizing multilayers.

The samples are fabricated with vacuum evaporation. Firstly combination of thickness of Pd and Fe layers is investigated. Multilayers with various combination of Pd and Fe such as (1nm, 4nm), (1nm, 5nm), (1nm, 6nm), (2nm, 6nm), (3nm, 6nm) where total Fe thickness is equal to 60nm were fabricated and their magnetization is measured with vibrating magnetometer. The thickness of the films are measured with X-ray reflectometer. Combination of 3nm-Pd and 6nm-Fe gave highest magnetization. Measured magnetic field is 1.51 T which is reasonable value comparing with bulk magnetization of 2.1 T for density reduction of 75% given by X-ray reflectivity.

Secondly, for comparison, various combination of Fe and other material was tested. Here Ge, Ti, Si were adopted other than Pd. The thickness of all non magnetic material is 2nm, and that of Fe is 6nm. The calibrated hysteresis curves are shown in the upper figure in Fig.1. Here Ge gives similar result as Pd. However, Pd gives a little higher field and smaller coercive force. These saturated magnetization was also confirmed with polarized neutron reflectivity.

The lower figure in Fig.1 shows polarized neutron reflectivity of Fe6nm-Pd2nm-Ge2nm-Pd2nm multilayer with 15 period. The rise of reflectivity in the region $Q_z > 0.06$ is due to the position dependent back ground. Other than this region, the reflectivity is well reproduced by the calculation in which saturated magnetic field is assumed as 1.51T.

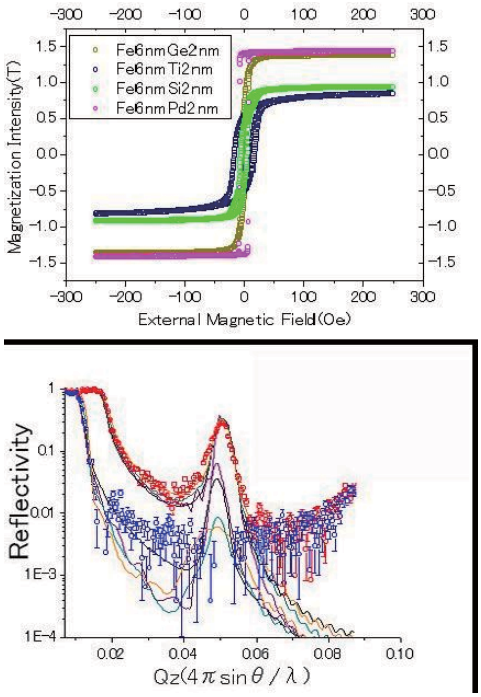


Fig. 1. The caribrated hysteresis curves of multilayers of Fe and various material (upper), and polarized neutron reflectivity of Fe6nm-Pd2nm-Ge2nm-Pd2nm multilayer with 15 period (lower).

1-7-5

Development of neutron optics with a curved supermirror

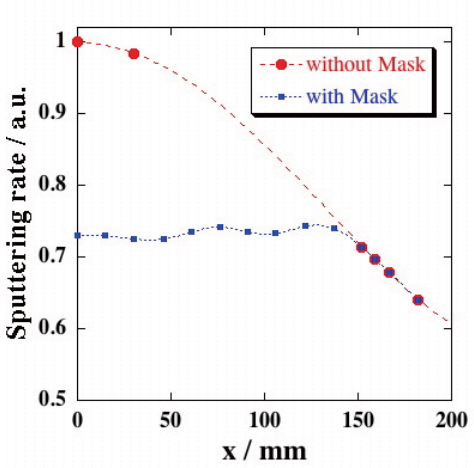
Ikeda K., Sato H., Hirota K., Mishima K.
Radiation Laboratory, RIKEN, 2-1 Hirosawa, Wako, 351-0198

We are developing real curved supermirror, which is deposited neutron supermirror on the substrate with a curved surface. First in our sputtering machine, we manage to keep the uniformity of layer thickness over the large area of tens to a hundred centimeter for large substrates with flat surface. But, when the curvature of surface is large and the surface is not considered to be flat, it's not easy to deposit supermirror uniformly on the curved surface as we can do on flat substrate. We then have to make the layer-thickness distribution to have conformity to curved surface, or find the way to compensate for the distribution.

We, at first, made the mask which is the meshes with stainless wires of 0.3mm in diameter in order to keep the uniformity of layer thickness over 300mm long area. Two kinds of meshed patterns and blank area were used for 300mm long substrate. Fig. 1 shows the sputtering rate in the case of with the mask and without the mask versus the position on the sample stage of our sputtering machine. The position x=0 is the center of the stage. We succeeded to decrease the differences of layer thickness from 28% to 4% between the center and the edge on the sample stage.

Second, we deposited 2.5Qc supermirror on the substrate with an ellipsoidal surface on which substrate 2.0Qc supermirror was requested. The performance of 2.5Qc to 2.0Qc supermirror was kept at the thinnest area to the thickest area, since the maximun reduction of the layer thickness was estimated to be 27% in the ellipsoidal surface. Fig. 2 shows the neutron reflectivity of 2.5Qc supermirror fabricated with the mask. The mirror has the performance of 2.1Qc supermirror and the neutron reflectivity at 2.0Qc was 95%. The supermirror is deposited on a flut substrate of Si at the center of the sample stage.

Next, we have to find the way to keep uniformity of layer thickness on the surface with large curvature. The larger distribution of layer thickness yields stronger stress in the layers. It thus results in the peeling layers off the substrate and prevents from developing higher-Qc supermirror with curved surface.



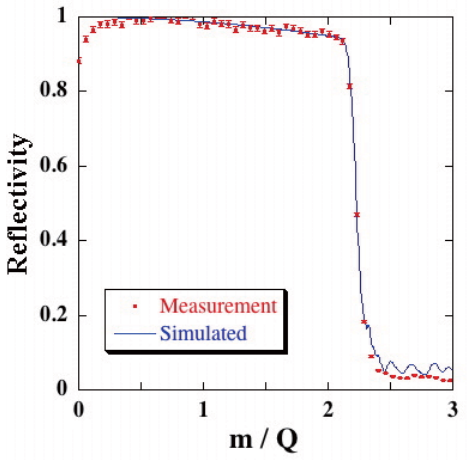


Fig. 1. Sputtering rate in the case of with the mask (circles) and without the mask (squares) versus the position on the sample stage of our sputtering machine. Fig. 2. Neutron reflectivity of 2.5Qc supermirror fabricated with the mask.

Activity Report on Neutron Scattering Research: Experimental Reports **15** (2008)
Report Number: 653

This is a blank page.

1. 中性子散乱 8) 装　置

1. Neutron Scattering　8) Instrument

This is a blank page.

1-8-1

Thermal diffuse scattering effect on neutron holography

K. Hayashi, K. Ohyama, S. Orimo, Y. Nakamori, H. Takahashi 1 and K. Shibata 2
1 IMR, Tohoku Univ., 2 Graduate School for Environmental Science, Tohoku Univ., 3 JAEA

In the previous experiment, we measured efficiently the neutron hologram of a palladium hydride single crystal using the powder diffrcatometer of HERMES in JRR-3M reactor, and found the thermal diffuse scattering effect in the measured hologram.1) In this study, we used again a palladium hydride single crystal as the measured sample and evaluated the temperature dependence of the sample on the thermal diffuse scattering in the hologram. The sample dimension was 10 mm in a diameter and 5 mm in a thickness, and it was coated by Cu not to desorb the hydrogen gas. Wavelength of the neutron was 0.182 nm. Sample was rotated in the range of 0 - 359 deg with the step of 1 deg, where rotation axis was parallel to the incoming beam direction. Neutrons incoherently scattered by hydrogen nuclei in the sample were detected by HERMES 150 He3 counters at each sample rotation angle. Polar angle of the measured hologram defined by the counter ranged from 7 deg to 157 deg. Dwelling time at each angle was 480 sec. The average neutron intensity at each pixel was about 500 counts. To reduce the effect of thermal diffuse scattering the cryostream cooler (Oxford: cryostream 70 series) was used for keeping the sample temperature at 100 K. Figures 1 (a) and (b) show the 2D angular distributions of the neutron intensities around the sample at room temperature and 100 K, respectively. The observed data were four-fold symmetrized using sample crystal symmetry in order to suppress statistical error, and then they were low-pass filtered. The displayed patterns exhibit strong spots reflecting the sample crystal symmetry, due to thermal diffuse scattering. However, the contrast of the pattern in Fig.1 (b) is weaker than that in Fig. 1 (a). Figure 1 (c) shows the intensities changes as a function of azimuthal angle at polar angle of 80 deg. The amplitude of the intensity change at room temperature was twice as much as that at 100 K. These results revealed that the effect of the thermal diffuse scattering effect was reduced by the sample cooling.

1) K. Hayashi, K. Ohoyama, S. Orimo, Y. Nakamori, H. Takahashi and K. Shibata, Jpn. J. Appl. Phys. in press.

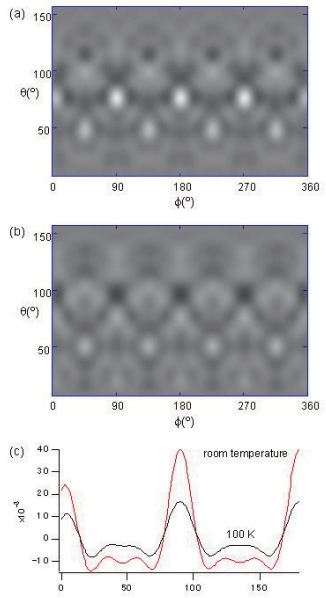


Fig. 1. Fig.1 2D angular distributions of the neutron intensities around the sample. (a) room temerature. (b) 100 K. (c) Intensities change at polar angle of 80 deg.

1-8-2

Development of A New Spin-Phase Contrast Imaging of Neutron

Seiji Tasaki, Masashi Kageyama, Masahiro Hino, Yuji Kawabata
Department of Nuclear Engineering Kyoto University

Spin-phase contrast imaging is a method of taking 2D image of the phase difference between spin-eigenfunctions of neutron. Since the phase difference is proportional to the magnetic integral along the neutron trajectory, the image shows the magnetic field distribution over the beam cross section.

The phase difference between the spin-eigenfunctions is measured using neutron spin interferometer (NSI), installed at C3-1-2-2 port of JRR-3M reactor in JAEA. In NSI, neutrons monochromated with 8.8Å($\Delta\lambda/\lambda = 2.7\%$) is polarized and is changed into superposition state of spin-parallel and antiparallel eigenstate to the guide magnetic field by $\pi/2$-flipper. In the middle of the set-up, the spin state of neutron is reversed by π-flipper, in order to realize spin echo of neutron, with which additional phase difference caused by outer magnetic field can be canceled. Then after going through the sample, neutron comes to the second $\pi/2$-flipper and spin-analyzer, where the measured neutron counts are proportional to the cosine of phase difference. Available beam area is 2mm(w)$\times$20mm(h).

In the experiments, neutron counts are measured via additional phase ϕ, the counts are fitted to $A(1+\cos(\phi_0+\phi))$ and ϕ_0 is the desired phase difference. In the present study, the additional phase is introduced as phase difference of rf-current to $\pi/2$ and π-flipper.

As neutron detector, we adopt 2D Photo Multiplier with Li-glass scintillator and neutron imaging plate (IP). The former has real-time read out system but low spatial resolution, where the latter has very high resolution but requires off-line read out.

With the former detector, we made preliminary experiments and confirmed the relation between magnetic field and phase difference in the case of magnetic coils (via electric current) and magnetic thin layer (via incident glancing angle).

With the IP, neutron imagines for different additional phase is recorded in a single IP. An example is shown in Fig. 1. The left picture is the sample, which is a 6Q polarizing supermirror with total thickness of magnetic layers is about 6μm. The sample was kept in non magnetic atmosphere for months. Hence the sample was demagnetized gradually. Left picture in Fig.1 is a photograph of the sample. Middle picture is normal transmission image, where no clear image is shown since almost all neutrons are transmitted. Right picture is the phase image, where inhomogeneous distribution of magnetic field is shown.

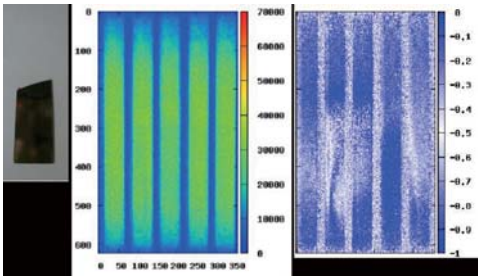


Fig. 1. The results of the spin-phase contrast imaging of neutron using imaging plate.

1-8-3

Development of transmittion geometry supermirror polarizer

M.Hino, M.Kitaguchi, H.Hayashida[1], Y.Kawabata, S. Tasaki[1]
KURRI, [1]Depart. Nucl. Eng., Kyoto Univ.

Magnetic multilayer mirror consisting of ferromagnetic layers and nonmagnetic layers is useful to polarize neutron beam. Polarizing supermirror is a stack of magnetic multilayer with gradually increasing value of the d-spacing. Polarizing supermirror is stable and it is easy to handle as neutron polarizer. Recently performance of He-3 spin filter is improved and it is better than supermirror when we need analyzer covering wide scattering angle for thermal neutron. When we use cold neutron and polarizer covering narrow beam cross section, polarizing supermirror is more useful than He-3 spin filter since transmission probability of supermirror is better than that of spin filter.

Recently we succeeded in fabricating m=4.9 Fe/Ge polarizing supermirror by using ion beam sputter (IBS) machine at KURRI[1]. The magnetic property of supermirror is better than Fe/Ge and Fe/Si ones by inserting thin Si layer in which thickness 0.5 nm between Fe and Ge layer. The measurement was carried out at C3-1-2-3 port (MINE2) at JRR-3M at JAEA. The average wavelength of incident neutron is 0.88 nm and the resolution is 2.7 % in full width half maximum. The divergent angle of neutron beam was smaller than 1 mrad. The strength of external magnetic field is 45 mT. The reflectivity and polarization efficiency of reflected neutron is estimated to be above 0.7 and 0.94, respectively. The reflectivity is very high, however, the polarization efficiency of transmitted neutron is 0.5. Because polarization efficiency of transmitted neutron P_t is related reflectivity R and it is given by the following equation $P_t \simeq P_r R/(2-R)$, where P_r is the polarization efficiency of reflected neutron.

The transmission geometry supermirror polarizer does not change neutron beam line and it is more useful and it is important for development of transmission geometry supermirror polarizer (analyzer) to enlarge utility of polarized neutron beam. Thus we started to develop transmission geometry supermirror polarizer.

The supermirrors were deposited on silicon wafer (150x60x0.6mm^3) using IBS at KURRI. The measurement was carried out at C3-1-2-2 port (MINE1) at JRR-3M at JAEA. The average wavelength of incident neutron is 0.81 nm and the resolution is 17.4 % in full width half maximum. The divergent angle of neutron beam was 1.9 mrad. The strength of external magnetic field is 60 mT. As shown in Fig.1, we succeeded in fabricating m=4 transmission geometry polarizing supermirror. The flipping ratio is higher than 20 at 2*le*m*le*4.1 and it is especially higher than 70 at 1.4*le*m*le*2.6. As a next step, we will improve the flipping ratio at m*ge*2.6.

[1] M.Hino, et al., ISSP Activity Report, Vol. 13 ,ibid, Physica B (2006) 385-386(2006)1187.

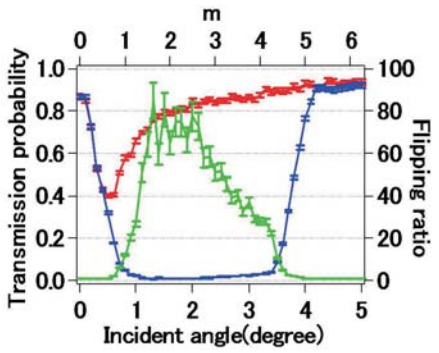


Fig. 1. Fig.1 Measured transmittion probabilities of up (blue) and down(red) spin neutron for m=4 Fe/$SiGe_3$(Si:0.5nm) magnetic supermirror. The green line indicates flipping ratio that transmittion probability of down spin neutron devided by that of up spin one.

1-8-4

Observation of superparamagnetic fluctuations in magnetic ferrofluid using MIEZE spectroscopy

M.Hino, H.Hayashida[1], M.Kitaguchi, N.Achiwa[2] and Y.Kawabata
KURRI, [1]Depart. Nucl. Eng., Kyoto Univ.,[2]Grad. Sch. Sci., Osaka Univ.

We have developed a MIEZE(Modulated IntEnsity by Zero Effort) spectrometer at C3-1-2-2(MINE1) port JRR-3M in order to install it to the high flux pulsed neutron source at J-PARC in the near future. In the MIEZE spectrometer the sample is placed after the analyzer and there are no optical components between sample and detector. When we measure NSE and NRSE signals on paramagnetic and ferromagnetic samples the maximum contrast is reduced to 0.5 or less. On the other hand the contrast of a MIEZE signal can be observed with almost 100 % contrast(1) even in magnetic scattering because the sample is placed after the analyzer. MIEZE signal is sensitive for dispersion of neutron trajectories from sample to detector. In other words MIEZE signal is reduced due to the dispersion alone even without in- and quasi-elastic scattering. We studied the correlation between experimental configuration and its resolution function using Monte Carlo simulation. We prepared a magnetite ferrofluid sample and examined the simulation model by experiments. The experimental results were reproduced with the simulation [1]. We studied dynamical structure-changes of the magnetite ferrofluid by using the MIEZE spectrometer. The ferrofluid consists of magnetite particles and solvent (heavy water). The magnetite particles with a diameter in the order of 10 nm are coated by oleic acid. There are two kind of dynamic modes in ferrofluid. One is diffusion of magnetite particles and the other is superparamagnetic fluctuation. When we observe the superparamagnetic fluctuation, we have to measure spin-flip scattering from magnetite particle. The intensity of magnetic scattering is much smaller than nuclear scattering and separate spin-flip and non-spin-flip scattering. Thus we placed second analyzer after sample in order to observe spin-flip scattering only. The second analyzer is transmission geometry magnetic supermirror to keep trajectories of scattering neutron. Figure 1 shows typical MIEZE signals with nuclear and spin flip(magnetic) scattering at Q=0.68 nm^{-1} at room temperature. As shown in Fig.1, the contrast of MIEZE signal with magnetic scattering reduced and we succeeded in observing superparamagnetic fluctuation.

[1] H.Hayashida, et al., *Measurement Science and Technology* (2008), in press.

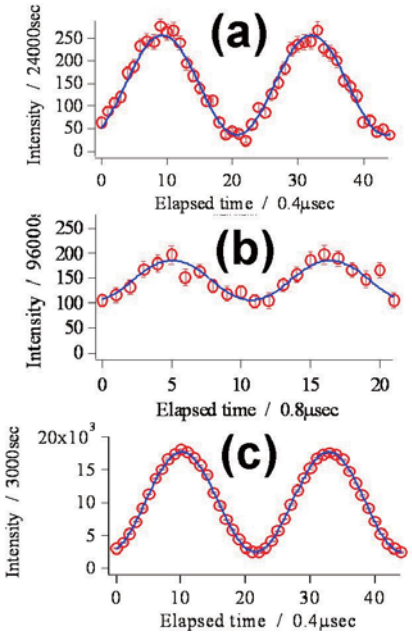


Fig. 1. Fig.1 Measured MIEZE signal(Q=0.68nm^{-1}) with (a) nuclear and (b) magnetic scattering in magnetic ferrofluid. (c) Measured MIEZE signal without sample.

1-8-5

Installation of a prototype of focusing-type small-angle neutron scattering instrument with an ellipsoidal supermirror

M. Furusaka(A), T. Satoh(B), Y. Sasaki(A), Y. Kawamura(C), T. Asami(C), Y. Otake(D), K. Ikeda(D), P. Mikula(E), Y. Kiyanagi(A), S. Naito(F), H. Yoshizawa(C)
(A)Grad. Sch. Eng., Hokkaido Univ. , (B)KUR, Kyoto Univ., (C)ISSP Univ. Tokyo, (D)RIKEN, (E)NPI, Czech Republic, (F)KENS, KEK

SANS is a very powerful and popular technique to study nano-scale structure in matters. Every neutron facilities all over the world have at least one or two such instruments, but very often, they are oversubscribed and not so easy to obtained machine time on these machines. We, therefore, decided to develop a prototype sans instrument, that is compact and low cost, hence can be easily installed at any neutron beam line.

Using a compact ellipsoidal mirror as a focusing device and high positional-resolution detectors, which have been developed in the last decade, we can now construct very compact and versatile focusing-type SANS instruments. We are now developing such instruments, and named it "Mini-focusing small-angle neutron scattering instrument (mfSANS)".

At first, we have conducted mock-up test experiments of a time-of-flight type mfSANS at a small pulsed cold-neutron source facility at Hokkaido University. The results looked very promising: from the preliminary results showed that we could measure minimum momentum transfer Q of the order of 2 $\times$ 10-2 nm-1 if the sample is a strong scatterer.

We have just finished a first phase construction of another prototype mfSANS instrument at the JRR-3 reactor at C1-3 position in October as shown in the figure. We put a new monochromator at just downstream of the ULS (ultra low-angle scattering) instrument in the same monochromator shielding. The total length of the instrument, from the monochromator to the detector, is only about 2.8 m. It is installed not horizontally, but installed above the beamline at the angle of 135° (45°) from the horizontal line. Aperture size of 1 to 10 mm can be selected remotely. A focusing mirror of 900 mm in length was used, that has a curved surface of a part of an ellipsoid of 2.5 m major and 20 mm minor axes, coated with 2.5 Qc supermirror. It is divided into three parts, each with 300 mm in length. Sample position is just after the mirror. A detector of 5 inch effective diameter that consists of a resistive-wire type photomultiplier with a ZnS scintillation plate is used. The position resolution of it is less than 1 mm.

Several very preliminary data were obtained with the instrument. Unfortunately, slight miss-alignments in the focusing mirrors were found. Even though, the miss-alignments were not so large, the direct beam focusing position was displaced by about 300 mm and it was blurred by almost a factor of 2. Even with such a geometry, we could measure fairly good small-angle scattering patterns and minimum Q of about 0.05 nm-1 using 2 mm aperture. Because of the long shutdown of the JRR-3 reactor, we will resume commissioning from July, 2008.

Activity Report on Neutron Scattering Research: Experimental Reports **15** (2008)
Report Number: 655

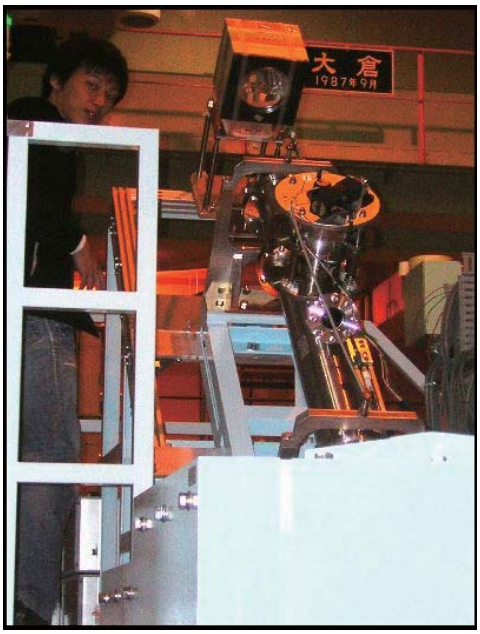


Fig. 1. Mini-focusing small-angle neutron scattering instrument (mfSANS) just installed above the ULS monochromator shielding.

1-8-6

Development of 10 GPa class cubic anvil type high pressure apparatus for neutron scattering experiments

Tetsuya Fujiwara[a], Kazuyuki Matsubayashi[b], Yoshiya Uwatoko[b], Naofumi Aso[b], Masakazu Nishi[b], Hideki Yoshizawa[b]
[a]*Yamaguchi Univ.*, [b]*ISSP, Univ. of Tokyo*

Over the past few decades, a considerable number of studies have been devoted the physical properties of Ce-, Yb- and U-based intermetallics, the so-called strongly correlated electron systems. In these systems, an external pressure is often a key to bring about a new type of ground state accompanied with exotic physical phenomena, such as a heavy fermion superconductivity or valence transition and so on. Accordingly, nowadays the concern with an application of high pressure generation techniques to various sorts of experimental measurements has been growing remarkably. In this work, we have developed a cubic anvil type high pressure cell (CAC). CAC can generate superior hydrostatic pressure to other high pressure apparatuses. In CAC, however, sample space is surrounded and enclosed by thick sliding anvil blocks made of tungsten carbide (WC) whose neutron transmittance is remarkably poor. So, to optimize CAC for neutron scattering experiments, We conducted a review of apparatus volume and a material of anvil block. Consequently, we succeeded in reducing the diameter of cell from 180 mmϕ to 80 mmϕ and the mass of apparatus from 26.8 kg to 1.4 kg. Fig. 1 is photograph of downsized CAC. Furthermore, anvil block made of ZrO_2 with superior neutron transmittance to WC was prepared. Pressurization examination was performed at room temperature. Daphne 7373 and a single crystal of NaCl were used as a pressure transmitting medium and a manometer, respectively. Transmittance of apparatus keeps up above $\sim$30 %. At present, applying external load, pressure distribution brings about materially, so that an intensity of NaCl (200) Bragg reflection remarkably decreases. There is room for improvement in homogenization of generated pressure.



Fig. 1. Downsized Cubic anvil type high pressure cell optimized for neutron scattering experiments

1-8-7

Development of Large 2D-PSD under collaboration with HANARO

Y. Noda, M. Watanabe, H. Kimura, Y. Dohi, Y. Ishikawa, T. Yamazaki, M. Moon(A) and Chang-Hee Lee(A)

IMRAM, Tohoku University, Katahira Sendai 980-8577, (A)HANARO, KOREA ATOMIC ENERGY RESEARCH INSTITUTE ,Taejon, 305-600, Korea

We have developed a large-scale two dimensional position sensitive detector (2D-PSD) under the collaboration with HANARO of KAERI. First, we have tested a small and flat 2D-PSD to evaluate the capability of the counter. The size of this plot-type detector is about 20cm x 20cm. Then, we have developed more realistic size detector to evaluate the capability, especially to apply structure analysis of relatively complicated system. The detector is bend one and size of this prototype detector is 63cm x 44cm. The upper panel of Fig. 1 shows the settlement of the 2D-PSD at T2-2 beam port.

First, we settled a Laser beam to adjust to the neutron beam path of FONDER. Then, goniometer with 4K-cryostat is put on the beam. This Laser beam evaluates sample position. The simple example to test oscillation photograph is that of NaCl, and shown in the lower panel of Fig.1. Condition of measurement is the following: omega speed is 0.2 degree/min. Each 0.4 degree, data is transferred to computer. All of parameters of 2D-PSD were determined by using the standard NaCl crystal. As shown in Fig.1, we can see the layer structure of NaCl from L=-1 to L=+2. We have developed new program to find peak position and intensity automatically. Peak position gives reasonable good lattice parameters. Then, we tried measurements of various crystals. Still we are developing new programs to do precise structure analysis. It seems to get good data from very efficient experiment. The lattice parameter of NaCl obtained by 2D-PSD is ; a=5.644(6) b=5.638(8) c=5.644(22)[A] alpha=89.8(2) beta=90.2(2) gamma= 90.2(2)[deg] vol.= 179.6(8) [A^3] These numbers can be compared with those taken by using FONDER : a=5.6569(11) b=5.6566(7) c=5.6542(45)[A] alpha=89.99(3) beta=89.92(3) gamma= 89.99(1)[deg] vol.=180.93(15) [A^3]. As other examples to test the detector, various different organic conductors was measured. We can get good lattice parameters. Now we are trying to do structure analysis for these complicated system.

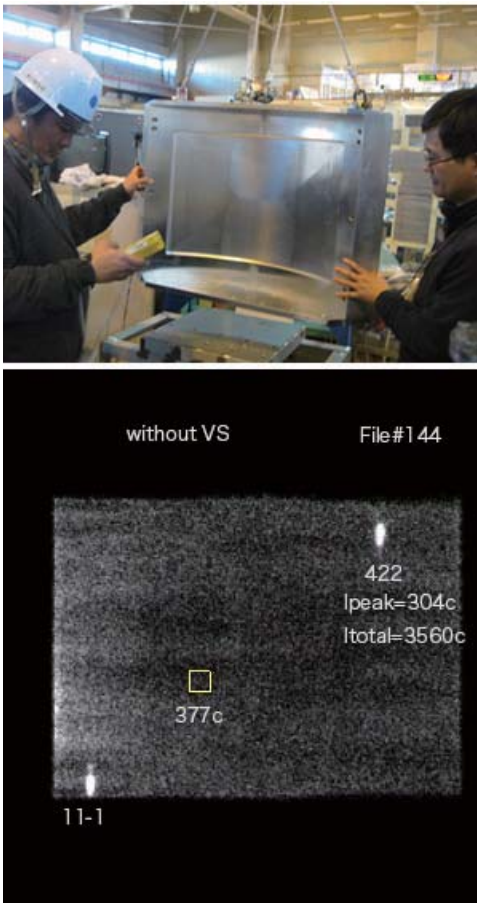


Fig. 1. Upper: The picture of the 2D-PSD at the settlement procedure. Lower: Snapshot of diffrcation from NaCl.

1-8-8

Neutron imaging measurement using newly developed inorganic gadolinium scintillator

J. H. Kaneko 1), S. Satoh 2), J. Haruna 1), S. Saeki 1), S. Kawamura 1), Y. Ohtake 3), M. Furusaka 1), Y. Kiyanagi 1)
1) Hokkaido University, 2) KEK, 3) RIKEN

1. Introduction

To improve experimental efficiency, neutron imaging measurement using a newly developed inorganic gadolinium scintillator was carried out. Cerium doped gadolinium pyrosilicate, i.e., GPS:Ce scintillator has been developed by Hokkaido University. This scintillator has two times light output higher than that of GSO scintillator; in addition, it has fast decay time of 50 to 60 ns. Several types of GPS scintillator plates were examined with combination of a position sensitive photo multiplier tube in the ULS.

2. Experimental

Polycrystalline GPS scintillator was grown by floating zone melting method. The GPS scintillator was grinded down and then fixed by several substrates by adhesive. Some of them were polished by mechanical way. Larger size of fabricated GPS scintillator plate was approximately 3 cm in diameter and 120 micrometer in thickness. A special circuit developed in KEK for a GPS scintillator was used. Figure 1 shows schematic drawing of the detection system.

3. Experimental results

Figure 2 shows an example of pulse height distribution from a charge sensitive preamplifier. Peaks caused by 33 keV internal conversion electrons and 77 keV that was sum of 33 keV internal conversion electron and 44 keV characteristics X-ray were clearly observed. Figure 3 shows neutron imaging of a character of “kita” made of cadmium plate. Although there was not high uniformity of scintillator, fine image was obtained successfully. Detection efficiency of 70% was confirmed by comparison between a Li glass scintillator. As future work, a uniform GPS scintillator plate should be developed for higher spatial resolution in neutron imaging.

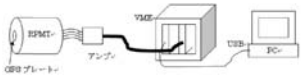


Figure 1 Schematic drawing of the detection system

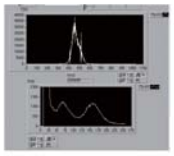


Figure 2 An example of pulse height distribution from a charge sensitive preamplifier



Figure 3 A neutron imaging of a character of gkitah made of cadmium plate

Fig. 1.

1-8-9

Performance Test of Neutron Detector for Engineering Diffractometer in J-PARC

K. Sakasai, T. Nakamura, S. Harjo, A. Moriai, M. Katagiri,
K. Soyama, S. Satoh[1], E. Shooneveld[2], and N. Rhodes[2]

J-PARC Center, JAEA, Tokai, Ibaraki 319-1195
[1]*Institute of Materials Structure Science, KEK,Tsukuba, 305-0801*
[2]*ISIS Science Diffraction and Muon Division, RAL, Didcot, OX11 0QX, UK*

A prototype linear scintillation neutron detector originally developed in RAL was fabricated for the engineering diffractometer in J-PARC. In this paper, some results of the performance test of the detector is described.

The fabricated detector was designed to have a small detection pixel with a spatial resolution of 3 mm. The detector had 120 pixels to establish a large neutron sensitive area. Scattered neutrons were detected based on a nuclear reaction of ^{6}Li(n,α) in ZnS/LiF scintillators in the pixel. Incident neutron position was determined by a $_2C_n$ coding method. The applied voltages of PMTs are individually set to have a gain of 3 x 10^7. The Si monochrometer was used for generation of 2.2 Å-neutrons. After comfirmation of fundamental performances such as output linearity, demonstration experiments for neutron diffraction were carried out. In the experiment, a two-phase iron sample that has both α-Fe and γ-Fe phases was used. Nickel powder and silicon powder were also used as reference sample.

Figure 1 shows neutron diffraction pattern of the two-phase sample after calibration of scattering angle using results of nickel and silicon powders. After determination of each scattering angle in the figure by Gaussian fitting method, lattice spacings of α-Fe and γ-Fe in the sample were determined according to an equation of neutron scattering intensity $I_{hkl}(\theta)$:

$$I_{hkl}(\theta) = K \cdot J \cdot A(\theta,\lambda)L(\theta)|F_{hkl}|^2,$$

where K is constant that is dependent on the experimental configuration, J is a multiplicity factor, $A(\theta,\lambda)$is an absorption factor, $L(\theta)$ is a Lorentz factor, and F_{hkl} is a structure factor. Table 1 summarizes the results. The estimated lattice spacings agreed very well to the values by Harjo et al. [1)]

In summary, the lattice spacing of a sample was well determined. New detectors that meet the actual requirements, e.g., a sensitive area of 196 mm × 1,000 mm and the secondary flight path of 2.0 m, are now under construction for first commissioning in 2008.

References

1) S. Harjo et al. :"Residual Thermal Phase Stresses in α-γ Fe-Cr-Ni Alloys Measured by a Neutron Diffraction Time-of-Flight Method", Mat. Trans., 43, 1696(2002).

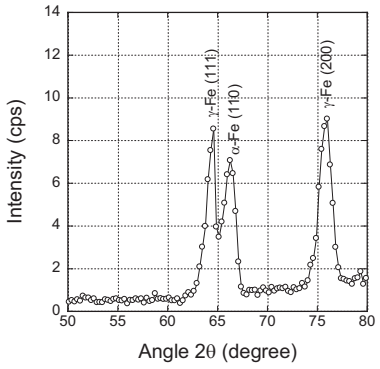


Figure 1: Neutron diffraction pattern of the two-phase sample.

Table 1: Estimated lattice spacing (Å)

Phase	This work	Harjo et al.	Diff.(%)
γ-Fe	3.593	3.59464	-0.05324
α-Fe	2.860	2.87084	-0.39245

原子炉：JRR-3　　装置：MUSASI(T2-3)　　分野：中性子散乱（装置）

1-8-10

Development of ^{3}He PSDs and Related Electronics for New Spectrometers in J-PARC

K. Nakajima[1], T. Yokoo[1,2], S. Satoh[1,2], K. Shibata[1], N. Takahashi[1], R. Kajimoto[1], T. Nakatani[1], Y. Inamura[1], N. Kaneko[1,2], Y. Yasu[3], K. Nakayoshi[3], E. Inoue[3], H. Sendai[3] and M. Arai[1]

[1]*Neutron Science Section, MLF Division, J-PARC Center*
[2]*Institute of Materials Structure Science, High Energy Accelerator Research Organization (KEK)*
[3]*Institute of Particle and Nuclear Studies, High Energy Accelerator Research Organization (KEK)*

Various novel types of ^{3}He position sensitive detectors (PSDs) and related data acquisition electronics (DAQ) including software, which are planed to be used at new spectrometers in J-PARC, have been tested at MUSASI port. Since the detector is one of the most important key components, it is indispensable to evaluate the feasibility and the performance of these new detectors and related electronics prior to actual construction of the instruments. We have continued these efforts from the beginning of our development work for J-PARC spectrometers and, in JFY2007, mainly following items have been subjected to be studied. 1. Performance and feasibility studies of U-type detectors. 2. Evaluation test of a new DAQ system using NEUNET. 3. Characterization studies of PSDs. U-type detectors are sequentially coupled detectors. Since the connector is shared by 2 pieces, we can reduce the installing space. Such type of detectors will be employed at Biomolecular Dynamics Spectrometer, DNA planned for J-PARC. We have tested several detectors from different benders and have obtained enough performance at the final moment. NEUNET is a new data processing module for ^{3}He PSDs. This module equips SiTCP developed by the University of Tokyo and can do high through put processing using Ethernet. Practical trials were performed at MUSASI port, and the expected performance has been proven. These modules have been already installed at several spectrometers in J-PARC. We have also carried out characterization studies of PSDs to obtain data which are necessary in operating existing PSDs and designing future purchasing detectors.

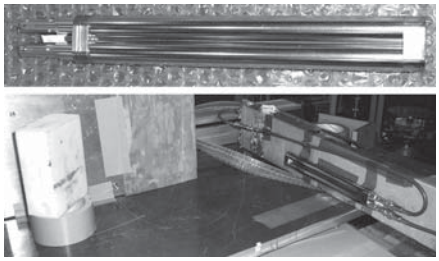


Figure 1: A prototype nunchakus-type detector (upper panel) and fully illuminated test setup, at which full part of the detector was illuminated by neutrons scattered at a polyethylene block (lower panel).

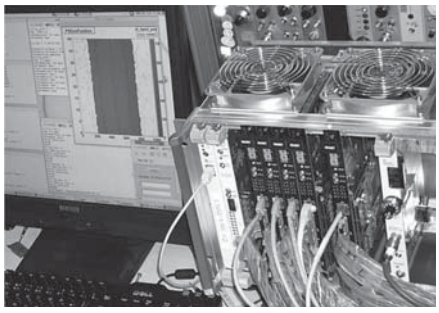


Figure 2: A DAQ system with NEUNET modules (5 black boards on the VME chassis) under the evaluation test at MUSASI port.

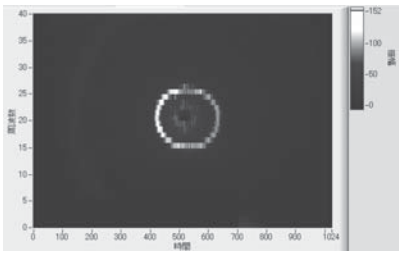


Figure 3: Obtained diffraction pattern from powder Si by using prototype DAQ system with NEUNET.

原子炉：JRR-3　　装置：MUSASI(T2-3)　　分野：中性子散乱（装置）

1-8-11

Development of Asymmetric Reflection-type Germanium Monochromator for Beam Flux Enhancement on HRPD

H. Yamauchi, Y. Ishii[1], N. Igawa, H. Fukazawa and W. Utsumi

Quantum Beam Science Directorate, Japan Atomic Energy Agency, Tokai, Ibaraki 319-1195
[1]*Radiation Application Development Association, Tokai, Ibaraki 319-1106*

The angle-dispersive neutron diffractometer, HRPD, installed at the research reactor JRR-3 in Japan Atomic Energy Agency can provide high resolution powder diffraction data that meet the many users' needs until recently. On the other hand, the demand of high efficiency and high intensity in measurements is growing in late years. However, HRPD is not suitable for high intensity measurements because fine Soller slit-type collimators are placed in front of each of the 64 detectors and fixed in an angular divergence of 6′, so that users cannot easily choose the appropriate resolution for high efficient measurements. In order to improve the source intensity of the monochromatic neutron beam, the authors tried to develop asymmetric reflection-type monochromators using mosaic germanium crystals.

According to theoretical considerations, the asymmetric reflection in compression geometry has an effect on spatial condensation of the neutron beam, which leads to the enhancement of the flux density per unit area. We used germanium single crystals as neutron monochromators, introducing the crystal mosaic of 20′ in the horizontal direction by hot pressing method. The mosaic crystals were cut at an angle of $\beta = 40°$ relative to the Ge(3 3 1) reflecting planes. Mosaicity check and assembling of all mosaic crystals were performed on TAS-2 and MUSASI-H.

Figure 1 shows the diffraction patterns of a standard powder sample (NIST 640c Si) measured by the new monochromator and existing symmetric type one. The diffraction results reveal that peak intensities by the asymmetric reflection-type monochromator are improved 1.2 times larger than those by the existing symmetric type one, but integrated intensities are almost comparable each other. For mosaic crystals, asymmetric reflections in compression geometry surely intensify the current density, but reflectivity is always less than that in symmetric reflections, and thus the suppression of the reflectivity just cancels out the enhancement of the current density [1,2]. This is the reason why the asymmetric reflection has no practical effect on the beam enhancement. In addition, it is reported that bent crystals behave quite differently from mosaic crystals and show an effective gain in the neutron current density [2].

References

1) S. A. Werner *et al.*, Phys. Rev. 140, A675 (1965).
2) G. Albertini *et al.*, Acta Cryst. A 33, 360 (1977).

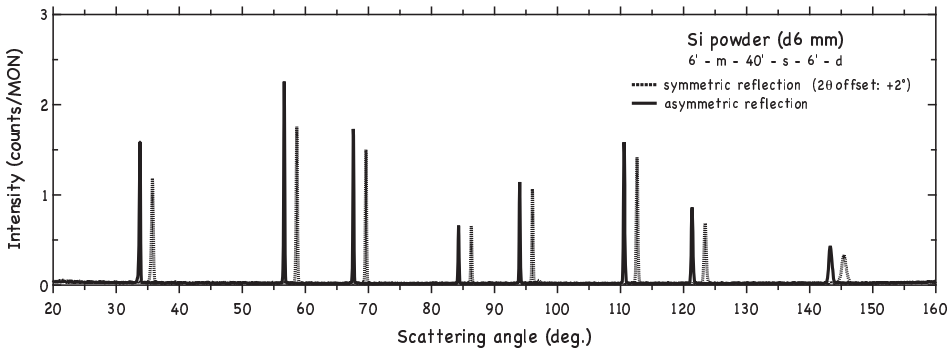


Figure 1: Diffraction patterns measured by the new monochromator and existing symmetric type one.

原子炉：JRR-3　　装置：TAS-2(T2-4)　　分野：中性子散乱（装置）

1-8-12

Development of High Quality Neutron Mirrors with Upgrading Compact Cold Neutron Bender System II

I. Tamura, R. Maruyama[1], D. Yamazaki[1], K. Yamamoto, K. Nakamura and K. Soyama[1]

Nuclear Science Research Institute, JAEA, Tokai, Ibaraki 319-1195
[1]J-PARC Center, JAEA, Tokai, Ibaraki 319-1195

The compact cold neutron bender system has been installed in JRR-3 beam hall to increase the number of beam ports with white neutron beam. A transportation efficiency of the compact cold neutron bender system was upgraded by using newly developed neutron mirrors within the last couple of years. We fabricated new high quality Ni/Ti multilayer double sided neutron supermirrors with m=3 on silicon substrates in this year. These supermirrors was employed the ion beam sputtering technique. Large and thin silicon substrates whose size 40mm in width x 160 mm in length and 0.2 mm in thickness were selected in order to improve the accuracy of installation position. The neutron mirrors were installed in the bender as curved neutron guides.

We report the neutron reflectivity of mirrors with the silicon substrates using cold neutron bender system.

The measurements of neutron reflectivity of newly produced neutron mirror have been carried out at SUIREN[1)] at JRR-3 in the Japan Atomic Energy Agency. The incident neutron wavelength was 3.93Å.

Neutron reflectivities of Ni/Ti supermirror on the both side of the silicon substrate are shown in figure 1 and figure 2. Figure 1 shows the neutron reflectivity of Ni/Ti supermirror on one side of the silicon substrate and figure 2 shows the neutron reflectivity on the other side of the same substrate. The reflectivities at the effective critical momentum transfer were almost 0.9. The performances of the reflectivities of mirrors on one side of substrate are almost same as that of the other side.

We succeeded in the manufacturing of the high reflectivity Ni/Ti multilayer neutron supermirrors with m=3 on both surfaces of the large and thin silicon substrate.

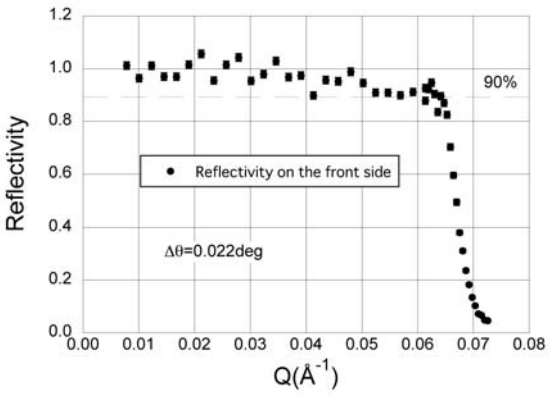


Figure 1: Neutron reflectivity on a front side of Ni/Ti multilayer supermirror carried out at SUIREN.

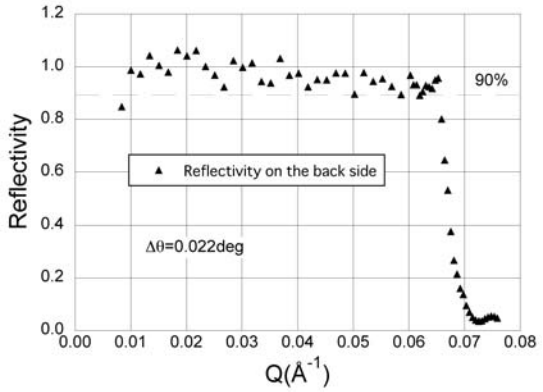


Figure 2: Neutron reflectivity on a back side of Ni/Ti multilayer supermirror carried out at SUIREN.

References

1) D. Yamazaki, et al. :"Development of a Neutron Reflectometer SUIREN at JRR-3", JAEA-Technology 2007-030 (2007).

原子炉：JRR-3　　装置：SUIREN(C2-2)　　分野：中性子散乱（装置）

1-8-13

Development of High Reflectivity Neutron Supermirror Using Ion Beam Sputtering Technique

R. Maruyama, D. Yamazaki, T. Ebisawa, and K. Soyama
J-PARC Center, JAEA, Tokai, Ibaraki 319-1195

The development of high-performance neutron supermirrors with high reflectivity and large m, where m is the ratio of the effective critical angle of the supermirror to that of natural nickel, is important in neutron experiments, since they lead to a considerable increase in available neutron intensity. We have developed neutron supermirrors using ion beam sputtering (IBS) since it enables the production of layers with high density and small grain size [1,2]. An IBS system with an effective deposition area of 2,000 cm^2 has been installed at JAEA to produce neutron guides, benders, and other optical devices based on supermirrors for the new spallation neutron source (Japan Proton Accelerator Research Complex, J-PARC). Ni/Ti supermirrors have been fabricated with large critical angles extending up to $m = 3$, 4, and 6.7 using the IBS system. The neutron reflectivity of the supermirrors at the critical angle is 0.82, 0.66, and 0.23, respectively [3,4].

Although supermirrors with large critical angle have been fabricated, the realization of higher reflectivity may be more important for neutron experiments. There is a technique of adding carbon atoms to the nickel layer to suppress interface roughness that leads to higher reflectivity [5]. We have also tested this technique and fabricated NiC/Ti supermirrors with $m = 3$ and 4. The measurement of neutron reflectivity was performed using the JRR-3/SUIREN reflectometer at JAEA. The incident average neutron wavelength was 0.39 nm with the resolution of 2.6% in the FWHM. The divergent angle of the neutron beam was less than 1 mrad. The reflectivity of those supermirrors at the critical angle was 0.88 and 0.82, respectively. The total number of layers was 403 and 1201, respectively. Test fabrication of the NiC/Ti supermirror with $m = 6$ was performed. The total number of layers was 6003. Although an anomalous reduction in the reflectivity was observed, the comparison of the measured reflectivity with that calculated demonstrated that a NiC/Ti supermirror with reflectivity of 0.40 at momentum transfer of 1.29 nm^{-1} ($m = 6$) can be fabricated with a higher-precision deposition rate. By adopting NiC/Ti multilayers instead of Ni/Ti multilayers, higher reflectivity has been realized [6]. We are therefore ready to contribute to the J-PARC project by providing neutron guides, benders, and other optical devices based on supermirrors.

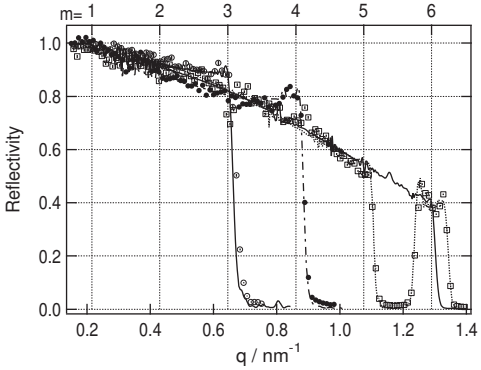


Figure 1: Reflectivity profiles of NiC/Ti supermirrors with $m = 3$, 4, and 6. Lines indicate the calculated reflectivity profiles.

References

1) K. Soyama, W. Ishikawa, and K. Murakami, "J. Phys. Chem. Solids" 60 1587(1999).
2) K. Soyama, H. Tsunoda, and K. Murakami, "Nucl. Instrum. Methods Phys. Res. A" 529 73(2004).
3) R. Maruyama, D. Yamazaki, T. Ebisawa, M. Hino, and K. Soyama, "Physica B" 385-386 1256(2006).
4) R. Maruyama, D. Yamazaki, T. Ebisawa, M. Hino, and K. Soyama, "Thin Solid Films" 515 5704(2007).
5) J. Wood, "SPIE" 1738 22(1992).
6) R. Maruyama, D. Yamazaki, T. Ebisawa, and K. Soyama, "Nucl. Instrm. Methods Phys. Res. A" in print.

原子炉：JRR-3　　装置：SUIREN(C2-2)　　分野：中性子散乱（装置）

1-8-14

Neutron Reflectometer SUIREN: Status and Developments in 2007

D. Yamazaki, M. Takeda[1], R. Maruyama, M. Hino[2] and K. Soyama

J-PARC Center, JAEA, Tokai-mura, Ibaraki 319-1195
[1]*Quantum Beam Science Directorate, JAEA, Tokai, Ibaraki 319-1195*
[2]*Research Reactor Institute, Kyoto University, Kumatori, Osaka 590-0494*

At neutron reflectometer SUIREN (C2-2), beam-line components has been developed for more effective measurements since the start of oparation in 2006. In 2007 following components were developed and installed:

- new higher-harmonics filters (polarizing/ unpolarizing)
- a polarization analyzer
- neutron spin flippers and guide magnets

The neutron wavelength have been changed into 3.928 Å due to the installation of the new higher-harmonics filters.

There are two higher-harmonics filters (a polarizing filter and unpolarizing one) both of which reflect only nominal wavelength 3.928 Å while higher-harmonics neutrons are transmitted and absorbed as shown in Fig. 1. The reflection angle of the 3.928Å neutrons is $\theta \simeq 1.57$deg, which corresponds to four times the critical reflection angle of pure nickel (denoted as m=4), for both filters.

Figure 1: Filtering of higher-harmonics with wideband multilayer filter.

The unpolarizing filter is a NiC/Ti supermirror coated on a float glass of 400 mm (L) × 100 mm (H) × 5 mm (T), and reflectivity is 0.77. Neutron intensity is 1.8×10^4 n/cm^2/s under collimation of $\Delta\theta = 0.08$ deg.

The polarizing filter and the polarization analyzer are Fe(Si)/Ge wideband-multilayer (m∼4, $\Delta d/d = 10\%$) coated on silicon wafers of 160 mm (L) × 60 mm (H) × 3 mm (T). Polarization is flipped by Mezei-type flippers and maintained with guide magnets which are composed of two parallel iron plates with four ferrite brace between them. Figure 2 shows measured polarization as a function of beam collimation. It can be seen that polarization

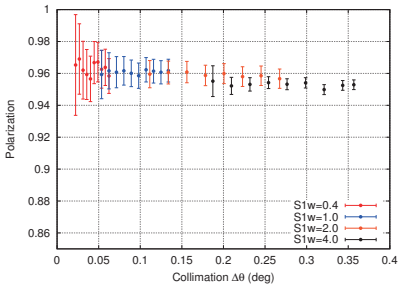


Figure 2: Polarization as a function of beam collimation.

is no less than 0.95 even for loose collimations. Neutron intensity is 7.6×10^4 n/cm^2/s under collimation of $\Delta\theta = 0.08$ deg. Resultant specifications of SUIREN are shown in Table 1.

Table 1: Specifications of SUIREN

λ	3.928 Å ($\Delta\lambda = 2.6\%$)
beam size	20 mm$^{\mathrm{W}}$ × 80 mm$^{\mathrm{H}}$
$I_{\mathrm{unpol.}}$	1.8×10^4 n/cm^2/s ($\Delta\theta = 0.08°$)
$I_{\mathrm{pol.}}$	7.6×10^3 n/cm^2/s ($\Delta\theta = 0.08°$)
P	> 0.95
backgound	4.5×10^{-3} n/s (shutter close)

SUIREN provided 67 days for the JAEA common-use program and the MEXT trial-use program and were used for measurement on samples including magnetic thin films and solid-liquid interfaces.

原子炉：JRR-3　　装置：SUIREN(C2-2)　　分野：中性子散乱（装置）

1-8-15

Upgrading Compact Cold Neutron Bender System II

I. Tamura, R. Maruyama[1], D. Yamazaki[1], K. Yamamoto, K. Nakamura,
K. Aizawa[1] and K. Soyama[1]

Nuclear Science Research Institute, JAEA, Tokai, Ibaraki 319-1195
[1]J-PARC Center, JAEA, Tokai, Ibaraki 319-1195

The compact cold neutron bender system was used to branch off a cold neutron beam from a straight neutron guide to create additional guide end positions. The bender has been installed in the C2 neutron guide at JRR-3 beam hall and the bender provides new white cold neutron beam ports

However, the intensity of divided neutron beams was too low to perform experiments effectively. Therefore, the neutron beam transportation efficiency of the cold neutron bender system was improved by using newly developed neutron mirrors.

Ni monolayer mirrors were replaced with Ni/Ti multilayer supermirror on the curved neutron guides section in the bender system before the JRR-3 operation in 2007.We report the measured spectrum at the end of C2-3-3 beam port using a chopper spectrometer.

The neutron chopper has a 1400mm diameter disk, which has a slit of 10 mm width.The disk of the neutron chopper operated with 5000rev/min rotation. A flight path length between the end of C2-3-3 beam port and the chopper was 1.7m and a length between the chopper and a detector was 1.3m.

The conversion factor from the time channel to the wavelength was calibrated on a dip in the spectrum, which formed by an upstream monochromator in the neutron guide.

Figure 1 shows measured neutron spectra at the end of C2-3-3 beam port by the time-of-flight method before and after upgrade. The characteristic wavelength of this beam port is 4.8 Å for after upgrade. The wavelength range of neutron beam was expanded and the intensity of neutron beam increased entire wavelength range. Measured neutron flux at C2-3-3 beam port was 1.6×10^{11}(n/m^{2}s) by the gold foil activation method. The neutron flux incresed by 10 times after upgrade.

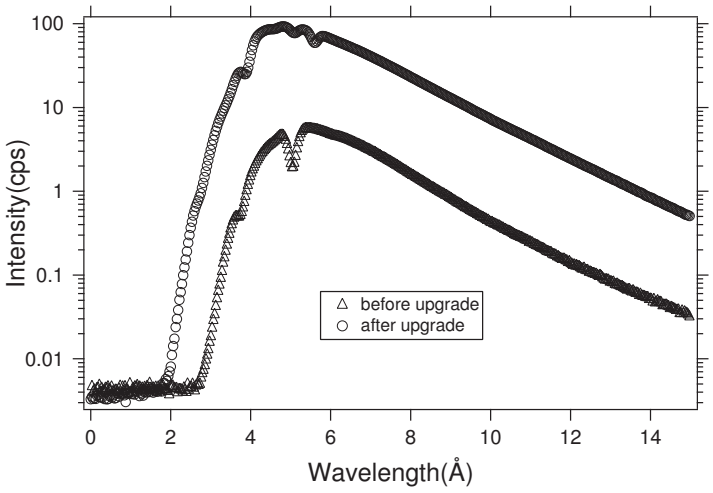


Figure 1: Neutron spectra measured at C2-3-3 beam port before and after upgrade.

原子炉：JRR-3　　装置：CHOP(C2-3-3)　　分野：中性子散乱（装置）

1-8-16

Neutron Detection by a MgB_2 Transition Edge sensor

S. Okayasu[1,2,5], M. Katagiri[1,5], K. Houjo[2,5], Y. Morii[1,5], S. Miki[3,5], H. Shimakage[3,5], Z. Wang[3,5] and T. Ishida[4,5]

[1] *Quantum Beam Science Directorate , JAEA, Tokai, Ibaraki 319-1195*
[2] *Advanced Science Research Center , JAEA, Tokai, Ibaraki 319-1195*
[3] *KansaiAdvanced Research Center, NICT, Kobe, Hyogo 651-2492*
[3] *Department of Physics and Electronics, Osaka Prefecture University, Sakai, Osaka 599-8531*
[3] *JST-CREST, 5 Sanbancho, Chiyoda, Tokyo 102-0075*

From the early stage of the discovery of a new superconducting material MgB_2 [1], we have been investigating for neutron detection with a MgB_2 transition edge sensor (TES) [2,3]. For the purpose, we developed a low noise detecting system for neutron, and confirmed the availability of the system by alpha ray from an americium-241 (^{241}Am) source [4]. Using the system, we have achieved the detection of a single neutron signal.

The ^{10}B atoms in MgB_2 have an extremely large cross section (3800 barns) with thermal neutrons to be expressed as ^{10}B (n, α)^{7}Li with yielding a large nuclear energy of 2.31MeV. The liberated energy destroys the superconducting state of MgB_2 locally, and a hot spot is generated in the sample. If the sample is kept on the superconducting transition edge, a sharp resistance change due to the hot spot can be observed.

Samples used in the detection experiments were fabricated by the Kansai group in NiCT. The sample preparations are described elsewhere [3,5]. The ^{10}B-rich MgB_2 samples (enriched 97% ^{10}B) were fabricated to increase the nuclear reaction.

A short meander line was used as shown in fig.1. A nuetron detected signal on the superconducting transition edge (Tc=26.3K) under constant current condition is also shown in fig.2. The detected pulse width is about 10^{-8}second indicating fast responding time of the sensor.

References

1) J. Nakamatsu, et al.:"Nature", 410, pp. 63 (2001).
2) K. Takahashi, et al.:"Physica C", 392-396, pp. 1501 (2003).
3) S. Miki, et al.:"Nucl. Instr. Meth. A", 529, pp. 405 (2004).
4) S. Okayasu, et al.:"Physica C", in press.
5) H. Shimakage, et al.:"Physica C", 392-396, pp. 1387 (2003).

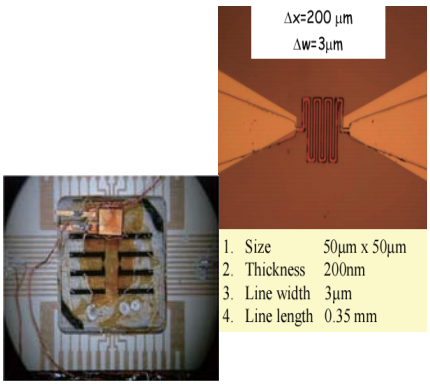


Figure 1: MgB_2 neutron detecting sensor

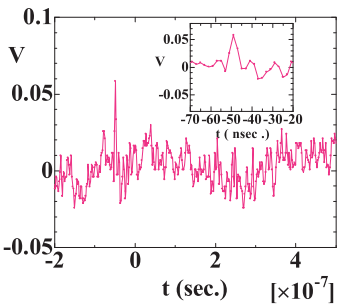


Figure 2: Example of a detecting neutron signal at 26.2K (I=-0.1mA).

原子炉：JRR-3　　装置：CHOP(C2-3-3)　　分野：中性子散乱（装置）

1-8-17

Application of a Magnetic Neutron Polarizing and Focusing Device to a Focusing-Geometry Small-Angle Polarized Neutron Scattering Instrument

T. Oku, T. Shinohara, T. Kikuchi, Y. Oba, H. Iwase[1], S. Koizumi[1], J. Suzuki

Quantum Beam Science Directorate, JAEA, Tokai, Ibaraki 319-1195
[1]*Advanced Science Research Center, JAEA, Tokai, Ibaraki 319-1195*

Quadrupole and sextupole magnets are considered to be ideal neutron-polarizing and polarized neutron-focusing devices, respectively, since no materials are required to be put on the beam axis so that the neutrons are free from neutron scattering and absorption by materials [1,2]. Therefore, we can construct an ideal focusing-geometry small-angle "polarized" neutron scattering instrument by utilizing the quadrupole magnet as a neutron polarizing device and the sextupole magnet as a neutron focusing device. In this study, we have installed the quadrupole magnet in the focusing geometry small-angle neutron scattering (FSANS) instrument SANS-J-II at JRR-3, in which the sextupole magnet has been already installed [3,4], and investigated the instrument's performance. By comparing the obtained results with those obtained with conventional magnetic super-mirror polarizers, we discuss the improvement of the performance.

The instrumental setup is shown in Fig.1. SANS-J-II is equipped with a magnetic neutron lens based on an extended Halbach-type permanent magnet together with magnetic Fe/Si supermirror polarizers P1 and P2 [3,4]. The polarization efficiencies of P1 and P2 are $\sim$ 0.96 and $\sim$ 0.99, respectively [3]. The quadrupole magnet is the Halbach-type permanent quadrupole magnet with an aperture size of 5 mm in diameter and a length of 600 mm. The magnetic field gradient $\partial |\mathbf{B}| / \partial r = 791.9 \pm 8.3$ Tm^{-1} is generated inside the magnet. In the aperture of the quadrupole magnet, positive polarity neutrons are confined around the magnet center axis, but negative polarity neutrons are accelerated away from the magnet center axis due to the magnetic field gradient. Therefore, a Cd slit with a 2 mm-ϕ pinhole (Slit2) is attached at the end of the magnet. Then only the positive polarity neutrons can pass through the quadrupole magnet aperture in this experimental condition. The neutrons are focused on the surface of the 2d-position-sensitive scintillation detector (2d-PSD) and the neutron intensity distributions are measured by the 2d-PSD.

Figs. 2 (a) and (b) show the radial distributions of the averaged intensity normalized by the measuring time and the peak-height intensities, I_{peak}, respectively. It is considered that the difference in the peak height of the intensity normalized by time is mainly caused by the difference in the neutron transmission property of the polarizing devices (Fig. 2(a)). Since P2 has a neutron transmission

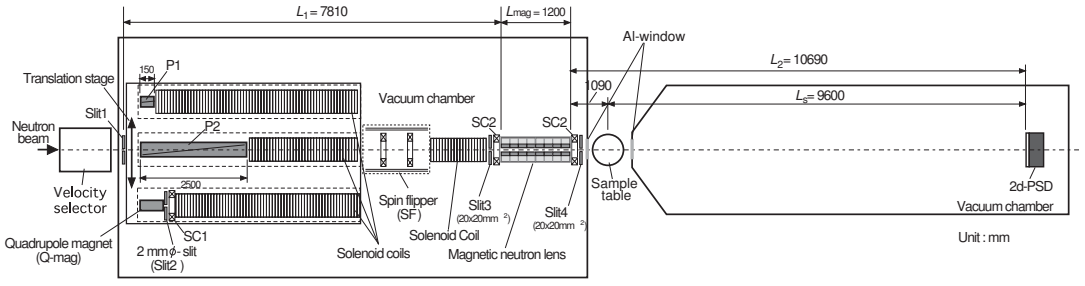


Figure 1: Experimental setup of SANS-J-II.

原子炉：JRR-3　　装置：NOP(C3-1-2-1)　　分野：中性子散乱（装置）

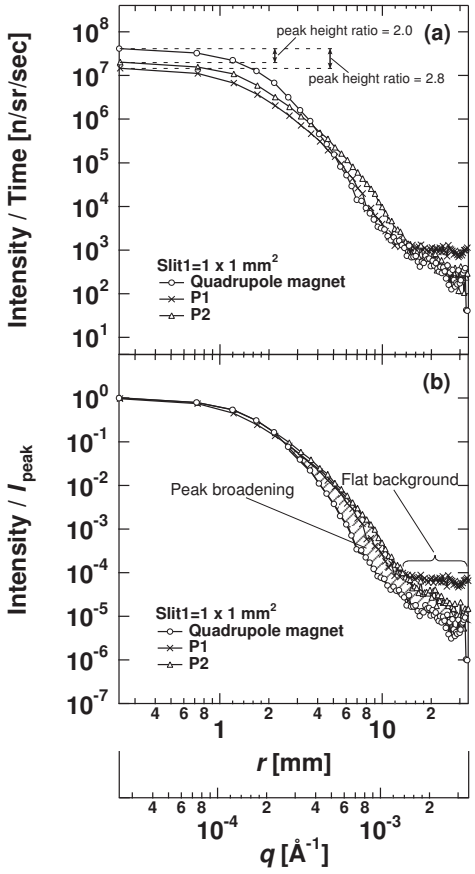


Figure 2: The radial averages of the intensity distributions. The intensities are normalized by (a) the measuring time and (b) the peak-height intensities $I_{\rm peak}$. r is the distance from the peak center.

$T_{\rm unpol} \sim 0.22$ for unpolarized neutrons with $\lambda = 6.5$Å [3], the neutron transmissions of the quadrupole magnet and P1 are estimated to be $T_{\rm unpol} \sim 0.44$ and $T_{\rm unpol} \sim 0.16$, respectively. Since the quadrupole magnet has very high polarization efficiency $P >\sim 0.99$ and includes no materials which absorb and scatter neutrons on the beam axis of the quadrupole magnet, such a higher neutron transmission can be obtained. In the case of using P1, a flat background intensity region was observed as indicated in Fig. 2 (b). This background intensity is created by the negative polarity neutrons, because they are defocused by the magnetic neutron lens and spread over the detector homogeneously. On the other hand, such a flat background region was not observed in the cases of using P2 and the quadrupole magnet with the higher polarizing efficiencies. In Fig. 2 (b), relatively large peak broadening of the intensity profiles was observed for P1 and P2 by comparing with the profile for the quadrupole magnet. The peak broadenings is considered to be the result of the neutron scattering from the mirror materials of the P1 and P2 and/or the neutron reflection on the Ni-side walls of the P2 [3]. As the results of this study, the excellent performance of the quadrupole magnet as the neutron-polarizing device based on its characteristics such as high neutron transmission and high polarization efficiency was demonstrated in the application to the FSANS instrument using the magnetic neutron lens. The weak aspect of the quadrupole magnet based polarizer is its small opening aperture, which is required to realize a sufficiently strong magnetic field gradient for the application. If the effective aperture of the quadrupole magnet is enlarged with keeping its polarizing power by employing an extended-Halbach circuit or a superconducting magnet, the performance of the FSANS instrument would be further improved and another kind of its application such as a highly efficient polarized-neutron transporting guide would be expected.

In summary, we conclude that the FSANS setup which is composed of the magnetic neutron lens and the neutron-polarizing device based on the quadrupole magnet is considered to be suit for small-angle polarized neutron scattering measurements with high angular resolution.

References

1) H.M. Shimizu, et al. :"NIM-A", 430, pp. 423-434 (1999).
2) T. Oku, et al. :"Physica B", 397, pp. 188-191 (2007).
3) T. Oku, et al. :"J. App 40, pp. s408-s413 (2007).
4) S. Koizumi, et al. : "J. Appl. Cryst.", 40, pp. s474-s479 (2007).

This is a blank page.

1. 中性子散乱 9)超伝導現象

1. Neutron Scattering 9)Superconductivity

This is a blank page.

1-9-1

Emergence of Magnetic Modulations in the Overdoped Phase of Bi2201 by Fe Doping

H. Hiraka, S. Wakimoto[1], M. Takeda[1], K. Kakurai[1], and K. Yamada[2]

IMR, Tohoku University, Sendai, Miyagi 980-8577
[1] *Quantum Beam Science Directorate, JAEA, Tokai, Ibaraki 319-1195*
[2] *AIMR(WPI), Tohoku University, Sendai, Miyagi 980-8577*

Inelastic neutron scattering studies revealed that the so-called "hourglass-like" magnetic-dispersion relation commonly exists in high-T_c cuprates [1–3], thus indicating the magnetic interaction as a prime candidate of pairing mechanism. However, no magnetic cross section has been ever reported in $Bi_2Sr_2CuO_{6+\delta}$ (Bi2201), which is one of the most typical cuprate superconductors. In order to resolve this puzzle, we grew large single crystals of Fe and Pb co-doped Bi2201 for neutron scattering experiments. The Fe atom is doped to enhance magnetic scattering, and the hole density of current Pb-doped samples was estimated to be $p \sim 0.25$ from T_c of as-grown crystals before Fe doping. Recently, by means of unpolarized neutron scattering, we discovered diffuse incommensurate peaks around (π, π) below $T_{neu} \sim 30$ K using a 9%-Fe doped single crystal. Unexpectedly, the incommensurability reaches to $\delta \sim 0.20$, which is much larger than that of magnetic modulations in La214 ($\delta^{max} \approx 0.13$) [4]. Further, the diffuse-peak width is very broad in the $(h, k, 0)_{ort}$ scattering plane, corresponding to a short correlation length of $1/\kappa < 10$ Å on the CuO_2 plane. Prior to further inspection, it is required to confirm its origin of this intriguing cross section at first.

Polarized neutron experiments were carried out on the TAS-1 at JRR-3 using the same 9%-Fe doped single crystal. A Heusler monochromator and an analyzer were used to generate spin polarized neutrons with energy of 14.7 meV. The plate-like sample with $5\times2\times30$ mm^3 in size was set to scan in the $(h, k, 0)_{ort}$ scattering plane. Figure 1 shows polarized neutron data under a spin-flip mode with horizontal field parallel to the scattering vector. The low-temperature **Q** spectrum at 3 K proves that the incommensurate cross section is magnetic in origin. This consequence is also supported by the disappearance at high temperature ($> T_{neu}$). The emergence of the incommensurate-peak pattern strongly suggests incommensurate magnetic correlations underlying in the Cu spin system. Now, we started searching for the "hourglass-like" magnetic excitations by unpolarized neutron scattering.

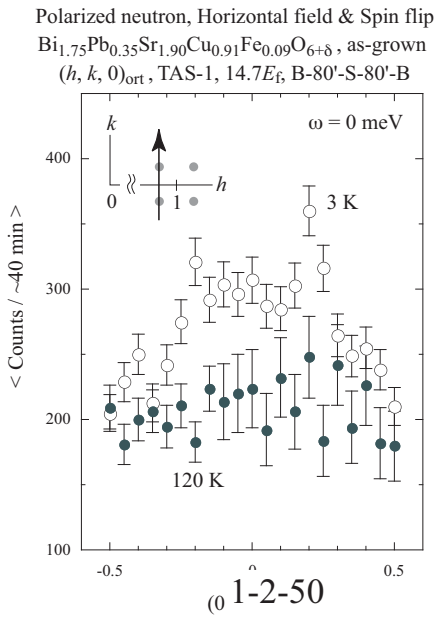


Figure 1: Polarized neutron data under the spin-flip mode with horizontal field of 10 Oe. The inset shows the scan trajectory through incommensurate peaks.

References

1) J.M. Tranquada *et al.*, Nature **429**, 524 (2004).
2) C. Stock *et al.*, Phys. Rev. B **71**, 024522 (2005).
3) B. Fauque *et al.*, Phys. Rev. B **76**, 214512 (2007).
4) K. Yamada *et al.*, Phys. Rev. B **57**, 6165 (1998).

原子炉：JRR-3　　装置：TAS-1(2G)　　分野：中性子散乱（超伝導）

1-9-2

Peculiar Field Response of Antiferromagnetism in non-centrosymmetric heavy fermion superconductor $CePt_3Si$

K. Kaneko[1], N. Metoki[1], T. Takeuchi[2], T.D. Matsuda[1], Y. Haga[1],R. Settai[3], Y. Ōnuki[1,3]

[1]*Advanced Science Research Center, Japan Atomic Energy Agency, Tokai, Naka, Ibaraki 319-1195*
[2]*Low Temperature Center, Osaka University, Toyonaka 560-0043*
[3]*Graduate School of Science, Osaka University, Toyonaka 560-0043*

Non-centrosymmetric heavy fermion superconductor $CePt_3Si$ attracts a surge of interest since novel superconducting properties are expected under a of inversion symmetry in a crystal structure[1]. $CePt_3Si$ exhibits an antiferromagnetic (AFM) transition at T_N=2.2 K, which is followed by a superconducting transition at T_{sc}∼0.45 K. In addition to the lack of inversion symmetry, the characteristics of the superconductivity in $CePt_3Si$ are its coexistence with the long range AFM order[2]. We clarified that the AFM order in $CePt_3Si$ is commensurate with $\boldsymbol{q}$=(0 0 1/2) in which reduced magnetic moment of 0.17 μ_B orients parallel to ⟨100⟩[2]. The AFM reflection does not exhibit an anomaly on passing through T_{sc} and persists down to the lowest temperature. In contrast to the temperature variation, AFM reflection intensity shows a peculiar response against external magnetic field; the intensity of AFM reflection is enhanced with applying fields, especially for $\boldsymbol{H}\|[0\,0\,1]$[3]. This response is opposite to an usual antiferromagnet. Since these measurements have been carried out only down to 1.5 K so far, we tried to extend the scan range to lower temperature in the present study.

Three single crystalline samples of $CePt_3Si$ with the total mass of 2 grams were assembled within 1 degree and used for the present study. Neutron diffraction experiments were carried out on the cold triple-axis spectrometer LTAS installed in the guide hall. A incident wavevector of 1.5 $Å^{-1}$ was employed, and the cooled Be filter was put on k_i in order to remove the higher order contamination. Horizontal field magnet was used together with the hand-made dilution insert.

Figure 1 shows the 0 0 1/2 reflection intensity at 0.56 K as a function of external magnetic field applied for $\boldsymbol{H}\|[0\,0\,1]$. The AFM intensity shows strong enhancement with applying fields at 0.56 K well below T_N. The intensity at 5 T becomes 4 times stronger than that at zero field and keeps increasing even around 5 T. This indicates that the AFM ordered moment becomes double at 5 T. Furthermore, the field dependence of intensity shows an inflection point around 4 T, which matches the reported additional boundary in the H-T phase diagram[4]. The origin of both the AFM moment enhancement and the additional phase boundary are unclear at present. Inelastic scattering experiments under fields are in progress in order to clarify these phenomena.

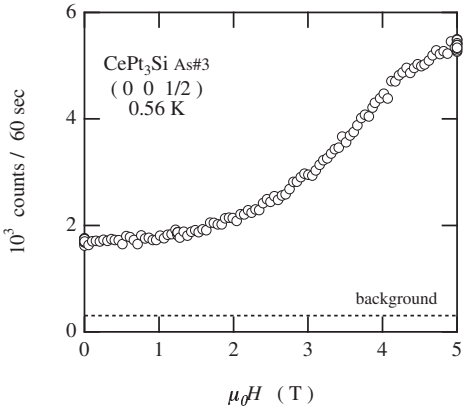


Figure 1: The 0 0 1/2 antiferromagnetic reflection intensity of $CePt_3Si$ at 0.56 K as a function of external magnetic field for $\boldsymbol{H}\|[0\,0\,1]$.

References

1) E. Bauer *et al.*, Phys. Rev. Lett. **92**, 027003 (2004).
2) N. Metoki *et al.*, J. Phys.: Condens. Matter **16**, L207 (2004).
3) K. Kaneko *et al.*, J. Phys. Soc. Jpn. **75**, Suppl. pp. 177 (2006).
4) T. Takeuchi *et al.*, J. Phys. Soc. Jpn., **76**, 014702 (2007).

原子炉：JRR-3　　装置：LTAS(C2-1)　　分野：中性子散乱（超伝導）

1. 中性子散乱 10）残留応力

1. Neutron Scattering 10）Residual Stress

This is a blank page.

1-10-1

Strain Evaluation of Rebar in Reinforced Concrete Using Neutron Diffraction

M. Kanematsu, T. Noguchi[1], M. Yasuda[2] and H. Suzuki[3]

Department of Architecture, Tokyo University of Science, Noda, Chiba 278-8510
[1]*Department of Architecture, University of Tokyo, Hongo, Bunkyo-ku, Tokyo 113-8656*
[2]*Toyo Construction Co., Ltd, Miura, Ibaraki 300-0424*
[3]*Quantum Beam Science Directorate, JAEA, Tokai, Ibaraki 319-1195*

Reinforced concrete is known as the composite material of concrete and rebar, so that the stress balance between rebar and concrete is affected by the bond condition between them. Therefore, it is very important to know the strain distribution on the rebar in the reinforced concrete in order to evaluate the bond condition. In this study, we applied neutron diffraction technique to measure the strain distribution on the rebar in the reinforced concrete.

At first, lattice strains of ferrite 110 reflection on the rebar was measured during uniaxial tensile loading in order to verify accuracy of the strain measurement of the rebar covered by concrete. Lattice strains were measured on the rebar with diameter of 18mm passed through the hole with diameter of 20mm machined in the rectangular concrete structure with the size of $a \times a \times 150$mm (a=50mm and 70mm). Figure 1 shows the result of change in diffraction angle with respect to the applied stresses. Average diffraction angles at some positions on the rebar were plotted in this figure. Diffraction angles were plotted near the same line as that of rebar without concrete regardless of sample conditions. Therefore, it was confirmed that effects of concrete conditions i.e., sample size and water content, on accuracy of strain measurement on the rebar were negligible.

Secondly, strain distributions on the rebar in the reinforced concrete were measured around cracks during tensile loading. Figure 2 shows the strain distributions on the rebar around cracks under applied stresses of approximately 150MPa and 300MPa as well as stress-free condition. Compressive residual strain can be observed in stress-free condition due to drying shrinkage. Strains transferred to the rebar were 60% to 80% of applied strains because of stress share with concrete. Moreover, scattering around cracks were observed due to stress relaxation around cracks and also due to stress concentration around rib. These results indicate that neutron diffraction technique probably enables to measure detailed strain distribution and to evaluate the damage region around cracks accurately.

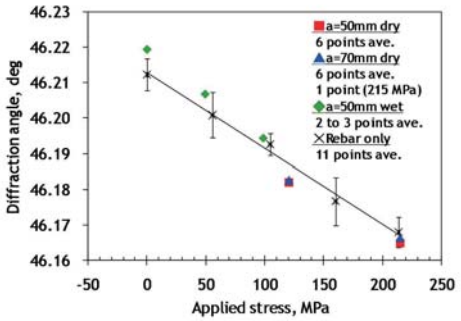


Figure 1: Changes in diffraction angle with respect to applied stress in each concrete sample and rebar only.

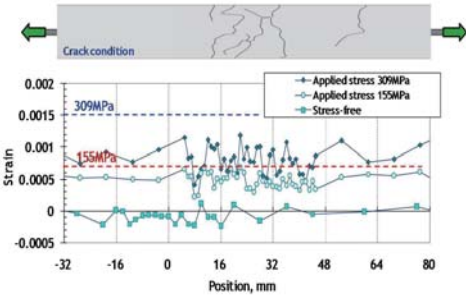


Figure 2: Strain distributions on the rebar around cracks in the reinforced concrete under tensile loading.

原子炉：JRR-3　　装置：RESA(T2-1)　　分野：中性子散乱（残留応力）

1-10-2

Residual Stress and Deformation Behavior on $Zr_{55}Al_{10}Ni_5Cu_{30}$ Bulk Metallic Glass Containing ZrC Particles

H. Suzuki, J. Saida[1] and M. Imafuku[2]

Quantum Beam Science Directorate, JAEA, Tokai, Ibaraki 319-1195
[1] *Center for Interdisciplinary Research, Tohoku University, Sendai 980-8578*
[2] *Materials Characterization Center, NSTR, Futtsu, Chiba 293-0011*

It has been developed that bulk metallic glasses containing hard particles or fibers exhibit higher strength and higher compressive plasticity as compared with monolithic bulk metallic glasses [1)]. In order to clarify the mechanism of these unique behavior, residual stress and deformation behavior of $Zr_{55}Al_{10}Ni_5Cu_{30}$ bulk metallic glass containing 10vol%ZrC particles (10%ZrC-BMG) were evaluated using neutron diffraction technique.

RESA diffractometer was utilized in this study. At first, residual stress and deformation behavior of ZrC particles, which are crystalline phase, were evaluated using neutron diffraction, and then, those of the metallic glass matrix were predicted by the composite law in assumption of stress balance between each phase.

Residual stresses in the ZrC phase and the metallic glass matrix were hydrostatic conditions of approximately 1.0GPa in compression and approximately 100MPa in tension, respectively. This relationship of residual stresses between each phase to develop during cooling could be explained by mismatch of the thermal expansion coefficients between each phase.

Figure 1 shows the elastic deformation behavior under uniaxial tensile loading. Linear response in both phases can be observed in this figure, and the deformation behaviors of each phase agreed well with those calculated by the Self-Consistent model. Figure 2 shows the compressive deformation behaviors of each phase up to 2.2GPa predicted by the Self-Consistent model with consideration of the residual stresses in each phase. Phase stress of the metallic glass matrix at 2.0GPa of applied stress, which is compressive fracture strength on the 10vol%ZrC-BMG, reached 1785MPa in compression which is close to the compressive strength, approximately 1.8GPa [1)], of the monolithic $Zr_{55}Al_{10}Ni_5Cu_{30}$ bulk metallic glass. This is probably one of the reasons why the compressive strength of the bulk metallic glass reinforced by hard particles is higher than that of the monolithic bulk metallic glass.

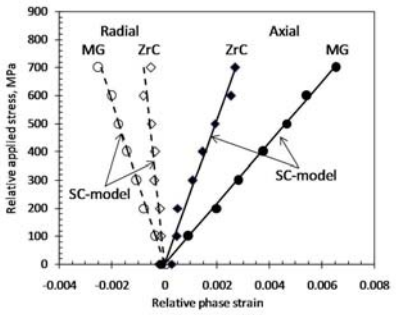


Figure 1: Elastic deformation behaviors of each phase under uniaxial tensile loading.

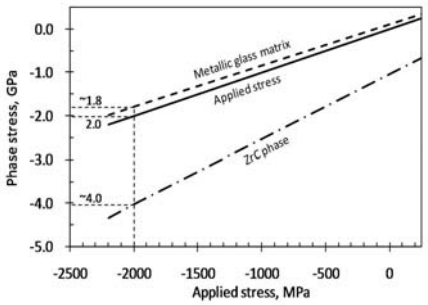


Figure 2: Compressive deformation behaviors predicted by the Self-Consistent model.

References

1) H. Kato et al, Scripta Mater., 43, 503(2000).

原子炉：JRR-3　　装置：RESA(T2-1)　　分野：中性子散乱（残留応力）

1-10-3

Bulky Measurement of Gradient Texture of an IF Steel by Neutron Diffraction

P.G. Xu, Y. Tomota, H. Suzuki[1] and S. Machiya[1]

Graduate School of Science and Engineering, Ibaraki University, Hitachi, Ibaraki, 316-8511
[1] *Quantum Beam Science Directorate, JAEA, Tokai, Ibaraki 319-1195*

1. Introduction

As one of the factors influencing on the mechanical/physical properties of steels, texture is usually measured by X-ray diffraction. The texture is heterogeneous so that bulky texture is determined by a serial sectioning method etc., but there is a limitation of accuracy. Because neutron penetrates a bulk sample and hence it is hopeful to determine the bulky average in a gradient textured material. In this study, 110, 200 and 211 pole figures of an interstitial-free (IF) steel were measured by neutron diffraction with an angular dispersion method.

2. Experimental Procedures

A 0.68mm-thick annealed IF steel containing 0.0018C-0.01Si-0.17Mn-0.013P-0.006S-0.01Cu- 0.01Ni-0.02Cr-0.003V-0.03Ti-0.026Nb-0.033Alsolute-0.0014Ntotal (mass%) was used. The 15×15mm sheets were stacked up to be a cubic sample with the consistent rolling direction and the edges of the sheets were adhered with a small amount of glue. The 110, 200 and 211 pole figures were measured with a neutron diffractometer, RESA, at JAEA with a neutron wavelength of 0.18nm, a 5mm×5mm slit for incident beam and a 5mm collimator before PSD.

3. Results and Discussion

Figure 1 shows the orientation mapping obtained by EBSD. As seen, microstructure changes through the sheet thickness. Perfect pole figures were obtained by neutron diffraction and crystal orientation distribution function (ODF) was calculated as shown in Fig. 2. Compared with the X-ray textures and the EBSD orientation mappings, the Gaussian integrated intensity obtained from each neutron diffraction profile can evaluate the bulk texture with a high accuracy.

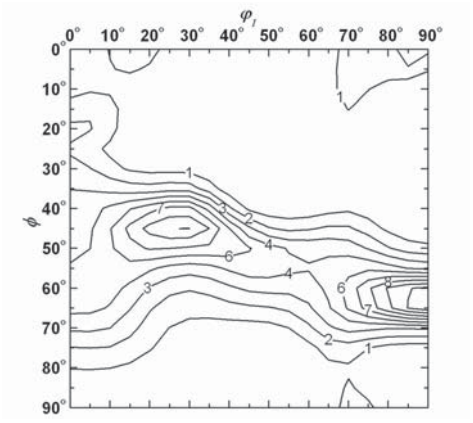


Figure 2: ODF determined by neutron diffraction.

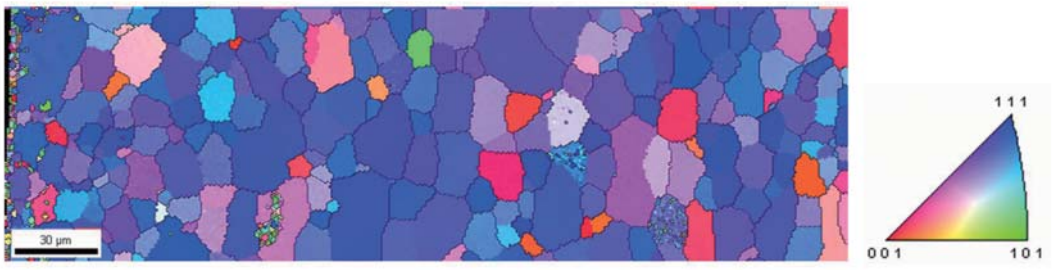


Figure 1: Crystal orientation mapping obtained by EBSD through the thickness direction (surface (left) to center).

原子炉：JRR-3　　装置：RESA(T2-1)　　分野：中性子散乱（残留応力）

1-10-4

Engineering diffractometer "RESA" and "RESA-II"

H. Suzuki, T. Saito, S. Machiya, Y. Tsuchiya, A. Moriai, Y. Shimojo, K. Akita and Y. Morii
Quantum Beam Science Directorate, JAEA, Tokai, Ibaraki 319-1195

Recently, the industrial users are interested in using the neutron stress measurement for ensuring the reliability of mechanical components, and the number of such users is rapidly increasing each year. As a result of that, measurement efficiency had to be improved by modifying the RESA diffractometer in order to satisfy many needs and the expectations from industrial users. Figure 1(a) shows the upgraded engineering diffratometer, RESA. Wavelength can be selected from approximately 0.16 nm to 0.21 nm by using asymmetrical bent crystal silicon monochromator. Large scale XYZ goniometer with the size of 1000 mm x 1000 mm top plate and the load capacity of 800 kgf was developed. Two axis diffractometer was replaced to low height type to get about 400 mm distance in maximum from beam height to top surface of the XYZ goniometer. The one-dimensional position sensitive detector (PSD) with 100 mm x 100 mm active area is installed for improving efficiency of the neutron detection, and the radial collimator system can be set before PSD to define the gauge volume (0.5 mm, 1.0 mm, 2.0 mm, 3.0 mm and 5.0 mm). These upgrades related to the detector will achieve single-digit measurement efficiency increase compared with RESA before upgrades. Sample oscillation function was added for allowing the stress measurement of large grain polycrystalline samples. These improvements of RESA would bring the further promotion of industrial use of neutron stress measurement.

As described above, the number of RESA users is rapidly increasing each year. Since there was only one diffratometer for engineering application, almost users could not get enough beam time to achieve their experiment. Therefore, the 2nd engineering diffratometer, called RESA-II, was installed at T2-3-2 beam port in the guide hall of the JRR-3, as shown in Fig. 1(b). Relatively small type diffractometer was installed on the steel board with the size of approximately 1500 mm x 2000 mm. PSD with 50 mm x 100 mm active area is utilized, and relationship of slits set before and after sample can define the gauge volume. Wavelength of RESA-II is fixed at approximately 0.21 nm. Small type of XYZ goniometer with the size of 300 mm x 300 mm top plate and load capacity of approximately 20 kgf can be installed, and the distance from beam height to top surface of the XYZ goniometer is approximately 245 mm in maximum. In addition, the quarter type Euler cradle can be installed. Operation of RESA-II is the same as that of RESA, so it is convenient for RESA users. Measurement efficiency is smaller than that of RESA, however, RESA-II can be sufficiently applied to not only residual stress measurement of small mechanical components but also microstructural analysis of deformed materials.

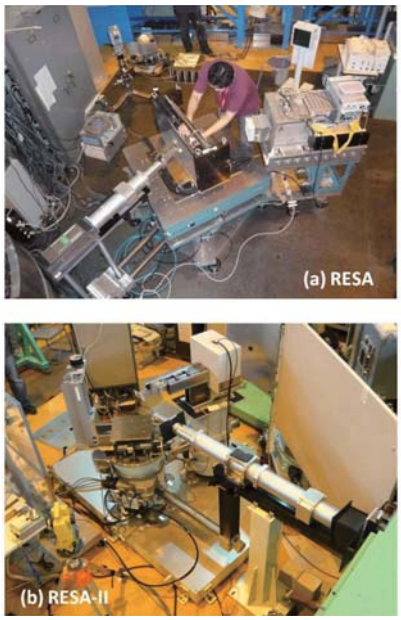


Figure 1: Upgraded RESA and 2nd engineering diffractometer RESA-II.

原子炉：JRR-3　　装置：RESA(T2-1), RESA-II(T2-3-2)　　分野：中性子散乱（残留応力）

2. 中性子ラジオグラフィ

2. Neutron Radiography

This is a blank page.

2-1

Fundamental Experiments for the Development of an Advanced Neutron Tomography

M. Kureta

Nuclear Science and Engineering Directorate, JAEA, Tokai, Ibaraki 319-1195

1. Introduction

Fundamental high-frame-rate neutron radiography and neutron tomography experiments were performed in order to develop the high-frame-rate (HFR) neutron tomography technique which is an advanced neutron visualization and measurement technique. Merit of the HFR neutron tomography techniques are one that neutron irradiation time becomes short, and second that its makes 4D visualization and measurement possible. The experiments were carried out in the TNRF of JRR-3.

2. Experimental Setup

High-frame-rate video camera with image intensifier system are used instead of the cooled CCD camera system. And the test object was rotated quickly on the turn table. Many kinds of test object were used for the development of the HFR neutron tomography technique such as a toy boat, bubbling water can, sandglass etc. Recording frame rate and rotating speed are changed as a test parameter. Neutron beam shutter is opened very short time compared with the CCD camera system such as 3 sec. There for, activation of the test object becomes very small. Nominal recording image size was 512x512 pixel, and the depth resolution was 10bit (1024 grayscale).

3. Experimental Results

Consecutive images of the neutron radiography were recorded while the test object is rotated. For example, 1000 consecutive and 360 degree revolved images are recorded when the 1000fps and 1rps while 1sec. If the test object was moved while the recording, we can observe the moving radiography image. After the recording, image processing method and visualization technique has been investigated based on the developed image data processing code NIPPON and visualization software JIPANG. Instantaneous 3D CT value distribution was successfully calculated.

4. Summary

For the development of an advanced neutron tomography technique, the HFR neutron tomography experiments has been carried out in the TNRF-2 of the JRR-3. Also, data processing code and visualization software are improved to correspond to the HFR neutron tomography. Consecutive instantaneous 3D CT value distribution could be calculated after the experiments. The development has been continued. At this moment, as this technique will be got a patent, detailed results will be opened after the patent is accepted.

原子炉：JRR-3　　装置：NRF(7R, C2-3-3-1)　　分野：中性子ラジオグラフィー（熱水力）

2-2

Development of an Ultra-High-Speed Scanning Neutron Tomography System for High-Quality and Four-Dimensional Visualizations

M. Kureta, H. Iikura[1]

Nuclear Science and Engineering Directorate, JAEA, Tokai, Ibaraki 319-1195
[1] *Quantum Beam Science Directorate, JAEA, Tokai, Ibaraki 319-1195*

A new neutron tomography imaging system was developed in order to realize a high-quality three-dimensional (3D) and four-dimensional (4D) visualizations by fusing high-frame-rate neutron radiography and computed tomography (CT) techniques. Fundamental idea (patent-JP2008-4247) is that the object is revolved with high rotating speed ranging from 0.1 to 10 rps and the neutron radiography images are recorded with a high-speed video camera and an image intensifier, and then the consecutive images are processed by 3D CT technique. When we need to visualize the time change of the 3D distribution, 3D CT data processing is continued on time axis in increments of more than one time step. Fundamental tests were carried out at the TNRF in the research reactor JRR-3 of JAEA to proof this new technique. Figure 1 shows an outside view of the 3D CT data (Fig. 1(a)) and the cut view (Fig. 1(b)). Object rotating speed for Fig. 1 condition was 1 rps, recording speed was 2,000 fps and projection number was 2,000 / 360 degree. We could get the fine 3D distribution of the CT values as shown in Fig. 1. 4D CT images of the sample (two sandglasses) were shown in Fig. 2. Object rotating speed was 0.25 rps, recording speed was 60 fps and projection number was 240 / 360 degree. These imaging conditions should be regulated depending on the research target. This new technique has also an advantage to reduce radio- activation of the object materials remarkably.

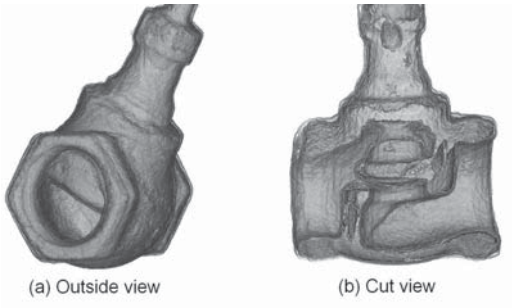


Figure 1: 3D-CT sample image (2,000 projection numbers; 2,000 fps; 1 revolution per second).



Figure 2: 4D-CT sample image (240 projection numbers; 60 fps; 0.25 revolution per second).

原子炉：JRR-3　　装置：NRF(7R, C2-3-3-1)　　分野：中性子ラジオグラフィー（原子炉用燃料・材料）

2-3

JRR-3M 熱中性子を利用した混相流の動態計測法の高度化-II

Development of Measurements for Multiphase Flow Dynamics -II
by Using Neutron Beam of JRR-3M

京都大学原子炉実験所 三島 嘉一郎

1. 研究目的

沸騰や凝縮を伴う混相流は、多くの動力プラント、化学プラントおよび空調・冷凍装置に関係し、これらの機器の最適設計を行う上で極めて重要である。近年、気液二相流や固液二相流に関して様々な数値解析手法が発達し、解析対象によっては精度の高い予測が可能となってきているが、高レイノルズ数流れや相変化を伴う混相流などについては必ずしも理解は十分ではなく、さらに検討を行う必要がある。

中性子ラジオグラフィはX線（あるいはγ線）ラジオグラフィと相補的な性質を有し、混相流計測に貴重な情報を提供する有力なツールの一つである。しかし、時間平均を対象としたボイド率計測やCT解析の技術はほぼ確立しているものの、混相流の動態計測法に至っては数多くの課題が残されている。

高速度で動態を計測する際の課題の一つは、画質の劣化である。これは中性子の計数誤差と撮像系のノイズに起因するが、もし中性子束の増大が望めないとすれば撮像系を改良するしか方法は残されていない。京都大学の研究グループでは、これまで高感度イメージ・インテンシファイアの光電面に中性子用蛍光コンバータと相性の良い半導体光電面（GaAsP）を選択し、高解像度高速度カメラと組み合わせることでノイズの低減を行ってきた [1]。しかし、蛍光コンバータを用いて高感度・高解像度を現在以上の高いレベルで両立させることは極めて困難であり、今後は撮像系の量子効率をさらに向上させるためには、中性子イメージ・インテンシファイアなどの開発が必要であろう [2,3]。

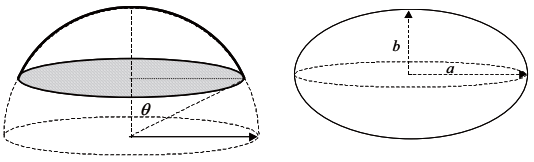
もう一つの課題としては、得られた画像から混相流の理解に対して有益な情報を抽出する計測処理手法を開発することである。これまでの共同利用では主に中性子ラジオグラフィ高速度撮像法とPIV(Particle Image Velocimetry)やPTV(Particle Tracking Velocimetry)を併用して、液体金属二相流の液相速度分布計測法を開発してきた [4]。しかしながら、これまでの体系は、急激な相変化を含む体系ではなかった。

今回の共同利用では、相変化を含む液体金属流を対象として実験を行い、得られた画像から熱流動研究に有用な物理量を算出することを目的とした。

2. 溶融金属中における液滴の直接接触蒸発現象

例えば、液体金属冷却高速増殖炉でシビアアクシデントが発生し、炉心が溶融した場合には燃料とスティールからなる沸騰プールが形成されることが予測されている。この場合、スティールの沸点が燃料の融点とほぼ等しいために、溶融燃料中で、構造材であるスティールが沸騰する。この沸騰二相流は液体と気体の密度比が通常の気液二相流と比較して1桁程度高く、高密度比の気液二相流を形成する。これまで、京都大学のグループではこの高密比気液二相流の特性を解明するために様々な実験を行ってきた。しかしながら、沸騰のソースとなるスティールの沸騰／蒸発現象には言及していない。本研究では、この高密度比体系における直接接触蒸発現象を対象として、溶融金属中－水の直接接触蒸発現象をとりあげた [5]。

加熱された溶融金属内に液滴を噴射させると、液滴は溶融金属内で蒸発しながら溶融金属中を上昇する。この場合、二相気泡の体積変化を中性子ラジオグラフィを用いて計測すれば蒸発速度が算出が可能である。次に界面における熱伝達率を特定するためには界面面積を求める必要があるが球形を仮定することで算出が可能である。したがって、本研究では、まず、球形を仮定して解析を行った。さらに、単一液滴を噴射させた場合には、通常の気液二相流と同様に水と蒸気からなる二相気泡は球形や楕円形、さらには笠状と変化する。多くの場合にはこれらの気泡形状は Fig.1 に示すように回転対称体となることが多く [5]、本研究では回転対称体を仮定して解析も行った。



Cap bubble　　Ellipsoidal bubble

Fig.1　Axial symmetrical bubble.

JRR-3M, TNRF-2,中性子ラジオグラフィを用いた構造解析

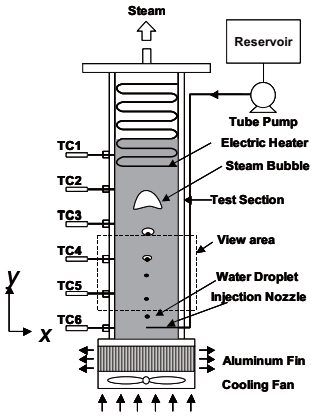


Fig.2 Schematic of Experimental Apparatus.

3. 実験装置及び実験方法

Fig.2 に実験装置の概略を示す。試験部はアルミニウム製矩形容器（高さ 600 mm、幅 100 mm、奥行き 20 mm）であり、試験部底部にはステンレス製液滴噴射ノズル（内径 0.5 mm）が設けられている。矩形容器上部には加熱用電気ヒータが取り付けてあり、試験部下部はアルミニウム製フィンおよび空冷ファンが取り付けられてある。容器上部を加熱、下部を冷却することにより、垂直方向に温度勾配を発生させ、安定な密度成層を実現することができる。流体としては、ニュートン合金（融点 95℃）および純水を用いた。 溶融金属の温度計測は、アルメル･クロメル熱電対により試験部底部から 2.5cm, 7.5cm, 10cm の 3 個所の位置で行った。液滴流量は、チューブポンプの回転数により調整した。実験は容器下部を約 100℃に保ち、Table1 に示すように液滴流量および容器の上部温度を変化させて行った。

Table 1 Experimental conditions

Run No.	TC1 [°C]	TC2 [°C]	TC3 [°C]	TC4 [°C]	TC5 [°C]	TC6 [°C]	Temperature Gradient $(\Delta T/\Delta z)_{ave}$ [K/m]	Comments
Run 4	104.4	105.8	106.2	106.1	103.7	100.1	25	Non boiling
Run 5	107.4	109.0	108.2	107.2	104.2	100.2	40	Non boiling
Run 6	111.2	111.7	110.3	107.5	103.9	100.0	64.5	Non boiling
Run 7	115.3	115.3	112.0	108.5	104.0	100.0	80.5	Boiling
Run 8	120.2	118.7	115.3	110.0	104.5	100.0	107.5	Boiling
Run 9	125.0	124.3	119.6	112.2	105.3	100.6	142.5	Boiling
Run 10	125.0	125.2	124.7	121.7	111.0	102.0	137	Boiling
Run 11	130.2	129.6	128.8	121.8	109.9	102.4	188.5	Boiling
Run 12	134.8	134.7	133.7	129.5	111.4	101.8	223	Boiling
Run 13	140.5	140.2	139.1	136.2	115.2	101.4	239	Boiling
Run 14	144.1	144.0	143.0	138.2	121.6	104.1	213.5	Boiling

4. 実験結果及び考察

Fig.3 に液滴の蒸発の様子を示す。撮像速度は毎秒 500 コマであるが、ここでは 80ms 毎の画像をならべている。画像中のほとんどを占める灰色の部分が溶融金属を示し、矢印の先端の黒い点は液滴を示す。Run4 は、上下の温度差が小さく、液滴は蒸発することなく溶融金属中を上昇する。しかし、Run11、Run13 に示すように上下の温度差が大きくなると直接接触

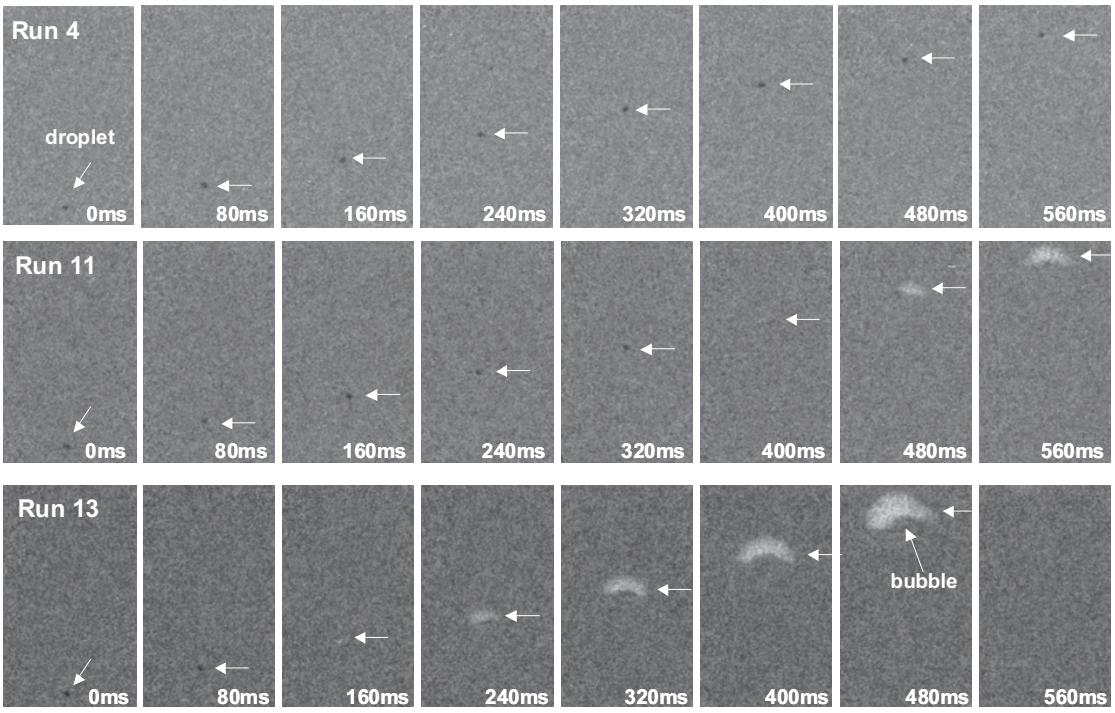


Fig.2 Water droplet evaporating in Newton's alloy taken by neutron radiography

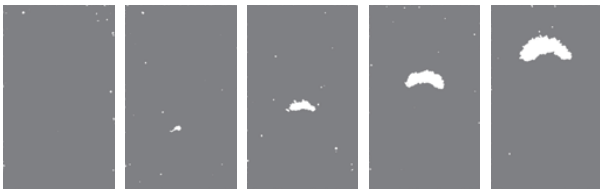


Fig.3 (a) Simple image binarization.

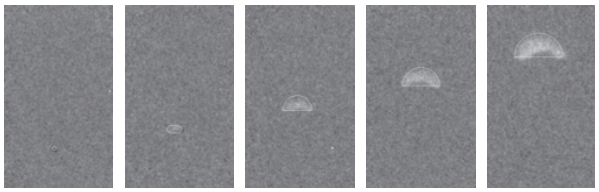


Fig.3 (b) Original image and calculated results.



Fig.3 (c) Calculated bubble shape.

Fig. 3. Consecutive bubble images.

熱伝達により液滴内で蒸発が起こり、二相気泡が生じていることがよくわかる。さらに画像から、二相気泡は楕円から笠状気泡に変化していることも明瞭に観察することができる。従来の報告 [6]では同じような体系で発生する二相気泡は縦長の気泡となることが報告されているがこれはノズル部における蒸気噴射による影響によるものと考えられる。

Fig.4 は画像処理による気泡形状の抽出結果を示す。Fig.4(a)は、二値化による画像処理である。この処理では、気泡の界面がノイズの影響を受けて滑らかではなく、二値化のための閾値も理論的に決定することが難しい。Fig.4(c)は回転対称を仮定した解析結果を、Fig.4(b)は現画像に Fig.4(c)で得られた気泡の輪郭を重ねて表示してある。これらの気泡形状の抽出結果からわかるように回転対称を仮定した計算結果は現画像の観察結果と良く一致することがわかる。また、この解析では二相気泡の体積をもとに気泡形状を算出するため、各時刻における体積は実験結果と同じである。抽出された気泡の高さおよび幅も良く一致していることから、本実験条件では二相気泡を回転対称体として仮定しても良いことが示唆された。

5. 結論

中性子ラジオグラフィを用いてより詳細な混相流研究を行うために、溶融金属中の液滴の直接接触蒸発現象を対象として実験を行い、発生した二相気泡の形状が回転対称体と仮定して気泡画像の抽出を行った。結果から、単なる二値化処理では界面はノイズの影響によりスムーズではなく、閾値の決定も難しいが、回転対称体を仮定した解析の場合には、各時刻で計測した体積を用いるために解析上、合理的に界面位置を決定することが可能であった。もちろん、この解析方法は回転対称が仮定できる条件にしか適用できないことに注意する必要がある。

今後の方針

これまで液滴の直接接触蒸発現象については、単一液滴を用いた実験を行ってきたが、今後はさらに現実的な問題として多数の液滴が蒸発する場合の実験を行う予定である。現在、当研究グループでは、共同利用研究の課題として「JRR-3M 熱中性子を利用した混相流の動態計測法の高度化-II」を行っているが、さらに継続して、今後も急激な相変化を伴う混相流の計測技術の開発を行いたいと考えている。

参考文献

[1] Y. Saito, K. Mishima, Y. Tobita, T. Suzuki, and M. Matsubayashi, Proc. 9th Int. Symposium on Flow Visualization, Edinburgh, U.K. 2000.

[2] W.B.Feller et al., "Gamma Insensitive Higly Borated Microchannel Plates for Neutron Imaging", Proc. 8th World Conference on Neutron Radiography, Gaithersburg, Maryland, USA. Oct.16-19. 2006.

[3] K.-I. Mochiki et al., "Neutron Color Image Intensifier", , Proc. 8th World Conference on Neutron Radiography, Gaithersburg, Maryland, USA. Oct.16-19. 2006.

[4] Y. Saito et al., "Application of High Frame Rate Neutron Radiography to Liquid-Metal Two-Phase Flow Research," Nucl. Instrum. Methods Phys. Res. A, vol.424, pp.229-234, 2005.

[5] Y. Saito et al., "Shape Measurement of Bubble in a Liquid-Metal", Proc. 6th Int. Topical Meeting on Neutron Radiography, Kobe, Japan, Sept. 14-18,2008.

[6] Y.Nishi et al., Proc. 11th IHTC, Kyongju, Korea, August 23-28, 1998

2-4

樹木の防御反応と水分動態

Defense Responses of Trees and Dynamics of Water Distribution

東京大学大学院農学生命科学研究科 山田利博、永石憲道、田野井慶太朗、中西友子

Graduate School of Agricultural and Life Sciences, the University of Tokyo

T. Yamada, N. Nagaishi, K. Tanoi and T.M. Nakanishi

I. 研究の目的と意義

中性子線は水素中での減衰率が大きいことから、中性子ラジオグラフィ（NRG）法は樹木の材内をはじめとする植物体内の水の分布を非破壊的に知る有用な手法である。樹木では材の病変部で健全部と異なる水分分布を示すが、これは樹木の防御反応との関連が考えられるため、両者の関係解明を目的とした。

非破壊的に水分分布の変化を捉えることができれば、樹木の診断や病態生理等さまざまな応用が考えられる。例えば、野外における樹木の倒壊の危険度診断に音響波伝達速度やγ線の透過率測定が用いられ始めている。これらを含め、腐朽部、空洞部を捉えるための非破壊診断法は腐朽程度だけでなく水分等の密度分布に左右される。材変色部、腐朽部の水分分布のパターンは樹種によって異なることが推測され、診断の確度を低くする要因となる。この水分分布の変動の検出、さらにその原因となる樹木の生理的な反応の追跡を実験的に行うために NRG が利用できると考えられる。

今回は、傷害に対する樹木木部の防御反応と水分分布が樹種によってどのように異なるかを知るために、いくつかの樹種を用い、まず最初に自然の傷害を受けた枝で、次に共通の人為的な傷害を与えた主幹および枝／苗木で、NRG による観察を行った。

なお、以下の実験はすべて JRR-3M 7R の TNRF を利用して行った。熱中性子のフラックスは 1.5×10^8 n/cm^2/s である。

II.自然傷害枝の観察

1. 緒言

樹木は自然にも多くの機械的傷害を受ける。傷害の形状は不定であるが、樹種特有の組織と反応に基づいた傷害部の様式を示すはずである。そこで、まず自然に傷害を受けた種々の樹木の枝について防御関連組織や水分の分布がどのようになっているかを調べた。

2. 実験

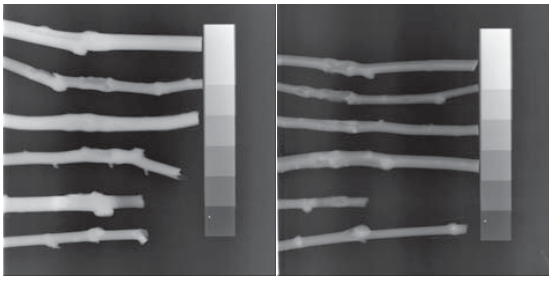
東京大学附属演習林田無試験地（西東京市）で、プラタナス、ヒノキ、イロハモミジの、(財)新技術開発財団植物研究園（熱海市）で、ヤマモモ、ヤブツバキ、シダレザクラの傷害枝（外部に露出した傷のある枝）を採取した。イメージングプレート（IP）で透過像を、また CCD カメラ（200mm レンズ）によって CT 像（横断面および縦断面）を得た。

同じ試料で新鮮時、乾燥時を比較することはできなかったが、いずれの樹種も新鮮な試料と乾燥した試料の観察で水分や防御関連物質の分布を検討した。

3. 結果

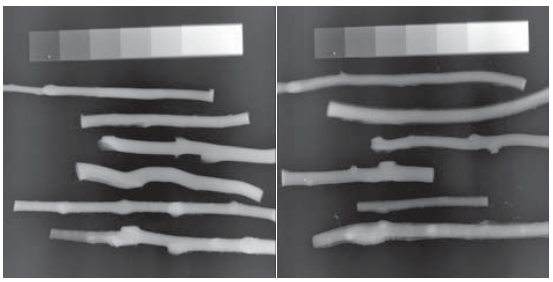
3-1. 透過像の観察

透過像（図-1）では針葉樹（ヒノキ）と広葉樹の特徴を区別することはできなかった。枝先枯れの場合は広葉樹でも乾燥が進むため NRG で生存部と区別することができた。また、防御関連物質の集積については傷害の方向によっては十分確認できた。



新鮮枝（田無試験地）　乾燥枝（田無試験地）

上からプラタナス、ヒノキ、モミジ（各 2 本）



新鮮枝（植物研究園）　乾燥枝（植物研究園）

上からヤマモモ、ヤブツバキ、シダレザクラ（各 2 本）

図-1. 自然傷害枝の透過像

スタンダードはテフロンのステップ

JRR-3M 7R　中性子ラジオグラフィ装置　樹木医学

枝が不整形の円柱状であることに加え、さらに形態の変異に富む傷害部を単なる透過像で解析するのは困難であった。こうした枝の解析には CT 像の構築が必要であると考えられる。

3-2. CT 像の観察

傷害部の中心付近で最も傷害が顕著な部位の横断面を CT 像により観察した（図-2）。また、縦断面での観察も行った（図-3）。

乾燥試料の観察から、どの樹種も病変部（材変色部）の周囲に不揮発性の物質が集積（防御関連物質と考えられる）していることが分かった。特に針葉樹のヒノキで顕著であった。この物質の集積は新鮮試料では水分によってマスクされ不明瞭になったことから、水分、防御関連物質の両者の分布状況を知るには新鮮試料と乾燥試料とを比較する必要があると考えられた。

針葉樹のヒノキでは防御組織を含む病変部で含水率の低下が確認された。しかし、広葉樹のプラタナス、モミジ、ヤブツバキ、ヤマモモでは含水率の低下は不明瞭であった。また、シダレザクラでは逆に防御関連物質とともに水の集積の可能性がみられた。

4. まとめ

同じ試料の新鮮時と乾燥時の比較はできなかったが、おおまかな各樹種の傷害様式の特徴をつかむことができた。傷害部内部の様子を非破壊で観察することで、傷害の履歴まである程度推測可能であった。病変部と水分との関係については広葉樹間では大きな差異がなかったが、針葉樹と広葉樹とで大きく異なっていた。

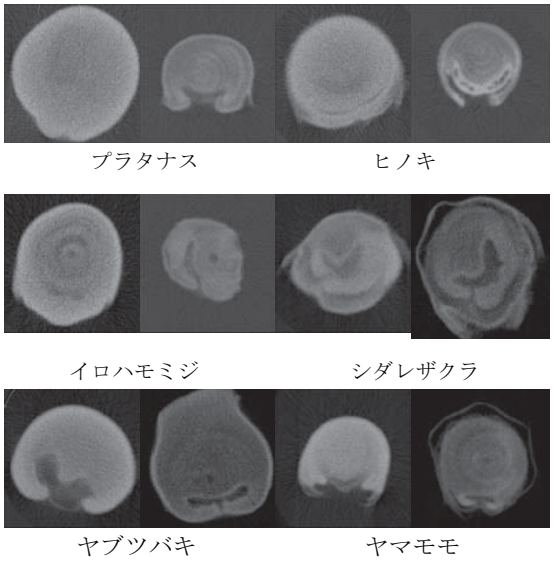


図-2. 自然傷害枝の横断面 CT 像
それぞれ、左が新鮮試料、右が乾燥試料

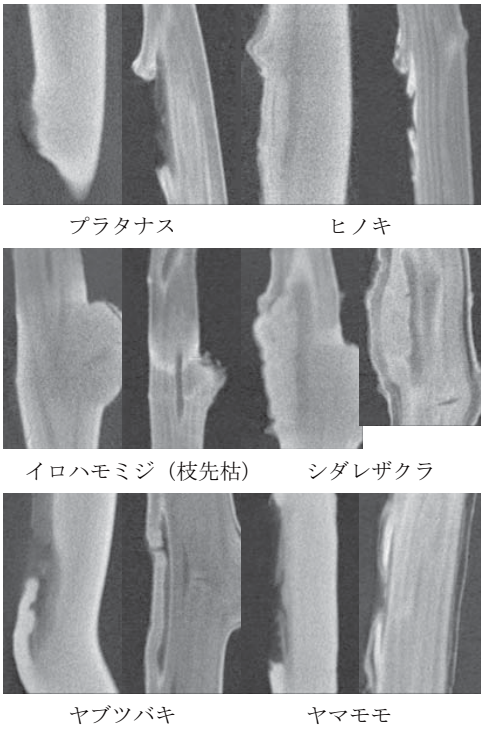


図-3. 自然傷害枝の縦断面 CT 像
それぞれ、左が新鮮試料、右が乾燥試料

III.人為傷害木の観察

1. 緒言

傷害に対する樹木の反応と水分分布の変化、材組織構造との関連を解明することを目的として、各種樹木に人為的な傷害を与える試験を行った。

2. 実験

袖ヶ浦市にある（株）富士植木長浦圃場で、夏季に針葉樹のイチョウ（ここでは針葉樹として扱う）、カヤ、広葉樹のマテバシイ、シラカシ（以上、放射孔材）、サルスベリ、ヒメシャラ、サクラ（関山）、タブノキ（以上、散孔材）の計 8 種の樹木の主幹に径 15mm のドリルで、また枝あるいは苗木に径 2.5mm のドリルで貫通する穿孔傷害を加えた。傷害の 1 週間、2 か月、1 年、3 年後に傷害部を採取した。主幹は約 10～12mm 厚の円板にして IP を用いて透過像を観察した。枝あるいは苗木は長さ約 20cm に切断して、CCD カメラ（105mm レンズ）で撮像し CT 像を構築した。

水分や防御関連物質の分布パターンを明らかにするため、上記試料のいずれも新鮮試料と絶乾試料の観察を行った。

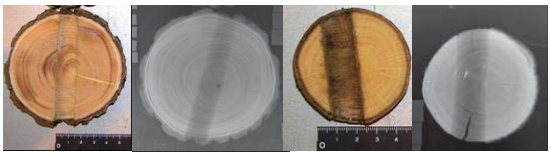
3. 結果

3-1. 主幹部の傷害－樹木円板の透過像

主幹部の傷害 1 週間後の観察例を図-4 に、3 年後の観察例を図-5 に示す。

針葉樹のイチョウやカヤでは 1 週間後の材変色は明瞭でなく、広がってもいなかった。材変色は 2 か月後には明瞭になり、その長さは 2 か月以降も拡大した。イチョウでは 1 週間後から材変色部の乾燥が認められた。カヤでは乾燥部は 2 か月後、1 年後でも透過像で確認されなかったが、3 年後の試料では認められた。

広葉樹についてみると、ヒメシャラでは、1 週間後には材変色部が明瞭に認められ、2 か月後にはさらに濃くなった。しかし、材変色の大きさは軸方向、接線方向ともほとんど広がることはなかった。透過像では材変色関連の乾燥部は全く認められなかったが、傷の周囲の物質（水あるいは防御関連物質）の集積は 1 週間後には既にみられた。マテバシイやシラカシも材変色部の形成・拡大あるいは傷の周囲の物質の集積についてはヒメシャラと同様であった。ただし、マテバシイでは 1 週間後の材変色はやや薄く、その軸方向の長さは 2 か月を越えても拡大した。タブノキも上記広葉樹と同様であったが、1 週間後の材変色はやや薄かった。1 週間後の幹では肉眼で軸方向に乾燥部がみられたが、透過像では確認できなかった。材変色の軸方向の長さは 2 か月を越えても拡大した。傷の周囲の物質は透過像で明瞭であり、特に 1 年後で上下に伸長していた。サクラも材変色は 1 週間後で明瞭で、材変色のその他の特徴や物質の集積については他の広葉樹と同様であった。1 週間後に肉眼で内層からの乾燥がみられたが透過像では不明瞭であった。サルスベリも材変色は 1 週間で明瞭で、材変色のその他の特徴や物質の集積については他の広葉樹と同様であった。

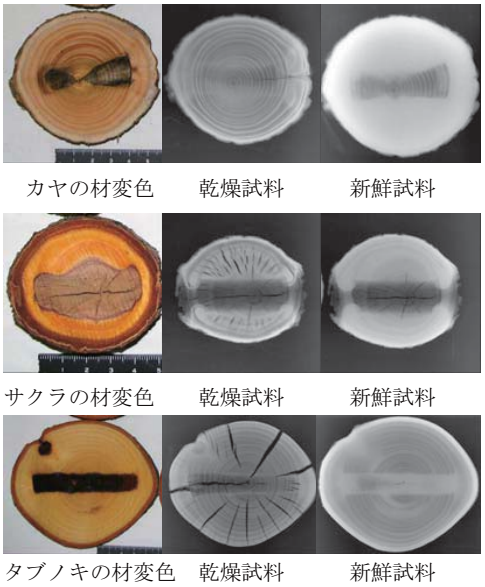


材変色不明瞭　乾燥試料　　材変色明瞭　　乾燥試料
イチョウ　　シラカシ

図-4. 傷害 1 週間後の材変色と乾燥試料の NRG 像

傷害 3 年後の観察でも、すべての樹種の乾燥試料で傷害 2 か月後、1 年後と同じく材変色部の周囲に形成された反応障壁に防御関連物質と推測される不揮発性物質の集積が認められた。

カヤでは傷害 1 年後と異なり、イチョウと同様な針葉樹に一般的な変化、つまり傷害部周囲の材変色部の乾燥が観察された。また、タブノキでは 1 年後にわずかに認められた材変色部への水の集積が顕著になった。他の広葉樹、シラカシ、サクラ、サルスベリでは付傷 1 年後と同じく材変色部の乾燥も水の集積も認められなかった。



カヤの材変色　乾燥試料　新鮮試料
サクラの材変色　乾燥試料　新鮮試料
タブノキの材変色　乾燥試料　新鮮試料

図-5. 傷害 3 年後の材変色と NRG 透過像

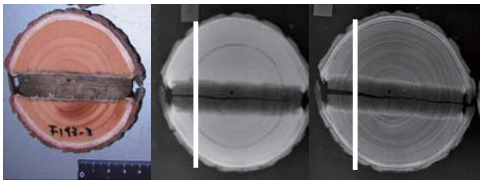
次に、針葉樹と広葉樹の代表例としてイチョウとタブノキの傷害 1 年後の試料について中性子透過度をグラフ化した（図-6）。

イチョウではタブノキに比べ元々の含水率が高いが、材変色部では極端に乾燥（グラフの中央の窪みでは新鮮試料と乾燥試料の線が近接）したのに対し、タブノキでは材変色部の乾燥は認められなかった。タブノキでは傷害孔があるにもかかわらずマスクされるほどなんらかの物質の集積が顕著であり、材変色部で水分が増加しているようである。

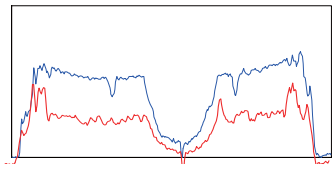
乾燥試料で防御関連物質についてみると、イチョウでは材変色部の周囲に薄い帯状に集積がみられ、そこより内側が乾燥していた。タブノキではイチョウほど顕著でないが集積が認められた。

以上のように、材変色は傷害 1 週間後では特に針葉樹では不明瞭であったが、2 か月後以降はどの樹種も明瞭になった。水平方向の材変色の範囲はどの樹種もほとんど広がらなかった。イチョウでは傷害部の周囲で早くから乾燥部が認められたが、同じ針葉樹でもカヤでは乾燥部の形成は普遍的でないか遅かった。広葉樹では材変色が生じても傷害部周囲の乾燥はほとんど認められず、タブノキのように逆に水の集積が推測される樹種があった。針葉樹、広葉

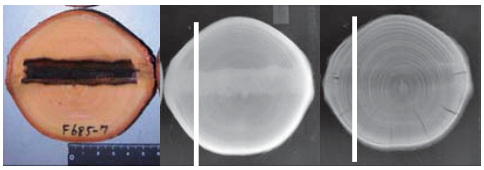
樹とも材変色部の境界で防御関連物質と思われる不揮発性物質の集積が 1 週間後にはすべての樹種で認められ、その量は時間の経過とともに増加した。防御組織形成の時間経過が同じであっても材変色部の水分分布が樹種によって異なることが確認された。



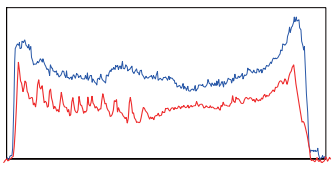
イチョウ　　新鮮試料　　乾燥試料



イチョウ



タブノキ　　新鮮試料　　乾燥試料



タブノキ

図-6. 傷害 1 年後の傷害部（白線部）の中性子透過阻害度
青線：新鮮試料、赤線：乾燥試料

3-2. 苗木／枝の傷害部の CT 観察

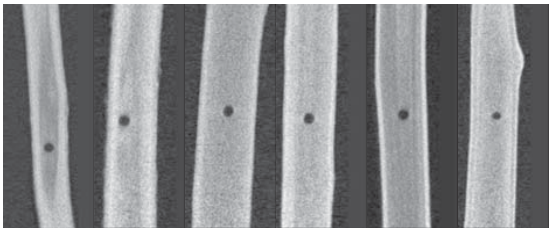
新鮮試料の縦断面断層像の例を図-7 に示す。

針葉樹：イチョウでは傷害 1 週間後には CT で既に軸方向に長い明瞭な乾燥部が観察され、その後の拡大は認められなかった。一般に材変色（特に傷害のみに起因する材変色）は接線方向の拡大は小さく接線方向に長いが、縦断面の CT 像観察が有効であることが確認された。カヤでは CT でも乾燥部はみられず、広葉樹と同じような像であった。

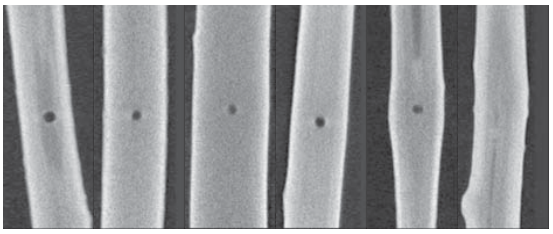
広葉樹：すべての広葉樹で傷害部の周囲に乾燥部は認められなかった。傷の周囲の物質（水あるいは防御関連物質）の集積も CT で確認された。特にタブノキの 1 年後で上下に伸長しているのが顕著であった。

CT でも病変部の周囲における防御関連物質の集積はどの樹種も傷害 1 週間後にわずかにみられ、2 か月後には増加して顕著になった。

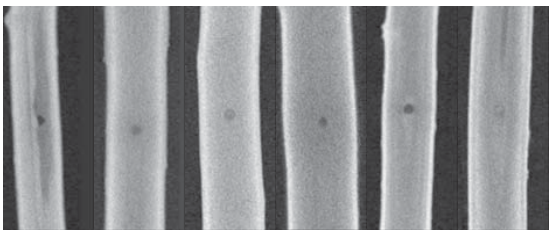
傷害 1 週間後



傷害 2 か月後



傷害 1 年後



イチョウ　カヤ　シラカシ マテバシイ タブノキ サクラ

図-7. 傷害枝新鮮試料の縦断面 CT 像

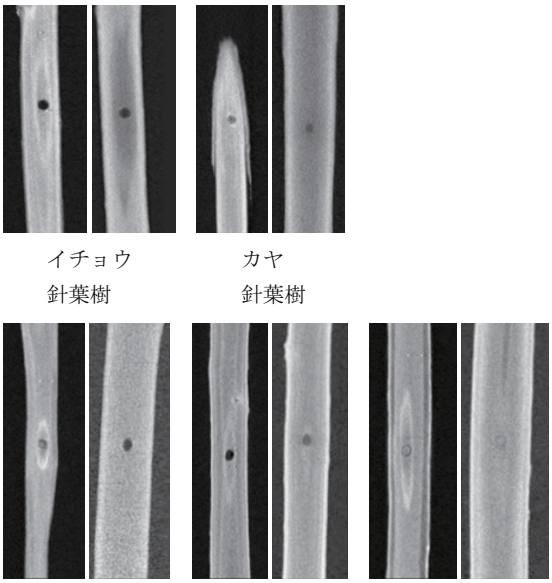
次に、傷害 1 年後の新鮮試料と乾燥試料との比較（水と防御関連物質の分布パターン）を図-8 に示す。

針葉樹では、イチョウで付傷部の周囲に早くから材変色部より広い縦長の乾燥部が形成された。これは、スギ、ヒノキでみられる乾燥部と共通と考えられる。しかし、針葉樹でもカヤではこのような乾燥部はみられなかった。シラカシ（放射孔材、常緑樹）、サクラ（散孔材、落葉樹）、ヒメシャラ（散孔材、落葉樹）といった広葉樹では材変色が生じても傷害部周囲の乾燥はほとんど認められなかった。タブノキ（散孔材、常緑樹）では逆に水の集積が推測された。

絶乾状態にした試料の観察では、IP による観察結果と同じく、針葉樹、広葉樹とも材変色部の境界で防御関連物質と思われる物質の集積が 1 週間後にはすべての樹種で認められ、その量は時間の経過とと

もに増加した。

散孔材（一部半環孔材）と放射孔材とで共通する特徴はなかった。水分分布に差異を生じる機構や、差異と樹木の構造や生理的性質との関連を検討する必要がある。本報告では省略するが、一つの試みとして各樹種の傷害部の組織化学的観察を行っている。



イチョウ　針葉樹　　カヤ　針葉樹

シラカシ　放射孔材　　タブノキ　散孔材　　サクラ　散孔材

図-8. 傷害 1 年後の縦断面 CT 像
それぞれ、左が乾燥試料、右が新鮮試料

4. まとめ

材変色は傷害後次第に明瞭になった。材変色の大きさは、水平方向ではどの樹種もほとんど広がらなかったが、軸方向に長くなった。イチョウでは傷害部の周囲で早くから軸方向に長い乾燥部が認められた。これはこれまでのスギやヒノキでの研究結果と一致し多くの針葉樹に共通する特徴と考えられたが、カヤでは明瞭でなかった。他の針葉樹についてもどちらのタイプか確認を要する。広葉樹では材変色が生じても傷害部周囲の乾燥はほとんど起こらず、逆に水の集積が推測される樹種があった。針葉樹、広葉樹とも材変色部の境界で防御関連物質と思われる固形物の集積が 1 週間後にはすべての樹種で認められ、その量は時間の経過とともに増加した。

IV. 今後の課題

新鮮試料と乾燥試料との比較、特に CT によって病変部の断層像を得ることで、樹種による病変部あるいは防御反応発現部位の特性の違いが明瞭に示された。今後は、NRG 以外の手法でもって、木部の組織構造あるいは防御反応のタイプと水分分布との関連を明らかにすることが必要である。

また、樹種による水分分布の差異が確認されたことから、現場での非破壊手法による腐朽診断ではこの点を考慮する必要がある。季節あるいは水ストレスによっても水分分布が変わることが予想されるので、この変化を NRG によって検出することも今後の課題である。

V. 成果の公表

Yamada, T., Yamato, M. & Nakanishi, T.M. (2005) Influence of water stress on lesion expansion in the xylem of *Cryptomeria japonica* seedlings inoculated with a canker fungus *Guignardia cryptomeriae* revealed by neutron radiography. International Forest Review 7(5):373 (XXII International Union of Forest Research Organizations World Congress Abstract)

山田利博 (2005) 中性子ラジオグラフィで見る樹木木部の傷害に対する反応. 第 3 回日韓中性子ラジオグラフィワークショップ「中性子ラジオグラフィ」専門研究会（平成 17 年度）報告書:128-143

Yamada, T. (2006) Influence of water stress and wetness of open wound on lesion expansion in the xylem of *Cryptomeria japonica* seedlings inoculated with a canker fungus *Guignardia cryptomeriae*.8th International Mycological Congress Abstracts Book:179

山田利博・永石憲道・山下得男・小山常夫・神庭正則・大島　渡 (2006) 中性子ラジオグラフィでみた傷害後の樹木の水分と防御組織の変化. 第 11 回樹木医学会大会講演要旨集 11:69

山田利博 (2007) 樹木の中を診る－材変色腐朽防止と正確な危険度診断のために－. グリーンエージ 2007 年 1 月号:30-33

山田利博・永石憲道・山下得男・小山常夫・神庭正則・大島　渡・飯倉　寛 (2007) 各種樹木における傷害後の水分分布の変化および防御組織形成. 第 118 回日本森林学会大会学術講演集:46

2-5

中性子イメージ・インテンシファイアのための動画撮像システムの開発

Development of Imaging System for Neutron Image Intensifier

持木幸一、和田泰明、岡崎道彦

K. Mochiki, Y. Wada and M. Okazaki

武蔵工業大学　Musashi Institute of Technology

1. はじめに

平成 16 年度から 17 年度にかけて 2 年間で行った中性子イメージ・インテンシファイア（ＩＩ）の性能試験は極めて良好な結果が得られた。この成果をふまえ、ＴＮＲＦ２における動画撮像用の撮像系の整備を行い、高速ＣＴ、ひいてはダイナミックＣＴ用の高性能な撮像システムの開発を行ったので報告する。

2. 中性子ＩＩを用いた中性子ＣＴ

従来の中性子用蛍光コンバータと高感度カメラから成る撮像装置では、中性子の検出効率が悪いために統計的な揺らぎが多く、ゆえにＣＴ用のデータを得るには長時間かけて撮像するのが一般的である。３次元ＣＴでは再構成処理のために多数の透過像を必要とするため、撮像作業は長時間に及び、また被検体の放射化も問題となっている。

中性子イメージ・インテンシファイア（以下中性子Ｉ．Ｉ.）はこれらの欠点を克服する撮像装置である。中性子に対し高い検出効率を持ち、より短時間で撮像作業を行えるようになる[1,2]。

2.1 中性子ＣＴシステム

中性子Ｉ．Ｉ．を用いたＣＴ用中性子透過像撮影システムの構成を図１に示す[3]。被検体を透過してきた中性子は撮像装置によって可視化され、その像を撮像素子(カメラ等)によって撮影する。ＣＴの再構成処理を行うためには、被検体を様々な角度から撮影した透過像が半回転分だけ必要となる。よって図に示すように被検体はターンテーブル上に置かれ、テーブルを一定速度で回転させながら被検体に中性子線を照射し、連続で透過像を撮影した。

実験では透過像の撮影に EPIX 社製 SV9M001 のＣＭＯＳビデオカメラと、特別に調整された東芝製３板式カラーＣＣＤビデオカメラを使用した。ＣＭＯＳカメラの画素数は 1280×1024 画素であり、30fps で 8bit もしくは 10bit グレースケール画像を撮影できる。ＣＣＤカメラの画素数は 640x480 画素であり、ＤＶＤビデオデッキに 30fps で 8bit グレースケール動画として記録した。また比較用として、中性子Ｉ．Ｉ．ではなく蛍光板による従来の撮像装置を用いて長時間撮像も行って透過像を取得した。この撮影には浜松製 C4880 冷却型ＣＣＤカメラを用いた。その画素数は 1024x1024 画素（1008x1023 で処理）であり、32bit グレースケール画像を撮影できる。よって今回の実験では、ＣＴ用透過像を３種類の条件でそれぞれ取得した。その撮像条件を表１に示す。

表１　撮像条件

撮像素子	撮像装置	画像解像度	撮像時間	撮像枚数
冷却型CCD	蛍光板	1008x1023	7200 秒	600
3板式カラーCCD	中性子II	640x480	18 秒	540
CMOS	中性子II	1280x1024	9 秒	270

被検体として、独自に製作した円筒形のＣＴ解像度評価用インジケータを使用した。インジケータはアルミニウム製であり、内部には様々な形状・大きさの空洞が存在し、その一部には鉄などが埋め込まれている。実験を行った施設は日本原子力研究開発機構（ＪＡＥＡ）のＪＲＲ－３Ｍである。ここではＬ／Ｄ＝１７６であり、照射される熱中性子束は $1.5\times10^{8}\,n/cm^{2}\cdot s$ である。

2.2 中性子イメージインテンシファイア

中性子ＣＴでは、中性子で得られる透過像の画質が、Ｘ線と異なり量子的揺らぎ成分のノイズの影響が強く受けるため、撮像系には高い検出効率が求められる。従来の撮像装置では、$Gd_2O_2S;Tb$ や $^{6}LiF;ZnS$ の中性子用蛍光板を用いるのが一般的である。この方式の構成を図２に示す。この方式では、蛍光をレンズで集光する過程で光量が大幅に減少するので、検出量子効率が低下してしま

ＪＲＲ－３Ｍ　７Ｒ　中性子ラジオグラフィ装置、中性子ＣＴ、イメージング

うという欠点がある。平均収集蛍光光子数をε、中性子束をφとすれば、この方式での中性子の検出効率は $S/N \propto \sqrt{\phi}/\sqrt{1+1/\varepsilon}$ となる。よって、この方式では十分な光量を得るために長時間かけて撮像を行うのが一般的である。

これに対して、中性子イメージ・インテンシファイアは中性子線の検出量子効率が高い撮像系である。図３、図４にそれぞれ中性子Ｉ．Ｉ．の外観と構造を示す。これは、平成 15 年度に株式会社東芝が試作したものを購入したものである。中性子Ｉ．Ｉ．は、入射してきた中性子を可視光に変換するだけでなく、微弱な光を明るくする機能を持った大型の電子管(真空管)である。中性子線源から放出された中性子は被検体を透過して中性子　　Ｉ．Ｉ．に入射する。入力蛍光面は、中性子に対して高感度な蛍光体が採用されており、入射した中性子は中性子強度(中性子の個数)に応じた光に変換され、蛍光面表面の光電膜で光電子を放出する。光電子は収束電極及び陽極で構成される電子レンズの作用で、加速されて出力蛍光面に集束される。加速された電子は出力蛍光面を励起して可視像に変換される。その際に輝度増倍が起こり、赤色成分の強い高輝度の可視像となる。従来の撮像方式と違い、撮影される可視像には光の分散の影響が少なく、平均収集蛍光光子数εが十分大きくなり無視されるため、中性子の検出効率は $S/N \propto \sqrt{\phi}$ となる。中性子 I.I.からの出力画像は､主に赤色成分で構成されているが､若干緑色、青色の波長成分も含まれている。このカラー画像をＲＧＢ成分それぞれを別々に撮影すれば、発光強度の違いから、それぞれ感度の異なる赤(R)、緑(G)、青(B)の画像を同時に取得できる。ただし、今回処理で使用した透過像は赤画像のみとした。

中性子Ｉ．Ｉ．の視野は９、６、及び４.５インチ径で可変である。視野を９インチの状態にすると横 18.29 cm、縦 13.72cm の視野での撮像が可能となっている。入射面の蛍光体は $Gd_2O_2S;Tb$ であり､出力蛍光面には Eu を添加した高輝度赤色発光体の $Y_2O_2S;Eu$ シンチレータが使用されている。赤色発光ピークは固体撮像素子の感度特性に適合しており、従来の緑色蛍光体を使用したＩ．Ｉ．と比較し、数倍の感度改善がなされている。

2.3 測定結果

冷却型ＣＣＤカメラによって撮像された透過像６００枚から、３枚ごとの最小値をとって１枚の画像を作成し、２００枚の透過像としてそのうち１８０枚をＣＴ再構成に使用する。３板式カラーＣＣＤカメラによって撮像された透過像は、３枚ごとの中心値をとってＣＴ用の１８０枚の透過像としている。ＣＭＯＳによって得られた透過像には窓幅 3x3 のメディアンフィルタをかけている。その後、各透過像について暗電流補正・シェーディング補正を行う。暗電流補正・シェーディング補正前までの各撮像法ごとの透過像を図５に示す。

Shepp-Logan フィルタ補正を行った後に重畳積分法により再構成を行った。再構成画像に、アルミの部分が輝度１００に、鉄の部分が輝度２００になるように補正したものを図６に示す。

再構成を行った直径 60mm のアルミ板の部分には直径 2.0mm、1.5mm、1.0mm の穴がそれぞれ１０個ずつ開いており、そのうち５つずつに鉄が埋め込まれている。またアルミ板の周囲には紙が巻かれている。

冷却型ＣＣＤおよびＣＭＯＳの再構成画像では鉄と空洞の両方の部分が確認できる。しかし３板式ＣＣＤの再構成画像では空洞部分は確認できなかった。また、各再構成画像からアルミ部分の一部を抜き出し､その標準偏差を求めた｡その結果、３板式ＣＣＤの再構成画像では冷却型ＣＣＤの１.４２倍、ＣＭＯＳは冷却型ＣＣＤの１.０６倍となった。これにより、中性子Ｉ．Ｉ．を用いてＣＭＯＳカメラで取得された透過像は、従来の撮像方法で取得した透過像と比べてもさほど品質の劣らないデータであるといえる。

3. まとめ

実験により、中性子ＩＩを用いれば僅か９秒の撮像時間で取得した透過像データでも、長時間撮像により取得されるデータとさほど品質の劣らないＣＴ再構成画像が得られることが実証された。

参考文献

1) 持木、松本、菊池、橋；平成 17 年度「中性子ラジオグラフィ」専門研究会、京大原子炉実験所 (2005)
2) 持木幸一、松本哲男、菊池秀、橋康達、中神賢士　「中性子イメージインテンシファイアを用いた中性子ＣＴ」　日本非破壊検査協会　平成 18 年度春季大会 pp.135-136 (2006)
3) 持木幸一、日塔光一　「中性子カラーイメージインテンシファイア」　応用物理、vol.75、No.11 pp.1349-1353 (2006)

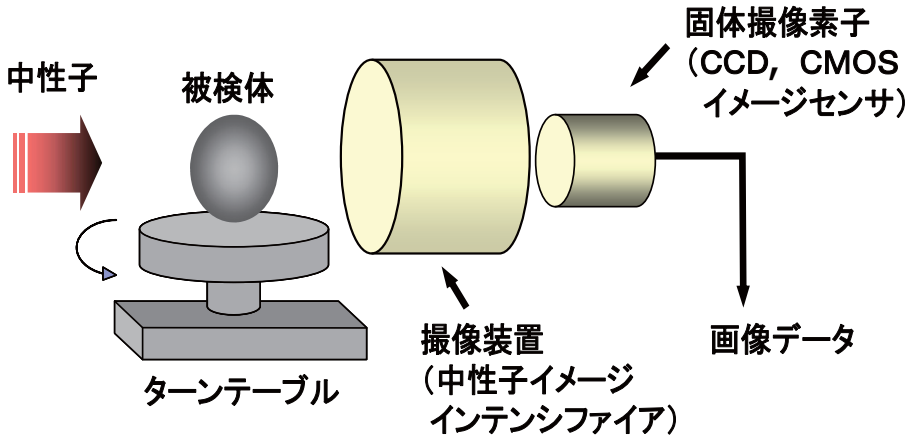


図１　ＣＴ用中性子透過像撮影システムの構成図

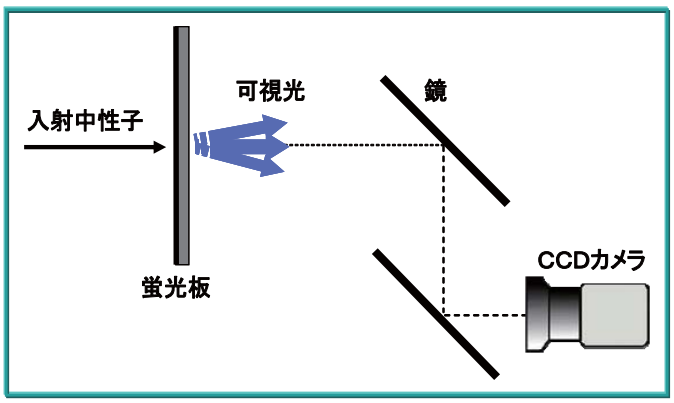


図２　従来の撮影装置

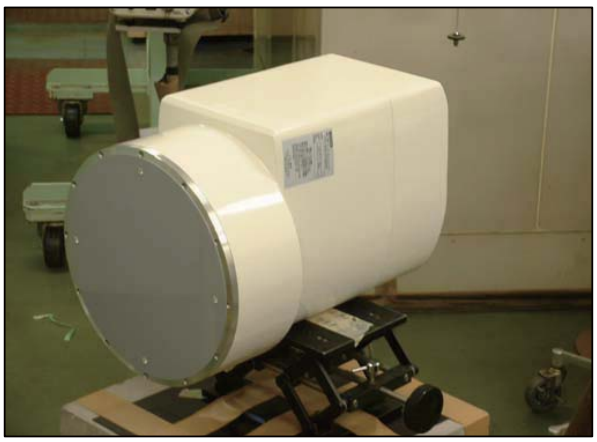


図３　中性子Ｉ．Ｉ．の外観

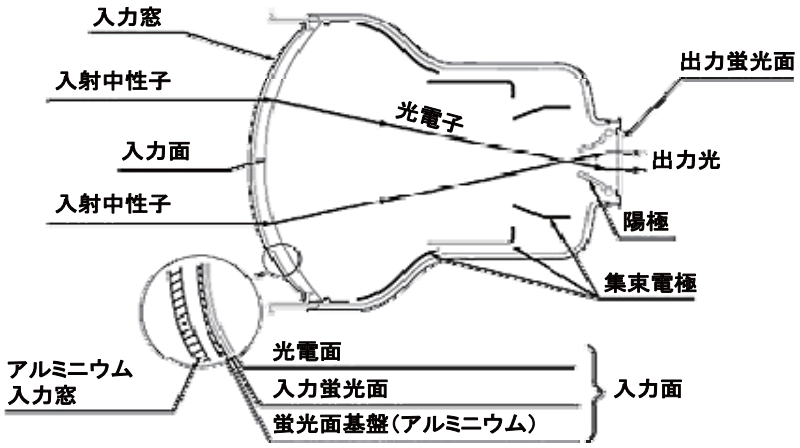


図４　中性子Ｉ．Ｉ．の構造図

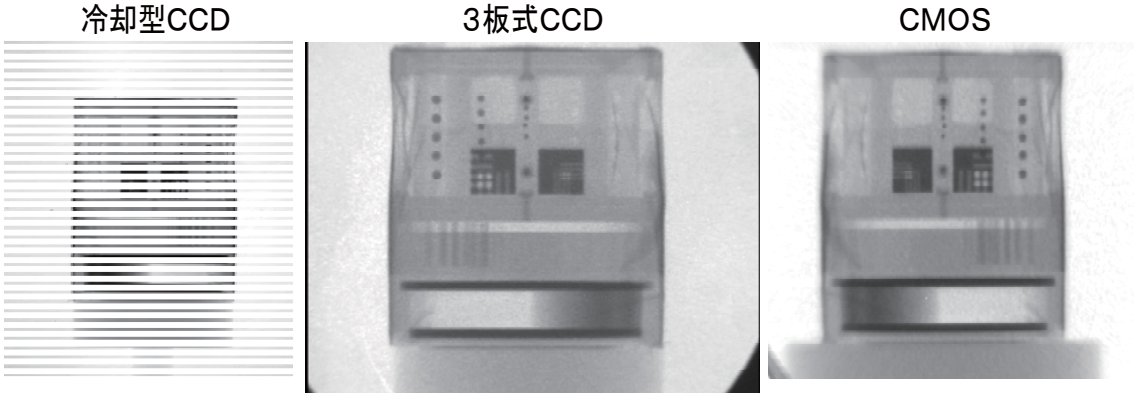


図５　各透過像

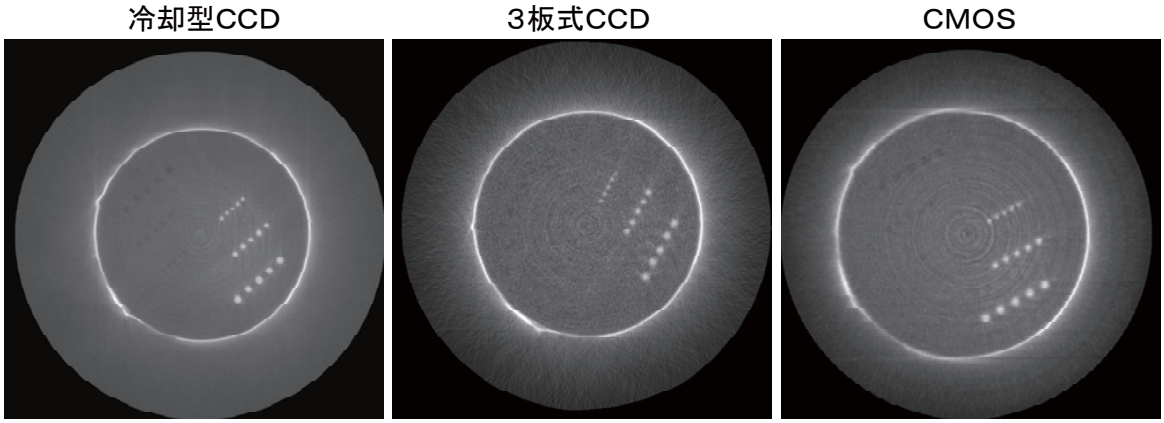


図６　各再構成画像

2-6

「7179　植物試料における水分布解析」

Analysis of water distribution in plant tissue.

東京大学大学院農学生命科学研究科

中西　友子

研究の目的と意義

植物体の実に 9 割は水が占め、植物におけるあらゆる生理反応は水溶液中で行われ、植物の活動は水の媒介無しにはおこりえない。特に、養分吸収や養分の転流においては水が大きな役割を果たしていることは周知の通りである。生きた植物において最も重要な役割を果たしている化学物質は何といっても水であるにもかかわらず、水そのものの知見については非常に少ない。そこで我々は、生きたままの植物体中の水の動きや分布を探るために、中性子ラジオグラフィー(NRG)を採用し、水に特異的な像を得ることを目的に実験を進めた。NRG は正確には水素の像の可視化であるが、植物試料の水について詳細に調べることができる方法は NRG を含め数少ない。

試料としてはマメ科で半乾燥地に良く生育する、アジア、アフリカにおける重要な穀物であるササゲを用いた。ササゲは、根付近に水が全くない状態を 2 週間以上続けても、再び水を与えると吸収を開始し生育を継続することができる植物である。しかし、なぜこのような強い乾燥耐性能を保持しているかについては不明な点が多い。ササゲの茎の一部には水分含量が高いものがあり、この組織が貯水組織として機能しているらしいと言われているものの、まだ実験的に貯水組織の機能について確かめられていない。乾燥に強いメカニズムを解くためには、乾燥時の植物体内水分布を詳細に把握する必要がある。本研究では、NRG を用いて、植物体内水分分布を解析した。

その研究をどのように行ったか

本研究では、アフリカの乾燥地域で自生しているササゲ約 2000 種から選抜された乾燥に耐性な品種と乾燥に感受性な品種を用いた。具体的には、乾燥耐性品種のササゲ 2 品種、*Vigna unguiculata* TVu11979, TVu11986 と、乾燥感受性品種のササゲ 2 品種 *Vigna unguiculata*　TVu7778、TVu9357 を使用した。種子表面にヤスリで傷をつけた後、水道水で湿らせたバーミキュライトへ播種し、暗所において 30℃で 2 日間処理し発芽させた。発芽後、5 日間 1/4Hogland 水耕液で生育させ、その後播種後 24 日目まで Hogland 水耕液で生育させた。水耕液は 7 日毎に交換した。生育環境は人工気象器(BIOTRON LPH300:NK system Co. Japan)内で温度 28℃、湿度 70%、明期 16 h、暗期 8 h、光条件 150 μ molm^{-2}sec^{-1} とした。一方のサンプルは引き続き改良 Hogland 水耕液で 3 日間生育させ、他方を 3 日間乾燥ストレス処理した(乾燥ストレス期間中の湿度も 70%とした)。

NRG の撮影は、日本原子力研究開発機構、東海研究所の研究用原子炉、FRR3 を用いて行なった。中性子ラジオグラフィ専用の中性子線取り出し口における熱中性子束は、1.5 x 10^{8}n/cm^{2}/s である。原子炉からの中性子線による照射像は、55 mm レンズ(空間分解能 200 μm、視野 20 cm×20 cm)により、5 枚を 1 セットとして撮影した。研究所内の室温は 20℃、湿度 27%であり、撮影室は室温 28℃、湿度 22%であった。また、撮影中、他のサンプルは人工気象器内で温度 28℃、湿度 70%、明期 16 h、暗期 8 h、光条件 150 μ molm^{-2}sec^{-1} に保った。撮影開始前には CCD カメラの暗電流画像とサンプルを置いていない状態での NRG 画像(バックグラウンド画像)を撮影した。

乾燥ストレス前・ストレス後それぞれ、ササゲ 4 品種、3 連で撮影した。5 枚の画像セットを 1 枚の画像に統合し（撮影した 5 枚セットの画像のピクセルごとの最低値をとり、1 枚の画像へ変換した)、暗電流画像とバックグラウンド画像を用いて植物体の中性子線透過画像を得た。この画像は中性子線が透過するほど明るく、減衰するほど暗く写っており、水分含量の多いところほど濃く写っていると考えられる。

また、2 次元の NRG 画像とは別に 3 次元 NRG 画像も撮影した。この実験は TVu7778 と TVu11979 について、乾燥処理の有無それぞれに 2 連で行った。播種後 19 日目のサンプルと、播種後 19 日目から乾

JRR3　NRG　　植物試料における水分布解析

燥ストレス条件下に 8 日間さらしたサンプルとを比較した。サンプルは第一葉の葉柄下 6 cm の部分(初出葉下 1 cm 程度までにあたる)の茎を切りだし、アルミホイルに包んで円柱状に加工した。直径 1 cm のアルミ製の円柱へサンプルを固定し、200 mm レンズ(空間分解能 50 μm、視野 5 cm×5 cm)を用いて、サンプルを 0.5 度ずつ 180 度回転させ、各回転角度において NRG 画像を撮影した。取得した 360 枚の画像を IPLab(Scanalytics,Inc.)によって処理し、3 次元 NRG 画像として構築した。まず、画像を横方向に輪切りにし、できた幅 1 ピクセルの細切れの画像をそれぞれ画像の横幅分のピクセル数だけ並べた。この正方形の画像を各角度で撮影した画像ごとに作り、おのおのの角度分回転させ、全て 1 枚に足し合わせた。こうして出来た画像にフーリエ変換ノイズ除去を行い、1 枚の断面像とした。そして、この断面像を最初に輪切りにした各画像分並べることで、3 次元 NRG 像を再構築した。

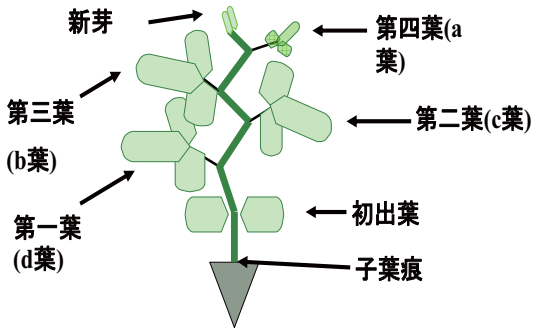


Fig1： ササゲ(*Vigna unguiculata* L. Walp.)

どのような結果を得たか

ササゲの乾燥感受性品種、TVu7778 ならびに TVu9357 について、乾燥ストレスを与える前と後において NRG 撮影を行なった。その結果を Fig. 2-1 に示した。また、乾燥耐性品種、TVu110979 ならびに TVu 11986 についての NRG 像を Fig. 2-2 に示した。まず、乾燥耐性の品種（Fig. 2-2）の方が、乾燥処理前後における形態や水分含量の差が少ないことが示された。

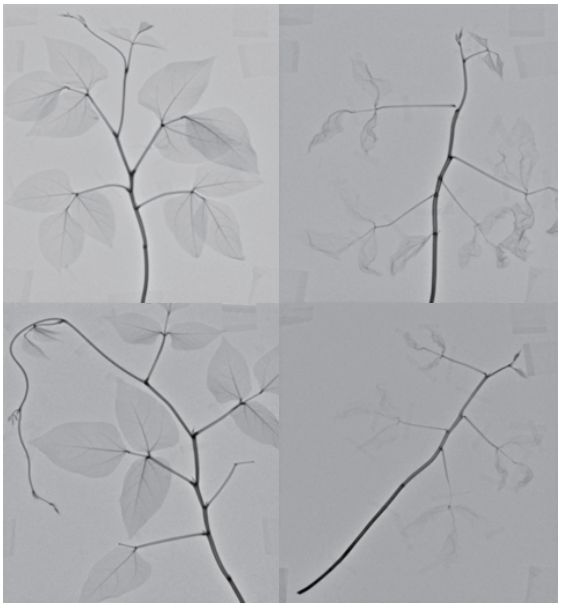


Fig. 2-1：**ササゲ乾燥感受性品種のNRG像**
左上：TVu7778**乾燥ストレス前**
右上：TVu7778**乾燥ストレス後**
左下：TVu9357**乾燥ストレス前**
右下：TVu9357**乾燥ストレス後**

さらに詳細に得られた像をみてみると、特に乾燥耐性品種においては、第一葉から第三葉の間の茎節（Fig. 1 参照）の水分含量が高い傾向が見られた(濃い影が見られた)(Fig. 2-1、2-2)。また、通常の環境条件下では、この茎の部位に水が多く含まれていることがわかった。乾燥ストレス処理をかけると、すべての品種において、下の葉から水分が減少していく様子が示された。しかし、乾燥耐性品種では特に葉からの水分減少が少ない、つまり葉が枯れにくいことがわかった。乾燥耐性品種と感受性品種を比較すると、乾燥耐性品種は、感受性品種よりも茎中の水含量が保たれていることも示された。これらのことから、乾燥耐性品種は、葉をなるべく枯らせない機構、つまり乾燥時に葉を保持する機構として、茎の水含量をあまり減らさない機構と、葉と茎それぞれに乾燥耐性に寄与する機構の存在が示唆された。特に、乾燥耐性品種では、茎が太く、含水率も高いことから、この部位が乾燥時に水の供給元として寄与していることが予想される。さらに、葉も枯れにくいことから、水が茎から葉へ移行し蒸発して失われることがないようなメカニズムが働いていることが考えられた。



Fig. 2-2：**ササゲ乾燥耐性品種のNRG像**
左上：TVu11979**乾燥ストレス前**
右上：TVu11979**乾燥ストレス後**
左下：TVu11986**乾燥ストレス前**
右下：TVu11986**乾燥ストレス後**



Fig. 3：**茎(初出葉付け根)の立体的NRG画像**
左上：TVu7778**乾燥ストレス前**
右上：TVu7778**乾燥ストレス後**
左下：TVu11979**乾燥ストレス前**
右下：TVu11979**乾燥ストレス後**

次に、ササゲの節の 3 次元 NRG 画像を撮影した。その結果、乾燥ストレスによって茎節の水分も抜けたことが確認できた。しかし、乾燥耐性品種、感受性品種ともに同様に茎節の水は失われていた。今回の状況まで乾燥させても、水を再度与えると生育が回復することから、茎節の水がない乾燥状況でも降雨等で生育が回復する際には、節部位に水が供給されることが判明した。しかし、その際に水供給機構は不明であった。また、この耐性機構はササゲとして保有しているものであり、ササゲの品種間差に寄与するものではないことが予想できた。

その結果に対する評価

植物体中に含まれる水のイメージング手法として中性子ラジオグラフィを用いた。中性子ラジオグラフィは対象物に中性子線を照射して中性子線の透過画像を得る手法である。中性子線の減衰原因として、植物体内ではその存在量からもH_2Oの影響が極めて大きいと考えられることから、植物体内の水分含量を非破壊的に測定できる有効な方法である。

本研究結果は、ササゲの耐性メカニズムを解明する目的で、ササゲ体内の水分含量および乾燥時の水分分布を解析した。その際には、3D による撮影に挑戦し、茎節部位での詳細な水分布が明らかとなった。本研究で得られた節部位での水含量変化は、ササゲ耐性メカニズムを解明するにあたり貴重な知見である。というのも、一旦水が抜けた組織に水を供給する、という仕組みは植物にとってとてもエネルギーの要る作業であり、ササゲの茎節部位でそのような行動をとっていることは、乾燥耐性機構に茎節部位が重要であることを示唆している。さらなる知見を得るには、再度水を供給した場合のササゲ節部位の水分布を撮影したり、より定量的なデータを示せるような解析を行う必要があるものと思われる。

成果の公表

本研究成果については、学会発表等では公表しておりません

This is a blank page.

3. 即発ガンマ線分析

3. Prompt Gamma-ray Analyses

This is a blank page.

3-1

Development of a Method of Measuring the Cadmium Concentration in Agricultural Produce with Prompt γ-ray Analysis

Y. Sakurai[1], H. Matsue[2], S. Miyamoto[1] and N. Kihou[1]

[1]*National Institute for Agro-Environmental Sciences, Tsukuba, Ibaraki 305-8604*
[2]*Quantum Beam Science Directorate, JAEA, Tokai, Ibaraki 319-1195*

1. Objective

Enhancement of regulations on standard levels of cadmium in foods is currently being studied both here in Japan and abroad. The most effective way of ensuring risk management of the cadmium concentration in agricultural produce and animal feed is to monitor the cadmium concentration in produce. Thus, we developed a method of measuring the cadmium concentration in agricultural produce and animal feed with PGA, which is a method of non-destructive analysis that does not require wet decomposition of samples, in order to measure cadmium concentrations rapidly and with a high level of accuracy. In 2007, we studied the effects of noise level attenuation and sample form on measurement accuracy in order to improve the sensitivity of cadmium detection.

2. Methods

An acrylic sheet (150 mm x 150 mm, d=2, 3, or 5 mm) was inserted as a noise filter in a neutron beam line prior to samples being analyzed with a PGA device, and the S/N ratio of the prompt γ ray peak (558 keV) of cadmium in brown rice (Cd: 2 μg/g) was measured for 1500 s. In addition, ground samples (5-6 g) of brown rice (Cd: 0.6 μg/g) were placed in aluminum rings and shaped into round pellets (Φ40 mm) with a hydraulic press (20t/cm^2), and the S/N ratio of the cadmium peak of these samples was compared to that of powdered and granular samples of brown rice.

3. Results

Effects of the insertion of an acrylic sheet in the beam line on cadmium measurements in brown rice are shown in Table 1, and effects of different forms of samples on the S/N ratio of cadmium are shown in Table 2.

Table 1: Thickness of the acrylic sheet filter and the S/N ratio of Cd in brown rice

Acrylic sheet thickness (mm)	S/N ratio of the Cd peak
0	0.121 ± 0.022
2	0.199 ± 0.012
3	0.179 ± 0.002
5	0.0788 ± 0.015

Table 2: Sample form and S/N ratio of Cd in brown rice

Form of brown rice sample	S/N ratio of the Cd peak
Pellets(6.1g)	0.0529 ± 0.0065
Powder(5g)	0.0446 ± 0.0039
Grains(5g)	0.0315 ± 0.0003

4. Discussion/Conclusion

Results of placing an acrylic sheet in the neutron beam and measuring the Cd peak in brown rice indicated that the S/N ratio improved about 1.5-fold when an acrylic sheet with a thickness up to 3 mm was inserted in the beam line. The sheet's effect, however, was limited, so the same measurements were made the following year as well. The sample form had an effect on the S/N ratio in the order of shaped pellets>powder>grains; this is believed to be the order of greater brown rice sample density in the neutron beam's target plane. Even when brown rice powder was molded into shape, doing so improved the S/N ratio of the powdered sample only 1.2-fold, so measured with a powdered sample is recommended because of its analysis efficiency.

原子炉：JRR-3　　装置：PGA(T1-4)　　分野：即発γ線分析実験（農・水産物）

3-2

Measurements of Hydrogen-Containing Samples Using MPGA

Y. Toh, M. Oshima, M. Koizumi, K. Furutaka, A. Kimura and Y. Murakami[1]

Nuclear Science and Engineering Directorate, JAEA, Tokai, Ibaraki 319-1195
[1] *JST Innovation Satellite Ibaraki, JST, Tsukuba, Ibaraki 305-0047*

Many of agricultural, medical and industrial samples contain large amounts of hydrogen. Hydrogen emits a 2.2MeV prompt gamma ray in a neutron capture reaction. The low-energy photons due to the Compton scattering of high energy γ rays from hydrogen obviously cause an increase in the background in the lower region of the γ spectrum, resulting in a decrease in the detection limit. Hydrogen emits only one prompt γ ray at a time at every neutron capture reaction. The multiple γ-ray detecting method, which is known as a coincidence method, is widely used in nuclear spectroscopy. In this method, only elements which simultaneously emit two or more prompt gamma ray in a capture reaction can be measured [1,2]. Therefore, by applying the multiple γ-ray detection method to PGA, the influence from hydrogen can be reduced.

A standard polymer sample (IRMM BCR681) which contain 22 ppm Cd was measured by the MPGA detector system. The event rate was about 220k count/sec. Cadmium emits some prompt γ rays mainly in the neutron capture reaction of ^{113}Cd(n, γ)^{114}Cd: 558-, 576-, 651- and 725-keV γ rays, for example. PGA and MGPA spectrum were compared in the Fig.1. In fig.1, the normalized projection spectra of the two-dimensional spectra with change in the scaling of the Y axis is shown for comparison. In the MPGA spectrum, hydrogen peak was reduced and signal-to-noise ratio of Cd was improved.

Polymer standard samples BCR680, B7 and a standard rice sample NIES CRM No.10 were also measured by the MPGA detector system. These samples contain different amounts of cadmium (BCR680 141 ppm , B7 4.8 ppm, CRM No.10 1.8 ppm) . A calibration curve for quantification of cadmium was obtained. The cadmium calibration curve exhibited good linearity in the range of 1.8 to 141ppm.

This research was partly conducted as the Practical Application Research and supported by JST Innovation Satellite Ibaraki.

References

1) Y.Toh, et al. :"Appl. Radiat. Isotopes", 64, pp. 751-754 (2006).
2) M.Oshima , et al. :"Proc. J. Radioanal. Nucl. Chem.", 271, 317 (2007).

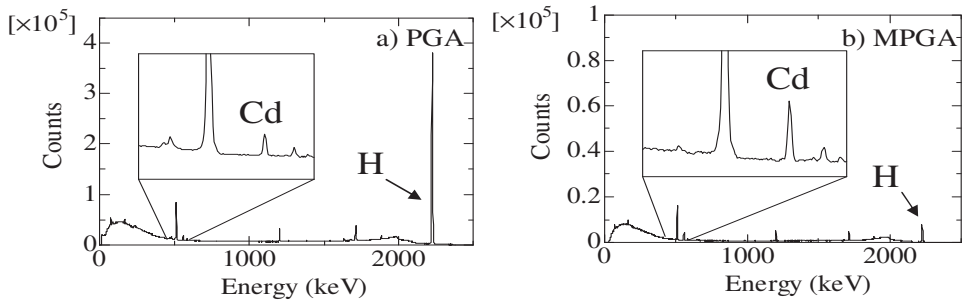


Figure 1: a) PGA and b) MPGA spectrum for a standard polymer sample (IRMM BCR681). The normalized projection spectra of the two-dimensional spectra with a change in the scaling of the X axis is shown for comparison to the PGA spectra.

原子炉：JRR-3　　装置：MPGA(C2-3-2)　　分野：即発γ線分析実験（農・水産物）

3-3

Determination of Boron in Ceramic Reference Materials by Prompt Gamma-ray Analysis Using Focused Neutron Guided Beam of JRR-3M

T. Miura[1] , H. Matsue[2], T. Kuroiwa[1] and K. Chiba[1]

[1]*NationalMetrologyInstituteofJapan − AIST, Ibaraki*305 − 8563
[2]*QuantumBeamScienceDirectorate, JAEA, Tokai, Ibaraki*319 − 1195

Prompt gamma-ray analysis (PGA) is useful for nondestructive determination of light elements such as B in bulk samples. However, a long counting time is generally required to measure sufficient gamma ray spectrum by straight neutron beam irradiation. Recently, a new beam focusing unit for JRR-3M was developed which increases beam flux increase by 3 times^{-1})[1,]. However, the profile of the focused neutron beam is usually less homogeneous than when compared with a straight neutron beam. Appropriate internal standards are required to correct the inhomogeneity of neutron flux and make the irradiation uniform enough for precise and accurate determination. The aim of this study was to evaluate the analytical performance of PGA using the focused neutron beam. The PGA was applied to the determination of B in SiC ceramics CRM (BAM S-003), and the effect of an internal standard and the measurement uncertainty in PGA were investigated.

The B standards were prepared from NMIJ primary standard solution. A series of B standards (0, 1.2, 4.7 and 10.6 ug of B) were prepared, each of which contained Si metal and ND4Cl as matrices. Another aliquot of 25 mg of ND4Cl was weighed and put into another FEP film bag to prepare the ND4Cl standard sample, which was used to measure the correction factor to correct the spectral interference. Three aliquots of 100 mg of BAM S-003 were weighed and put into the FEP film bags. The FEP film bags were heat-sealed to make the sample packages smaller than 15 mm x 15 mm. The blank levels of B in Si metal and ND4Cl had been measured by the PGA and were less than 0.3 ug both in 250 mg of Si metal and 25 mg of ND4Cl. The samples and standards were irradiated by the focused neutron beam at JRR-3M. The prompt gamma ray spectrum was measured with Compton suppression PGA system for 1000 to 8000 s according to the spectrum intensity. The B gamma ray peaks were analyzed by Covell ' s method and by the non-linear least squares method[2)]. The determination of B was carried out by linear calibration curves using an internal standard. The Cl 1601 keV peaks were used as an internal standard. The analytical result of B in BAM CRM S003 (63.3 mg/kg ± 3.0 mg/kg, k=2)[3)] is in good agreement with the certified value (63 mg/kg ± 7 mg/kg, k=2) which was characterized by the analytical results obtained by ICP-OES, DCarc-OES and molecular absorption spectrometry. The main component of the standard uncertainty was the sample measurement repeatability for BAM CRM S-003.

PGA using the focused neutron beam was applied to the determination of B in ceramic CRM. The internal standard method was found to be useful for the focused neutron beam irradiation method. PGA using the focused neutron beam can be determined in the range of 0 to 10 ug of B in ceramics sample without any sample dissolution.

References

1) S. Yamada et al :"Physica B", 385-386, 1243(2006).
2) M. Magara and C. Yonezawa :"Nucl. Instr. and Meth",A454, 389(2000).
3) CRM BAM-S003 Certificate :Federal Institute for Material Research and Testing, BAM, Berlin, 2004.

原子炉：JRR-3　　装置：PGA(T1-4)　　分野：即発γ線分析実験（工業材料）

3-4

Non-Destructive Analysis of Ancient Egyptian Vitreous Relics by Neutron

S. Yoshida

Department of Energy Science and Technology, Tokai University, Kanagawa 259-1292

On our laboratory, ancient Egyptian vitreous relics (faience) and sand or rock which become those raw materials are analyzed by the non-destructive simultaneous multi-elements measurement using the prompt gamma-ray analysis (PGA) by neutron beam, because it is extremely a very small amount of the residual radioactivity after irradiation when neutron flux is low. Our goal in this study is to examine what archeological characteristics in those distributions of some component elements of main elements and trace elements specified exist, such as times nature and regional nature. The analysis has been carried out by the thermal neutron prompt gamma-ray analysis used the T1-4-1 beam port of the JRR-3 institution. Many analysis samples were faience of ancient Egyptian vitreous relics or sand and rock of the orient area, many samples of about 5cm x 10cm at the maximum (thickness a little less than 1cm) were sealed up with an FEP film individually, and analyzed while irradiating it by 3,000-5,000 seconds per one sample on the sample stage center in the whole He-gas atmosphere after a set. The relations with Fe/Si ratio (ratio of the peak area net count rate of the full-energy peak of Fe (E γ =352keV) for the one of Si (E γ =3539keV) which is a main element) and Co/Si ratio (mainly, the Nile central part, the Akoris remains) in each faience and local sand, were shown in Fig. 1. We have been investigated that Fe ratio in sand (Si) was strongly proportional related to Co ratio, however, could not find a regional characteristic. In addition, it follows that the existence ratio between each element in faience accords with the one in sand. But it is considered that cobalt was elemental addition at the time of faience production and it was showed to present distribution that it came off from existence distribution of the sand (inside points of the dotted line in Fig. 1). Furthermore, the existence ratio distribution with Co element and Cu element which it was detected in faience without it being detected into sand was shown in Fig.2. By the distribution that the existence ratio of the Co and Cu become 1 as for the dotted line crossing the center at the opposite angle, it has been revealed that two groups formed characteristic distribution that the upper domain where the existence ratio of the Cu is big in comparison with the Co and the lower domain where the existence ratio of the Cu is small.

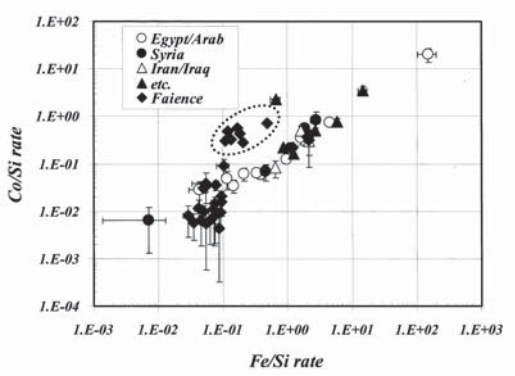


Figure 1: Comparison of the existence ratio of Fe and Co in faience and sand.

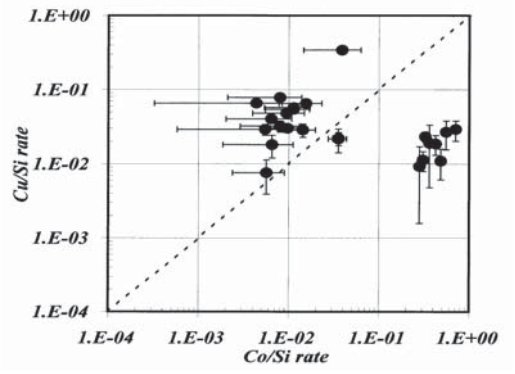


Figure 2: Comparison of the existence ratio of Co and Cu in faience.

原子炉：JRR-3　　装置：PGA(T1-4)　　分野：即発γ線分析実験（考古学）

3-5

Development of Temperature Variable Neutron In-beam Mössbauer Spectrometer

M. K. Kubo, Y. Kobayashi[1], Y. Yamada[2], Y. Watanabe[3], T. Takayama[3]Y. Sakai[3], H. Shoji[4], W. Sato[5], A. Shinohara[5], M. Segawa[6], H. Matsue[6]

Department of Chemistry, International Christian University, Tokyo 181-8585
[1]*Applied Nuclear Physics Laboratory, RIKEN, Saitama 351-0198*
[2]*Department of Chemistry, Tokyo University of Science, Tokyo 162-8061*
[3]*Daido Institute of Technology, Nagoya 457-8530*
[4]*Graduate School of Science, Tokyo Metropolitan University, Tokyo 192-0039*
[5]*Department of Chemistry, Graduate School of Science, Osaka University, Osaka 560-0043*
[6]*Japan Atomic Energy Agency, Ibaraki 319-1195*

Emission Mössbauer spectroscopy is a useful tool in the investigation of the trace amount of chemical species formed by nuclear reactions and radioactive decays. The large transmission power of γ-ray used by the Mössbauer effect enables non-destructive analysis of the inside of solid materials in which nuclear events occur. We have been developing a new ^{57}Fe in-beam Mössbauer spectroscopic system in order to investigate the chemical and physical behaviors of the species produced after the neutron capture reaction of ^{56}Fe in materials. This year we introduced a liquid N_2 cryostat to try freezing and keeping thermally unstable initial nuclear event products and meaure their Mössbauer specta.

Pyrite (FeS_2) was chosen as a sample material because it has high Fe content and a simple cubic structure. A conventional cryostat for absorption Mössbauer spectroscopy was used after slight modification. Since scattered neutrons and the neutron beam itself react with every material in addition to the target in their paths and cause unnecessary γ-ray background. The amount of material of the cold head holding the sample was minimized. An aluminum foil of 12 μm thickness was used as the sample contact part of the aluminum (4N) cold head extending 20 cm from the nitrogen vessel. This was planned to minimize the background originating from the cryostat body by placing the cryostat as far from the beam line as possible while holding the sample at low tempratures. The cryostat windows were 45 mmϕ holes covered with 50 μm thick Kapton foils to reduce the amount of material hit by the beam while keeping the vacuum of the cryostat.

At room temperature the neutron in-beam Mossbauer spectrum of pyrite was composed of two doublets. At 78K the spectrum of pyrite was decomposed into three doublets (Figure 1). Component A had similar Mossbauer parameters as the parent pyrite. Doublet B showing IS=0.08(5) mms^{-1} and QS = 1.0(1) mms^{-1} could be Fe(III) in low spin state, and doublet C with IS=0.68(8) mms^{-1} and QS = 1.27(13) mms^{-1} might be Fe(II) in high spin state. At this point we cannot determine the details of these two new species. But it could safely be said that the spectrum at low temperature is different from the one at room temperature and more than two species appeared in the spectrum might be attributable to species produced by the nuclear event but could not be observed at room temperature due to their thermal instability.

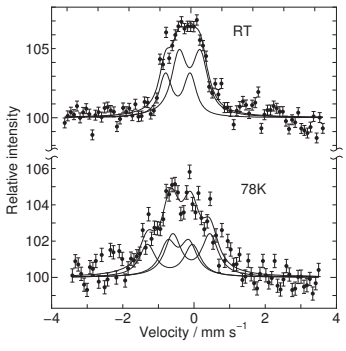


Figure 1: Neutron in-beam Mössbauer spectrum of pyrite.

原子炉：JRR-3　　装置：PGA(T1-4)　　分野：即発γ線分析実験（その他）

This is a blank page.

4. 放射化分析

4. Neutron Activation Analyses

This is a blank page.

4-1

研究テーマ：中性子放射化分析法を用いた環境試料中 ^{129}I 濃度の把握

表　　題：東海再処理施設周辺の畑土中 ^{129}I 濃度調査

東海再処理施設周辺の畑土中 ^{129}I 濃度調査

國分　祐司、中野　政尚、武石　稔

日本原子力研究開発機構　核燃料サイクル工学研究所　放射線管理部環境監視課

【はじめに】

東海再処理施設では、1977 年のホット試験開始以来、2007 年度までに約 1140 トンの使用済燃料が再処理された。排気、排水中の ^{129}I は、その大部分が除去されたのち大気および海洋へ管理放出されてきた。しかし、^{129}I は物理的半減期が 1570 万年と長く、微量であっても長期的な観点から土壌等を対象に分布および挙動を調査している。

【畑土中 ^{129}I の分析・測定方法】

調査は、過去の全方位の水準調査結果に基づき[1)]、主な風下方向である南西方向の畑土を対象とした。

畑土を 70℃で乾燥後、2mm メッシュの篩で分け、専用燃焼装置で燃焼し、燃焼ガス中のヨウ素を活性炭に捕集した。溶媒抽出法によりヨウ素を精製し、石英アンプル内に封入し、原子炉（JRR-3 又は JRR-4）で中性子を照射した。再度溶媒抽出法で照射試料を精製し、放射化された微量の臭素等を除去しヨウ化銀沈殿とした。最終的に、^{127}I（n,2n）^{126}I、^{129}I（n, γ）^{130}I 反応により生成した ^{126}I および ^{130}I を Ge 半導体検出器で測定し、^{127}I および ^{129}I 濃度を定量した。別に ICP-MS で測定した ^{127}I 濃度と中性子放射化分析による ^{127}I 濃度の比率により分析回収率を求め、^{129}I の値を補正した。

【畑土中 ^{129}I 濃度】

図 1 に 1982 年から 2007 年にかけての南西方向の畑土中 ^{129}I 濃度の経年変化を示す。図 1 より、顕著な増加は認められていないことがわかる。また、2007 年度の測定結果を表 1 に示す。表 1 から、南西 2km および 3km 地点が 12mBq／kg・乾と高く、1km、8km の順に低くなった。これらの濃度は、再処理施設からの放出量及び気象観測データを用いた拡散計算により、保守的に再現される[2)]。また濃度的には、過去の大気圏内核実験フォールアウトに起因する表土中 ^{137}Cs 濃度（原子力機構周辺 2007 年度：7.1～18Bq／kg・乾）と比べ数 100 分の 1 以下であり、環境安全上、問題はないレベルであった。

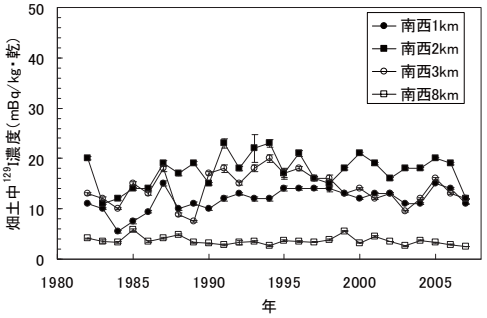


図 1　東海再処理施設周辺の畑土中 ^{129}I 濃度の経年変化

表 1　東海再処理施設周辺の畑土中 ^{129}I 濃度（2007 年度）

単位：mBq／kg・乾

南西1km	南西2km	南西3km	南西8km
11	12	12	2.5

参考文献

1）武石他，環境試料中の ^{127}I 及び ^{129}I の中性子放射化分析法，PNC TN843-85-39，（1985）

2）Nakano,M. et al, Proceeding of the International Symposium on Environmental Modeling Radioecology ,（2006）, 216-222.

原子炉：JRR-3　　装置：水力照射設備　　分野：放射化分析（環境科学）

4-2

研究テーマ：放射線防護・線量評価に関する研究
表　　題：水銀中生成トリチウムの性状解明

水銀中に核反応で生成されるトリチウムの化学形に対し水分濃度が及ぼす影響

真辺健太郎、横山須美
独立行政法人日本原子力研究開発機構　原子力基礎工学研究部門　放射線防護研究グループ

大強度陽子加速器施設（J-PARC）の物質・生命科学実験施設に設置される中性子源は、液体金属ターゲットに 3 GeV の陽子ビームを入射し核破砕反応を起こさせ、中性子を生成させる施設である。水銀ターゲットは、核破砕反応により大量に発生する熱を処理するための機器、陽子ビームの衝撃波による内圧の変化を緩衝するヘリウムガスを充填したサージタンク等を備えたターゲット台車内を循環する。核破砕反応で生成する多様な放射性核種は、アマルガム化して水銀とともに循環、あるいは沈澱または気化してサージタンクに貯蔵される。

水銀ターゲット中に生成する放射性核種のうち、放射能の約 6 割はトリチウムである。トリチウムは気化しやすいため空気中に浮遊し、内部被ばくを引き起こす可能性がある。したがって、トリチウムに対する線量評価が重要となるが、トリチウムはその化学形により摂取量当たりの線量が大きく異なる。そのため、トリチウムによる線量を見積もるには化学形に関する知見が不可欠である。

昨年度までに我々は、微量のリチウムを含む水銀試料を熱中性子照射し、水銀マトリクス中にホットなトリチウムを生成させ、トリチウム水（HTO）とトリチウムガス（HT）に分別し回収する方法を確立した [1]。今年度は、水銀に含まれる微量の水分がトリチウムの化学形割合に与える影響を調べた。

水分含有量を調整した水銀試料は、液相に僅かに溶存する気体量は気相の分圧に比例することを利用し、任意の水分圧に調整したガスを気相に導入し調整した。試料の熱中性子照射は、JRR-4 の中性子ビーム設備を使用した。ビーム孔前に試料と Co フラックスモニタを設置し、熱中性子モード I で 6 時間照射した。放射化した Co のγ線スペクトロメトリにより求めた熱中性子フラックスは約 1.6×10^9 cm^{-2} s^{-1} であった。生成したトリチウムは HTO と HT に分別、回収し、液体シンチレーションカウンタにより放射能を計測した。収率はほぼ 100%であった。

図 1 に、試料容器気相の水分圧（P_{water}）と、生成したトリチウムのうち HTO が占める割合（R_{HTO}）の関係を示す。R_{HTO} と P_{water} には正の相関があり、図 1 から関係式を得た。

$$R_{HTO}\,(\%) = 62 + 4.1 \times \ln(P_{water} / \mathrm{Pa}).$$

すなわち、この式を用いれば、サージタンクに導入するガスの水分圧から、水銀ターゲット中に生成するトリチウムの化学形の割合が推測できる。これにより、トリチウムの化学形を考慮した線量評価が可能になると考えられる。

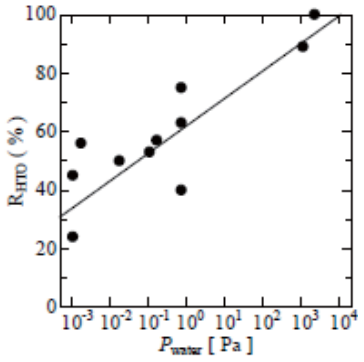


図 1　試料容器気相の水分圧と生成したトリチウムのうち HTO が占める割合の関係

参考文献

1) K. Manabe and S. Yokoyama, Appl. Radiat. Isotopes 66 (2008) 122-125.

使用原子炉：JRR-4　　装置名：中性子ビーム設備　　利用分野：放射化分析・その他

4-3

縞状炭酸塩堆積物（トゥファ）の層別元素分析

Analysis of element in annually layered terrestrial carbonates (Tufa)

九州大学 アイソトープ総合センター　杉原真司
九州大学　大学院理学府　森長一朗、広瀬篤志

（1）　はじめに

縞状炭酸塩堆積物（トゥファ）は、陸域で生成する炭酸塩堆積物であり、石灰岩地域の湧泉や河川、湖の溢流部に堤や滝を形成する。多孔質で、藻類・植物根などの痕跡をもち、細粒質の炭酸カルシウムがゆるく固結した堆積物である。水の蒸発、脱二酸化炭素により炭酸カルシウムで過飽和になった水から、シアノバクテリア（藍藻類）、緑藻類、蘚苔類による光合成によりさらに溶存二酸化炭素が消費されて過飽和が進行し、炭酸カルシウムが沈殿すると考えられている。そのためトゥファは、年輪のように縞状に発達する。縞には堆積当時の環境を保持している。このため、縞の数を計測することにより、絶対年代が推定可能であり、その縞に含有する元素分布を測定すれば、その当時の環境汚染物質等の降下の影響を知ることができる。今回、福岡県の石灰岩地区である平尾台で採取したトゥファについて、中性子放射化分析を適応し、元素分布を測定し、北九州地区における環境汚染の歴史を解明する。

栗崎らは、同試料を用いて、表流水とのイオン交換反応によって保持している大気汚染の指標となるSO_4^{2-}濃度の測定から、北九州地区における過去の大気汚染の変遷の復元を行うことができた。今回は、大気汚染物質等の環境情報を抽出するために、各元素濃度を測定した。

（2）　実験と方法

試料は、福岡県の平尾台で採取した。乾燥後、層別に分別し分析用試料とした。

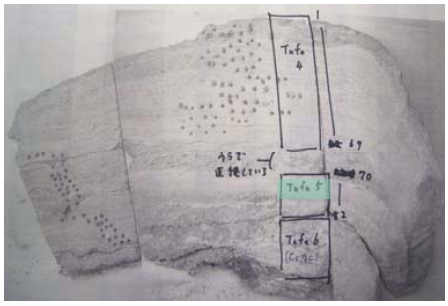


図１　トゥファ試料

照射は、JRR-4 気送管（10 秒照射、直後に測定）、S パイプ（3 時間照射、1 週間、1 ヶ月冷却後測定）で行った。試料約 30ｍｇをポリエチレン袋、約 20ｍｇを石英管に封入しそれぞれ照射した。比較標準は JB-1 を利用し、3 時間照射については、K0 法も適応した。

試料は、新しい部分（No. 1）から No. 82 まであり、年縞の計測が確かであれば約 80 年に相当する。

（3）　結果と考察

栗崎らによる、年縞から年代づけされたトゥファのSO_4^{2-}濃度の測定結果を図２に示す。

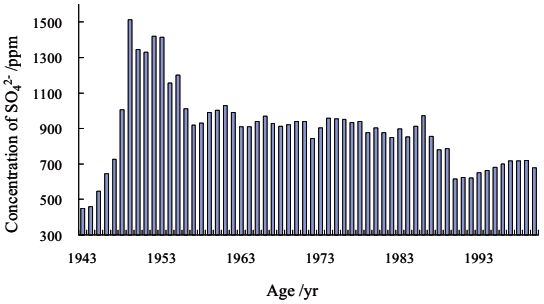


図２　トゥファ中のSO_4^{2-}濃度年変化

平尾台は、北九州市の南方約 20km にある。北九州市は、1946 年の八幡製鉄稼動により急速に工業化され環境汚染が発生している。図２からトゥファ中の硫酸イオン濃度も同時期から急激に上昇しているが、60 年代からはほぼ均一の濃度をしめし、90 年代では低下している。トゥファ表面の部分（約 10 年分）は、外観上も異なっている。しかし、硫酸イオン濃度から大気汚染の影響はこのようにトゥファ中に観測することができた。

今回、放射化分析で測定した元素は、Al, Ca, Ce, Co, Cr, Eu, Fe, Hf, La, Mn, Sc, Sm, Th, Ti, V, Lu, Mg, Na, Se, Yb, Ba, Cs, Ta, U である。全ての元素が、各試料に検出されたわけではないので、50%以上の試料で検出された、15 元素について、変動をみた。

JRR-4　気送管　Sパイプ　環境試料放射化分析

まず、Ca の分布であるが、トゥファの主成分である炭酸 Ca の濃度は、平均して 96%であり、Ca 濃度は約 3.8×10^5 ppm となる。

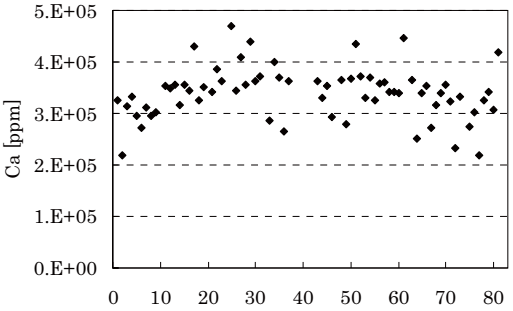


図３　トゥファ中の Ca 濃度の分布

Ca 濃度は、硫酸イオン濃度の変化と比べて、大きな変化はなく、トゥファ自体の生成条件に大きな変動はなかったことがわかる。

その他の元素では、表面から 10～12 番目にかけて大きな変動が見られる元素と、見られない元素に大きく大別できた。変動が見られる元素の例として、Al と Fe の濃度分布を図 4 に示す。

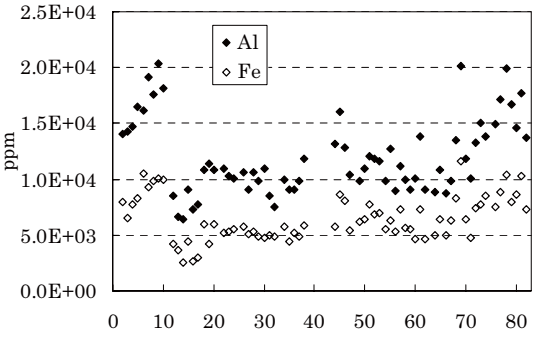


図４　トゥファ中の Al、Fe 濃度分布

表層 10 番目まで濃度が増加し、その後急激に減少してその後 70 番目まではほぼ均一、更にその後上昇する。同様の変動を示す元素は、Ce, Co, Cr, La, Mn, Sc, Sm, Th, Ti, V, Lu であった。表層の変化は硫酸イオン濃度でも同様の変化を示し、外観上も表面は若干色が異なるため、比較的新しい（10 年程度）部分はトゥファに取り込まれる粘土鉱物等の組成が異なり何らかの環境変動が起こったことが考えられる。しかし、この年代に相当する平尾台におけるイベントについてははっきりしない。更なる検索が必要である。古い部分の濃度上昇についても、原因はまだわからない。

採取地点は、通常人が出入りする所ではないので、大気からの降下量の変動か、周辺の開発（植林等）による小河川への流入の変動影響かが考えられる。

次に濃度の変動があまりない元素は、Mg, Na, Eu, Hf　であり、前 2 元素の濃度変化を図５に示す。

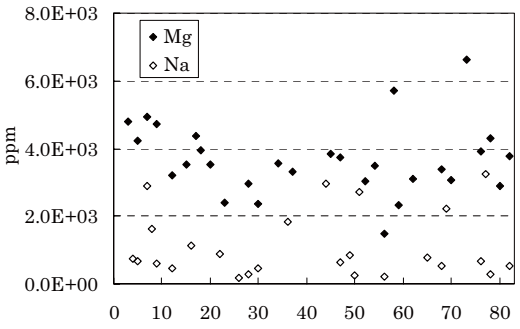


図５　トゥファ中の Mg, Na 濃度分布

図 4 に見られたような変動はない。

定量した元素（Ca を除く）の平均濃度を計算すると、多い方から Al(1.2%), Mg(0.4%),Na(0.06%), Fe(0.05%)となり残りは、数十 ppm である。これらの 4 元素で変動が異なることから、2 種類の粘土鉱物の組成が異なったのではないかと考えれる。

さらに、大気汚染物質等の環境情報抽出については、周辺の環境変動との選別を行う必要があるため現状では断定できない。

周辺土壌の影響を評価するために、トゥファ生成場所の上流地点で、土壌コアを 2 本採取し、2cm ごとに切断し乾燥後、Ge 半導体検出器でガンマ線を測定した。表面土壌コアにおける ^{137}Cs と ^{210}Pb の深度分布を図６、７に示す。

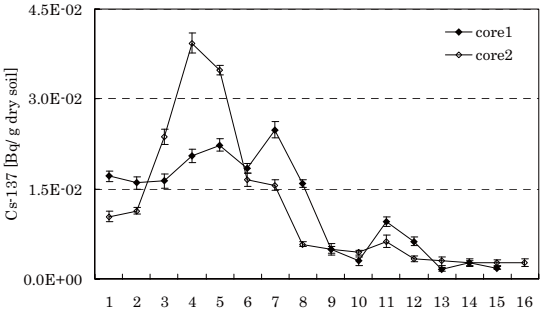


図６　土壌コア中の ^{137}Cs 深度分布

コア１では、表層が少し浸食・撹乱されている

が、コア２では、60 年代前半と思われる ^{137}Cs のピークが残っている。このように明らかに上層約 20cm に大気降下物由来放射性核種の蓄積が見られるので、トゥファ生成時にこれらの大気降下物が取り込まれ保存されていることが確認できた。

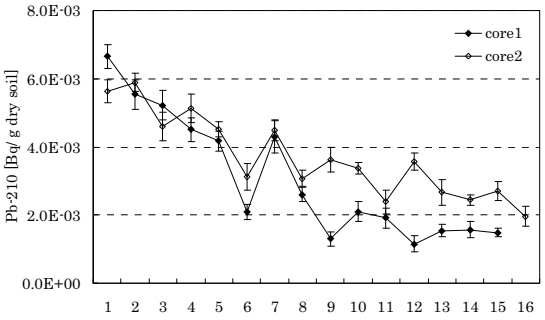


図７　土壌コア中の ^{210}Pb 深度分布

^{210}Pb 深度分布においても、約 20cm まで徐々に減少し浸食・撹乱の大きな変化は観測されない。

今回採取した、トゥファ試料について、放射化分析によって元素分析を行った。硫酸イオン濃度に観測されたような変動を観測することができたが、その原因については、大気汚染の影響なのか周辺環境の変動なのかを、明らかにすることは出来なかった。しかし、元素濃度の分布パターンが異なる元素が存在し、トゥファの生成環境の変化が見られることがわかり、その原因について更なる調査が必要である。

大気汚染だけでなく、周辺環境の変動を推察する手段としては、多元素を分析し総合的に判断する手法は有意義であり、平尾台の開発の歴史等と照合して、変動の原因を探ることが可能である。

（４） 参考文献

栗崎弘輔：Extraction of environmental information from annually layered terrestrial carbonates. 平成 15 年度九州大学大学院理学府修士論文

4-4

「工場跡地における土壌汚染植物浄化法の検討」

Studies on Phytoremediation of Soil Pollutions at the trace of a factory

川西幸子(武蔵野学院大学)、野川憲夫、巻出義紘(東京大学アイソトープ総合センター)
澤幡浩之、川手稔、石本光憲(東京大学大学院工学系研究科原子力専攻共同利用管理本部)
松江秀明（原子力機構原子力科学研究所量子ビーム応用研究部門中性子産業利用技術研究ユニット）

１．研究の目的と意義

今、全国で土壌汚染の報告が相次ぎ、その６割が環境基準を越えている。汚染対策には２法律、農地に対しての農用地土壌汚染防止法、市街地を対象にした土壌汚染対策法がある。しかし、放置化、除去した汚染土の行方など重要な問題点が上がっている。土壌に化学試薬などを加えずに、汚染元素をリサイクルできる形で回収する方式として植物による抽出法を検討してきた。

２．実験概要

工場跡地に隣接する土壌を入手し、その均一化した試料について、アンチモン、亜鉛、鉄、カドミウム汚染量を機器中性子放射化分析（INAA）および即発γ線分析（PGA)により定量した。これらの元素を効率よく吸収する植物を検討した。先ず水耕栽培で２種の植物,セイヨウキズタ Hedera helix Linn.(ウコギ科)およびジャノヒゲ Ophiopogon japonicus Ker-Gawl.(ユリ科)が種々の植物を検討した結果から選ばれた。次に両者の植物の土壌栽培による吸収力を検討した。

2.1.工場跡地近傍土壌および予備実験土壌

工場跡地の敷地境界から８m道路を隔てた外部の土地で、深さ０－1m 前後掘り返した土壌を入手し、石、瓦礫等を除き、乾燥粉末化し汚染標準土壌試料とした。植物のスクリーニングには市販園芸土壌を用い、汚染元素を添加して実験した。

2.2. 水耕栽培実験

キズタなど種々の植物の幼苗をポットで入手し、根を出来るだけ傷つけないように水中で株ごとに分離し洗浄した。各添加元素水溶液は NaOH,HCl で中和後、植物を入れ、戸外で水耕栽培をおこなった。

2.3. 土壌栽培実験

市販園芸用土或は汚染土壌に試薬溶液,Sb,ZnCd（予め NaOH,HCl で中和した溶液）を加えた後、更に水を充分に加えて水層を保つ状態で生育させた。

2.4. 栽培後の分析試料調製

栽培後の植物は水洗後、更に精製水を入れたビーカーに入れ超音波洗浄機で洗浄し、ペーパータオルに土がつかなくなるまで、何回か洗浄を繰り返し、ペーパータオルにくるみ、60℃の乾燥機で乾燥した。乾燥植物を地上部と地下部に分け、一部地下部の塊根(麦門冬)を分離し、セラミック製小型粉砕機にかけ粉末化した。

2.5. 中性子放射化分析条件

各試料は厚さ 0.05mm ポリ袋に入れてシールし、東洋ろ紙 51A を挟み、さらに同ポリ袋に入れてシールし、INAA 分析試料とした。

INAA は日本原子力研究所東海研究所ＪＲＲ－３原子炉、照射孔：ＰＮ－1&2, 照射位置：下段、5.2&4.7×1017／cm²・sec, 20 分間照射、また、ＪＲＲ－４原子炉、簡易照射筒Ｔパイプ、5.3&4.3×1017／cm²・sec, 20 分間照射,10 日後より測定を開始した。測定は東京大学アイソトープ総合センターで、MODEL SC100L 放射能測定用遮蔽体付オートサンプルチェンジャー(東洋メディック)を用いて, 10,000sec で測定した。 PGA は粉末試料約 400mg を 13mmφのペレットにし、FEP フィルムに封入して、テフロンフレームに吊り下げて、PGA 照射装置に設置する。JRR－3M 即発γ線分析装置(Ｔ１―4―1)で中性子ビーム：冷中性子、測定時間 2000 秒、Cd は 558KeV のピーク面積を標準物質と比較定量した。

研究施設と装置名：JRR-3,JRR-4 の INAA, JRR－3M 即発γ線分析装置(T1―4―1)　　研究分野：環境科学　.

3．結果と考察

実験結果を表１にまとめる。

表１．中性子放射化分析及び即発γ線分析（カドミウムのみ）による測定値［相乗平均値］

1.1.汚染土壌の分析値

	アンチモン		亜鉛		カドミウム	
	濃度（ppm）	分配比（%）	濃度（ppm）	分配比（%）	濃度（ppm）	分配比（%）
工場付近汚染土	49		999		15.5	
同上HCl抽出部	21	16	3,099	83		
同上抽出残部	39	84	201	17		

1.2.水耕栽培及び土壌栽培による植物の元素抽出量

	植物種	栽培条件	部位	アンチモン 濃度（ppm）	アンチモン 分配比（%）	亜鉛 濃度（ppm）	亜鉛 分配比（%）	カドミウム 濃度（ppm）	カドミウム 分配比（%）
水耕栽培	セイヨウキヅタ	各2.5mg/pot	茎葉部	5	1	104	10		
			根部	489	30	340	28		
			水残部	577	69	2,126	62		
	ジャノヒゲ	Sb,Zn 各2.5mg/pot	茎葉部	20	2	33	48		
			塊根部	201	8	11	7		
			根部	427	41	20	26		
			水残部	3,346	49	572	19		
土壌栽培	セイヨウキヅタ	汚染土＋Sb,Zn 各2.5mg/pot	茎葉部	5	2	208	10		
			根部	34	1	126	28		
			土残部	67	97	208	62		
		汚染土 magnet処理後栽培	magnet吸着部	56	14	930	12		
			magnet洗液部	106	1	1,619	1		
			根部	2	2	72	5		
			土残部	53	83	915	82		
	ジャノヒゲ	汚染土＋Sb,Zn,Cd 各2.5mg/pot	茎葉部	2	1	83	2		
			根部	36	13	166	1	81.3	
			土残部＊	17	86	935	97		
		＊土残部	土残部HCl部	16	33	1817	91		
			土残部HCl残部	18	67	87	9		

工場付近土壌はINAAにより、アンチモン（50ppm）、亜鉛（1,000ppm）、PGAによりカドミウム（15.5ppm）の汚染を確認した。通常、土壌中のアンチモン定量値は１N塩酸抽出による分析値である。従って、1N塩酸で抽出すると、アンチモンは21ppm 16%（残部を含めた含量を100として）、亜鉛は3,000ppm 、83%（同左）となった。

これらの植物で水耕栽培の結果はアンチモンで、セイヨウキズタ根部490ppm収量30%、ジャノヒゲ根部430ppm植物全体で５割回収、亜鉛の場合では植物全体で、セイヨウキズタ４割、ジャノヒゲで８割回収されるとの結果が得られた。因みにジャノヒゲの塊根部は生薬麦門冬として使用されるが、この部分のアンチモン、亜鉛の吸収量は8%で低いことがわかった。

これらの植物で土壌栽培し、吸収量を残部と比較すると、セイヨウキズタでアンチモン3%、亜鉛40%弱、ジャノヒゲでアンチモン14%、亜鉛3%となった。ジャノヒゲのアンチモン吸収は塩酸による抽出16%に比較し、一応アンチモンの浄化法として使用できると思われる。しかし、ジャノヒゲ栽培後の土壌を１N塩酸抽出すると残部のアンチモン３割、亜鉛９割が抽出された。

また、汚染土壌をマグネットで処理し、吸着部及び洗液部を集め、INAAで定量すると、アンチモン15%、亜鉛13%回収できる。その土壌で植物を栽培すると、予想通り植物の吸収量はアンチモン、亜鉛共2～5%と低くなった。

これらの結果は土壌中における鉄とアンチモン、亜鉛の錯化合物の挙動と考えられる。土壌中に鉄粉を撒き、マグネットで回収する方法が有機塩素化合物の分解浄化[1)]と共に汚染元素の除去に有効であることが示唆された。

一方、カドミウムについてはPGAにより、ジャノヒゲの根部に81.3ppmの蓄積が見られた。ジャノヒゲの根部と汚染土壌のPGAのスペクトルを図2に

示す。珪素、アルミニウム、チタン、炭素、クロム、サマリウムなどのシグナルがほぼ消え、カルシウム、鉄、カリウム、塩素、ホウ素、ナトリウムがカドミウムと共存していることがわかる。

結果に対する評価はこれから本格的研究に入る段階であるため低く継続出来ないのが残念である。

1）戸田工業 KK：朝日新聞 2008.4.18 朝刊

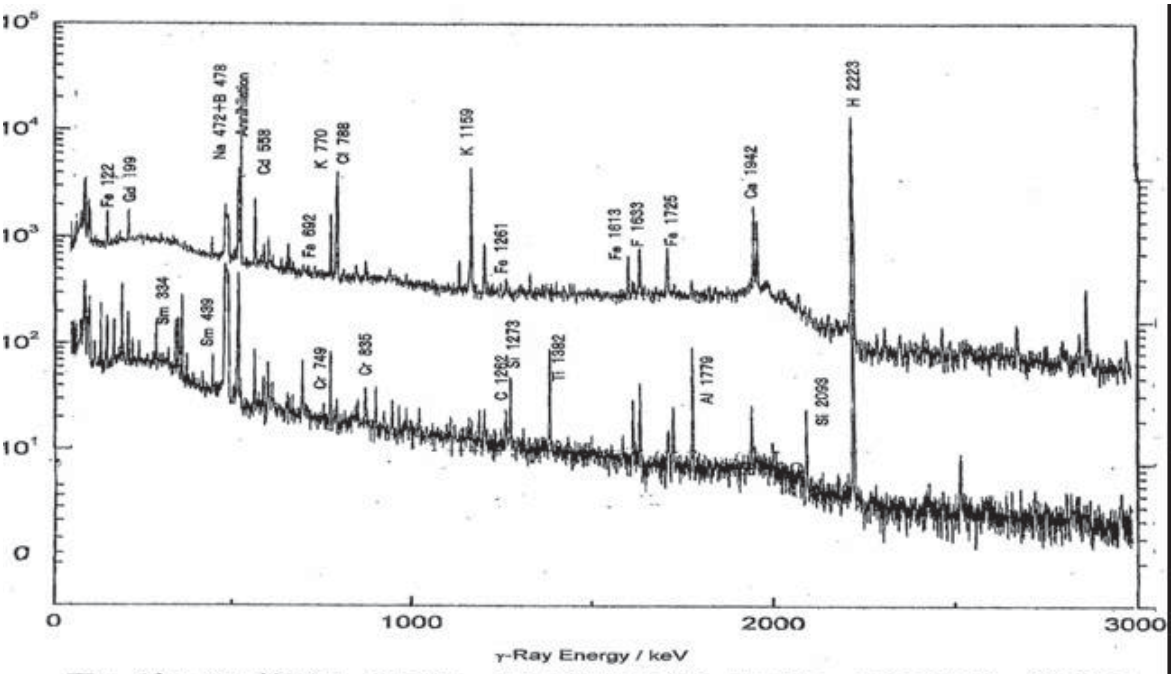


図1．ジャノヒゲ根（上、左スケール）と汚染土（下、右スケール）の即発γ線分析

４．成果の公表

川西幸子、野川憲夫、澤幡浩之、野村貴美「環境に関わるヘデラ属植物について（その２）セイヨウキズタにおけるアンチモンおよび亜鉛集積性」武蔵野学院大学研究紀要　第３輯 p.37－43（2006）

4-5

中子性子放射化分析による九州地方の火山活動を含む物質循環のキャラクタライゼーション

Instrumental Neutron Activation Analyses of volcanic rocks from Kyushu island:
Characterization of Material Circulation through Volcanism

熊本大学 大学院自然科学研究科　長谷中 利昭，三好 雅也，奈須 隆志，
下野 まどか，枝村 拓也，谷田 康介，関口 悠子，森永 麻衣子，高江 友佳，上村 伸樹

1. はじめに

火山岩の微量元素組成は，マグマの起源物質について重要な情報を与えてくれる．特に海洋プレートの沈み込みが関与した島弧，大陸縁の火山岩と，沈み込みが関与しない海洋島や大陸内部に産する火山岩は，さまざまな微量元素のプロットにおいて明瞭に異なる組成を示し，マグマの成因の違いを反映していることが知られている．

本研究地域である西南日本弧には，若い海洋プレートが島弧の下にあるマントルに沈み込んでおり，古い海洋プレートが沈み込む東北日本弧などの成熟した島弧とは異なる物質循環が起こっていることが考えられている．これまでの研究で，島弧的な火山岩，島弧的な特徴が非常に少ない火山岩，大陸内部に見られるようなアルカリ玄武岩，海洋プレートが直接成因に関わったと考えられるアダカイトや高マグネシウム安山岩など多様なマグマが活動していることが分かってきた．微量元素を使ってマグマの成因の違いを考える上で非常に興味あるフィールドである．

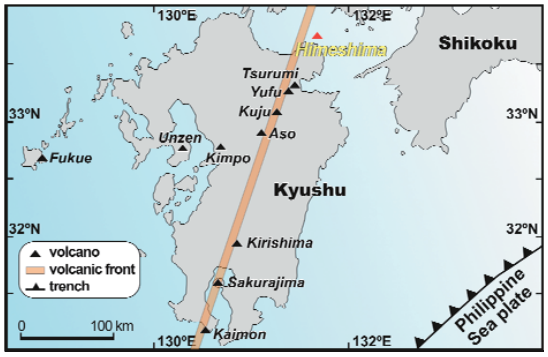


Fig. 1 九州の主な第四紀火山の分布

これまで，九州地方に分布する火山岩の化学組成，特に微量元素について我々のグループは精力的に調査，分析してきたが， 今回は九州の火山フロント最北端に位置する姫島火山噴出物の分析結果を報告する (Fig. 1).

姫島火山は，約 30～10 万年前に活動した第四紀火山であり，複数の溶岩ドームからなる．火山直下には若いフィリピン海プレート（四国海盆：約 150 万年前）が沈み込んでいると考えられている（伊藤，1989）. 本論では姫島火山から採集した火山岩数試料に対して，偏光顕微鏡観察，主成分，微量元素組成分析を行った結果を報告する．

姫島火山の地質や岩石については伊藤（1989，1990）が詳しい報告をしているが，柴田ら（2005）は，マグマの特異な組成に注目し，同位体組成を報告した姫島およびその近くの由布岳，鶴見岳火山のマグマが，一般的な島弧マグマの成因とは異なるアダカイトである可能性を指摘した．典型的な島弧においては，沈み込む海洋プレートに含まれる含水鉱物が高圧で分解して生じた流体が，島弧下マントルに付加し，島弧的な組成のマグマが生じるという説が広く受け入れられている．これに対して姫島，由布岳，鶴見岳に見られるマグマの組成は，一般的な島弧マグマ成因の仮説では説明できず，沈み込む海洋プレート自体が溶融して生じたマグマが関与したアダカイトであるというものである．我々は放射化分析を含めた微量元素の化学分析結果から，この仮説を検証した．

2. 分析試料，分析手法

放射化分析用試料は次の手順によって準備した．

（1）火山岩試料を粉末化し，それぞれ約 60 mg を

JRR-3M PN-1, JRR-4 T パイプ　　**地球科学試料・放射化分析**

秤量.
（2）粉末試料をポリエチレン・バイアル（10mmφ，20mm L）に挿入.
（3）ハンダゴテでバイアルの蓋を融封.
（4）バイアルをポリエチレン袋に入れてシーラーで封入.

放射化分析の実験条件および手順は次の通りである．JRR-4 原子炉 T パイプで 100kW 出力の下，6 時間照射した．JRR-4 号炉が使えない時は，JRR-3 号炉の PN-1 気送管で 20 分間照射した．照射一週間後に試料カプセルを開封，ポリエチレン袋を交換し，大学開放研究室の実験利用棟 113, 115 実験室のガンマ線検出器（ASC-20）を用いて短寿命核種のガンマ線測定を行った．また，一ヵ月後には長寿命核種のガンマ線測定を行った．

主成分元素といくつかの微量元素含有量は，同じ岩石粉末試料に四ホウ酸リチウムの融剤を加えて，ビード・サンプラーでガラスビードを作成し，北九州自然史・歴史博物館の蛍光 X 線分析装置（フィリップス社製 PANalytical MagiX PRO）を用いて分析した.

3. 分析結果・考察

姫島火山岩類は，斑晶鉱物組合せによって以下の 2 つのグループに大別されることが分かった.

1）普通角閃石 (Hb)＋斜長石 (Pl) を含むデイサイトおよび流紋岩.

2）ザクロ石 (Grt) 微斑晶を含む流紋岩.

グループ 1 はグループ 2 に比べて Sr, Zr に著しく富むことが特徴である (Fig. 2a).

グループ 1 は Sr/Y 比が大きく，アダカイトの領域に入るが，ざくろ石を微斑晶に含むグループ 2 火山岩アダカイトの領域には入らない (Fig. 2b).

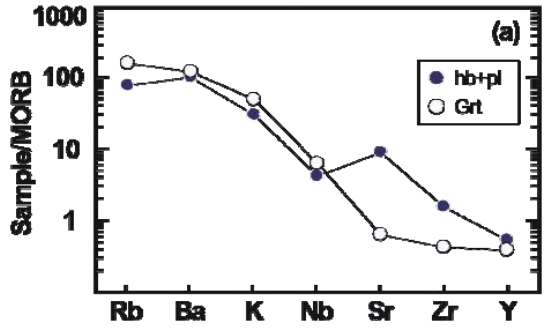


Fig. 2 (a) 姫島火山岩類の液相濃集元素パターン (平均値を n-MORB の値で規格化). ※ n-MORB の値は Sun and McDonough (1989) を引用した.

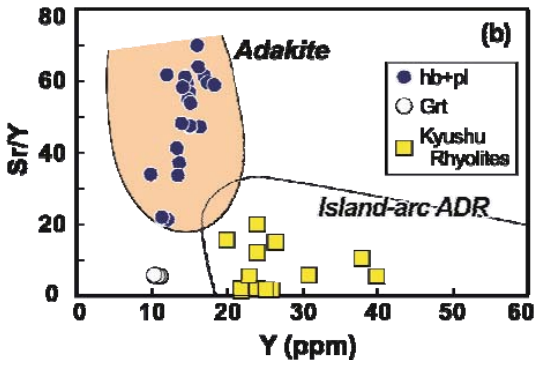


Fig. 2 (b) 姫島火山岩類の Y-Sr/Y 図 (Defant and Drummond, 1990).

姫島は黒曜石が産することで考古学的にも注目されているが，図 2（b）においては，九州各他の火山から採集した黒曜石（流紋岩類）の分析値も合わせてプロットした．姫島の流紋岩のみが特異な組成を示すことが明瞭である.

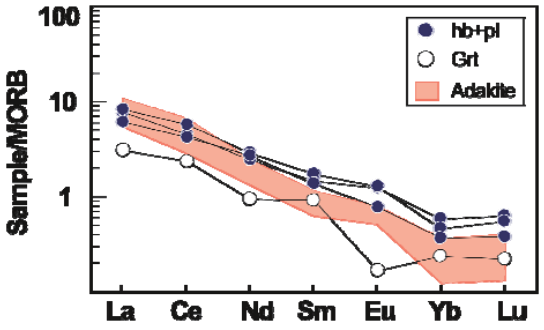


Fig. 3 姫島火山岩類の希土類元素組成 (n-MORB の値で規格化). ※ n-MORB の値は Sun and McDonough (1989) を引用. アダカイトの化学組成は Wen et al. (2008) を引用した.

希土類元素組成については，グループ 1 の流紋岩，デイサイトがグループ 2 の流紋岩に比べて軽希土，重希土の両方に富むことがわかる (Fig. 3). 特にヨーロッピウムの含有量は両グループ間で大きく異なる (グループ 1＞＞2).

世界各地から報告されたアダカイトの組成と比較すると，グループ 1 の流紋岩，デイサイトはアダカイト報告値とほぼ同等の軽希土類元素の含有量を示すが，重希土類元素に関してはアダカイト報告値と比べてやや富む傾向がある．一方，グループ 2 の流紋岩はアダカイトの報告値に比べて軽希土類元素が乏しいことがわかる (Fig. 3).

4. まとめ

（1）姫島火山岩類のうち，グループ 1 の流紋岩，デイサイトは記載岩石学的特徴 (普通角閃石＋斜長石)，微量元素含有量ともに Defant and Drummond (1990) が定義したアダカイトの特徴を示している．一方，グループ 2 の流紋岩は記載岩石学的特徴 (ザクロ石を含むこと), 微量元素含有量ともにアダカイトの特徴を示さないことがわかった．

（2）両グループの微量元素パターンが大きく異なることから，両者のマグマの起源物質化学組成は異なる可能性がある．グループ 1 がアダカイト組成を示すことは，姫島直下に沈み込んだフィリピン海プレート自体が部分溶融した可能性を示唆している．

（3）両グループのマグマが同じ海洋地殻の部分溶融によって生成されたと仮定すると，グループ 2 がグループ 1 に比べて Sr, Zr や軽希土類元素（特に Eu）に乏しいことは，グループ 1 マグマ生成後の Sr, Zr, LREE に枯渇した海洋地殻の部分溶融によってマグマ 2 が生成した可能性を示唆している．両者の成因関係については今後の課題である．

（4）以上に示したとおり，本研究で得られた結果は，九州における火成活動による物質循環にはいくつかの異なったパターンがあることを示した．

謝辞

中性子放射化分析を行う上で共同利用実験計画，試料準備，測定器利用などにおいて澤幡浩之氏，川手稔氏，石本光憲氏をはじめとする大学開放研究室の皆様には実験遂行にあたって多大のアドバイス，ご援助を受けました．皆様のサポートなくしては本研究の遂行は難しかったと思います．深く感謝いたします．また分析方法に関して立正大学の福岡孝昭教授にご教示いただきました．合わせて感謝いたします．

5. 引用文献

伊藤順一，姫島火山群の地質と火山活動，火山 第 2 集，34，1−17，1989.

伊藤順一, 姫島火山群の岩石学, 岩鉱, 85, 541-558, 1990.

柴田 知之，伊藤 順一，竹村 恵二，姫島火山群第四紀火山岩類の Sr・Nd・Pb 同位体組成，地球惑星科学関連学会，2005 年合同大会予稿集，J030-003，2005.

Sun, S.S. and McDonough, W.F., Chemical and isotopic systematics of oceanic basalts: implications for mantle composition and processes. In: Saunders, A.D., Norry, M.D. (Eds.), Magmatism in the Ocean Basins. Geol. Soc. London. Spec. Publ. 42, 315-345, 1989.

Defant, M.J., Drummond, M.S., Derivation of some modern arc magmas by melting of young subducted lithosphere. Nature 347, 662-665, 1990.

Wen, D.-R., Chung, S.L., Song, B., Iizuka, Y., Yang, H.-J., Liu, J. Ji, D. and Gallet, S., Late Cretaceous Gangdese intrusions of adakitic geochemical characteristic, SE Tibet: petrogenesis and tectonic implications, Lithos, 105, 1-11, 2008.

６．研究成果の公表

学会誌

Miyoshi, M., Shimono, M., Hasenaka, T., Sano, T., Fukuoka, T., Determination of boron contents in volcanic rocks by prompt-gamma ray analysis: an application to magma genesis in Kyushu island, SW-Japan. Journal of Radioanalytical and Nuclear Chemistry, 278, 343-347, 2008.

Miyoshi, M., Nasu, T., Tajima, T., Kido, M., Mori, Y., Hasenaka, T., Shibuya, H., Nagao, K., K-Ar ages of high-magnesian andesite lavas from northern Kyushu, Japan. Journal of Mineralogical and Petrological Sciences, 103, 183-191, 2008.

Miyoshi, M., Fukuoka, T., Sano, T. and Hasenaka, T., Subduction influence of Philippine Sea plate on the mantle beneath northern Kyushu, SW Japan: an examination of Boron contents in basaltic rocks. Journal of Volcanology and Geothermal Research, 171, 73-87, 2008.

Sano T, T. Hasenaka, H. Sawahata, T. Fukuoka, Determination of Ti, K, Sm, and Gd Values in Geological Survey of Japan Reference Materials by Prompt Gamma Neutron Activation Analysis, Geostandards and Geoanalytical Research, 30, 31-36, 2006.

三好雅也，長谷中利昭，森康，山下茂，阿蘇カルデラ西部に分布する栃ノ木溶岩中にみられる組成不均質とその成因．岩石鉱物科学，日本岩石鉱物鉱床学会，36，15-29，2007.

三好雅也，長谷中利昭，佐野貴司，阿蘇カルデラ形成後に活動した多様なマグマとそれらの成因関係について．火山，日本火山学会，50，269-283，2005.

学会発表

Miyoshi, M., Shimono, M., Hasenaka, T., Sano, T. and Fukuoka, T., Subduction influence of Philippine Sea plate on the mantle beneath Kyushu, SW Japan: An examination of boron contents in basaltic rocks. IAVCEI General Assembly, Reykjavik, Iceland, 2008.

Miyoshi, M., Shimono, M., Hasenaka, T., Sano, T. and

Fukuoka, T., Subduction influence of Philippine Sea plate on the mantle beneath Kyushu, SW Japan: An examination of boron contents in basaltic rocks. 18th Goldschmidt Conference, Vancouver, Canada, 2008.

新正裕尚，折橋裕二，角井朝昭，福岡孝昭，長谷中利昭，佐野貴司，瀬戸内火山岩類のホウ素含有量，地球惑星科学関連学会，2008 年合同大会，千葉県幕張メッセ，2008.

関口悠子，長谷中利昭，長岡信治，姶良カルデラ形成に至る前駆的なマグマ活動:マグマ混合の可能性，日本火山学会秋季大会，岩手大学，2008.

Miyoshi, M., Shimono, M., Hasenaka, T., Sano, T., Fukuoka, T., Furukawa, K., and Shinmura, T., The evolving fluid flux from the subducting plate beneath Aso area: evidence from Boron in volcanic products. Cities on Volcanoes 5, Shimabara, Japan, 2007.

Shimono, M., Miyoshi, T., Fukuoka, T., M., Sano, T. and Hasenaka, T., Along-arc variation of Boron data: the influence of Philippine Sea plate on the composition of mantle beneath Kyushu, SW Japan arc. Cities on Volcanoes 5, Shimabara, Japan, 2007.

Hasenaka, T., Morinaga, M. and Miyoshi, M., Kusasenrigahama pumice cone from Aso volcano, Kyushu, Japan: Petrological characteristics of pumice and coeval volcanic products representing one of the largest eruption after caldera-formation, Cities on Volcanoes 5, Shimabara, Japan, 2007.

関口悠子，長谷中利昭，長岡信治，森康，姶良カルデラにおける 100-29ka のマグマ供給システムの変遷，火山都市国際会議 5，島原，2007.

Miyoshi, M., Shimono, M., Hasenaka, T., Sano, T. and Fukuoka, T., Determination of boron contents in volcanic rocks by prompt-gamma ray analysis: an application to magma genesis in Kyushu island, SW-Japan. 12th International Conference on Modern Trends in Activation Analysis (MTAA-12), Tokyo, Japan, 2007.

Miyoshi, M., Shimono, M., Hasenaka, T., Sano, T., Fukuoka, T. and Shinmura, T., Temporal changes of the subduction components in volcanic products from Aso area, SW Japan. 17th Goldschmidt Conference, Koln, Germany, 2007.

Shimono, M., Miyoshi, M., Fukuoka, T., Sano, T. and Hasenaka, T., The influence of Philippine Sea plate on the composition of mantle beneath Kyushu, SW Japan arc: Along-arc variation of B data. 17th Goldschmidt Conference (Koln, Germany, 2007.

Sekiguchi, Y., Hasenaka, T., Nagaoka, S. and Mori, Y., Precursory magma activities leading to Aira caldera-forming eruptions in southern kyushu, Japan, American Geophysical Union, Fall meeting, San Francisco, 2007.

三好雅也, 下野まどか, 長谷中利昭, 佐野貴司, 福岡孝昭, 北部九州玄武岩類中のホウ素含有量の時間的・空間的変化．日本鉱物科学会，2007 年度年会, 東京大学, 2007.

関口悠子，長谷中利昭，長岡信治，森康，姶良カルデラにおける 100-29ka の噴出物の岩石学的特徴，地球惑星科学関連学会, 2007 年合同大会, 千葉県幕張メッセ，2007.

Miyoshi, M., Shimono, M., Fukuoka, T., Sano, T., Hasenaka, T., Slab influence of hot Philippine Sea plate on the subarc mantle: An examination of Boron contents in basaltic rocks from northern Kyushu, SW Japan, 16th Goldschmidt conference, Melbourne, Australia, 2006.

Shimono, M., Miyoshi, M., Fukuoka, T., Sano, T. and Hasenaka, T., Temporal and spatial influence of Philippine Sea plate on the composition of basaltic rocks from southern Kyushu, SW Japan arc -- a study from boron analysis, 16th Goldschmidt conference, Melbourne, Australia, 2006.

三好雅也, 下野まどか, 福岡孝昭, 佐野貴司, 長谷中利昭, フィリピン海プレートの沈み込みが北部九州のソースマントルに与えた影響－火山岩のホウ素含有量を用いた検討－．日本火山学会， 2006 年度秋季大会，熊本県阿蘇，2006.

下野まどか, 三好雅也, 福岡孝昭, 佐野貴司, 長谷中利昭, 2006．九州南部に産する火山岩起源物質中のホウ素含有量の空間的・時間的変化．日本火山学会，2006 年度秋季大会，熊本県阿蘇，2006.

Miyoshi, M., Shimono, M., Fukuoka, T., Sano, T. and Hasenaka, T., Subduction metasomatism beneath northern Kyushu: an examination from spatial and temporal variations of boron contents in basalts. 地球惑星科学関連学会, 2006 年合同大会, 千葉県幕張メッセ, 2006.

下野まどか, 三好雅也, 福岡孝昭, 佐野貴司, 長谷中利昭, 九州南部に産する火山岩起源物質へのフィリピン海プレートの寄与について～ホウ素を用いた研究，地球惑星科学関連学会，2006 年合同大会，千葉県幕張メッセ，2006.

Miyoshi, M., Shimono, M., Fukuoka, T., Sano, T. and Hasenaka, T., Spatial and temporal variations of Boron contents of basaltic rocks from northern Kyushu, SW Japan arc. American Geophysical Union, fall meeting, San Francisco, USA, 2005.

高江友佳，奈須隆志，長谷中利昭，開聞岳火山溶岩組成の年代変化から推定したマグマ溜まりでの過程，地球惑星科学関連学会，2005 年合同大会，千葉県幕張，2005.

4-6

酸性温泉周辺地域におけるヒ素動態調査

Origin and fate of arsenic in volcanic hot spring area

木川田喜一，大井隆夫，早津岳宏，佐野淳子，井上綾，小田幸平，藤宏之，大野有希子，
京免賢一，佐藤直子 （上智大学理工学部化学科）

Yoshikazu Kikawada, Takao Oi, Takehiro Hyatsu, Junko Sano, Aya Inoue, Kohei Oda,
Hiroyuki Fuji, Yukiko Ohno, Ken-ichi Kyomen, Naoko Sato
(Department of Chemistry, Faculty of Science and Technology, Sophia University)

１．研究の背景と目的

ヒ素は毒性を有する元素として社会的に広く知られているが，実際には特別な元素ではなく，工業的に古くから用いられ，現在においても半導体材料として利用されるなど，現代社会には欠くことのできない元素である．火山地域にはごく普通にヒ素が存在しており，火山性温泉の中にも相当量のヒ素を含むものが存在する．たとえば，秋田県の玉川温泉では，その源泉水が流下する河川において，ヒ素化合物を含む沈殿物が認められている[1].

我々はこれまでの研究で，群馬県草津温泉地域の万代鉱源泉が，1990 年代後半以降，10 ppm 前後の高いヒ素濃度にあり，その年間ヒ素供給量が 50 トン近くにも達することを明らかにした[2]. この大量の源泉起源のヒ素は，最終的には地域内の河川へと流入し，域外へと運搬される．草津温泉の源泉はそのすべてが強酸性であることから，それらが流入する河川は酸性河川であり，今日，国土交通省による河川中和事業が行われている．したがって河川水の中和がこの地域のヒ素の挙動に大きな影響を与えていることは間違いない．本研究では，このような背景のもと，草津温泉地域の源泉起源のヒ素が環境中をどのように移動，運搬されているのかを可能な限り定量的に求め，当該地域におけるヒ素の動態を明らかにすることを目的とした．

２．草津温泉地域の概要

草津温泉は群馬県北西部，草津白根火山の東麓に位置する，日本を代表する温泉のひとつである．地域内には多くの源泉が湧出するが，そのいずれもが強酸性である．地域内の代表的源泉とその pH を図 1 に示す．この中で，万代鉱源泉(BND)と草津湯畑源泉(KYB)の 2 源泉により，草津温泉の温泉街で利用される源泉水のほとんどが占められている．

地域内で最大の湧出量を有する万代鉱源泉は，1970 年に硫黄鉱山の掘削中に坑道内より湧出を開始した比較的新しい源泉である．万代鉱源泉の源泉水は引湯パイプにより温泉街に供給されるが，未利用源泉水の一部は，源泉湧出口近くに設けられた放出池，ならびに域内の河川へ直接放出されている[3].

草津温泉が位置する草津白根山東麓には，湯川水系に属する 3 つの河川，「大沢川」，「谷沢川」，

JRR-3 PN-1, PN-2 ; JRR-4 T-pipe, S-pipe,　地球化学的試料放射化分析

「湯川」が存在し(図 1)，そのいずれもが強酸性の温泉水ならびに湧水の流入により酸性の河川となっている．この中で湯川は，万代鉱源泉，草津湯畑源泉に加え，温泉街に湧出する小規模な源泉からの未利用源泉水を集水し，さらには温泉街での利用後の廃湯をも併せて草津温泉の温泉街中心部を流れている．湯川水系では国土交通省による河川中和事業が行われており，3 河川のすべてにおいて石灰乳液の中和剤が投入されている．中和剤を投入されたあとの 3 河川は，中和沈殿物の捕集と中和の促進を目的として作られた品木ダムにおいて合流する．品木ダムからは送水管を通して湯川発電所に送られ，白砂川に合流する．白砂川は吾妻川に合流し，最終的には利根川へと繋がっている．

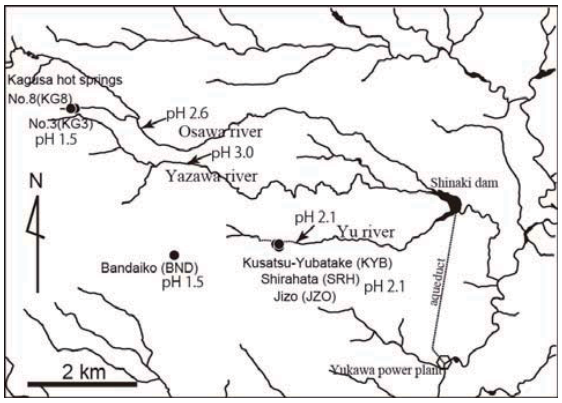


図 1 草津温泉地域の源泉水と河川水の pH

●は地域内の主要源泉を示す.

3．試料の採取と分析

3.1 温泉水ならびに河川水試料

上智大学理工学部化学科に保存されている，1964 年以降の湯川の中和前試料水を分析に供した．前述の通り，湯川は万代鉱源泉水が流入する河川である．さらに，草津温泉地域の源泉水ならびに湯川の河川水を新たに採取し，これも分析に供した．河川水については中和剤の投入前と投入後においてそれぞれ採取した(図 2)．中和後の河川水の場合，中和剤と中和生成物により激しく懸濁しているため，アドバンテック東洋の No. 2 濾紙を用いて濾過した．また一部の試料については，溶存するヒ素の化学形態を推察するため，ピロリジンジチオカルバミン酸(PDC)共沈法[4]を用いた As(III)と As(V)の分別定量を試みた．

試料水中の全溶存ヒ素濃度は，試料水を濾紙の小片に含浸させ，これを照射試料として中性子放射化分析法により定量した．また一部については，水素化物発生法による原子吸光分光法も併用した．PDC 共沈法では，採水直後に試料水にアンモニウムピロリジンジチオカルバミン酸(APDC)と硝酸鉛を加え，生じた $Pb(PDC)_2$ の沈殿をメンブランフィルタによりろ別回収した．この $Pb(PDC)_2$ には As(III)が選択的に共沈する．回収した $Pb(PDC)_2$ の沈殿は非破壊中性子放射化分析法に供し，得られたヒ素濃度から試料水中の As(III)濃度を求め，全ヒ素濃度から As(III)濃度を差し引くことで As(V)濃度を求めた．

試料水の水温，pH は採水時に測定し，主要成分濃度は炎光光度法，ICP 発光分析法，イオンクロマトグラフィーにより定量した．

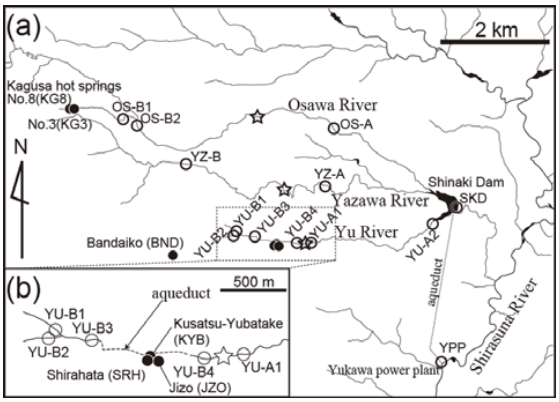


図 2 河川水試料の採水地点

●は源泉水，○は河川水の採水地点を示す．河川採水地点に付された“A”は中和後，“B”は中和前をそれぞれ示す．☆は河川中和地点を示す.

3.2 河川中和生成物

河川水の中和後に生じる中和生成物に含まれるヒ素量を求めるため，河川中和生成物を採取した．中和後の懸濁物を含む河川水を，孔径 0.45 μ

m のメンブランフィルタを用いて吸引濾過し，フィルタ上に捕集された懸濁物を回収した．また河床に沈着した褐色の中和生成物を採取した．

フィルタにより回収した懸濁物，ならびに粉砕した河床沈着物は，非破壊中性子放射化分析法によりヒ素濃度を求めた．また，河床沈着物についてはフッ化水素酸により分解，溶液化し，炎光光度法，ICP 発光分析法により主要成分の定量を行うとともに，断面の EPMA 分析ならびに，X 線粉末回折(XRD)による化学種の同定を試みた．

3.3 土壌試料

草津温泉地域の各所から，スパイラルディガーもしくはピートコアサンプラーを用いて土壌試料を採取した．スパイラルディガーを用いた場合には地表下 10 cm 以下の土壌を，また，コアサンプラーを用いた場合には，得られた地表下 30 cm までのコア試料を数 cm ごとに分割して以後の分析に供した．

ヒ素濃度は非破壊中性子放射化分析法により求め，主要成分濃度はフッ化水素酸により分解，溶液化して，炎光光度法，ICP 発光分析法，イオンクロマトグラフィーにより定量した. また XRD による鉱物種の同定を試みた．

3.4 中性子放射化分析の実際

中性子放射化分析は既報の手順に則って行った[5]．液体試料については，0.5 mL を濾紙に含浸させたものを，また固体試料については数～数 10 mg を精秤したものをポリエチレンバッグに二重に封入して照射試料とした．比較標準試料としては，原子吸光用ヒ素標準溶液を濾紙に含浸させたものを同時照射した．中性子照射は JRR-3 の PN-1，PN-2，もしくは JRR-4(定格出力)の T パイプ，S パイプを用いて 3 分から 5 分間照射し，冷却時間 1 日，数 1000 秒の測定時間で，大学開放研究室の測定器を利用してガンマ線スペクトロメトリを実施した．

4．結果と考察

4.1 湯川の溶存ヒ素濃度の経年変化

図 3 には，湯川の中和前の溶存ヒ素濃度の経年変化を，万代鉱源泉の溶存ヒ素濃度経年変化とともに示す．これを見ると，湯川のヒ素濃度の経年変化は万代鉱源泉のヒ素濃度の経年変化と相似的であり，湯川のヒ素濃度は万代鉱源泉からの流入水に完全に支配されている．

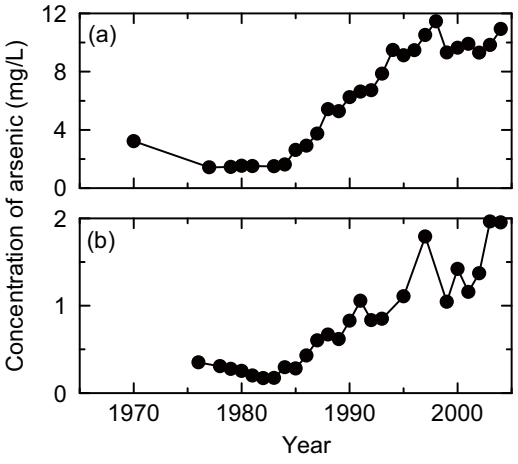


図 3 溶存ヒ素濃度の経年変化

(a)は万代鉱源泉水，(b)は湯川の中和前の河川水.

4.2 河川水中のヒ素濃度とヒ素運搬量

表 1，2 に，湯川水系の 3 河川におけるヒ素濃度の分析結果を河川流量[6]とともに示す. 表 1 から，中和前の河川では湯川の溶存ヒ素濃度が最も高く，最大 3 mg/L に達している．溶存ヒ素濃度と河川流量から各河川のヒ素運搬量を見積もると(表 1)，湯川のヒ素運搬量が圧倒的に高く，年間 28 トンと見積もられた．これはこの地域の河川により運搬されるヒ素の 99%を占めている. 一方，中和後の河川のヒ素濃度はいずれも検出限界未満(< 0.01 mg/L)であった(表 2)．したがって，中和前の河川水に含まれていたヒ素のほとんどが河川中和によって生じる中和生成物に捕集され，懸濁態となって河川を流下していることを意味する．

表1 中和前の河川水の溶存ヒ素濃度とヒ素運搬量の見積もり結果

Sampling location		Sampling date	Arsenic content		Flow rate*	Amount of arsenic transported
			(mg /L)	[Ave.]	(L /min)	(ton /year)
Yu River	YU-B1	30-Nov-2004	0.08		-	
	YU-B2	30-Nov-2004	3.04		-	
	YU-B3	30-Nov-2004	1.29		-	
	YU-B4	29-Jul-2004	1.95	(1.60)	33000	28
		30-Nov-2004	1.37			
		4-Jun-2005	1.55			
		27-Jul-2005	1.51			
Yazawa River	YZ-B	29-Jul-2004	ND	(0.01)	8800	0.05
		27-Jul-2005	0.01			
Osawa River	OS-B1	2-Aug-2004	0.32	(0.26)	-	
		2-Aug-2005	0.19			
	OS-B2	2-Aug-2005	0.03		10000	0.16

* Data cited from Hirabayashi and Mizuhashi [6]

表2 中和後の河川水の溶存ヒ素濃度

Sampling location		Sampling date	Arsenic content (mg /L)
Yu River	YU-A1	29-Jul-2004	ND
	YU-A2	29-Jul-2004	ND
		27-Jul-2005	ND
Yazawa River	YZ-A	29-Jul-2004	ND
		27-Jul-2005	ND
Osawa River	OS-A	30-Jul-2004	ND
		27-Jul-2005	ND
Shinaki Dam	SKD	3-Aug-2003	ND
		31-Jul-2005	ND
	YPP	29-Jul-2004	ND
		27-Jul-2005	ND

ND: Not detected (< 0.01 mg /L)

ところで，ここ数年のヒ素濃度とその湧出量からすれば，万代鉱源泉から供給されるヒ素は年間45トンと見積もられるのに対し，湯川が運搬するヒ素は年間 28 トンに過ぎない．したがって，その差としての年間 10 数トンのヒ素が行方不明となっている．この行方不明のヒ素の多くは，余剰の万代鉱源泉水を放出池に投入する際に周辺土壌に浸透する源泉水や，湯川が流下する過程で河床や河岸から土壌中に浸透する河川水に伴い失われたものと思われる．すなわち，万代鉱源泉ならびに湯川の流域では，土壌中に年間 10 トン以上のヒ素が浸透，拡散している可能性がある．

一方，中和後の河川水に溶存態のヒ素がほとんど認められないということは，河川により運搬されるヒ素のほとんどが懸濁物として品木ダムに堆積していることを意味する．品木ダムから白砂川への放出口となる湯川発電所の放出水中のヒ素濃度を求めると，懸濁態をも含めた全ヒ素濃度は 0.12 mg/L であった．仮に品木ダムに流入する3 つの河川の合計流量と，湯川発電所を介して白砂川に流入する水量とが等しいとするならば，白砂川には年間約 3 トンのヒ素が流入することになる．これが草津温泉地域から域外へと運搬されるヒ素の総量である．なお，品木ダムでは中和生成物や流入土砂の堆積によるオーバーフローを避けるため，定常的にダム内の浚渫を行っており，回収したダム堆積物はダム周辺の処分場において埋め立て処分される．したがって，高濃度にヒ素を含む土砂がダム周辺に蓄積されているのが現状である．この堆積処分場からのヒ素の二次的な拡散については，環境負荷の観点から今後十分に検討する必要があるものと考えられる．

4.3 中和生成物へのヒ素の取り込み

先に示したように，河川水に溶存するヒ素は中和により生じる懸濁物に取り込まれている．そこで，メンブランフィルタにより捕集した中和後の湯川ならびに品木ダムの懸濁物のヒ素濃度を求めたところ，1 wt%前後の高いヒ素濃度が得られた(表 3)．さらに中和直後の湯川の河床から採取した赤褐色の沈着物を分析したところ，10 wt%前後ときわめて高いヒ素濃度を示し(表 4)，中和直後からヒ素が選択的に中和生成物に吸着，沈殿していることが明らかになった．この河床沈殿物の切断面を EPMA により局所分析したところ，ヒ素含有量と鉄含有量との間にきわめて良い相間が認められ(図 4)，河川中和によって生成する水酸化鉄にヒ素が共沈しているものと考えられる．XRD 測定の結果，この河床沈着物は非晶質であり，その化学形態を知ることはできなかった．しかしながら湯川の水質からすれば，ヒ素はゲーサイトやヘマタイトなどの鉄酸化水酸化物と，鉄硫酸塩鉱物であるシュベルトマナイトに取り込まれるような形で沈着物中に存在しているもの

と推察される．鉄酸化水酸化物やシュベルトマナイトは，ヒ素の捕集剤として広く知られているものである[7,8].

表3 中和後の河川懸濁物のヒ素濃度(乾燥重量基準)

Sampling location		Sampling date	Arsenic content (wt.%)
Yu River	YU-A1	29-Jul-2004	1.2
	YU-A2	29-Jul-2004	1.2
Shinaki Dam	SKD	3-Aug-2003	1.6
	YPP	29-Jul-2004	0.8

表4 中和直後の湯川から採取した河床沈着物の化学組成

	Content (wt.%)		
	dark brown	whitish brown	reddish brown
Na	0.07	0.03	0.02
Mg	0.15	0.11	0.03
Al	1.07	4.93	1.70
Si	15.0	20.3	20.5
P	1.45	1.27	2.02
K	0.12	0.09	0.03
Ca	1.85	0.78	0.20
Ti	0.21	0.23	0.04
Mn	0.04	0.04	0.04
Fe	21.73	28.43	29.62
As	8.8	7.6	9.1

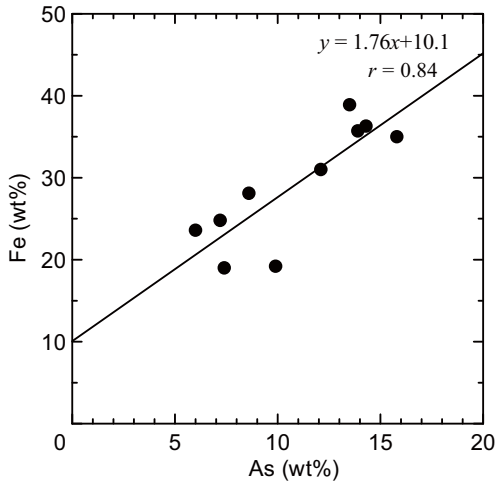


図4 湯川河床沈着物のEPMAの局所分析により得られたAsとFeの濃度相間

4.4 河川水の流下に伴う溶存ヒ素の酸化

図5には，源泉ならびに湯川の溶存As(III)/As(V)濃度を示した．湧出直後の源泉水中のヒ素はそのほとんどがAs(III)であるのに対し，中和前の湯川ではAs(III)よりもAs(V)の方が卓越することから，源泉水が温泉街で利用され，河川を運搬される過程でヒ素がAs(III)からAs(V)へと酸化されていることが示される．一方，中和直後の湯川では全ヒ素濃度が約半分となるとともに，溶存するヒ素のほとんどがAs(III)であることから，As(V)が選択的に中和生成物に取り込まれているものと思われる．さらに中和後の湯川がその下流の品木ダムに流入する段階においては，全ヒ素濃度はさらに低下するが，As(V)濃度とほぼ同程度であることから，流下する過程でAs(III)がAs(V)に酸化され，生じたAs(V)が順次，中和生成物に取り込まれているものと考えられる．

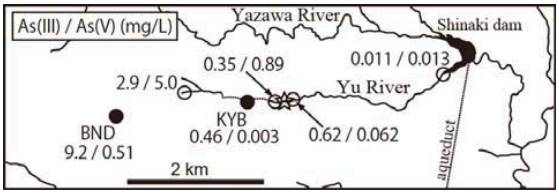


図5 源泉水および河川水のAs(III)とAs(V)濃度
●は源泉，○は河川水を示す．☆は中和地点．図中の濃度表記は“As(III)濃度／As(V)濃度”でmg/L単位.

4.5 土壌中のヒ素濃度の分布

ヒ素濃度を求めた土壌の採取位置を図6に示す．また得られたヒ素濃度を表5に示す．ヒ素濃度の地域的分布を見てみると，草津温泉地域の外縁部では濃度が低く，報告されている国内の地殻や河川堆積物におけるヒ素濃度(7～9 mg/kg)[9,10]とほぼ同等であるのに対し，草津温泉の中心部においては高いヒ素濃度が認められ，特に万代鉱源泉周辺の土壌中にきわめて高い濃度が散見される．したがって，草津温泉地域全体に，温泉水起源のヒ素が広く浸透，拡散しているものと見られる．

万代鉱源泉周辺の土壌についてより詳細に見てみると，万代鉱の湧出口周辺の土壌にはさほど高いヒ素濃度は認められず，余剰の万代鉱源泉水

が湯川に放出される地点の近傍(Nos. 6 – 8)でのヒ素濃度がきわめて高い．湯川への源泉水の放出は，急斜面の下部において，埋設された引湯パイプを通じて直接的に源泉水を投入することでなされており，この地点が事実上の湯川の起点となっている．この放出地点の湯川河岸の土壌(No. 8)で高いヒ素濃度が見いだされるのは，明らかに源泉水の浸透に伴いヒ素が土壌中に取り込まれていることを示している．一方，放出点のある斜面の上部(No. 6)においても高いヒ素濃度が認められるが，こちらは引湯パイプからの漏水により，土壌中に源泉水が浸透している可能性が高い．

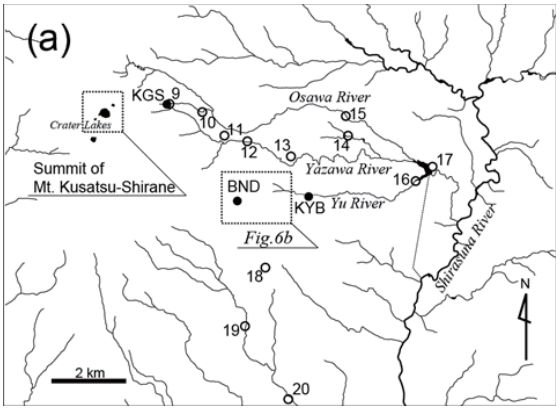


図 6 土壌試料の採取地点と試料番号

(a) 草津白根火山東麓全域図，(b) 万代鉱源泉周辺拡大図．○は土壌採取位置，●は源泉．(b) 図における点線矢印は万代鉱源泉水の引湯経路を示す．

表5 草津温泉地域の土壌中のヒ素濃度

Sampling location	Sample No.	Depth (cm)	As content * (mg/kg)
1	1	20	15 ± 1
2	2	10	21 ± 2
3	3A	25	37 ± 11
	3B	15	31 ± 7
	3C	45	36 ± 5
4	4	31	17 ± 4
5	5	15	28 ± 2
6	6	15	170 ± 2
		52	87 ± 21
7	7A	19	36 ± 6
		25	7 ± 2
	7B	17	19 ± 11
	7C	17	33 ± 4
8	8	28	130 ± 30
9	9	12	41 ± 9
10	10	10	46 ± 13
11	11	10	21 ± 3
12	12	20	24 ± 2
13	13	25	19 ± 2
14	14	20	35 ± 15
15	15	22	10 ± 5
16	16	20	38 ± 1
17	17	20	9 ± 1
18	18	55	8 ± 1
19	19	45	13 ± 1
20	20	53	11 ± 2

* The error twice the standard deviation (±2σ) of the mean values (n = 3).

高いヒ素濃度を示した湯川における源泉水放出地点周辺の 2 点(Nos. 6, 7)において，そのヒ素濃度を深度別に見てみると，下層より上層でヒ素濃度が高い結果となった．放出地点の湯川河岸の土壌の化学組成や鉱物組成からは，明らかに深部では酸性変質が進行していた．この酸性変質層よりも上部に最大ヒ素濃度が見られるので，強度に酸性変質が進行した土壌にはヒ素は保持されないことがわかる．したがって，万代鉱源泉の放出地点周辺では，地表下の比較的浅い部分を水平方向に広がるようにヒ素が分布しているものと考えられる．

4.6 土壌中でのヒ素の形態

今回の土壌試料中で最大のヒ素濃度を示した No.6 地点の試料に対し，土壌分析で用いられる逐

次溶解法[11]を適用した．逐次溶解法では，STEP1 において弱酸可溶性ならびにイオン交換態の成分を，STEP2 において酸化物態(還元溶解性)の成分を，STEP3 において還元態(酸化溶解性)ならびに有機物態の成分を，それぞれ段階的に抽出し，抽出液の化学組成から土壌中での各成分の化学形態を類推することが可能である．表 6 には逐次溶解の結果を示した．

表6 逐次溶解による土壌試料(No.6)の元素抽出量

Depth	Element		Extracted amount		
			STEP1	STEP2	STEP3
0-5 cm	Al	mg/g	0.88	5.6	4.2
	Fe	mg/g	0.024	0.90	3.4
	Ca	mg/g	0.11	0.072	0.037
	Mg	mg/g	0.011	0.017	0.012
	Ti	mg/g	0.0002	0.005	0.053
	Na	mg/g	0.086	0.087	0.17
	K	mg/g	0.15	0.0014	0.039
	As	μg/g	0.24	2.9	21
5-10 cm	Al	mg/g	1.09	7.5	6.4
	Fe	mg/g	0.041	0.91	4.4
	Ca	mg/g	0.10	0.051	0.020
	Mg	mg/g	0.013	0.012	0.008
	Ti	mg/g	0.0007	0.005	0.061
	Na	mg/g	0.072	0.067	0.13
	K	mg/g	0.44	0.047	0.090
	As	μg/g	0.42	3.8	30
10-15 cm	Al	mg/g	0.94	6.4	4.7
	Fe	mg/g	0.029	0.93	4.0
	Ca	mg/g	0.12	0.066	0.029
	Mg	mg/g	0.015	0.015	0.011
	Ti	mg/g	0.0004	0.005	0.067
	Na	mg/g	0.099	0.10	0.22
	K	mg/g	0.44	0.059	0.12
	As	μg/g	0.25	3.6	25

表 6 を見ての通り，ヒ素は STEP3 において抽出される割合が最も高く，土壌中ではその多くが還元態として存在していることを示している．ヒ素以外の成分では，鉄がヒ素と類似の抽出挙動を示し，STEP3 での抽出が卓越している．このことは，土壌中でヒ素が鉄とともに還元態の化合物を構成していることを示唆し，少なくともヒ素が酸化態である鉄酸化物等に吸着しているのではないことを意味する．おそらくは，ヒ素は As(III)として鉄とともに硫化物のような形態で土壌中に保持されているものと見られる．しかしながら，このヒ素の還元化合物が源泉水による直接的作用によって形成されたものなのか，それとも生物学的作用によって二次的に形成されたものなのかは現段階ではわからない．

５．まとめ

草津温泉地域におけるヒ素の動態を明らかにするべく，同地域内の源泉水，河川水，土壌中のヒ素濃度を種々の手法で求めた．この結果，以下のことが明らかになった．

(1) 草津温泉地域の源泉水ならびに河川水のヒ素濃度に基づくマスバランス計算の結果，当該地域において万代鉱源泉が最大のヒ素供給源であり，年間約 45 トンのヒ素を放出している．また，万代鉱源泉水が流入する湯川では，年間約 28 トンのヒ素が運搬されている．源泉からのヒ素供給量と河川によるヒ素運搬量の差からすれば，年間 10 トン以上のヒ素が，当該地域の土壌中に浸透，拡散していると見られる．

(2) 河川水中のヒ素は，当該地域の酸性河川中和事業により生じる中和生成物に捕集され，その大半が品木ダムに蓄積している．品木ダムには年間約 25 トンのヒ素が蓄積し，年間 3 トンのヒ素が地域外に懸濁物として運搬されていると見積もられた．

(3) 河川中和事業では，As(V)が選択的に中和生成物に取り込まれ，As(III)は河川の流下に伴い徐々に As(V)に酸化されることで，順次，中和生成物へと吸着除去される．

(4) 万代鉱源泉の周辺の土壌中には，源泉水の浸透の結果として高いヒ素濃度が見いだされる．土壌中のヒ素は As(III)として鉄とともに固定されていると見られる．

参考文献

[1] 佐藤比奈子，石山大三，水田敏夫，世良耕一

郎，秋田県玉川温泉の大噴と湯川の温泉水と沈殿物の特徴．NMCC 共同利用研究成果報文集，**12**，205-211，2004.

[2] 木川田喜一，大井隆夫，川井智，長谷川潤，小坂美紀子，金田哲人，早津岳宏，佐野淳子，久野吉郎，西野剛弘，草津白根山周辺温泉の微量元素溶存濃度の経年変化とその地球化学的解釈．平成 16 年度原研施設利用共同研究成果報告書，59-65，2005.

[3] 小坂丈予，小坂知子，平林順一，大井隆夫，大場武，野上健治，木川田喜一，飛田典子，万代鉱源泉の湧出に伴う草津温泉源泉群の水質変化について． 温泉科学，**47**，166-178，1998.

[4] Y. C. Sun, J. Y. Yang, Simultaneous determination of arsenic (III,V), selenium (IV,VI), and antimony (III,V) in natural water by coprecipitation and neutron activation analysis. *Anal. Chim. Acta*, **395**, 293-300, 1999.

[5] Y. Kikawada, S. Kawai, T. Oi, Determination of arsenic and bromine in hot spring waters by neutron activation analysis. *J. Radioanal. Nucl. Chem.*, **261**, 381-386, 2004.

[6] 平林順一，水橋正英，草津白根山から放出される揮発性成分量，第 4 回草津白根火山の集中総合観測報告書，167-174，2004.

[7] K. Fukushi, M. Sasaki, T. Sato, N. Yanase, H. Amano, H. Ikeda, A natural attenuation of arsenic in drainage from an abandoned arsenic mine dump. *Appl. Geochem.*, **18**, 1267-1278, 2003.

[8] M. L. Pierce, C. B. Moore, Adsorption of arsenite and arsenate on amorphous iron hydroxide, *Water Res.*, **16**, 1247-1253, 1982.

[9] S. Togashi, N. Imai, Y. Okuyama-Kusunose, T. Tanaka, T. Okai, T. Koma, Y. Murata, Young upper crustal chemical composition of the orogenic Japan Arc. *Geochem. Geophys. Geosyst.*, **1**, doi:10.1029/2000GC000083, 2000.

[10] 今井登，寺島滋，太田充恒，御子柴（氏家）真澄，岡井貴司，立花好子，富樫茂子，松久幸敬，金井豊，上岡晃，谷口政碩，日本の地球化学図．地質ニュース，**604**，30-36，2004.

[11] G. Rauret, J. F. López-Sánchez, A. Sahuquillo, R. rubio, C. Davidson, A. Ure, P. Quevauviller, Improvement of the BCR three step sequential extraction procedure prior to the certification of new sediment and soil reference materials. *J. Environ. Monit.*, **1**, 57-61, 1999.

成果の公表

学術論文

- 木川田喜一，川井智，大井隆夫 (2006) 草津温泉主要源泉における溶存ヒ素濃度経年変化とヒ素負荷量の見積．地球化学，**40**，125-136.
- Sano, J., Kikawada, Y., Oi, T. (2008) Determination of As(III) and As(V) in hot spring and river waters by neutron activation analysis with pyrrolidinedithiocarbamate coprecipitation technique. *J. Radioanal. Nucl. Chem.*, **278**, 111-116.
- Kikawada, Y., Kawai, S., Shimada, K., Oi, T. (2008) Arsenic originating in Kusatsu hot springs, Gunma, Japan, and arsenic pollution status of Kusatsu rivers. *J. Disaster Res.*, **3**, 261-269.
- Kikawada, Y., Fuji, H, Ohono, Y, Oi, T. (2008) Mobility of arsenic in hot spring water accompanying its penetration into the ground. *J. Radioanal. Nucl. Chem.*, **278**, 323-326.

紀要等

- 木川田喜一，本多照幸，大井隆夫（2006）草津温泉主要源泉および周辺河川によるヒ素負荷量の見積． 武蔵工業大学原子力研究所所報，**32**，6-13.
- 木川田喜一（2006）火山性温泉に見る溶存ヒ素濃度の経年変化と環境問題．地下水技術，**48**（12），1-9.

学会発表

- Kikawada, Y., Kawai, S., Oi, T.（2007）Effect of Acidic River Water Neutralization on Mobility of Arsenic in Kusatsu-Shirane Volcano Area, Gunma, Japan. Cities on Volcano 5（COV5）[Shimabara, Japan], 13-O-12.
- Kikawada, Y., Fuji, H., Ohno, Y., Oi, T.（2007）Mobility of arsenic in hot spring water accompanying penetration of water into ground. 12th International Conference on Modern Trends on Activation of Analysis（MTAA-12）[Hachioji, Japan], A087.
- Kikawada, Y., Kawai, S., Shimada, K., Oi, T.（2006）Origin and fate of dissolved arsenic in acidic rivers in the Kusatsu hot spring area, Gunma, Japan. 16th Annual V.M. Goldschmidt Conference [Melbourne, Australia], Geochim. Cosmochim. Acta, 70, Suppl. 1, p.15.
- 佐野淳子，川井智，木川田喜一，大井隆夫（2005）草津白根山西麓陸水のヒ素濃度，2005 年度日本地球化学会年会講演要旨集，p.156.
- 木川田喜一，川井智，佐野淳子，大井隆夫（2005）群馬県草津白根山東麓源泉ならびに河川におけるヒ素の物質収支，2005 年度日本地球化学会年会講演要旨集，p.283.
- 佐野淳子，川井智，木川田喜一，大井隆夫（2006）$Pb(PDC)_2$ 共沈法を利用した中性子放射化分析による As 価数別定量法，2006 年度日本地球化学会講演要旨集，p.3.
- 佐野淳子，木川田喜一，大井隆夫（2007）草津白根火山の火山活動に連動した万座温泉主要源泉の溶存ヒ素濃度経年変化．日本地球惑星科学連合 2007 年大会（2007 年 5 月 23 日，幕張メッセ）

4-7

畑地における有機性廃棄物に由来する土壌改良資材の施用が各種元素の土壌蓄積と作物吸収に及ぼす影響

Accumulation of elements in an arable field with soil amendments (organic un-used resources) and its uptake by cultivated crop

千葉大学：鈴木弘行・熊谷 宏
東京大学：野川憲夫

(1) 研究の目的、意義、計画について

平成 14 年～16 年度に実施した原研施設利用共同研究[1)]において有機性廃棄物を再利用した土壌改良資材である下水汚泥コンポストを放射化分析した結果，Zn，Ag，La 等多数の重金属が含まれていることが明らかとなった。また，そのような下水汚泥コンポストを施用した圃場の土壌において Ag が蓄積していることも明らかになった。しかし，下水汚泥コンポストの投入量から推定した圃場の土壌の Ag 含有率（分散する土層を 15cm と仮定）は実測値より低くなるため，その原因を調査する必要があると考えられた。

このため,平成 17 年～19 年度の原研施設利用共同研究においては，別年度に採取した土壌試料を用いて各元素の土壌含有率について再評価を行った。また，土壌改良資材である下水汚泥コンポストの施用下で栽培した作物について重金属やその他の様々な元素の含有率を調べ，化学肥料のみを施用した場合と比較した。その結果について報告する。

(2) 試料および方法

1)試験区の概要

千葉大学園芸学部内の圃場にトレンチ(長さ 2m，幅 1m，深さ 40cm）を掘り，1998 年 8 月に褐色森林土を充填した。褐色森林土は千葉県暖地園芸研究所内の畑より採取した。試験区は化学肥料区とオガクズ汚泥コンポスト区，モミガラ汚泥コンポスト区の 3 区を設置した。

化学肥料区は A 社製の化学肥料（N：P_2O_5：K_2O=8:8:5)を 1 作あたり 1.25 t ha^{-1} または 1.88t ha^{-1} 施用した。オガクズ汚泥コンポスト区には B 市においてオガクズと下水汚泥を混合し堆肥化したオガクズ汚泥コンポストと化学肥料区と同量の化学肥料を施用した。モミガラ汚泥コンポスト区には，C 市においてモミガラと下水汚泥を混合し堆肥化したモミガラ汚泥コンポストと化学肥料区と同量の化学肥料を施用した。オガクズ汚泥コンポストとモミガラ汚泥コンポストはそれぞれ乾物として初回のみ 12t ha^{-1}，以降は各作ごとに 10t ha^{-1} 施用した。試験は 1998 年 10 月に開始し 2001 年 10 月までの 3 年間にコンポストは合計 6 回施用した。その施用状況と栽培作物については表 1 に示した。

2)土壌試料および作物試料の調整

土壌試料は 2001 年および 2002 年の 5 月に化学肥料，オガクズ汚泥コンポスト，モミガラ汚泥コンポストの施用前に，各試験区からランダムに 3 箇所を選び，それぞれの表層土（0～15cm）を採取した。採取した土壌は乾燥後粉砕し 0.5mm の篩を通過させて分析に供試した。栽培作物の分析は 2001 年 5 月に採取したエンバクと 2001 年 10 月に採取したニンジンについて行った。エンバクとニンジンは採取後，蒸留水を用いて洗浄し土壌粒子等を除去した。水洗後，エンバクからは穂，ニンジンからは主根の皮や葉柄基部などの非可食部（以下皮と表記)，皮を除いた主根（以下可食部と表記）を分離し，80℃で 48 時間乾燥した。乾燥後，各部分を粉砕し放射化分析用の試料とした。

3)中性子放射化分析

各試料と標準試料（National Institute of Standards and Technology の Peach Leaves SRM1547，China National Analysis Center for Iron and Steel の Stream Sediment NCS DC 73317）の 10～50mg を秤量し，ポリエチレン製の小袋に封入した。この小袋はさらに別の小袋に封入し二重にした。二重化した小袋は照射用のキャプセルに充填した後，日本原子力研究所東海研究所の原子炉(JRR-4 または JRR-3M)において放射化した。放射化分析では標準試料から検出された，Na，Mg，Cl，K，Ca，Sc，Cr，Mn，Fe，Co，Zn，As，Br，Rb，Sr，Zr，Ag，Sb，Cs，Ba，La，Ce，Sm，Eu，Yb，Lu，Ta，Th，U の 29 元素を定量の対象とした。試料の照射条件と測定核種を表 2 に示した。測定はゲルマニウム半導体検出器を用い

JRR-3M (PN-1); JRR-4 (気送管, T パイプ A), 中性子利用分析・放射化分析

て行い，γ線エネルギーと半減期を基に放射化された核種の同定を行った。そして，各試料中の放射化された核種の放射能を標準試料中の放射化された核種の放射能と比較して定量を行った。

4) 統計処理

統計解析ソフト Statcel[2)]を用いて，土壌と栽培作物のデータの分散分析と多重検定（Bonferroni/Dunn 法）を行った。

(3) 結果および考察

1)下水汚泥コンポストと化学肥料中の元素

オガクズ汚泥コンポスト，モミガラ汚泥コンポストおよび化学肥料の分析結果を表 3 に示した。オガクズ汚泥コンポストとモミガラ汚泥コンポストからは測定の対象とした 29 元素，化学肥料からは Ag を除いた 28 元素が検出された。

これらの元素の中では Zn について，土壌に蓄積しやすい重金属として規制値が示されており，2001 年に改正された肥料取締法においては 900mg kg^{-1} 以上含む場合に表示の義務付けがなされている。オガクズ汚泥コンポストとモミガラ汚泥コンポストの Zn 含有率は約 500mg kg^{-1} であり，化学肥料よりも約７倍高い値を示した。Zn のように化学肥料と比べて７倍以上高い含有率を示した元素には，オガクズ汚泥コンポストにおいて Mn，Fe，Ag，Ba，La，Ce が，モミガラ汚泥コンポストにおいて Mn，Ag，Ba があった。これらの元素については，長期にわたる施用では Zn 同様に土壌への蓄積について慎重に検討する必要があると思われる。

2)土壌中の元素

平成 14 年～16 年度の原研施設利用共同研究において 2001 年に採取された土壌においては Ag が検出されたが，測定に用いた ^{110m}Ag について冷却期間と測定時間を十分に取り 658keV のガンマ線について半減期を検証すると共に 885keV，937keV，1384keV，1505 keV のガンマ線の存在についても検証した結果，土壌試料からは Ag は検出されていないと結論した。このため，2001 年および 2002 年に採取したオガクズ汚泥コンポスト区，モミガラ汚泥コンポスト区，化学肥料区の土壌からは Ag を除いた 28 元素が検出された（表 4)。

2001 年に採取した土壌ではオガクズ汚泥コンポスト区の Rb の含有率がモミガラ汚泥コンポスト区よりも有意に高くなったが，両汚泥コンポスト区とも化学肥料区とは Rb の含有率に有意な違いは認められなかった。また他の元素の含有率には 3 つの試験区の土壌間で有意差は認められなかった。

一方 2002 年に採取した土壌ではオガクズ汚泥コンポスト区において Zn，Sb，Ba，La，Ce，の含有率が化学肥料区よりも有意に高くなり，La と Ce の含有率についてはモミガラ汚泥コンポスト区とも有意差が認められた。モミガラ汚泥コンポスト区においては Zn と As の含有率が化学肥料区やオガクズ汚泥コンポスト区よりも有意に高くなった。

化学肥料区と有意差が認められた汚泥コンポスト区の元素について，汚泥コンポスト区と化学肥料区との差を元素の増加分（実測値）として理論値（3 年間の下水汚泥コンポストの施用に伴って投入された元素が土層 15cm までに分散した場合の化学肥料区との差）と比較した場合（表 3）と比較した場合，実測値の Zn，As，Sb，Ba，La，Ce の含有率の増加分は理論値の 88%，63%，55%，107%，65%，52%に相当した。このため，これらの元素については投入された元素量の 50%以上が土層 15cm までに存在すると考えられた。しかし，これらの元素を 2001 年と 2002 年の含有率で比較すると，Zn のように投入量としては 2002 年の方が多いにもかかわらず 2001 年の方が高い傾向を示している場合もある。このような元素含有率の年次変動は作付け条件等の影響があるのかもしれない。このため，土壌における元素の蓄積を正確に把握するためには多年度にわたる年次変動についてデータを集める必要がある。

本研究の結果から，オガクズ汚泥コンポストやモミガラ汚泥コンポストを褐色森林土に 3 年間投入した限りにおいては，Zn，As，Sb，Ba，La，Ce は土壌に蓄積しやすい性質があると考えられた。また下水汚泥コンポストと化学肥料中の元素の測定からは Mn，Fe，Ag，についても土壌への蓄積を慎重に検討する必要があると思われたが 2001 年と 2002 年の土壌中の元素含有率には 3 つの試験区間で有意差が認められなかったことについても，年次変動の影響があるのかも知れない。

3)栽培作物中の元素

栽培作物であるエンバクの穂とニンジンの可食部および皮の分析結果を表 5 に示した。

エンバクの穂からは Na，Mg，Cl，K，Ca，Sc，Cr，Mn，Fe，Co，Zn，Br，Rb の 13 元素が検出された。オガクズ汚泥コンポスト区では Cl と Zn について，モミガラ汚泥コンポスト区では Zn と Br について化学肥料区よりも元素含有率が有意に高くなった。コンポストの投入によって含有率が化学肥料を投入した場合よりも高くなった。Cl については環境中に広く分布すること，Br については米，麦，雑穀の残留基準値(50～180mg kg^{-1})[3)]を下回っていることから，人体に対する安全性には問題がないと考えられる。Zn については，食品の微量元素含量表 [4)]によれば，

標準的なエンバクの玄穀の Zn 含有量は新鮮重 100g あたり 1.9mg であり，乾物当たりに換算すれば 21mg kg^{-1} に相当する。本実験におけるエンバクの穂の Zn 含有率は，化学肥料区（Zn 23.5 mg kg^{-1}）において標準レベルを若干上回っていた。また，オガクズ汚泥コンポスト区とモミガラ汚泥コンポスト区の Zn 含有率は標準レベルのほぼ 2 倍に相当した。国民栄養調査による成人男女のその他の穀類の 1 日摂取量（0.294g）[5]と食品の微量元素含量表 [4]にある水分量を基にオガクズ汚泥コンポスト区のエンバクの穂を 0.294g 喫食した場合の Zn 量を算出した場合，その値は 9.32μg となり，日本人の Zn の 1 日摂取量（8.67mg）に占める割合は約 0.1%と少なかった（表 6）[6]。また，ラットに対する塩化亜鉛の LD_{50} は 350 mg kg^{-1} であることからも，3 年間のオガクズ汚泥コンポストやモミガラ汚泥コンポストの施用によってエンバクの穂の Zn 含有率が化学肥料施用時よりも高くなったとしても食品として安全性には問題のない水準にあると考えられた。

一方，ニンジンの場合，皮からは Na，Mg，Cl，K，Ca，Sc，Cr，Mn，Fe，Co，Zn，Br，Rb，Sr，Cs，Ba，La，Sm，Eu，Yb，Lu が検出された。オガクズ汚泥コンポスト区＞化学肥料区の関係が認められた元素は Mg，Sc，Mn，Zn，Br，Ba，La の 7 元素であり，モミガラ汚泥コンポスト区＞化学肥料区の関係は Mg，Mn，Br の 3 元素に認められた。可食部については Na，Mg，Cl，K，Ca，Mn，Fe，Co，Zn，Br，Rb，Sr，Cs，Ba の 14 元素が検出された。Zn と Mn についてはオガクズ汚泥コンポスト区≒モミガラ汚泥コンポスト区＞化学肥料区の関係が，Fe と Co にはオガクズ汚泥コンポスト区＞化学肥料区の関係が，Cl と Br にはモミガラ汚泥コンポスト区＞化学肥料区の関係が認められた。

多くの元素の含有率が可食部よりも皮において高い値を示したことから，コンポストを投入した土壌で栽培したニンジンからの不要な元素の人体への流入を軽減するためには皮やへた等の非可食部の除去が有効であると考えられた。食品の微量元素含量表 [4]によれば，ニンジンの Zn と Mn の含有量は新鮮重 100g あたり 170μg であり，乾物当たりでは 20mg kg^{-1} に相当する。この値を標準的なニンジンの値とした場合，本実験におけるニンジンの可食部の Zn と Mn の含有率は，化学肥料区（Zn 28.8 mg kg^{-1}，Mn 12.7 mg kg^{-1}）において Zn は標準レベルを既に上回っているが，Mn は標準レベルを下回っていた。オガクズ汚泥コンポスト区とモミガラ汚泥コンポスト区のニンジンの可食部の Zn と Mn の含有率は標準レベルの 2 倍以内であった。Fe の場合，食品標準成分表 [7]から求めた乾物あたりの含有率は約 83 mg kg^{-1} であったので，本実験におけるニンジンの可食部の含有率は，いずれの区も標準レベルを下回っていた。Co については微量元素含量表 [4]から求めた乾物当たりの含有率が 0mg kg^{-1} であるため，本実験における Co 含有率（化学肥料区 0.03 mg kg^{-1}）は標準的なニンジンよりも高いと考えられた。国民栄養調査による成人男女のニンジンの 1 日摂取量（24.2g）[5]と食品の微量元素含量表 [4]にある水分量を基にオガクズ汚泥コンポスト区のニンジンの可食部を 24.2g 喫食した場合の Zn，Mn，Fe，Co 量を算出した場合，その値はそれぞれ 69.6μg，81.6μg，65.7μg，0.2μg となった（表 6）。これらの値の日本人の Zn と Mn の 1 日摂取量 [6]，旧厚生省の定めた Fe の 1 日所要量 [8]，香川県における人の Co の 1 日摂取量 [6]に占める割合では Zn で約 0.8%，Mn で約 2.2%，Fe で約 0.5〜0.7%，Co で約 4.2%となり Mn や Co については Zn や Fe よりも 1 日摂取量 [6]に占める割合がやや高い傾向が認められた。しかし，ラットに対する塩化亜鉛，塩化マンガン，塩化第一鉄，塩化コバルトの LD_{50} は 350 mg kg^{-1}，250mg kg^{-1}，984 mg kg^{-1}，766 mg kg^{-1} であることから，本研究においてはオガクズ汚泥コンポストやモミガラ汚泥コンポストを 3 年程度施用すればニンジンの可食部の Zn，Mn，Fe，Co の含有率が化学肥料区よりも高くなることがあっても，安全性の点では問題のない水準であると考えられた。また，モミガラコンポスト区のニンジン可食部の Cl と Br の含有率についても，エンバクの穂の場合と同様な理由で，人体に対する安全性では問題がないレベルと考えられた。

以上をまとめると，オガクズ汚泥コンポストやモミガラ汚泥コンポストを 3 年間施用することによって，栽培作物の Mn や Zn 等の元素の含有率が化学肥料を施用した場合よりも高くなることが明らかになった。しかし，食品となるエンバクの穂やニンジンの可食部では，汚泥コンポストの施用によって元素の含有率が増加しても，安全性の点では問題がない水準であると考えられた。

要約

褐色森林土の畑圃場に 2 種類の下水汚泥コンポスト（オガクズ汚泥コンポストとモミガラ汚泥コンポスト）を 3 年間施用し，土壌と栽培作物（エンバクとニンジン）に含まれる様々な元素の量を化学肥料のみを施用した場合と比較した。

オガクズ汚泥コンポストには Mn，Fe，Zn，Ag，Ba，La，Ce が，モミガラ汚泥コンポストには Mn，Zn，

Ag, Ba が化学肥料と比べて７倍以上高い含有率で含まれていた。オガクズ汚泥コンポスト区，モミガラ汚泥コンポスト区，化学肥料区の土壌の各元素の含有率を比較した結果，オガクズ汚泥コンポストやモミガラ汚泥コンポストを褐色森林土に３年間投入した限りにおいては，Zn，As，Sb，Ba，La，Ce が土壌に蓄積しやすい可能性があると考えられた。

エンバクの穂についてはオガクズ汚泥コンポストの施用によって Mg，Cl，Ca，Zn の含有率が，モミガラ汚泥コンポストの施用によって Mg，Ca，Zn，Br の含有率が化学肥料のみを施用した場合よりも有意に高くなった。また，ニンジンの可食部についてはオガクズ汚泥コンポストの施用によって Mn, Fe, Zn, Co，Br の含有率が，モミガラ汚泥コンポストの施用によって Cl，Mn，Zn，Br の含有率が化学肥料のみを施用した場合よりも有意に高くなった。

下水汚泥コンポスト施用した場合のエンバクの穂やニンジン可食部の Mn，Fe，Zn，Co の含有率について安全性を検討した結果，1 日摂取量に対する量やラットによる LD_{50} の点から食品としての安全性に問題はない水準であると考えられた。

(4) 今後の方針

2001 年と 2002 年の土壌の元素含有率を比較すると，Zn のように投入量としては 2002 年の方が多いにもかかわらず 2001 年の方が高い傾向を示している場合もある。このため，土壌における元素の蓄積を正確に把握するためには多年度にわたる年次変動についてデータを集める必要がある。

(5) 引用文献

1) 鈴木弘行・村松雅子・鈴木悠一・荻山慎一・熊谷宏・野川憲夫：アーバスキュラー菌根を形成した植物の微量元素分析と植物保護技術としてのアーバスキュラー菌根菌の利用可能性の検討.，原研施設利用共同研究成果報告書，**44**, 49-58 (2006)

2) 柳井久江：4Step エクセル統計， p.110～162，オーエムエス出版，所沢 (1998)

3) 農薬残留分析法研究班：最新農薬の残留分析法，p.423～424，中央法規出版，東京 (1995)

4) 鈴木泰夫編：食品の微量元素含量表，第一出版，東京 (1993)

5) 吉池信男：残留農薬の暴露量試算のための食品摂取量基準データの検討- 1995～1997 年国民栄養調査，食品衛生研究，50，7～27 (2000)

6) 西岡千鶴・吉田明美・藤田久雄・毛利孝明・塚本武・黒田弘之：香川県における日常食品中の無機元素の摂取量について (第２報)，香川県環境保健研究センター所報，1，91～100 (2002)

7) 科学技術庁資源調査会編：四訂日本食品標準成分表，p.216～217，大蔵省印刷局，東京 (1982)

8) 毛利孝明・西岡千鶴・石川英樹・黒田弘之：香川県における日常食品中の金属の一日摂取量について，香川県衛生研究所報，**14**，71～78 (1985)

(6) 成果の公表

(論文)

Suzuki, H., Suzuki, Y., Kumagai, H., Nogawa, N., Kawate, M., Sawahata, H., Sakamoto, K. and Inubushi, K.: Influence of sewage sludge compost applications on uptake of element by cultivated crops in a brown forest soil - measurement by the neutron activation analysis- ., Radioisotopes, **55**, 135-145 (2006)

Ogiyama, S., Sakamoto, K., Suzuki, H., Ushio, S., Anzai, T. and Inubushi, K.: Measurement of concentrations of trace metals in arable soils with animal manure application using instrumental neutron activation analysis and the concentrated acid digestion method., Soil Science and Plant Nutrition, **52**, 114-121 (2006)

表1　各試験区への下水汚泥コンポストおよび化学肥料の施用量と栽培作物

栽培回数	施用および播種年月	施用量（t ha^{-1}）			栽培作物
		オガクズ汚泥コンポスト区およびモミガラ汚泥コンポスト区		化学肥料区	
		オガクズ汚泥コンポストまたはモミガラ汚泥コンポスト	化学肥料	化学肥料	
1	1998.11	12	1.25	1.25	エンバク
2	1999.6	10	1.25	1.25	大豆
3	1999.11	10	1.25	1.25	エンバク
4	2000.6	10	1.88	1.88	ニンジン
5	2000.10	10	1.25	1.25	エンバク
6	2001.6	10	1.88	1.88	ニンジン
7	2002.5	0	0	0	アルファルファ
8	2003.5	0	0	0	サツマイモ
9	(2004～2005)	0	0	0	無作付

表2　照射条件および測定核種

照射原子炉（設備）	最大熱中性子束 ($m^{-2}\cdot s^{-1}$)	照射時間	冷却時間	測定試料	測定元素（測定核種）
JRR-4（気送管）	3.2×10^{17}	10秒 20秒	3～5分 1～3分	土壌，各汚泥コンポスト．化学肥料 エンバク，ニンジン	Cl(^{38}Cl)，Ca(^{49}Ca)，Mg(^{27}Mg)，Mn(^{56}Mn)
JRR-4（Tパイプ A） またはJRR-3M（PN-1）	5.3×10^{17} 5.2×10^{17}	10分 10分	1週間 1週間	全試料	Na(^{24}Na)，K(^{42}K)，Sc(^{46}Sc)，Cr(^{51}Cr)，Fe(^{59}Fe)，Co(^{60}Co)，Zn(^{65}Zn)，As(^{76}As)，Br(^{82}Br)，Rb(^{86}Rb)，Sr(^{85}Sr)，Zr(^{95}Zr)，Ag(^{110m}Ag)，Sb(^{122}Sb)，Cs(^{134}Cs)，Ba(^{131}Ba)，La(^{140}La)，Ce(^{141}Ce)，Sm(^{153}Sm)，Eu(^{152}Eu)，Yb(^{175}Yb)，Lu(^{177}Lu)，Ta(^{182}Ta)，Th(^{233}Pa)，U(^{239}Np)
JRR-4（Tパイプ A） またはJRR-3M（PN-1）	5.3×10^{17} 5.2×10^{17}	10分 10分	2～6ヶ月 2～6ヶ月	全試料	Ag(^{110m}Ag)

表3　下水汚泥コンポストおよび化学肥料中の元素含有量と下水汚泥コンポストに由来する元素の理論増加量

元素	下水汚泥コンポストおよび化学肥料（mg kg^{-1} D.W.）			下水汚泥コンポストに由来する元素の理論増加量[1]（mg kg^{-1} D.W.）	
	オガクズ汚泥コンポスト	モミガラ汚泥コンポスト	化学肥料	オガクズ汚泥コンポスト区	モミガラ汚泥コンポスト区
Na	143	188	132	5.91	7.77
Mg	6.93×10^{3}	9.07×10^{3}	3.54×10^{3}	286	375
Cl	841	947	23.0×10^{3}	34.8	39.1
K	2.54×10^{3}	946	74.6×10^{3}	105	39.1
Ca	20.6×10^{3}	6.04×10^{3}	78.7×10^{3}	851	250
Sc	1.18	1.86	0.85	0.05	0.08
Cr	28.0	16.1	9.1	1.16	0.67
Mn	1.63×10^{3}	1.46×10^{3}	232	67.4	60.4
Fe	11.7×10^{3}	31.6×10^{3}	3.06×10^{3}	484	1306
Co	4.98	3.14	1.20	0.21	0.13
Zn	516	527	74	21.3	21.8
As	6.21	15.1	7.04	0.26	0.62
Br	32.7	22.4	86.6	1.35	0.93
Rb	4.50	6.67	10.6	0.19	0.28
Sr	183	92.7	148	7.56	3.83
Zr	29.2	47.5	53.6	1.21	1.96
Ag	6.4	36.1	＜ 0.1	0.26	1.49
Sb	1.29	1.50	1.06	0.05	0.06
Cs	0.48	0.49	0.55	0.02	0.02
Ba	1.25×10^{3}	754	107	51.7	31.2
La	183	3.3	18.4	7.56	0.14
Ce	228	4.0	18.2	9.42	0.17
Sm	4.25	0.51	3.13	0.18	0.02
Eu	0.62	0.10	0.60	0.03	0.004
Yb	0.38	0.29	0.91	0.02	0.12
Lu	0.05	0.06	0.16	0.002	0.002
Ta	0.23	0.10	0.07	0.01	0.004
Th	1.39	0.64	0.98	0.06	0.03
U	0.46	0.50	3.69	0.02	0.02

1）施用した下水汚泥コンポスト中の元素が全て作土層（0～15cm）に留まった場合に，土壌密度を 1kg m^{-3}と仮定して算出した.

表4　2001年と2002年に採取した各試験区における土壌中の各種元素含有率 *)

元素	試験区	2001		2002	
Na	オガクズ汚泥コンポスト区	10.6×10^{3} ± 1.2×10^{3}	a	7.84×10^{3} ± 0.13×10^{3}	a
	モミガラ汚泥コンポスト区	11.1×10^{3} ± 0.5×10^{3}	a	7.82×10^{3} ± 0.20×10^{3}	a
	化学肥料区	11.5×10^{3} ± 0.7×10^{3}	a	8.02×10^{3} ± 0.46×10^{3}	a
Mg	オガクズ汚泥コンポスト区	29.3×10^{3} ± 6.3×10^{3}	a	27.0×10^{3} ± 4.3×10^{3}	a
	モミガラ汚泥コンポスト区	32.4×10^{3} ± 9.6×10^{3}	a	31.8×10^{3} ± 8.8×10^{3}	a
	化学肥料区	26.1×10^{3} ± 6.0×10^{3}	a	33.4×10^{3} ± 8.8×10^{3}	a
Cl	オガクズ汚泥コンポスト区	320 ± 151	a	459 ± 298	a
	モミガラ汚泥コンポスト区	482 ± 167	a	329 ± 139	a
	化学肥料区	519 ± 206	a	335 ± 122	a
K	オガクズ汚泥コンポスト区	8.94×10^{3} ± 1.16×10^{3}	a	8.87×10^{3} ± 0.31×10^{3}	a
	モミガラ汚泥コンポスト区	9.84×10^{3} ± 0.87×10^{3}	a	8.76×10^{3} ± 0.67×10^{3}	a
	化学肥料区	10.3×10^{3} ± 1.8×10^{3}	a	9.23×10^{3} ± 0.50×10^{3}	a
Ca	オガクズ汚泥コンポスト区	13.6×10^{3} ± 2.8×10^{3}	a	19.6×10^{3} ± 3.0×10^{3}	a
	モミガラ汚泥コンポスト区	16.1×10^{3} ± 2.5×10^{3}	a	10.5×10^{3} ± 2.1×10^{3}	a
	化学肥料区	16.7×10^{3} ± 2.8×10^{3}	a	14.8×10^{3} ± 5.4×10^{3}	a
Sc	オガクズ汚泥コンポスト区	33.9 ± 0.1	a	29.1 ± 0.1	a
	モミガラ汚泥コンポスト区	33.5 ± 0.8	a	29.5 ± 0.4	a
	化学肥料区	34.1 ± 1.4	a	29.5 ± 0.6	a
Cr	オガクズ汚泥コンポスト区	48.5 ± 4.4	a	50.0 ± 4.0	a
	モミガラ汚泥コンポスト区	55.6 ± 12.2	a	53.4 ± 0.8	a
	化学肥料区	56.1 ± 2.7	a	90.5 ± 61.2	a
Mn	オガクズ汚泥コンポスト区	1.12×10^{3} ± 0.10×10^{3}	a	1.25×10^{3} ± 0.30×10^{3}	a
	モミガラ汚泥コンポスト区	1.15×10^{3} ± 0.17×10^{3}	a	1.04×10^{3} ± 0.14×10^{3}	a
	化学肥料区	1.10×10^{3} ± 0.10×10^{3}	a	1.19×10^{3} ± 0.18×10^{3}	a
Fe	オガクズ汚泥コンポスト区	65.7×10^{3} ± 2.6×10^{3}	a	60.8×10^{3} ± 0.7×10^{3}	a
	モミガラ汚泥コンポスト区	64.5×10^{3} ± 0.8×10^{3}	a	63.6×10^{3} ± 1.5×10^{3}	a
	化学肥料区	66.4×10^{3} ± 1.9×10^{3}	a	62.5×10^{3} ± 0.6×10^{3}	a
Co	オガクズ汚泥コンポスト区	22.1 ± 1.7	a	19.4 ± 0.2	a
	モミガラ汚泥コンポスト区	20.5 ± 0.5	a	20.4 ± 0.9	a
	化学肥料区	24.0 ± 0.9	a	19.4 ± 0.5	a
Zn	オガクズ汚泥コンポスト区	177 ± 11	a	142 ± 4	b
	モミガラ汚泥コンポスト区	169 ± 4	a	142 ± 1	b
	化学肥料区	155 ± 11	a	118 ± 1	a
As	オガクズ汚泥コンポスト区	5.26 ± 0.48	a	5.19 ± 0.20	a
	モミガラ汚泥コンポスト区	5.39 ± 0.53	a	6.18 ± 0.27	b
	化学肥料区	5.13 ± 0.33	a	5.21 ± 0.25	a
Br	オガクズ汚泥コンポスト区	9.22 ± 0.28	a	9.88 ± 0.12	a
	モミガラ汚泥コンポスト区	8.97 ± 0.78	a	9.81 ± 0.31	a
	化学肥料区	9.25 ± 0.35	a	9.59 ± 0.45	a
Rb	オガクズ汚泥コンポスト区	59.9 ± 15	b	40.2 ± 0.6	a
	モミガラ汚泥コンポスト区	30.0 ± 2.3	a	40.8 ± 2.1	a
	化学肥料区	34.5 ± 0.5	ab	38.5 ± 1.4	a
Sr	オガクズ汚泥コンポスト区	139 ± 53	a	154 ± 6	a
	モミガラ汚泥コンポスト区	128 ± 47	a	113 ± 34	a
	化学肥料区	121 ± 36	a	155 ± 13	a
Zr	オガクズ汚泥コンポスト区	99.3 ± 32.3	a	76.3 ± 24.9	a
	モミガラ汚泥コンポスト区	104 ± 25	a	89.0 ± 3.7	a
	化学肥料区	112 ± 4	a	88.8 ± 4.1	a
Ag	オガクズ汚泥コンポスト区	ND		ND	
	モミガラ汚泥コンポスト区	ND		ND	
	化学肥料区	ND		ND	
Sb	オガクズ汚泥コンポスト区	0.34 ± 0.04	a	0.43 ± 0.02	b
	モミガラ汚泥コンポスト区	0.37 ± 0.08	a	0.41 ± 0.00	ab
	化学肥料区	0.30 ± 0.08	a	0.34 ± 0.04	a
Cs	オガクズ汚泥コンポスト区	3.58 ± 0.43	a	3.36 ± 0.11	a
	モミガラ汚泥コンポスト区	3.65 ± 0.22	a	3.25 ± 0.24	a
	化学肥料区	3.72 ± 0.42	a	3.59 ± 0.15	a
Ba	オガクズ汚泥コンポスト区	386 ± 67	a	373 ± 9	b
	モミガラ汚泥コンポスト区	377 ± 35	a	362 ± 18	ab
	化学肥料区	334 ± 22	a	325 ± 9	a
La	オガクズ汚泥コンポスト区	19.9 ± 2.9	a	24.7 ± 1.2	b
	モミガラ汚泥コンポスト区	16.2 ± 0.6	a	15.0 ± 0.3	a
	化学肥料区	14.9 ± 2.0	a	13.0 ± 0.4	a
Ce	オガクズ汚泥コンポスト区	31.3 ± 5.0	a	39.5 ± 2.5	b
	モミガラ汚泥コンポスト区	24.1 ± 1.2	a	25.2 ± 0.4	a
	化学肥料区	24.2 ± 1.1	a	21.6 ± 0.4	a
Sm	オガクズ汚泥コンポスト区	3.78 ± 0.20	a	3.69 ± 0.27	a
	モミガラ汚泥コンポスト区	3.53 ± 0.09	a	3.34 ± 0.12	a
	化学肥料区	3.66 ± 0.11	a	3.26 ± 0.07	a
Eu	オガクズ汚泥コンポスト区	1.08 ± 0.01	a	1.11 ± 0.05	a
	モミガラ汚泥コンポスト区	1.07 ± 0.04	a	1.04 ± 0.03	a
	化学肥料区	1.08 ± 0.06	a	1.04 ± 0.03	a
Yb	オガクズ汚泥コンポスト区	2.31 ± 0.26	a	2.43 ± 0.08	a
	モミガラ汚泥コンポスト区	2.23 ± 0.27	a	2.44 ± 0.05	a
	化学肥料区	2.38 ± 0.28	a	2.35 ± 0.06	a
Lu	オガクズ汚泥コンポスト区	0.44 ± 0.05	a	0.47 ± 0.02	a
	モミガラ汚泥コンポスト区	0.45 ± 0.02	a	0.51 ± 0.02	a
	化学肥料区	0.42 ± 0.02	a	0.47 ± 0.02	a
Ta	オガクズ汚泥コンポスト区	0.29 ± 0.07	a	0.32 ± 0.01	a
	モミガラ汚泥コンポスト区	0.31 ± 0.02	a	0.30 ± 0.01	a
	化学肥料区	0.30 ± 0.05	a	0.29 ± 0.02	a
Th	オガクズ汚泥コンポスト区	4.68 ± 0.51	a	4.53 ± 0.94	a
	モミガラ汚泥コンポスト区	4.24 ± 0.13	a	3.94 ± 0.14	a
	化学肥料区	4.42 ± 0.18	a	3.65 ± 0.26	a
U	オガクズ汚泥コンポスト区	1.18 ± 0.34	a	1.35 ± 0.16	a
	モミガラ汚泥コンポスト区	1.06 ± 0.14	a	1.18 ± 0.13	a
	化学肥料区	1.13 ± 0.18	a	1.25 ± 0.11	a

*) 表中の値は平均値と標準偏差（n=3)., また表中の英文字はBonferroni/Dunn法による統計処理結果を示す（同一英文字は$p<0.05$で同一年度の試験区間で有意差がないことを示す), ND：検出限界以下.

表5　各試験区において栽培したエンバクの穂およびニンジンの可食部と皮の各種元素含有率[a]

元素	エンバクの穂（mg kg^{-1} D.W.）			ニンジンの可食部（mg kg^{-1} D.W.）			ニンジンの皮（mg kg^{-1} D.W.）		
	オガクズ汚泥コンポスト区	モミガラ汚泥コンポスト区	化学肥料区	オガクズ汚泥コンポスト区	モミガラ汚泥コンポスト区	化学肥料区	オガクズ汚泥コンポスト区	モミガラ汚泥コンポスト区	化学肥料区
Na	30.4 ± 1.3 a	76.2 ± 16.3 a	40.0 ± 11.5 a	401 ± 14 a	348 ± 22 a	420 ± 66 a	338 ± 27 ab	244 ± 28 a	402 ± 49 b
Mg	1.64×10^{3} ± 0.10×10^{3} a	2.42×10^{3} ± 1.69×10^{3} a	6.49×10^{2} ± 1.71×10^{2} a	1.82×10^{3} ± 0.69×10^{3} a	1.19×10^{3} ± 0.03×10^{3} a	1.23×10^{3} ± 0.22×10^{3} a	2.65×10^{3} ± 0.27×10^{3} b	2.67×10^{3} ± 0.30×10^{3} b	1.87×10^{3} ± 0.05×10^{3} a
Cl	2.33×10^{3} ± 0.19×10^{3} b	1.74×10^{3} ± 0.05×10^{3} a	1.68×10^{3} ± 0.10×10^{3} a	3.13×10^{3} ± 0.07×10^{3} a	4.79×10^{3} ± 0.20×10^{3} b	3.55×10^{3} ± 0.53×10^{3} a	4.89×10^{3} ± 0.25×10^{3} a	5.43×10^{3} ± 0.26×10^{3} a	4.55×10^{3} ± 0.39×10^{3} a
K	9.35×10^{3} ± 1.21×10^{3} a	6.97×10^{3} ± 1.82×10^{3} a	11.4×10^{3} ± 1.6×10^{3} a	27.9×10^{3} ± 1.6×10^{3} a	31.6×10^{3} ± 1.5×10^{3} a	25.3×10^{3} ± 4.1×10^{3} a	38.1×10^{3} ± 1.5×10^{3} a	44.8×10^{3} ± 2.1×10^{3} ab	48.3×10^{3} ± 2.9×10^{3} b
Ca	2.54×10^{3} ± 0.26×10^{3} a	2.22×10^{3} ± 0.26×10^{3} a	1.97×10^{3} ± 0.36×10^{3} a	2.80×10^{3} ± 0.11×10^{3} a	3.17×10^{3} ± 0.22×10^{3} a	2.74×10^{3} ± 0.49×10^{3} a	6.84×10^{3} ± 0.17×10^{3} a	5.72×10^{3} ± 0.51×10^{3} a	6.53×10^{3} ± 0.84×10^{3} a
Sc	0.0041 ± 0.0002 a	0.0050 ± 0.0002 a	0.0287 ± 0.0006 b	ND	ND	ND	0.181 ± 0.004 b	0.164 ± 0.020 ab	0.134 ± 0.002 a
Cr	10.9 ± 3.3 a	5.48 ± 0.43 a	8.81 ± 0.21 a	ND	ND	ND	0.839 ± 0.214 a	0.721 ± 0.105 a	0.470 ± 0.033 a
Mn	132 ± 10 a	132 ± 8 a	118 ± 9 a	39.6 ± 0.6 b	37.2 ± 2.8 b	12.7 ± 1.8 a	80.2 ± 1.6 c	59.4 ± 3.8 b	29.4 ± 2.8 a
Fe	88.3 ± 16.4 a	60.1 ± 10.7 a	125 ± 1 b	31.9 ± 3.1 b	24.2 ± 1.5 a	24.6 ± 1.2 a	310 ± 2 a	271 ± 24 a	236 ± 39 a
Co	0.16 ± 0.04 b	0.08 ± 0.01 a	0.10 ± 0.01 ab	0.102 ± 0.033 b	0.0620 ± 0.019 ab	0.0280 ± 0.0020 a	0.326 ± 0.108 a	0.265 ± 0.090 a	0.136 ± 0.008 a
Zn	35.4 ± 2.4 c	28.6 ± 0.8 b	23.5 ± 0.7 a	33.8 ± 0.8 b	32.4 ± 1.4 b	28.8 ± 0.6 a	43.3 ± 0.4 b	37.2 ± 1.8 a	35.3 ± 1.3 a
As	ND	ND	ND	ND	ND	ND	ND	ND	ND
Br	1.73 ± 0.15 a	2.36 ± 0.12 b	1.57 ± 0.14 a	4.23 ± 0.19 a	6.21 ± 0.11 b	4.71 ± 0.23 a	8.66 ± 0.19 b	10.7 ± 0.1 c	7.10 ± 0.32 a
Rb	15.4 ± 0.3 b	10.1 ± 0.8 a	14.8 ± 0.5 b	19.4 ± 1.3 b	16.3 ± 0.1 a	20.8 ± 0.3 b	31.0 ± 0.4 ab	28.3 ± 1.4 a	32.2 ± 0.9 b
Sr	ND	ND	ND	20.5 ± 2.6 a	19.7 ± 1.2 a	19.6 ± 1.5 a	77.3 ± 7.2 b	49.1 ± 3.7 a	64.2 ± 2.6 ab
Zr	ND	ND	ND	ND	ND	ND	ND	ND	ND
Ag	ND	ND	ND	ND	ND	ND	ND	ND	ND
Sb	ND	ND	ND	ND	ND	ND	ND	ND	ND
Cs	ND	ND	ND	0.033 ± 0.003 a	0.031 ± 0.001 a	0.046 ± 0.004 a	0.080 ± 0.007 a	0.063 ± 0.007 a	0.080 ± 0.014 a
Ba	ND	ND	ND	17.2 ± 1.3 b	10.1 ± 1.3 a	13.4 ± 0.9 ab	36.6 ± 0.9 b	17.2 ± 3.4 a	19.8 ± 0.9 a
La	ND	ND	ND	ND	ND	ND	0.200 ± 0.010 b	0.145 ± 0.013 a	0.146 ± 0.019 a
Ce	ND	ND	ND	ND	ND	ND	ND	ND	ND
Sm	ND	ND	ND	ND	ND	ND	0.046 ± 0.003 a	0.040 ± 0.005 a	0.053 ± 0.008 a
Eu	ND	ND	ND	ND	ND	ND	0.021 ± 0.010 a	0.009 ± 0.008 a	0.015 ± 0.002 a
Yb	ND	ND	ND	ND	ND	ND	0.033 ± 0.007 a	0.027 ± 0.006 a	0.030 ± 0.002 a
Lu	ND	ND	ND	ND	ND	ND	0.007 ± 0.000 a	0.004 ± 0.003 a	0.010 ± 0.003 a
Ta	ND	ND	ND	ND	ND	ND	ND	ND	ND
Th	ND	ND	ND	ND	ND	ND	ND	ND	ND
U	ND	ND	ND	ND	ND	ND	ND	ND	ND

a）表中の値は平均値と標準偏差（n=3）．また表中の英文字はBonferroni/Dunn法による統計処理結果を示す（同一英文字はp<0.05で試験区間で有意差がないことを示す），ND：検出限界以下．

表6　Zn，Mn，Fe，Coの1日摂取量とオガクズ汚泥コンポスト区のエンバクの穂およびニンジンの可食部からの推定摂取量

元素	1日の摂取量[a]	本実験のエンバクを0.236g喫食した場合の各元素の1日の摂取量[b]	本実験のニンジンを24.2g喫食した場合の各元素の1日の摂取量[d]
Zn	8.67 mg	9.32 μg	69.6 μg
Mn	3.69 mg	—[d]	81.6 μg
Fe	男　10 mg 女　12 mg	—	65.7 μg
Co	4.8 μg	—	0.2 μg

a）ZnおよびMn:1985～2001年までの日本人による元素の一日摂取量の平均値　Fe：旧厚生省が定めた1日所要量　Co：1985～2001年までの香川県における人の一日摂取量の平均値

b）国民栄養調査による成人男女のその他の穀類の1日の摂取量（0.294g）食品の微量元素含量表にある水分量（100gあたり10.3g），オガクズ汚泥コンポスト区のエンバクの穂の各元素含有率を基に算出した．

c）国民栄養調査による成人男女のニンジンの1日の摂取量（85.4g）食品の微量元素含量表にある水分量(100gあたり91.5g)，オガクズ汚泥コンポスト区のニンジンの可食部の各元素含有率を基に算出した．

d）オガクズ汚泥コンポスト区あるいはモミガラ汚泥コンポスト区の値が化学肥とは統計的に有意差を示さなかったので算出しなかった．

5. その他

5. Others

This is a blank page.

5-1

研究テーマ：中性子捕捉療法適応癌腫の治療プロトコールの確立
表　　題：

頭頸部癌に対する硼素中性子捕捉療法
Boron neutron capture therapy for head and neck malignancies.

平塚純一、粟飯原輝人[1]、宇野雅子[1]、
熊田博明[2]、小野公二[3]、原田保[1]

川崎医科大学放射線医学(治療)
[1]川崎医科大学耳鼻咽喉科
[2]日本原子力開発機構
[3]京都大学原子炉実験所

Departments of Radiation Oncology, and [1]Otolaryngology Head and Neck Surgery, Kawasaki Medical School, Kurashiki, Japan
[2]Japan Atomic Energy Agency
[3]Radiation Oncology Research Laboratory, Research Reactor Institute, Kyoto University, Osaka, Japan

（１）　はじめに

頭頸部癌治療は、外科的治療、放射線治療、抗癌剤治療の 3 者を至適に組み合わせる方法が主流である。各治療法の技術は改良され治癒率は向上してきているが、発見が遅れた進行癌や治療後の再発癌では、ほとんどの症例が従来の治療法での完全治癒を期待することは難しい。頭頸部が機能上・美容上その温存が大変重要な領域であり、従来の治療法では、制御困難と思われる進行病巣・再発病巣を正常臓器を損なうことなく治療できれば、患者の大きな負荷は勿論のこと治療後の高い QOL が期待できる。そのような治療法開発はより重要かつ急務となる。

アミノ酸代謝が亢進した癌細胞に特異的に集積する p-boronophenylalanine (BPA)を用いた中性子捕捉療法（BNCT）は、主に癌組織に集積した硼素（^{10}B）と熱中性子との核反応で生じる高 LET 放射線(α粒子)により癌細胞だけにエネルギーを集中させる事が可能であり癌治療に理想的である[1)]。また BPA の腫瘍集積は ^{18}F-BPA PET での定量が可能で、その結果から抗腫瘍効果が予測可能である[2)]。

我々は上記理論に基いて、2003 年 10 月から川崎医科大学倫理委員会承認のもと、進行頭頸部癌患者に中性子捕捉療法を行っており、2007 年に BNCT を行った症例の詳細を報告する。

（２）対象と方法

対象は 2007 年 1 月から 2007 年 12 月までの間に、(1)頭頸部癌標準治療にて制御困難、または、標準治療では手術以外の選択肢が無く、治療後の QOL 低下が著しいと考えられる、(2)PS≦2、(3)遠隔転移を認めない、または認めても予後に大きく関与しない、(4)18F－BPA PET 検査にて腫瘍/正常組織集積比が 2.5 以上、(5)文章で同治療法について同意が得られた、のすべて条件を満たした頭頸部癌 13 例である。

性別は男性 8 例・女性 5 例、年齢は 39 歳から 74 歳（平均 59）であった。

組織型は腺様嚢胞癌 4 例、悪性黒色腫 4 例、扁平上皮癌 3 例、乳頭状腺癌 1 例、腺癌 1 例であった。全症例の観察期間は、6-17 ヶ月(平均 11.3)であった。

照射方法は照射前に病変部を画像(CT または MRI)撮影したものを、BNCT 専用治療計画ソフトを用いて評価し、皮膚線量が 15Gy-Eq、眼球線量が 10Gy-Eq を超えない範囲で腫瘍最低線量を 20Gy-Eq 以上とした。

照射日に BPA500mg/kg を 3 時間かけて点滴静注を行い、終了直後に照射体位のセッティング後、照射直前に血中ホウ素濃度を測定した。直前ホウ素濃度と、15 分間の中性子線量から最終的な照射時間を決定した。

（３）結果

全 13 症例の治療効果は、CR : 8 例、PR : 4 例、NC : 1 例であり、奏功率は 92.3%であった。生存例 8 例の現在までの平均観察期間は 14.8 ヶ月であった。死亡は 5 例であった。死亡例の内訳は、現病死 4 例、他因死 1 例であり、平均生存期間は 5.8 ヶ月であった。

照射に伴う GradeII 以上の合併症は認められず、その他の合併症も認められなかった。現在のところ晩期放射線合併症は認められていない。

（４）考察とまとめ

標準の頭頸部癌治療で制御不可能な症例に対して行った本治療では、奏功率 92.3%と非常に高いものであった。しかし、進行および再発癌の場合は、明らかな病変以外に転移が隠れている事が否定できず、我々の症例でも潜在病変が予後を大きく左右した。しかしながら、再発病変に対する二次治療としての有効性は我々の最初の症例 [3] や本結果から明らかであり、加藤らもその有効性を高く評価している [4]。その結果を踏まえ我々は BNCT を頭頸部癌治療の Neoadjuvant therapy として治療を行うことが可能で、我々は当大学倫理委員会承認のもと、頭頸部癌の初期治療として BNCT を行っている。現在 3 例(2007 年の 2 例を含む)の進行頭頸部癌に対して本治療を初期治療として行い、3 例の平均観察期間が 18 ヶ月を越えた現在でも、全例無病生存中である。今後もその治療効果を検討する予定である。

参考文献

1)Y, Mishima. Neutron capture treatment of malignant melanoma using 10B-chlorpromazine. Pigment Cell Res. 1:215-221,1973

2)Y Imahori, S Ueda, Y Ohmori, T Kusuki, K Ono, R Fujii and T Ido. Fluorine-18-labeled fluoroboronophenylalanine PET in patients with glioma. J. Nucl. Med.39:325-333,1998

3)Teruhito Aihara, Junichi Hiratsuka, Norimasa Morita, et al : First clinical case of boron neutron capture therapy for head and neck malignancies utilizing 18F-BPA PET. Head and Neck.-DOI 10 850-855 2006

4) I Kato, K Ono, Y Sakurai, M Ohmae, A Maruhashi, Y Imahori, M Kirihata, M Nakazawa and Y Yura. Effectiveness of BNCT for recurrent head and neck malignancies. Applied Radiation and Isotopes 61:1069-1073,2004

原子炉：JRR-4　　装　置：BNCT 医療照射装置　　分　野：その他(臨床医学)

5-2

β線検出 NMR-ON による核物性の研究

Study of Hyperfine Interaction using β ray detected NMR-ON

大矢　進，大坪　隆，泉川卓司[1]，武藤　豪[2]，西村克彦[3]

S. Ohya,T. Ohtsubo, T. Izumikawa, S. Muto, K. Nisimura

新潟大学自然科学研究科

Graduate School of Science and Technology, Niigata University

[1]新潟大学アイソトープ総合センター

[1]Radioisotope Center, Niigata University

[2]高エネルギー加速器研究機構中性子研究所

[2]Neutron Science Laboratory, KEK

[3]富山大学工学部

[3]Faculty of Engineering, Toyama University

１．はじめに

我々新潟大学低温核整列グループはこれまで NMR-ON((Nuclear Magnetic Resonance on Oriented Nuclei)法を用いて、多くの原子核の磁気モーメント、電気的四重極モーメントを精密に測定してきた．また内部磁場、緩和時間などの核物性の研究も行ってきた。その手法は低温核偏極からのγ線の異方性の崩れを検出して核磁気共鳴を得ることであった。γ線は ^{3}He/^{4}He 希釈冷凍機の外側から検出でき、容易であるが、次のような場合、原理的に観測が出来ないか、非常に難しい場合が多い．

★核スピンが１／２の場合，γ線に異方性が無い。

★核スピンが３／２のような場合、β崩壊の影響でγ線の異方性が小さいことが多い．

★親核の娘核の基底状態の直接β遷移がほとんどの場合、γ崩壊が観測できない．

そこでこれらの問題を解決するため数年前からβ検出器を ^{3}He/^{4}He 希釈冷凍機の内部に設置して、パリティの破れによるβ線の異方性を検出して NMR-ON の実験を行ってきて，いくつかの原子核の磁気モーメントを決定してきた．この方法をさらに発展させて，これまで測定が困難であった超微細相互作用をβ線放出核の NMR-ON の方法で研究する．

本実験では ^{59}Fe のニッケル中の NMR-ON を行い、共鳴の観測，緩和時間の測定に成功しニッケル中の ^{59}Fe の内部磁場の精度よい測定が出来た。それらの結果について報告する。

２．試料製作

^{59}Fe*Ni* の試料は定同位元素 ^{58}Fe を原子炉で照射することにより製作した。 98.2%に濃縮された安定同位元素 ^{58}Fe を高純度のニッケルに約 0.17%溶かしたものを（数回，電子ビームによる溶融）ローラで約 3 ミクロン薄くしたものを用いた。これを直径３ｍｍの円形に

JRR-3 水力照射設備　HR-1,2　　原子核物理学，核物性物理学分野

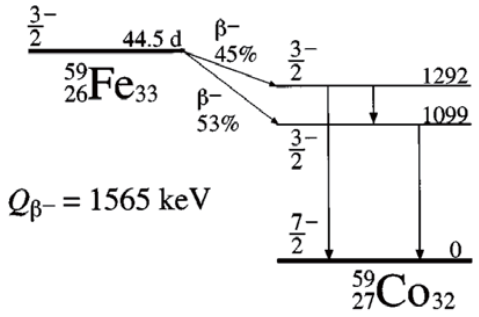


図１　^{59}Fe の崩壊様式

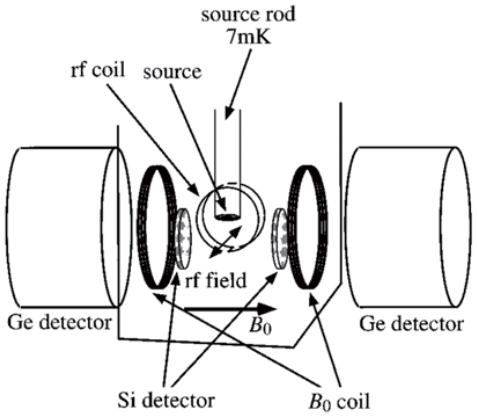


図２　検出器の配置図

切り取り，東海の日本原子力研究開発機構の３号炉で熱中性子の照射により ^{59}Fe*Ni* を製作した。照射後は真空中で温度 800 度で１時間熱処理をした。温度計は試料と一緒に半田された ^{60}Co*Fe* を用いた。

図１に ^{59}Fe の崩壊様式を示す。^{59}Fe からの β 崩壊は，ほとんどが最大エネルギー 475keV（５１％）と 273keV（４９％）で ^{59}Co の 1292keV, 1099keV 励起準位に崩壊して，そこからガンマー線を放出している。このガンマー線の角分布係数は小さく，低温核整列では，ガンマー線の異方性が小さいことが知られている「１」。ベータ線の観測では異方性があり，すでに我々は鉄中の ^{58}Fe NMR-ON の測定に成功している「２」。

３．　低温核偏極

試料を銅のソースロッドに低温半田でつけて，^{3}He/^{4}He 希釈冷凍機で冷却した。外部磁場を 0.2T かけて整列させ，ガンマー線は０度方向と 90 度方向に置かれた 2 台の Ge 半導体検出器で測定した。β 線は ^{3}He/^{4}He 希釈冷凍機の内部に設置した 2 台の Si(50mm^2, 厚さ 0.7mm) 検出器で測定した。　その配置図を図２で示す。Si 検出器は窓なしで直接 β 線を測定できるように 0.7k のシールドに取り付けられている。外部磁場 B_0 は超伝導電磁石で印加される。

また得られた β 線のスペクトルを図３に示す。矢印の領域は共鳴をモニターするのに使用した。　それ以上にエネルギーの高いのは，わずかではあるが基底状態に直接フイードするものである。エネルギーの低いところはノイズでありこれが変動するので無視した。

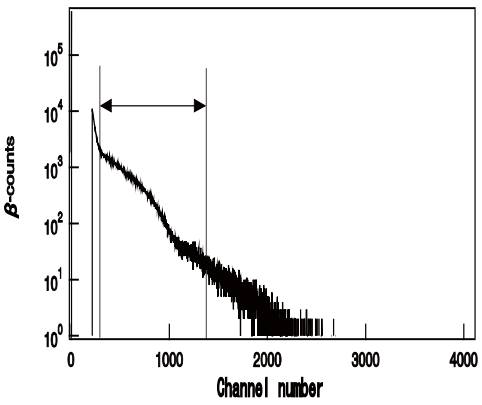


図３　^{59}Fe の β 線スペクトル

４．　^{59}Fe*Ni* のNMR-ON実験

^{3}He/^{4}He 希釈冷凍機で ^{59}Fe*Ni* を約 10mK の温

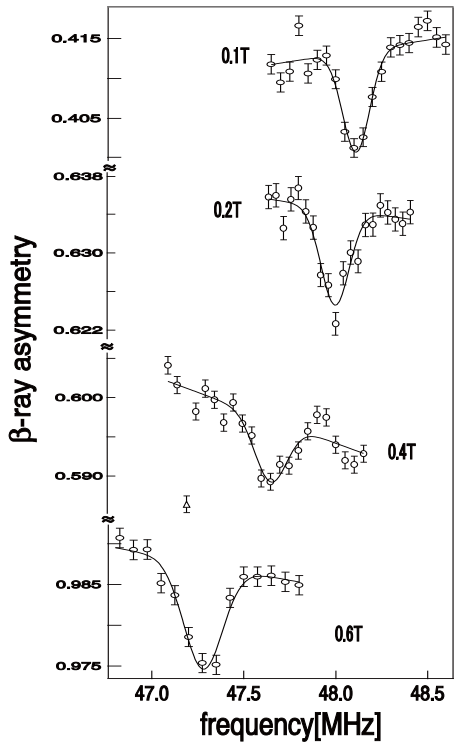


図４　^{59}FeNi の各外部磁場に対する共鳴

度に冷却した。　最初外部磁場 0.2T で FM（frequency modulation）1MHz で予想共鳴領域をサーチしたその結果，48MHz 付近で共鳴を得た。　そこで FM 幅を狭くして，共鳴を外部磁場 0.1T、0.2T、0.4T、0.6T でそれぞれ測定した。図４に観測された共鳴線を示す。それぞれの外部磁場 0.1, 0.2, 0.4, 0.6T に対しての典型的な共鳴線が観測された。縦軸はベータ線の 0 度と 180 度の非対称性（スケールは任意）を示す。　横軸は印加された高周波の周波数である。図４の共鳴の実線はガウス形とバックグラウンドを直線でフィットしたものである。その結果，外部磁場 0.1T で共鳴周波数は 48.11(1)MHz，幅 0.073MHz（FM±0.1MHz），外部磁場 0.2T で共鳴周波数は 47.997(7)MHz，幅 0.076MHz（FM±0.075MHz），

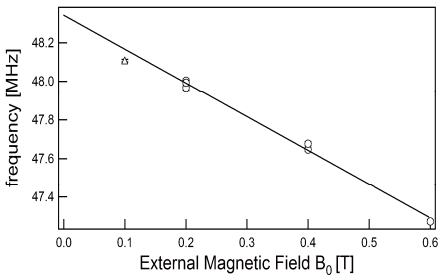


図５　共鳴周波数の外部磁場依存性

外部磁場 0.4T で共鳴周波数は 47.67(1)MHz，幅 0.089MHz（FM±0.075MHz），外部磁場 0.6T で共鳴周波数は 47.31（1)MHz，幅 0.093MHz（FM±0.075MHz）であった。

共鳴周波数の外部磁場依存性を表したものを図５に示す。純粋な磁気相互作用であると共鳴周波数は次のようになる

$$h\nu = | g \{ B_{\mathrm{hf}} + (1+K)B_0 \} | \mu_{\mathrm{N}}.$$

ここで B_{hf} は内部磁場，K はナイトシフト，g は核の g-factor を表わす。外部磁場 B_0=0.1T の場合、外部磁場が小さいと磁化が不十分なため，他とは条件が異なるということで直線のフィッティングから外した。その結果，外部磁場 B_0 = 0T のときの共鳴周波数 ν_0 ＝48.341(8)MHz を得た。^{59}Fe の磁気モーメントは我々の他の実験で測定されており、μ ＝ −0.3358(4) μ_N「３」である。したがってこの値を用いるとニッケル中の ^{59}Fe のに内部磁場は

$$\therefore\ B_{hf} = -28.33(3)T$$

となった。これはメッスバウアー法で求めた値 28.2(2)T「４」と誤差の範囲内で一致するが，精度の桁は一桁良くなった。

５．^{59}Fe*Ni* の緩和時間測定

^{59}Fe*Ni* の緩和時間を測定するために，外部磁場0.2Tのときの共鳴周波数48.0MHzを中心にFMをON,OFFすることで求めた。図６に緩和時間のスペクトルを示した。フィッティングした結果、緩和時間 T_1＝30(25)秒を得た。

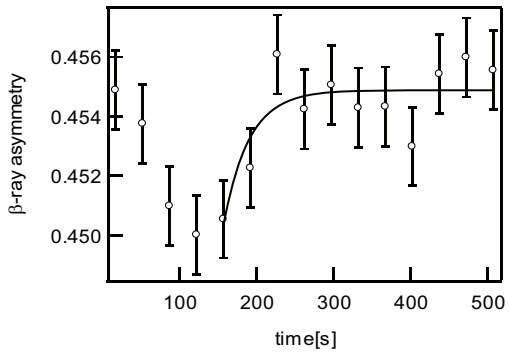


図６　^{59}Fe*Ni* の外部磁場0.2Tの緩和時間測定

鉄中の^{59}Fe*Fe* の緩和時間は共鳴周波数57.38MHzで17(3)分である「５」。

参考文献

「１」N. J. Stone, At. Data and Nucl. Data Tables 90(2005)75

「２」K.S. Krane, S.S. Rosenblum and W. A. Steyert, Phys. Rev. C14 (1976) 653

「３」T. Ohtsubo, D.J. Cho, Y.Yanagihashi and S. Ohya, Phys. Rev. C54 (1996) 554

「４」V.G. Bhide and G. K. Shenoy, J. Phys. Soc. Japan 21(1966)625

「５」T. Ohtsubo, D.J. Cho, Y.Yanagihashi, K. Komatsuzaki, K. Mizushima, S. Muto and S. Ohya, Proceedings of the 10th International Conference on Hyperfine Interactions； Hyperfine Interactions (C) (1996) 577

成果の公表

１．T. Ohtsubo, S. Ohya and S. Muto, Magnetic moment of the 3/2$^-$ ground state of ^{185}W, Hyperfine Interaction 195(2004)277

２．T. Ohtsubo, S. Ohya, K. Nishimura, T. Izumikawa, J. Got, M. Tanigaki, A. Taniguchi, Y. Ohkubo, Y. Kawase, and S. Muto, Bohr Weisskopf effect measurements using NMR-ON, 2nd Joint Meeting of the Nuclear Physics Divisions of the American Physical Society and the Physical Society of Japan, Sep. 18-22, 2005, Hawaii.

３．大矢進，大坪隆，平野晴誉，久保徹，山田亮太，渡部亮太，西村克彦， W.D.Hutchison, 武藤豪：^{59}FeNi のNMR-ON，日本物理学会，第63回年次大会，2008年3月

5-3

中性子捕捉療法の難治性癌治療への適応拡大に関する基礎的・臨床的研究

Basic & Clinical Research for Application of Neutron Capture Therapy to Highly Advanced Cancer

- **Measurement of Boron in Tumours by Neutron Capture Autoradiography following intra-arterial Administration of Boron Entrapped Water-in-Oil-in-Water Emulsion**

Yanagie Hironobu[1,2], Mikado Shoji[3], Yasuda Nakahiro[4], Higashi Syushi[5], Ikushima Ichiro[5], Mizumachi Ryuji[6], Murata Yuji[6], Morishita Yasuyuki[7], Shinohara Atsuko[8], Ogura Koichi[3], Sugiyama Hirotaka[2], Ryohei Nishimura[9],Takamoto Sinichi[2,10], Eriguchi Masazumi[2,11], and Takahashi Hiroyuki[1,2]

[1]Department of Nuclear Engineering & Management, Graduate School of Engineering, The University of Tokyo,Tokyo, JAPAN, [2]Cooperative Unit of Medicine & Engineering, The University of Tokyo Hospital, Tokyo, JAPAN, [3]Department of Physics, College of Industrial Technology, Nihon University, Chiba, JAPAN, [4]Department of Physics, National Institute of Radiological Sciences, Chiba, JAPAN, [5]Miyakonojyo Metropolitan Hospital, Miyazaki, JAPAN, [6]Department of Pharmacology, Kumamoto Institute Branch, Mitsubishi Chemical Safety Institute Ltd, Kumamoto, JAPAN, [7]Department of Human & Molecular Pathology, Graduate School of Medicine, The University of Tokyo, Tokyo, JAPAN, [8]Department of Humanities, The Graduate School of Seisen University, Tokyo, JAPAN, [9]Department of Veternary Surgery, The University of Tokyo Veternary Hospital, Tokyo, JAPAN, [10]Department of Cardiac Surgery, The University of Tokyo Hospital, Tokyo, JAPAN, [11]Department of Microbiology, Syowa University School of Pharmaceutical Sciences, Tokyo, JAPAN

Corresponding Author: Hironobu Yanagie, MD, PhD ; TEL: +81-3-5800-9194 ; FAX: +81-3-5800-9195 ; E-mail: yanagie@n.t.u-tokyo.ac.jp

---

1. Introduction

The cytotoxic effect of BNCT is due to a nuclear reaction between ^{10}B and thermal neutrons ($^{10}B + {}^{1}n \rightarrow {}^{7}Li + {}^{4}He + 2.31$ MeV (93.7 %) / 2.79 MeV (6.3 %)). The resultant lithium ions and α particles on neutron capture reaction are high LET(linear energy transfer) particles with relatively high biological efficiency. These particles (α and ^{7}Li) destroy cells within about 10μm path length from the site of the capture reaction. It is theoretically possible to kill tumour cells without affecting adjacent healthy cells, if the former can selectively accumulate ^{10}B atoms. So It is very important to develop selective boron delivery systems for effective

JRR3, Thermal Neutron Irradiation Facility, Neutron Capture Autoradiography

BNCT therapy (Yanagie, 1991, 1997, 2004, 2006a). BNCT has been used clinically in patients with malignant brain tumours and melanoma.

Liposomes have been investigated extensively as carriers for anticancer drugs in attempts to direct active agents to tumours or to protect sensitive tissues from toxicity. We have reported that ^{10}B atoms delivered by immunoliposomes are cytotoxic to human pancreatic carcinoma cells (AsPC-1) after thermal neutron irradiation *in vitro*(Yanagie, 1991). The intra-tumoural injection of boronated immunoliposomes can increase the retention of ^{10}B atoms in tumour cells, causing suppression of tumour growth *in vivo* following thermal neutron irradiation (Yanagie, 1997). We prepared polyethylene- glycol binding liposomes (PEG-liposomes) as an effective ^{10}B carrier to obviate phagocytosis by RES.

Hepatocellular carcinoma (HCC) is difficult to cure with operation, chemotherapy, or radiation therapy. Iodized poppy-seed oil (IPSO) has a property of depositing itself selectively in the cells of HCC, and the usefulness of iodized poppy-seed oil (IPSO) for detecting or treating liver cancer was first reported. The oil has the property of depositing itself selectively in the cells of HCC. Kanematsu et al. reported a method that mixed a water-soluble antitumour agent with IPSO. In their reports, an aqueous solution of an anticancer drug, doxorubicin, was mixed with 60% urografin, a water-soluble contrast medium, before the solution was mixed with the oil (IPSO) (Kanematsu, 1989).

Higashi et al prepared a long term inseparable, water-in-oil-in-water emulsion (WOW) containing 8-60 mg of epirubicin for use in arterial injection therapy for patients with HCC (Figure 1) (Higashi, 1993, 1995). Higashi et al had reported that tumour size of HCC was reduced in six of seven patients, and a 50% or greater decrease of initial alpha-fetoprotein (AFP) levels within 14 days was observed in all four patients who showed abnomal levels of serum AFP before treatment (Higashi, 1995).

According to the Higashi's clinical results, we would like to apply BNCT to treatment of Hepatocellular Carcinoma (HCC) for increasing the selection of therapies of HCC's patients (Yanagie, 2006b). In this study, we develop BSH entrapped WOW emulsion and evaluate the emulsion as selective boron delivery carrier to cancer tissues.

The accurate measurement of ^{10}B distributions in biological samples with a sensitivity in the ppm range is essential for evaluating the potential usefulness of various boron-containing compounds for BNCT.

We applied CR-39 (polyallyldiglycol carbonate) plastic track detectors to alpha-autoradiographic measurements of the ^{10}B biodistribution in sliced whole body hepatic samples of VX-2 tumour bearing rabbit. The subsequent use of an alpha-track radiographic image analysis system enabled a discrimination between alpha-tracks and recoiled proton tracks was made by track size selection method. This enabled to estimate quantitatively the distributions of ^{10}B concentrations within the tissue sections comparing using suitable standards (Yanagie, 1999).

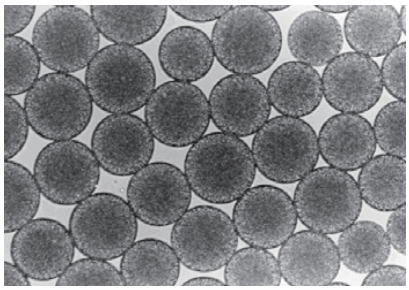


Figure 1. Microphotograph of WOW emulsion

In our study, we performed the neutron capture autoradiography (NCAR) using CR-39 track etch detectors to qualitatively and quantitatively determine the ^{10}B biodistribution in hepatic samples of VX-2 tumours after intra-arterial injection of ^{10}B entrapped WOW emulsion.

2. Materials & Methods

Chemicals : Sodium salt of undecahydro-mercaptocloso-dodecaborate ($Na_2{}^{10}B_{12}H_{11}SH$) was obtained by Wako Chemical Co. Ltd. (Tokyo, Japan). Iodized poppy-seed oil (IPSO, Lipiodol Ultrafluid, Kodama, Co., Ltd., Tokyo, Japan) is composed of iodized ethyl esters of the fatty acids obtained from poppy-seed oil and contains 37% iodine.

Preparation of Boron entrapped WOW emulsion : Three hundred milligrams of BSH was dissolved in 5 ml of a 5% glucose solution and filtrated of controlled pore glass membrane emulsifying into 5 ml of IPSO containing surfactant, to form the water-in-oil emulsion (WO). The WO emulsion was then emulsifyied again with aqueous phase containing 5 ml of saline and surfactant. With this double emulsifying technique, the BSH entrapped WOW emulsion was prepared (Higashi, 1995, Yanagie, 2006b). The particle size distributions of the vesicles of WOW and IPSO microdroplets were determined with a laser-diffraction particle-size analyzer SALD-2000 (Shimadzu Corp., Kyoto, Japan). The boron concentration entrapped in WOW vesicles was determinated by ICP- Mass Spectroscopy at Jyuntendo University.

In vivo Experiments : VX-2 rabbit squamous cell carcinoma cell line was cultured in vitro supplemented with of 10% fetal bovine serum and 500mg streptomycin/penicillin in 5% CO2 condition. The VX-2 cells were inocculated onto the foot pad of the rabbits, and then, the tumours of VX-2 were formed after one week feeding. The nodules of VX-2 tumour were inocculated to left hepatic lobe of liver, then, the hepatic tumour models were constructed after two weeks feedings. After 2 weeks tumour inocculation, BSH entrapped WOW emulsions were administered with intra-arterial injections via the hepatic artery propria compared with ^{10}BSH-Lipiodol mixed conventional emulsion (^{10}BSH : 75 mg/kg rabbit) on VX-2 rabbit hepatic tumour models. One and three days after arterial injections, the boron concentrations of the tumour nodules and normal liver tissues were determinated by ICP-Mass Spectroscopy at Jyuntendo University. (Yanagie, 1999).

Preparation of standard samples and sliced mice samples : In order to examine the biodistribution of the ^{10}B entrapped WOW emulsion after intra-arterial injections to the hepatic artery propria, we carried out Neutron-Capture Auto Radiography(NCAR). Rabbits were sacrificed 1 and 3 days after the injection of ^{10}B-WOW emulsion, and the hepatic samples were frozen at -60 ℃. Subsequently, the frozen samples were cut sagittally into 40 μm thick sections mounted on a thin 3M Scotch tape, freeze-dried at -20℃ for two weeks and air-dried for one more week. Thus, the dried samples were prepared. Boron-containing standard samples were also prepared using drying filter paper sheets wetted by BSH solutions of four different ^{10}B concentrations(10, 50, 100, 500 ppm of ^{10}BSH), respectively. The ^{10}B concentrations of ^{10}BSH solutions were determined by ICP-Mass Spectroscopy at Jyuntendo University.

Neutron irradiation : The sliced sections were put in close contact with the CR-39 plates (HARZLAS TD-1; Fukuvi Chemical Industry, Japan) using thin adhesive tape. The set of hepatic samples of VX-2 tumour bearing rabbit were simultaneously exposed in the JRR3 reactor of Japan Atomic Energy Research Institute. The thermal neutron fluence irradiation was varied according to the experimental objectives.

For alpha track counting (i.e. ^{10}B distribution measurements) : 2.0×10^{10} n/cm^2.
For the visible observation of NCAR image: 2.0×10^{12} n/cm^2.

Etching procedure : For NCAR imaging utilizedα- and Li tracks as well as protons of recoiled and/or produced by ^{14}N (n, p) reaction,

where ^{14}N is the biogenically abundant nuclide, the CR-39 detector plates were etched in a 7 N NaOH solution at 70 ℃ for 2 hours to reveal tracks.

3. Results & Discussion

We prepared BSH entrapped WOW emulsion. The mean ^{10}B concentration was 13000 ppm by ICP-MAS. The size of WOW was controlled to 50μm.

The ^{10}B concentration in VX-2 tumour was 141 ppm, 61 ppm by WOW emulsion after 1 day, or 3 day intra-arterial injection, respectively. The ^{10}B concentration of tumour was 58, 24ppm by Lipiodol mix emulsion after 1 day, or 3 day same injection, respectively (Table 1).

The histological staining showed the superior accumulation of the fat droplets of WOW emulsion in tumour site compared with Lipiodol mix emulsion. Electromicroscopic figure of hepatocellular carcinoma after arterial- injection chemotherapy using WOW emulsion : The microdroplets of Iodized poppy-seed oil was retained in the cytoplasm of the cancer cell in the same conformation as preparation time, but there was no accumulation of fat droplets in Lipiodol emulsion. The ^{10}B concentrations of samples were determined by ICP-Mass Spectroscopy at Juntendo University

From NCAR image of sliced samples, we can estimate the ^{10}B accumulations in the organs. ^{10}B accumulations were estimated for the strongly concentrated part of the tumour at day 3 after injection by WOW emulsion. In order to show the imaging of ^{10}B accumulation in tumour, we obtained NCAR image of sliced samples of VX-2 hepatic tissues using CR-39 track etch detector. NCAR image consists of a large number of etch pits, such as proton, α- and Li tracks. The track area of the opening mouth of each etch pit as well as its position was analyzed by the automated digital imaging optical microscope (HSP-1000), whose image acquisition speed is 50-100 times faster than conventional microscope system[15]. NCAR

Table 1. ^{10}B concentration of VX-2 hepatic tumour bearing rabbit model after intra-arterial injection of ^{10}B-WOW emulsion or ^{10}B-Lipiodol mix

WOW	Tumour	Normal Liver	Blood
Day-1	141.8	6.1	1.2
Day-3	61.7	4.3	0.1

Lipiodol	Tumour	Normal Liver	Blood
Day-1	58.0	14.6	0.4
Day-3	24.5	3.9	0.2

images of tumour in hepatic tissues are shown in Fig. 2. These images were reconstructed by means of scatter plots for the *x-y* coordinate of the observed whole tracks. Each dot appearing in Fig. 2 corresponds to tracks one by one. Figure 2 shows NCAR of tumour or normal liver site of VX-2 hepatic tissues from a set of VX-2 hepatic cancer bearing rabbit that have received intra-arterial injections of 150 mg of ^{10}B by WOW emulsion or Lipiodol mix solution. The slices of sacrificed and frozen sections were prepared 3 days after injection.

It is difficalt to assess ^{10}B accumulation and distribution in the sample, because the images of Fig. 2 were contaminated by proton tracks. In order to know the efficiency of intra-arterial boron delivery carrier for BNCT, it is necessary to discriminateα- tracks from proton tracks. Generally, etch pit size of the track in the plastic track detector depends on the LET value of the incident particle. In this case, LET values for protons are less than 100 keV/μm. The tracks with LET greater than 100keV/μm are actually due to α- and Li particles from the^{10}B(n, α)^{7}Li reaction and the maximum values are 2.4 x10^2 keV/μm and 3.9 x 10^2 keV/μm, respectively[16]. Therefore, two peaks of track size appear in the track area distribution, the lower peak corresponds to proton tracks, and the higher one is due to α- and Li tracks. It is considered that the

contribution of Li tracks is not so large because of the short range of Li particles. The track size discrimination betweenα- and proton tracks has been done using observed track area distribution and subtracted proton tracks from Fig. 2. The results are shown in Fig. 3. The distribution of α-tracks was obtained, then we are able to recognize accurate ^{10}B accumulation and distribution in the VX-2 tumours. It is readily apparent that theα-etch pit reveals the existence of ^{10}B atoms delivered by WOW emulsion into the VX-2 tumour. Accurate ^{10}B accumulation in the VX-2 tumours was achieved by WOW emulsion. When the ^{10}B Lipiodol mix solution was injected to the tumour bearing rabbit, the accumulation of ^{10}B atoms in the tumour was small. Theα-track densities of normal liver is not detected at 3 days after intra-aterial injection, so the clearance of WOW emulsion and Lipiodol mix solution in the healthy tissue is very rapid.

The measurement of ^{10}B distributions in biological samples with a sensitivity in the ppm range is essential for evaluating the potential usefulness of various boron-containing compounds for BNCT. ^{10}B accumulations in the tumour varies by boron delivery systems, so we find the strong and weak, concentrated parts of the tumour after injection (Yanagie, 1999. It is necessary to supply the boron atoms homogeneously in the tumours for effective BNCT. The study of the microdosimetry of ^{10}B atoms is ongoing, and CR-39 radiography using track counting will be possible to determine the micro- or fine structure, i.e. *micro-autoradiography*, of ^{10}B distribution in the tumour (Ogura, 2001).

Clinically, administration of WOW emulsion drug encapsulated anti-cancer reagent in inner droplets, is surprisingly effective for both terminal and multi-originated in HCC when the drug is injected to suffered liver through a catheter inserted in liver artery. ^{10}B entrapped WOW emulsion is possible to deliver and transport the boron atoms to the cancer cell in tumour tissues. These results have shown that ^{10}B entrapped WOW emulsion is most useful for intra-arterial boron delivery carrier on BNCT to cancer. We now plan in vivo evaluation of ^{10}B entrapped WOW emulsion, and the clinical trial of BNCT for HCC patients, and hope to perform first BNCT trial with WOW emulsion in near future.

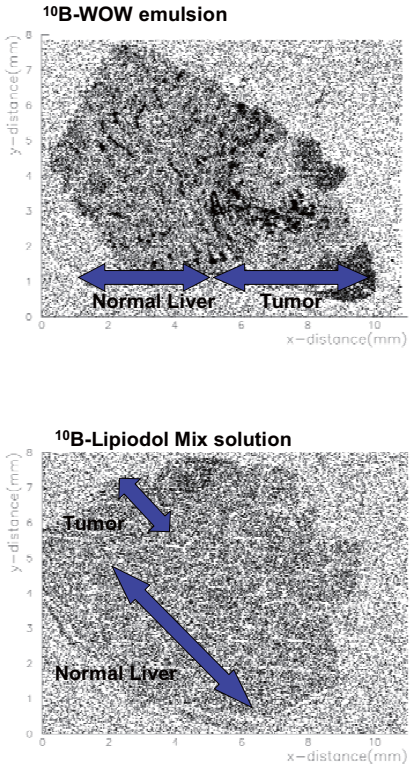


Figure 2 . Alpha and proton track etch pits distributions of the tumour after 3 days injection of ^{10}B entrapped WOW emulsion (Left) / 10B Lipiodol mix solution (Right) on VX-2 hepatic tumour bearing rabbit. This image shows tumour or normal liver site of a neutron-capture radiograph from a set of VX-2 hepatic cancers bearing rabbit that have received intra-arterial injection of 150 mg of ^{10}B. The slices of sacrificed and frozen tissues were prepared 3 days after injection.

4. Conclusion

We will be able to apply boron entrapped WOW emulsion to BNCT for hepatocellular carcinoma, and NCAR technique for detection

of effective 10B carrier in BNCT for cancer.

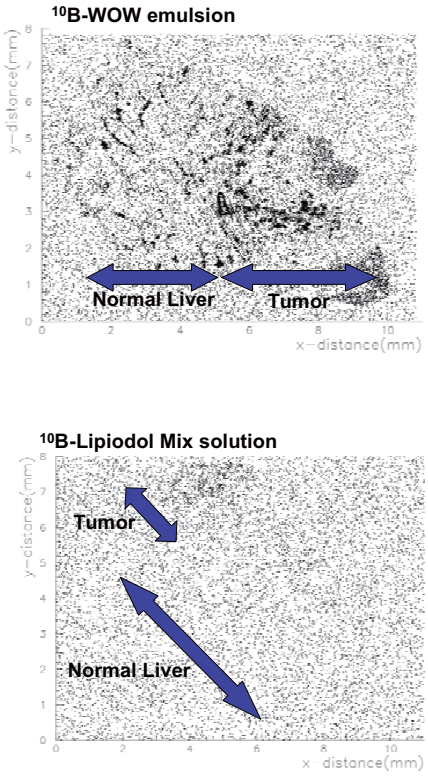


Figure 3. ^{10}B distributions of the tumour after 3 days injection of ^{10}B entrapped WOW emulsion (Left) / 10B Lipiodol mix solution (Right) on VX-2 hepatic tumour bearing rabbit. Images were obtained by the subtraction of proton track data from Fig. 2.

Acknowledgements

This work was supported in part by a Grant-in-Aid from the Ministry of Education, Science and Culture, Japan (No. 11691202 and No. 11557092 to Hironobu Yanagie). The thermal neutron irradiation was carried out using the JAEA (Tokai) JRR3 facility supported by the Inter-University Program for the Joint Use of JAEA Facilities.

5. Publications

Yanagie. H, et al. 2008. Measurement of Boron in Tumours by Neutron Capture Autoradiography following intra-arterial Administration of Boron Entrapped Water-in-Oil-in-Water Emulsion. Proc. of 13th International Congress of Neutron Capture Therapy, pp713-718.

Mikado S., Yanagie.H, et al. 2008. Application of Neutron Capture Autoradiography to Boron Delivery Seeking Techniques for Selective Accumulation of Boron Compounds to Tumor with Intrarterial Administration of Boron Entrapped Water-in-oil-in-water Emulsion. NIMA inpress.

Yanagie H, et al. 2006. Selective Enhancement of Boron Accumulation with Boron-Entrapped Water-in-oil-in-water Emulsion in VX-2 Rabbit Hepatic Cancer Model for BNCT. Proc. of 12th International Congress of Neutron Capture Therapy, pp211-214.

Amemiya H., yanagie H., et al. 2005. High-resolution nuclear track mapping in detailed cellular histology using CR-39 with the contact microscopy technique. RadiationMeasurements, 40, Issues 2-6, 283-288.

5-4

中性子捕捉療法の難治性癌治療への適応拡大に関する基礎的・臨床的研究

Basic & Clinical Research for Application of Neutron Capture Therapy to Highly Advanced Cancer

- Inhibition of Tumor Growth of Mouse Colon Cancer Cell Line by Boron Neutron Capture Therapy & Immunotherapy
- Feasible Evaluation of Neutron Capture Therapy for Local Recurrenced Breast Cancer

H. Yanagie[1,2], K. Kakimi[2,3], A. Hosoi[2,3], A. Ogata[2], K. Mouri[2], K. Eguchi[2], Y. Morishita[4], A. Shinohara[5], H. Kumada[6], T. Nakamura[6], Y. Furuya[7], S. Takamoto[2,8], M. Eriguchi[2,9], and H. Takahashi[1,2]

[1]Department of Nuclear Engineering & Management, Graduate School of Engineering, The University of Tokyo, [2] Cooperative Unit of Medicine & Engineering, The University of Tokyo Hospital, [3]Department of Immunotherapeutics (Medinet), The University of Tokyo Hospital, [4]Department of Human & Molecular Pathology, Graduate School of Medicine, The University of Tokyo, [5]Department of Hygenes, School of Medicine, Jyuntendo University, Tokyo, [6]Japan Atomic Research Institute, Ibaraki, [7]Department of Surgery, Satukidai Hospital, Chiba, [8]Department of Cardiac Surgery, The University of Tokyo Hospital, Tokyo, [9]Department of Microbiology, Syowa University School of Pharmaceutical Sciences, Tokyo, JAPAN

Corresponding Author: Hironobu Yanagie, MD, PhD ; TEL: +81-3-5800-9194 ; FAX: +81-3-5800-9195 ; E-mail: yanagie@n.t.u-tokyo.ac.jp

1. Introdeuction

The cytotoxic effect of BNCT is due to a nuclear reaction between ^{10}B and thermal neutrons ($^{10}B + {}^{1}n \rightarrow {}^{7}Li + {}^{4}He$ + 2.31 MeV (93.7 %) / 2.79 MeV (6.3 %)). The resultant lithium ions and α particles are high linear energy transfer (LET) particles which give important biological effect. Their short range in tissue (5 - 9 μm) restricts radiation damage to those cells in which boron atoms are located at the time of neutron irradiation.

Liposomes can contain a large amount of ^{10}B compound, which can be delivered to tumor cells. We have reported that ^{10}B atoms delivered by immunoliposomes are cytotoxic to human pancreatic carcinoma cells (AsPC-1) with thermal neutron irradiation *in vitro* (Yanagie, 1991), and intratumoural injection of boronated immunoliposomes can increase the retention of ^{10}B atoms in tumour cells, and suppress tumour growth *in vivo* under thermal neutron irradiation (Yanagie, 1997).

Dendritic Cells (DCs) are potent antigen-presenting cells that can both activate innate and acquired immune responses, so it is now being focused on the role of DCs in eliciting antitumor

JRR4, Thermal Neutron Irradiation Facility of Reactor, JCDS, BNCT

immunity and in potential therapeutic applications. For example, administration of DCs loaded ex vivo with tumor-associated antigens can elicit antitumor immunity resulting in tumor regression in various murine tumor models, and DCs pulsed with tumor derived peptides, proteins, genes or tumor lysates, as well as DCs fused with tumor cells, have all been studied as therapeutic cancer vaccines (Chang, 2002). Candido et al had reported that they evaluated the effect of IT injections of bone marrow derived DCs on the subcutaneous growth of the murine MT-901 breast tumor (Candido, 2001). They demonstrate that DCs can efficiently uptake apoptotic MT-901 tumor cells and that local injections of DCs alone can result in regression of this breast tumor *in vivo*, which is dependent on host CD8 T-cell immunity.

Recently, it has been reported that combined immuno and radiation therapy results in effective tumor growth suppression. Radiation therapy is currently applied in the treatment of a wide array of human cancers. Recent evidence indicates that besides exerting direct toxic effects on tumor cells, ionizing radiation also exhibits various immunomodulatory effects. Inflammatory responses are triggered within irradiated tissues recruiting DCs to sites of inflammation. At the site, DCs acquire antigens, undergo maturation, and then migrate to the draining lymph node, where they present processed antigens to T cells. Irradiated tumor cells have been shown to serve effectively as a source of Tumor Associated Antigens (TAAs) to elicit specific T-cell responses *in vitro* when processed and presented by DCs (Strome, 2002).

We would like to apply BNCT, to radioresistant conditions as recurring & advanced breast cancer, hepatocellular carcinoma, liver metastases, or lung cancer.
Incidence of breast cancers is increasing, so it is also more important to plan treatment protocols for recurring cases (Ballo, 1999, Liao, 2000). Breast cancer may recur after primary resection both locally (thoracic wall :23%, local lymph nodes :19%) and in distant sites (bone :23%, lung : 18%, and liver : 4%). The treatment of local recurrences may be curative or palliative to avoid the occurrence of bleeding, ulcer formations, bad smelling. Radiation therapy is commonly used to this purpose (Nielsen, 2006, Touboul, 1999, Willner, 1997). Skin ulcer, and bone necrosis may apper after irradiation due to the lower tolerance of the thoracic wall after mastectomy. So a dose of about 40~50 Gy is recommended for recurrences.

In our study, we prepared the cationic liposome (COATSOME-EL) as the effective ^{10}B carrier to deliver the boron atomes into the cancer cells as the manner of gene delivery systems, and we evaluated the synergic anti-cancer effects of immune-responces with dendritic cells intratumoral injection after BNCT.

We also evaluate neutron flux dosimetry in horizontal irradiation position using a phantom model of a mammary gland at Kyoto University Research Reactor, and also evaluate the BNCT simulation for a breast cancer patient with MRI images using JCDS at Japan Atomic Energy Research Institute.

2. Materials & Methods

Chemicals : Sodium salt of undecahydro-mercaptocloso-dodecaborate ($Na_2{}^{10}B_{12}H_{11}SH$) was obtained by Wako Chemical Co. Ltd. (Tokyo, Japan).

Preparation of Liposomes containing ^{10}B-Compound : A cationic empty liposome (COATSOME EL-C-01 : Nichiyu liposome Co. Ltd.) is composed with L-a-dipalmitoyl phosphatidylcholine (26 μmoles), cholesterol (20 μmoles), and stealylamine (4 μmoles). BSH (10mg/ml) solution was added to the COATSOME EL-C-01, and made the ^{10}B-liposome solution (Yanagie, 1999). The boron concentration entrapped in COATSOME-EL vesicles was determinated by ICP- Masspectroscopy of Jyuntendo University.

Generation of Bone Marrow-Derived DCs : Bone marrow cells obtained from femurs and tibias of BALB/c mice were cultured in RPMI 1640 medium supplemented with 10% FCS, 12.5 mM HEPES, 5

x 10^{-5} M 2-mercaptoethanol, 1 x 10^{-5} M sodium pyruvate, 1% NEAA, 10 mg/ml Penicillin/Streptomycin and 20 ng/ml GM-CSF (PeproTech, Rocky Hill, NJ) for 7 days. On day 7, DCs were harvested by gentle pippetting, washed twice with PBS and resuspended at 1 x 10^7 cells/0.1 ml PBS for intratumoral injection (Saji, 2006).

Splenocytes : **Spleen cells, harvested from BALB/c mice, were treated with ammonium chloride-potassium lysis buffer (0.83% ammonium chloride, 0.1% KHCO3, and 0.004% EDTA) for 5 min to deplete erythrocytes and washed twice with HBSS. They were then enumerated and resuspended in HBSS for injection (Saji, 2006).**

BNCT procedure : **The Colon26 (1 x 10^6) cells were injected subcutaneously into the back of the male BALB/C mice (Nihon SLC). Ten days after injection, when an average diameter of 10 mm was reached , 150 µl of ^{10}B-liposome solution were injected(IT). The mice injected with ^{10}B-liposome solutions were irradiated with thermal neutrons (2 x 10^{12} n/cm^2) at JRR4 reactor of Japan Atomic Energy Research Institute.**

DC treatment : **On day 10, when the tumors reached an average diameter of 10 mm, BNCT on mice IT injected with ^{10}B entrapped liposome was performed and, at that time,**
syngeneic DCs(1 x 10^7 cells/mouse) were injected IT with the schedule 1 (day 0, day 3 , day 6), or schedule 2 (day 0, day 3, day 6, day9, day 12, day 15, day 18). After BNCT+DCs injections, the effect of treatment was calculated on the basis of tumor volume and morphological findings of the tumors at 4-day intervals.

ELISPOT Assay. : **Tumor-specific T cell responses were evaluated by ELISPOT assays. Erythrocyte-depleted splenocytes harvested from treated or control mice 40 days after tumor inoculation or from age matched naive mice (5 x 10^4 splenocytes in 100 µl of CM) were placed into each well and incubated for 24 h at 37°C, 5% CO_2 in the absence or presence of irradiated (60 Gy) Colon26 tumor cells (5 x 10^3 cells in 100 µl of CM). The assays were performed and developed using anti-mouse IFN-γmAb according to the kit manufacturer's instructions (BD Pharmingen). All experiments were performed in duplicate and the data correspond to the mean value.**

Adoptive Transfer Model. : **Splenocytes harvested from treated mice on day 40 after tumor inoculation were transferred intraveneously to syngeneic mice. Two days after spleen cells transfer, Colon26 cells (5 x 10^5 cells) were injected subcutaneously. The effect of anti-tumor immunity was evaluated on the basis of tumor volume (Saji, 2006).**

Animal Etics : **The procedures for the tumor implantation and the sacrifice of the animals were in accordance with approved guidelines of the Institution's Animal Ethics Committee.**

Neutron dosimetry with JAERI Computational Dosimetry System (JCDS) for a breast cancer patient: : BNCT was simulated in a 64 years patient with a 3 cm tumour in the lower half of the R breast. LiF collimation was used to selectively irradiate the tumor while sparing the adjacent normal organs (lung, heart). The Neutron Beam Facility at JRR4 enables to carry out boron neutron capture therapy with epithermal neutron beam. The JAERI Computational Dosimetry System (JCDS), which can estimate distributions of radiation doses in a patient's head by simulating in order to support the treatment planning for epithermal neutron beam BNCT, was developed. We applied this JCDS for evaluation the neutron dosimetry for this case.

3. Results & Discussion

In order to evaluate that local BNCT followed by IT-DC can inhibit primary tumor growth, BALB/c mice were injected s.c. with Colon26 tumor cells. On day 10, the tumors reached an average diameter of 10 mm, BNCT on IT with ^{10}B entrapped liposome was done at that time and

syngeneic DCs were injected intratumorally with the schedule 1 (day 0, day 3 , day 6), or schedule 2 (day 0, day 3, day 6, day9, day 12, day 15, day 18). On schedule 1, although the tumors grew rapidly following treatment with saline alone, and IT-DC, the group treated BNCT + IT-saline and the combination of BNCT + IT-DC resulted in significant suppression of tumor growth (Figure 1). Almost all animals treated with BNCT + It-saline, and BNCT + IT-DC became tumor-free. On schedule 2, 30% tumor growth suppression was achieved on IT-DC group, and also the group treated BNCT + IT-saline, and the combination of BNCT + IT-DC resulted in significant suppression of tumor growth compared to non-treated group (Figure 2).

Because both components of the combined treatment, BNCT+DC, are delivered directly to the tumor, we investigated whether this protocol could induce a systemic antitumor response. It has been reported that *in vitro* tumor-specific IFN-γproduction by host-derived T cells correlated with systemic antitumor immunity *in vivo*. We evaluated whether treatment of Colon26 tumor-bearing mice with BNCT+DCs could elicit tumor-specific IFN-γsecreting T cells using ELISPOT assays . Splenocytes retrieved on day 40 after tumor inoculation from mice subjected to the BNCT+ 3 times DCs combined therapy showed slightlyactivated tumor-specific IFN-γ-secreting cells, while schedule 2 with BNCT+ 7 times DCs resulted in significantly more tumor-specific IFN-γ-secreting cells compared with splenocytes from control groups (data not shown).

To examine whether tumor-specific immune response was induced in BNCT-DC treated mice, splenocytes harvested from treated mice on day 40 after tumor inoculation were transferred i.v. to syngeneic mice, and, Colon26 cells (5 x 10^5 cells) were injected subcutaneously. In tumor challenged mice, that received spleen cells from DC-treated mice and BNCT-treated mice, tumor growth was suppressed by 25%. Fifty % reduction in tumor growth was observed in mice that received spleen cells from BNCT+DCs treated mice (Figure 3).

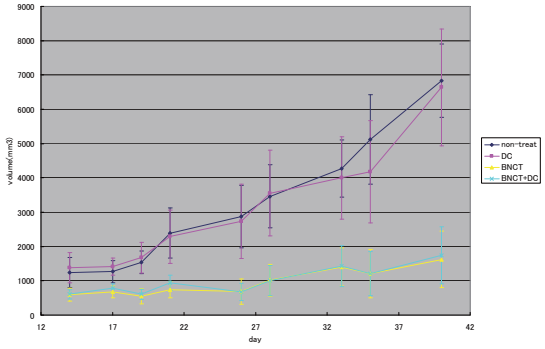


Figure 1. Effect of combination treatment with BNCT and IT-DC on Colon26 tumors.

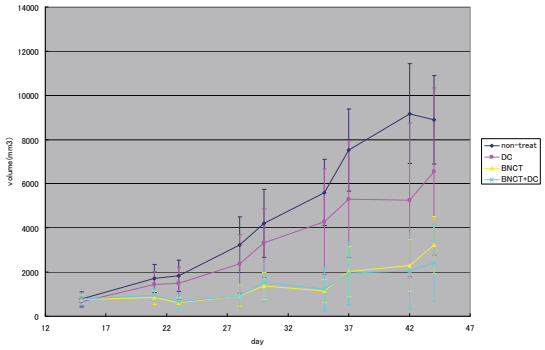


Figure 2. Enhancement of tumor growth suppression with increased intratumoral injections of DCs on BNCT and IT-DC treatments.

Celluzzi *et al.* had reported that it is possible that radiation augments the antitumor efficacy of DC administration by modifying tumor cells to become more immunogenic (Celluzzi, 1998). This would allow *ex vivo* generated functional DCs to acquire TAAs from irradiated tumor cells more efficiently than they would acquire them from nonirradiated tumor cells. One of the hallmarks of inflammation is an increase in the permeability of the local vasculature that leads to recruitment of circulating leukocytes into surrounding tissues. Recently, it has been shown that necrotic tumor cells can serve as a source of multiple TAAs to pulse DCs as effectively as apoptotic tumor cells (Kotera, 2001). Radiation has been reported to induce

cytokines, chemokines, and inflammatory mediator release and to upregulate the expression of adhesion molecules, co-stimulatory molecules, and heat shock proteins in tumor, stromal, and endothelial cells (Friedman, 2002). Thus, the proinflammatory microenvironment within irradiated tumors could provide DCs with maturation-inducing stimuli critical for eliciting effective antigen presentation. Radiation facilitates the extravasation of both antigen-presenting cells (Nikitina, 2001) and effector T cells (Quarmby, 1999) into solid tumors.

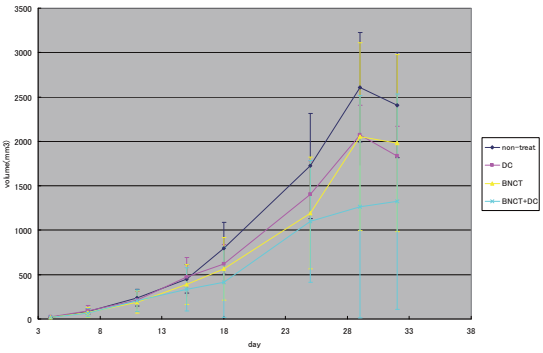


Figure 3. Tumor growth suppression with adoptive immunity by BNCT+DCs on new challenging Colon26 tumor

In these experiments, our data indicate that DC administration combined with BNCT induces tumor antigen-specific cellular-mediated immune responses in tumor bearing mice. DCs combined with BNCT of a solitary tumor confers protection against tumor rechallenge. It is thought that tumor antigens derived from necrosis, apoptosis, and inflammation induced by BNCT had been presented to DCs in BNCT+DCs combined therapy. The growth of Colon26 tumors was highly suppressed in mice that received splenocytes from BNCT+DCs treated mice. Regulatory T cells and suppressor macrophage will be necessary to delete in the adoptive splenocytes for more stimulation the anti-tumor immunity (*not clear)*. We hope to apply this direct DC immunotherapy for enhancing the BNCT effects in clinical trials.

Kumada et al had reported that JCDS is a software that creates a 3-dimensional head model of a patient by using CT scan and MRI images, and that generates a input data file automatically calculation of neutron flux and gamma-ray dose distributions in the brain with the Monte Carlo code MCNP, and that displays these dose distributions on the head model for dosimetry by using the MCNP calculation results (Kumada, 2001). JCDS has the following advantages; (1) a detailed 3D model of the patient's head can be easily obtained from the CT and MRI data, (2) the three-dimensional head image is editable to simulate the state of a head after surgery, (3) JCDS can provide information for the Patient Setting System which can support to set the patient to an actual irradiation position swiftly and accurately.

We performed the dosimetry with JCDS in the condition of BNCT using epithermal neutron beams(Figure 4). To decrease the skin side effects, the skinRBE dose limited to 10Gy-Eq. The minimum tumor RBE dose is 11.3 Gy-Eq, the mean tumor RBE dose is 28.9 Gy-Eq, and the maximum tumor RBE dose is 42.2 Gy-Eq. The two dimensional distributions of neutron beam revealed that the peak of the beam was a little shifted from the tumor site(Figure 5). For calibration of the beam peaks to tumor, t is necessary to perform a few change the beam direction, and addition of some void to the neighbor site of tumors.

4. Conclusion

Colon26 tumor growth was suppressed in the groups of BNCT and BNCT with DC injections relative to controls. The growth of colon26 tumors was highly suppressed in mice that received spleen cells from DC-treated mice, suggesting that anti-tumor immunity was induced by DC treatment. Direct DC immunotherapy can enhance the anti-cancer effect of BNCT and have promising clinical application in near future.

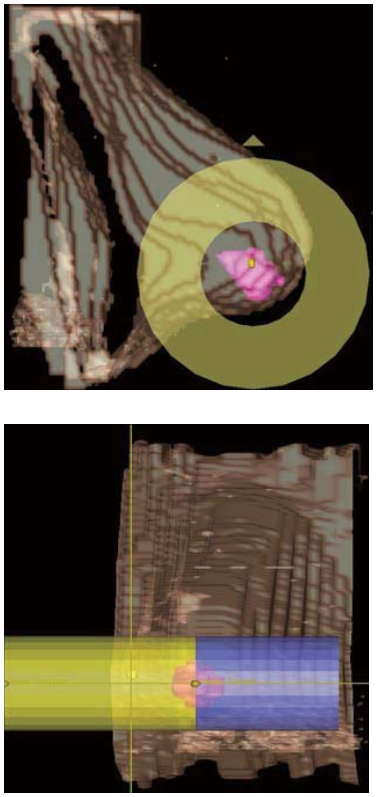


Figure 4. JCDS simulation for rt breast cancer patient. Upper : lateral view, Lower : frontal view

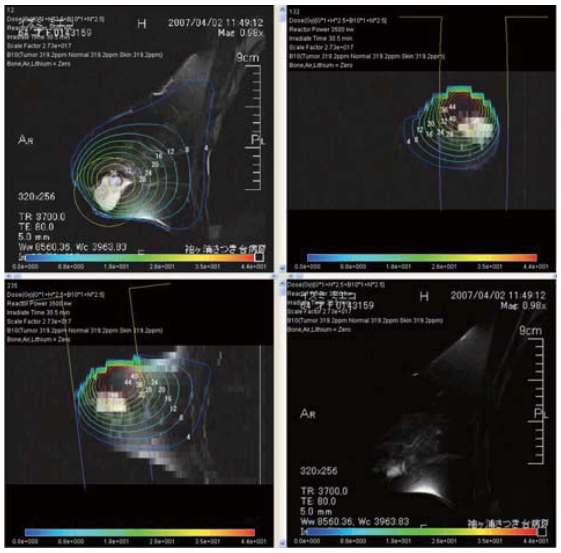


Figure 5. Two dimensional distributions of epithermal neutron beam at JRR4 using JCDS evaluation.

We applied the JCDS to dosimetry of epithermal neutron, direction of neutron beam, and patient's positioning on BNCT. We also evaluate the epithermal neutron dose to decreas the skin side effect. High resolution whole body dosimetry system, as JCDS will be very useful to evaluate the thermal neutron dosimetry and the application of BNCT to recurring or advanced breast cancer.

Acknowledgements

This work was supported in part by a Grant-in-Aid from the Ministry of Education, Science and Culture, Japan (No. 11691202 and No. 11557092 to Hironobu Yanagie). The thermal neutron irradiation was carried out using the JAEA (Tokai) JRR4 facility supported by the Inter-University Program for the Joint Use of JAEA Facilities.

5. Publications

Yanagie H, et al., 2008. Feasible Evaluationof Neutron Capture Therapy for Local Recurrenced Breast Cancer. Proc. of 13th International Congress of Neutron Capture Therapy, pp34-37.

Yanagie H, et al., 2008. Inhibition of Tumor Growth of Mouse Colon Cancer Cell Line by Boron Neutron Capture Therapy & Immuno-therapy. Proc. of 13th International Congress of Neutron Capture Therapy, pp358-361.

Yanagie H, et al., 2007. Evaluation of neutron dosimetry on pancreatic cancer phantom model for application of intraoperative boron neutron-capture therapy, Biomedicine & Pharmacotherapy, 61(9), 505-514.

Yanagie H, et al. 2006. Application of boron-entrapped stealth lipsomes to inhibition of growth of Tumour cells in the in vivo boron neutron-capture therapy model; Biomedicine & Pharmacotherapy, 60 : 43-50.

Yanagie H, et al. 2006. Selective Enhancement of Boron Accumulation with Boron-Entrapped Water-in-oil-in-water Emulsion in VX-2 Rabbit Hepatic Cancer Model for BNCT. Proc. of 12th International Congress of Neutron Capture Therapy, pp211-214.

Yanagie H, et al. 2006. Production of Polyoxoboronate as Novel Boron Compound. Proc. of 12th International Congress of Neutron Capture Therapy, pp251-252.

Yanagie H, et al. 2006. Application of Boron-Entrapped WOW Emulsion as boron delivery carrier for boron neutron capture therapy on VX-2 rabbit hepatic cancer model. European Journal of Surgical Oncology, Volume 32, Supplement 11(1) pp S19.

柳衛宏宣, 2008. 中性子捕捉療法の一般外科領域癌への応用と展望, 第 1 回東大放射線アライアンスワークショップ、2008 年 3 月 11 日、東京大学武田先端知ホール

お わ り に

本報告書は、研究炉（JRR-3、JRR-4）を利用した利用者の協力を基に、研究炉の成果を提出して頂き、研究炉利用課で編集したものであります。この成果を公表する事で、研究炉の今後の有効利用並びに利用拡大に役立つ事を期待します。

謝　　辞

本報告書の発刊にあたり、多くの皆様から多大なご協力を頂きました。

原稿を提出して頂いた利用者の皆様のご協力に感謝するとともに、今後も研究炉が有効に利用され、種々の研究がさらに進展されることを期待します。

編集に際し、ご協力頂いた、研究炉加速器管理部長 丸尾　毅氏、研究炉加速器管理部NSRR管理課長 村山洋二氏に深く感謝致します。

This is a blank page.

付　録

Appendixes

This is a blank page.

付 録

原科研研究炉の利用設備一覧

１．ＪＲＲ－３

１）実験設備

実　験　孔	実　　験　　装　　置
１Ｇ	高分解能粉末中性子回折装置（ＨＲＰＤ）
１Ｇ－Ａ	生体高分子用中性子単結晶回折装置-3（ＢＩＸ－Ⅲ）
１Ｇ－Ｂ	生体高分子用中性子単結晶回折装置-4（ＢＩＸ―Ⅳ）
２Ｇ	三軸型中性子分光器（ＴＡＳ－１）
３Ｇ	精密中性子光学装置（ＰＮＯ）
４Ｇ	汎用三軸型中性子分光器（ＧＰＴＡＳ）
５Ｇ	偏極中性子散乱装置（ＰＯＮＴＡ）
６Ｇ	東北大学中性子散乱分光器（ＴＯＰＡＮ）
７Ｒ	熱中性子ラジオグラフィ装置（ＴＮＲＦ）
Ｔ１－１	中性子偏極回折装置（ＨＱＲ）
Ｔ１－２	単結晶中性子回折装置（ＫＳＤ）
Ｔ１－３	粉末中性子回折装置（ＫＰＤ）
Ｔ１－４－１	即発ガンマ線分析装置（ＰＧＡ）
Ｔ１－４－２	多重即発ガンマ線分析装置（ＭＰＧＡ）
Ｔ１－４－３	ＴＯＦ型中性子反射率計（ＴＯＦ）
Ｔ１－４－４	中性子ラウエ回折装置（ＬＡＵＥ）
Ｔ１－４－５	中性子ベータ崩壊基礎測定装置
Ｔ１－４－６	多目的単色熱中性子実験ポート（高角）（ＭＵＳＡＳＩ）
Ｔ２－１	中性子応力測定装置-1（ＲＥＳＡ-1）
Ｔ２－２	中性子４軸回折装置（ＦＯＮＤＥＲ）
Ｔ２－３－１	多目的単色熱中性子実験ポート（低角）（ＭＵＳＡＳＨＩ）
Ｔ２－３－２	中性子応力測定装置-2（ＲＥＳＡ-2）
Ｔ２－４	高分解能三軸型中性子分光器（ＴＡＳ－２）
Ｃ１－１	高エネルギー分解能三軸型中性子分光器（ＨＥＲ）
Ｃ１－２	二次元位置測定小角散乱装置（ＳＡＮＳ－Ｕ）
Ｃ１－３	超高分解能後方散乱装置（ＵＬＳ）
Ｃ２－１	冷中性子三軸型中性子分光器（ＬＴＡＳ）
Ｃ２－２	偏極中性子反射率計（ＳＵＩＲＥＮ）
Ｃ２－３－１	中性子スピンエコー分光器（ＮＳＥ）
Ｃ２－３－２－１	多重即発ガンマ線分析装置（ＭＰＧＡ）
Ｃ２－３－２－２	即発ガンマ線分析装置（ＰＧＡ）
Ｃ２－３－３－１	冷中性子ラジオグラフィ（ＣＮＲＦ）
Ｃ２－３－３－２	パルス中性子機器開発装置（ＣＨＯＰ）
Ｃ２－３－３－３	ＴＯＦ型中性子反射率計（ＴＯＦ）
Ｃ２－３－３－４	中性子ラウエ回折装置(ＬＡＵＥ)
Ｃ３－１－１	高分解能パルス冷中性子分光器（ＡＧＮＥＳ）
Ｃ３－１－２－１	中性子光学システム評価装置（ＮＯＰ）
Ｃ３－１－２－２	多層膜中性子干渉計／反射率計（ＭＩＮＥ）
Ｃ３－２	集光型偏極中性子超小角散乱装置（ＳＡＮＳ－Ｊ）

２）照射設備

水力照射設備	ＨＲ－１，２
気送照射設備	ＰＮ－１，２
放射化分析用照射設備	ＰＮ－３
均一照射設備	ＳＩ－１
回転照射設備	ＤＲ－１
垂直照射設備	ＶＴ－１，ＲＧ－１～４ ＢＲ－１～４，ＳＨ－１

２．ＪＲＲ－４

１）実験設備

プール
中性子ビーム設備
散乱実験設備
冷却水循環ループ
医療照射設備（ＢＮＣＴ）
即発ガンマ線分析装置

２）照射設備

簡易照射筒	Ｔパイプ（水力）
	Ｓパイプ
	Ｄパイプ
	Ｎパイプ
気送管照射設備	ＰＮ

国際単位系（SI）

表１．SI 基本単位

基本量	SI 基本単位	
	名称	記号
長さ	メートル	m
質量	キログラム	kg
時間	秒	s
電流	アンペア	A
熱力学温度	ケルビン	K
物質量	モル	mol
光度	カンデラ	cd

表２．基本単位を用いて表されるSI組立単位の例

組立量	SI 基本単位	
	名称	記号
面積	平方メートル	m^2
体積	立法メートル	m^3
速さ，速度	メートル毎秒	m/s
加速度	メートル毎秒毎秒	m/s^2
波数	毎メートル	m^{-1}
密度，質量密度	キログラム毎立方メートル	kg/m^3
面積密度	キログラム毎平方メートル	kg/m^2
比体積	立方メートル毎キログラム	m^3/kg
電流密度	アンペア毎平方メートル	A/m^2
磁界の強さ	アンペア毎メートル	A/m
量濃度(a)，濃度	モル毎立方メートル	mol/m^3
質量濃度	キログラム毎立法メートル	kg/m^3
輝度	カンデラ毎平方メートル	cd/m^2
屈折率(b)	（数字の） 1	1
比透磁率(b)	（数字の） 1	1

(a) 量濃度（amount concentration）は臨床化学の分野では物質濃度（substance concentration）ともよばれる。
(b) これらは無次元量あるいは次元１をもつ量であるが、そのことを表す単位記号である数字の１は通常は表記しない。

表３．固有の名称と記号で表されるSI組立単位

組立量	SI 組立単位			
	名称	記号	他のSI単位による表し方	SI基本単位による表し方
平面角	ラジアン(b)	rad	1 (b)	m/m
立体角	ステラジアン(b)	sr(c)	1 (b)	m^2/m^2
周波数	ヘルツ(d)	Hz		s^{-1}
力	ニュートン	N		m kg s^{-2}
圧力，応力	パスカル	Pa	N/m^2	m^{-1} kg s^{-2}
エネルギー，仕事，熱量	ジュール	J	N m	m^2 kg s^{-2}
仕事率，工率，放射束	ワット	W	J/s	m^2 kg s^{-3}
電荷，電気量	クーロン	C		s A
電位差（電圧），起電力	ボルト	V	W/A	m^2 kg s^{-3} A^{-1}
静電容量	ファラド	F	C/V	m^{-2} kg^{-1} s^4 A^2
電気抵抗	オーム	Ω	V/A	m^2 kg s^{-3} A^{-2}
コンダクタンス	ジーメンス	S	A/V	m^{-2} kg^{-1} s^3 A^2
磁束	ウエーバ	Wb	Vs	m^2 kg s^{-2} A^{-1}
磁束密度	テスラ	T	Wb/m^2	kg s^{-2} A^{-1}
インダクタンス	ヘンリー	H	Wb/A	m^2 kg s^{-2} A^{-2}
セルシウス温度	セルシウス度(e)	℃		K
光束	ルーメン	lm	cd sr(c)	cd
照度	ルクス	lx	lm/m^2	m^{-2} cd
放射性核種の放射能(f)	ベクレル(d)	Bq		s^{-1}
吸収線量, 比エネルギー分与, カーマ	グレイ	Gy	J/kg	m^2 s^{-2}
線量当量, 周辺線量当量, 方向性線量当量, 個人線量当量	シーベルト(g)	Sv	J/kg	m^2 s^{-2}
酸素活性	カタール	kat		s^{-1} mol

(a)SI接頭語は固有の名称と記号を持つ組立単位と組み合わせても使用できる。しかし接頭語を付した単位はもはやコヒーレントではない。
(b)ラジアンとステラジアンは数字の１に対する単位の特別な名称で、量についての情報をつたえるために使われる。実際には、使用する時には記号radおよびsrが用いられるが、習慣として組立単位としての記号である数字の１は明示されない。
(c)測光学ではステラジアンという名称と記号srを単位の表し方の中に、そのまま維持している。
(d)ヘルツは周期現象についてのみ、ベクレルは放射性核種の統計的過程についてのみ使用される。
(e)セルシウス度はケルビンの特別な名称で、セルシウス温度を表すために使用される。セルシウス度とケルビンの単位の大きさは同一である。したがって、温度差や温度間隔を表す数値はどちらの単位で表しても同じである。
(f)放射性核種の放射能（activity referred to a radionuclide）は、しばしば誤った用語で"radioactivity"と記される。
(g)単位シーベルト（PV,2002,70,205）についてはCIPM勧告2（CI-2002）を参照。

表４．単位の中に固有の名称と記号を含むSI組立単位の例

組立量	SI 組立単位		
	名称	記号	SI 基本単位による表し方
粘度	パスカル秒	Pa s	m^{-1} kg s^{-1}
力のモーメント	ニュートンメートル	N m	m^2 kg s^{-2}
表面張力	ニュートン毎メートル	N/m	kg s^{-2}
角速度	ラジアン毎秒	rad/s	m m^{-1} s^{-1}=s^{-1}
角加速度	ラジアン毎秒毎秒	rad/s^2	m m^{-1} s^{-2}=s^{-2}
熱流密度，放射照度	ワット毎平方メートル	W/m^2	kg s^{-3}
熱容量，エントロピー	ジュール毎ケルビン	J/K	m^2 kg s^{-2} K^{-1}
比熱容量，比エントロピー	ジュール毎キログラム毎ケルビン	J/(kg K)	m^2 s^{-2} K^{-1}
比エネルギー	ジュール毎キログラム	J/kg	m^2 s^{-2}
熱伝導率	ワット毎メートル毎ケルビン	W/(m K)	m kg s^{-3} K^{-1}
体積エネルギー	ジュール毎立方メートル	J/m^3	m^{-1} kg s^{-2}
電界の強さ	ボルト毎メートル	V/m	m kg s^{-3} A^{-1}
電荷密度	クーロン毎立方メートル	C/m^3	m^{-3} sA
表面電荷	クーロン毎平方メートル	C/m^2	m^{-2} sA
電束密度，電気変位	クーロン毎平方メートル	C/m^2	m^{-2} sA
誘電率	ファラド毎メートル	F/m	m^{-3} kg^{-1} s^4 A^2
透磁率	ヘンリー毎メートル	H/m	m kg s^{-2} A^{-2}
モルエネルギー	ジュール毎モル	J/mol	m^2 kg s^{-2} mol^{-1}
モルエントロピー, モル熱容量	ジュール毎モル毎ケルビン	J/(mol K)	m^2 kg s^{-2} K^{-1} mol^{-1}
照射線量（X線及びγ線）	クーロン毎キログラム	C/kg	kg^{-1} sA
吸収線量率	グレイ毎秒	Gy/s	m^2 s^{-3}
放射強度	ワット毎ステラジアン	W/sr	m^4 m^{-2} kg s^{-3}=m^2 kg s^{-3}
放射輝度	ワット毎平方メートル毎ステラジアン	$W/(m^2$ sr)	m^2 m^{-2} kg s^{-3}=kg s^{-3}
酵素活性濃度	カタール毎立方メートル	kat/m^3	m^{-3} s^{-1} mol

表５．SI 接頭語

乗数	接頭語	記号	乗数	接頭語	記号
10^{24}	ヨタ	Y	10^{-1}	デシ	d
10^{21}	ゼタ	Z	10^{-2}	センチ	c
10^{18}	エクサ	E	10^{-3}	ミリ	m
10^{15}	ペタ	P	10^{-6}	マイクロ	μ
10^{12}	テラ	T	10^{-9}	ナノ	n
10^9	ギガ	G	10^{-12}	ピコ	p
10^6	メガ	M	10^{-15}	フェムト	f
10^3	キロ	k	10^{-18}	アト	a
10^2	ヘクト	h	10^{-21}	ゼプト	z
10^1	デカ	da	10^{-24}	ヨクト	y

表６．SIに属さないが、SIと併用される単位

名称	記号	SI 単位による値
分	min	1 min=60s
時	h	1h =60 min=3600 s
日	d	1 d=24 h=86 400 s
度	°	1°=(π/180) rad
分	’	1’=(1/60)°=(π/10800) rad
秒	”	1”=(1/60)’=(π/648000) rad
ヘクタール	ha	$1ha=1hm^2=10^4m^2$
リットル	L, l	$1L=11=1dm^3=10^3cm^3=10^{-3}m^3$
トン	t	$1t=10^3$ kg

表７．SIに属さないが、SIと併用される単位で、SI単位で表される数値が実験的に得られるもの

名称	記号	SI 単位で表される数値
電子ボルト	eV	$1eV=1.602\ 176\ 53(14)\times10^{-19}J$
ダルトン	Da	$1Da=1.660\ 538\ 86(28)\times10^{-27}kg$
統一原子質量単位	u	1u=1 Da
天文単位	ua	$1ua=1.495\ 978\ 706\ 91(6)\times10^{11}m$

表８．SIに属さないが、SIと併用されるその他の単位

名称	記号	SI 単位で表される数値
バール	bar	1 bar=0.1MPa=100kPa=10^5Pa
水銀柱ミリメートル	mmHg	1mmHg=133.322Pa
オングストローム	Å	1 Å=0.1nm=100pm=10^{-10}m
海里	M	1 M=1852m
バーン	b	$1\ b=100fm^2=(10^{-12}cm)2=10^{-28}m^2$
ノット	kn	1 kn=(1852/3600)m/s
ネーパ	Np	SI単位との数値的な関係は、対数量の定義に依存。
ベル	B	
デジベル	dB	

表９．固有の名称をもつCGS組立単位

名称	記号	SI 単位で表される数値
エルグ	erg	$1\ erg=10^{-7}$ J
ダイン	dyn	$1\ dyn=10^{-5}$N
ポアズ	P	1 P=1 dyn s cm^{-2}=0.1Pa s
ストークス	St	1 St =$1cm^2$ s^{-1}=$10^{-4}m^2$ s^{-1}
スチルブ	sb	1 sb =1cd cm^{-2}=10^4cd m^{-2}
フォト	ph	1 ph=1cd sr cm^{-2} 10^4lx
ガル	Gal	1 Gal =1cm s^{-2}=$10^{-2}ms^{-2}$
マクスウェル	Mx	1 Mx = 1G cm^2=10^{-8}Wb
ガウス	G	1 G =1Mx cm^{-2} =10^{-4}T
エルステッド(c)	Oe	1 Oe≙ $(10^3/4\pi)$A m^{-1}

(c) ３元系のCGS単位系とSIでは直接比較できないため、等号「 ≙ 」は対応関係を示すものである。

表10．SIに属さないその他の単位の例

名称	記号	SI 単位で表される数値
キュリー	Ci	$1\ Ci=3.7\times10^{10}Bq$
レントゲン	R	$1\ R = 2.58\times10^{-4}C/kg$
ラド	rad	$1\ rad=1cGy=10^{-2}Gy$
レム	rem	$1\ rem=1\ cSv=10^{-2}Sv$
ガンマ	γ	1γ=1 nT=10-9T
フェルミ		1フェルミ=1 fm=10-15m
メートル系カラット		1メートル系カラット = 200 mg = 2×10-4kg
トル	Torr	1 Torr = (101 325/760) Pa
標準大気圧	atm	1 atm = 101 325 Pa
カロリー	cal	1cal=4.1858J（「15℃」カロリー），4.1868J（「IT」カロリー）4.184J（「熱化学」カロリー）
ミクロン	μ	1 μ =1μm=10^{-6}m

（第8版，2006年改訂）

この印刷物は再生紙を使用しています